

AD-A246 057



2

NAVAL POSTGRADUATE SCHOOL Monterey, California



DTIC
ELECTE
FEB 14 1992
S D

THESIS

EFFECTS OF CENTRIFUGAL
INSTABILITIES ON
LAMINAR/TURBULENT TRANSITION
IN CURVED CHANNELS WITH
40 TO 1 ASPECT RATIOS

by

Michael R. Kendall

June 1991

Thesis Advisor

P.M. Ligrani

Approved for public release; distribution is unlimited.

92-03695



92 2 12 171

REPORT DOCUMENTATION PAGE				Form Approved OMB No 0704-0188	
1a REPORT SECURITY CLASSIFICATION Unclassified			1b RESTRICTIVE MARKINGS		
2a SECURITY CLASSIFICATION AUTHORITY			3 DISTRIBUTION/AVAILABILITY OF REPORT Approved for public release; distribution is unlimited.		
2b DECLASSIFICATION/DOWNGRADING SCHEDULE					
4 PERFORMING ORGANIZATION REPORT NUMBER(S)			5 MONITORING ORGANIZATION REPORT NUMBER(S)		
6a NAME OF PERFORMING ORGANIZATION Naval Postgraduate School		6b OFFICE SYMBOL (If applicable) 34	7a NAME OF MONITORING ORGANIZATION Naval Postgraduate School		
6c ADDRESS (City, State, and ZIP Code) Monterey, CA 93943-5000			7b ADDRESS (City, State, and ZIP Code) Monterey, CA 93943-5000		
8a. NAME OF FUNDING / SPONSORING ORGANIZATION Propulsion Directorate		8b OFFICE SYMBOL (If applicable)	9 PROCUREMENT INSTRUMENT IDENTIFICATION NUMBER MIPR C-30030-P		
8c. ADDRESS (City, State, and ZIP Code) US Army Aviation R/T Act. AVSCOM NASA-Lewis; Cleveland, OH 45433			10 SOURCE OF FUNDING NUMBERS		
			PROGRAM ELEMENT NO	PROJECT NO	TASK NO
11 TITLE (Include Security Classification) EFFECTS OF CENTRIFUGAL INSTABILITIES ON LAMINAR/TURBULENT TRANSITION IS CURVED CHANNELS WITH 40 TO 1 ASPECT RATIOS					
12 PERSONAL AUTHOR(S) Michael R. Kendall					
13a TYPE OF REPORT Engineer's Thesis		13b TIME COVERED FROM 7/90 TO 6/91	14 DATE OF REPORT (Year, Month, Day) June 1991		15 PAGE COUNT 306
16 SUPPLEMENTARY NOTATION The views expressed in this thesis are those of the author and do not reflect the official policy or position of the Department of Defense or the U.S. Government.					
17 COSATI CODES			18 SUBJECT TERMS (Continue on reverse if necessary and identify by block number) Dean vortices, centrifugal instabilities, turbulence, rectangular curved channel, laminar/turbulent transition		
FIELD	GROUP	SUB-GROUP			
19 ABSTRACT (Continue on reverse if necessary and identify by block number) Dean vortices in curved channels with 40 to 1 aspect ratios were measured and studied over the range of Dean numbers from 50 to 450. At low Dean numbers (50) the flow is fully laminar. At higher Dean numbers, the development of vortex pairs as the primary instability was a function of Dean number and the angle of curvature. Higher Dean numbers required less curvature to produce the vortices. At Dean numbers from 75 to 200, secondary instabilities developed in the form of vortex pair undulations, vortex pair twisting, and in the form of events where vortex pairs appear and disappear. These secondary instabilities are also a function of Dean number and curvature. Twisting leads to increases in longitudinal fluctuating intensities, particularly in the upwash region from the concave wall, which are especially significant at Dean numbers above 150. Fluctuation increases eventually lead to fully turbulent conditions and depend on location in the spanwise/radial plane relative to a					
20 DISTRIBUTION/AVAILABILITY OF ABSTRACT <input checked="" type="checkbox"/> UNCLASSIFIED/UNLIMITED <input type="checkbox"/> SAME AS RPT <input type="checkbox"/> DTIC USERS			21 ABSTRACT SECURITY CLASSIFICATION Unclassified		
22a NAME OF RESPONSIBLE INDIVIDUAL P. M. Ligrani			22b TELEPHONE (Include Area Code) (408) 646-3382		22c OFFICE SYMBOL 69Li

Unclassified

SECURITY CLASSIFICATION OF THIS PAGE

(19) Continued:

vortex pair structure, where upwash regions from the concave wall are the most unstable. Fully turbulent flow develops at Dean numbers greater than about 400.

Approved for public release; distribution is unlimited.

Effects of centrifugal instabilities
on laminar/turbulent transition
in curved channels with
40 to 1 aspect ratios

by

Michael R. Kendall
Lieutenant, United States Navy
B.S., University of the State of New York, 1985

Submitted in partial fulfillment of the
requirements for the degrees of

MASTER OF SCIENCE IN MECHANICAL ENGINEERING
and
MECHANICAL ENGINEER

from the

NAVAL POSTGRADUATE SCHOOL
June 1991

Accession For	
NTIS CRA&I	<input checked="" type="checkbox"/>
DTIC TAB	<input type="checkbox"/>
Unannounced	<input type="checkbox"/>
Justification	
By	
Distribution/	
Availability Codes	
Dist	Avail and/or Special
A-1	

Author:

Michael R. Kendall

Michael R. Kendall

Approved by:

Philip M. Ligrani

P.M. Ligrani, Thesis Advisor

Anthony S. Healey

Anthony S. Healey, Chairman

Department of Mechanical Engineering

Richard S. Elster

Richard S. Elster

Dean of Instruction



ABSTRACT

Dean vortices in curved channels with 40 to 1 aspect ratios were measured and studied over the range of Dean numbers from 50 to 450. At low Dean numbers (<50) the flow is fully laminar. At higher Dean numbers, the development of vortex pairs as the primary instability was a function of Dean number and the angle of curvature. Higher Dean numbers required less curvature to produce the vortices. At Dean numbers from 75 to 200, secondary instabilities developed in the form of vortex pair undulations, vortex pair twisting, and in the form of events where vortex pairs appear and disappear. These secondary instabilities are also a function of Dean number and curvature. Twisting leads to increases in longitudinal fluctuating intensities, particularly in the upwash region from the concave wall, which are especially significant at Dean numbers above 150. Fluctuation increases eventually lead to fully turbulent conditions and depend on location in the spanwise/radial plane relative to a vortex pair structure, where upwash regions from the concave wall are the most unstable. Fully turbulent flow develops at Dean numbers greater than about 400.

TABLE OF CONTENTS

I. INTRODUCTION.....	1
A. BACKGROUND.....	1
B. OBJECTIVES.....	2
C. ORGANIZATION.....	2
II. EXPERIMENTAL FACILITIES.....	4
A. CURVED CHANNEL DESCRIPTIONS.....	4
B. DEAN NUMBER DETERMINATION.....	5
III. EXPERIMENTAL PROCEDURES.....	7
A. STREAMWISE, SPANWISE AND RADIAL VELOCITY SURVEYS.....	7
1. Five-hole Pressure Probe Description.....	7
2. Experimental Details.....	8
3. Probe Calibration.....	8
4. Curved Channel Procedures.....	9
a. Traversing Mechanism.....	9
b. Measurements.....	9
c. Data Reduction.....	10
B. CONVEX WALL TURBULENCE SURVEYS.....	12
1. 17 Element Hot-film Probe Description.....	12
2. Experimental Details.....	12
3. Curved Channel Procedures.....	12
a. Measurements.....	12
b. Data Reduction.....	13
C. FLOW VISUALIZATION.....	14
D. DEAN NUMBER SURVEYS OF POWER SPECTRA AND LONGITUDINAL VELOCITY FLUCTUATIONS.....	15
1. Experimental Details.....	15
2. Probe Calibration and Measurement Procedures.....	17

IV. EXPERIMENTAL RESULTS.....	18
A. SURVEYS OF TIME AVERAGED QUANTITIES.....	19
1. Total Pressure.....	19
2. Streamwise Velocity.....	19
3. Velocity Perturbation.....	20
4. Vorticity Components.....	20
a. Streamwise Vorticity.....	20
b. Radial Vorticity.....	20
c. Spanwise Vorticity.....	20
B. TIME-AVERAGED AND SPATIALLY RESOLVED FLOW PROPERTIES NEAR THE CONVEX SURFACE.....	21
C. SPECTRAL AND LONGITUDINAL VELOCITY FLUCTUATION VARIATIONS WITH DEAN NUMBER.....	23
D. ANALYSIS OF APPEARANCE AND DISAPPEARANCE PHENOMENA FROM FLOW VISUALIZATION RESULTS.....	26
V. SUMMARY AND CONCLUSIONS.....	29
APPENDIX A - UNCERTAINTY ANALYSIS.....	32
A. DEAN NUMBER UNCERTAINTY.....	32
1. Pressure Drop Uncertainty.....	32
2. Mass Flow Rate Uncertainty.....	32
B. FIVE-HOLE PROBE VELOCITY MEASUREMENT UNCERTAINTY.....	32
1. Validyne Transducer Calibration Uncertainty.....	32
2. Probe Calibration Uncertainty.....	33
3. Curved Channel Measurement Uncertainty.....	33
C. HOT-WIRE PROBE VELOCITY MEASUREMENT UNCERTAINTY.....	34
1. Probe Calibration Uncertainty.....	34
2. Curved Channel Measurement Uncertainty.....	34
APPENDIX B - SOFTWARE DIRECTORY.....	35
A. GENERAL PROGRAMS.....	35
B. FIVE-HOLE PRESSURE PROBE PROGRAMS.....	35
C. 12 ELEMENT HOT-FILM PROBE PROGRAMS.....	38
D. HOT-WIRE PROBE PROGRAMS.....	38

APPENDIX C - DYNAMIC SIGNAL ANALYZER OPERATION.....	40
A. FREQUENCY RESPONSE.....	40
B. POWER SPECTRUM.....	41
APPENDIX D - TABLES.....	43
APPENDIX E - FIGURES.....	49
APPENDIX F - INDIVIDUAL SPECTRA.....	161
LIST OF REFERENCES.....	281
INITIAL DISTRIBUTION LIST.....	283

LIST OF TABLES

Table 1. 12 ELEMENT HOT-FILM PROBE LOCATIONS.....	43
Table 2. VORTEX PAIR APPEARANCE AND DISAPPEARANCE OCCURRENCES.....	44
Table 3. VORTEX PAIR APPEARANCE AND DISAPPEARANCE FREQUENCIES.....	45
Table 4. VORTEX PAIR APPEARANCE AND DISAPPEARANCE NON-DIMENSIONAL FREQUENCIES.....	46
Table 5. HOT-WIRE PROBE SENSING LOCATIONS RELATIVE TO VORTEX PAIR STRUCTURE.....	47
Table 6. HOT-WIRE SPECTRA SIGNAL CONDITIONER SETTINGS.....	48

LIST OF FIGURES

Figure 1. Transparent Curved Channel.....	49
Figure 2. Blower Assembly.....	50
Figure 3. Curved Channel Test Facility Schematic.....	51
Figure 4. Orifice Pressure Drop vs. De	52
Figure 5. Five-hole Pressure Probe Tip.....	53
Figure 6. Five-hole Pressure Probe Geometry.....	54
Figure 7. Five-hole Pressure Probe Dimensions and Connections.....	55
Figure 8. Five-hole Survey Data Acquisition and Traversing Control...	56
Figure 9. 12 Element Hot-film Probe.....	57
Figure 10. 12 Element Hot-film Survey Data Acquisition.....	58
Figure 11. Constant Temperature Anemometry Bridge and Low Speed Data Acquisition Systems.....	59
Figure 12. Radial/Spanwise Plane Flow Visualization.....	60
Figure 13. Flow Visualization Still Photography.....	61
Figure 14. Hot-wire Survey Processing and Data Acquisition.....	62
Figure 15. HP-3562A Dynamic Signal Analyzer Measurements.....	63
Figure 16. Hot-wire Probe Locations with Respect to Vortex Pair Structure, $De=104.2$, 120° Curvature.....	64
Figure 17. Total Pressure Contours $De=50.4$ to $De=200.3$	65
Figure 18. Total Pressure Contours $De=175.2$ to $De=325.5$	66
Figure 19. Total Pressure Contours $De=275.2$ to $De=424.8$	67
Figure 20. Streamwise Velocity Contours $De=50.4$ to $De=200.3$	68
Figure 21. Streamwise Velocity Contours $De=175.2$ to $De=325.5$	69
Figure 22. Streamwise Velocity Contours $De=275.2$ to $De=424.8$	70
Figure 23. Velocity Perturbation Contours $De=50.4$ to $De=200.3$	71
Figure 24. Velocity Perturbation Contours $De=175.2$ to $De=325.5$	72
Figure 25. Velocity Perturbation Contours $De=275.2$ to $De=424.8$	73
Figure 26. Streamwise Vorticity Contours $De=50.4$ to $De=200.3$	74

Figure 27. Streamwise Vorticity Contours De=175.2 to De=325.5.....	75
Figure 28. Streamwise Vorticity Contours De=275.2 to De=424.8.....	76
Figure 29. Radial Vorticity Contours De=50.4 to De=200.3.....	77
Figure 30. Radial Vorticity Contours De=175.2 to De=325.5.....	78
Figure 31. Radial Vorticity Contours De=275.2 to De=424.8.....	79
Figure 32. Spanwise Vorticity Contours De=50.4 to De=200.3.....	80
Figure 33. Spanwise Vorticity Contours De=175.2 to De=325.5.....	81
Figure 34. Spanwise Vorticity Contours De=275.2 to De=424.8.....	82
Figure 35. Hot-film Probe Locations with Respect to Vortex Pair Structure, De=104.2, 120° Curvature.....	83
Figure 36. Correlation vs. z/d Probes 2,4,6,8,10,12,wrt 2, De=50.25...	84
Figure 37. Correlation vs. z/d Probes 2,4,6,8,10,12,wrt 2, De=100....	85
Figure 38. Correlation vs. z/d Probes 2,4,6,8,10,12,wrt 2, De=149.9...	86
Figure 39. Correlation vs. z/d Probes 2,4,6,8,10,12,wrt 2, De=200.7...	87
Figure 40. Correlation vs. z/d Probes 2,4,6,8,10,12,wrt 2, De=250.4...	88
Figure 41. Correlation vs. z/d Probes 2,4,6,8,10,12,wrt 2, De=299.6...	89
Figure 42. Correlation vs. z/d Probes 2,4,6,8,10,12,wrt 2, De=350.5...	90
Figure 43. Correlation vs. z/d Probes 2,4,6,8,10,12,wrt 2, De=399.8...	91
Figure 44. 3-D Correlations vs. z/d Probes 2,4,6,8,10,12,wrt 2, from De=50.25 to De=399.8.....	92
Figure 45. Correlation vs. z/d Probes 2,4,6,8,10,12,wrt 12, De=50.25...	93
Figure 46. Correlation vs. z/d Probes 2,4,6,8,10,12,wrt 12, De=100....	94
Figure 47. Correlation vs. z/d Probes 2,4,6,8,10,12,wrt 12, De=149.9...	95
Figure 48. Correlation vs. z/d Probes 2,4,6,8,10,12,wrt 12, De=200.7...	96
Figure 49. Correlation vs. z/d Probes 2,4,6,8,10,12,wrt 12, De=250.4...	97
Figure 50. Correlation vs. z/d Probes 2,4,6,8,10,12,wrt 12, De=299.6...	98
Figure 51. Correlation vs. z/d Probes 2,4,6,8,10,12,wrt 12, De=350.5...	99
Figure 52. Correlation vs. z/d Probes 2,4,6,8,10,12,wrt 12, De=399.8...	100
Figure 53. 3-D Correlations vs. z/d Probes 2,4,6,8,10,12,wrt 12, from De=50.25 to De=399.8.....	101
Figure 54. Average Vrms/Vmean vs. De Probes 2,4,6,8,10,12.....	102
Figure 55. Vrms/Vmean / Vrms399.8/Vmean399.8 vs. z/d from De=50.25 to De=399.8.....	103

Figure 56. Length Scales vs. De Probes 2,4,6,8,10,12.....	104
Figure 57. Correlation vs. z/d Probes 1,2,3,4,5,6, wrt 1, De=49.2....	105
Figure 58. Correlation vs. z/d Probes 1,2,3,4,5,6, wrt 1, De=100.1...	106
Figure 59. Correlation vs. z/d Probes 1,2,3,4,5,6, wrt 1, De=150.7...	107
Figure 60. Correlation vs. z/d Probes 1,2,3,4,5,6, wrt 1, De=200.9...	108
Figure 61. Correlation vs. z/d Probes 1,2,3,4,5,6, wrt 1, De=249.6...	109
Figure 62. Correlation vs. z/d Probes 1,2,3,4,5,6, wrt 1, De=299.2...	110
Figure 63. Correlation vs. z/d Probes 1,2,3,4,5,6, wrt 1, De=350.2...	111
Figure 64. Correlation vs. z/d Probes 1,2,3,4,5,6, wrt 1, De=400.3...	112
Figure 65. 3-D Correlations vs. z/d Probes 1,2,3,4,5,6, wrt 1, from De=49.2 to De=400.3.....	113
Figure 66. Correlation vs. z/d Probes 1,2,3,4,5,6, wrt 6, De=49.2....	114
Figure 67. Correlation vs. z/d Probes 1,2,3,4,5,6, wrt 6, De=100.1...	115
Figure 68. Correlation vs. z/d Probes 1,2,3,4,5,6, wrt 6, De=150.7...	116
Figure 69. Correlation vs. z/d Probes 1,2,3,4,5,6, wrt 6, De=200.9...	117
Figure 70. Correlation vs. z/d Probes 1,2,3,4,5,6, wrt 6, De=249.6...	118
Figure 71. Correlation vs. z/d Probes 1,2,3,4,5,6, wrt 6, De=299.2...	119
Figure 72. Correlation vs. z/d Probes 1,2,3,4,5,6, wrt 6, De=350.2...	120
Figure 73. Correlation vs. z/d Probes 1,2,3,4,5,6, wrt 6, De=400.3...	121
Figure 74. 3-D Correlations vs. z/d Probes 1,2,3,4,5,6, wrt 6, from De=49.2 to De=400.3.....	122
Figure 75. Average Vrms/Vmean vs. De probes 1,2,3,4,5,6.....	123
Figure 76. Vrms/Vmean / Vrms400.3/Vmean400.3 vs. z/d from De=49.2 to De=400.3.....	124
Figure 77. Length Scales vs. De Probes 1,2,3,4,5,6.....	125
Figure 78. Digital Mean Streamwise Velocity vs. De, Positions 1,2,3,4,5.....	126
Figure 79. Analog Mean Streamwise Velocity vs. De, Positions 1,2,3,4,5.....	127
Figure 80. Digital Longitudinal Turbulence Intensity vs. De, Positions 1,2,3,4,5.....	128
Figure 81. Analog Longitudinal Turbulence Intensity vs. De, Positions 1,2,3,4,5.....	129
Figure 82. Digital Normalized Longitudinal Turbulence Intensity vs. De, Positions 1,2,3,4,5.....	130

Figure 83. Analog Normalized Longitudinal Turbulence Intensity vs. De, Positions 1,2,3,4,5.....	131
Figure 84. Hot-wire Probe Low Frequency Power Spectra Settings.....	132
Figure 85. Peak Frequency vs. De, Position 1.....	133
Figure 86. Peak Frequency vs. De, Position 2.....	134
Figure 87. Peak Frequency vs. De, Position 3.....	135
Figure 88. Peak Frequency vs. De, Position 4.....	136
Figure 89. Peak Frequency vs. De, Position 5.....	137
Figure 90. Low Frequency Power Spectrum, De=50, Position 1.....	138
Figure 91. Low Frequency Power Spectrum, De=150, Position 1.....	139
Figure 92. Low Frequency Power Spectrum, De=50, Position 1.....	161
Figure 93. Low Frequency Power Spectrum, De=100, Position 1.....	162
Figure 94. Low Frequency Power Spectrum, De=150, Position 1.....	163
Figure 95. Low Frequency Power Spectrum, De=160, Position 1.....	164
Figure 96. Low Frequency Power Spectrum, De=170, Position 1.....	165
Figure 97. Low Frequency Power Spectrum, De=180, Position 1.....	166
Figure 98. Low Frequency Power Spectrum, De=200, Position 1.....	167
Figure 99. Low Frequency Power Spectrum, De=250, Position 1.....	168
Figure 100. Low Frequency Power Spectrum, De=300, Position 1.....	169
Figure 101. Low Frequency Power Spectrum, De=350, Position 1.....	170
Figure 102. Low Frequency Power Spectrum, De=400, Position 1.....	171
Figure 103. Low Frequency Power Spectrum, De=450, Position 1.....	172
Figure 104. Low Frequency Power Spectrum, De=50, Position 2.....	173
Figure 105. Low Frequency Power Spectrum, De=100, Position 2.....	174
Figure 106. Low Frequency Power Spectrum, De=150, Position 2.....	175
Figure 107. Low Frequency Power Spectrum, De=160, Position 2.....	176
Figure 108. Low Frequency Power Spectrum, De=170, Position 2.....	177
Figure 109. Low Frequency Power Spectrum, De=180, Position 2.....	178
Figure 110. Low Frequency Power Spectrum, De=200, Position 2.....	179
Figure 111. Low Frequency Power Spectrum, De=250, Position 2.....	180
Figure 112. Low Frequency Power Spectrum, De=300, Position 2.....	181

Figure 113. Low Frequency Power Spectrum, De=350, Position 2.....	182
Figure 114. Low Frequency Power Spectrum, De=400, Position 2.....	183
Figure 115. Low Frequency Power Spectrum, De=450, Position 2.....	184
Figure 116. Low Frequency Power Spectrum, De=50, Position 3.....	185
Figure 117. Low Frequency Power Spectrum, De=100, Position 3.....	186
Figure 118. Low Frequency Power Spectrum, De=150, Position 3.....	187
Figure 119. Low Frequency Power Spectrum, De=160, Position 3.....	188
Figure 120. Low Frequency Power Spectrum, De=170, Position 3.....	189
Figure 121. Low Frequency Power Spectrum, De=180, Position 3.....	190
Figure 122. Low Frequency Power Spectrum, De=200, Position 3.....	191
Figure 123. Low Frequency Power Spectrum, De=250, Position 3.....	192
Figure 124. Low Frequency Power Spectrum, De=300, Position 3.....	193
Figure 125. Low Frequency Power Spectrum, De=350, Position 3.....	194
Figure 126. Low Frequency Power Spectrum, De=400, Position 3.....	195
Figure 127. Low Frequency Power Spectrum, De=450, Position 3.....	196
Figure 128. Low Frequency Power Spectrum, De=50, Position 4.....	197
Figure 129. Low Frequency Power Spectrum, De=100, Position 4.....	198
Figure 130. Low Frequency Power Spectrum, De=150, Position 4.....	199
Figure 131. Low Frequency Power Spectrum, De=160, Position 4.....	200
Figure 132. Low Frequency Power Spectrum, De=170, Position 4.....	201
Figure 133. Low Frequency Power Spectrum, De=180, Position 4.....	202
Figure 134. Low Frequency Power Spectrum, De=200, Position 4.....	203
Figure 135. Low Frequency Power Spectrum, De=250, Position 4.....	204
Figure 136. Low Frequency Power Spectrum, De=300, Position 4.....	205
Figure 137. Low Frequency Power Spectrum, De=350, Position 4.....	206
Figure 138. Low Frequency Power Spectrum, De=400, Position 4.....	207
Figure 139. Low Frequency Power Spectrum, De=450, Position 4.....	208
Figure 140. Low Frequency Power Spectrum, De=50, Position 5.....	209
Figure 141. Low Frequency Power Spectrum, De=100, Position 5.....	210
Figure 142. Low Frequency Power Spectrum, De=150, Position 5.....	211
Figure 143. Low Frequency Power Spectrum, De=160, Position 5.....	212

Figure 144. Low Frequency Power Spectrum, De=170, Position 5.....	213
Figure 145. Low Frequency Power Spectrum, De=180, Position 5.....	214
Figure 146. Low Frequency Power Spectrum, De=200, Position 5.....	215
Figure 147. Low Frequency Power Spectrum, De=250, Position 5.....	216
Figure 148. Low Frequency Power Spectrum, De=300, Position 5.....	217
Figure 149. Low Frequency Power Spectrum, De=350, Position 5.....	218
Figure 150. Low Frequency Power Spectrum, De=400, Position 5.....	219
Figure 151. Low Frequency Power Spectrum, De=450, Position 5.....	220
Figure 152. Hot-wire Probe High Frequency Power Spectra Settings.....	140
Figure 153. Peak Magnitude vs. De, Positions 1,2,3,4,5.....	141
Figure 154. High Frequency Power Spectrum, De=170, Position 2.....	142
Figure 155. High Frequency Power Spectrum, De=50, Position 1.....	221
Figure 156. High Frequency Power Spectrum, De=100, Position 1.....	222
Figure 157. High Frequency Power Spectrum, De=150, Position 1.....	223
Figure 158. High Frequency Power Spectrum, De=160, Position 1.....	224
Figure 159. High Frequency Power Spectrum, De=170, Position 1.....	225
Figure 160. High Frequency Power Spectrum, De=180, Position 1.....	226
Figure 161. High Frequency Power Spectrum, De=200, Position 1.....	227
Figure 162. High Frequency Power Spectrum, De=250, Position 1.....	228
Figure 163. High Frequency Power Spectrum, De=300, Position 1.....	229
Figure 164. High Frequency Power Spectrum, De=350, Position 1.....	230
Figure 165. High Frequency Power Spectrum, De=400, Position 1.....	231
Figure 166. High Frequency Power Spectrum, De=450, Position 1.....	232
Figure 167. High Frequency Power Spectrum, De=50, Position 2.....	233
Figure 168. High Frequency Power Spectrum, De=100, Position 2.....	234
Figure 169. High Frequency Power Spectrum, De=150, Position 2.....	235
Figure 170. High Frequency Power Spectrum, De=160, Position 2.....	236
Figure 171. High Frequency Power Spectrum, De=170, Position 2.....	237
Figure 172. High Frequency Power Spectrum, De=180, Position 2.....	238
Figure 173. High Frequency Power Spectrum, De=200, Position 2.....	239
Figure 174. High Frequency Power Spectrum, De=250, Position 2.....	240

Figure 175. High Frequency Power Spectrum, De=300, Position 2.....	241
Figure 176. High Frequency Power Spectrum, De=350, Position 2.....	242
Figure 177. High Frequency Power Spectrum, De=400, Position 2.....	243
Figure 178. High Frequency Power Spectrum, De=450, Position 2.....	244
Figure 179. High Frequency Power Spectrum, De=50, Position 3.....	245
Figure 180. High Frequency Power Spectrum, De=100, Position 3.....	246
Figure 181. High Frequency Power Spectrum, De=150, Position 3.....	247
Figure 182. High Frequency Power Spectrum, De=160, Position 3.....	248
Figure 183. High Frequency Power Spectrum, De=170, Position 3.....	249
Figure 184. High Frequency Power Spectrum, De=180, Position 3.....	250
Figure 185. High Frequency Power Spectrum, De=200, Position 3.....	251
Figure 186. High Frequency Power Spectrum, De=250, Position 3.....	252
Figure 187. High Frequency Power Spectrum, De=300, Position 3.....	253
Figure 188. High Frequency Power Spectrum, De=350, Position 3.....	254
Figure 189. High Frequency Power Spectrum, De=400, Position 3.....	255
Figure 190. High Frequency Power Spectrum, De=450, Position 3.....	256
Figure 191. High Frequency Power Spectrum, De=50, Position 4.....	257
Figure 192. High Frequency Power Spectrum, De=100, Position 4.....	258
Figure 193. High Frequency Power Spectrum, De=150, Position 4.....	259
Figure 194. High Frequency Power Spectrum, De=160, Position 4.....	260
Figure 195. High Frequency Power Spectrum, De=170, Position 4.....	261
Figure 196. High Frequency Power Spectrum, De=180, Position 4.....	262
Figure 197. High Frequency Power Spectrum, De=200, Position 4.....	263
Figure 198. High Frequency Power Spectrum, De=250, Position 4.....	264
Figure 199. High Frequency Power Spectrum, De=300, Position 4.....	265
Figure 200. High Frequency Power Spectrum, De=350, Position 4.....	266
Figure 201. High Frequency Power Spectrum, De=400, Position 4.....	267
Figure 202. High Frequency Power Spectrum, De=450, Position 4.....	268
Figure 203. High Frequency Power Spectrum, De=50, Position 5.....	269
Figure 204. High Frequency Power Spectrum, De=100, Position 5.....	270
Figure 205. High Frequency Power Spectrum, De=150, Position 5.....	271

Figure 206. High Frequency Power Spectrum, De=160, Position 5.....	272
Figure 207. High Frequency Power Spectrum, De=170, Position 5.....	273
Figure 208. High Frequency Power Spectrum, De=180, Position 5.....	274
Figure 209. High Frequency Power Spectrum, De=200, Position 5.....	275
Figure 210. High Frequency Power Spectrum, De=250, Position 5.....	276
Figure 211. High Frequency Power Spectrum, De=300, Position 5.....	277
Figure 212. High Frequency Power Spectrum, De=350, Position 5.....	278
Figure 213. High Frequency Power Spectrum, De=400, Position 5.....	279
Figure 214. High Frequency Power Spectrum, De=450, Position 5.....	280
Figure 215. Vortex Pair Split Visualization, De=100, $\theta=115^\circ$ Interval 1/30 s.....	143
Figure 216. Vortex Pair Collapse Visualization, De=100, $\theta=115^\circ$ Interval 1/30 s.....	144
Figure 217. Vortex Pair Appearances and Disappearances Macroscopic Time Line, De=100, $\theta=115^\circ$	145
Figure 218. Vortex Pair Appearances and Disappearances Microscopic Time Lines, De=100, $\theta=115^\circ$	146
Figure 219. Vortex Pair Appearance and Disappearance Frequencies vs. De, $\theta=85^\circ$	147
Figure 220. Vortex Pair Appearance and Disappearance Non-dimensional Frequencies ($\pi fd/\bar{U}$) vs. De, $\theta=85^\circ$	148
Figure 221. Vortex Pair Appearance and Disappearance Frequencies vs. De, $\theta=95^\circ$	149
Figure 222. Vortex Pair Appearance and Disappearance Non-dimensional Frequencies ($\pi fd/\bar{U}$) vs. De, $\theta=95^\circ$	150
Figure 223. Vortex Pair Appearance and Disappearance Frequencies vs. De, $\theta=105^\circ$	151
Figure 224. Vortex Pair Appearance and Disappearance Non-dimensional Frequencies ($\pi fd/\bar{U}$) vs. De, $\theta=105^\circ$	152
Figure 225. Vortex Pair Appearance and Disappearance Frequencies vs. θ , De=75.....	153
Figure 226. Vortex Pair Appearance and Disappearance Frequencies vs. θ , De=100.....	154
Figure 227. Vortex Pair Appearance and Disappearance Frequencies vs. De, $\theta=85^\circ$ to 135° Composite w/o Curve Identification.....	155
Figure 228. Vortex Pair Appearance and Disappearance Frequencies vs. De, $\theta=85^\circ$ to 105°	156

Figure 229. Vortex Pair Appearance and Disappearance Frequencies vs. De , $\theta=115^\circ$ to 135°	157
Figure 230. Vortex Pair Appearance and Disappearance Non-dimensional Frequencies ($\pi fd/\bar{U}$) vs. De , $\theta=85^\circ$ to 135° Composite w/o Curve Identification.....	158
Figure 231. Vortex Pair Appearance and Disappearance Non-dimensional Frequencies ($\pi fd/\bar{U}$) vs. De , $\theta=85^\circ$ to 105°	159
Figure 232. Vortex Pair Appearance and Disappearance Non-dimensional Frequencies ($\pi fd/\bar{U}$) vs. De , $\theta=115^\circ$ to 135°	160

LIST OF SYMBOLS AND ABBREVIATIONS

A	Hot-wire Probe Temperature Slope
A ₀	Hot-wire Probe Calibration Constant
A ₁	Hot-wire Probe First Order Calibration Constant
A ₂	Hot-wire Probe Second Order Calibration Constant
A ₃	Hot-wire Probe Third Order Calibration Constant
A _{ch}	Curved Channel Cross Sectional Area
A _{or}	Orifice Cross Sectional Area
A _p	Pipe Cross Sectional Area
b	Hot-wire Probe Normal Velocity Coefficient
CCPF	Curved Channel Poiseuille Flow
COR	Correlation
COV	Covariance
\bar{C}	Average Transducer Calibration Coefficient
C _p	Five-hole Probe Pitch Constant
C _y	Five-hole Probe Yaw Constant
C _{pp}	Five-hole Probe Pitch Pressure Calibration Coefficient
C _{ps}	Five-hole Probe Static Pressure Calibration Coefficient
C _{pt}	Five-hole Probe Total Pressure Calibration Coefficient
C _{pts}	Five-hole Probe Total Static Pressure Calibration Coefficient
C _{py}	Five-hole Probe Yaw Pressure Calibration Coefficient
d	Channel Height ($r_o - r_i$)
De	Dean Number
De _c	Critical Dean Number
d _p	Pipe Diameter
\bar{E}	Average Transducer Voltage
e'	Rms Voltage
E, E _o , E _{obs}	Observed Voltage

\bar{E}_o, \bar{E}_{obs}	Average Observed Voltage
EOC	Hot-wire Probe Linearized Zero Velocity Voltage
EOM	Hot-wire Probe Zero Velocity Voltage
Eref	Reference Probe Instantaneous Voltage
\bar{E}_{ref}	Reference Probe Average Voltage
f	Frequency
f_{nd}	Non-dimensional Frequency
HP	Hewlett Packard
K	Flow Coefficient
K_p	Five-hole Probe Pitch Calibration Coefficient Slope
K_{ts}	Five-hole Probe Total Static Calibration Coefficient Slope
K_y	Five-hole Probe Yaw Calibration Coefficient Slope
LS, L_x	Length Scale
\dot{m}	Mass Flow Rate
n	Hot-wire Probe Normal Velocity Exponent
ohr	Overheat Ratio
P	Pressure
ΔP	Pressure Drop
P_1	Five-hole Probe #1 Port Pressure
P_2	Five-hole Probe #2 Port Pressure
P_3	Five-hole Probe #3 Port Pressure
P_4	Five-hole Probe #4 Port Pressure
P_5	Five-hole Probe #5 Port Pressure
\bar{P}	Five-hole Probe Average Pressure $(P_2+P_3+P_4+P_5)/4$
$P_{manometer}$	Manometer Pressure
ΔP_{or}	Orifice Pressure Drop
P_s	Static Pressure
P_t	Total Pressure
r_i	Inner Radius
r_o	Outer Radius
Re	Reynolds Number

Re_{ch}	Curved Channel Reynolds Number
Re_p	Pipe Reynolds Number
rms	Root-Mean-Square
T_{cal}	Calibration Temperature
U	Total Velocity
\bar{U}	Average, Mean or Bulk Streamwise Velocity
u'	Streamwise Velocity Fluctuation
U_{ccpf}	Curved Channel Poiseuille Flow Streamwise Velocity
U_{lim}	Limiting Linear Velocity for Hot-wire Probe
U_n	Normal Streamwise Velocity
U_x, U_θ	Streamwise Velocity
U_y, U_r	Radial Velocity
U_z	Spanwise Velocity
x	Streamwise Direction
x'	Spatial Distance from Reference Probe
y	Radial Direction
y_{len}	Radial Distance between Port #1 and Port #4 or #5 Centers
Y	Expansion Coefficient
z	Spanwise Direction
Δz	Spanwise Distance between Active Probes
z_{len}	Spanwise Distance between Port #1 and Port #2 or #3 Centers
α	Spanwise Wavenumber
α_c	Critical Spanwise Wavenumber
δ	Uncertainty Estimate
η	Radius Ratio (r_i/r_o)
θ	Angle of Curvature, Streamwise Curvature Location
λ	Spanwise Spacing
π	Circular Circumference/Diameter Ratio
ρ	Density
ν	Kinematic Viscosity
ω_x, ω_θ	Streamwise Vorticity

ω_y, ω_r

Radial Vorticity

ω_z

Spanwise Vorticity

ACKNOWLEDGMENT

The work done in the curved channels was sponsored by the Propulsion Directorate, U.S. Army Aviation Research and Technology Activity, AVSCOM. Dr. K.C. Civinskas was the program monitor.

I am extremely gratified and would like to express my sincere appreciation to all the people who made this research work possible: Professor Phil Iigrani, who guided the project; Professor Mani Subramanian, who helped get past the software and data acquisition humps; Jim Schofield and Tom Christian, who helped with the electronic interfacing; Charles Crow and Mardo Blanco in the machine shop who always dropped everything they were doing to help when I needed it; Andy Sarakon and Mitch Nichols for the photo work; and especially to my family, Cheri, Jennifer and Keith, whose love, support and help mattered the most.

I. INTRODUCTION

The influences of curvature on flow behavior are important to a variety of machines including pump impellers, radial compressors, nozzles and diffusers, axial flow compressors, and axial flow turbines. To develop predictions of these flows, bench mark experimental results are required. The present study is part of an experimental effort to achieve this aim. In it, flow instabilities in a constant cross section channel with constant curvature are examined. These results not only enhance understanding of flows in more complex geometries, but also provide a building block for the development of improved prediction schemes and more efficient machine designs.

A. BACKGROUND

Until recently, only two laminar flows were known to occur prior to the onset of turbulence in curved channels. At low enough Re , the most basic laminar flow occurs. This is curved channel Poiseuille flow (CCPF). At higher Re , secondary flow develops due to centrifugal instability of CCPF. This second laminar flow consists of an array of streamwise-oriented, counter-rotating pairs of vortices and is called Dean vortex flow.

If the spanwise spacing of vortex pairs is λ , then a non-dimensional spanwise wavenumber of the vortex pairs is $\alpha = 2(d/2)\pi/\lambda$. For given α and radius ratio η , classical linear stability analysis predicts the neutrally stable De which sets the lower limit where such vortices may be present. The minimum of the neutral stability curve for the primary instability then occurs at De_c and α_c . For $\eta = 0.979$, $De_c = 36.92$.

Recent numerical work by Finlay et al. [Ref. 1] predicts these Dean vortices become unstable at higher Re to two types of travelling waves, resulting in two kinds of wavy vortex flows, referred to as undulating

Dean vortex flow and twisting Dean vortex flow. The first mention of experimentally observed waviness is given by Kelleher et al. [Ref. 2], and the first photographic evidence of vortex motions believed to be twisting is presented by Ligrani and Niver [Ref. 3]. Additional experimental evidence of wavy vortex flow in a rotating, curved channel is given by Matsson and Alfredsson [Ref. 4]. Finlay and Nandakumar [Ref. 5] provide experimental evidence of undulating Dean vortex flow and twisting Dean vortex flow which are compared to wavy vortex results obtained by direct simulation of the time-independent three-dimensional Navier-Stokes equations. The experimental results were obtained using the same large aspect ratio curved channel described by Ligrani and Niver [Ref. 3].

Another category of motions which has been observed is related to appearances and disappearances of Dean vortex pairs across the span of the channel. Evidence of such behavior for channel flow was first provided by Ligrani and Niver [Ref. 3] in the form of photographic sequences showing small secondary vortex pairs observed temporarily in spanwise/radial planes for De ranging from 75 to 220. Additional study of different phenomena that result in these appearances and disappearances is presented by Ligrani et al. [Ref. 6].

B. OBJECTIVES

The present study focuses on the behavior of Dean vortices in rectangular curved channels with 40 to 1 aspect ratios. Methods are employed to study flows at De from 49.2 to 450. This range of De represents flow regimes from laminar CCPP to fully turbulent flow. Of particular interest are undulation, twisting, appearances of vortex pairs, disappearances of vortex pairs, and their connections to the development of fully turbulent flow.

C. ORGANIZATION

Chapter II describes the construction and operation of the curved channels used for the present study. Included is information on the

determination of bulk flow rates in the channels. Chapter III describes equipment used for measurement of pressure and velocity surveys plus techniques used to obtain real time flow visualization results. Chapter IV presents experimental results. Chapter V presents the summary and conclusions. Appendix A contains uncertainty analysis results. Appendix B describes the software employed. Appendix C contains sequential Dynamic Signal Analyzer steps to obtain power spectra plots. Appendix D contains all tables. Appendix E contains photographs, schematics and result figures. Appendix F contains individual power spectra plots.

II. EXPERIMENTAL FACILITIES

A. CURVED CHANNEL DESCRIPTIONS

Two nearly identical curved channels, a transparent channel and a heat transfer channel, were utilized. A photograph of the transparent channel, a photograph of the blower assembly, and a schematic of the channel are shown in Figures 1, 2 and 3, respectively. The channel is described in detail by Ligrani and Niver [Ref. 3]. The facility is an open-circuit suction facility designed for low-speed transition studies. At the inlet, an aluminum honeycomb and three screens reduce spatial non-uniformities in the flow. These are followed by a two-dimensional nozzle with a 20 to 1 contraction ratio which accelerates the flow into a 2.44 m long straight duct. The straight section provides fully developed laminar flow at the inlet of the curved section which then follows, for Dean numbers up to 640 [Ref. 3]. The radii of the concentric convex and concave walls in the curved section are 596.9 mm and 609.6 mm, respectively. The 180 degree curved section is then followed by another 2.44 m long straight duct, and then a honeycomb, several screens, a diffuser and an outlet plenum. From the inlet of the first straight section to the outlet of the second straight section, the interior dimensions of the facility are 1.27 cm for the height and 50.80 cm for the width, providing an aspect ratio of 40 to 1. Tolerances for the height and width are 0.015 cm and 0.050 cm, respectively, maintained using longitudinal and cross-beam supports along the length of the test section. These supports are connected to two continuous, seamless sheets of polycarbonate (commercial name is Lexan) which form the two primary interior walls adjacent to the flow stream. The outlet plenum (labeled #1 in Figure 3) is connected to a second plenum (labeled #2 in Figure 3) using 50.8 mm diameter piping. Plenum #2 is maintained at low pressure by a 1/3 horsepower (250 W) blower manufactured by ICG Industries, Inc. A brass gate valve is used to adjust the flow

rate, which is determined from the pressure drop across an orifice plate located in the pipe between the two plenum chambers.

In the transparent channel a slot, 3.2 mm wide and 76.2 mm long is located in the convex wall. It is aligned in the spanwise direction 50.8 mm off the centerline at a location 120 degrees from the start of curvature. A support block of polycarbonate (152.4 mm by 63.5 mm by 22.2 mm) is joined using epoxy to the wall surrounding the slot to maintain the convex wall's dimensional integrity, and to minimize the deflection of the curved wall in the vicinity of the slot. Foam is used to line the slot to allow probe insertion with no air leakage to the channel interior. This foam is carefully positioned to avoid any bumps or discontinuities in the flow. Additional details are given by Ligrani, et al. [Ref. 7]

In the second curved channel, a slot identical to the one previously described is located straddling the centerline, aligned in the spanwise direction, and positioned 19.05 cm downstream of the convex surface. This channel is configured for heat transfer measurements, but the slot location is the only significant difference pertaining to this study. Additional details are given by Hughes. [Ref. 8]

B. DEAN NUMBER DETERMINATION

Dean number, channel Reynolds number, channel bulk velocity and mass flow rate are determined by measuring the pressure drop across the 3.81 cm (1.5 inch) diameter ASME sharp edged orifice plate. Also measured are barometric pressure, and ambient temperature. The expansion coefficient Y is then calculated from Holman and Gajda [Ref. 10]. An initial Dean number guess is then made by interpolating a table of Dean number versus orifice pressure drop compiled by Niver [Ref. 11]. The density of air is computed using the ideal gas law. An initial mass flow rate is subsequently calculated based on the initial Dean number. The Reynolds number through the pipe is calculated using the equation given by:

$$Re_p = \dot{m} \frac{d_p}{\rho v A_p}$$

Flow coefficient K is interpolated from ASME tables [Ref. 12]. With this, mass flow rate is determined using an equation of the form:

$$\dot{m} = K A_{o_r} Y \sqrt{2 \rho \Delta P_{o_r}}$$

Iterations continue until convergence to within 1% of previous mass flow rate. Channel bulk velocity, channel Reynolds number and Dean number are then calculated using the equations:

$$\bar{U} = \frac{\dot{m}}{\rho A_{ch}}$$

$$Re_{ch} = \bar{U} \frac{d}{\nu}$$

and

$$De = Re_{ch} \sqrt{\frac{d}{r_1}}$$

respectively. A plot of pressure drop versus De is shown in Figure 4 for a barometric pressure of 29.92 inches and an ambient temperature of 19 degrees Celsius.

III. EXPERIMENTAL PROCEDURES

A. STREAMWISE, SPANWISE AND RADIAL VELOCITY SURVEYS

1. Five-hole Pressure Probe Description

A photograph and two schematic diagrams of the miniature five-hole pressure probe are shown in Figures 5, 6 and 7, respectively. The diameter of the probe tip is 1.38 mm. The probe is arranged such that the central tube is surrounded by four other tubes. The ends of each of the surrounding tubes are beveled at a 45° angle with respect to the mouth of the central tube. Each of the five-hole tubes is made from stainless steel hypodermic tubing with inner and outer diameters of 0.203 mm and 0.406 mm, respectively. The probe was constructed by first spot welding together these five tubes. The tubes were then bent in a 90° turn with a radius of 1.52 mm to avoid any tube crimping. Silver solder was then used to join the five tubes together continuously along their length. Finally, portions of the probe tip were beveled to appropriate angles using a surface grinder. This approach is slightly different than the one described by Treaster and Houtz. [Ref. 13]

Figure 6 shows that the present probe tip extends 5.08 mm (4 tip diameters) beyond the bend in the stem to minimize the effects of stem flow blockage at the measuring location. Similarly, the tip is 22.9 mm (19 tip diameters) from the 9.53 mm diameter mounting cylinder. Within this cylinder, each tube is connected to a 1.60 mm diameter tube using a small manifold for each tube connection. The mounting cylinder was sized for easy handling and mounting. On top of the cylinder is a second set of manifolds with five male connectors for attachment to 6.35 mm outer diameter/4.67 mm inner diameter Imperial Eastman Polyflo tubing.

The miniature five-hole probe was designed to minimize the adverse effects of flow blockage and spatial resolution when used for measurements in the curved channel. When in place for measurements at the centerline

of the channel, the mounting cylinder is not exposed to the flow, and the probe produces 4.8% blockage over a 12.7 mm x 12.7 mm area. A five-hole rather than a four-hole design was chosen since it was easier to calibrate and because corrections for spatial resolution are more readily applied [Ref. 14]. The tip was conical rather than prismatic to minimize near-wall flow blockage effects, which are particularly severe for prismatic type probes.

2. Experimental Details

Figure 8 shows a schematic of the measurement chain used for the five-hole pressure probe. Each tube of the five-hole probe is connected via flexible plastic tubing (less than 20 cm in length to minimize the volume of air in the tubes) to a Validyne model DP103-06 variable reluctance differential pressure transducer. A separate transducer is used to measure pressure relative to the atmosphere for each port of the five-hole probe. Each transducer has a full-scale range of 2.5 mm of water differential pressure. Shielded cables connect the transducers to separate Celesco CD01D carrier demodulator units. The carrier demodulator units produce DC voltage output proportional to the pressure signals from the transducers. Each carrier demodulator output is connected to a Hewlett Packard (HP) 3498A extender which is controlled by an HP 3497A data acquisition/control unit. The HP 3497A is controlled by an HP Series 300, Model 236 computer which also processes the data. Voltage samples are recorded sequentially from the five channels using an overall sampling rate of about 10 Hz.

3. Probe Calibration

The probe was calibrated by Fields [Ref.15] using a procedure similar to Ligrani, et al. [Ref. 7]. During calibration, the probe was mounted in a calibration sled and placed in an open-circuit blower tunnel which provided uniform flow in the test section. A manually operated traverse was used to position the probe through a five yaw angle and five pitch angle array. Total pressure was measured with a Kiel probe, and

tunnel static pressure was measured near the probe position using wall static taps. For each probe position during calibration, yaw, pitch, total and total minus static pressure coefficients were calculated.

4. Curved Channel Procedures

a. Traversing Mechanism

When measurements are made in the channel, the probe is oriented using a mount which allows initial yaw and pitch angles to be adjusted within $\pm 0.1^\circ$ and $\pm 0.5^\circ$, respectively. The mounting block is attached to a travelling block which is part of an automated two-dimensional (X-Y) traversing mechanism. Moving parts are driven by 20 thread per inch (0.8 thread per mm) drive screws which are rotated by Superior Electric type M092-FD310 stepping motors. These motors are controlled by a MITAS Motion Controller, which directs movement of the probe according to instructions from the computer.

b. Measurements

The probe is positioned and aligned before measurements are made. The probe is first inserted in the slot of the insulated channel at a spanwise location 25.4 mm from the centerline so that it just touches the straight wall farthest from the slot. It is then visually aligned with the flow and then moved to the channel position at the midpoint of the spanwise-radial plane using the MITAS controller. Small adjustments are made to the yaw and pitch angle by adjusting the probe mount. Software program ORIENT, described in Appendix B, is used to check yaw and pitch coefficients as this is undertaken until the yaw coefficient is zero and the pitch coefficient is sufficiently small. The final orientation of the probe gives a yaw coefficient of 0.0 ± 0.01 and a pitch coefficient of -0.4. This is equivalent to $+3.0^\circ$ offset. More accurate pitch alignment forces the probe against the edge of the slot, hence the pitch offset is accounted for during data reduction. No offset is applied or needed for the yaw angle.

In a typical spanwise/radial traverse, the probe moves in the radial direction from the concave wall to the convex wall as measurements are made. To begin measurements at a new spanwise location, the probe first moves 2.54 mm in the spanwise direction, then in the reverse span direction 1.27 mm, and finally toward the concave wall until it is 1.27 mm away. A new radial or spanwise measuring traverse then begins. This procedure reduces the adverse effects of backlash and gives repeatable data regardless of the direction of spanwise probe motion.

When measurements are made at a particular location, 50 samples of each pressure are averaged. This is done by sampling pressure from probe ports in sequence so that a long averaging time is provided for each channel, thereby minimizing the influence of brief unsteadiness in the channel. For each probe location, about 3 min of acquisition and processing time is required. A traverse over an entire plane requires about 8 h. The entire process is computer controlled and generally performed at night when there is minimal unsteadiness at the channel inlet from laboratory disturbances.

c. Data Reduction

Measured pressures from each probe port are stored by the computer during each traverse. These data are then corrected to account for the effect of finite spatial resolution using procedures described by Ligrani et al. [Ref. 14]. The procedure corrects pressures to account for the fact that they are not measured at the same physical location by adjusting pressures from ports 2, 3, 4 and 5 so that they appear to be measured at port 1. The correction primarily affects secondary flow velocity vectors in the plane normal to the bulk flow direction. With the corrections, these secondary vector magnitudes may change as much as 15% at locations where velocity gradients are largest.

Yaw and pitch pressure coefficients are then calculated for each location. Using these coefficients and measured pressures, pitch and yaw angles are calculated at each location. The total minus static

pressure coefficient is then calculated. From this total velocity magnitude is calculated using the equation:

$$U = \sqrt{2 C_{pts} \frac{(P_1 - P)}{\rho}}$$

The three velocity components are subsequently given by:

$$U_\theta = U \cos(y) \cos(p)$$

$$U_r = U \sin(y)$$

and

$$U_z = U \cos(y) \sin(p)$$

where y and p are the yaw and pitch angles, respectively. Mean vorticity components are then calculated using finite difference schemes applied to the three components of mean velocity. Equations for the vorticity components as functions of velocity are given by:

$$\omega_\theta = \partial \frac{U_r}{\partial z} - \partial \frac{U_z}{\partial r}$$

$$\omega_r = -\partial \frac{U_\theta}{\partial z}$$

and

$$\omega_z = \frac{U_\theta}{r} + \partial \frac{U_\theta}{\partial r}$$

Streamwise derivatives are neglected when calculating radial and spanwise vorticities. In the final phase of data reduction, corrections are made to account for deflection of flow streamlines near the probe tip in the presence of transverse gradients of the streamwise velocity. This is referred to as the downwash velocity correction [Ref. 14], and is based on the idea that the downwash velocity in a particular direction scales with the transverse gradient of streamwise velocity in the same direction.

B. CONVEX WALL TURBULENCE SURVEYS

1. 12 Element Hot-film Probe Description

A photograph of the hot-film array is shown in Figure 9. The array has 12 hot-film anemometers mounted equidistant from each other on a specially designed aluminum frame. Probe locations are tabulated in Table 1, which indicates that probe 1 is positioned 56.95 mm from the channel spanwise centerline. Each probe is silver plated platinum with a diameter of 0.625 microns and an active length of 0.102 mm. The frame is designed to fit snugly into the slot located 120° from the start of curvature in the transparent curved channel. With thin shims placed under the ends of the frame, the probe is mounted so that the measuring plane of the gages is flush with the convex wall.

2. Experimental Details

Figure 10 shows a schematic of the measurement chain, including the probes, and data acquisition and processing equipment. With the present setup, any six probes can be connected to each of six different DANTEC 56C17 Constant Temperature Anemometer bridge units shown in the photograph Figure 11. Bridge outputs are sent simultaneously to a HP 3497A Data Acquisition/Control Unit and to DANTEC 56N20 Signal Conditioning Units. In the discussion which follows, the former signals are referred to as raw signals, whereas the latter are referred to as conditioned signals. The output of each signal conditioning unit is directed to the HP 3497A Data Acquisition/Control Unit which is controlled by an HP Series 300, Model 236 Computer which also processes the data. With the control unit and computer, voltage samples are recorded sequentially from the six channels using an overall sampling rate of about 5.9 Hz.

3. Curved Channel Procedures

a. Measurements

The data acquisition system is arranged so that the signal from the hot-film gage closest to the spanwise centerline is sampled

first. Signals from adjacent gages across the span of the array are then sampled in sequence. The sequence is repeated until 1000 sampled voltages for each gage are obtained. Each bridge uses an overheat ratio setting of 1.6. Each signal conditioning unit is set with filters to pass signals with frequencies from 0.1 Hz to 1.0 kHz. A gain setting of 500 is also used.

b. Data Reduction

After sampled voltages are stored in the computer, they are reduced by a factor of 500 to account for the amplifier gain. Mean values of the raw and conditioned voltage signals are then determined. In addition, rms voltage for each conditioned channel is also determined. Normalized rms voltage for each channel is computed as the ratio of rms voltage to the raw mean voltage.

Covariances are determined for the conditioned voltage signals using the equation:

$$COV = \frac{1}{n} \sum_{i=1}^n (Eref_i - \bar{E}ref) (Eobs_i - \bar{E}obs)$$

Here, n is the number of samples, ref is the reference channel and obs is the observed channel. This is equivalent to:

$$\overline{e'(x) e'(x+x')}$$

Two different probe configurations were utilized. First, covariances for probes 2, 4, 6, 8, 10 and 12 with respect to probe 2 located at $z/d=4.73$ were determined for De from 50.25 to 399.8. This sequence is termed 'in to out'. Covariances for probes 12, 10, 8, 6, 4 and 2 with respect to probe 12 located at $z/d=7.23$ were determined for $De=50.25$ to 399.8. This sequence is termed 'out to in'. Second, 'in to out' covariances for probes 1 through 6 with respect to probe 1 located at $z/d=4.48$ were determined for De from 49.2 to 400.3. 'Out to in' covariances for probes 6, 5, 4, 3, 2 and 1 with respect to probe 6 located at $z/d=5.73$ were

determined for $De=49.2$ to 400.3 . After determining covariances, spatial correlations are determined using the equation:

$$COR = \frac{COV}{(rmsE_{ref})(rmsE_{obs})}$$

This equation is equivalent to:

$$\frac{\overline{e'(x)e'(x+x')}}{\sqrt{\overline{e'(x)^2}}\sqrt{\overline{e'(x+x')^2}}}$$

Length scale, representing the area under a curve of correlation versus z/d is determined by the equation:

$$LS = \sum_{i=1}^n (COR) (\Delta Z)$$

or alternatively:

$$L_x = \int COR dz$$

Here, ΔZ is the spanwise distance between active probes. The summation was used to calculate length scales and is an approximation to the exact integral method.

C. FLOW VISUALIZATION

In order to obtain information on secondary flow motions resulting from the vortices, air in the transparent channel was partially contaminated with smoke and then photographed. The device used to generate the smoke is described by Ligrani and Niver. [Ref. 3] Smoke patterns were illuminated in spanwise/radial planes using spotlights directed at spanwise slits through black paper used to line the convex surface exterior of the channel. A Sony DXC-M3 video camera with a Fujinon-TVZ 1:1.7/10-140 mm DCL-914BY zoom lens was used to record the illuminated, time-varying patterns as shown in Figure 12. The camera was connected to a Sony VO-6800 portable videocassette recorder which collects

images at rates as high as 60 frames per second. Recorded images are then played back using a Sony VO-5800 videocassette recorder connected to a SONY PVM-1910 Trinitron color monitor. By employing the scan/stop action feature of this recorder, photographs of instantaneous images using the setup shown in Figure 13 were obtained and then arranged in sequences to show time-varying phenomena. New time-varying sequences are presented in Chapter IV. This chapter additionally gives results from analysis of video tapes previously obtained by Ligrani et al. [Ref. 6]. Data were analyzed at De from 60 to 150 at angles from the start of curvature from 85° to 135° . Of primary interest were frequencies of different appearance and disappearance events described by Ligrani et al. [Ref. 6]. Tabulations of results are given in Tables 2 and 3. In making these tabulations, vortex pairs which moved into or out of the field of view during the time sequences were ignored. All frequencies were also converted to non-dimensional form using the equation:

$$f_{nd} = \frac{\pi f d}{U}$$

These are also tabulated in Table 4.

The two new time-varying sequences presented here were obtained using the setup of Figure 13 using a Canon A-1 SLR camera with a 35-70 mm, f3.5-22 lens. Settings of 55 mm, f5.6 and speed 1/8 second for Kodak Tri-X pan, 400 ASA film were utilized following the recommendations of Longest [Ref. 16].

D. DEAN NUMBER SURVEYS OF POWER SPECTRA AND LONGITUDINAL VELOCITY FLUCTUATIONS

1. Experimental Details

A DANTEC 55P14 single hot-wire probe is used to obtain surveys of power spectra and longitudinal velocity fluctuations. The probe sensor is platinum plated tungsten wire with a diameter of 5 microns and a sensor length of 1.25 mm. Because support prongs are bent, they are approximately parallel to the flow direction at the sensor location, which

places the sensor normal to the bulk flow direction. During measurements, the probe is rigidly mounted in an X-Y traverse such that the sensor itself is oriented in the spanwise direction normal to the flow at a streamwise location 120° from the start of curvature. Surveys were obtained at each of five locations. These locations are listed in Table 5 and shown in Figure 16 relative to vortex pair structures. The probe is operated at an overheat ratio of 1.8 using a DISA 55M10 Constant Temperature Anemometer bridge. The output from the bridge is routed through a DANTEC 56N20 Signal Conditioning Unit. Settings on the signal conditioner were varied with Dean number range as shown in Table 6. The output from the signal conditioner was routed to a DANTEC 56N22 Mean Value Unit set at a 10 second integration interval. The output from the signal conditioner was additionally sent to a Hewlett Packard 6944A Multiprogrammer. This high speed data acquisition system was controlled by a Hewlett Packard 300 Series Model 9000 computer which also stored and processed the data. Acquisition sampling rate was 2500 Hz if De was less than 275 or 5000 Hz if Dean number was higher than 275.

Another output from the bridge was directed to a second signal conditioner operated with amplifier gain of 500, low pass filter of 1.0 kHz, and a high pass filter of 0.1 Hz. The output from this signal conditioner was then sent to a DISA 56N25 RMS Unit set with a 10 second integration interval.

After the DISA 56N20 Signal conditioner, signals were also sent to the Hewlett Packard 3562A Dynamic Signal Analyzer. This device is used to obtain spectra of the time-varying signals from the hot-wire bridge. Figure 14 shows the setup for measurement, data acquisition and processing. Figure 15 gives an overview of the internal measurement chain of the dynamic signal analyzer. Step by step details are given for setup and use of the dynamic signal analyzer for spectral measurements in Appendix C.

With settings on the signal conditioning units adjusted as shown in Table 6, frequency spectra were obtained between 0.1 and 25 Hz and between 0.1 and 10000 Hz.

2. Probe Calibration and Measurement Procedures

The probe was calibrated in the test section of the wind tunnel located in the Department of Mechanical Engineering laboratory of the Naval Postgraduate School. From the calibration, $N=0.45$, $B=3.750916$, and $EOC=2.653925$, where the equation given by:

$$U = \left(\frac{E^2 - EOC^2}{B} \right)^{1/n}$$

is valid when the sensor is subjected to forced convection. For $Re_d < 0.07$ mixed convection affects sensor response and the relationship between velocity and voltage is given by the equation:

$$Y = A_0 + A_1 X + A_2 X^2 + A_3 X^3$$

where $Y = U^N$, $X = E^2 - EOC^2$, $A_0 = -0.68058$, $A_1 = 0.99448$, $A_2 = -0.24088$ and $A_3 = 0.024986$.

With the experimental arrangement, longitudinal velocity fluctuation magnitudes are determined from digital processing of hot-wire bridge voltage signals and from signals read from the DISA 56N25 RMS unit. For the former, 20000 voltage samples were obtained. For the latter, the normalized streamwise velocity fluctuation magnitudes are calculated using the equation from given by:

$$\frac{u'}{U} = \frac{2}{n} \frac{\overline{E_o} e'}{(\overline{E_o}^2 - A)}$$

[Ref. 17].

APPENDIX B - SOFTWARE DIRECTORY

Programs written in Hewlett Packard BASIC 4.0 language for the HP 300 Series computers utilized in these studies are listed. A description of what the program does, significant user inputs required and significant output is provided.

A. GENERAL PROGRAMS

DEAN15M Calculates the Dean number as described in Chapter II.

user input

- barometric pressure
- ambient temperature
- orifice pressure drop

output

- expansion coefficient Y
- flow coefficient K
- mass flow rate
- channel Reynolds number
- Dean number
- bulk velocity

B. FIVE-HOLE PRESSURE PROBE PROGRAMS

C4 Data file of calibration coefficients: pitch, yaw, C_{py} , C_{pp} , C_{pt} , C_{ps} , and C_{pts} .

P4 Data file of calibration pressures: pitch, yaw, P_1 , P_2 , P_3 , P_4 , and P_5 .

FIVEHOLE Acquires pressure measurements at each of the five ports and directs probe positioning.

user input

- date/time
- estimated dean number
- orifice size
- number of spanwise and radial points
- spanwise and radial resolutions
- spanwise and radial starting positions
- wait time for pressure to stabilize
- number of transducers
- number of samples per channel

and curvature of 115° on the right side of the channel. Still photography timed sequences showing a collapsing occurrence and a splitting occurrence are presented also. For each De , these data were obtained from spanwise/radial plane observations which were video tape recorded at angles from 85° to 135° from the start of curvature.

A. SURVEYS OF TIME-AVERAGED QUANTITIES

Surveys of time-averaged quantities determined from five-hole pressure probe measurements are presented in figures 17 through 34. Figures 17 through 19 present total pressure contours. Figures 20 through 22 present streamwise velocity contours. Figures 23 through 25 present streamwise velocity perturbations. Figures 26 through 28 present streamwise vorticity components. Figures 29 through 31 present radial vorticity components. Figures 32 through 34 present spanwise vorticity components.

1. Total Pressure

In Figures 17 through 19, surveys of $P_{amb}-P_{total}$ (in Pascals) representing ambient pressure minus measured total pressure are given. The higher the index in the flow, the higher the difference in pressure, i.e., the higher the vacuum measured. Pressure deficits near the concave surface in the form of humps are upwash regions between counter-rotating vortex pairs. At $De=75$ the flow shows evidence of portions of at least five deficit regions. At $De=125.1$ the number of deficits is reduced to two. The highest deficits occur at $De=175.2$. At $De \geq 300$, the surveys show reasonable spanwise uniformity.

2. Streamwise Velocity

Surveys of streamwise velocity normalized by bulk velocity are displayed in Figures 20 through 22. These show velocity deficits near the concave wall which are nearly identical qualitatively to the total pressure deficits in Figures 17 through 19. These deficits are less intense than ones measured in the curved portion of the channel by Fields [Ref. 15] because the mechanism to produce the vortices and accompanying secondary flows (centrifugal instabilities) is not present.

3. Velocity Perturbation

In order to show streamwise velocity perturbations, curved channel Poiseuille flow is subtracted from streamwise velocity. Such perturbations are presented in Figures 23 to 25. At $De=100.3$ a regular perturbation pattern is present across the span of the measurement plane. The perturbations become spanwise uniform for $De \geq 300$.

4. Vorticity Components

Vorticity components in Figures 26 through 34 have positive and negative signs. Positive vorticity is contained within the solid contour lines while negative vorticity is contained within the dashed contour lines. As the plots are arranged so that streamwise flow moves into the page, positive streamwise vorticity is clockwise.

a. Streamwise Vorticity

Streamwise vorticity contours are shown in Figures 26 through 28. The streamwise vorticity distributions correlate nicely to total pressure and streamwise velocity such that velocity/pressure deficits are present between the two vortices within each counter-rotating pair. Counter-rotating vortex pairs are clearly evident at the locations of the two largest total pressure deficits for $De=100.3$. At $De=175.2$ two pairs of well defined vortices again correspond to the locations of the velocity deficits. At De greater than about 300 streamwise vorticity contours tend toward spanwise uniformity.

b. Radial Vorticity

Radial vorticity contours are shown in Figures 29 through 31. As De increases, the flow becomes spanwise periodic at $De=75$, until $De \geq 300$ when the flow becomes spanwise uniform.

c. Spanwise Vorticity

Spanwise vorticity contours are shown in Figures 32 through 34. These contours are consistent with the total pressure contours and

contours of streamwise velocity, where negative vorticity components closely match the velocity/pressure deficits. Flow is spanwise uniform at $De=50.4$ and for $De \geq 300$.

B. TIME-AVERAGED AND SPATIALLY RESOLVED FLOW PROPERTIES NEAR THE CONVEX SURFACE

Results presented in this section were obtained using an array of hot-film gages mounted on the convex surface of the channel ($y/d=1.0$) 120° from the start of curvature. Figure 35 shows the locations of the 12 hot-film elements with respect to vortex pairs. Table 1 gives probe locations with respect to individual vortices. One expects results from probes near similar vortex characteristics to be correlated with each other. Figures 36 through 43 give correlations versus z/d referenced to probe 2 for probes 2, 4, 6, 8, 10 and 12, for De from 50.25 to 399.8. Figure 44 is then a 3-D composite of Figures 36 through 43. Figures 45 through 52 give correlations versus z/d referenced to probe 12 for probes 2, 4, 6, 8, 10 and 12, for De from 50.25 to 399.8. Figure 53 is then a 3-D composite of Figures 45 through 52.

Referring to Figures 44 and 53 shows that, in all cases, correlation magnitudes decrease as the distance from the reference probe increases. Reference probes are probe 2, located at $z/d=4.73$, for Figure 44 and probe 12, located at $z/d=7.23$ for Figure 53. In Figure 44, sign variations of correlations versus z/d are evident at De from 50.25 to 299.6. These variations give evidence of regions of positive and negative correlation between different parts of vortex pair structures. For $De=100$, probe 2 is located directly over a downwash region. Probe 4, the nearest active probe, is located directly over an upwash region and its signal correlates negatively with the signal from probe 2. At $De \geq 299.6$, correlations have fully turbulent characteristics, dropping to values which do not vary significantly with z/d .

Similar qualitative trends are evident in Figure 53. For $De=100$, probe 12 is located over a region of negative vorticity. Probe 10, the

nearest active probe, is located over a region of positive vorticity and its signal correlates negatively with the signal from probe 12. At $De \geq 250.4$, correlations have fully turbulent characteristics, dropping to values which do not vary significantly with z/d .

Figure 54 shows the average (over all gages employed) normalized rms voltage versus De from 50.25 to 399.8. This curve indicates an increase in V_{rms}/V_{mean} as De increases from 150 to 200. At De higher than 300, the variations with De have lower slopes.

Figure 55 shows scaled, normalized rms voltage versus z/d for each De surveyed. The normalized rms voltage for each channel is scaled by the normalized rms voltage measured at $De=399.8$. Thus the scaled values at this De are equal to 1.0. These curves show that spatially varying structures occur at $De=149.9$, 200.7, 250.4, 299.6 and 350.5.

Length scales shown in Figure 56 represent integrations of the correlations with respect to z/d . These evidence spatially varying structures between $De=100$ and $De=250$.

The previous results were discussed for an active probe spacing of 6.35 mm. For a second set of measurements, active probe spacing was reduced to 3.18 mm. Results are now presented which were obtained using the array of hot-film gages with the smaller probe spacing. Figures 57 through 64 give correlations versus z/d referenced to probe 1 for probes 1, 2, 3, 4, 5 and 6, for De from 49.2 to 400.3. Figure 65 is then a 3-D composite of Figures 57 through 64. Figures 66 through 73 give correlations versus z/d referenced to probe 6 for probes 1, 2, 3, 4, 5 and 6, for De from 49.2 to 400.3. Figure 74 is then a 3-D composite of Figures 66 through 73.

Referring to Figures 65 and 74 shows that, in all cases, correlation magnitudes decrease as the distance from the reference probe increases. Reference probes are probe 1, located at $z/d=4.48$, for Figure 65 and probe 6, located at $z/d=5.73$ for Figure 74. In Figure 65, sign variations of correlations versus z/d are evident at De from 49.2 to 200.9. These

variations give evidence of regions of positive and negative correlation between different parts of vortex pair structures. For $De=100$, probe 1 is located directly over a region of positive vorticity. Probe 2, the nearest active probe, is located directly over a downwash region and its signal correlates negatively with the signal from probe 1. At $De \geq 249.6$, correlations have fully turbulent characteristics, dropping to values which do not vary significantly with z/d .

Similar qualitative trends are evident in Figure 74. For $De=100$, probe 6 is located over a downwash region. Probe 5, the nearest active probe, is located over a region of positive vorticity and its signal correlates negatively with the signal from probe 6. At $De \geq 350.2$, correlations have fully turbulent characteristics, dropping to values which do not vary significantly with z/d .

Figure 75 shows the average (over all gages employed) normalized rms voltage versus De from 49.2 to 400.3. This curve indicates an increase in V_{rms}/V_{mean} as De increases from 200 to 250. At De higher than 250, the variations with De have lower slopes.

Figure 76 shows scaled, normalized rms voltage versus z/d for each De surveyed. The normalized rms voltage for each channel is scaled by the normalized rms voltage measured at $De=400.3$. Thus, as for Figure 55, the scaled values at this De are equal to 1.0. These curves show that the spatially varying structures occur at $De=100.1$, 150.7, 200.9, 249.6, 299.2 and 350.2.

Length scales shown in Figure 77 represent integrations of correlations with respect to z/d . These evidence spatially varying structures between $De=100$ and $De=200$.

C. SPECTRAL AND LONGITUDINAL VELOCITY FLUCTUATION VARIATIONS WITH DEAN NUMBER

Figure 16 shows the five hot-wire probe locations where surveys were taken in the spanwise/radial plane 120° from the start of curvature. At each of these locations, time-averaged streamwise velocity and

longitudinal turbulence intensity were measured using a single hot-wire probe at De from 50 to 450. The five locations were chosen to obtain information on different parts of the vortex pair structure. As shown in Figure 16, position 1 is located near the concave wall at the base of an upwash region (with respect to the concave wall). Position 2 is located in an upwash region at the channel radial centerline. Position 3 is located near the concave wall near the base of a downwash region (with respect to the concave wall). Position 4 is located near the concave wall directly under a vortex. Position 5 is located in a downwash region at the channel radial centerline.

The streamwise mean velocity and longitudinal turbulence intensity were each determined two ways. With a digital method, the instantaneous streamwise velocity was calculated for each of 20000 samples. The average of the 20000 instantaneous velocities is then the mean streamwise velocity. The longitudinal velocity fluctuation intensity was then determined as the root-mean-square of the instantaneous longitudinal velocities. With an analog method, mean velocity and longitudinal turbulence intensity were calculated based on mean and rms voltages integrated over 10 second time intervals.

Figures 78 and 79 show plots of the average streamwise velocity using digital and analog techniques, respectively, versus De for the five probe positions listed in Table 5. The digital and analog streamwise velocities coincide nicely. All positions show a velocity increase that is generally linear with De . The behavior of the velocity for positions 1, 3 and 4 varies because spatial locations of upwash regions vary with De . The proximity of positions 1, 3 and 4 to the concave wall causes associated velocity magnitudes to be generally lower than for positions 2 and 5.

Figures 80 and 81 show longitudinal turbulence intensities determined using digital and analog techniques, respectively, versus De for the five probe positions. The digital and analog data coincide with each other reasonably well. For $De \leq 160$, the intensities are very small for all five

probe positions . At De higher than 160, intensities generally increase with De approximately linearly. Positions 2 and 5 have lower intensities because they are farther away from the effects of the concave surface than positions 1, 3 and 4.

Normalized longitudinal turbulence intensities are shown in Figures 82 and 83. Digital and analog data coincide well at most all De , except for values of $De=50$ when the digitally obtained values are incorrectly indicated to be too high. For De higher than 160, longitudinal turbulence intensity increases with De . The variations at position 4 are due to time-averaged spatial location variance of the upwash regions with De . Over this range of De , values for probe positions 2 and 5 are lower than others because positions 2 and 5 are farther away from the concave wall.

Figure 84 gives settings used on the dynamic signal analyzer to obtain power spectra over frequencies from 0.1 to 25 Hz. Summaries of observed local frequency maxima are given in Figures 85 through 89 for $De=50$ to $De=200$ for each of the five probe positions 1 through 5, respectively. Frequencies of 1 Hz to 2 Hz, 5 Hz to 6 Hz, 8 Hz, and 20 Hz to 21 Hz exist for all five probe positions. An additional frequency of about 3 Hz exists for probe positions 3, 4 and 5. Figures 90 and 91 are two examples of power spectra used to obtain such information. Figures 85 through 89 were compiled from data presented in Figures 92 through 151, which show individual frequency spectra for all five probe positions at De from 50 to 450.

Figure 152 gives settings used on the dynamic signal analyzer to obtain high frequency power spectra over frequencies from 0.1 Hz to 10.0 kHz. Figure 153 shows the average of five power spectra at probe position 2 at $De=170$. Clearly evident is a principal peak between 90 Hz and 100 Hz. Also apparent are harmonic peaks at about 180 Hz, 280 Hz and 400 Hz. Such variations are believed to be due to twisting [Ref. 18]. Figure 154 shows a plot of principal peak magnitudes versus De for all five probe positions at De from 150 to 200. In this figure, peak magnitudes are

shown to be dependent on De and probe position, where peak magnitudes generally increase with increasing De . The highest peak magnitudes observed are for $De=180$ at probe position 4 and for $De=200$ at probe position 1. Such behavior suggests higher instability near the upwash region close to the concave surface. Figure 154 was compiled from data shown in Figures 155 through 214 which are individual power spectra for all five probe positions at De from 50 to 450.

D. ANALYSIS OF APPEARANCE AND DISAPPEARANCE PHENOMENA FROM FLOW VISUALIZATION RESULTS

Appearances and disappearances of already developed vortex pairs along with accompanying alterations of spanwise vortex pair spacing are discussed by Ligrani et al. [Ref. 6] At the time of this writing, there is evidence of two types of appearance events and four types of disappearance events. Appearance events are categorized as growth or splitting. Growth events occur when vortex pairs emerge from the flow region near the concave wall. Splitting events occur when one vortex pair is rearranged into two vortex pairs. Splitting is also observed after a vortex pair decreases in size with simultaneous emergence of two new vortex pairs nearby from flow near the concave surface.

Disappearance events are categorized as engulfment, cancellation, merging and collapse. Engulfment refers to the absorption of a vortex pair by another vortex pair where contact occurs between vortices with the same sign of vorticity. Cancellation occurs when vortices of the opposite sign collide. Typically, these vortex pairs rock slightly toward each other as they move together. With merging, a smaller vortex pair merges into the upwash region of a larger pair. Collapse events are evidenced by the disappearance of a pair into the flow region near the concave surface.

Figure 215 shows a new type of splitting event which was unrecognized prior to the present work. Here, the center vortex pair in the field of view shrinks in size until it disappears into the flow near the concave surface while two new vortex pairs emerge simultaneously from the base of

the shrinking vortex pair. The sequence starts at the top with frame 1. Each photo shows the full channel height, 12.7 mm, and a channel width of 50.8 mm, and gives a spanwise/radial plane view with the concave surface at the bottom and streamwise flow into the plane of the page. In frames 1 through 5 the center vortex pair begins to shrink. In frame 6, dark spots begin to form on each side at the base of the shrinking vortex pair. Both spots rapidly grow in frames 7 and 8 while the original vortex pair shrinks even more. In frame 9 the original vortex pair is no longer evident. In frame 10 the two new vortex pairs are fully developed. In frames 11 and 12 the larger of the two new vortex pairs rocks to the left. Also in frames 11 and 12, the new vortex pair on the left begins to shrink toward the concave wall. The larger of the two new vortex pairs is now displaced to the left.

Figure 216 shows a collapsing type of disappearance event. Here, the second vortex pair from the right will shrink until it disappears into the flow near the concave wall. Frames 1 through 4 show the smallest vortex pair present growing to full size. In frames 5 and 6, it twists slightly counterclockwise and begins to shrink. Frames 7 through 10 then show the rapid collapse into the flow near the concave wall by the small vortex pair and then the translation to the left, as it fills the void left behind, by the large vortex pair at the right side of the frames. Frames 11 and 12 also show the center vortex pair enlarging to occupy a larger space.

Figure 217 shows a time history of appearance and disappearance events observed over an 80 second interval at $De=100$ and 115° from the start of curvature as observed on the right side of the channel. Figure 218 gives magnified views of three regions of Figure 217. The scale on these three time lines allows determination of the time intervals between discrete events. The time lines show that most appearance events are followed by disappearance events, and vice-versa.

Frequencies of appearance and disappearance events are given in Tables 2, 3 and 4 in dimensional and non-dimensional forms. The tabular data from Tables 3 and 4 is also shown in Figures 219 to 232. Figures 219, 221 and 223 present frequencies of appearance and disappearance events versus De for angles of 85° , 95° and 105° from the start of curvature respectively. Figures 220, 222 and 224 present the same information in non-dimensional form as in Figures 219, 221 and 223 respectively. Figures 225 and 226 present frequencies of appearance and disappearance events versus θ at $De=75$ and $De=100$ respectively. Figure 227 shows frequencies of total appearance and total disappearance events versus De for angles from 85° to 135° after the start of curvature. Figures 228 and 229 provide curve identification for Figure 227. Figures 230, 231 and 232 present the same information in non-dimensional form as in Figures 227, 228 and 229 respectively. Frequencies of appearance and disappearance events generally increase with increasing De for Figures 219 through 224 and 227 through 232. Figure 225 shows that frequencies of appearance and disappearance events generally increase with increasing θ at $De=75$. Figure 226 shows that frequencies of appearance and disappearance events generally decrease with increasing θ at $De=100$. In all cases, growth type appearance events and collapse type disappearance events occur most often. In Figures 219 and 225, local minima of total appearance and total disappearance event frequencies occur at $De=125$ and 85° after the start of curvature and $De=75$ and 115° after the start of curvature respectively.

V. SUMMARY AND CONCLUSIONS

Instabilities in curved channel flow were studied over conditions ranging from fully laminar to fully turbulent. Primary instabilities in the form of regularly spaced Dean vortices develop in the flow due to centrifugal effects. After the primary instabilities, secondary instabilities develop which affect the behavior of the vortices. These secondary instabilities take the form of undulation and twisting of the vortices, plus phenomena where vortex pairs appear and disappear. Two curved channels with 40 to 1 aspect ratios were used to obtain information on these instabilities.

Time-averaged total pressure, mean velocity, velocity perturbation and vorticity component surveys were obtained using a miniature five-hole pressure probe at De from 50.4 to 424.8 at a streamwise location in the second straight section located downstream of the curved portion of the channel. At $De \leq 75$, results show that flow is spanwise uniform. As De increases, results provide evidence of vortex pairs located at spanwise locations across the measurement plane. At De higher than about 300, flow again becomes spanwise uniform.

Time-averaged and spatially resolved flow correlations were obtained using a 12 element hot-film probe located 120° from the start of curvature at $y/d=1.0$ (flush with the convex wall) for De from 49.2 to 400.3. Six probe elements were used in two different probe configurations with element spacings of 6.35 mm and 3.18 mm respectively. In all cases, correlation magnitudes decrease as the spanwise distance from the reference probe increases. Sign variations of correlations versus z/d evidence regions of positive and negative correlation between different parts of vortex pair structures. For the first configuration, average (over all gages employed) normalized rms voltage increases as De increases from $De=150$ to $De=200$. Scaled, normalized local rms voltages versus z/d

show spatially varying structures at De from 150 to 350. Length scales indicate spatially varying structures at De from 100 to 250. Qualitatively, the second probe configuration is in close agreement with the first configuration.

Power spectra, streamwise velocity and longitudinal turbulence intensity surveys were obtained using a hot-wire probe at De from 50 to 450. Each survey was obtained at each of five positions in the spanwise/radial plane 120° from the start of curvature. Digital and analog methods were used to determine streamwise velocity and longitudinal turbulence intensity. Results from both methods are in close agreement. Streamwise velocity generally increases linearly over the range of De . The behavior of velocity for positions near the concave wall varies because spatial locations of upwash regions with respect to the concave wall vary with De . Longitudinal turbulence intensity increases with De higher than 160. Positions near the concave wall have higher intensities than the positions at the radial centerline. Observed local frequency maxima from low frequency power spectra evidence frequencies of 1 Hz to 2 Hz, 5 Hz to 6 Hz, 8 Hz, and 20 Hz to 21 Hz for all five probe positions. Local frequency maxima also exist at 3 Hz for probe positions away from upwash regions. For high frequency power spectra, principle peak magnitudes increase with increasing De . Highest peak magnitudes occur at positions near the base of the upwash region which evidence twisting [Ref. 18].

Frequencies of events where vortex pairs appear and disappear are obtained for De from 60 to 150. Time lines showing these events are shown at $De=100$. Still photography time lapse sequences are presented showing the collapse of a vortex pair and one type of splitting of a vortex pair. These data were obtained for each De from spanwise/radial plane observations which were video tape recorded at angles from 85° to 135° from the start of curvature. Time line results indicate that should an appearance event occur, the likelihood is that a disappearance event will

occur next, and vice-versa. Frequencies of total appearance and total disappearance events are nearly equal in all cases. Frequencies generally increase with increasing De . Growth type of appearance events and collapse type of disappearance events occur most often. Highest total appearance and total disappearance frequencies observed are at $De=125$ and 95° after the start of curvature. Local minima of total appearance and total disappearance event frequencies occur at $De=125$ and 85° after the start of curvature and at $De=75$ and 115° after the start of curvature.

APPENDIX A - UNCERTAINTY ANALYSIS

The uncertainty analysis presented below for sections A. and B. is taken from Baun [Ref. 9]. The present study utilizes much of the same peripheral equipment and studies flow situations similar to those studied by Baun in the same channels.

A. DEAN NUMBER UNCERTAINTY

The Dean number is a function of orifice pressure drop. The uncertainty for the pressure drop across the orifice is analyzed at $De=150$.

1. Pressure Drop Uncertainty

$$\delta \Delta P_{or} = \pm 0.001 \text{ in. H}_2\text{O}$$

2. Mass Flow Rate Uncertainty

$$\delta A_{or} = \pm 0.012 \text{ in}^2$$

$$\delta K = \pm 0.001$$

$$\delta Y = \pm 0.02$$

$$\delta \rho = \pm 0.002 \text{ lbm/ft}^3$$

$$\delta \dot{m} = \pm 0.0004 \text{ lbm/sec (95\% confidence level)}$$

$$\delta A_{ch} = \pm 0.0052 \text{ in}^2$$

$$\delta De = \pm 4.4 \text{ (95\% confidence level)}$$

B. FIVE-HOLE PROBE VELOCITY MEASUREMENT UNCERTAINTY

Five-hole probe velocity component uncertainties are derived from calibration uncertainties and measurement uncertainties. Values at $De=100.3$, $y/d=0.5$ and $z/d=0.0$ are listed below. The probe calibration uncertainty is for yaw= -10° and pitch= 0.0° .

1. Validyne Transducer Calibration Uncertainty

$$\delta P_{manometer} = \pm 0.001 \text{ in. H}_2\text{O}$$

$$\delta E = \pm 0.0007 \text{ Volts}$$

$\delta\bar{C}=\pm 0.000072$ in. $H_2O/Volt$ (bias error is disregarded because pressure differentials are calculated)

2. Probe Calibration Uncertainty

$\delta\bar{E}=\pm 0.0004$ Volts

$\delta P_1=\pm 0.0006$ in. H_2O

$\delta P_2=\pm 0.0001$ in. H_2O

$\delta P_3=\pm 0.0005$ in. H_2O

$\delta P_4=\pm 0.0002$ in. H_2O

$\delta P_5=\pm 0.0003$ in. H_2O

$\delta P_s=\pm 0.00004$ in. H_2O

$\delta P_t=\pm 0.0007$ in. H_2O

$\delta P=\pm 0.00015$ in. H_2O

$\delta C_{py}=\pm 0.025$

$\delta C_{pp}=\pm 0.011$

$\delta C_{pts}=\pm 0.045$

$\delta K_y=\pm 0.004$ degrees⁻¹

$\delta K_p=\pm 0.004$ degrees⁻¹

$\delta K_{ts}=\pm 0.003$ degrees⁻¹

3. Curved Channel Measurement Uncertainty

$\delta\bar{E}=\pm 0.0007$ Volts

$\delta\bar{C}=\pm 0.000072$ in. $H_2O/Volt$

$\delta P_1=\pm 0.0002$ in. H_2O

$\delta P_2=\pm 0.0002$ in. H_2O

$\delta P_3=\pm 0.0002$ in. H_2O

$\delta P_4=\pm 0.0002$ in. H_2O

$\delta P_5=\pm 0.0002$ in. H_2O

$\delta\bar{P}=\pm 0.0001$ in. H_2O

$\delta C_{py}=\pm 0.134$

$\delta C_{pp}=\pm 0.141$

$\delta yaw=\pm 1.33^\circ$

$\delta pitch=\pm 1.4^\circ$

$$\delta(P_t - P_s) = \pm 0.0004 \text{ in. H}_2\text{O}$$

$$\delta U = \pm 0.063 \text{ m/s}$$

$$\delta U_\theta = \pm 0.062 \text{ m/s}$$

$$\delta U_r = \pm 0.062 \text{ m/s}$$

$$\delta U_z = \pm 0.030 \text{ m/s}$$

C. HOT-WIRE PROBE VELOCITY MEASUREMENT UNCERTAINTY

The uncertainty associated with the hot-wire probe velocity is derived from probe calibration uncertainty and the uncertainty of voltages produced by the probe and bridge network.

1. Probe Calibration Uncertainty

$$\delta B = \pm 0.0216 \text{ Volts}^2 \text{ s}^{.45} \text{ m}^{-.45}$$

$$\delta \bar{E}_0 = \pm 0.0005 \text{ Volts}$$

$$\delta EOC = \pm 0.0005 \text{ Volts}$$

$$\delta EOM = \pm 0.0005 \text{ Volts}$$

$$\delta \Delta P = \pm 0.0005 \text{ in. H}_2\text{O}$$

2. Curved Channel Measurement Uncertainty

$$\delta E_0 = \pm 0.0005 \text{ Volts}$$

$$\delta U_x = \pm 0.048 \text{ m/s}$$

APPENDIX B - SOFTWARE DIRECTORY

Programs written in Hewlett Packard BASIC 4.0 language for the HP 300 Series computers utilized in these studies are listed. A description of what the program does, significant user inputs required and significant output is provided.

A. GENERAL PROGRAMS

DEAN15M Calculates the Dean number as described in Chapter II.

user input

- barometric pressure
- ambient temperature
- orifice pressure drop

output

- expansion coefficient Y
- flow coefficient K
- mass flow rate
- channel Reynolds number
- Dean number
- bulk velocity

B. FIVE-HOLE PRESSURE PROBE PROGRAMS

C4 Data file of calibration coefficients: pitch, yaw, C_{py} , C_{pp} , C_{pt} , C_{ps} , and C_{pts} .

P4 Data file of calibration pressures: pitch, yaw, P_1 , P_2 , P_3 , P_4 , and P_5 .

FIVEHOLE Acquires pressure measurements at each of the five ports and directs probe positioning.

user input

- date/time
- estimated dean number
- orifice size
- number of spanwise and radial points
- spanwise and radial resolutions
- spanwise and radial starting positions
- wait time for pressure to stabilize
- number of transducers
- number of samples per channel

- number of standard deviations
- calibration coefficients
- ambient pressure

output

- **FIVxxx** data file with: $y, z, C_{pp}, C_{py}, P_1, \bar{P}, De$
- **FIVPxxx** data file with $y, z, P_1^p, P_2^p, P_3^p, P_4^p, P_5^p, \bar{P}, De$
- average De

PADJUST Corrects spatial resolution described in Chapter III.

user input

- **FIVPxxx** data file
- Y_{len}
- z_{len}

output

- **FIVPxxxA** data file with $y, z, C_y, C_p, P_1, \bar{P}, De$

ORIENT Orients the five-hole probe in the flow such that $P_2=P_3$ at yaw=0° and pitch=0°

user input

- number of samples per channel
- number of standard deviations
- transducer calibration coefficients
- barometric pressure

output

- mean velocity
- C_y
- C_p
- $P_1^p, P_2^p, P_3^p, P_4^p, P_5^p$

VELOCITY1 Computes the three mean velocity components

user input

- **C4** data file
- **P4** data file
- number of yaw and pitch points
- **FIVPxxxA** data file
- pitch angle offset (4.3°)
- yaw angle offset (1.0°)
- y and z direction downwash velocity corrections (0.011, 0.011)

output

- **Vxxx** data file with $y, z, P_t, U, U_\theta, U_r, U_z$

Ux1 Plots mean streamwise velocity contours

user input

- **Vxxx** data file

- number and spacing of contour levels

output

- contour plot with level table

PTOT1 Plots Pamb minus Ptotal contours

user input

- Vxxx data file
- number and spacing of contour levels

output

- contour plot with level table

CCPF1 Calculates CCPF

user input

- Vxxx data file

output

- PFxxx data file with y, z, U_{ccpf} , $U_x - U_{ccpf}$

UX_UCCPF1 Plots streamwise velocity perturbations

user input

- PFxxx data file
- number and spacing of contour levels

output

- contour plot with level table

VORTICITY Computes the three mean vorticity components

user input

- Vxxx data file

output

- VVxxx data file with y, z, ω_θ , ω_r , ω_z

VORTICITY1 Plots any desired vorticity contour

user input

- VVxxx data file
- number and spacing of contour levels
- minimum threshold intensity to plot
- type of vorticity to plot (x,y or z)

output

- contour plot with level table

3DPLOT1xxx Plots a 3-D array of up to seven of the following type of plots. **Um** plots streamwise velocity. **Ucc** plots velocity perturbations. **Pt** plots P_{amb} minus P_{total} . **Vx** plots ω_θ . **Vy** plots ω_r . **Vz** plots ω_z . All user inputs are identical to those listed in the previously mentioned plotting programs with the additional information needed, i.e., the number of plots and the identification of all data files to plot. Output is a 3-D plot of all graphs.

C. 12 ELEMENT HOT-FILM PROBE PROGRAMS

12FILM1 Acquires raw and conditioned bridge output voltage for six active hot-film probes.

user input

- active probe numbers
- De

output

- overall sampling frequency
- individual channel sampling frequency
- **FDATAxxx** data file with active probes, raw and conditioned voltages

COV2 Analyzes data acquired by **12FILM1**

user input

- **FDATAxxx** data file

output

- mean raw voltages
- conditioned rms voltages
- normalized rms voltages
- covariances
- correlations
- correlation versus z/d plots for increasing and decreasing z

D. HOT-WIRE PROBE PROGRAMS

PROBE_003 Calibration data for the hot-wire probe containing: T_{cal} , A , ϕ_{hr} , n , B , EOC , U_{lim} and coefficients $A0$, $A1$, $A2$, and $A3$

CNT_BUF_AD Data file used to configure the HP 6944A multiprogrammer supplied with the instrument

HOTWIRESPM Computes instantaneous streamwise velocities and velocity fluctuations. Stores 5000 instantaneous velocities in a data file.

user input

- sampling frequency
- barometric pressure
- ambient temperature
- bulk velocity
- bridge output zero offset
- signal conditioner gain
- PROBE 003 data file
- analog mean voltage
- analog rms voltage

output

- WDATxxxxx data file containing 5000 U_0
- channel Re
- De
- digital average U_0
- digital u'^2

HOTWIREVEL Computes normalized velocities both digital and analog.
Plots U_0 versus time.

user input

- WDATxxxxx data file
- U bulk for the given De

output

- analog \bar{U}
- analog u'^2
- analog and digital u'
- analog and digital u'/\bar{U}
- analog and digital u'^2/\bar{U}^2
- plot of U_0

APPENDIX C - DYNAMIC SIGNAL ANALYZER OPERATION

The following sections list sequential operations to acquire frequency response and power spectra plots using the Hewlett Packard 3562A Dynamic Signal Analyzer. Keys with [] codes are permanent hard keys. Keys with { } codes are user input soft keys with CRT menus. Keys with () codes are permanent hard keys shifted to alpha-numeric code.

A. FREQUENCY RESPONSE

A power spectrum plot from frequency response is obtained as follows:

- Power up the dynamic signal analyzer
- Connect the input BNC connector
- [MEAS MODE]
- {LINEAR RES}
- [SELECT MEAS]
- {FREQ RESP}
- [MEAS DISPLAY]
- {POWER SPEC1}
- [FREQ]
- {FREQ SPAN}
- [0][.][1][,][2][5]
- {Hz}

This sets up a frequency response from 0.1 to 25 Hz.

- [SOURCE]
- {SOURCE OFF}
- [WINDOW]
- {HANN}
- [AVG]
- {STABLE (MEAN)}
- {NUMBER AVGS}
- [5]

This sets up 5 stable averages.

- [A]
- [SINGLE]
- [COORD]
- {MAG (LOG)}
- {NEXT}
- {LOG X}
- {RETURN}
- [UNITS]
- {P SPEC UNITS}
- {V²/Hz (PSD)}
- {RETURN}
- {Hz (SEC)}
- {TRACE TITLE}

- (D)(E)(A)(N)(BL)(=)(BL)[1][0][0]
- {ENTER}

This makes the title DEAN = 100.

- [SCALE]
- {X FIXD SCALE}
- [0][.][1][,][2][5]
- {Y FIXD SCALE}
- [0][.][0][0][0][0][0][0][0][0][1][,][1][0][0]
- [STATE/TRACE]

This checks the setup.

- [STATE/TRACE]
- [START]

Wait until the CRT indicates the measurement is complete.

Ensure the plotter is ready.

- [PLOT]

B. POWER SPECTRUM

A power spectrum plot is obtained as follows:

- Power up the dynamic signal analyzer
- Connect the input BNC connector
- [MEAS MODE]
- {LINEAR RES}
- [SELECT MEAS]
- {POWER SPEC}
- {CH1 ACTIVE}
- [MEAS DISPLAY]
- {POWER SPEC1}
- [FREQ]
- {FREQ SPAN}
- [0][.][0][0][0][1][,][1][0]
- {kHz}

This sets up a frequency response from 0.1 to 10000 Hz.

- [SOURCE]
- {SOURCE OFF}
- [WINDOW]
- {HANN}
- [AVG]
- {STABLE (MEAN)}
- {NUMBER AVGS}
- [5]

This sets up 5 stable averages.

- [A]
- [SINGLE]
- [COORD]
- {MAG (LOG)}
- {NEXT}
- {LOG X}

- {RETURN}
- [UNITS]
- {P SPEC UNITS}
- {V²/Hz (PSD)}
- {RETURN}
- {Hz (SEC)}
- {TRACE TITLE}
- (D)(E)(A)(N)(BL)(=)(BL){1}[0][0]
- {ENTER}

This makes the title DEAN = 100.

- [SCALE]
- {X FIXD SCALE}
- [0][.][1][,][1][0][0][0][0]
- {Y FIXD SCALE}
- [0][.][0][0][0][0][0][0][0][0][1][,][1][0][0]
- [STATE/TRACE]

This checks the setup.

- [STATE/TRACE]
- [START]

Wait until the CRT indicates the measurement is complete.

Ensure the plotter is ready.

- [PLOT]

APPENDIX C - TABLES

Table 1. 12 ELEMENT HOT-FILM PROBE LOCATIONS

PROBE #	z/d	REGION CHARACTERISTIC
1	4.48	POSITIVE VORTICITY
2	4.73	DOWNWASH
3	4.98	NEGATIVE VORTICITY
4	5.23	UPWASH
5	5.48	POSITIVE VORTICITY
6	5.73	DOWNWASH
7	5.98	NEGATIVE VORTICITY
8	6.23	UPWASH
9	6.48	POSITIVE VORTICITY
10	6.73	POSITIVE VORTICITY
11	6.98	DOWNWASH
12	7.23	NEGATIVE VORTICITY

Table 2. VORTEX PAIR APPEARANCE AND DISAPPEARANCE OCCURRENCES

Dean	θ	APPEARANCES			DISAPPEARANCES					Time
		Grow	Split	Total	Coll.	Merge	Engulf	Cancel	Total	
60	85	0	0	0	0	0	0	0	0	54
	95	0	0	0	0	0	0	0	0	56
	105	0	0	0	0	0	0	0	0	56
	115	39	0	39	39	0	0	0	39	53
	125	5	0	5	5	0	0	0	5	64
	135	47	0	47	43	1	0	2	46	48
75	85	28	0	28	28	0	0	0	28	60
	95	67	0	67	68	0	0	2	70	60
	105	91	1	92	83	1	0	0	84	61
	115	37	9	46	21	27	0	3	51	64
	125	102	1	103	54	18	7	24	103	60
	135	64	1	65	33	20	5	12	70	58
100	85	169	3	172	131	25	0	1	157	57
	95	136	10	146	116	33	3	9	161	59
	105	119	6	125	43	30	15	39	127	59
	115	122	9	131	36	36	26	25	123	60
	125	111	0	111	23	31	28	23	105	55
125	85	62	6	68	23	19	13	5	60	58
	95	212	9	221	84	64	30	24	202	58
	105	83	5	88	20	20	23	11	74	60
150	85	146	9	155	63	45	42	10	160	59
	95	146	13	159	73	32	54	20	179	61

Table 3. VORTEX PAIR APPEARANCE AND DISAPPEARANCE FREQUENCIES

Dean	θ	APPEARANCES			DISAPPEARANCES				
		Grow	Split	Total	Collapse	Merge	Engulf	Cancel	Total
60	85	0.00	0.00	0.00	0.00	0.00	0.00	0.00	0.00
	95	0.00	0.00	0.00	0.00	0.00	0.00	0.00	0.00
	105	0.00	0.00	0.00	0.00	0.00	0.00	0.00	0.00
	115	0.74	0.00	0.74	0.74	0.00	0.00	0.00	0.74
	125	0.08	0.00	0.08	0.08	0.00	0.00	0.00	0.08
	135	0.98	0.00	0.98	0.90	0.02	0.00	0.04	0.96
75	85	0.47	0.00	0.47	0.47	0.00	0.00	0.00	0.47
	95	1.12	0.00	1.12	1.13	0.00	0.00	0.03	1.16
	105	1.49	0.02	1.51	1.36	0.02	0.00	0.00	1.38
	115	0.58	0.14	0.72	0.33	0.42	0.00	0.05	0.80
	125	1.70	0.02	1.72	0.90	0.30	0.12	0.40	1.72
	135	1.10	0.02	1.12	0.57	0.35	0.09	0.21	1.22
100	85	2.96	0.05	3.01	2.30	0.44	0.00	0.02	2.76
	95	2.31	0.17	2.48	1.97	0.56	0.05	0.15	2.73
	105	2.02	0.10	2.12	0.73	0.51	0.25	0.66	2.15
	115	2.03	0.15	2.18	0.60	0.60	0.43	0.42	2.05
	125	2.02	0.00	2.02	0.42	0.56	0.51	0.42	1.91
125	85	1.07	0.10	1.17	0.40	0.33	0.22	0.09	1.04
	95	3.66	0.16	3.82	1.45	1.10	0.52	0.41	3.48
	105	1.38	0.08	1.46	0.33	0.33	0.38	0.18	1.22
150	85	2.48	0.15	2.63	1.07	0.76	0.71	0.17	2.71
	95	2.39	0.21	2.60	1.20	0.53	0.89	0.33	2.95

Table 4. VORTEX PAIR APPEARANCE AND DISAPPEARANCE NON-DIMENSIONAL FREQUENCIES

Dean	θ	APPEARANCES			DISAPPEARANCES				
		Grow	Split	Total	Collapse	Merge	Engulf	Cancel	Total
60	85	0.00	0.00	0.00	0.00	0.00	0.00	0.00	0.00
	95	0.00	0.00	0.00	0.00	0.00	0.00	0.00	0.00
	105	0.00	0.00	0.00	0.00	0.00	0.00	0.00	0.00
	115	.057	0.00	.057	.057	0.00	0.00	0.00	.057
	125	.006	0.00	.006	.006	0.00	0.00	0.00	.006
	135	.076	0.00	.076	.070	.002	0.00	.003	.075
75	85	.029	0.00	.029	.029	0.00	0.00	0.00	.029
	95	.069	0.00	.069	.070	0.00	0.00	.002	.072
	105	.093	.001	.094	.084	.001	0.00	0.00	.085
	115	.036	.009	.045	.020	.026	0.00	.003	.049
	125	.105	.001	.106	.056	.019	.007	.025	.107
	135	.068	.001	.069	.035	.021	.005	.013	.074
100	85	.138	.003	.141	.107	.020	0.00	.001	.128
	95	.107	.008	.115	.091	.026	.002	.007	.126
	105	.094	.005	.099	.034	.024	.012	.031	.101
	115	.095	.007	.102	.028	.028	.020	.019	.095
	125	.094	0.00	.094	.019	.026	.024	.019	.088
125	85	.040	.004	.044	.015	.012	.008	.003	.038
	95	.136	.006	.142	.054	.041	.019	.015	.129
	105	.052	.003	.055	.012	.012	.014	.007	.045
150	85	.077	.005	.082	.033	.024	.022	.005	.084
	95	.074	.007	.081	.037	.016	.027	.010	.090

Table 5. HOT-WIRE PROBE SENSING LOCATIONS RELATIVE TO
VORTEX PAIR STRUCTURE

PROBE POSITION	z/d	y/d	REGION CHARACTERISTIC
1	6.30	0.10	UPWASH BASE
2	6.30	0.50	UPWASH CENTER
3	6.95	0.10	DOWNWASH BASE
4	6.60	0.10	BENEATH VORTEX
5	6.95	0.50	DOWNWASH CENTER

Table 6. HOT-WIRE SPECTRA SIGNAL CONDITIONER SETTINGS

Type meas.	Dean	SIGNAL CONDITIONING UNITS					
		1. Analog \bar{E}			2. Analog e'		
		Filter		Gain	Filter		Gain
		High	Low		High	Low	
Data acq.	<275	DC	10 kHz	2.0	0.1 Hz	1.0 kHz	500*
	>275	DC	3 kHz	2.0			
LF plot	All	0.1 Hz	0.1 kHz	100			
HF plot		0.1 Hz	3 kHz	100			

* Or as high as possible to not saturate the rms unit

APPENDIX E - FIGURES

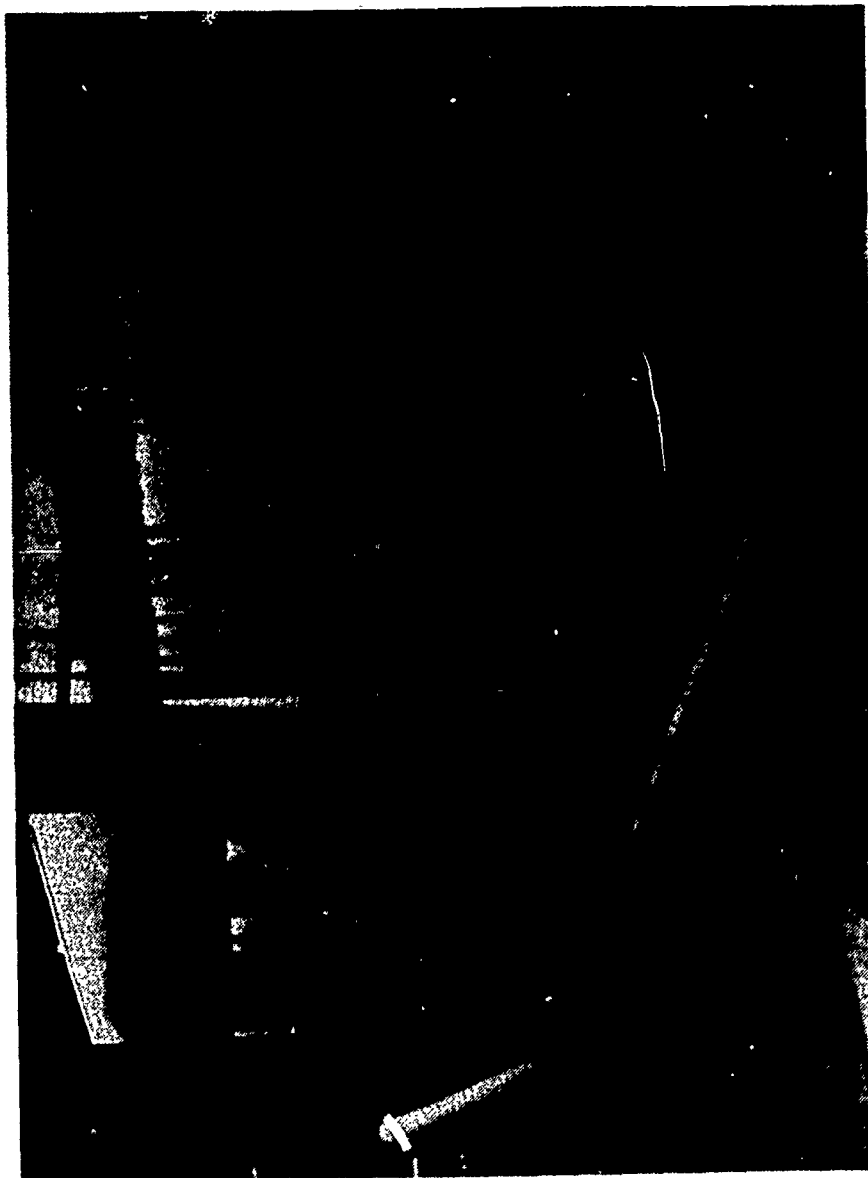


Figure 1. Transparent Curved Channel



Figure 2. Blower Assembly

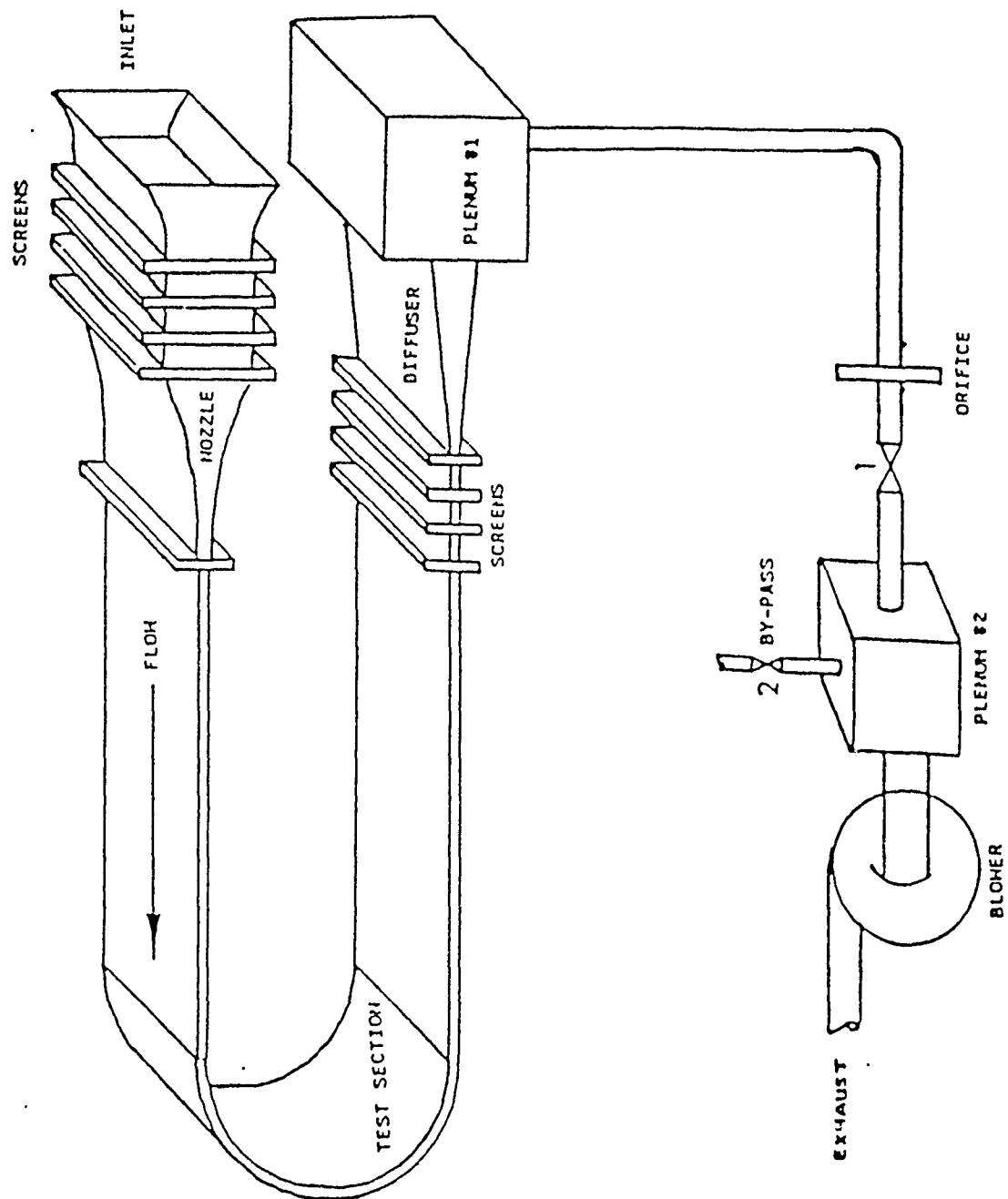


Figure 3. Curved Channel Test Facility Schematic

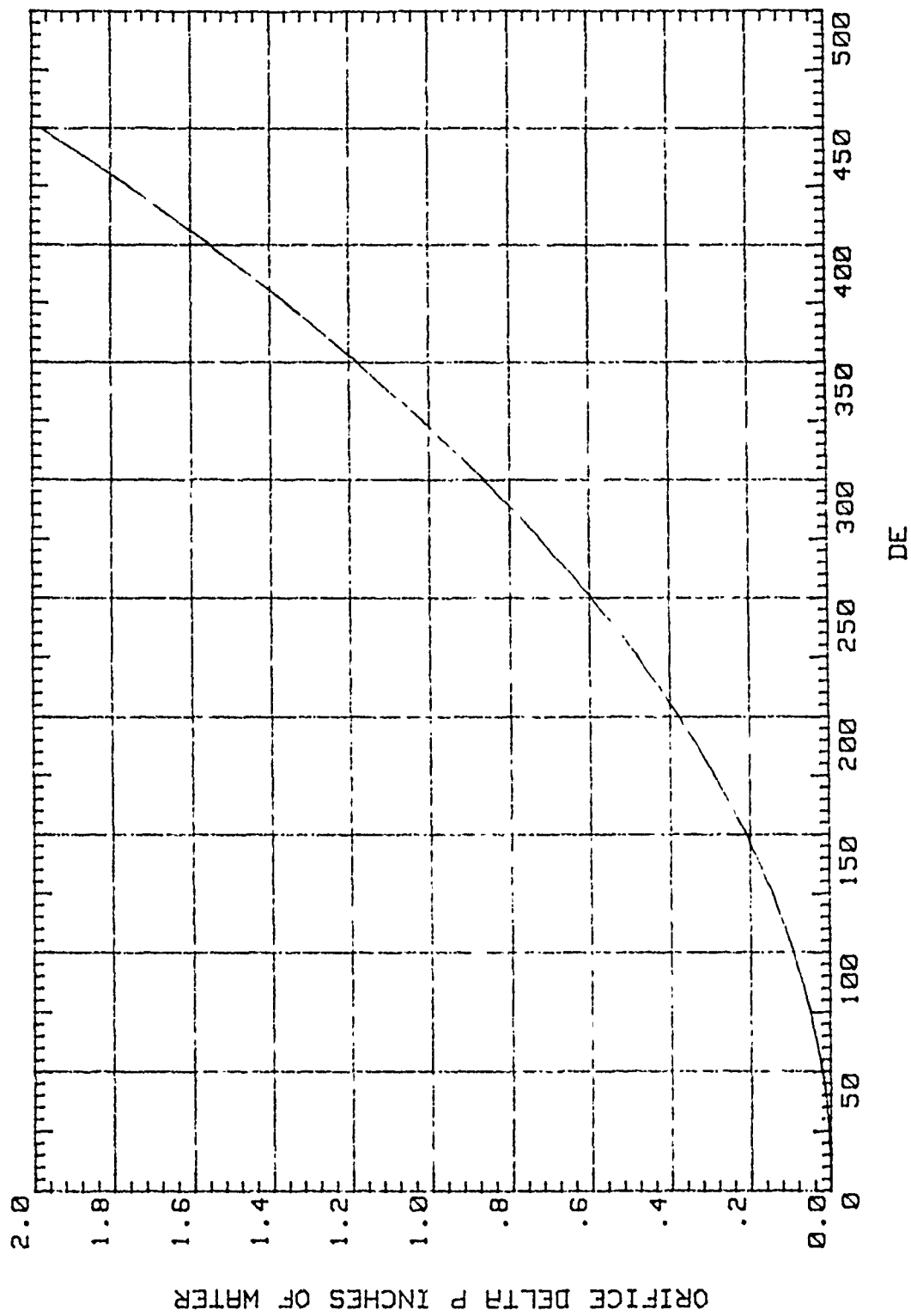


Figure 4. Orifice Pressure Drop vs. De



Figure 5. Five-hole Pressure Probe Tip

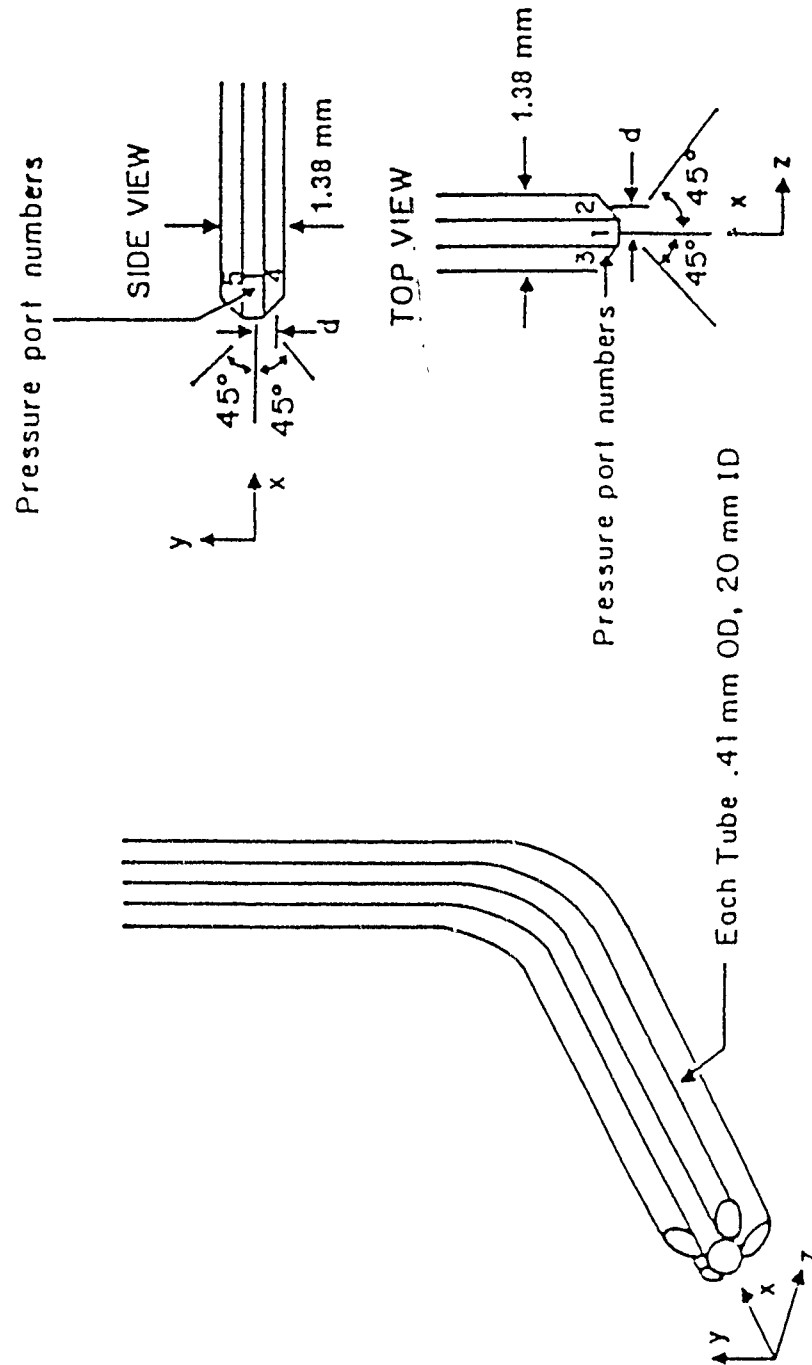


Figure 6. Five-hole Pressure Probe Geometry

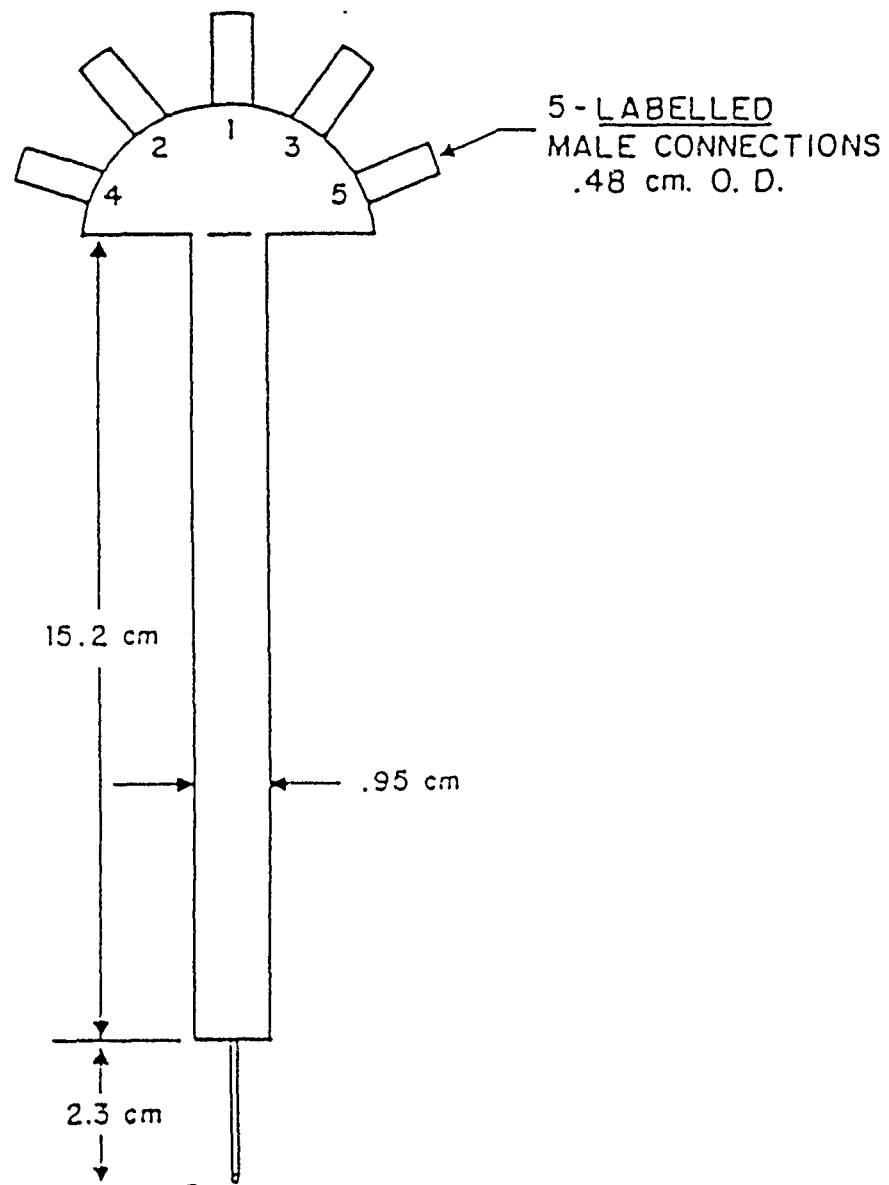


Figure 7. Five-hole Pressure Probe Dimensions and Connections

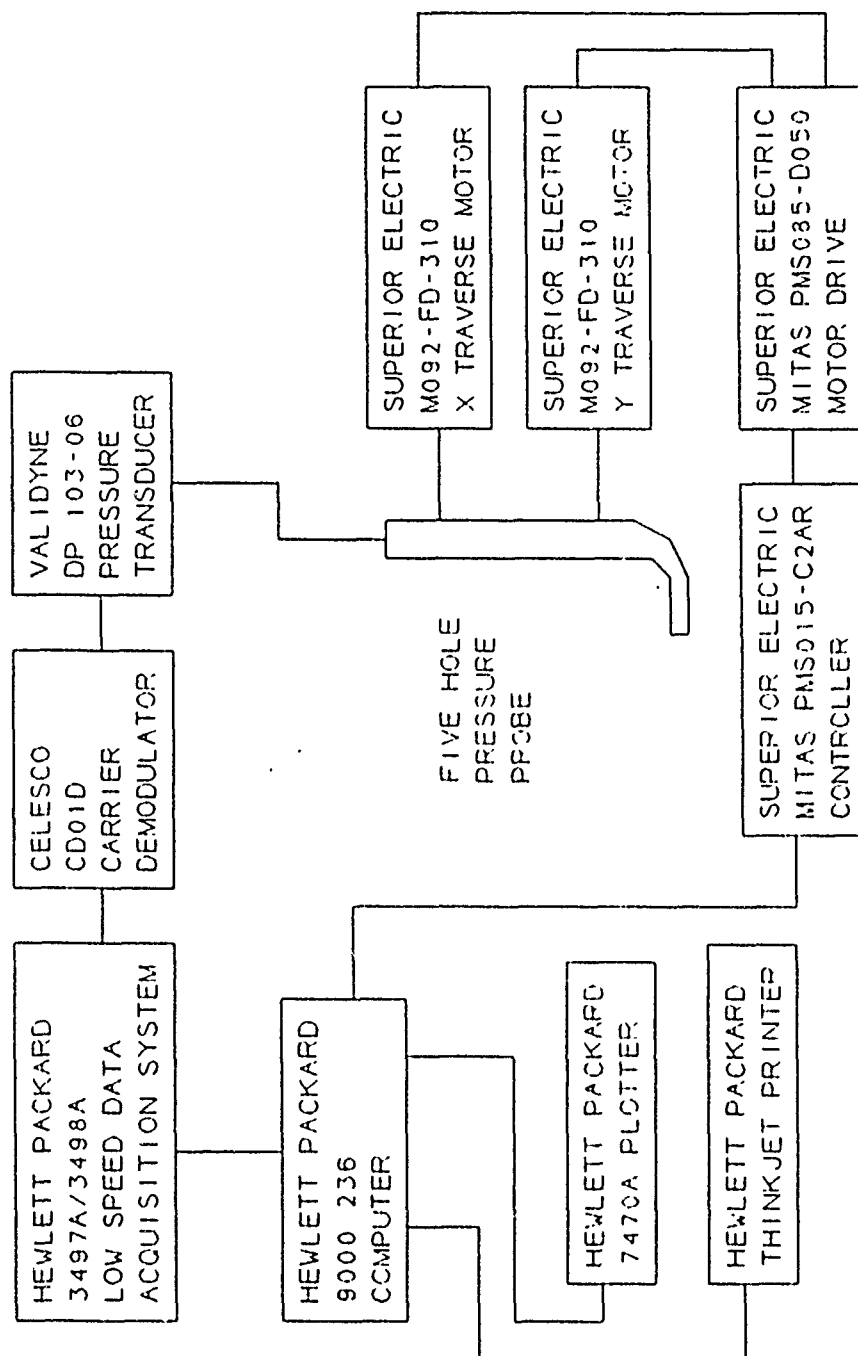


Figure 8. Five-hole Survey Data Acquisition and Traversing Control



Figure 9. 12 Element Hot-film Probe

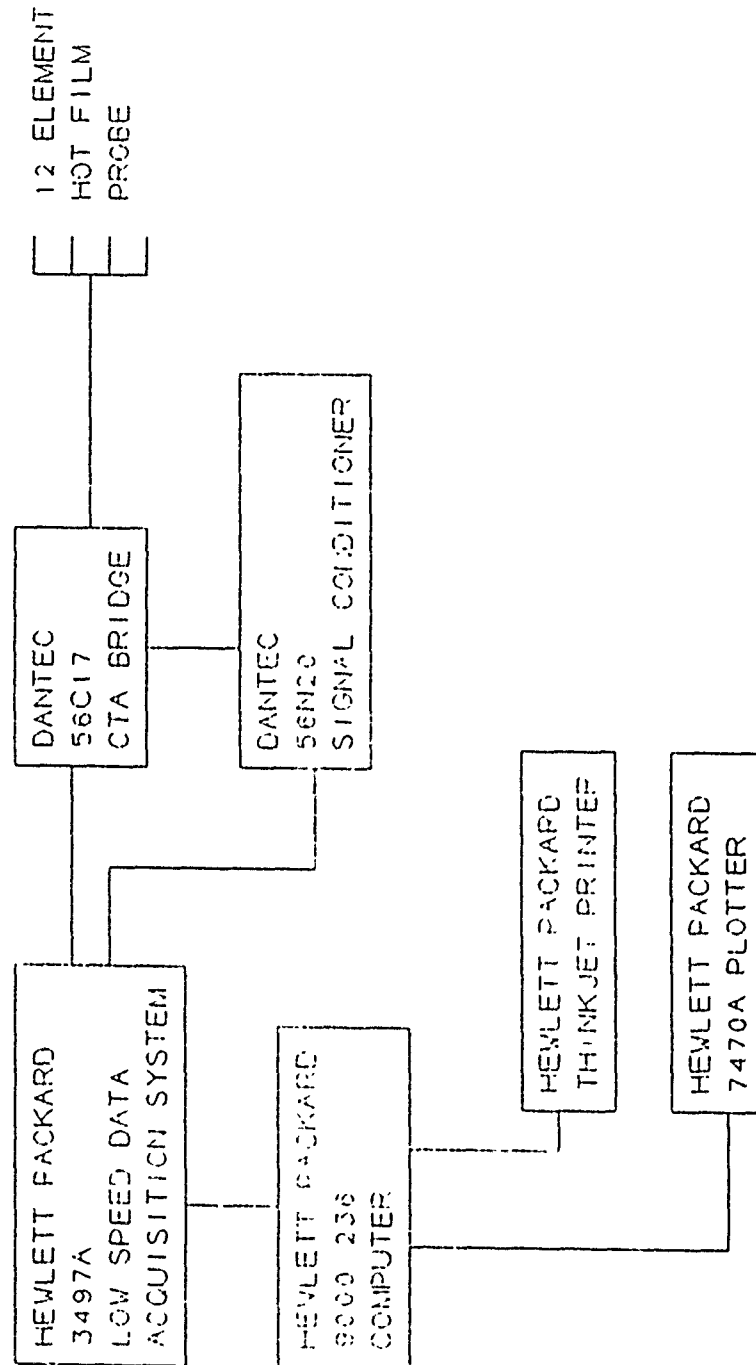


Figure 10. 12 Element Hot-film Survey Data Acquisition

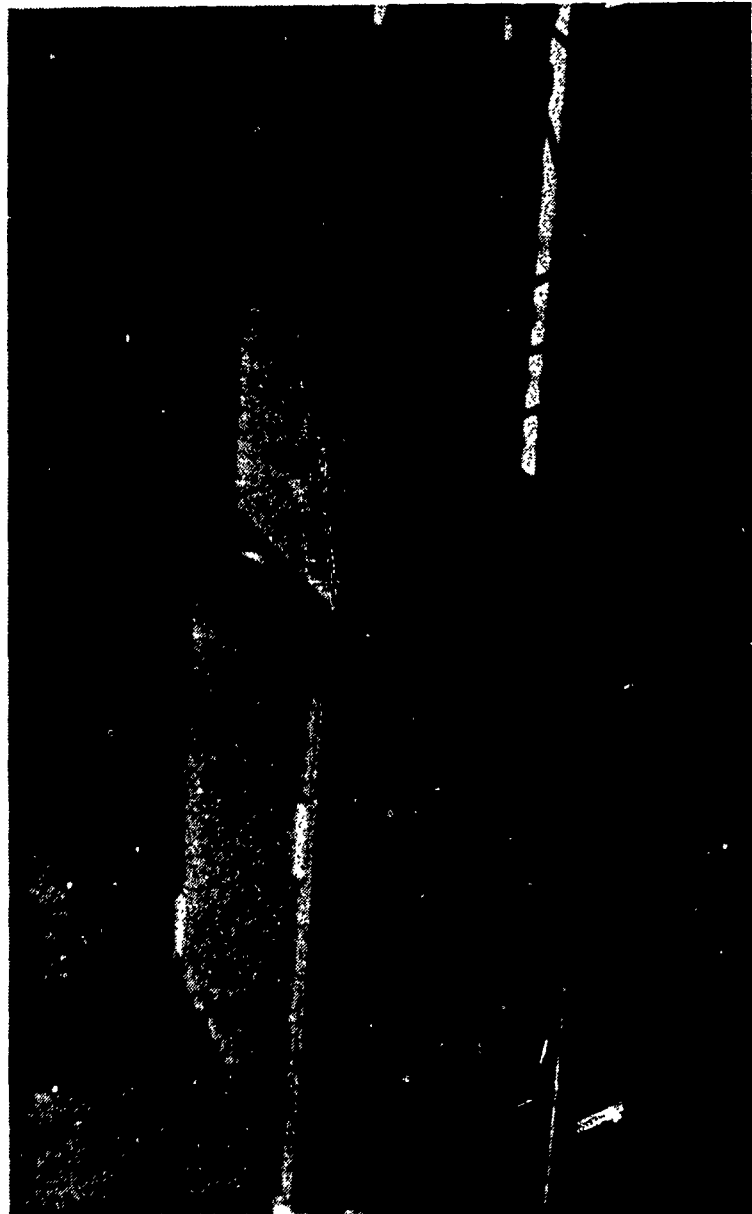


Figure 11. Constant Temperature Anemometry Bridge and Low Speed Data Acquisition Systems

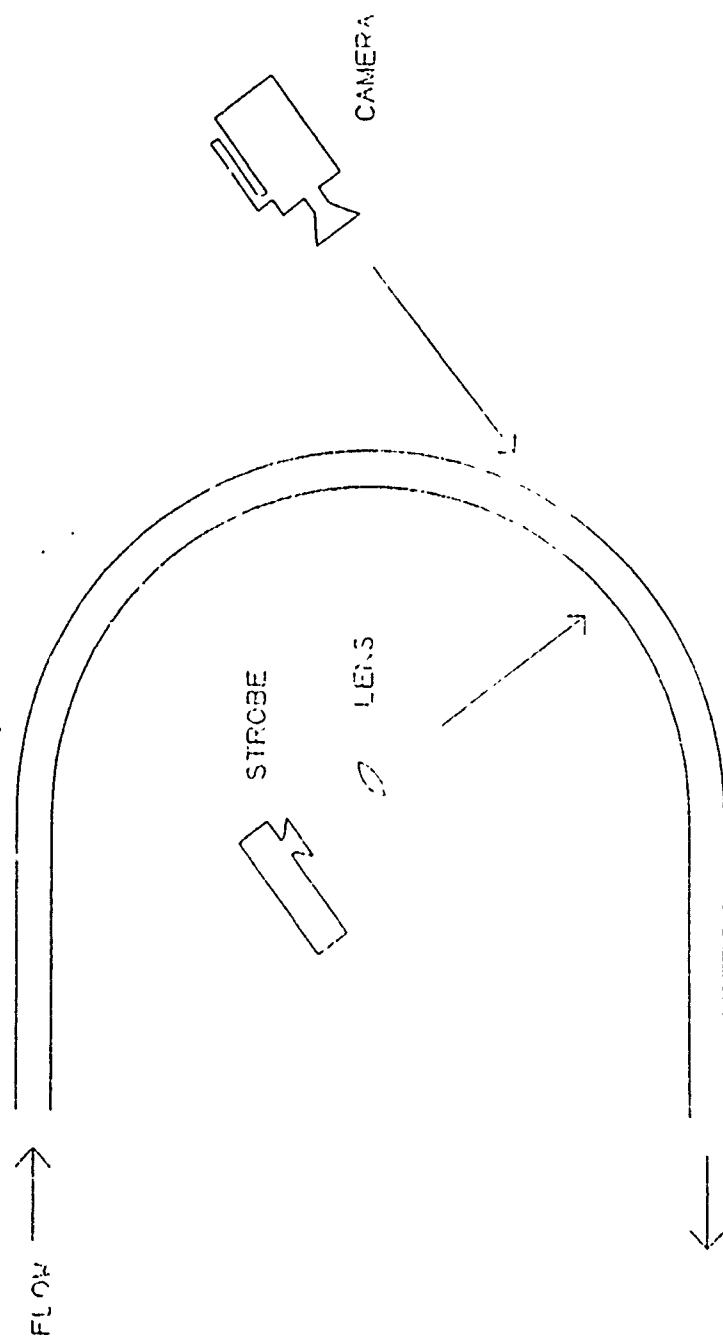


Figure 12. Radial/Spanwise Plane Flow Visualization

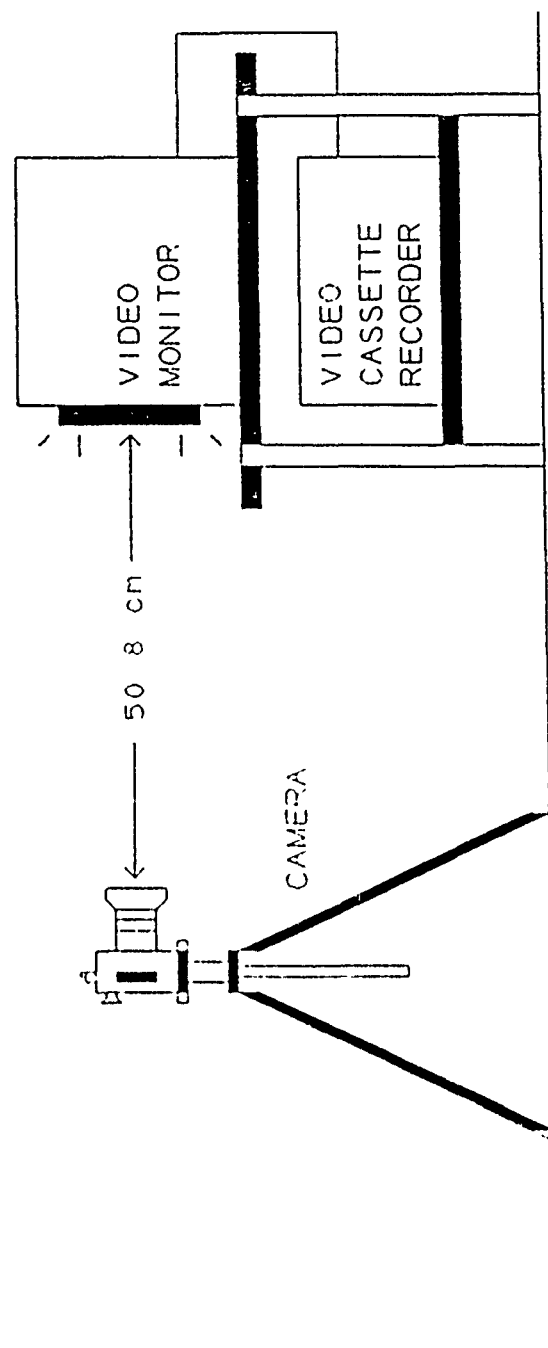


Figure 13 Flow Visualization Still Photography

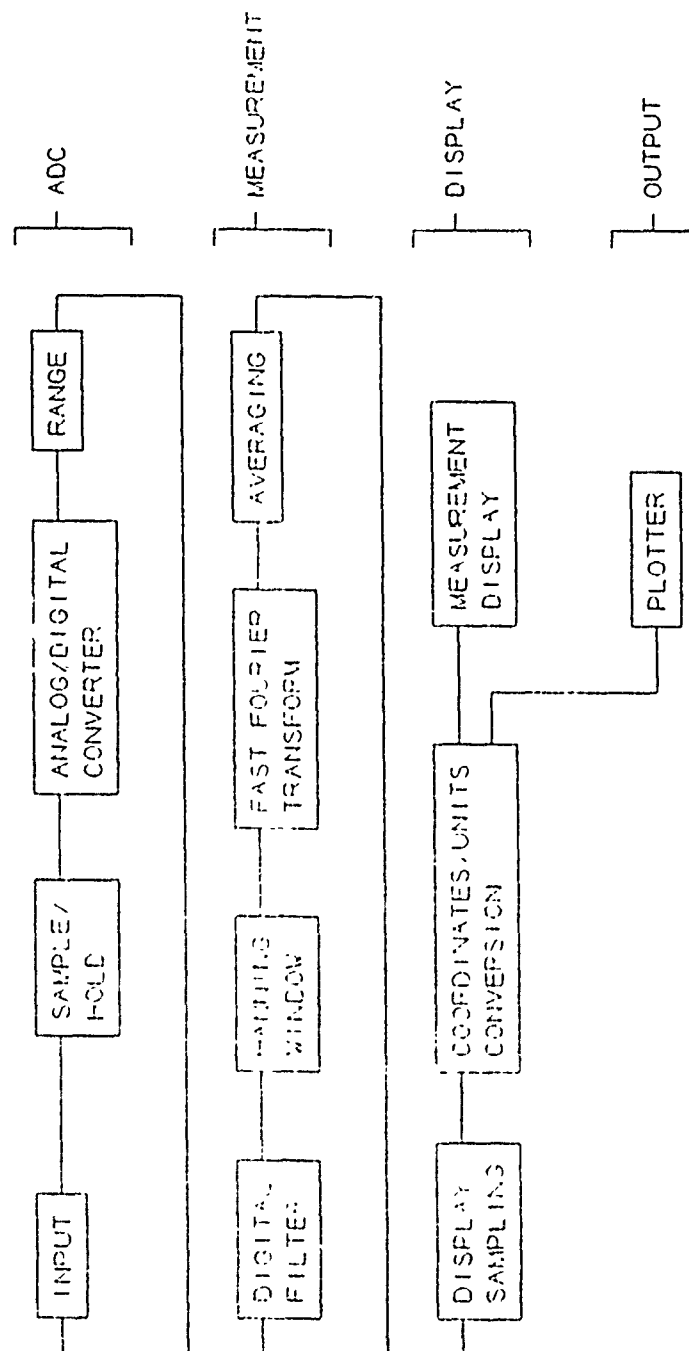


Figure 15. HP-3562A Dynamic Signal Analyzer Measurements

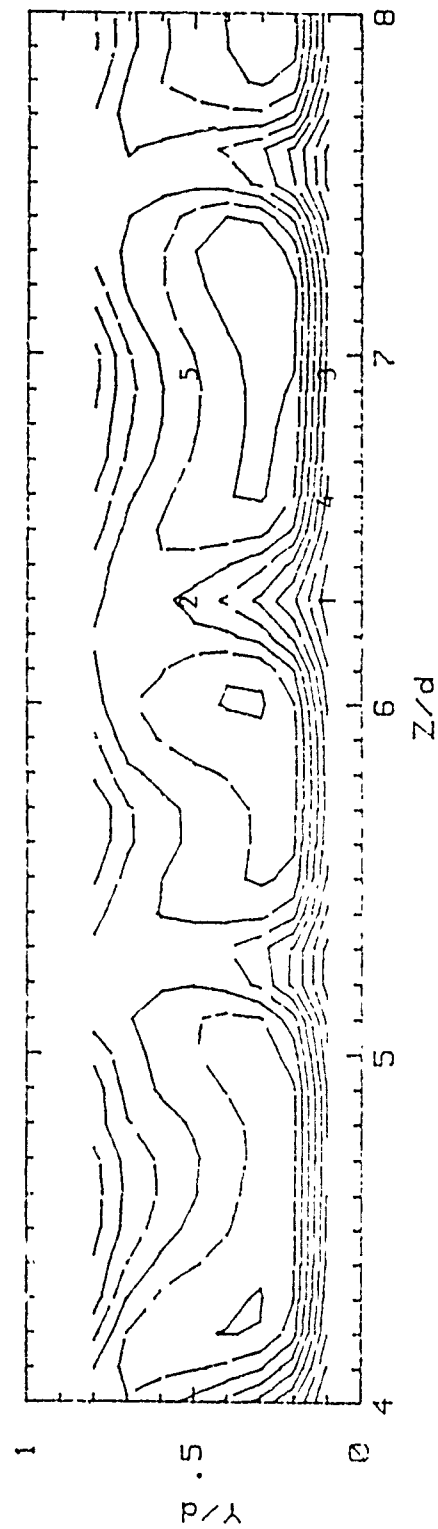


Figure 16. Hot-wire Probe Locations with Respect to Vortex Pair Structure, $De=104.2$, 120° Curvature

$P_{amb} - P_{total}$
RANGES IN PASCALS

0: 0.88 TO 0.91
1: 0.91 TO 0.94
2: 0.94 TO 0.97
3: 0.97 TO 1.00
4: 1.00 TO 1.03
5: 1.03 TO 1.06
6: 1.06 TO 1.09
7: 1.09 TO 1.12
8: 1.12 TO 1.16

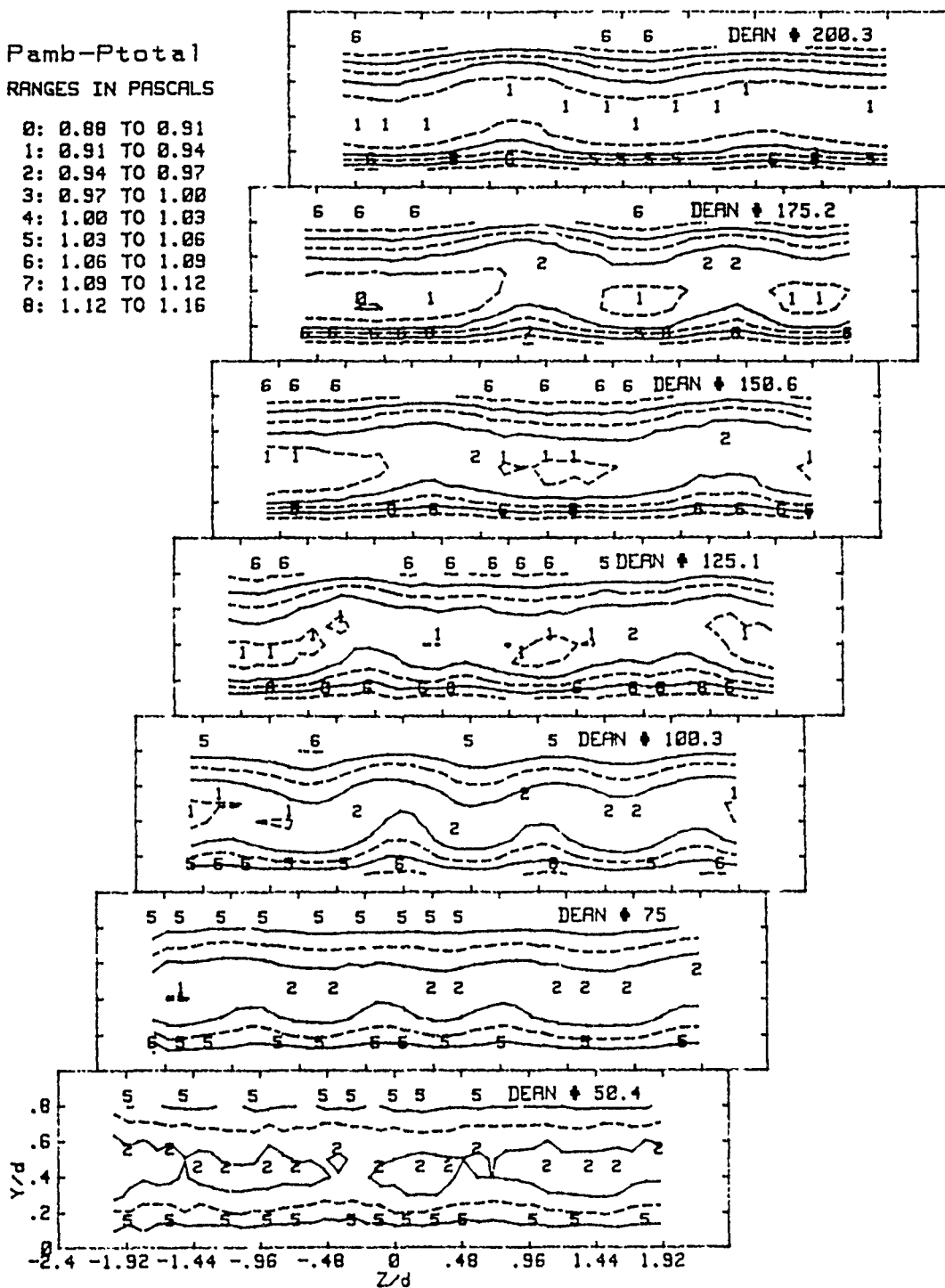


Figure 17. Total Pressure Contours $De=50.4$ to $De=200.3$

$P_{amb} - P_{total}$
RANGES IN PASCALS

- 0: 0.88 TO 0.91
- 1: 0.91 TO 0.94
- 2: 0.94 TO 0.97
- 3: 0.97 TO 1.00
- 4: 1.00 TO 1.03
- 5: 1.03 TO 1.06
- 6: 1.06 TO 1.09
- 7: 1.09 TO 1.12
- 8: 1.12 TO 1.16

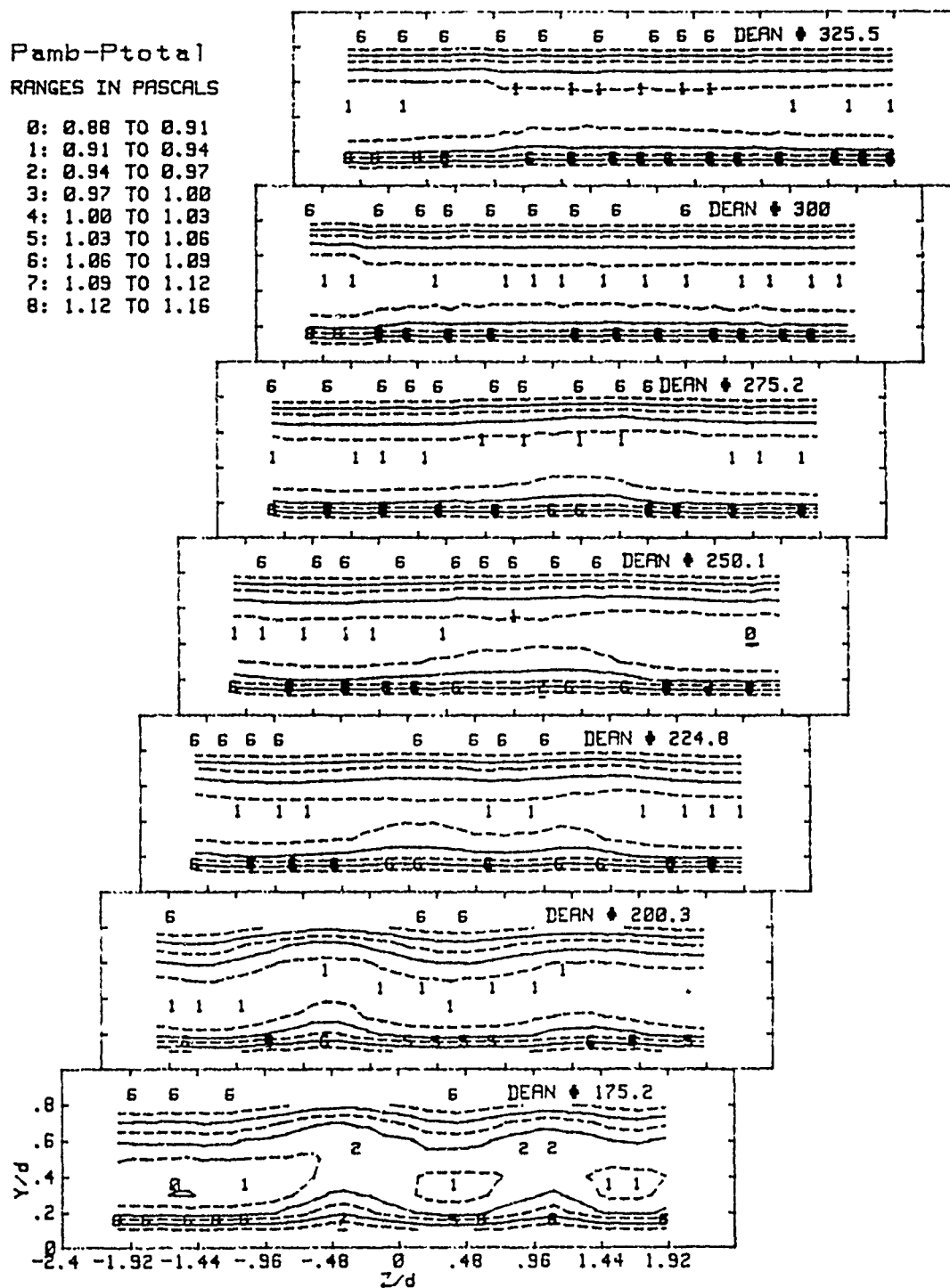


Figure 18. Total Pressure Contours $De=175.2$ to $De=325.5$

Pamb-Ptotal
RANGES IN PASCALS

- 0: 0.88 TO 0.91
- 1: 0.91 TO 0.94
- 2: 0.94 TO 0.97
- 3: 0.97 TO 1.00
- 4: 1.00 TO 1.03
- 5: 1.03 TO 1.06
- 6: 1.06 TO 1.09
- 7: 1.09 TO 1.12
- 8: 1.12 TO 1.16

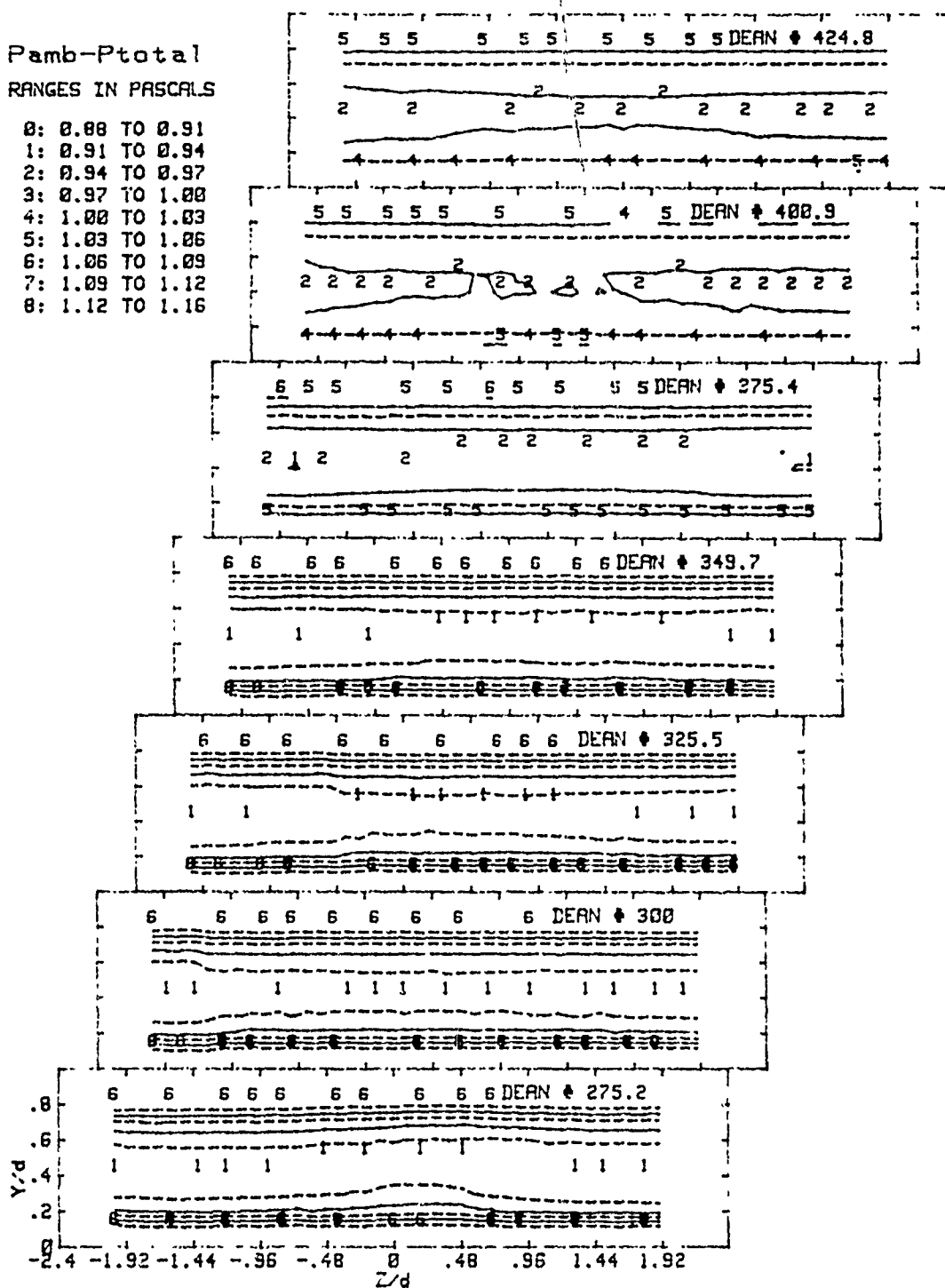


Figure 19. Total Pressure Contours $De=275.2$ to $De=424.8$

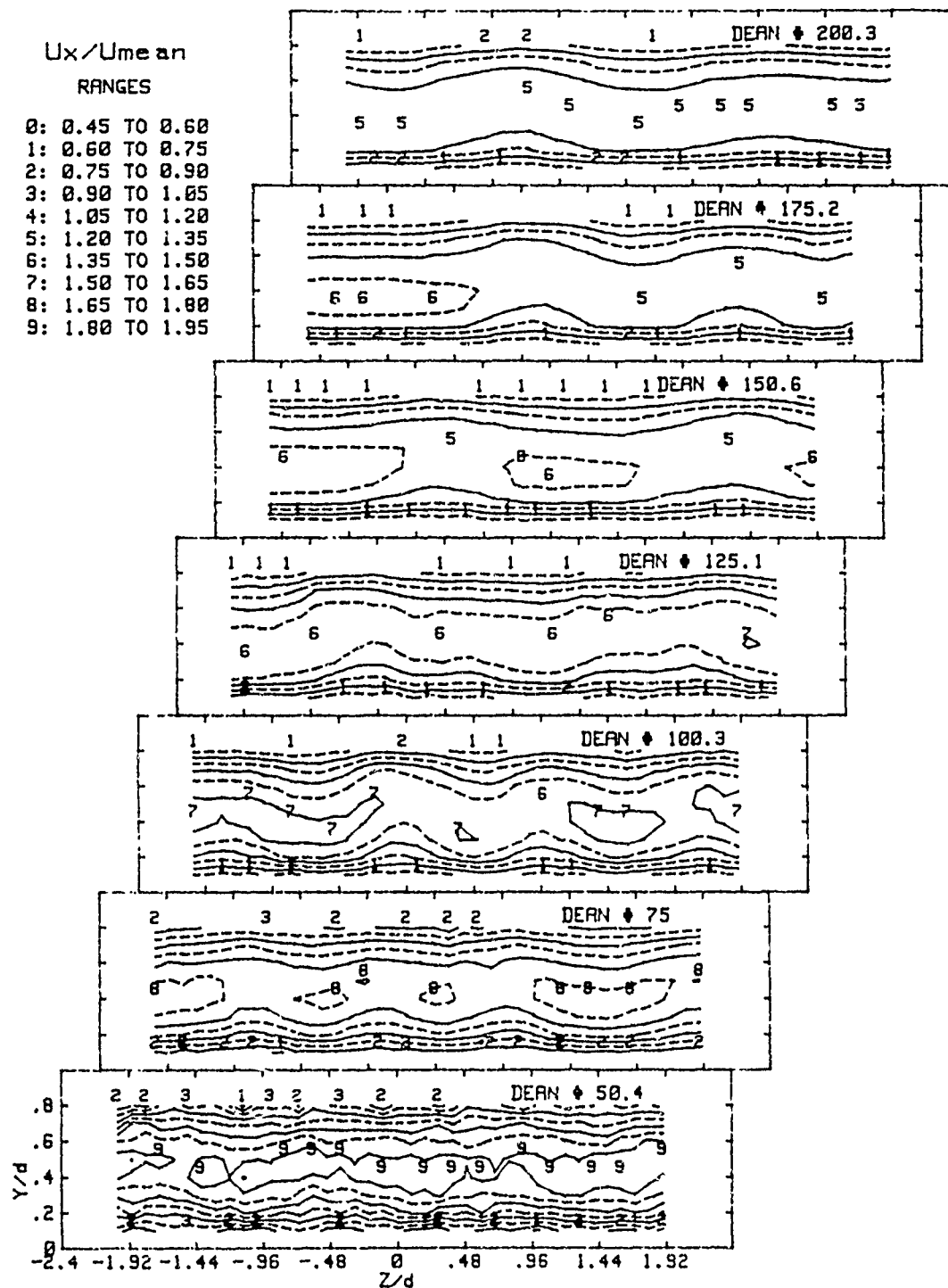


Figure 20. Streamwise Velocity Contours $De=50.4$ to $De=200.3$

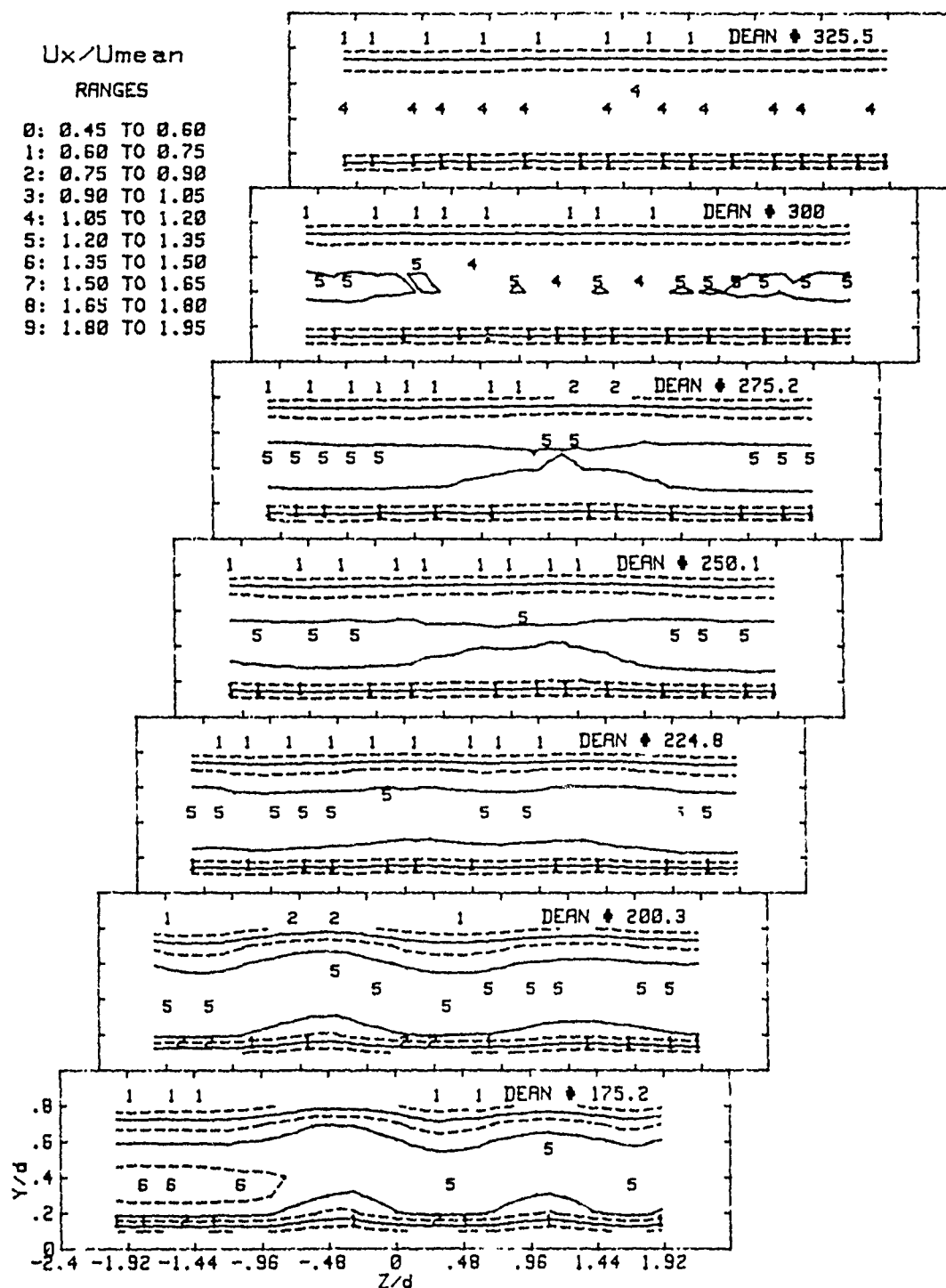


Figure 21. Streamwise Velocity Contours $De=175.2$ to $De=325.5$

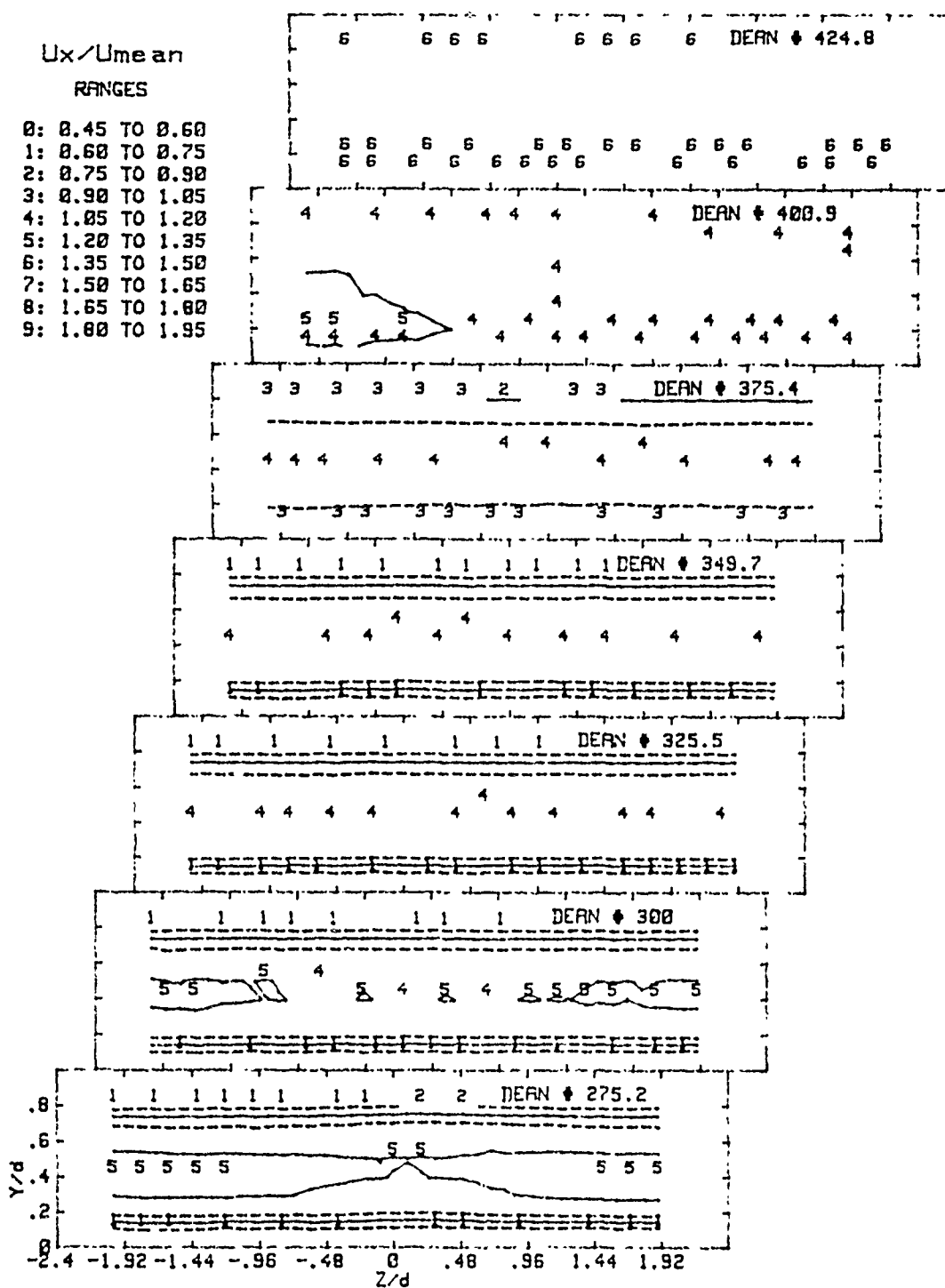


Figure 22. Streamwise Velocity Contours $De=275.2$ to $De=424.8$

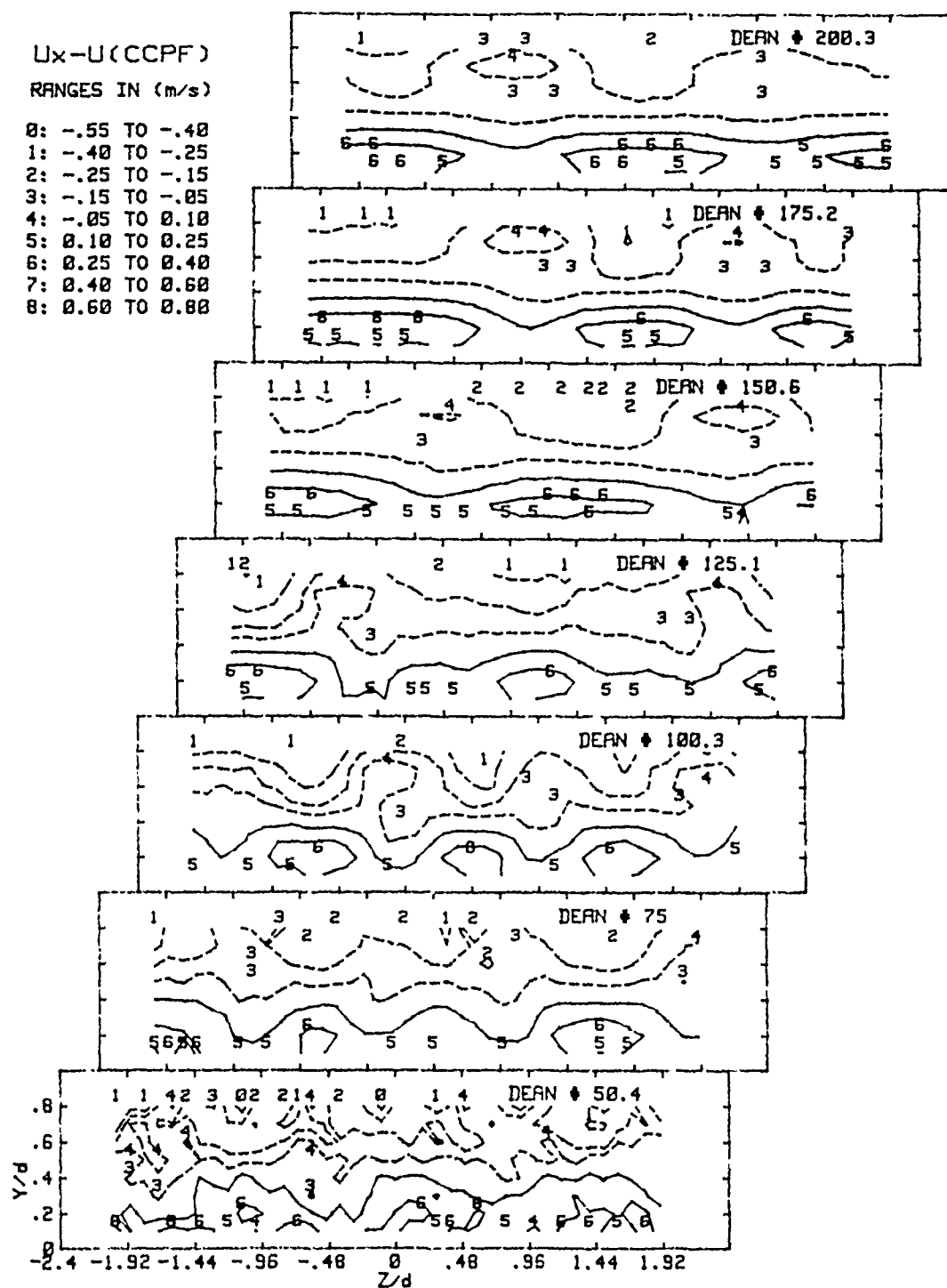


Figure 23. Velocity Perturbation Contours $De=50.4$ to $De=200.3$

$U_x - U$ (CCPF)

RANGES IN (m/s)

0: -.55 TO -.40

1: -.40 TO -.25

2: -.25 TO -.15

3: -.15 TO -.05

4: -.05 TO 0.10

5: 0.10 TO 0.25

6: 0.25 TO 0.40

7: 0.40 TO 0.60

8: 0.60 TO 0.80

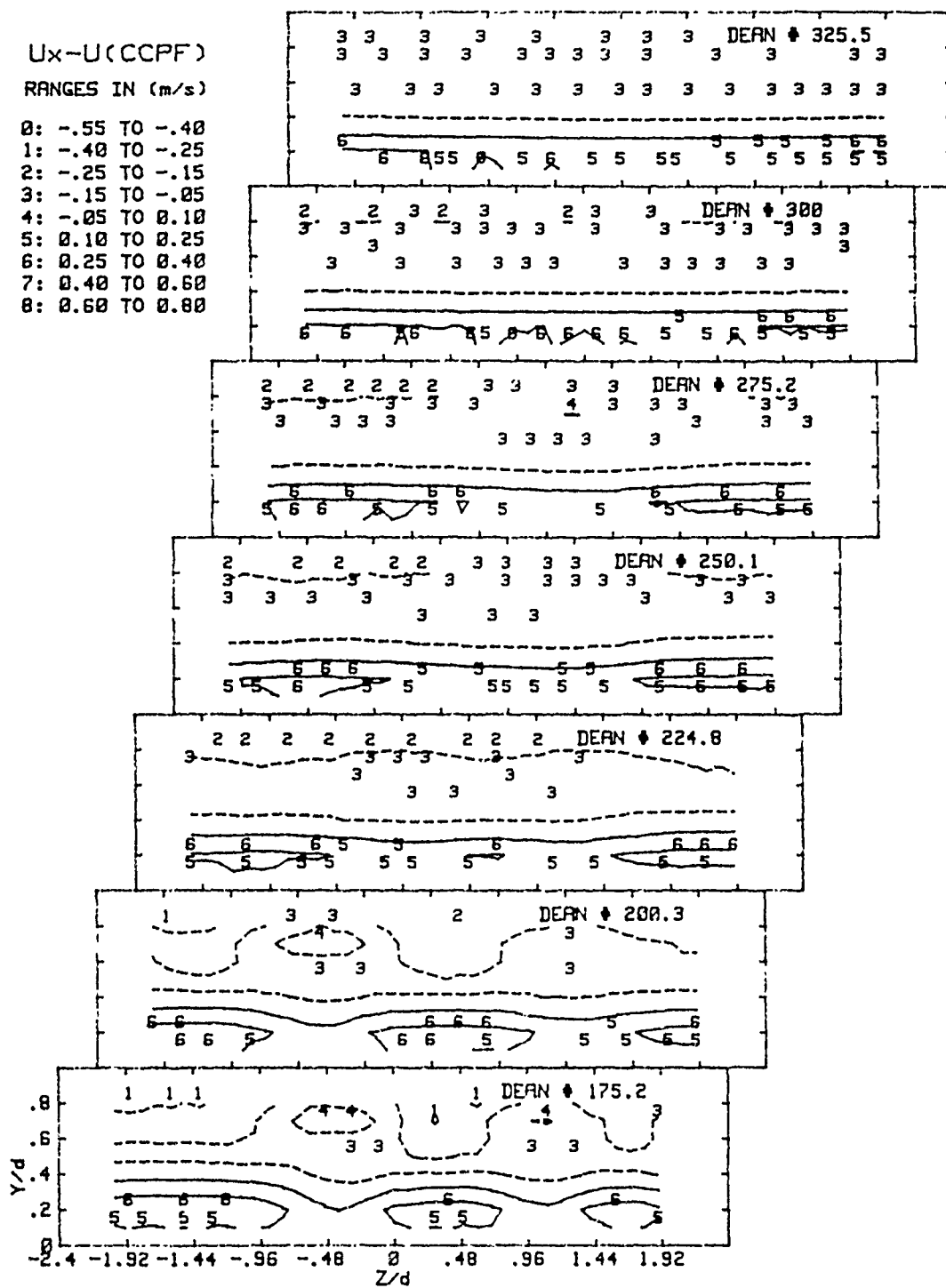


Figure 24. Velocity Perturbation Contours $De=175.2$ to $De=325.5$

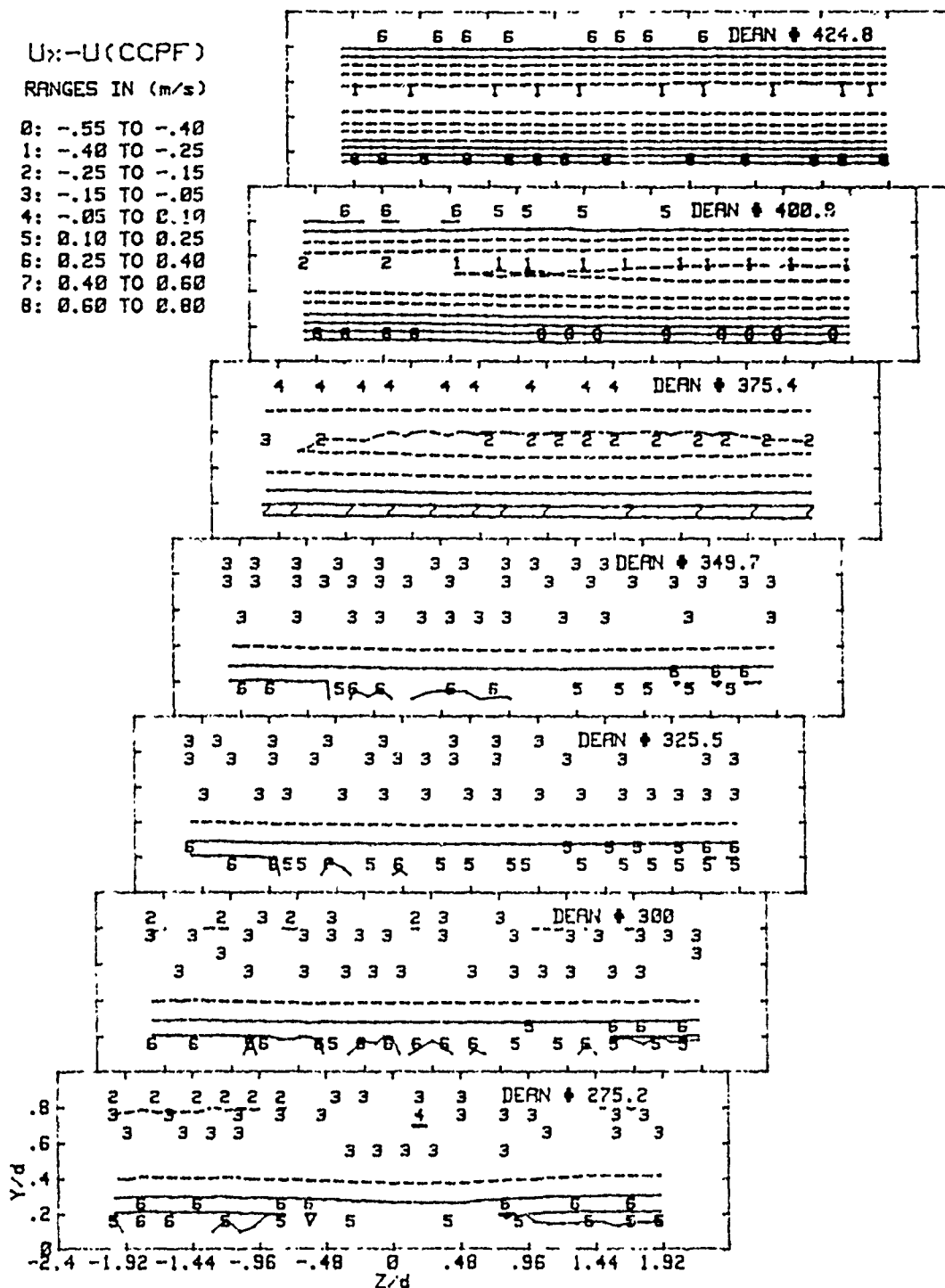


Figure 25. Velocity Perturbation Contours $De=275.2$ to $De=424.8$

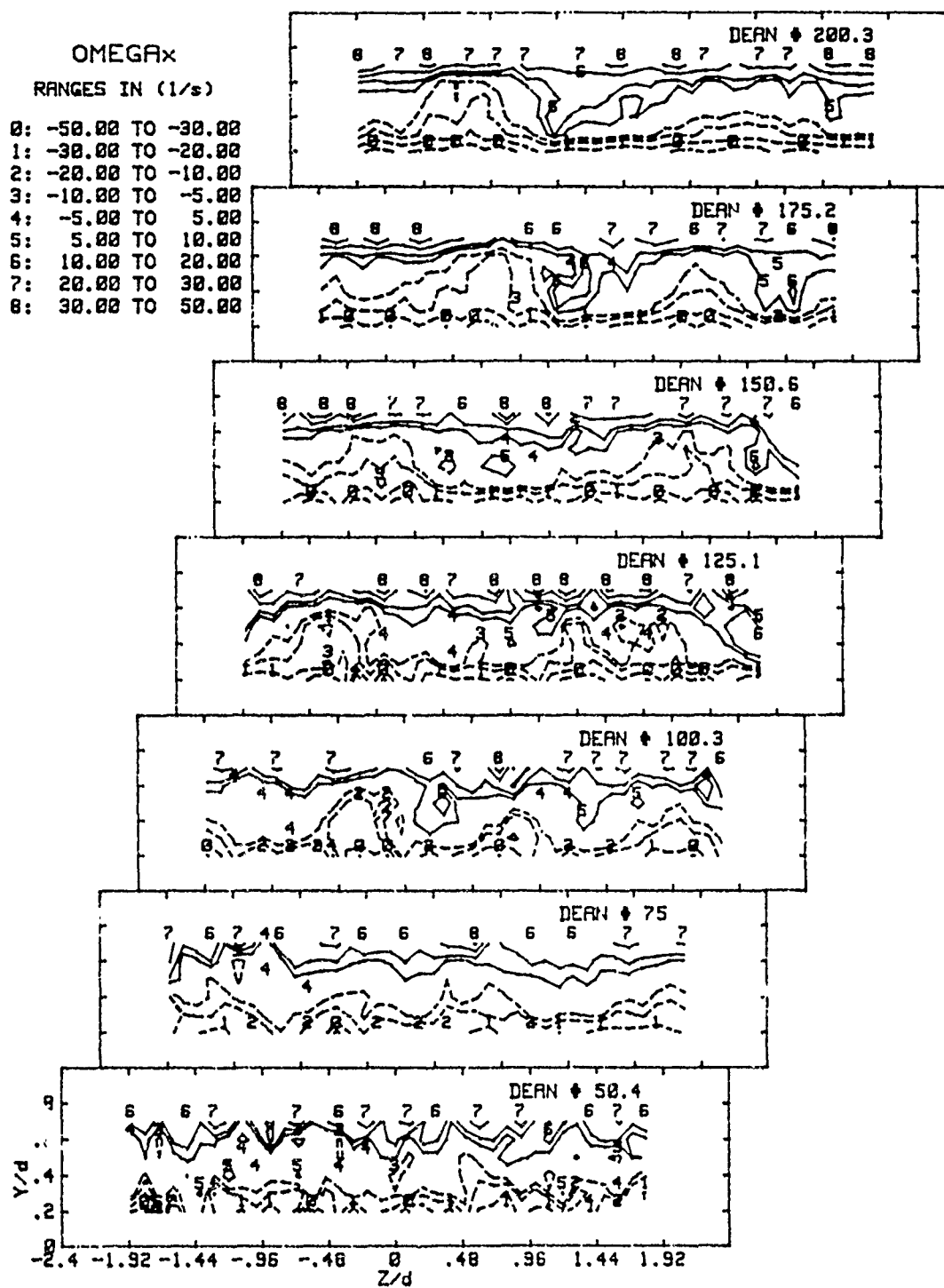


Figure 26. Streamwise Vorticity Contours $De=50.4$ to $De=200.3$

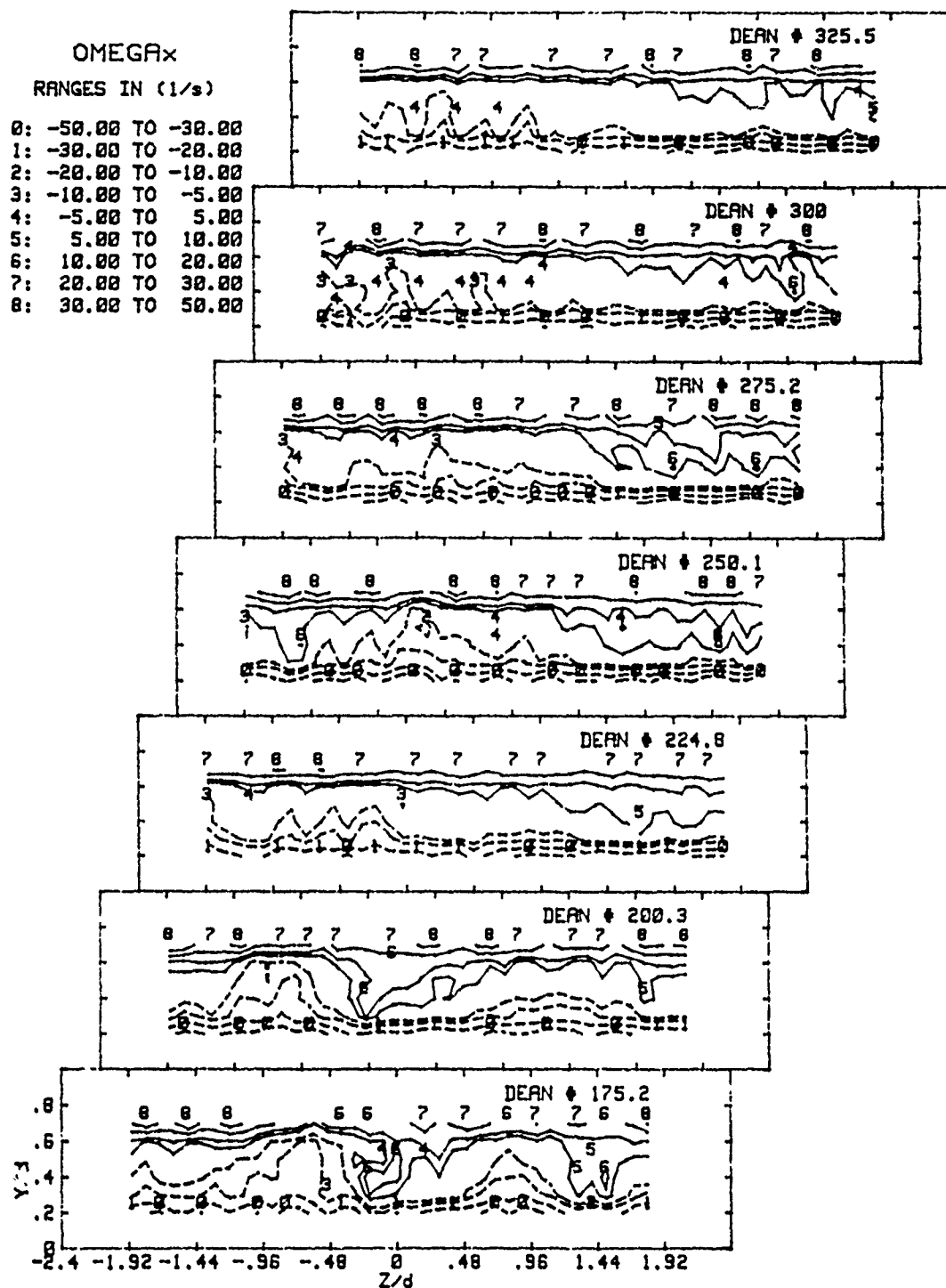


Figure 27. Streamwise Vorticity Contours $De=175.2$ to $De=325.5$

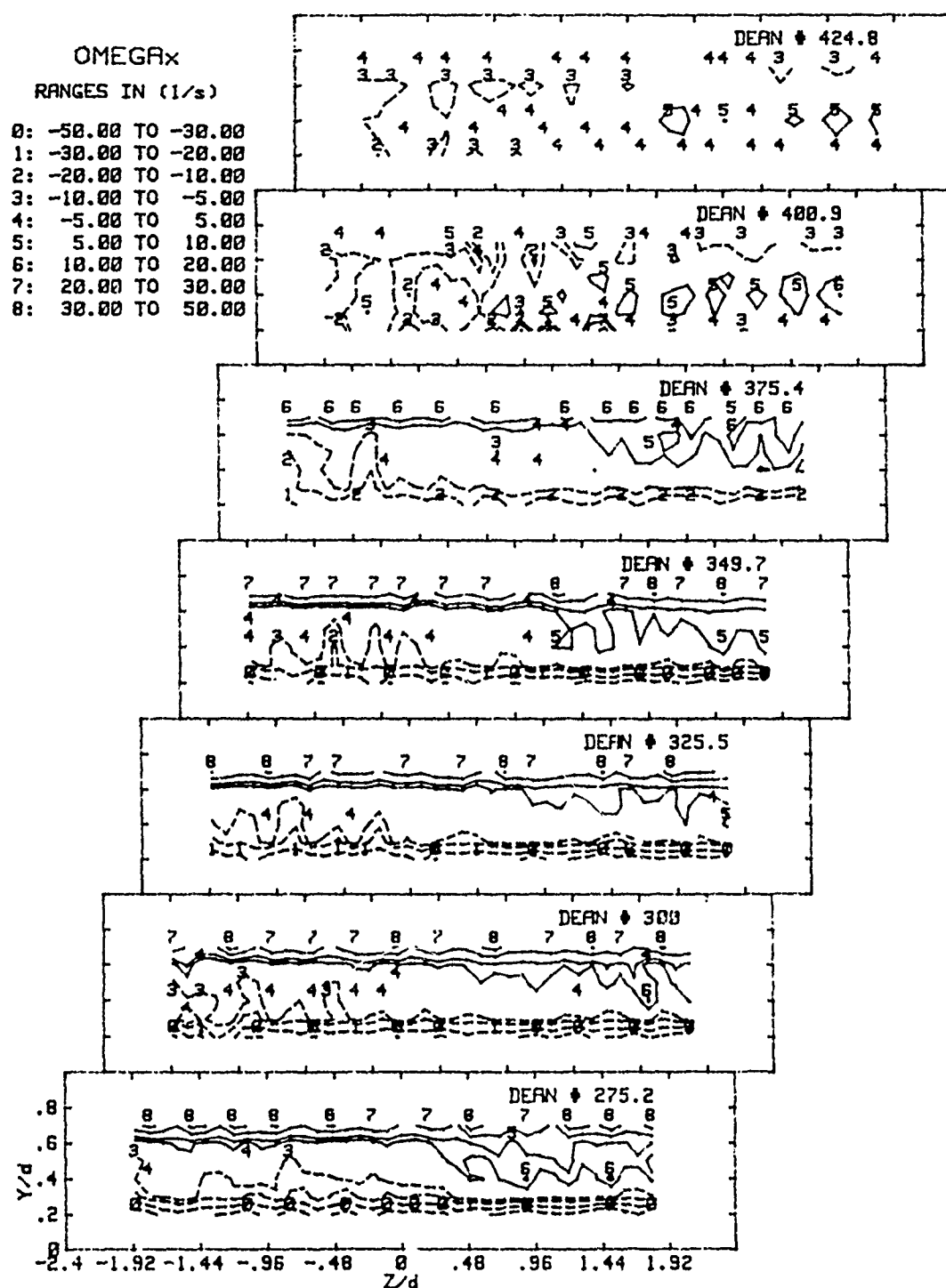


Figure 28. Streamwise Vorticity Contours $De=275.2$ to $De=424.8$

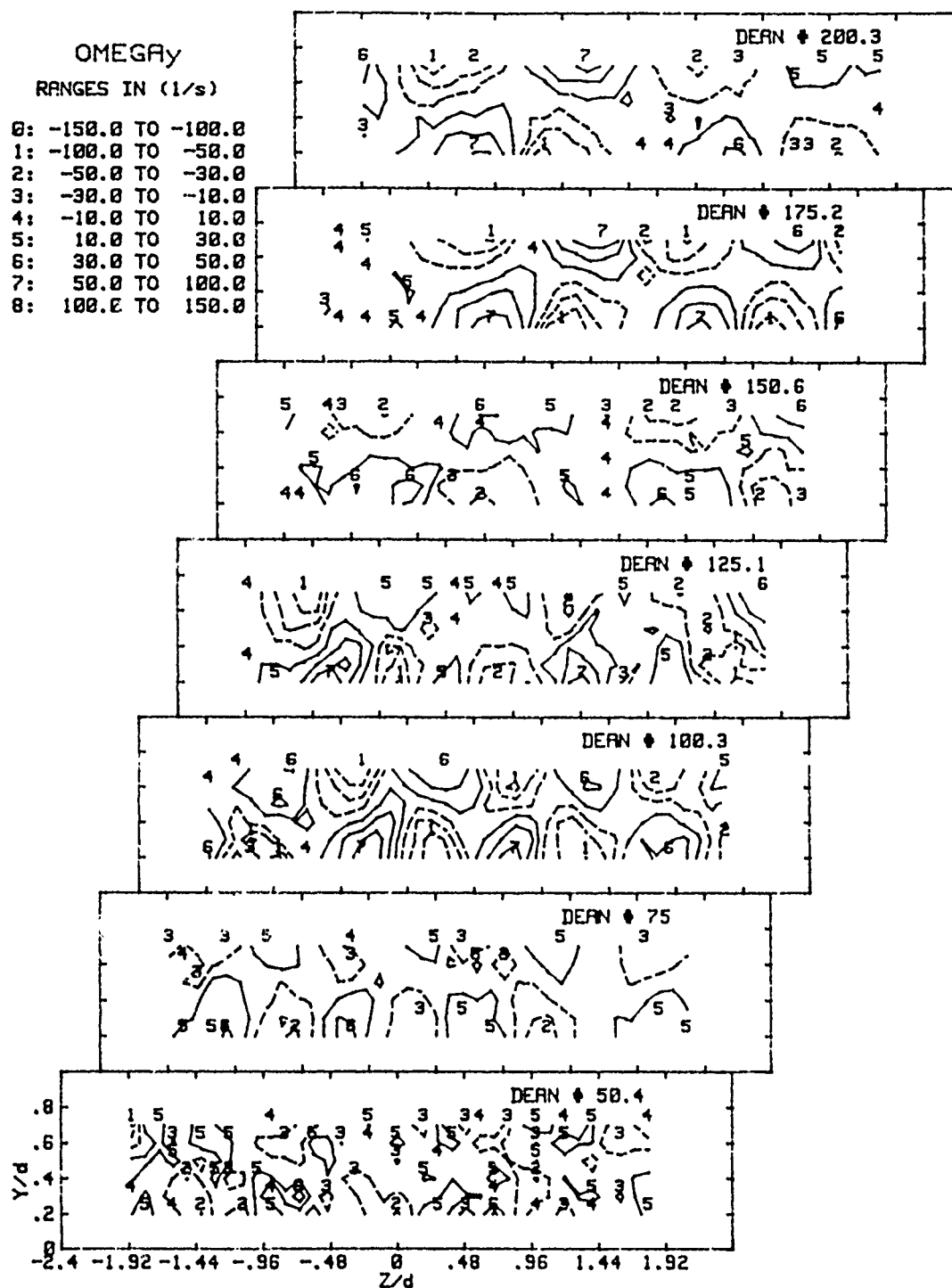


Figure 29. Radial Vorticity Contours $De=50.4$ to $De=200.3$

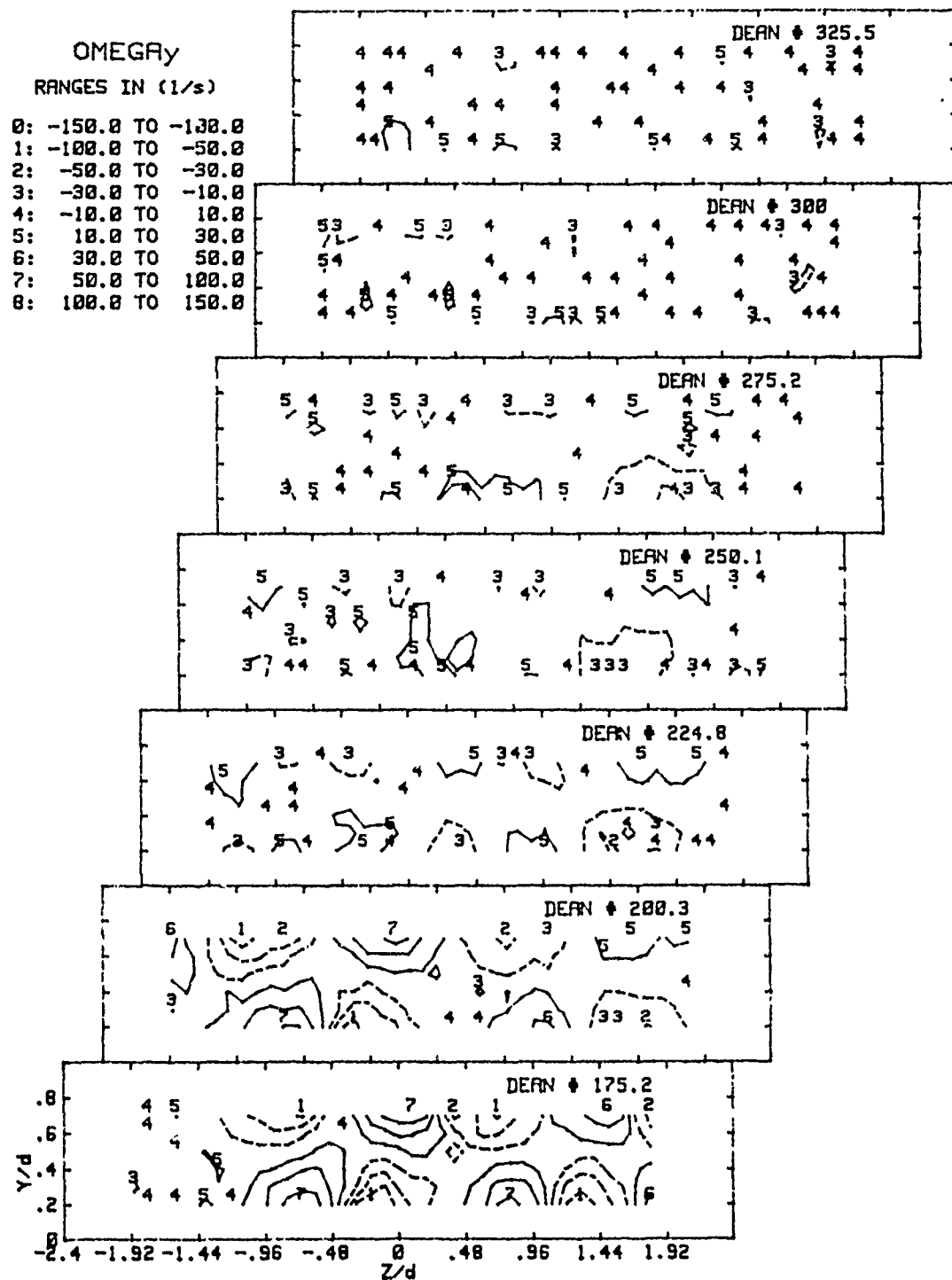


Figure 3C. Radial Vorticity Contours $De=175.2$ to $De=325.5$

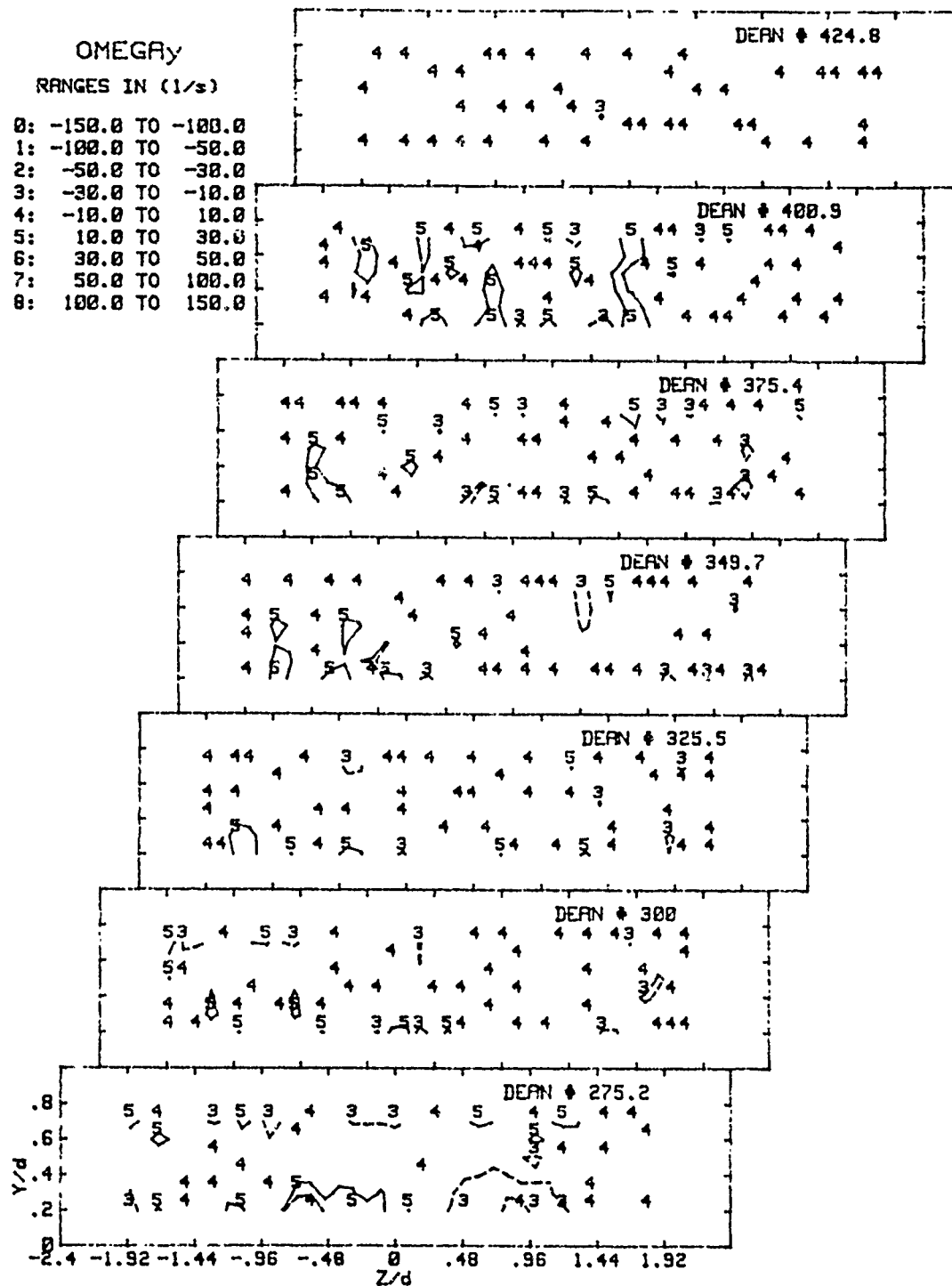


Figure 31. Radial Vorticity Contours $De=275.2$ to $De=424.8$

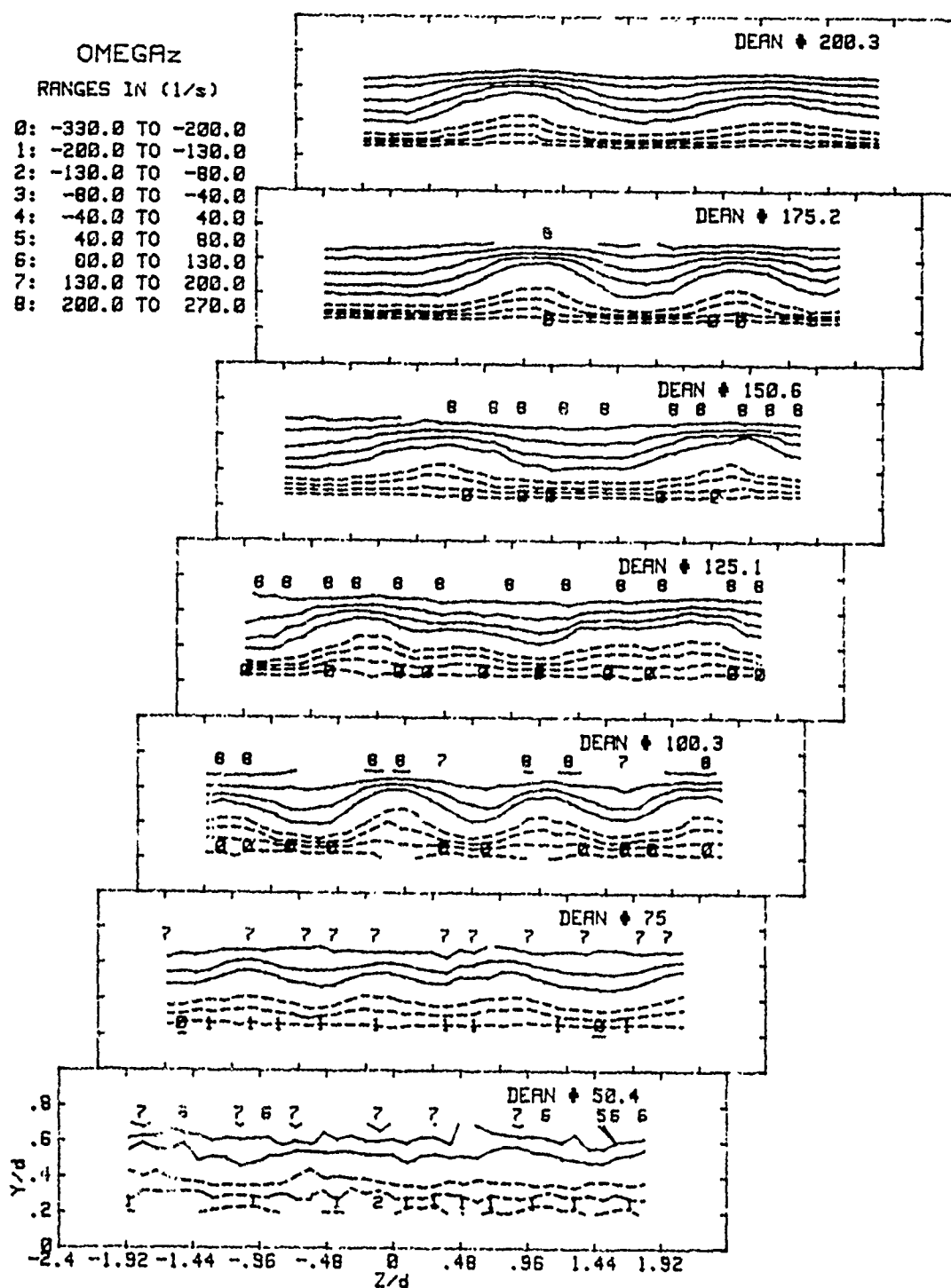


Figure 32. Spanwise Vorticity Contours $De=50.4$ to $De=200.3$

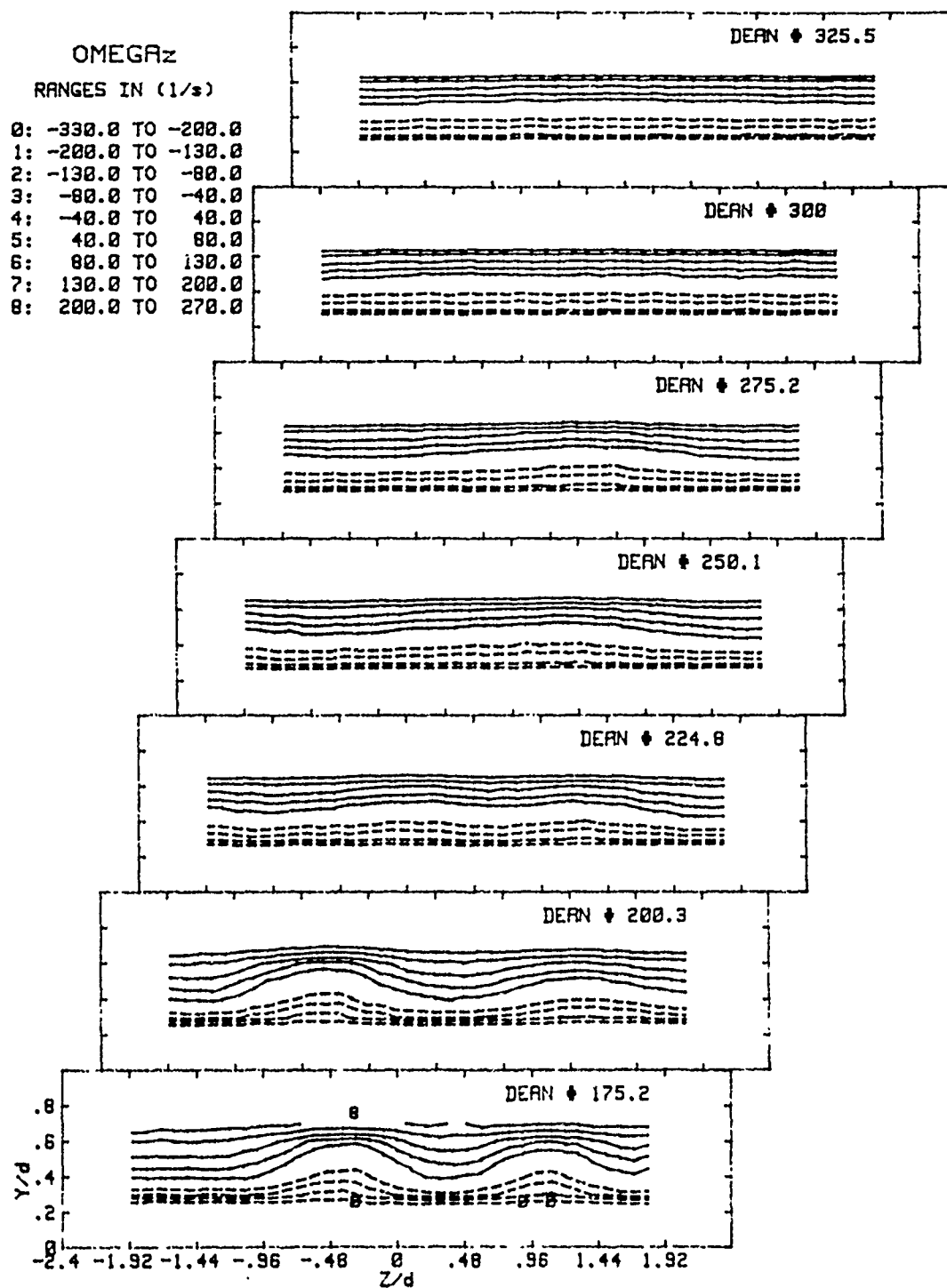


Figure 33. Spanwise Vorticity Contours $De=175.2$ to $De=325.5$

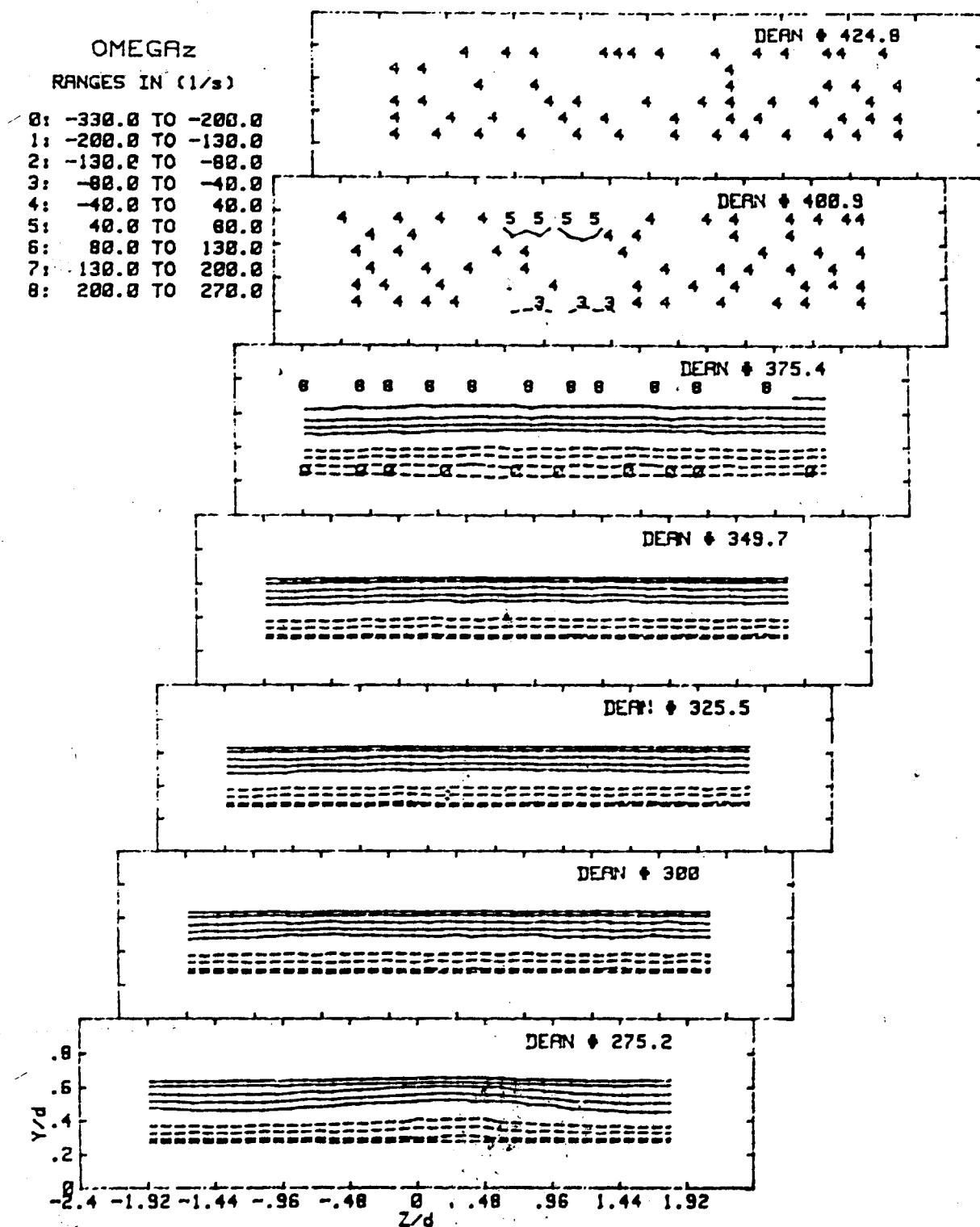


Figure 34. Spanwise Vorticity Contours $De=275.2$ to $De=424.8$

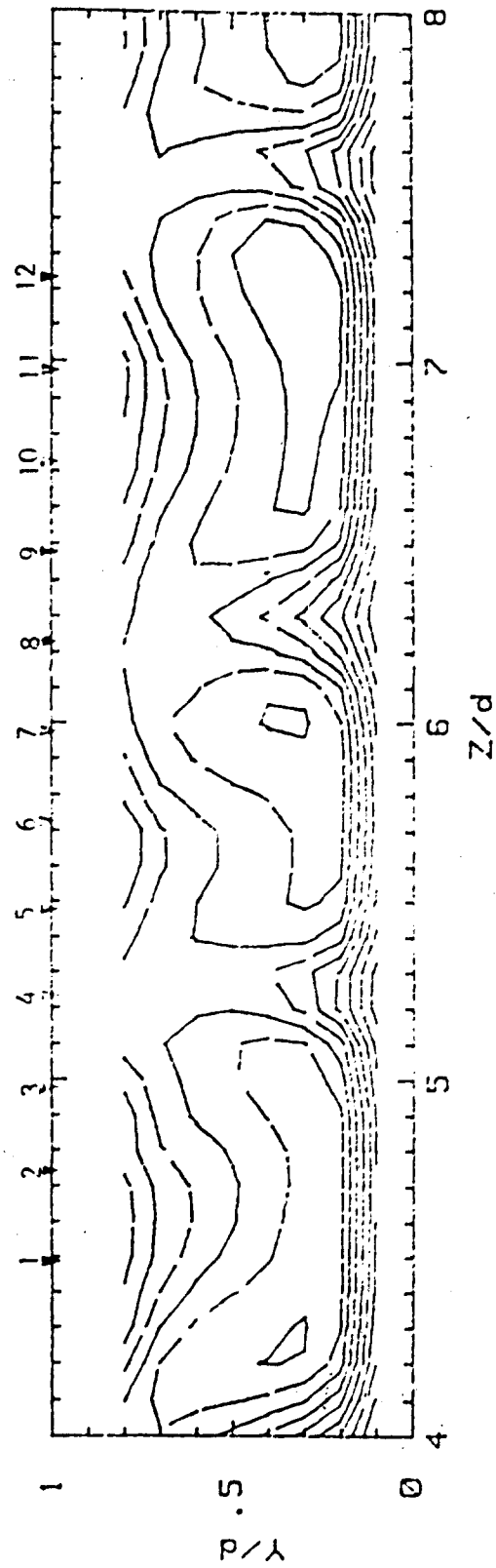


Figure 35. Hot-film Probe Locations with Respect to Vortex Pair Structure, $De=104.2$, 120° Curvature

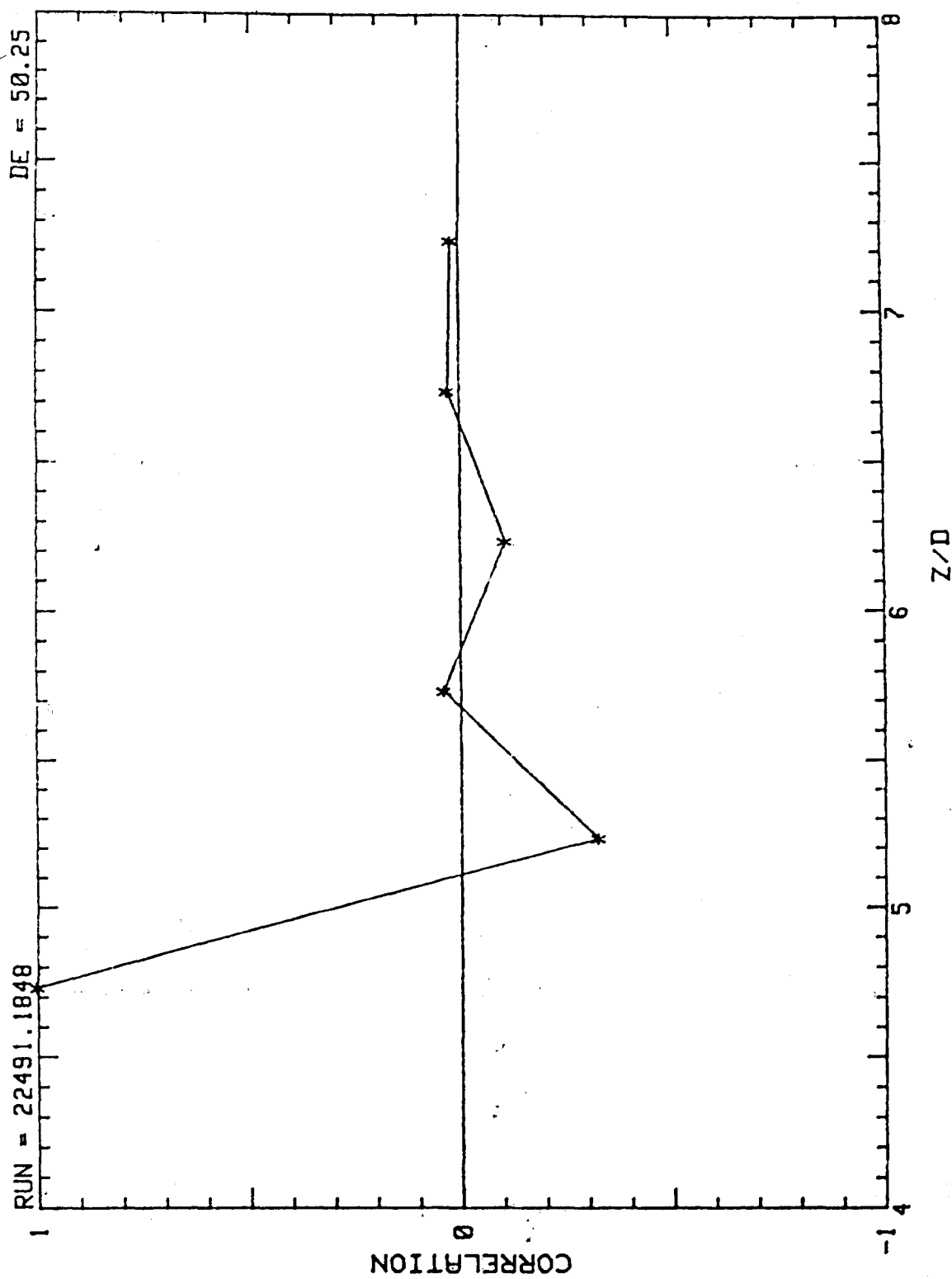


Figure 36. Correlation vs. z/d Probes 2,4,6,8,10,12,wrt 2, $De=50.25$

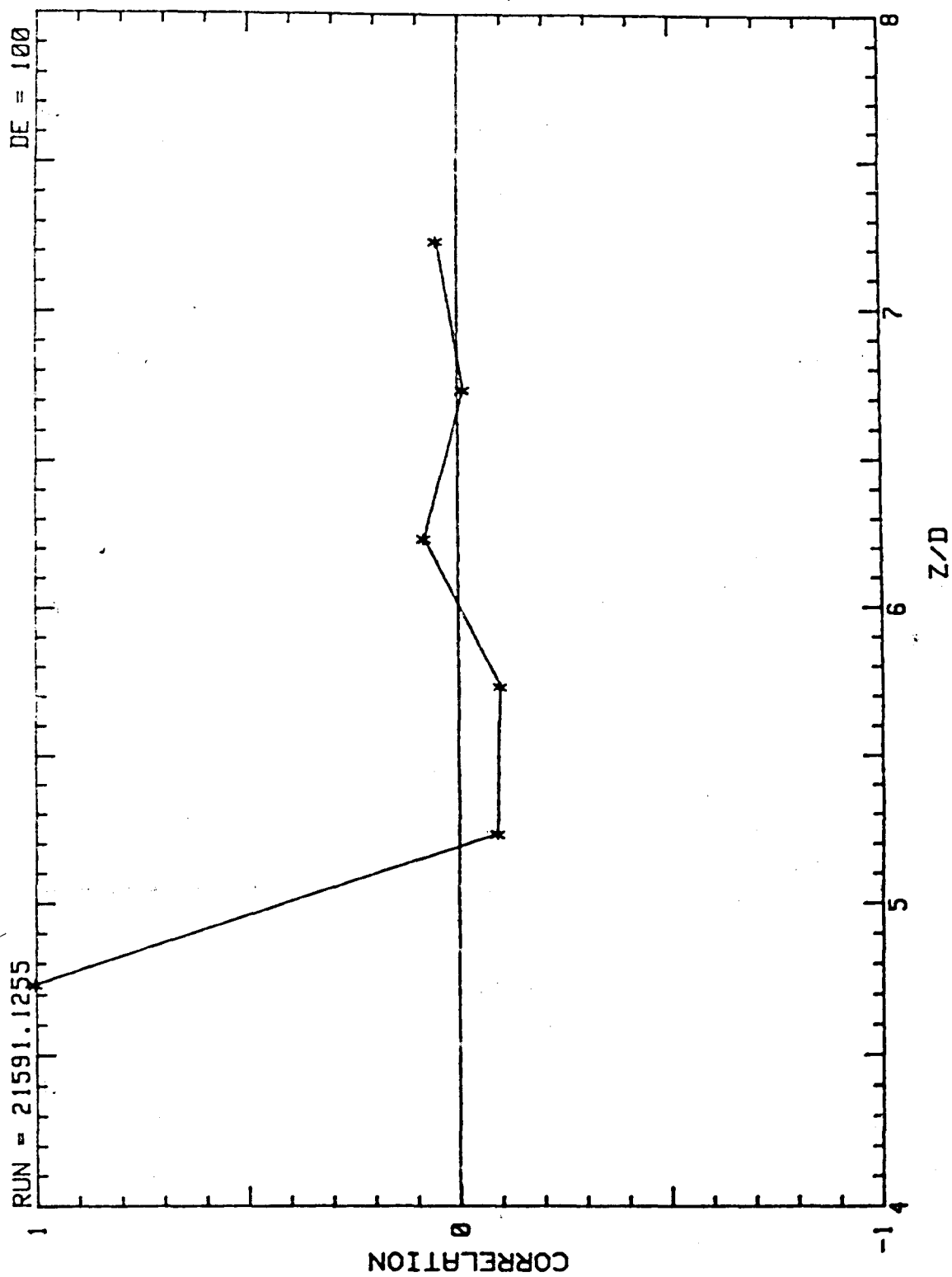


Figure 37. Correlation vs. z/d Probes 2,4,6,8,10,12,wrt 2, $De=100$

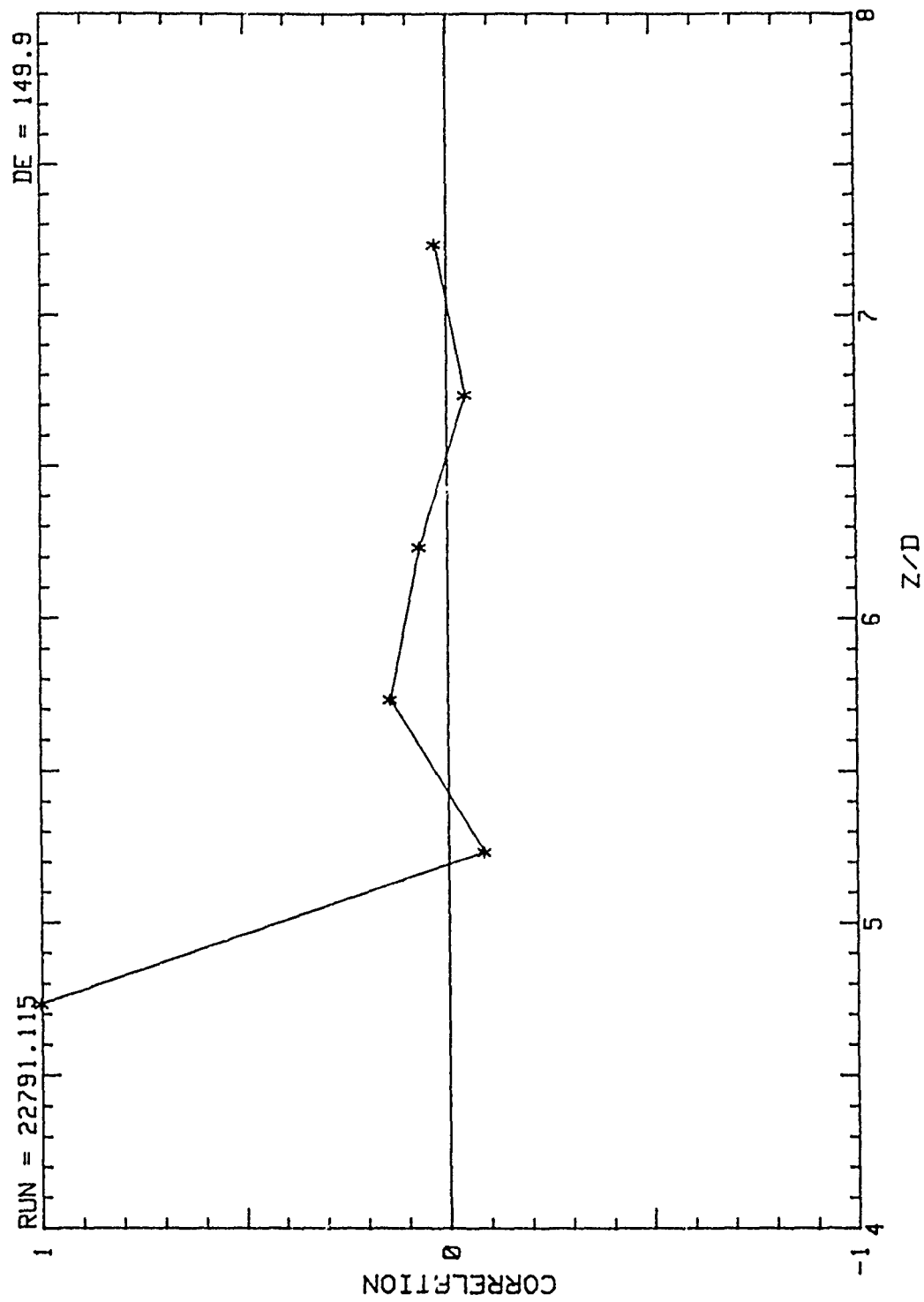


Figure 38. Correlation vs. z/d Probes 2,4,6,8,10,12,wrt 2, De=149.9

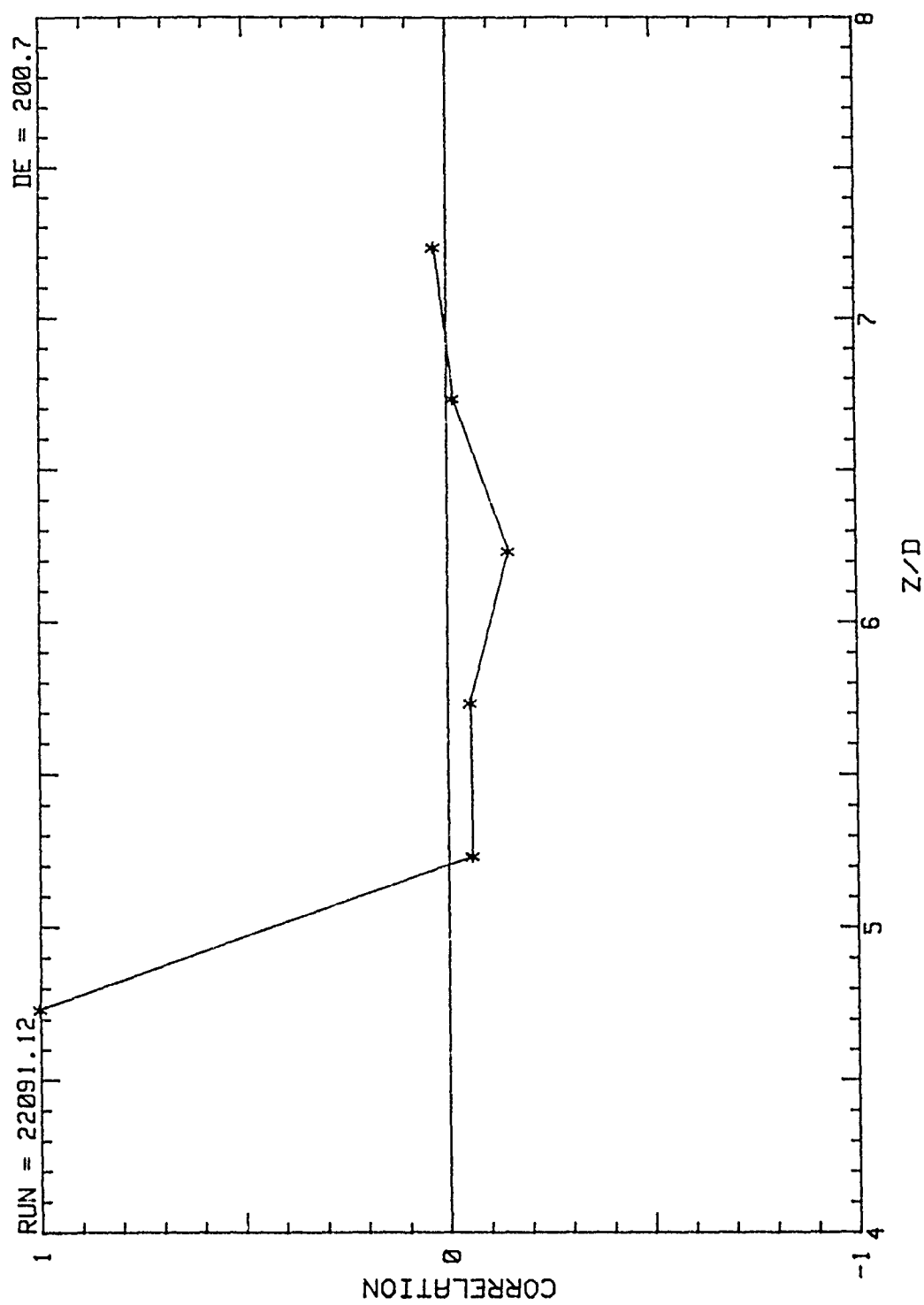


Figure 39. Correlation vs. z/d Probes 2,4,6,8,10,12,wrt 2, $De=200.7$

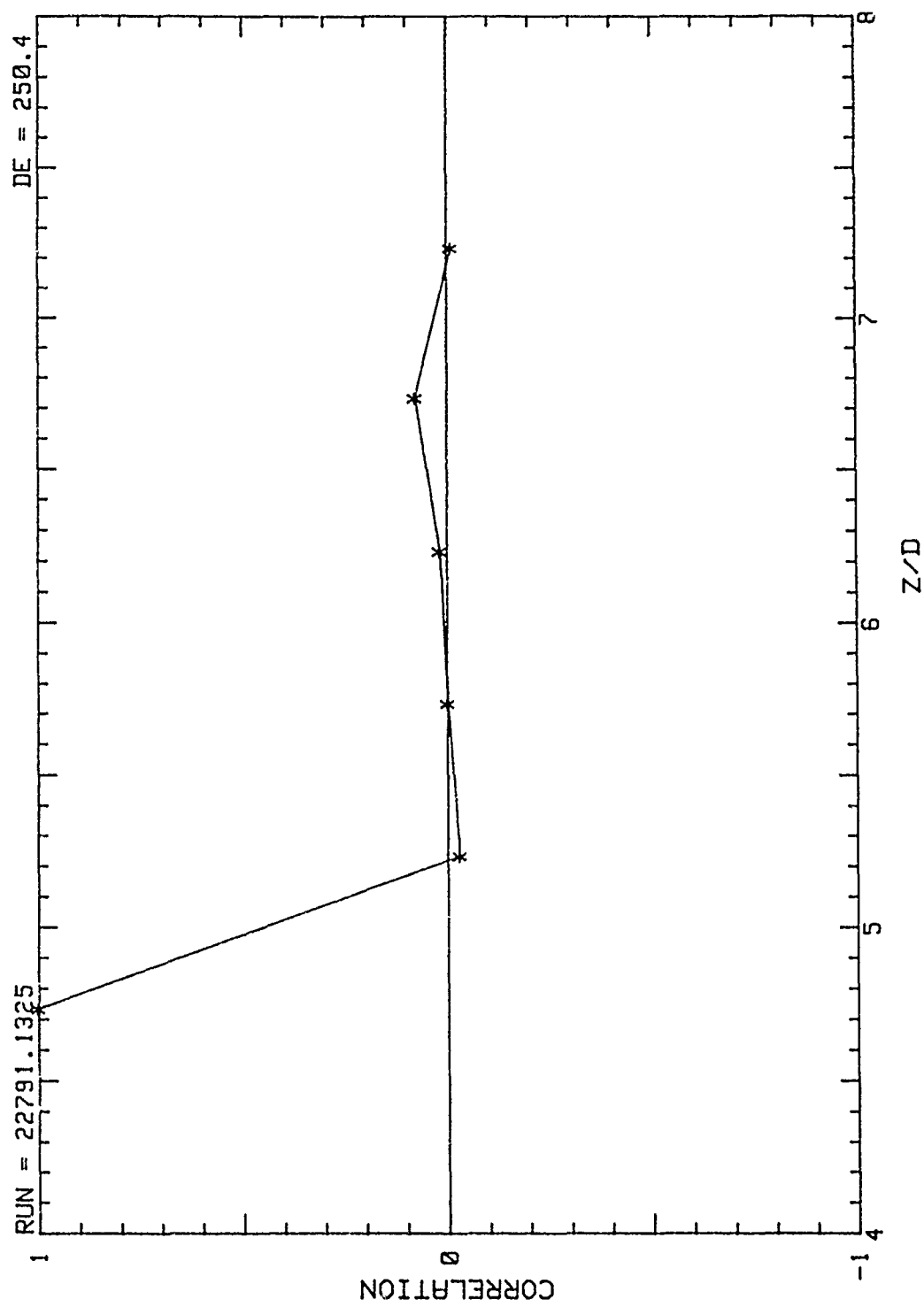


Figure 40. Correlation vs. z/d Probes 2,4,6,8,10,12,wrt 2, De=250.4

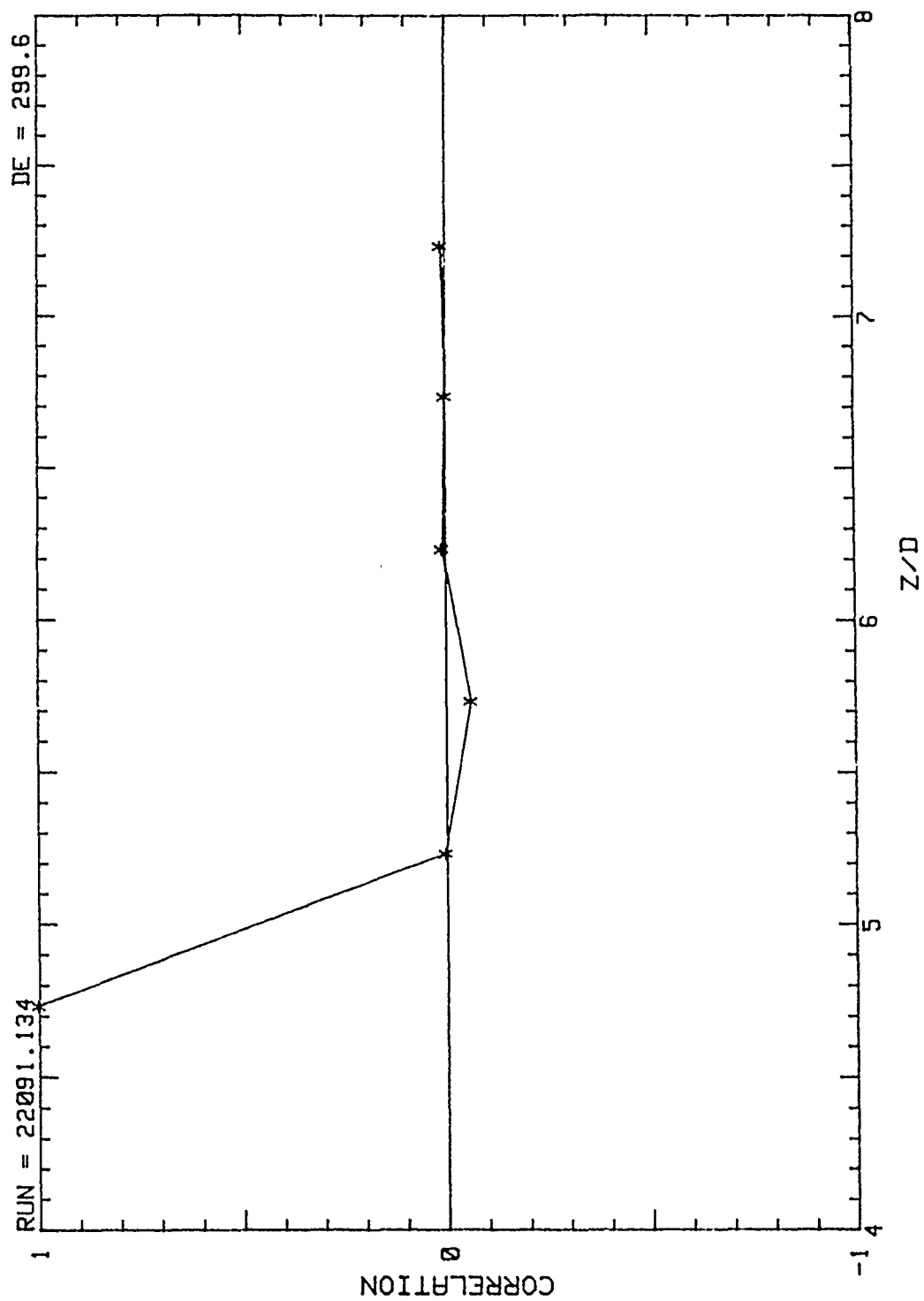


Figure 41. Correlation vs. z/d Probes 2,4,6,8,10,12,wrt 2, $De=299.6$

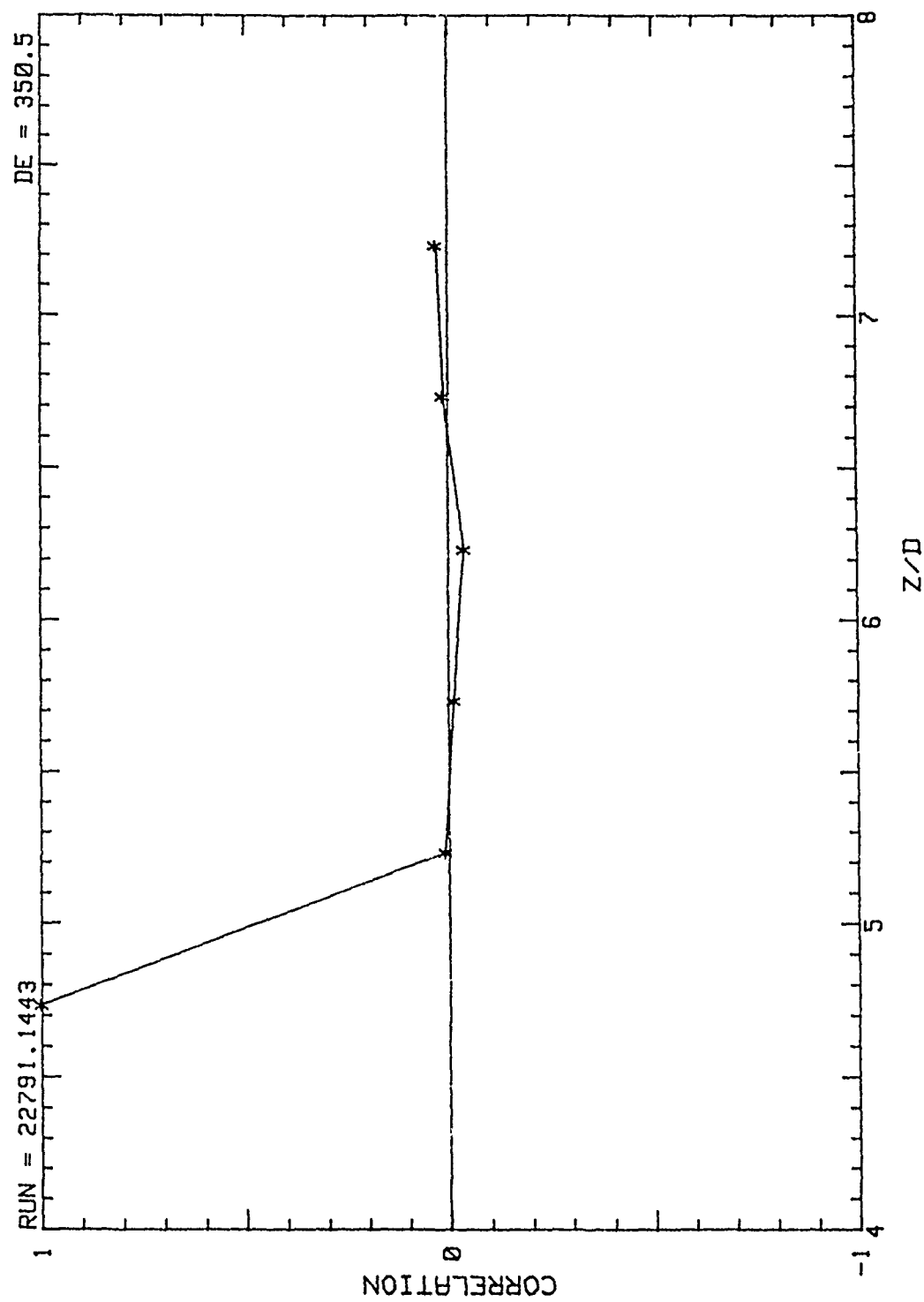


Figure 42. Correlation vs. z/d Probes 2,4,6,8,10,12,wrt 2, $De=350.5$

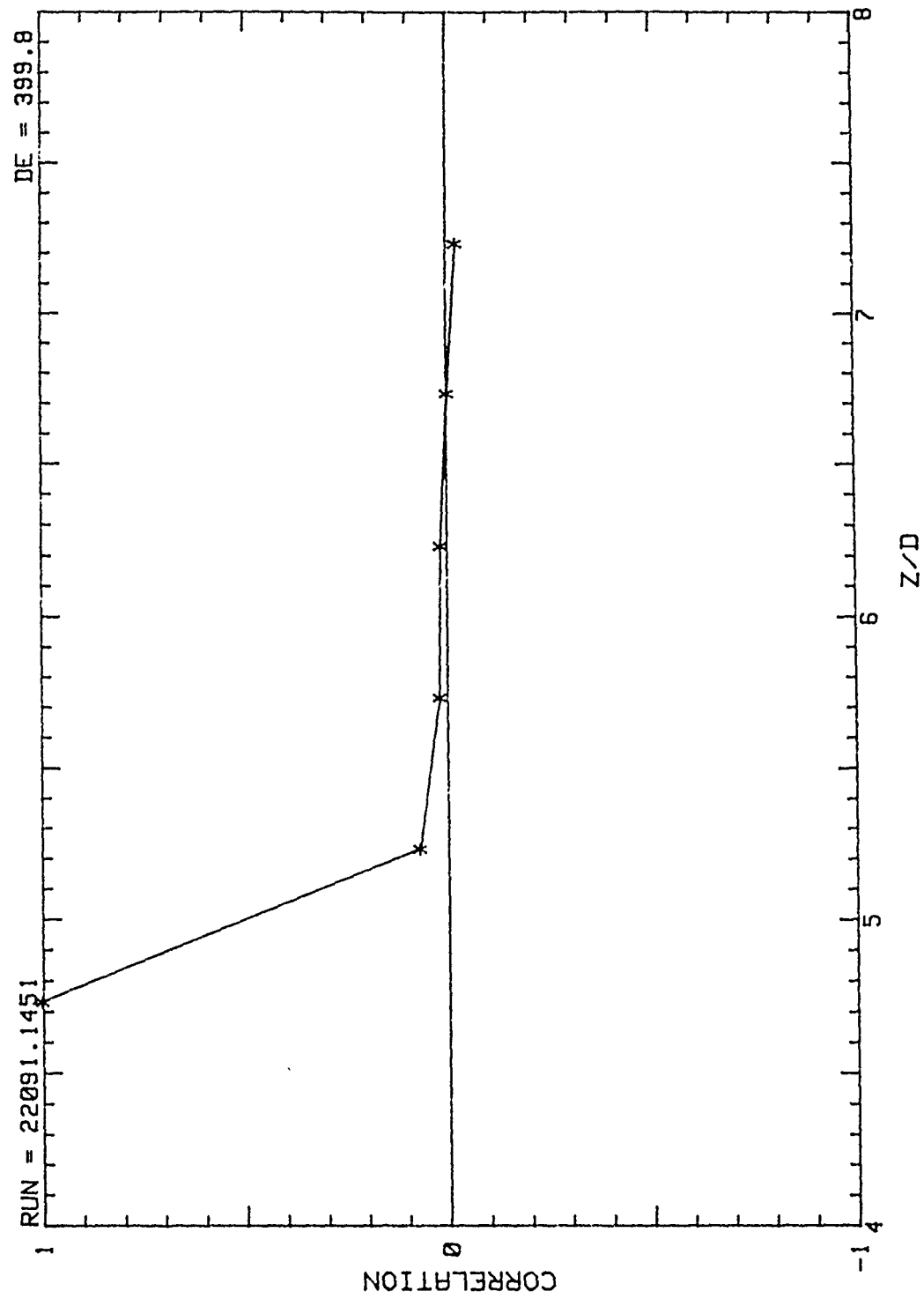


Figure 43. Correlation vs. z/d Probes 2,4,6,8,10,12,wrt 2, $De=399.8$

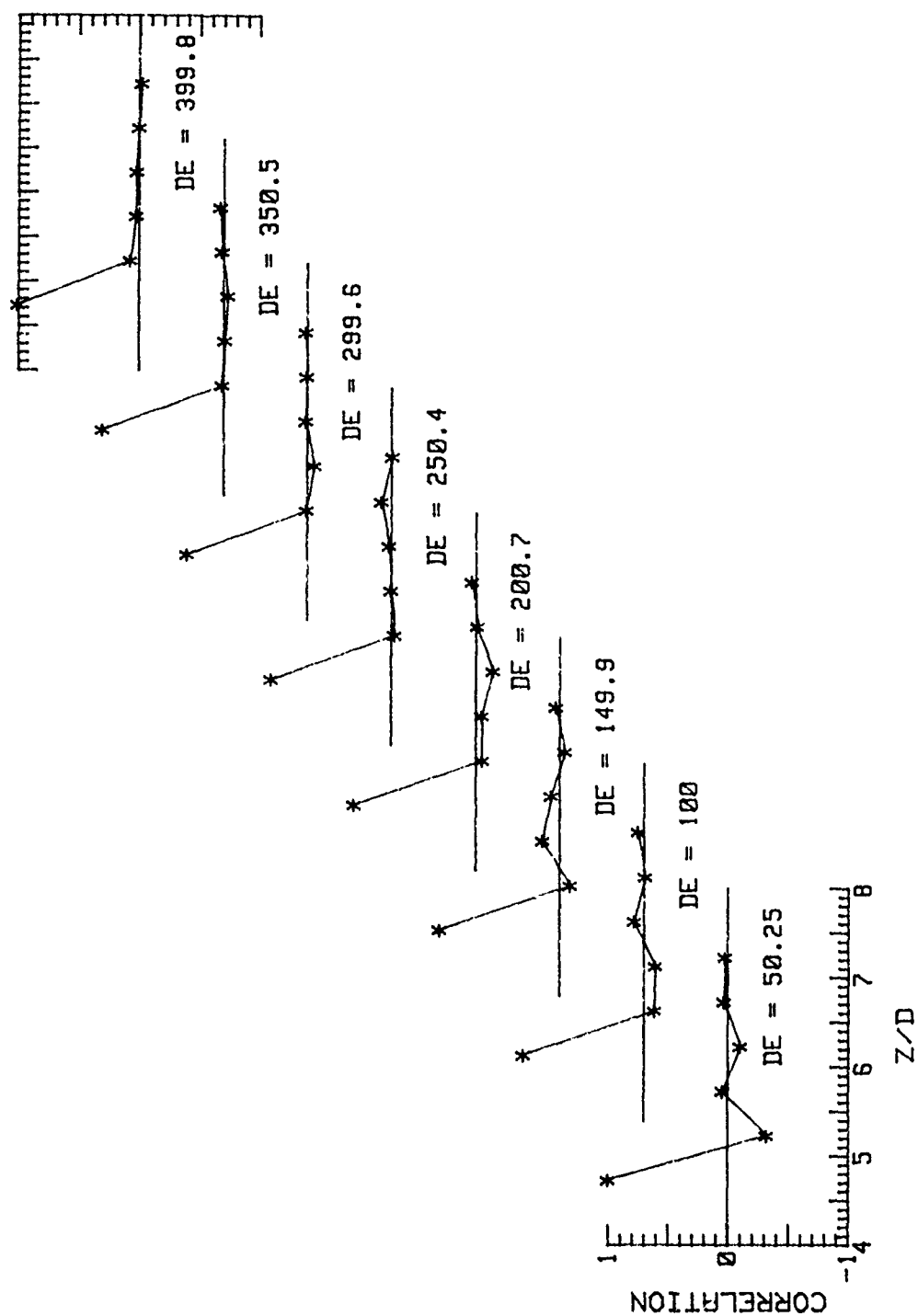


Figure 44. 3-D Correlations vs. z/d Probes 2,4,6,8,10,12,wrt 2, from $De=50.25$ to $De=399.8$

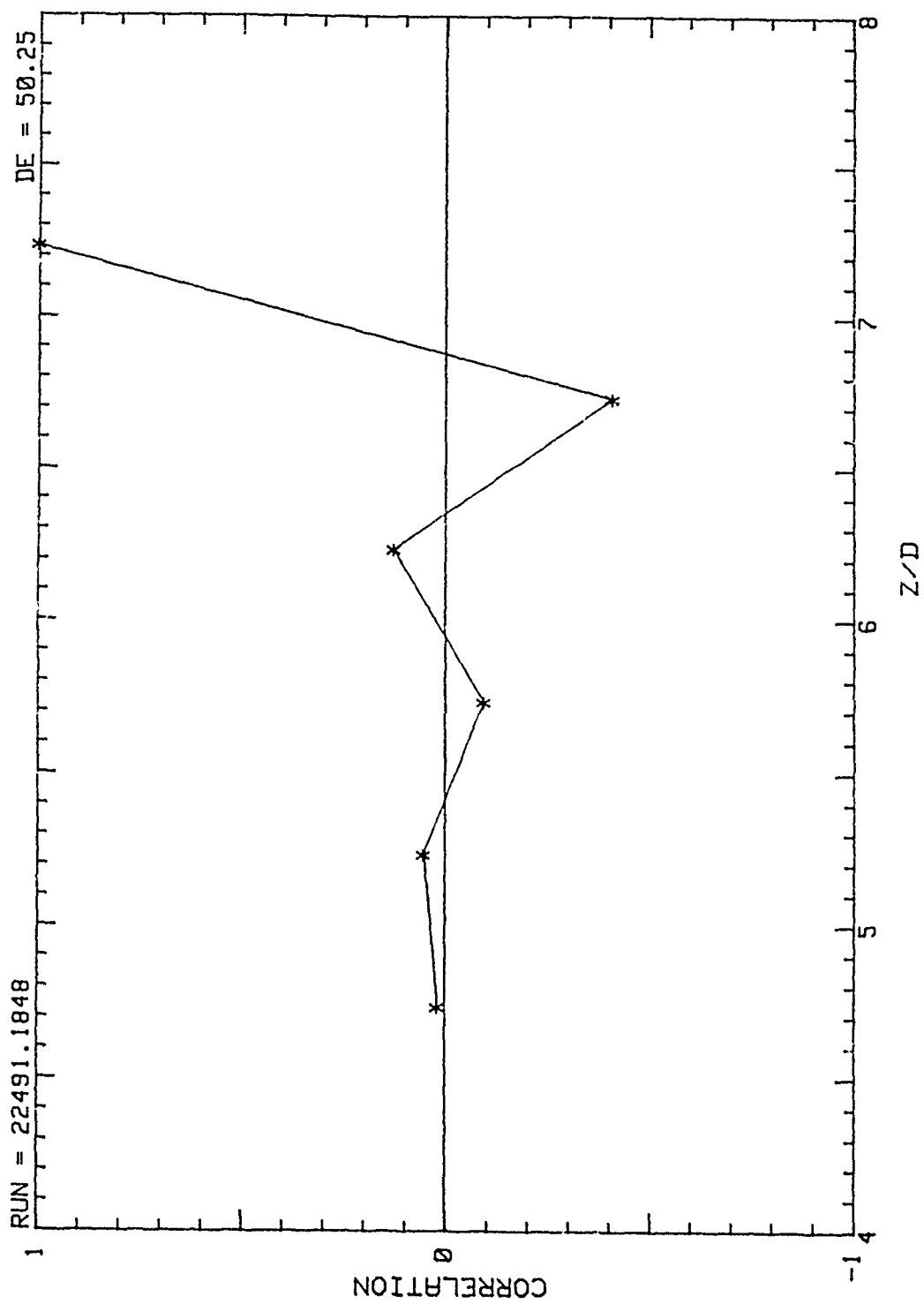


Figure 45. Correlation vs. z/d Probes 2,4,6,8,10,12,wrt 12, $De=50.25$

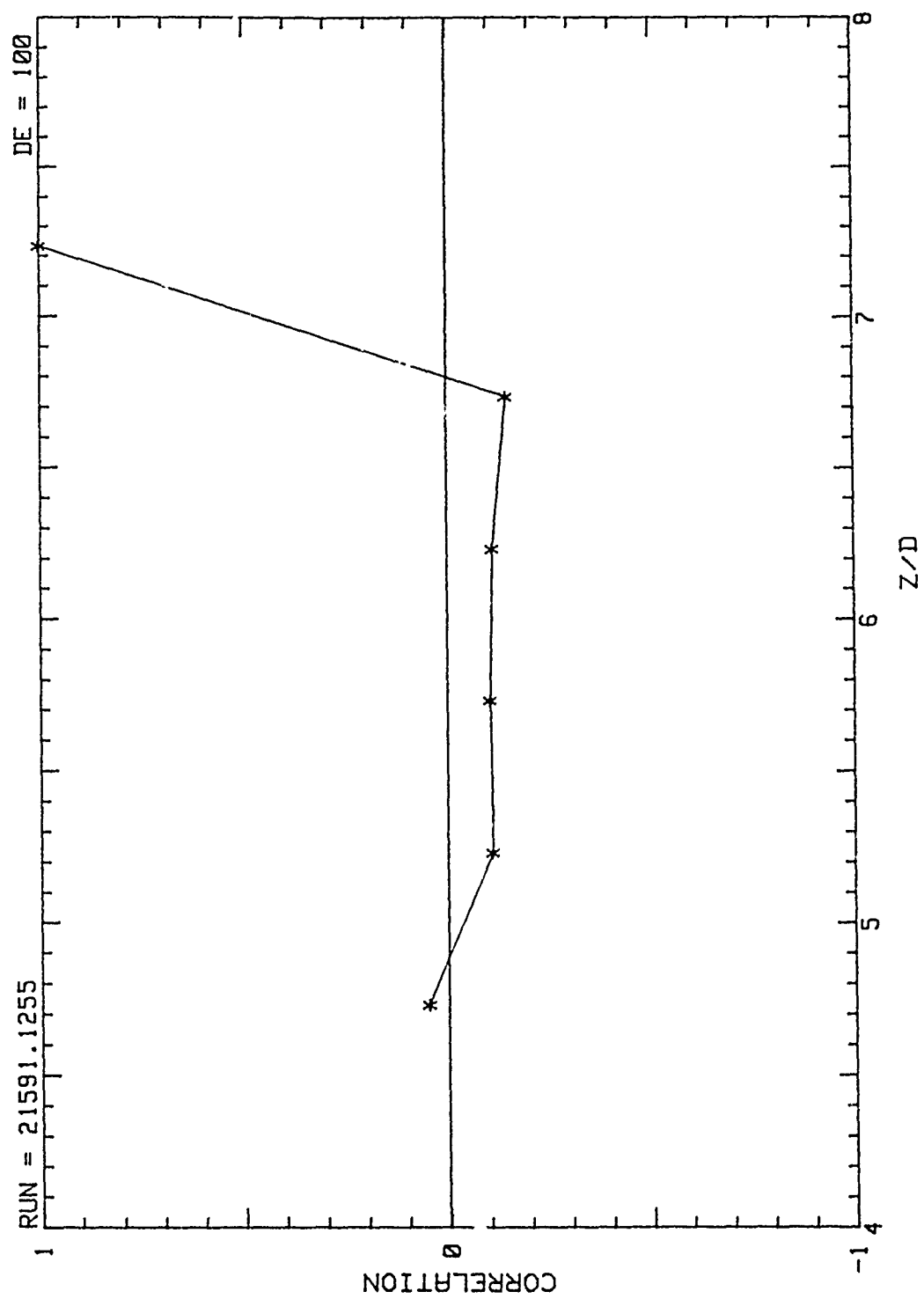


Figure 46. Correlation vs. z/d Probes 2,4,6,8,10,12,wrt 12, $De=100$

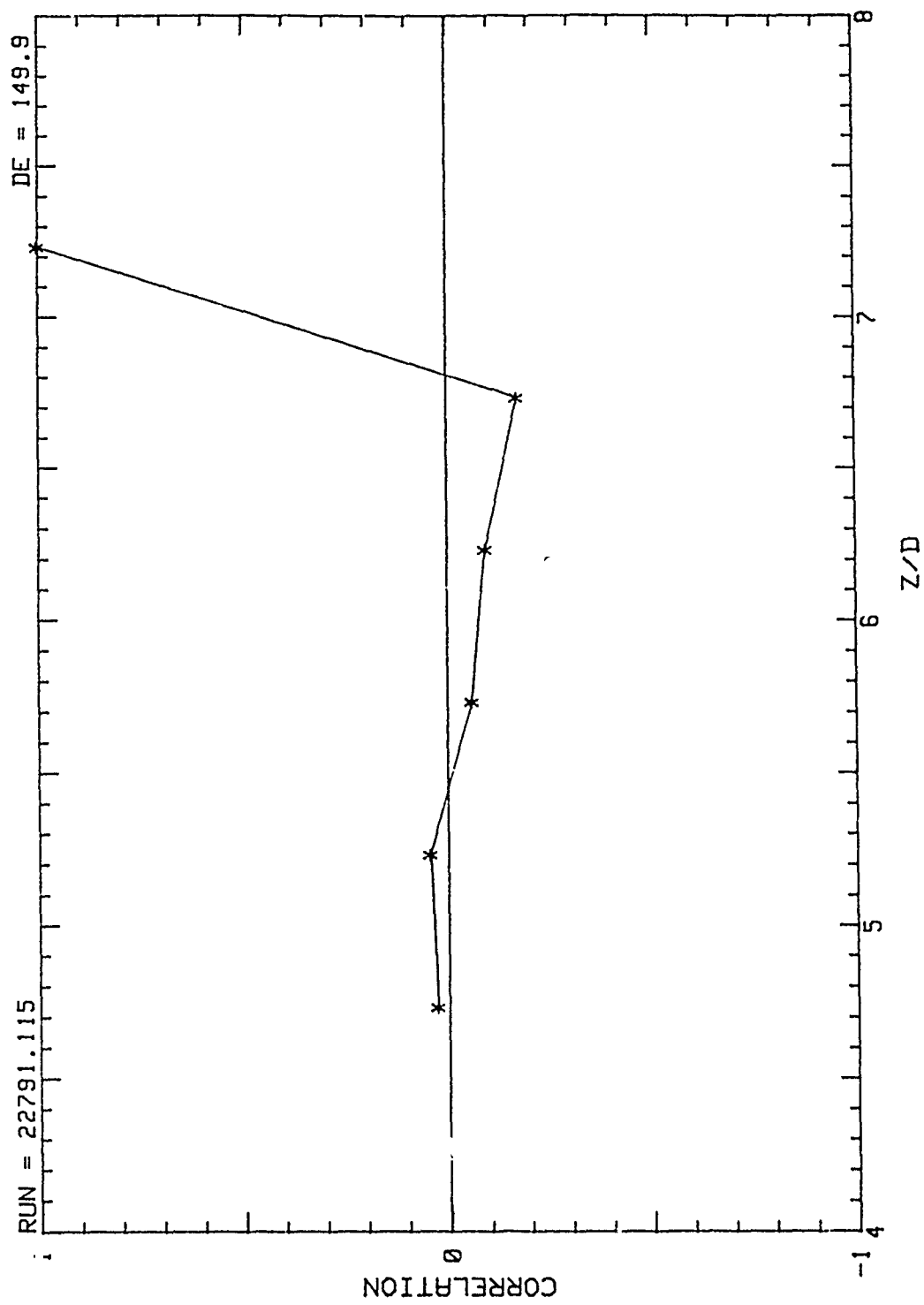


Figure 47. Correlation vs. z/d Probes 2,4,6,8,10,12,wrt 12, $De=149.9$

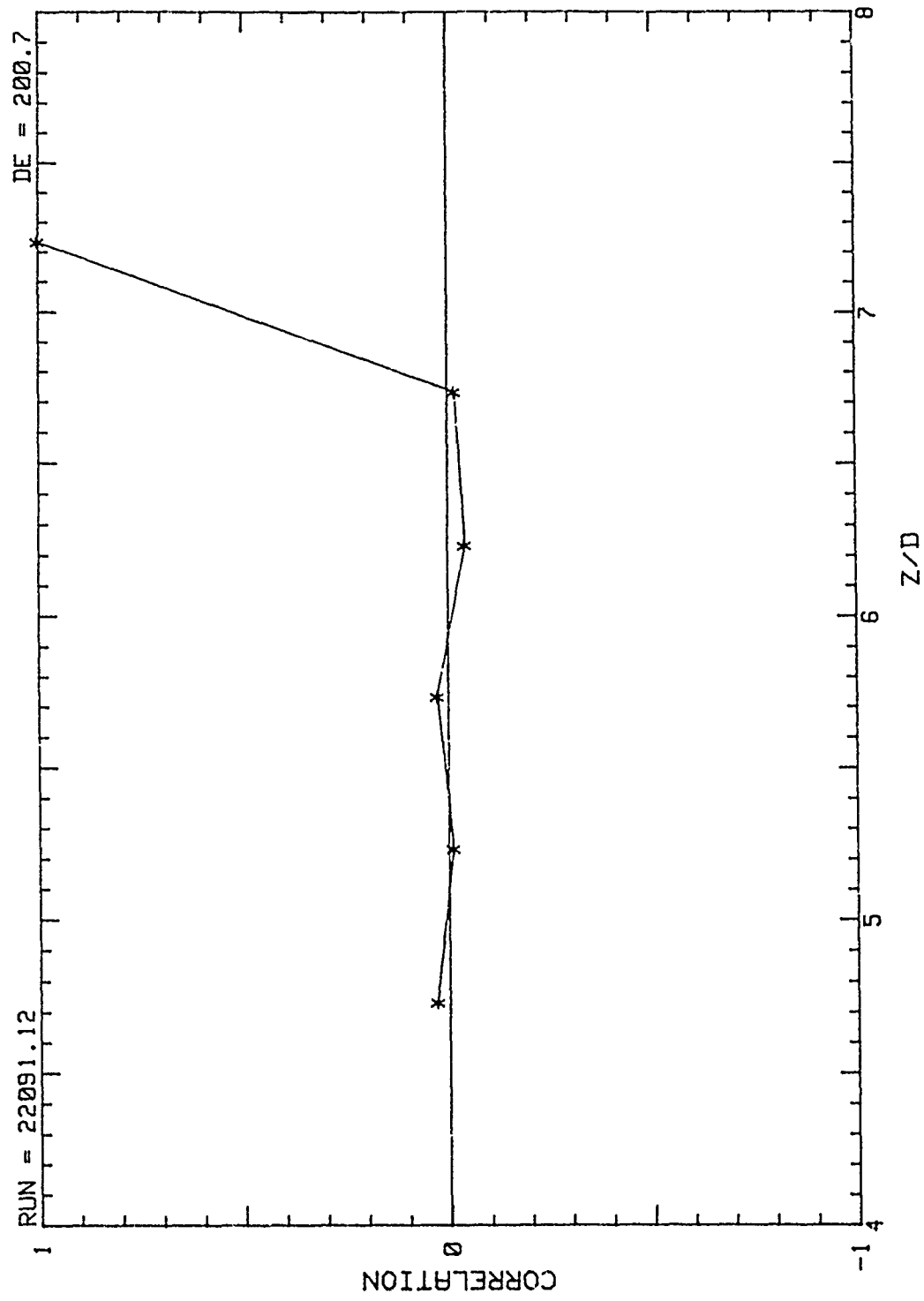


Figure 48. Correlation vs. z/d Probes 2,4,6,8,10,12,wrt 12, $De=200.7$

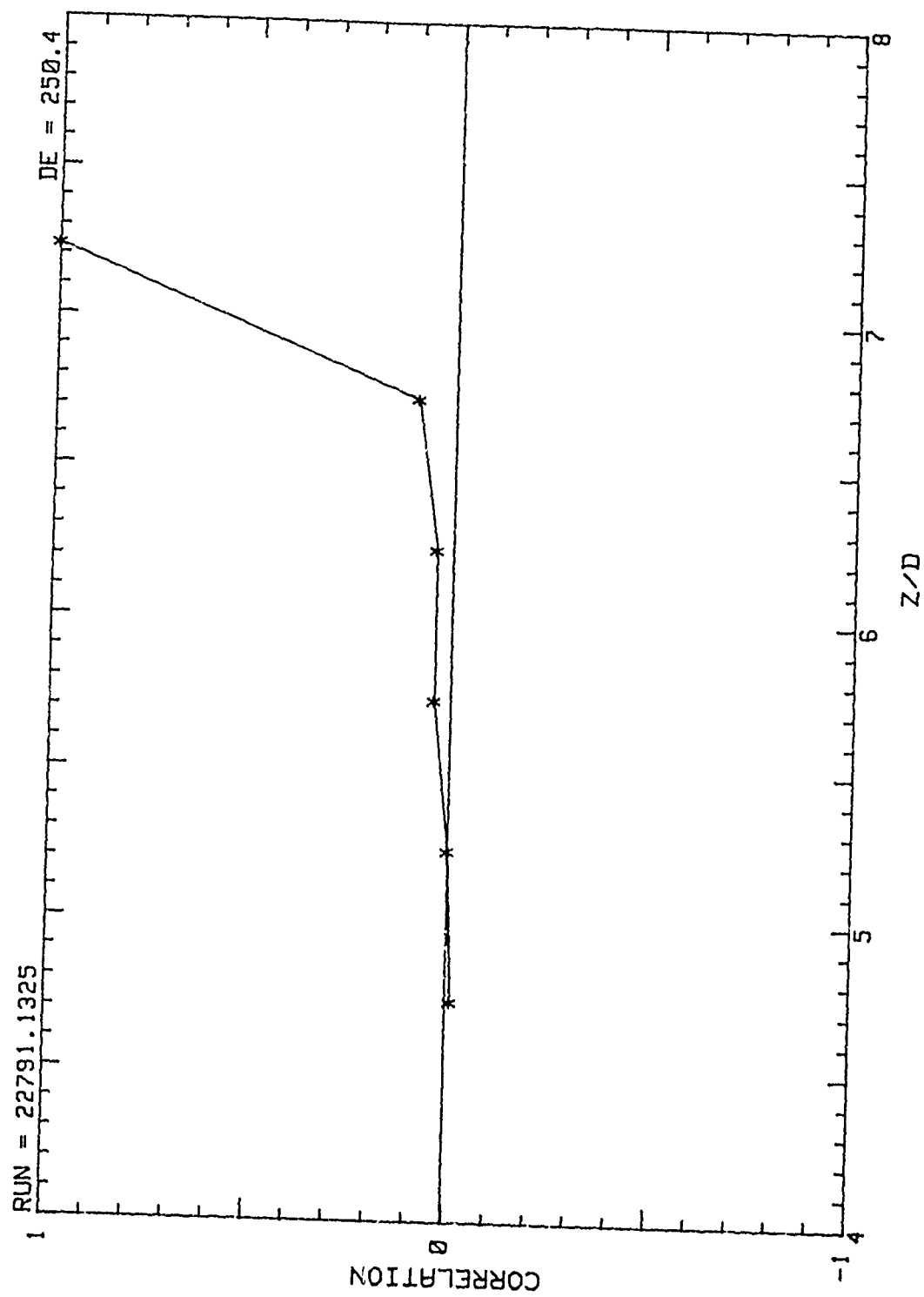


Figure 49. Correlation vs. z/d Probes 2,4,6,8,10,12,wrt 12, $De=250.4$

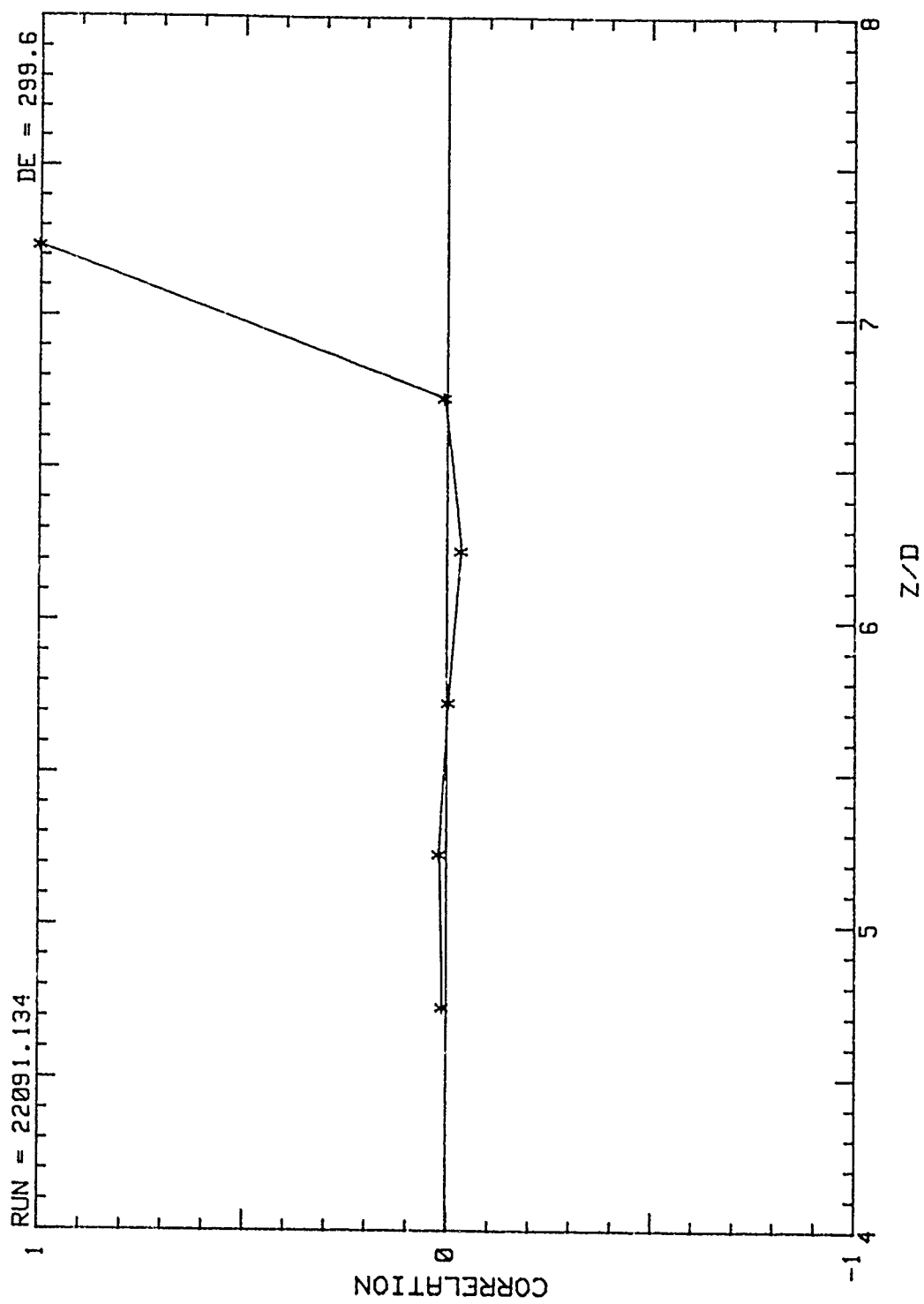


Figure 50. Correlation vs. z/d Probes 2,4,6,8,10,12,wrt 12, $De=299.6$

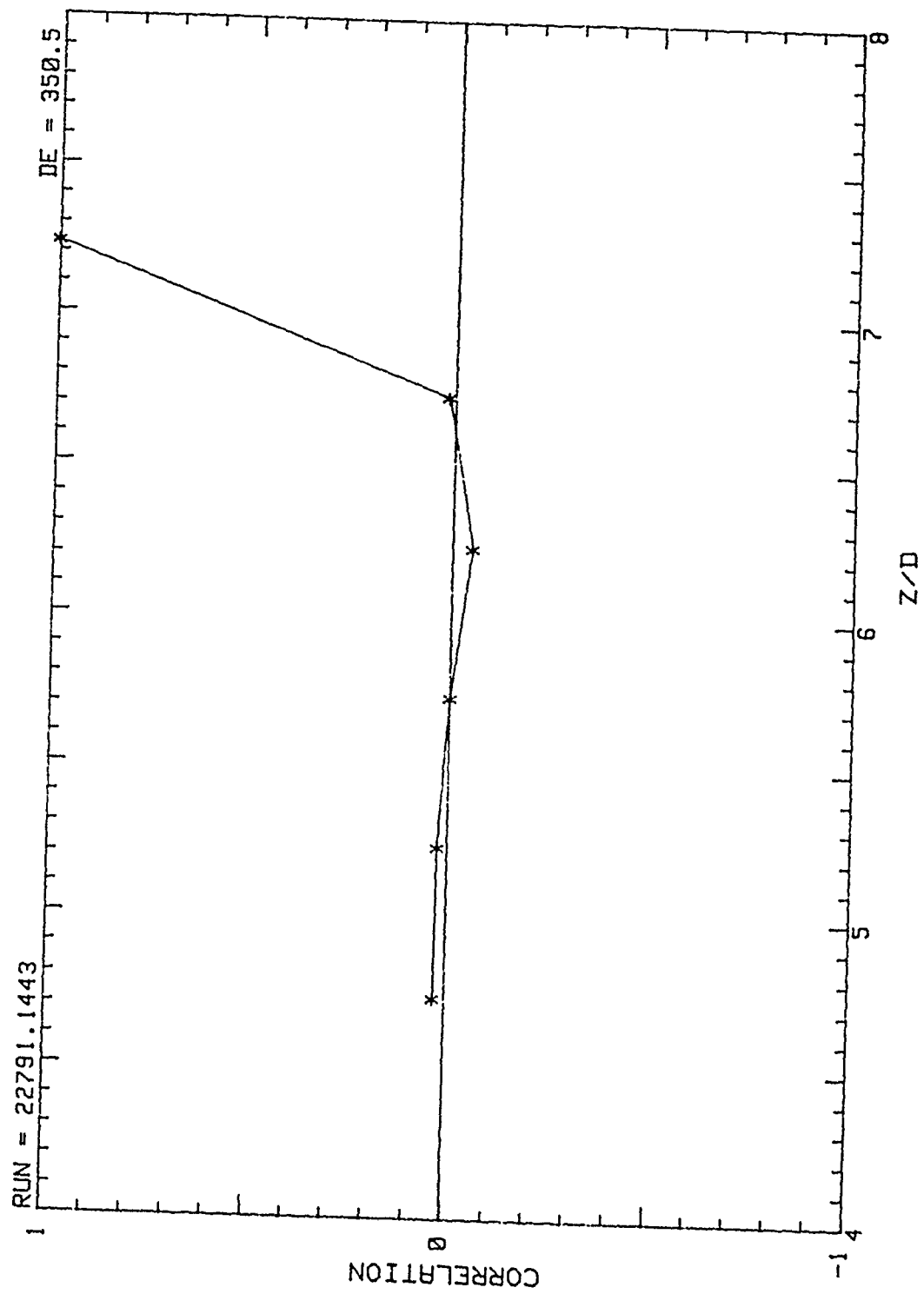


Figure 51. Correlation vs. z/d Probes 2,4,6,8,10,12,wrt 12, $De=350.5$

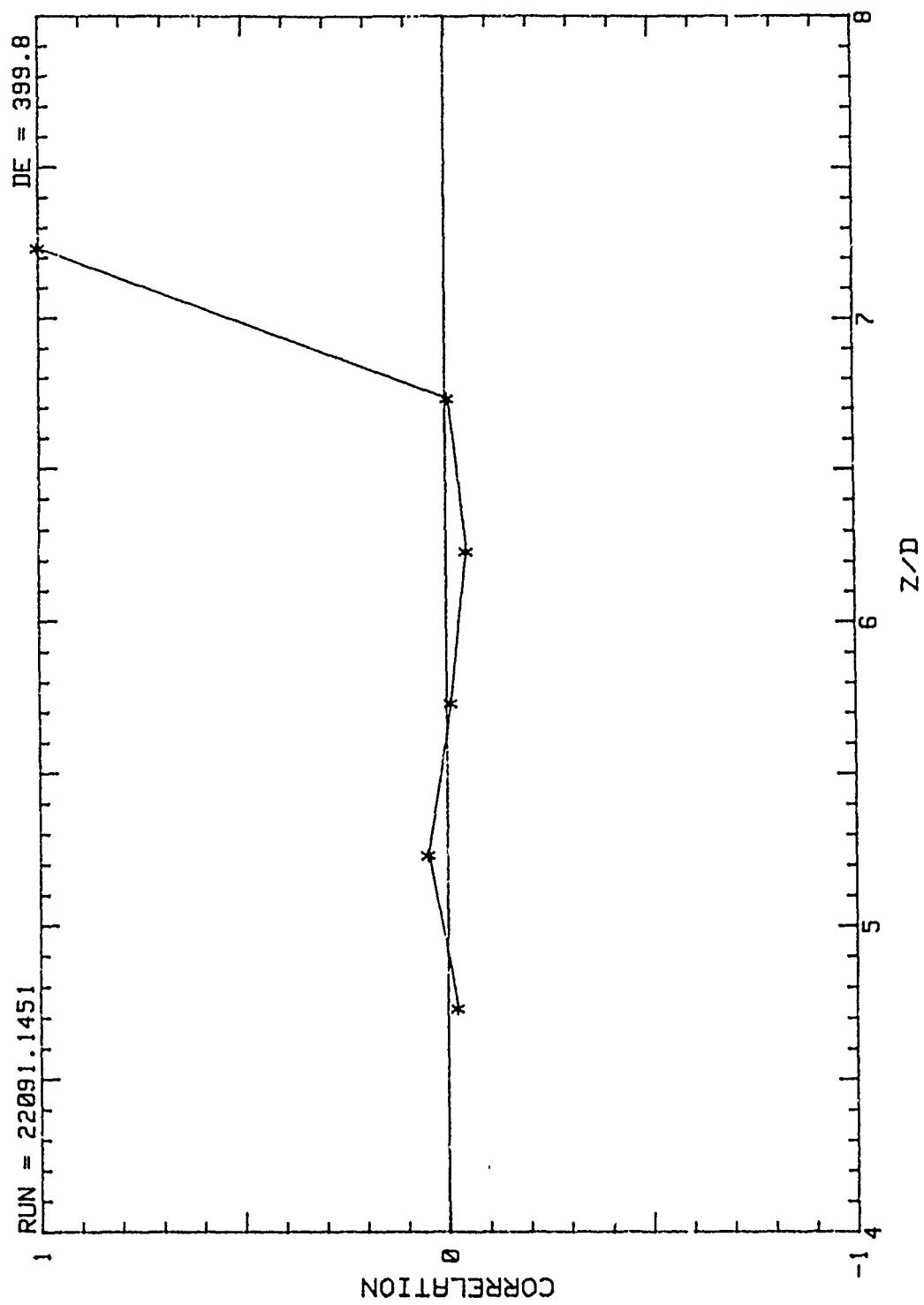


Figure 52. Correlation vs. z/d Probes 2,4,6,8,10,12,wrt 12, $De=399.8$

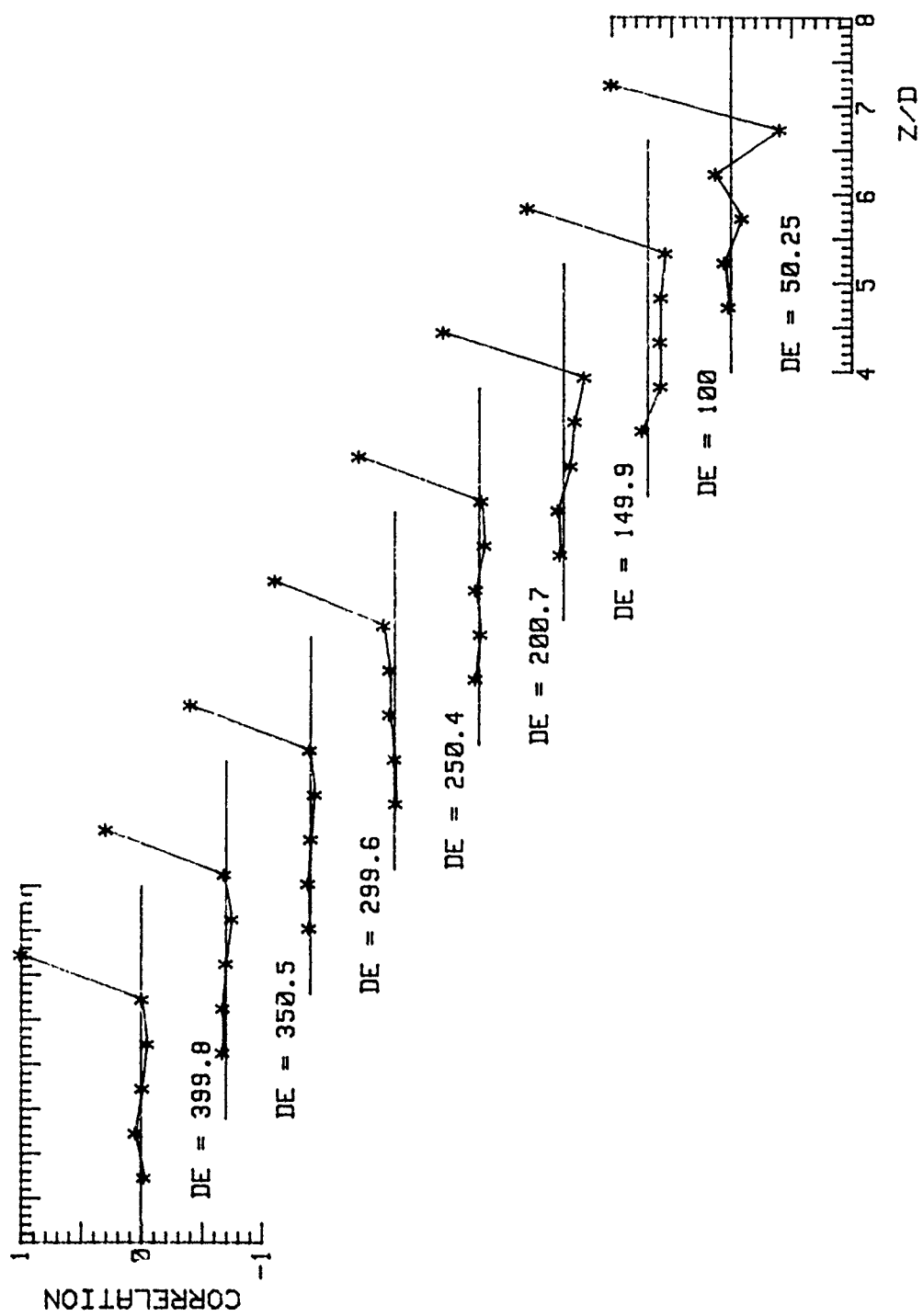


Figure 53. 3-D Correlations vs. z/d Probes 2,4,6,8,10,12,wrt 12, from $De=50.25$ to $De=399.8$

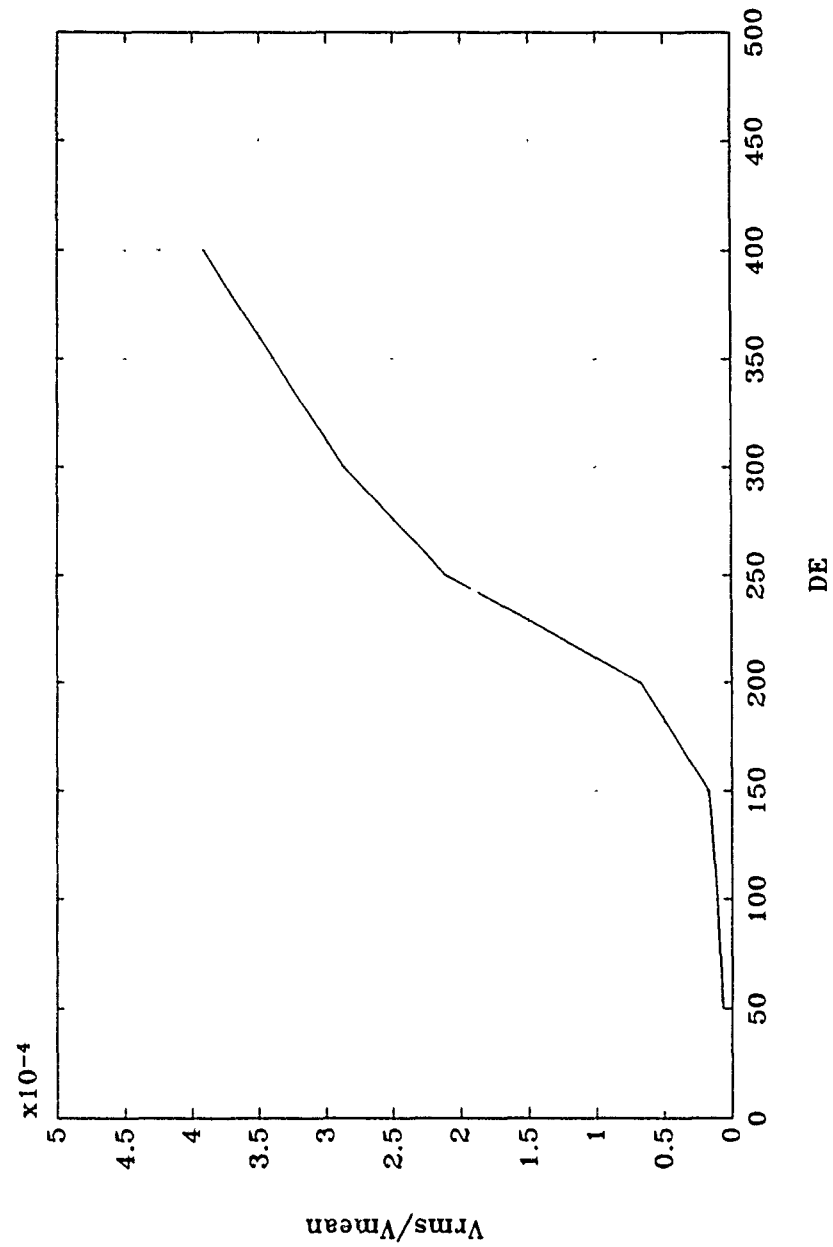


Figure 54. Average V_{rms}/V_{mean} vs. DE Probes 2,4,6,8,10,12

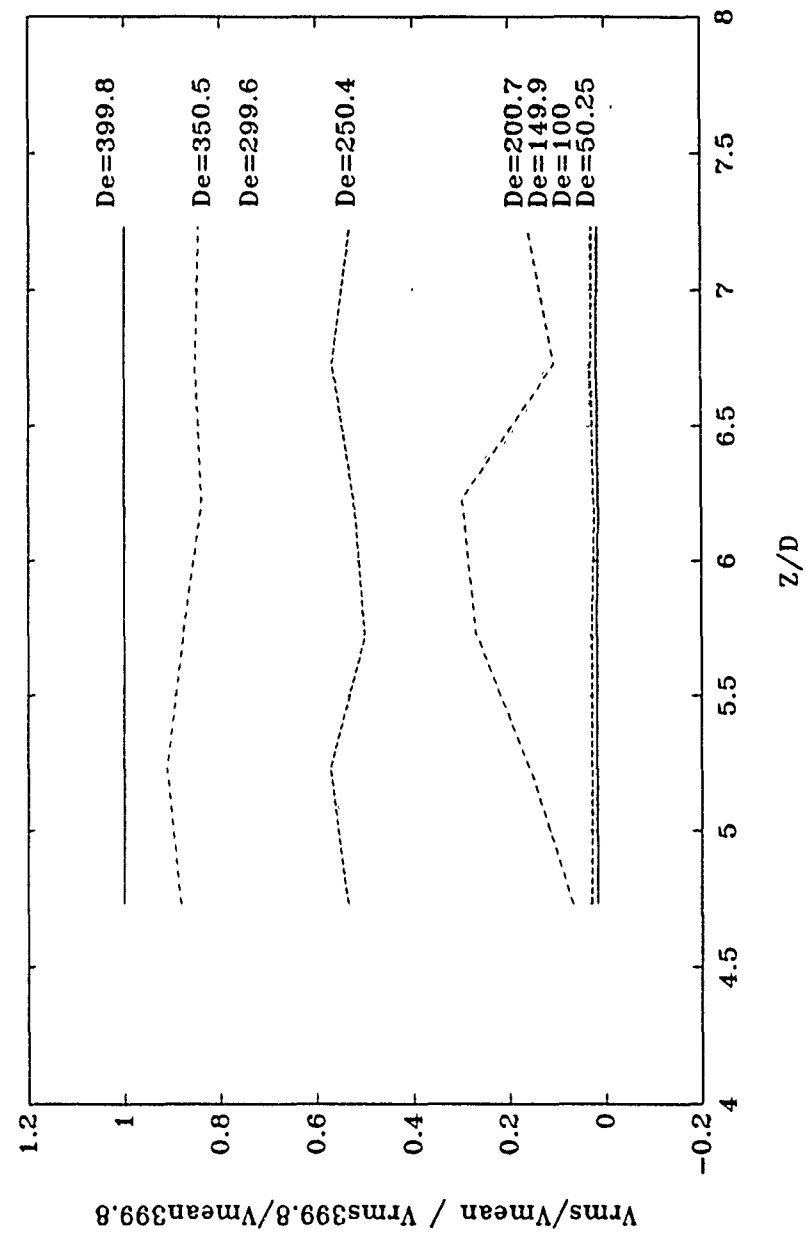


Figure 55. $V_{rms}/V_{mean} / V_{rms399.8}/V_{mean399.8}$ vs. z/d from $De=50.25$ to $De=399.8$

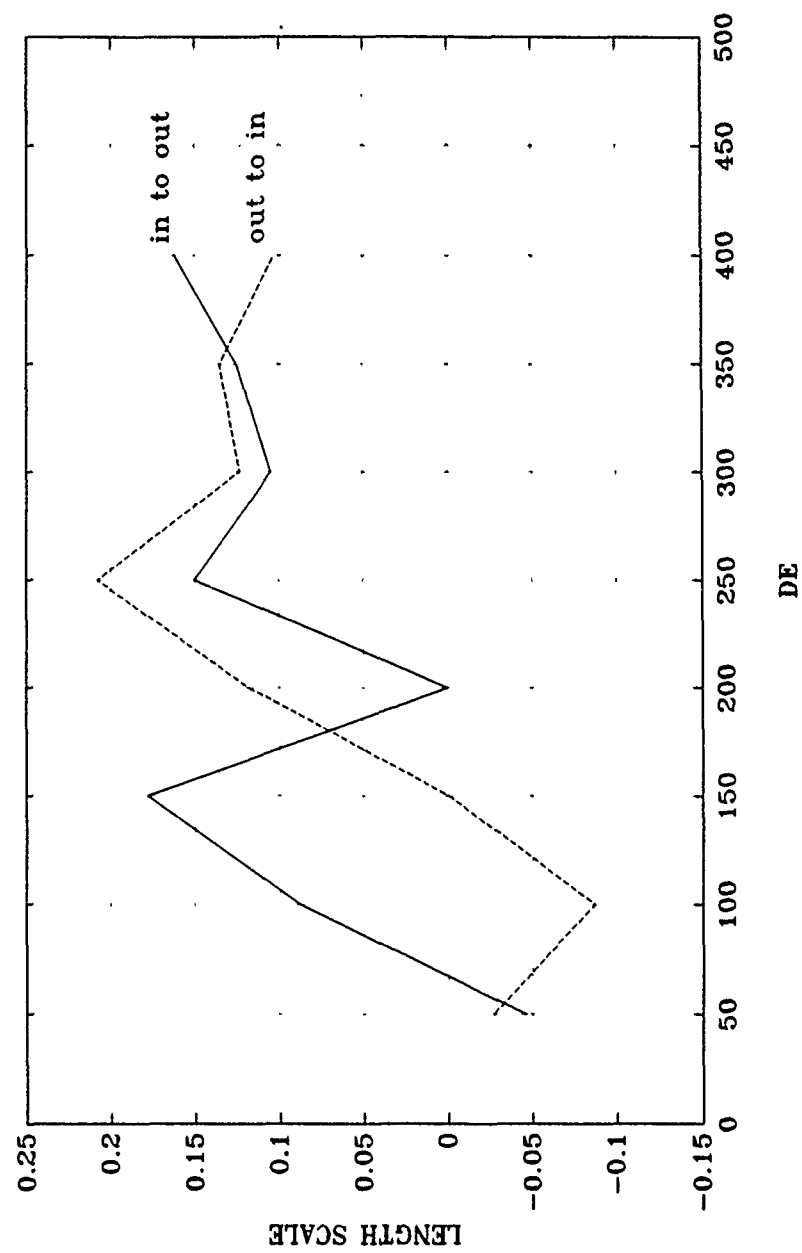


Figure 56. Length Scales vs. De Probes 2,4,6,8,10,12

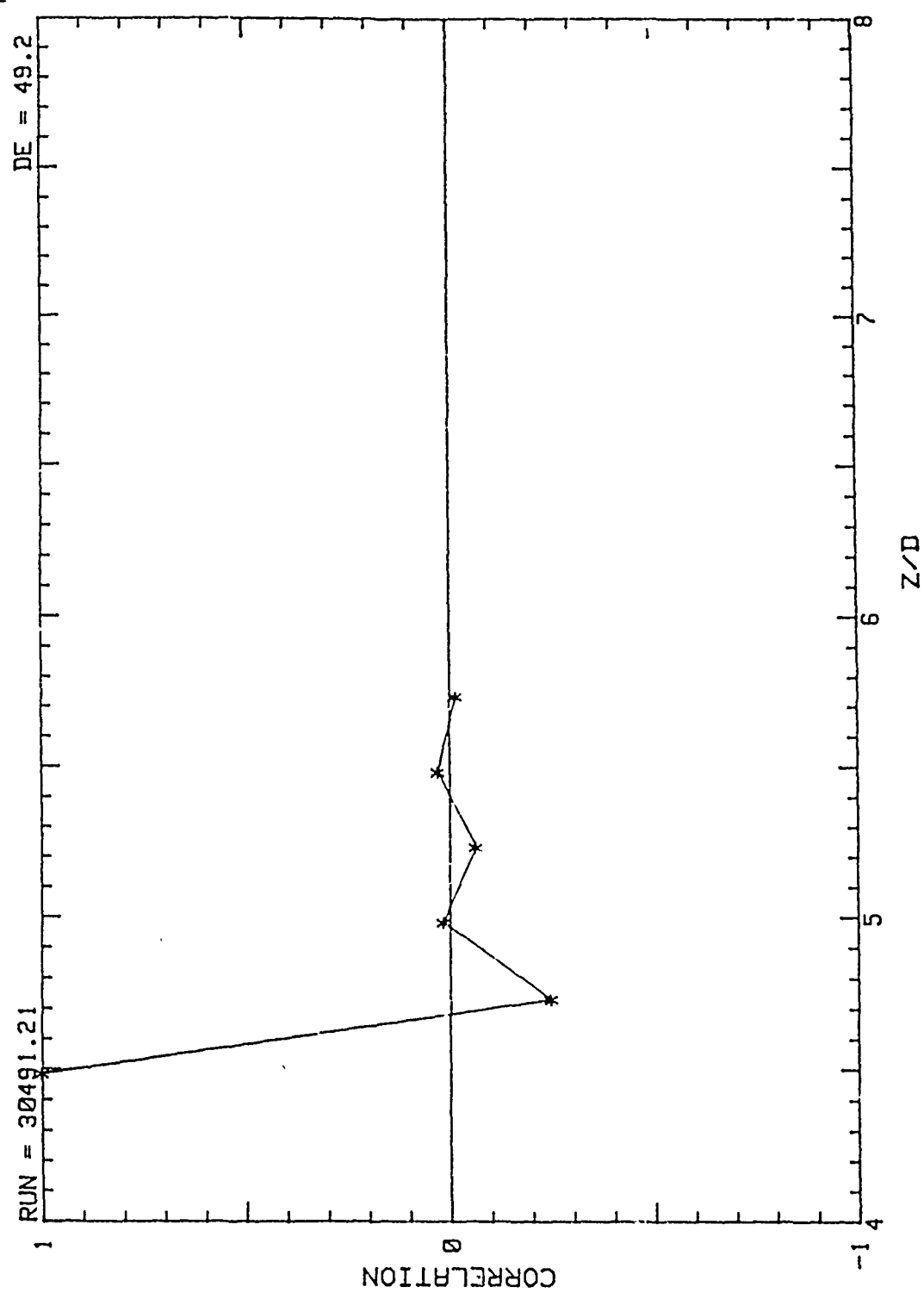


Figure 57. Correlation vs. z/d Probes 1,2,3,4,5,6, wrt 1, $De=49.2$

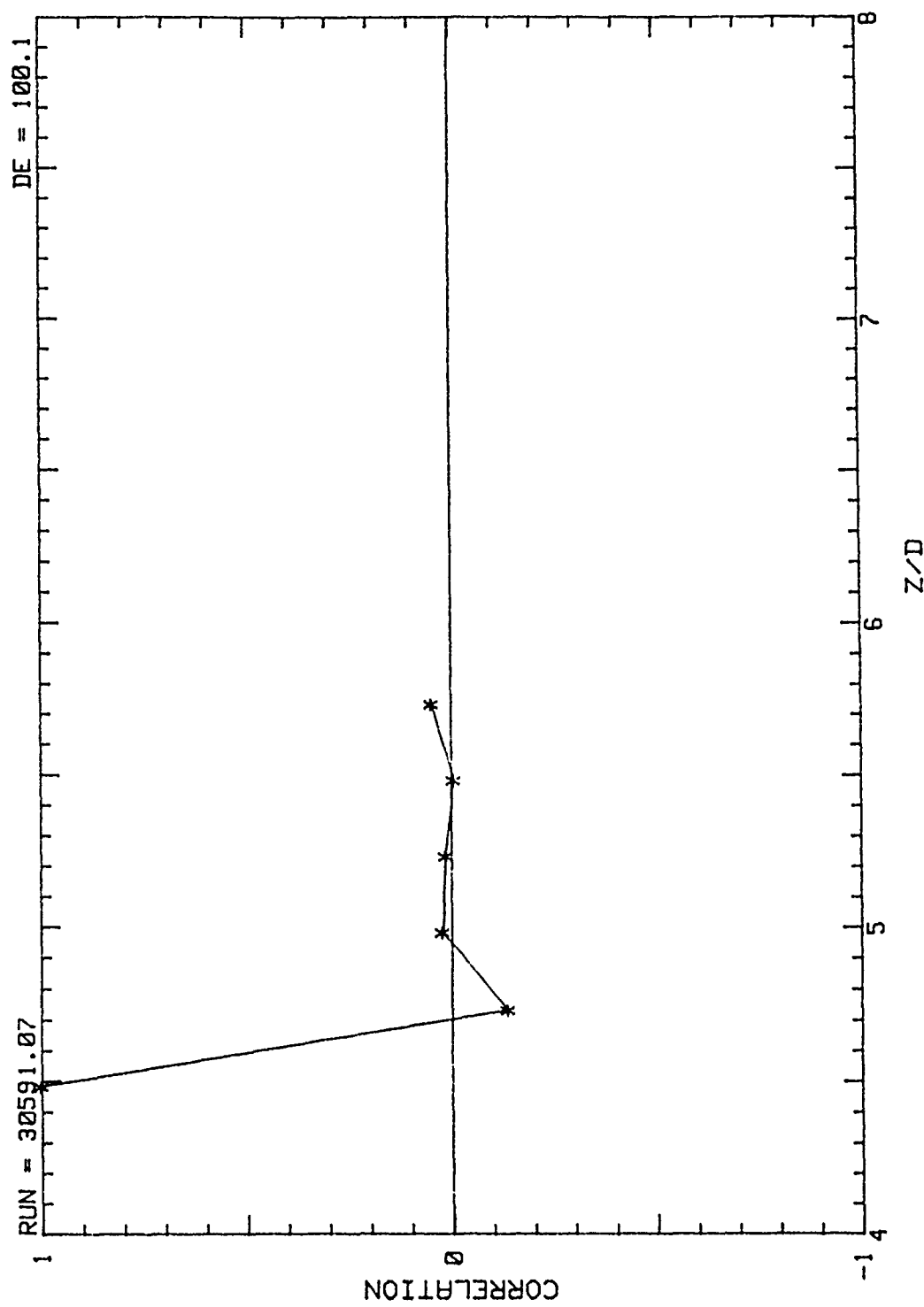


Figure 58. Correlation vs. z/d Probes 1,2,3,4,5,6, wrt 1, $De=100.1$

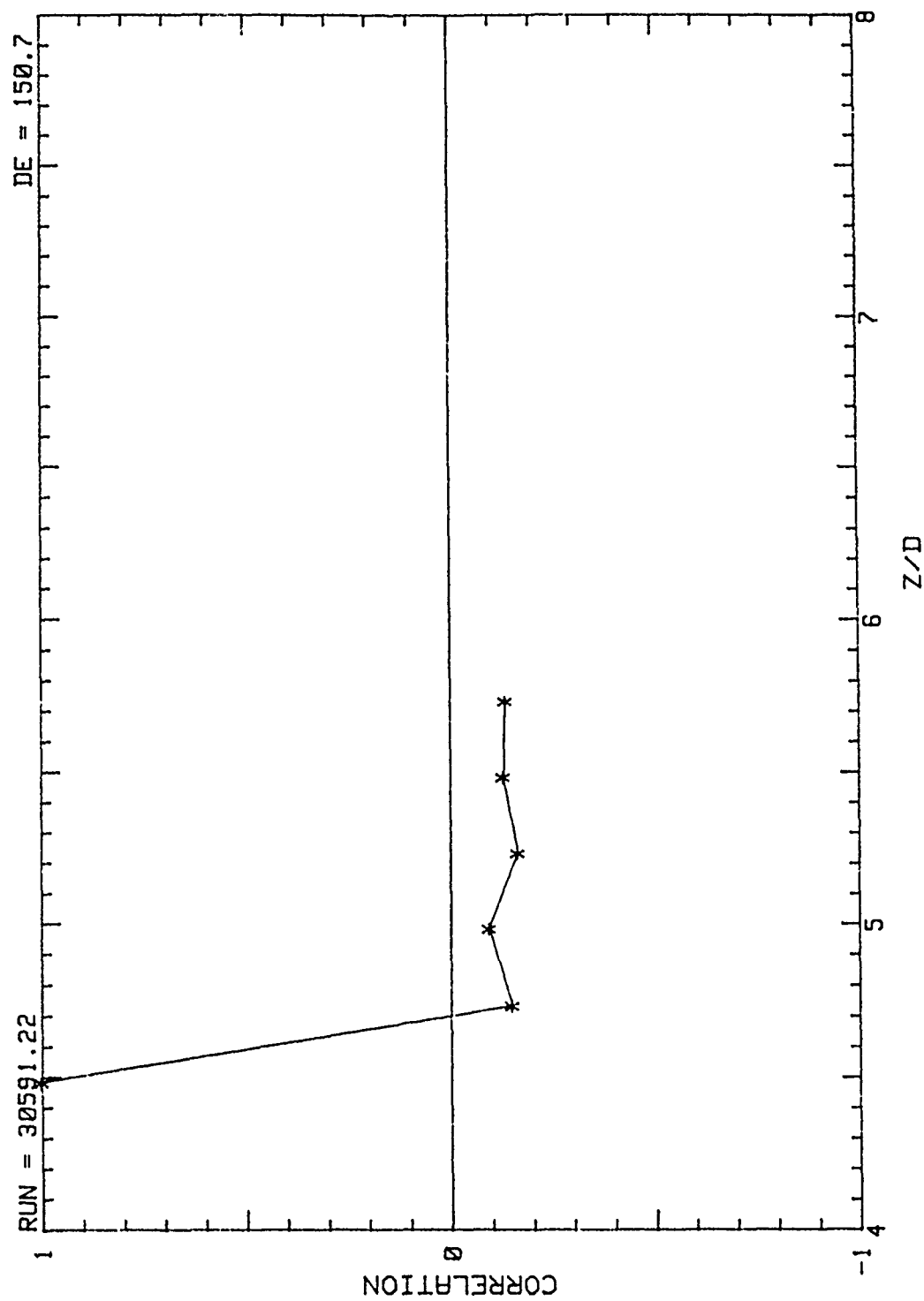


Figure 59. Correlation vs. z/d Probes 1,2,3,4,5,6, wrt 1, $De=150.7$

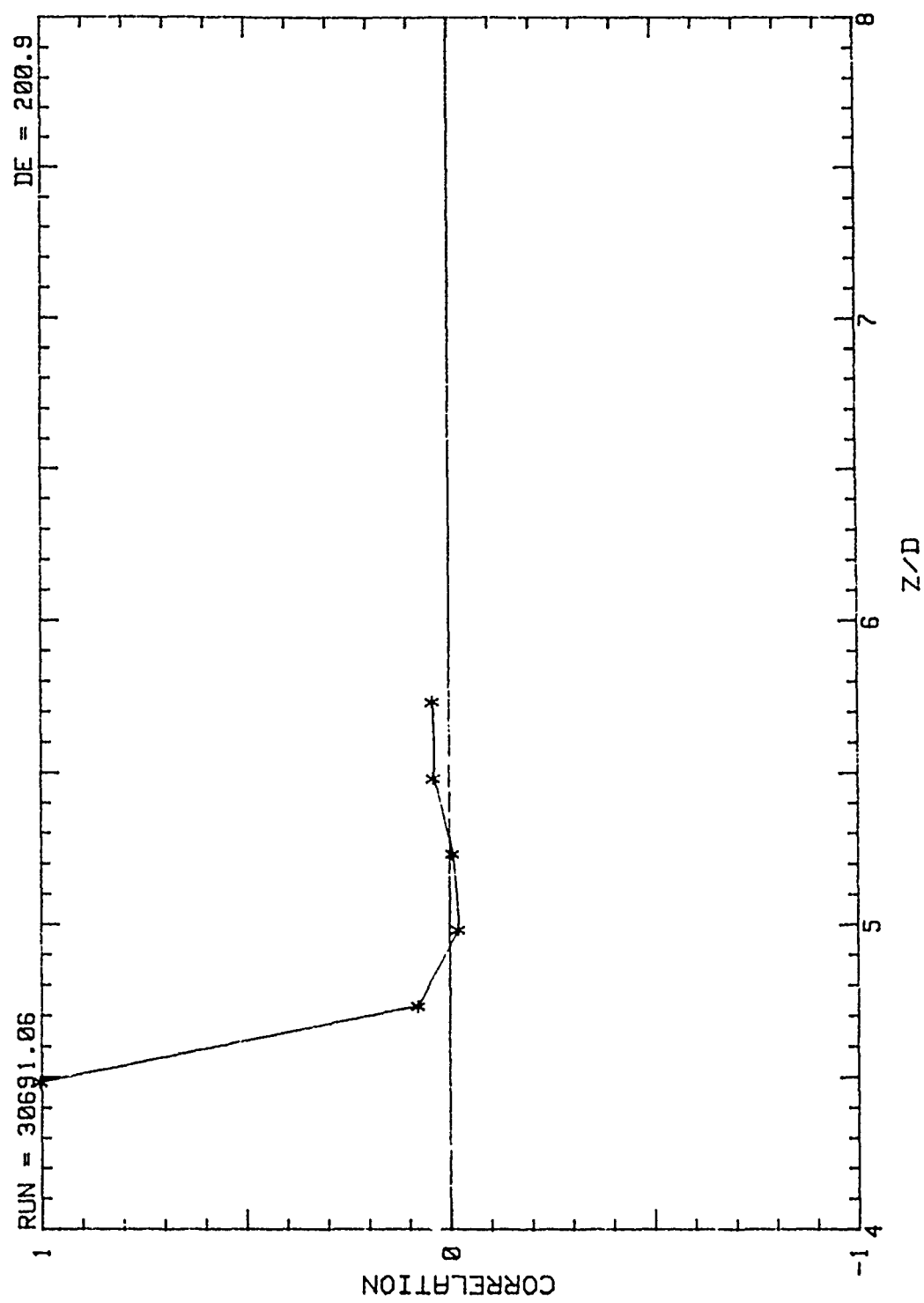


Figure 60. Correlation vs. z/d Probes 1,2,3,4,5,6, wrt 1, $De=200.9$

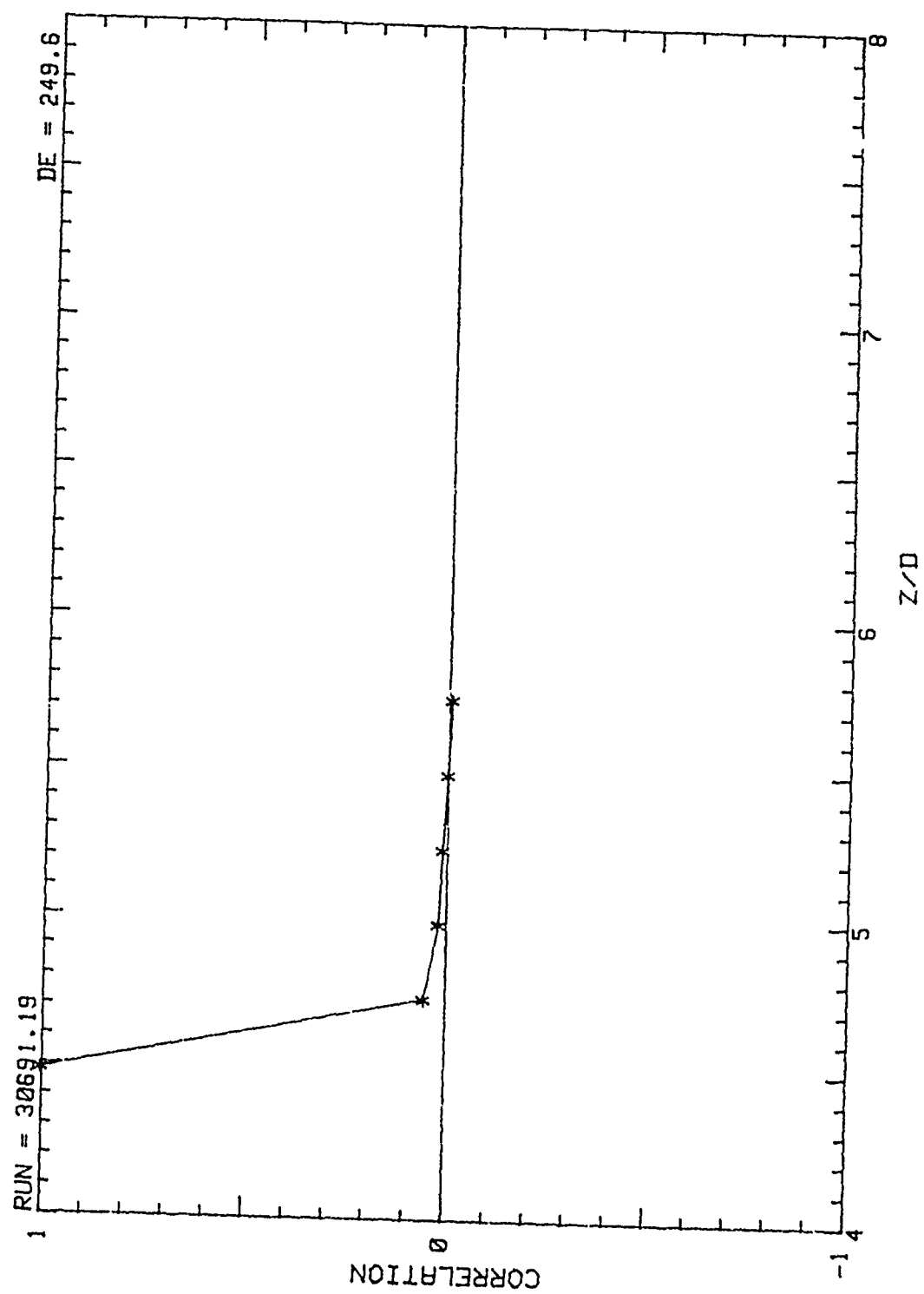


Figure 61. Correlation vs. z/d Probes 1,2,3,4,5,6, wrt 1, De=249.6

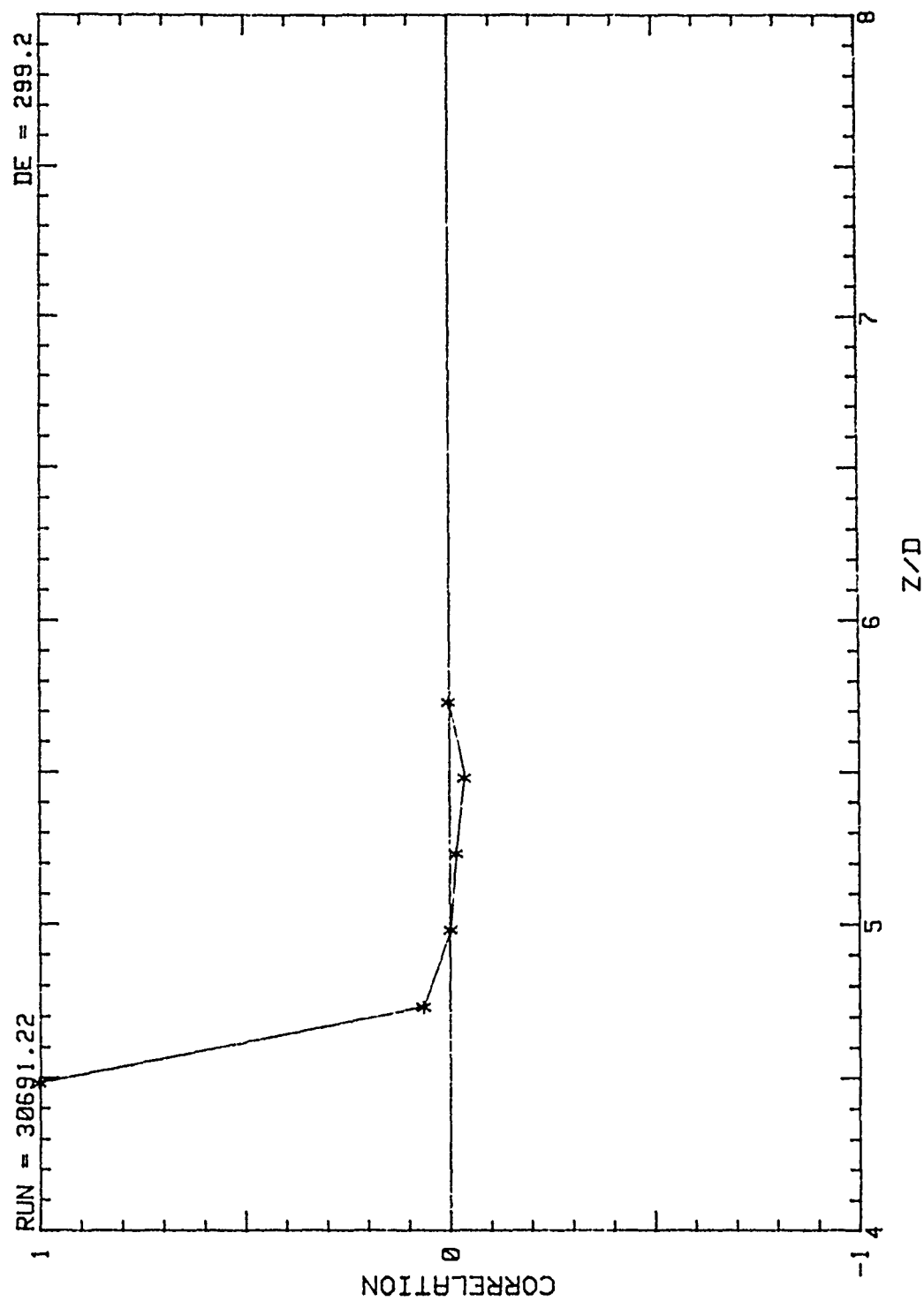


Figure 62. Correlation vs. z/d Probes 1,2,3,4,5,6, wrt 1, $De=299.2$

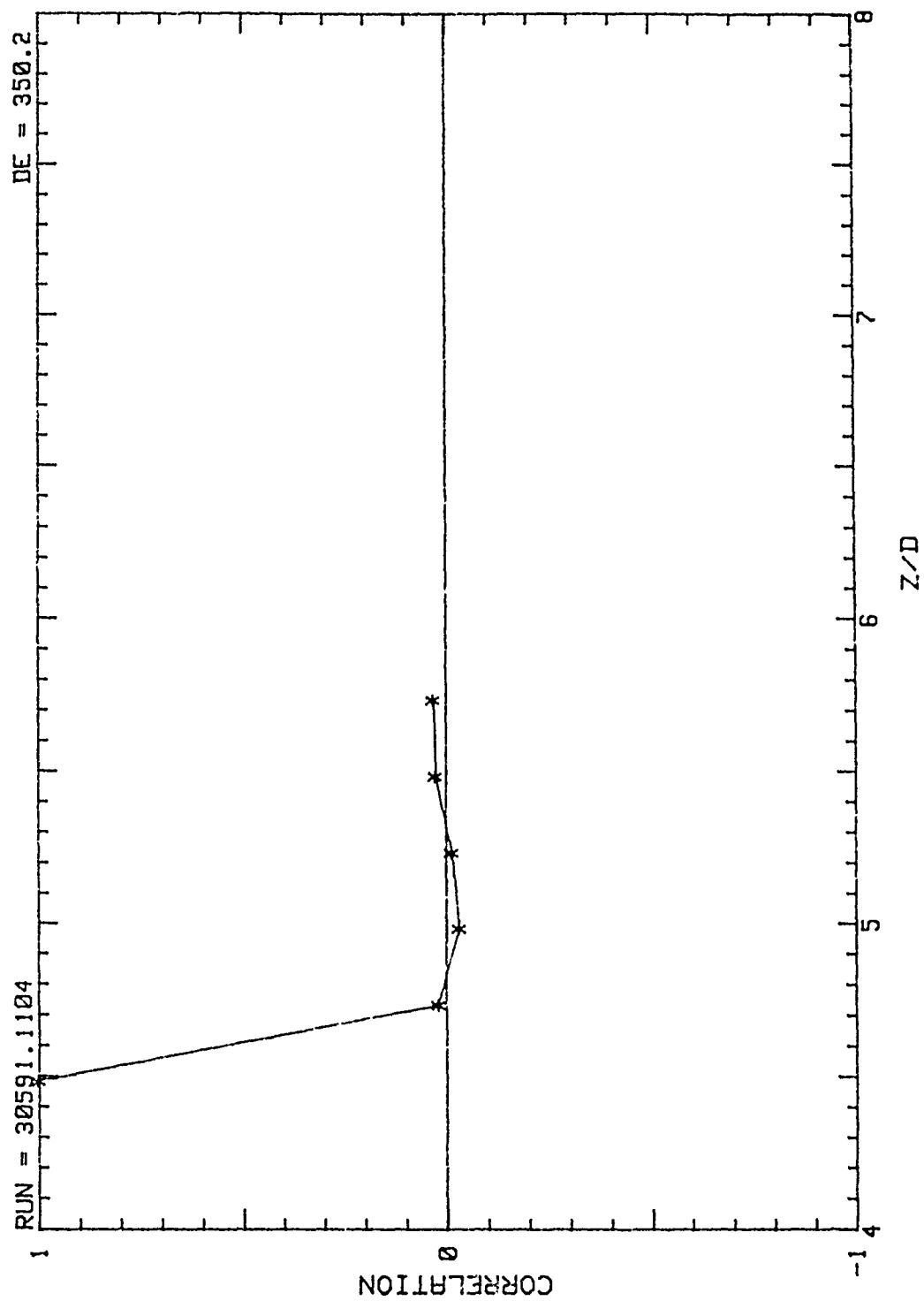


Figure 63. Correlation vs. z/d Probes 1,2,3,4,5,6, wrt 1, $De=350.2$

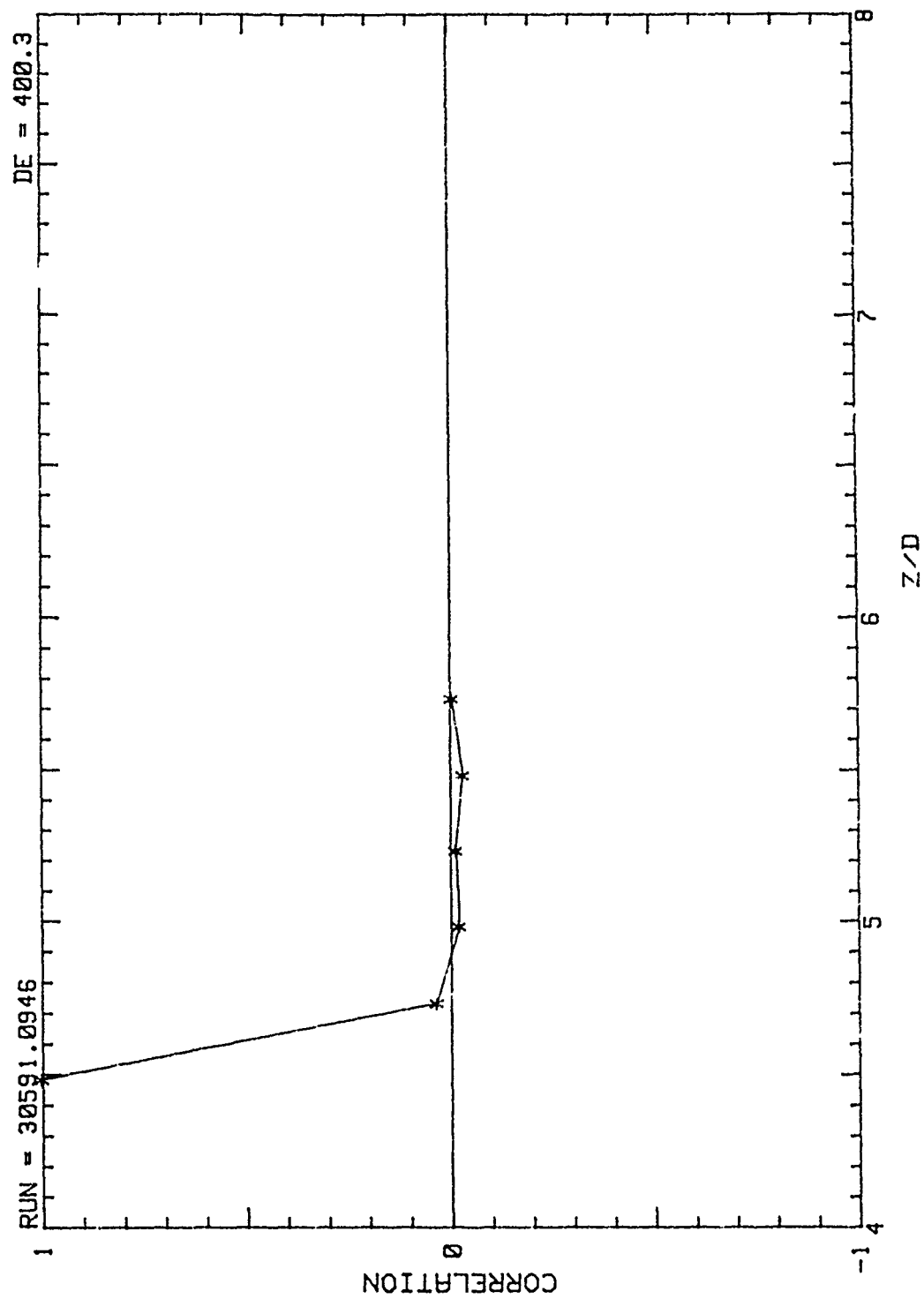


Figure 64. Correlation vs. z/d Probes 1,2,3,4,5,6, wrt 1, De=400.3

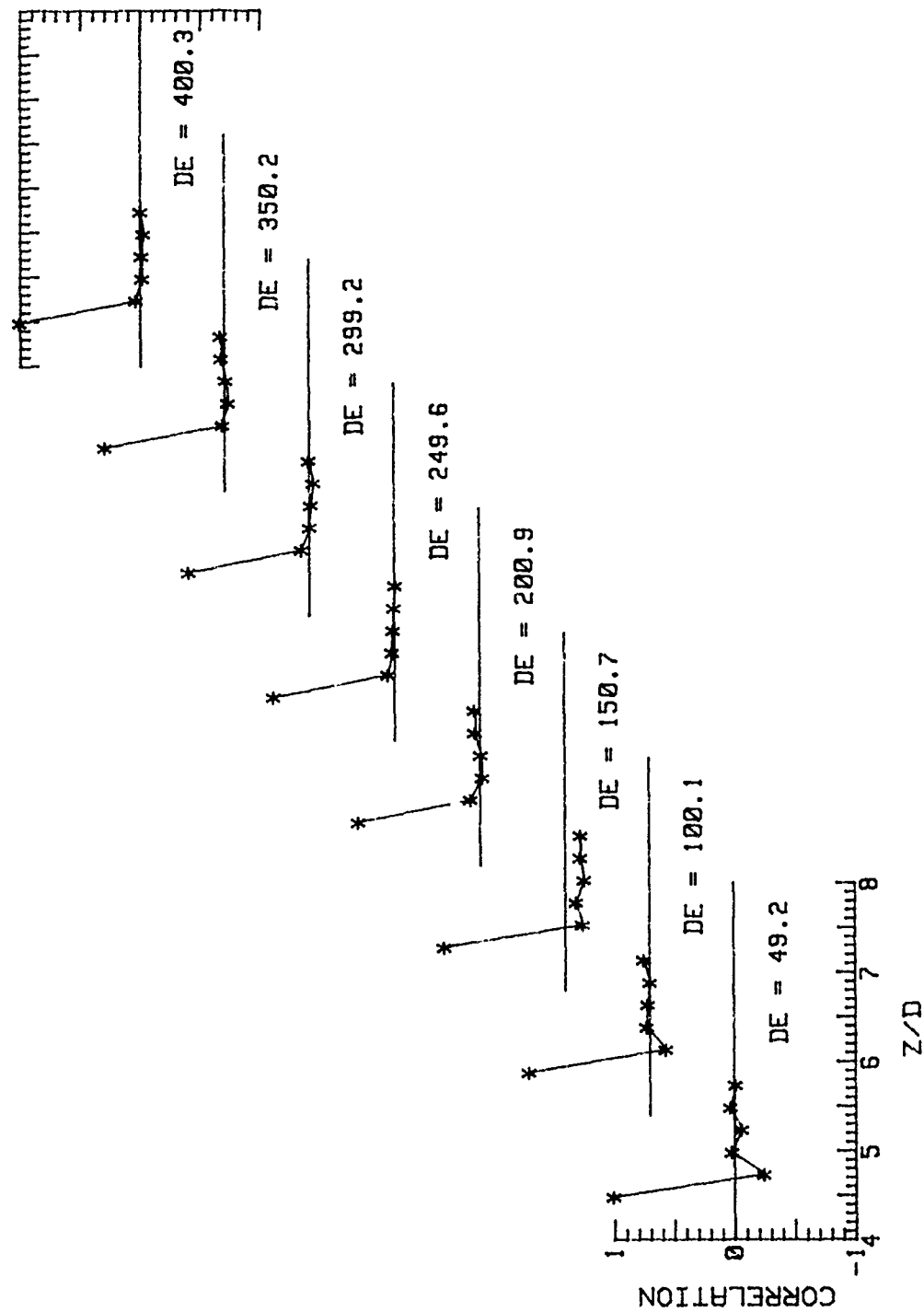


Figure 65. 3-D Correlations vs. z/d Probes 1,2,3,4,5,6, wrt 1, from $De=49.2$ to $De=400.3$

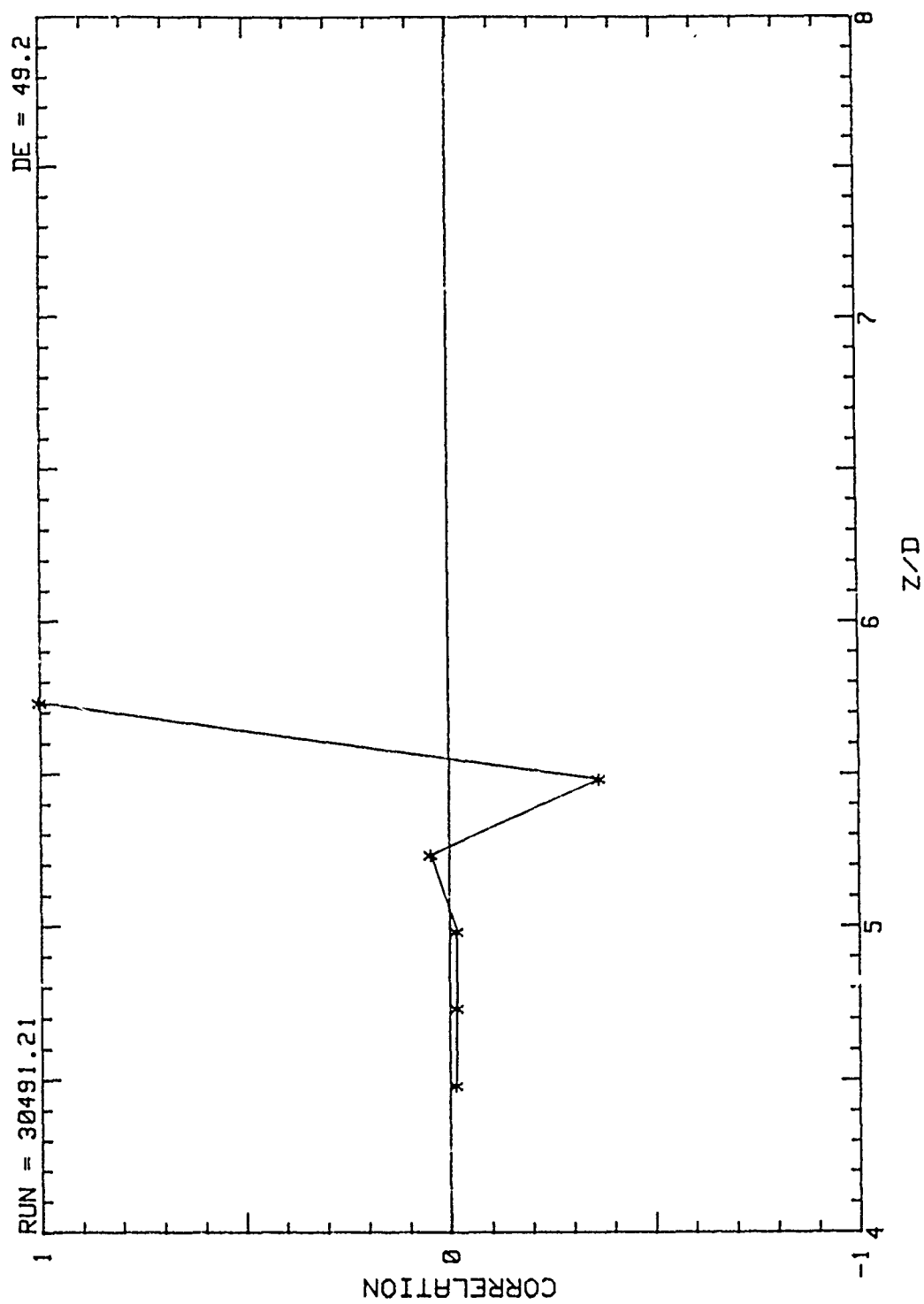


Figure 66. Correlation vs. z/d Probes 1,2,3,4,5,6, wrt 6, $De=49.2$

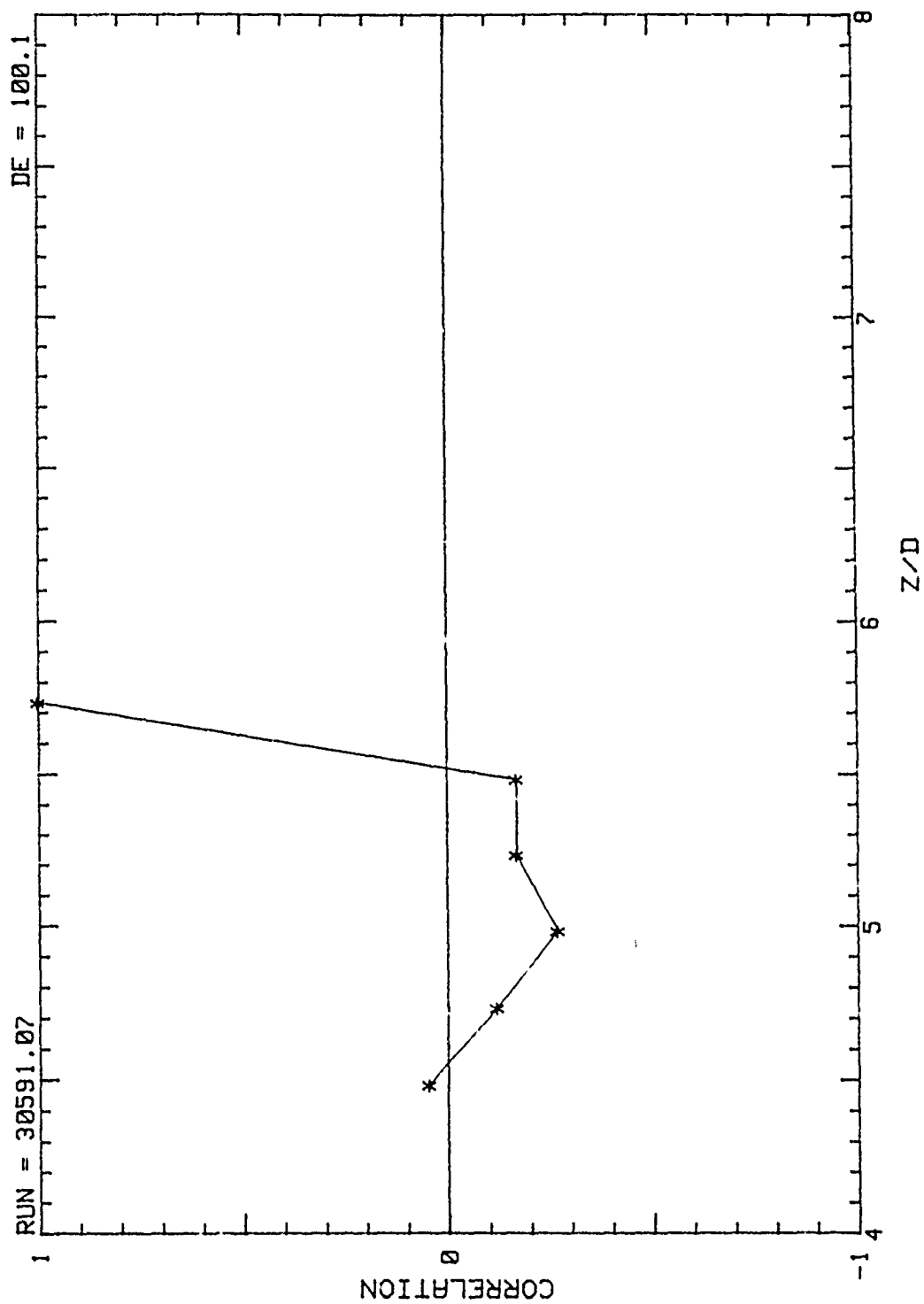


Figure 67. Correlation vs. z/d Probes 1,2,3,4,5,6, wrt 6, $De=100.1$

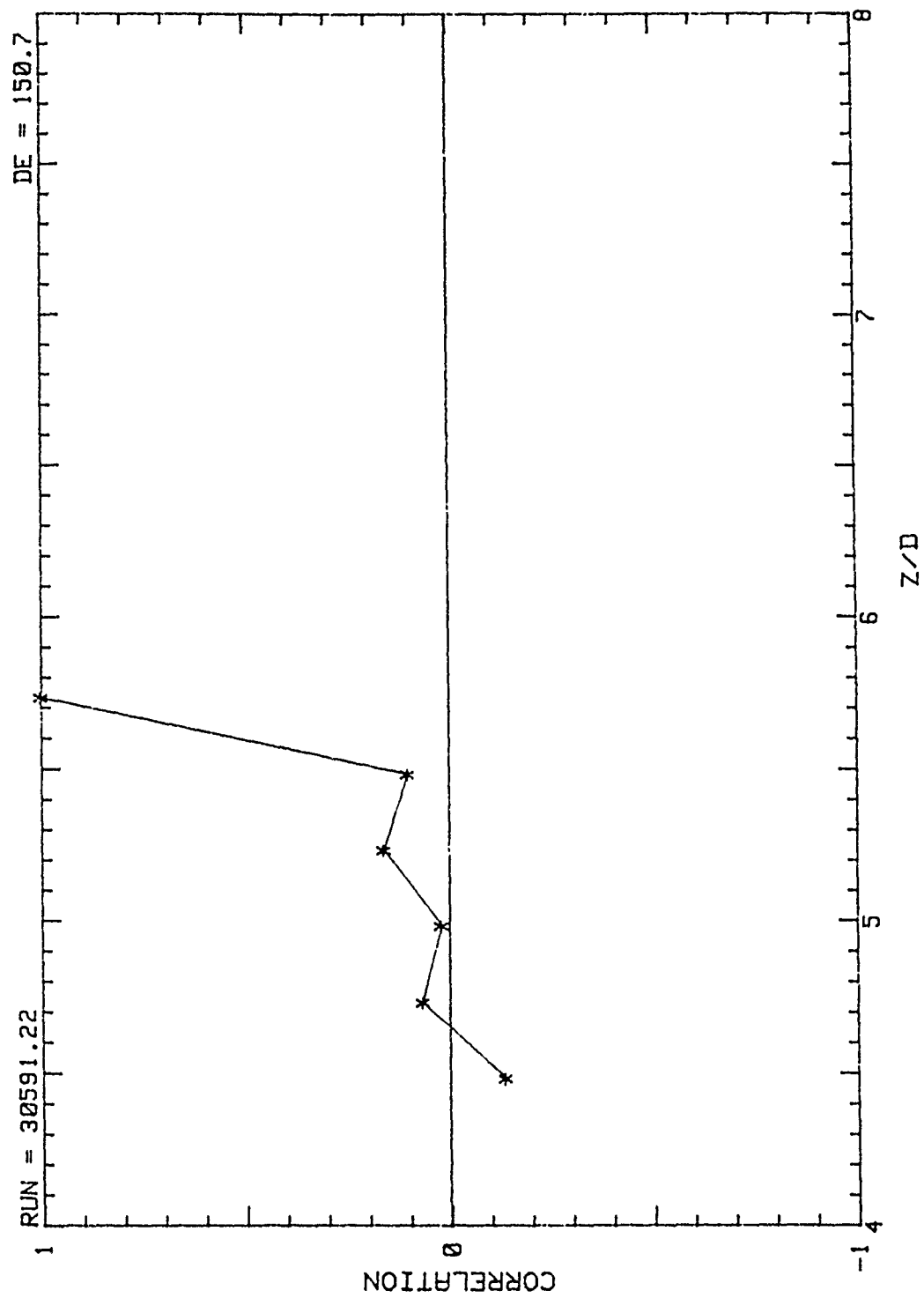


Figure 68. Correlation vs. z/d Probes 1,2,3,4,5,6, wrt 6, $De=150.7$

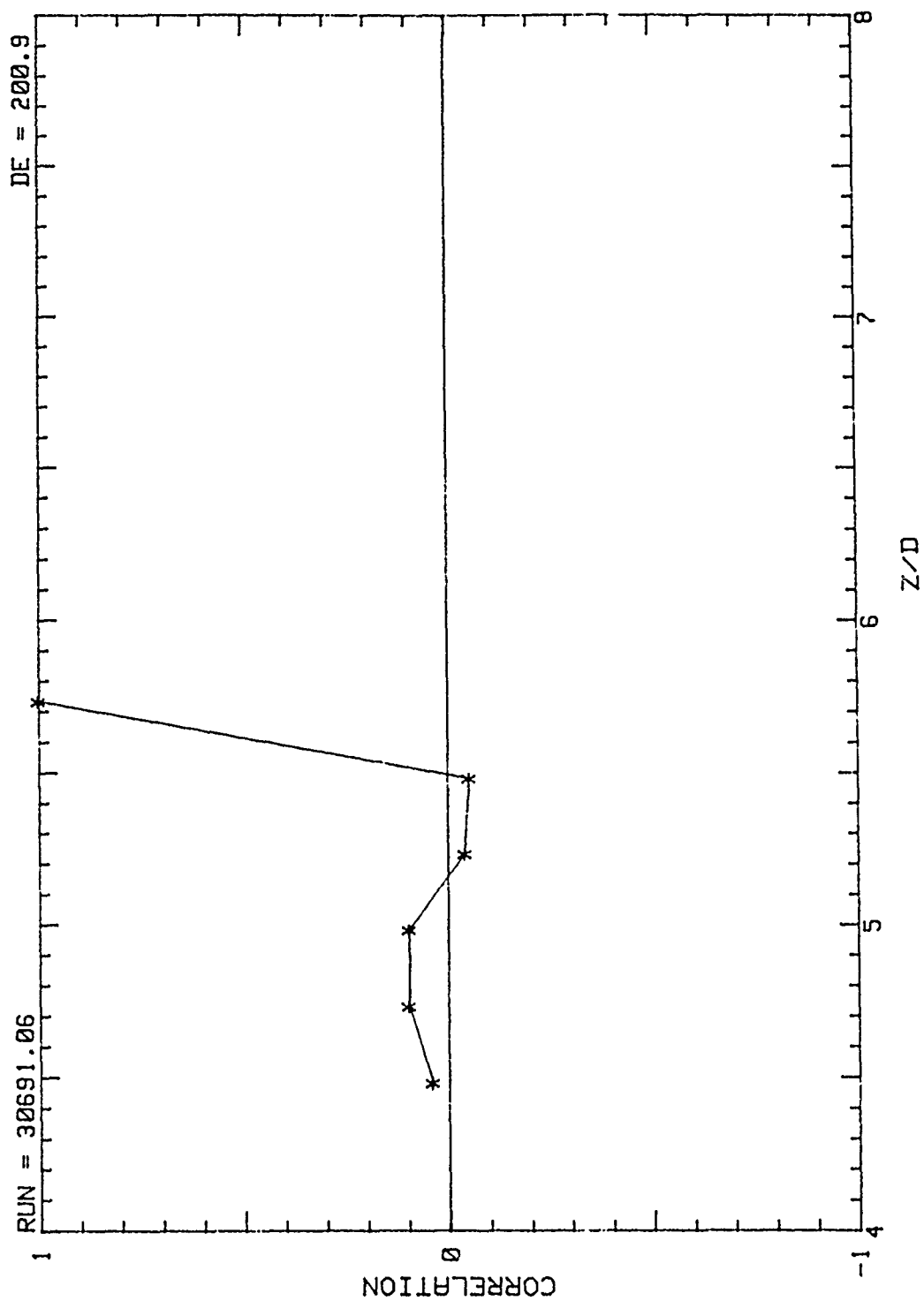


Figure 69. Correlation vs. z/d Probes 1,2,3,4,5,6, wrt 6, $De=200.9$

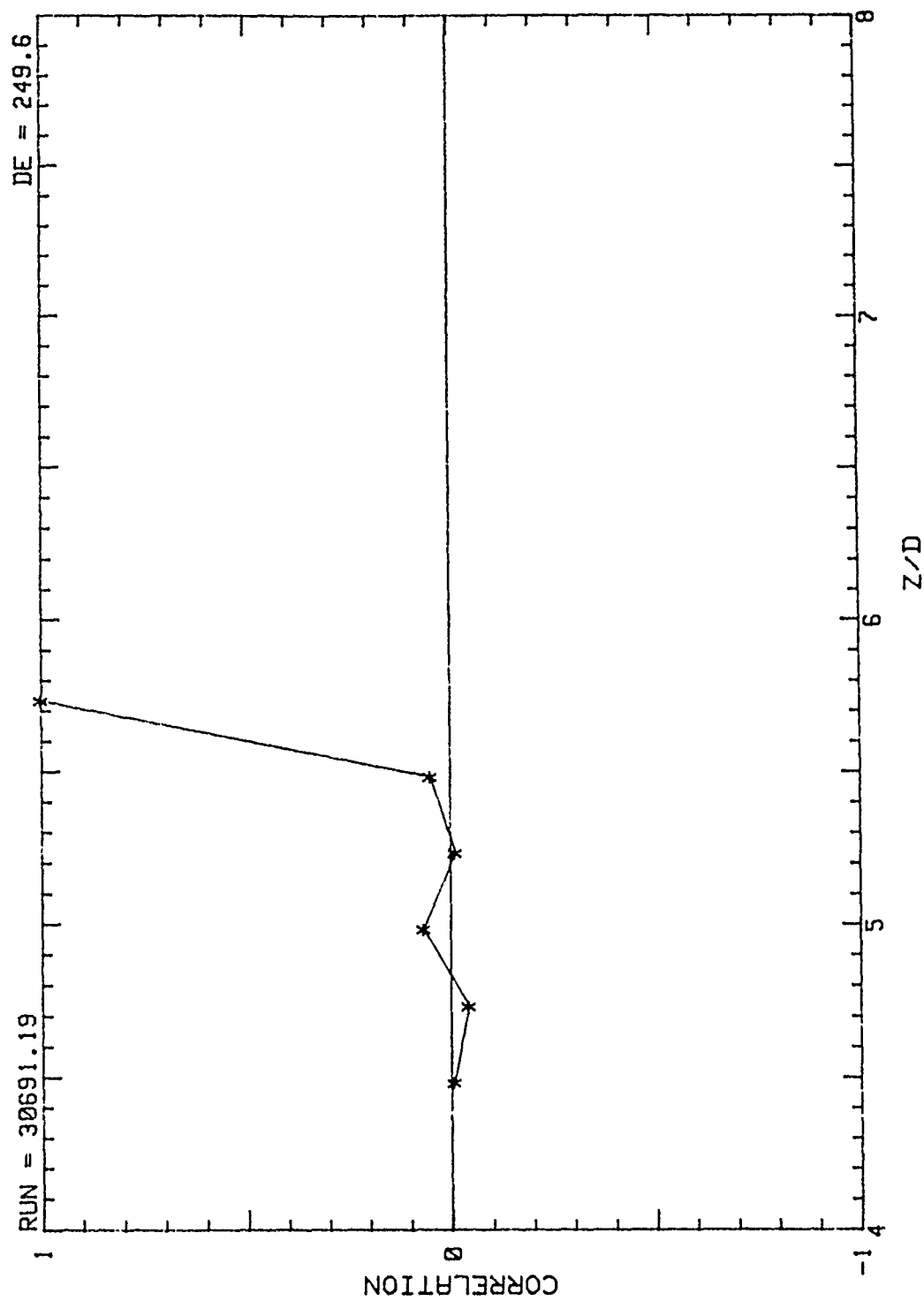


Figure 70. Correlation vs. z/d Probes 1,2,3,4,5,6, wrt 6, De=249.6

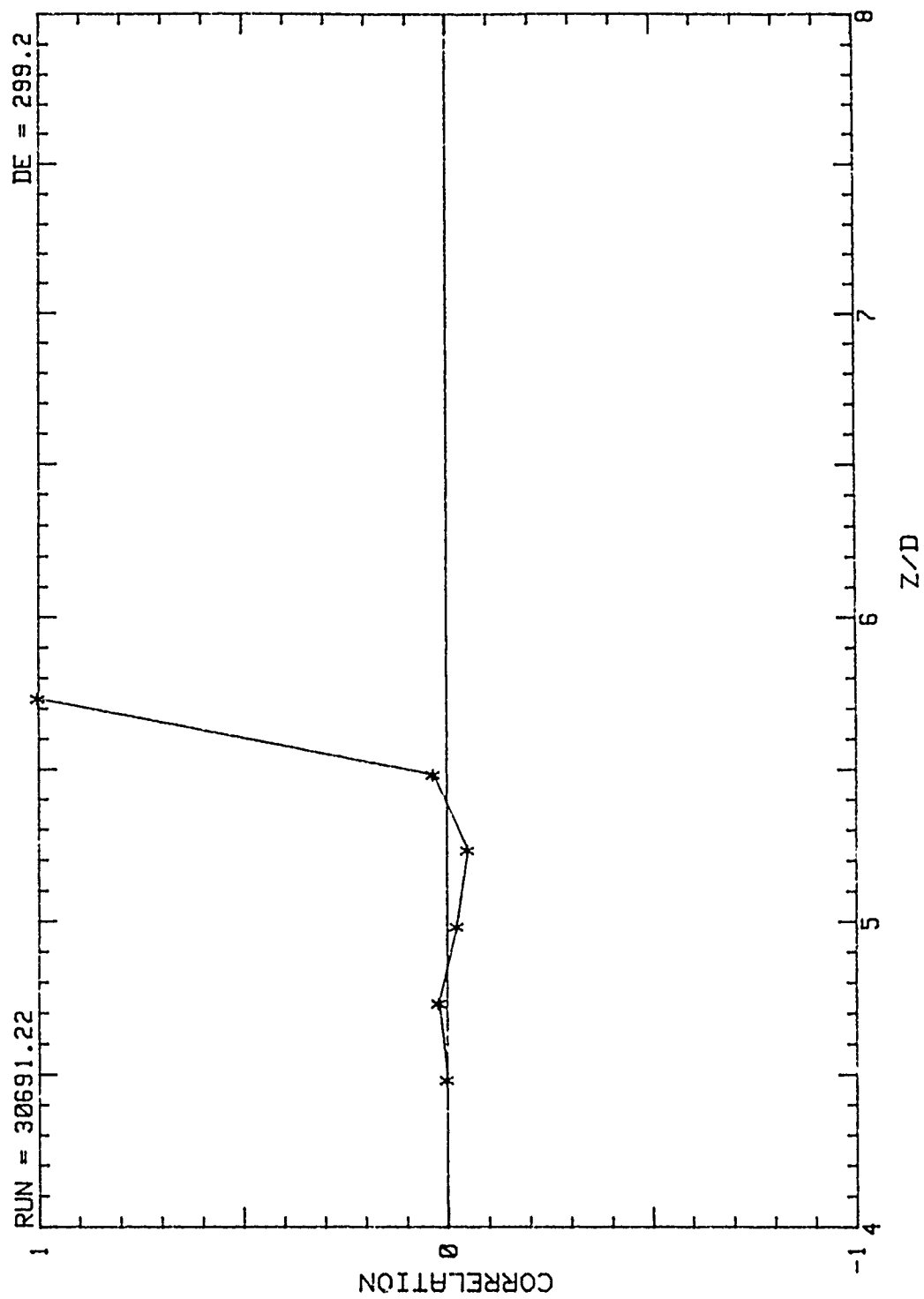


Figure 71. Correlation vs. z/d Probes 1,2,3,4,5,6, wrt 6, De=299.2

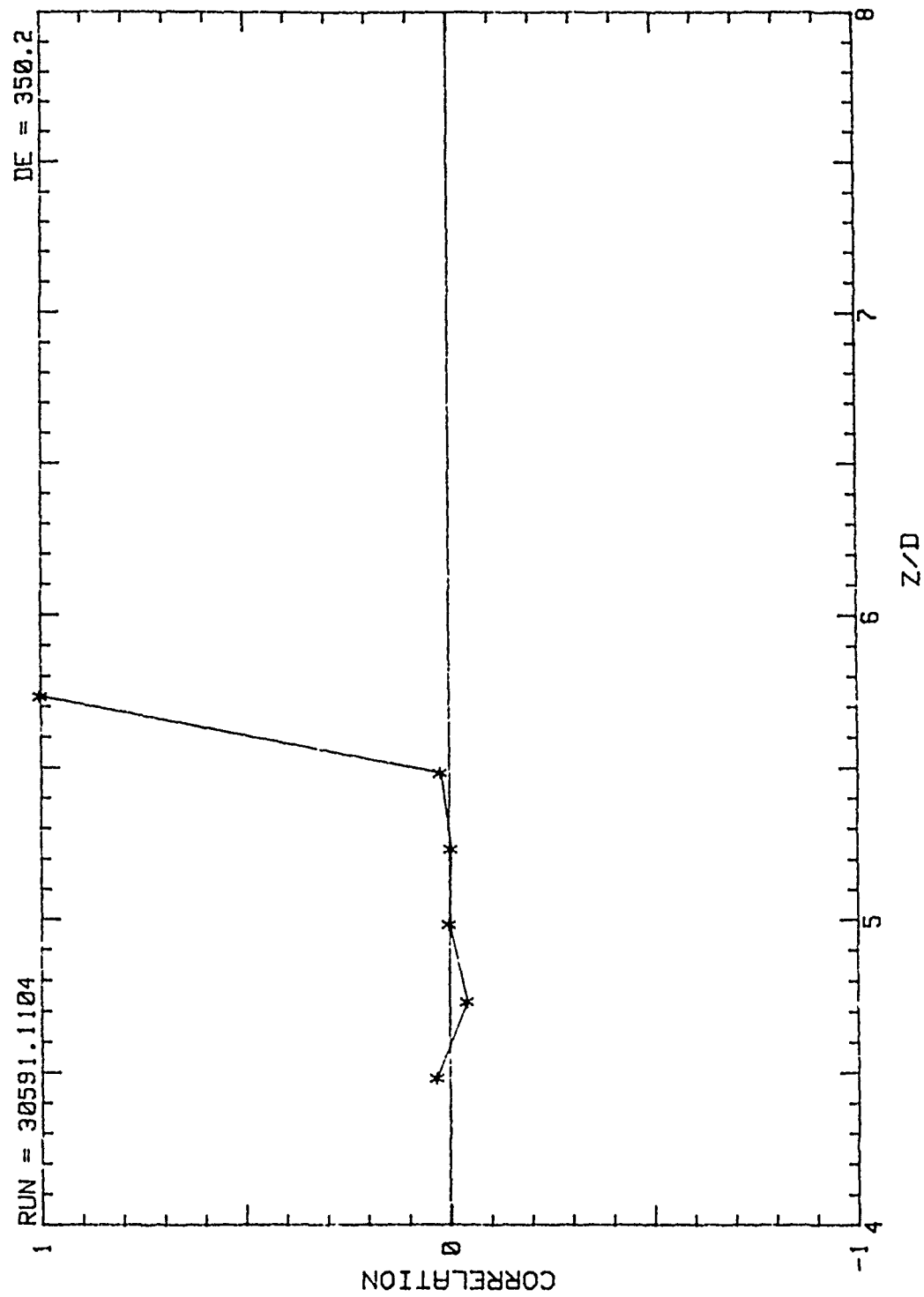


Figure 72. Correlation vs. z/d Probes 1,2,3,4,5,6, wrt 6, De=350.2

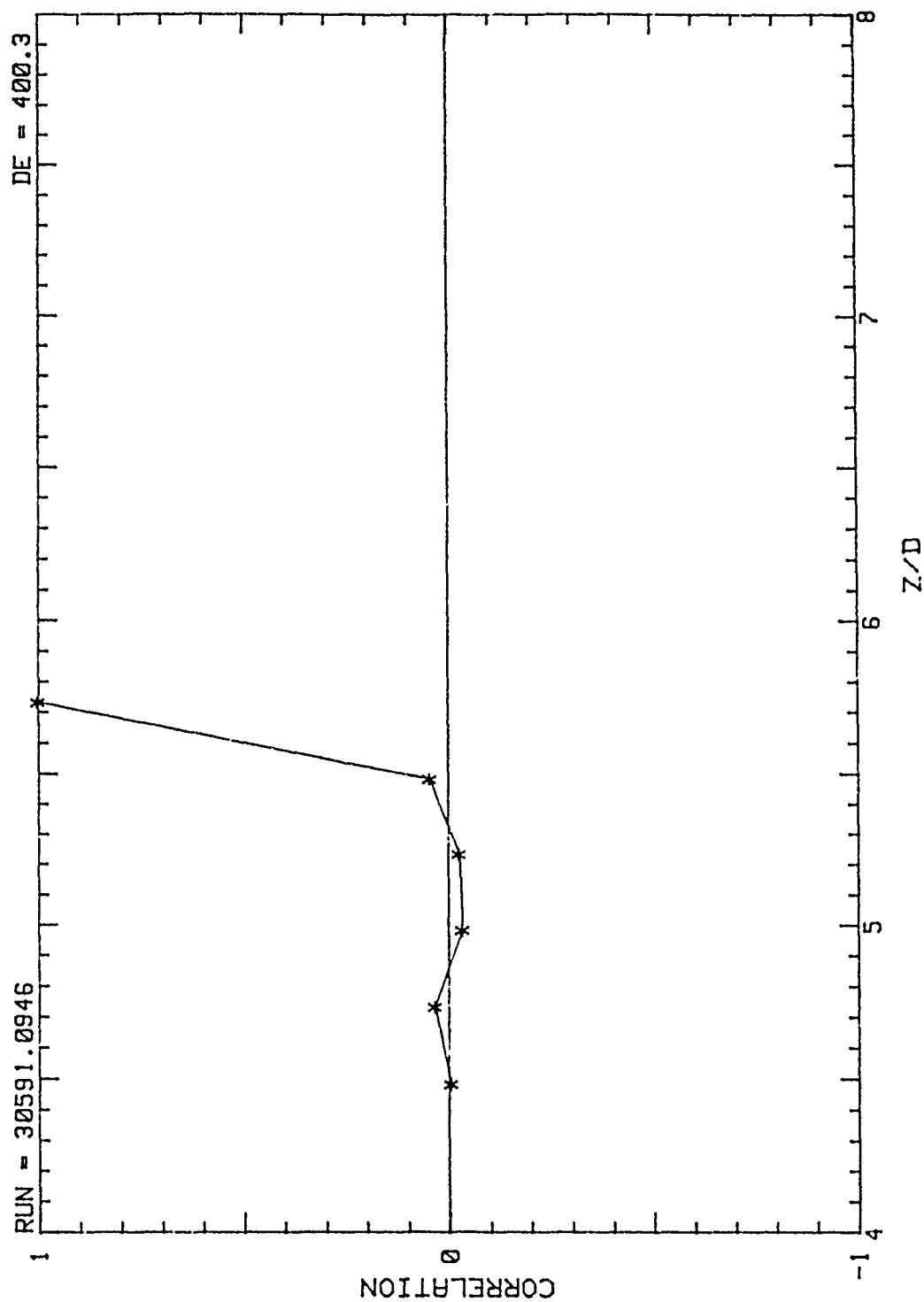


Figure 73. Correlation vs. z/d Probes 1,2,3,4,5,6, wrt 6, $De=400.3$

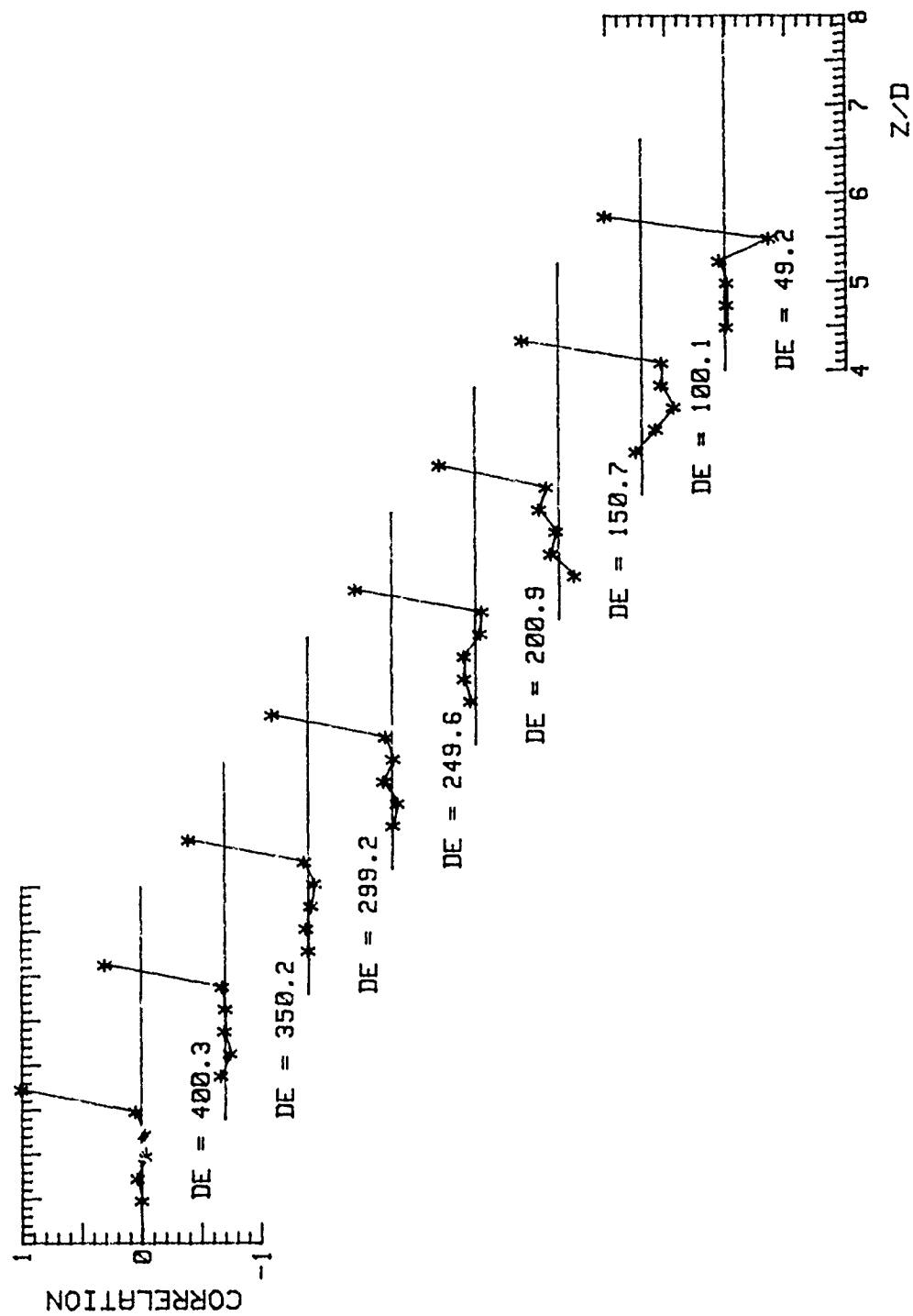


Figure 74. 3-D Correlations vs. z/d Probes 1,2,3,4,5,6, wrt 6, from $De=49.2$ to $De=400.3$

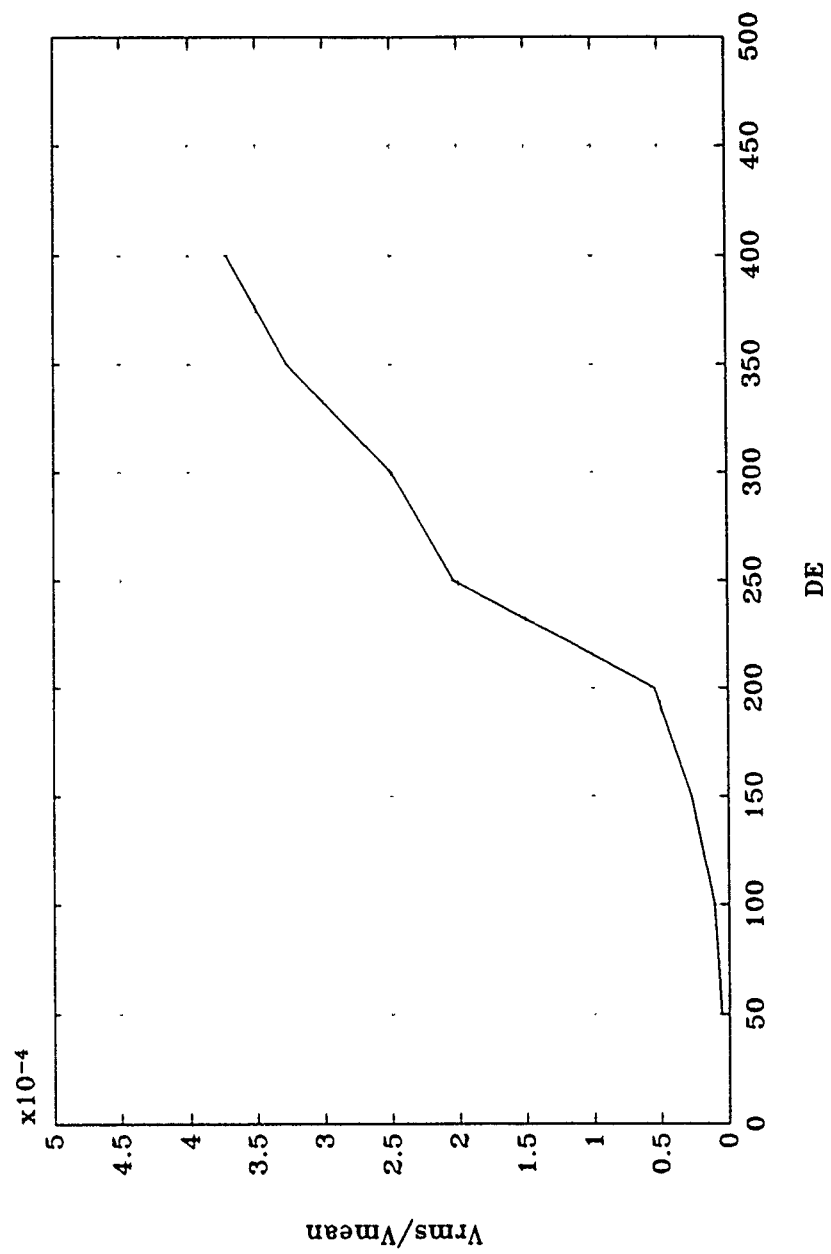


Figure 75. Average V_{rms}/V_{mean} vs. DE probes 1,2,3,4,5,6

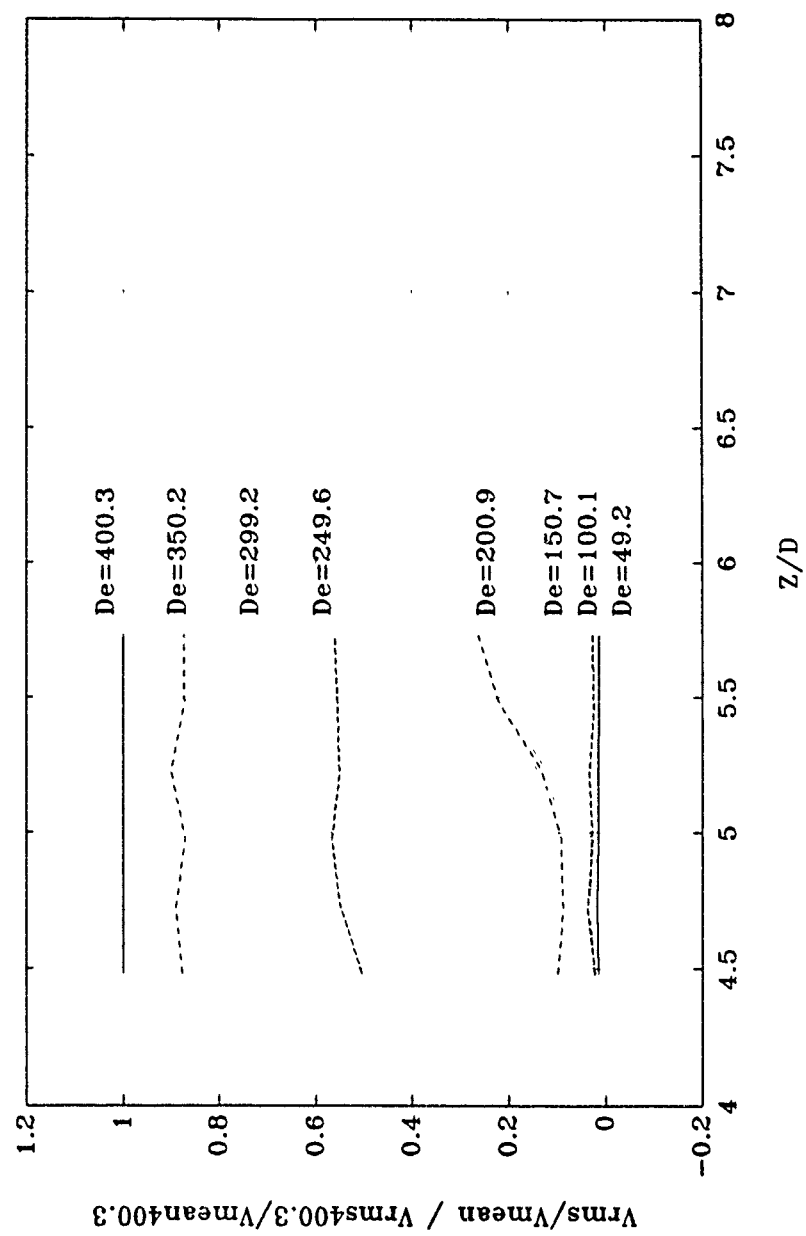


Figure 76. $V_{rms}/V_{mean} / V_{rms400.3}/V_{mean400.3}$ vs. z/d from $De=49.2$ to $De=400.3$

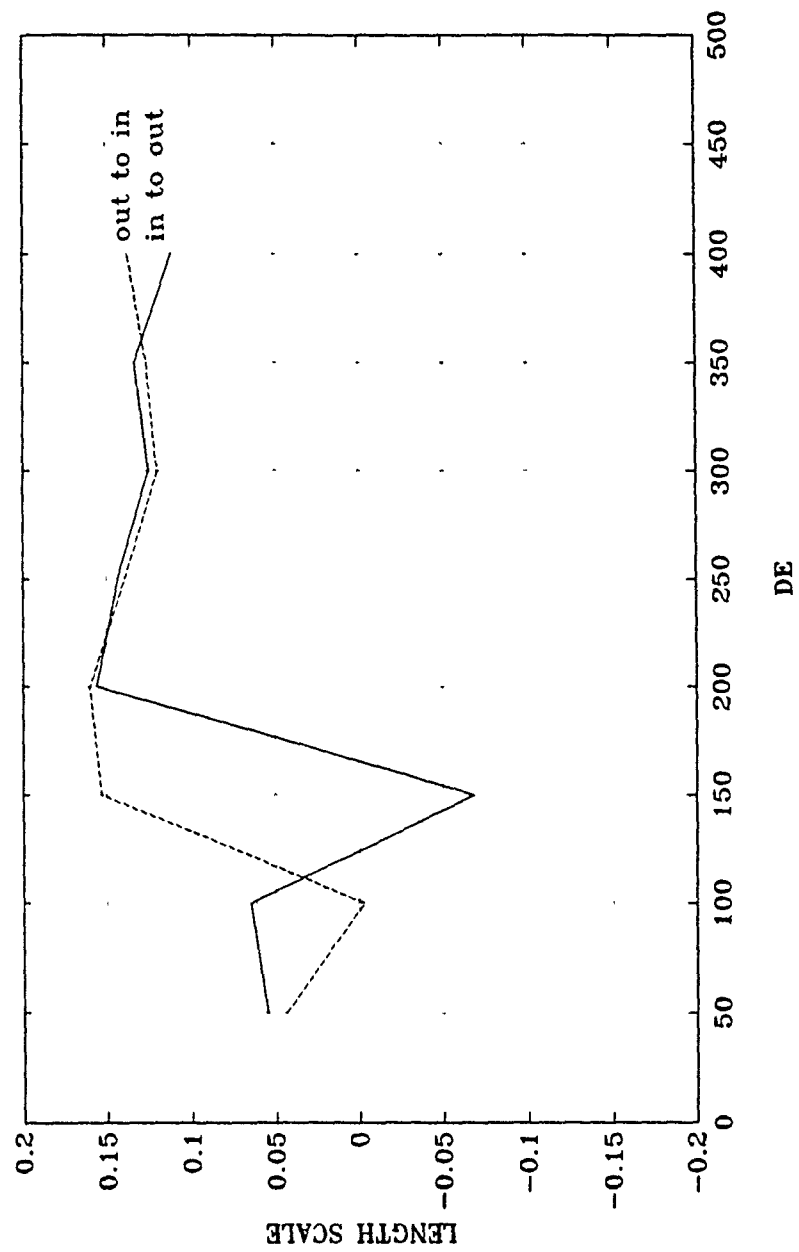


Figure 77. Length Scales vs. De Probes 1,2,3,4,5,6

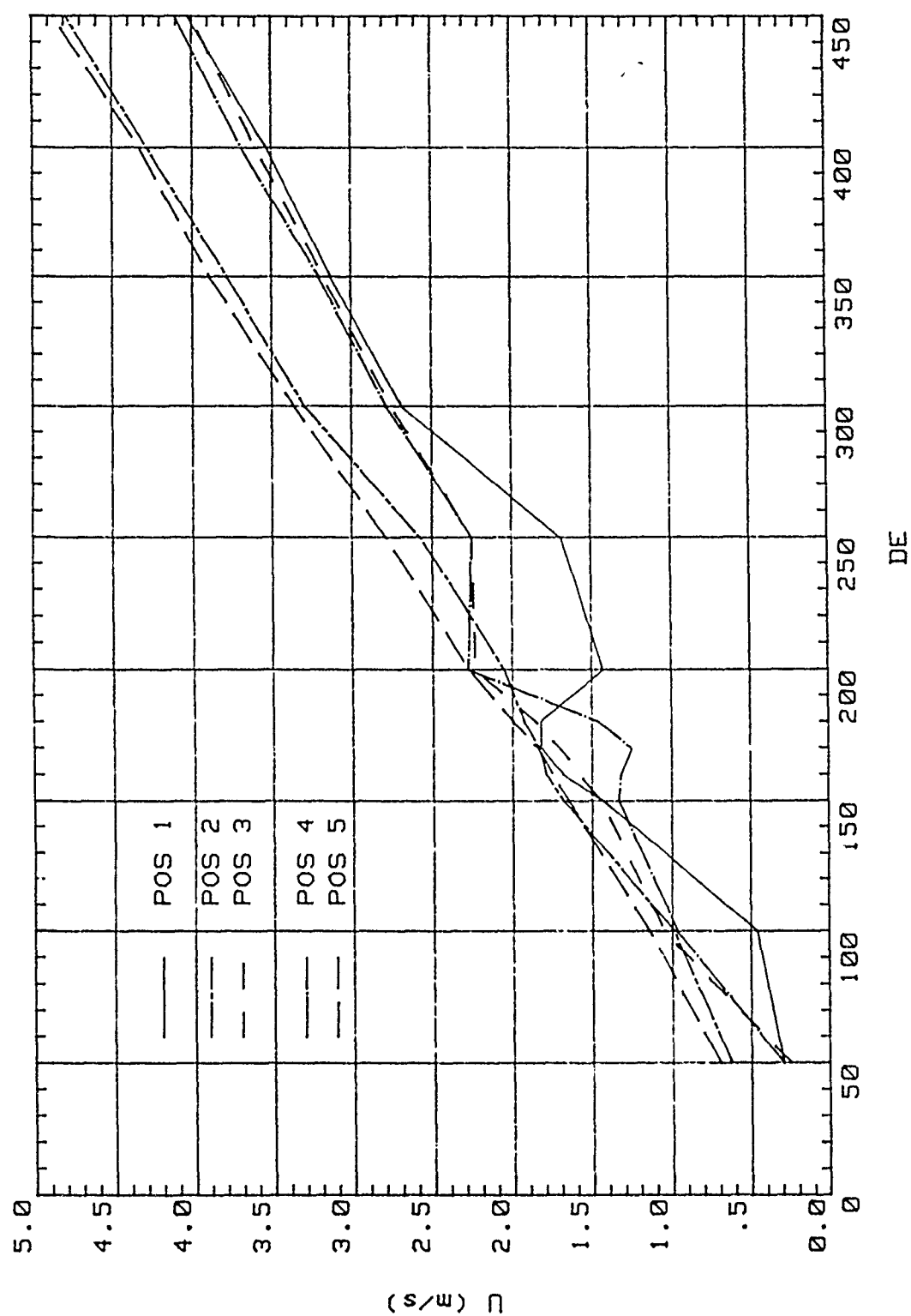


Figure 78. Digital Mean Streamwise Velocity vs. De , Positions 1,2,3,4,5

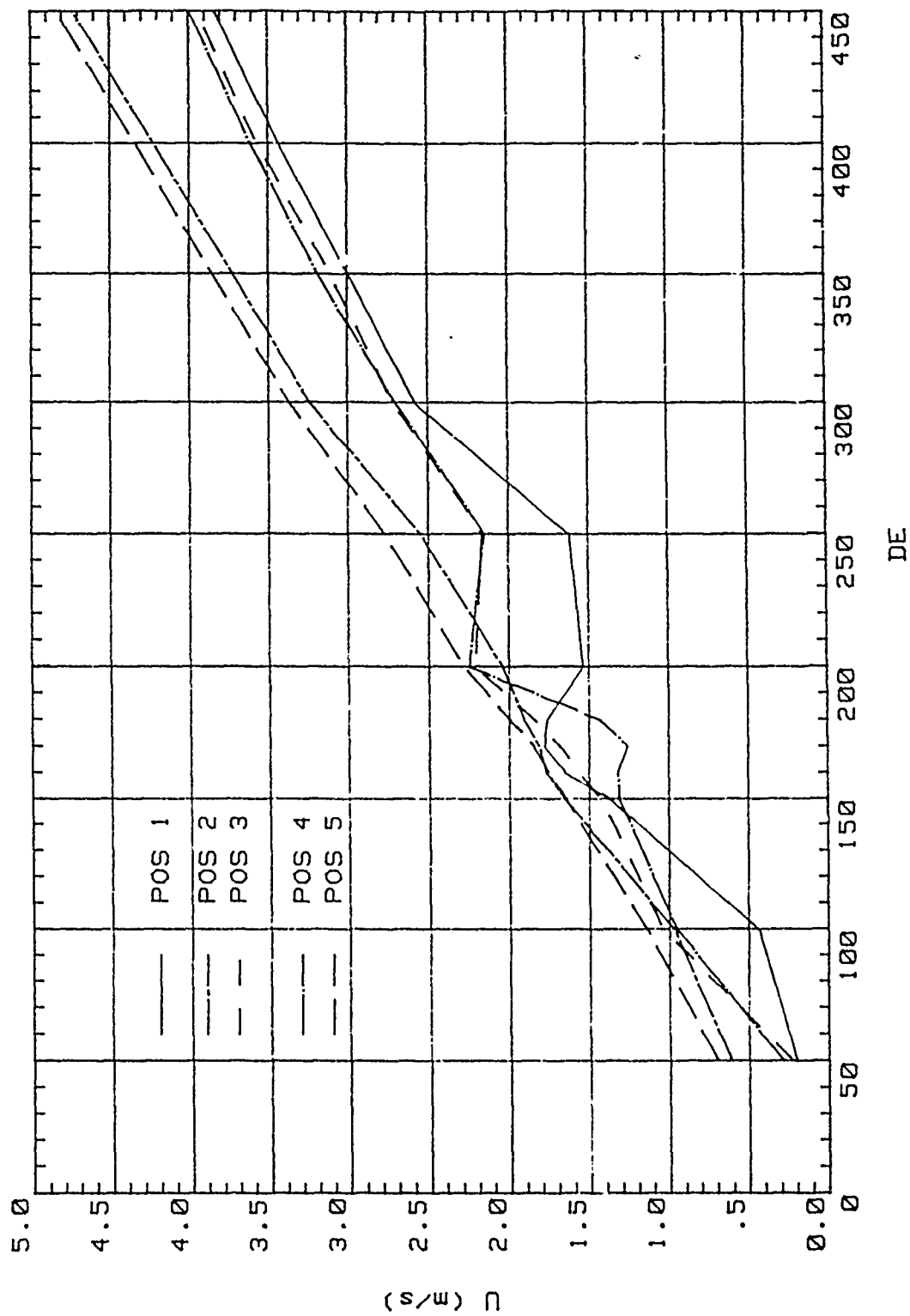


Figure 79. Analog Mean Streamwise Velocity vs. De , Positions 1,2,3,4,5

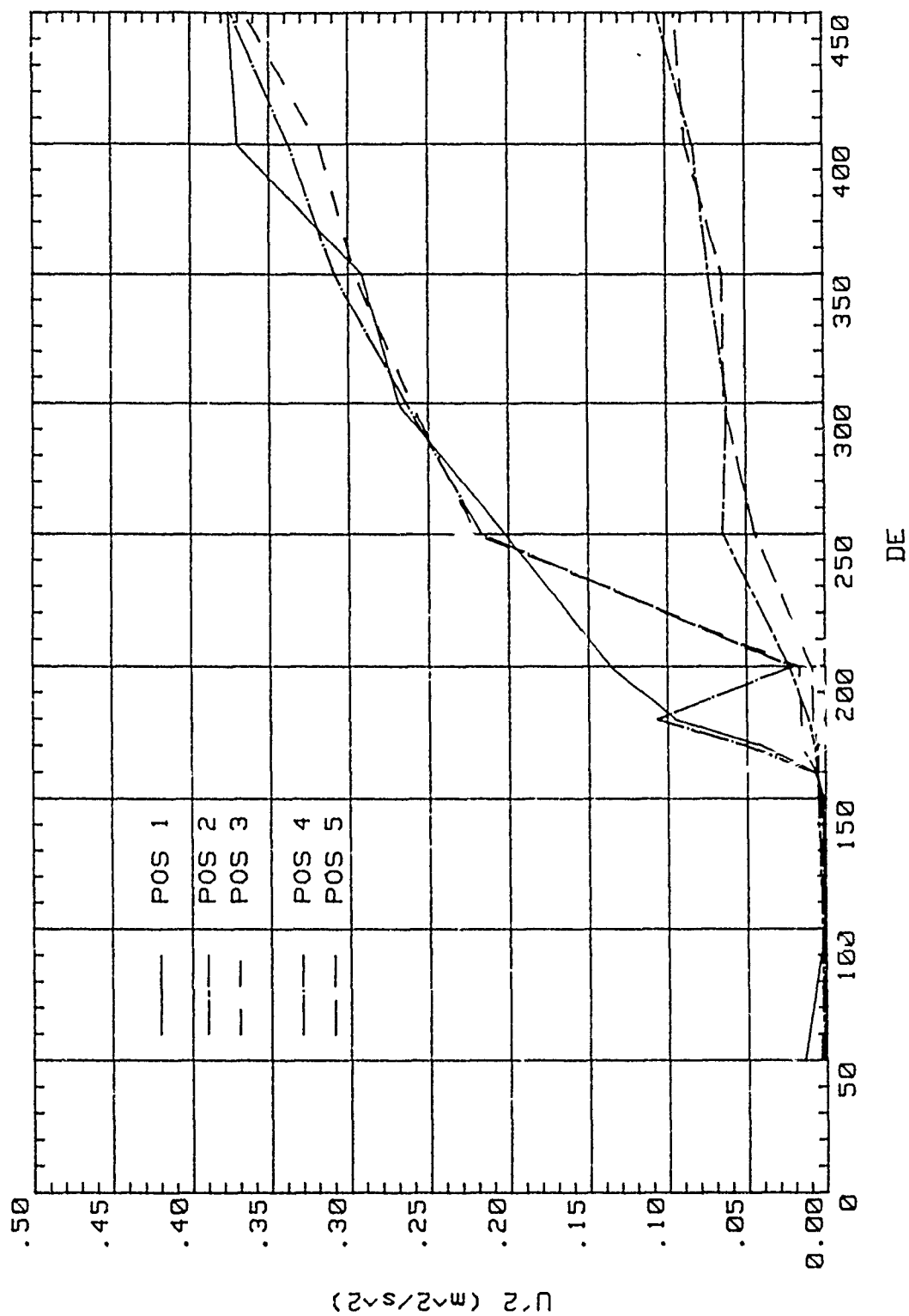


Figure 8C. Digital Longitudinal Turbulence Intensity vs. De, Positions 1,2,3,4,5

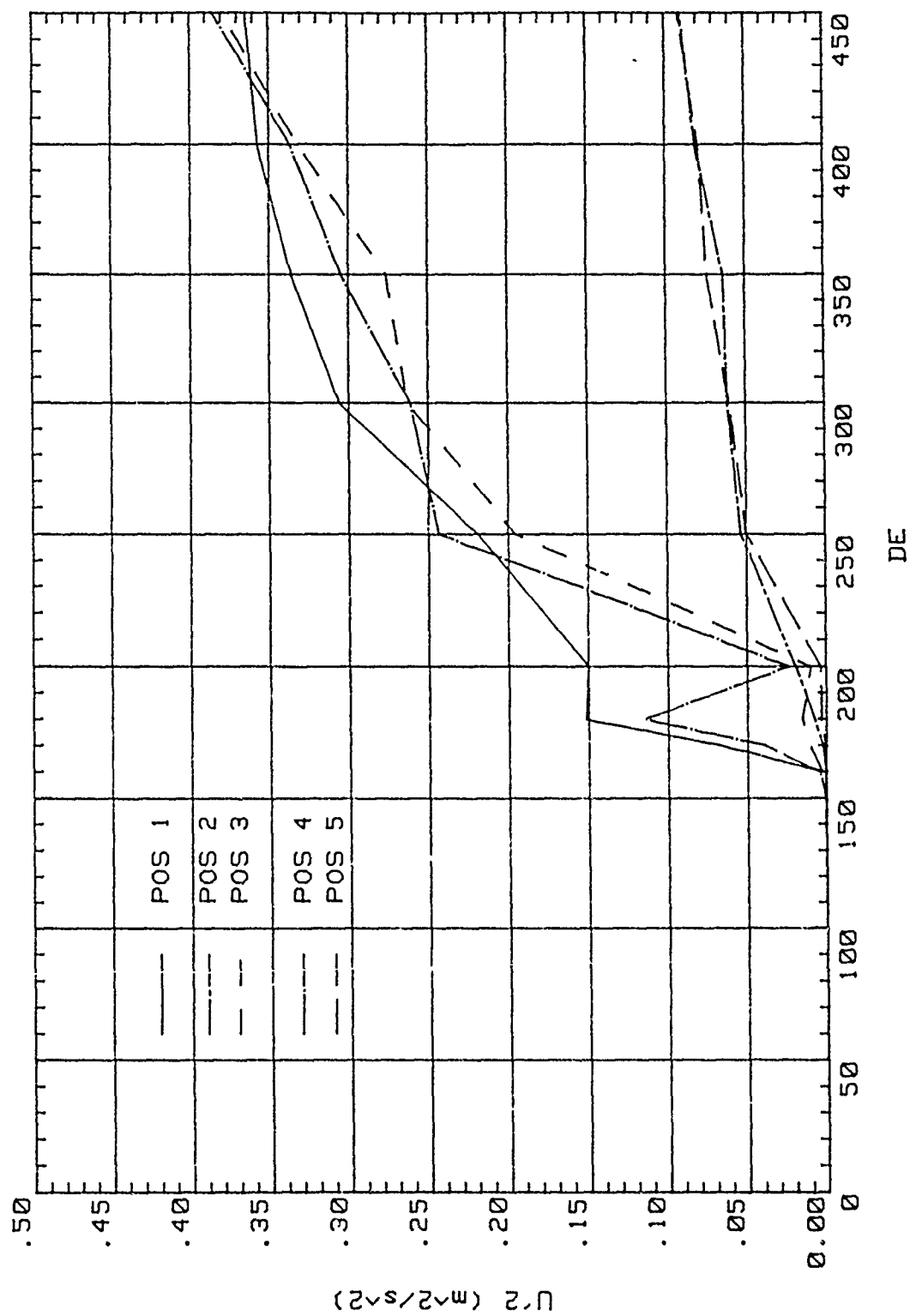


Figure 81. Analog Longitudinal Turbulence Intensity vs. De, Positions 1,2,3,4,5

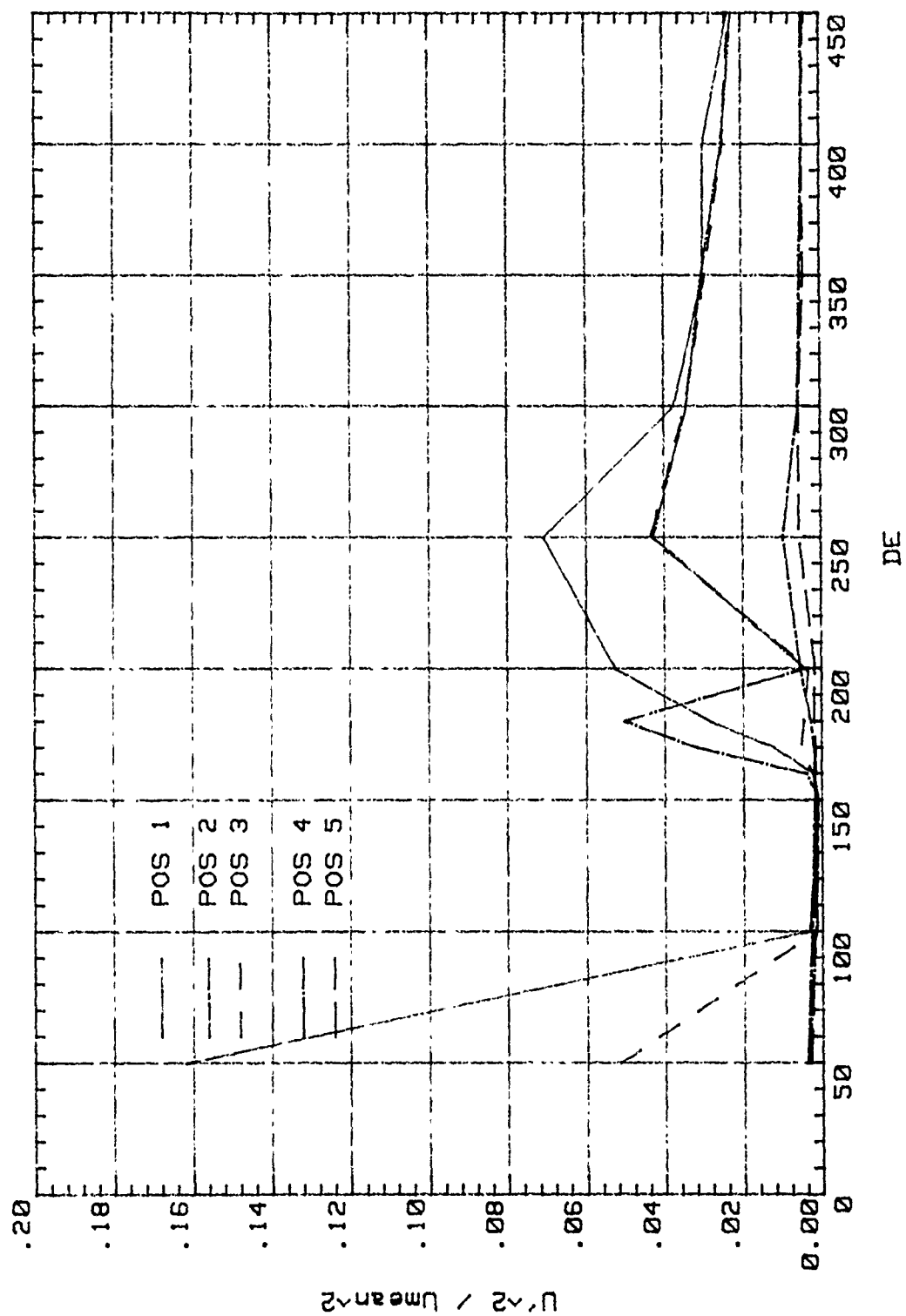


Figure 82. Digital Normalized Longitudinal Turbulence Intensity vs. DE , Positions 1,2,3,4,5

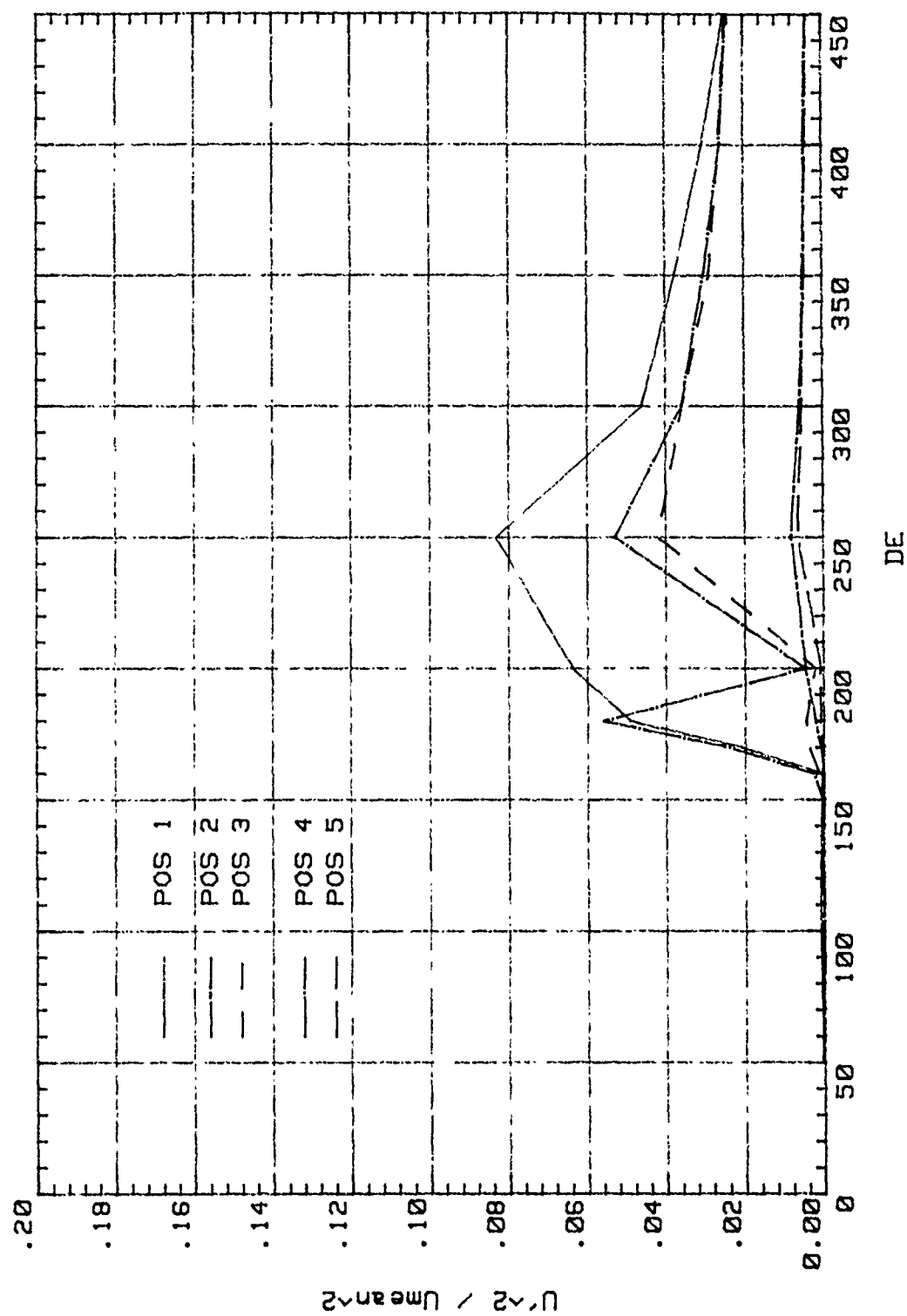


Figure 83. Analog Normalized Longitudinal Turbulence Intensity vs. De, Positions 1,2,3,4,5

Linear Resolution				
MEASURE:	CHAN 1 Freq Resp	CHAN 2 Freq Resp		
WINDOW:	CHAN 1 Hanning	CHAN 2 Hanning		
AVERAGE:	TYPE Stable	# AVGS 5	OVERLAP 0%	TIME AVG Off
FREQ:	CENTER 12.5 Hz		SPAN 25.0 Hz	BW 46.9mHz
	REC LGTH 32.0 S	Δt 15.6ms		
TRIGGER:	TYPE FreeRun	LEVEL 0.0 Vpk	SLOPE Pos	PREVIEW Off
INPUT:	RANGE	ENG UNITS	COUPLING	DELAY
CH 1	AutoRng↑	1.0 V/EU	DC (F1t)	0.0 S
CH 2	AutoRng↑	1.0 V/EU	DC (F1t)	0.0 S
SOURCE:	TYPE Off		LEVEL 0.0 Vpk	OFFSET 0.0 Vpk

Figure 84. Hot-wire Probe Low Frequency Power Spectra Settings

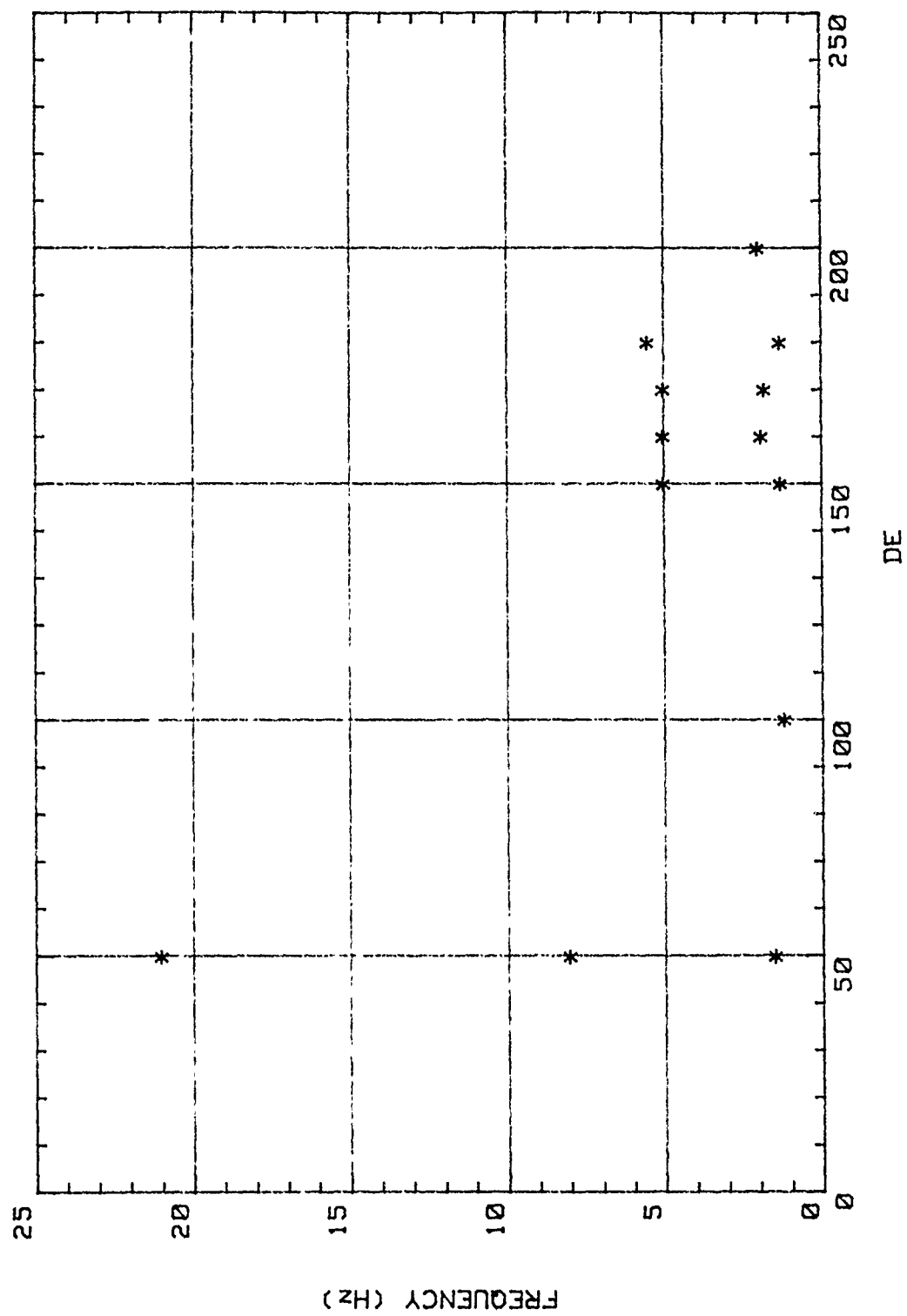


Figure 85. Peak Frequency vs. De, Position 1

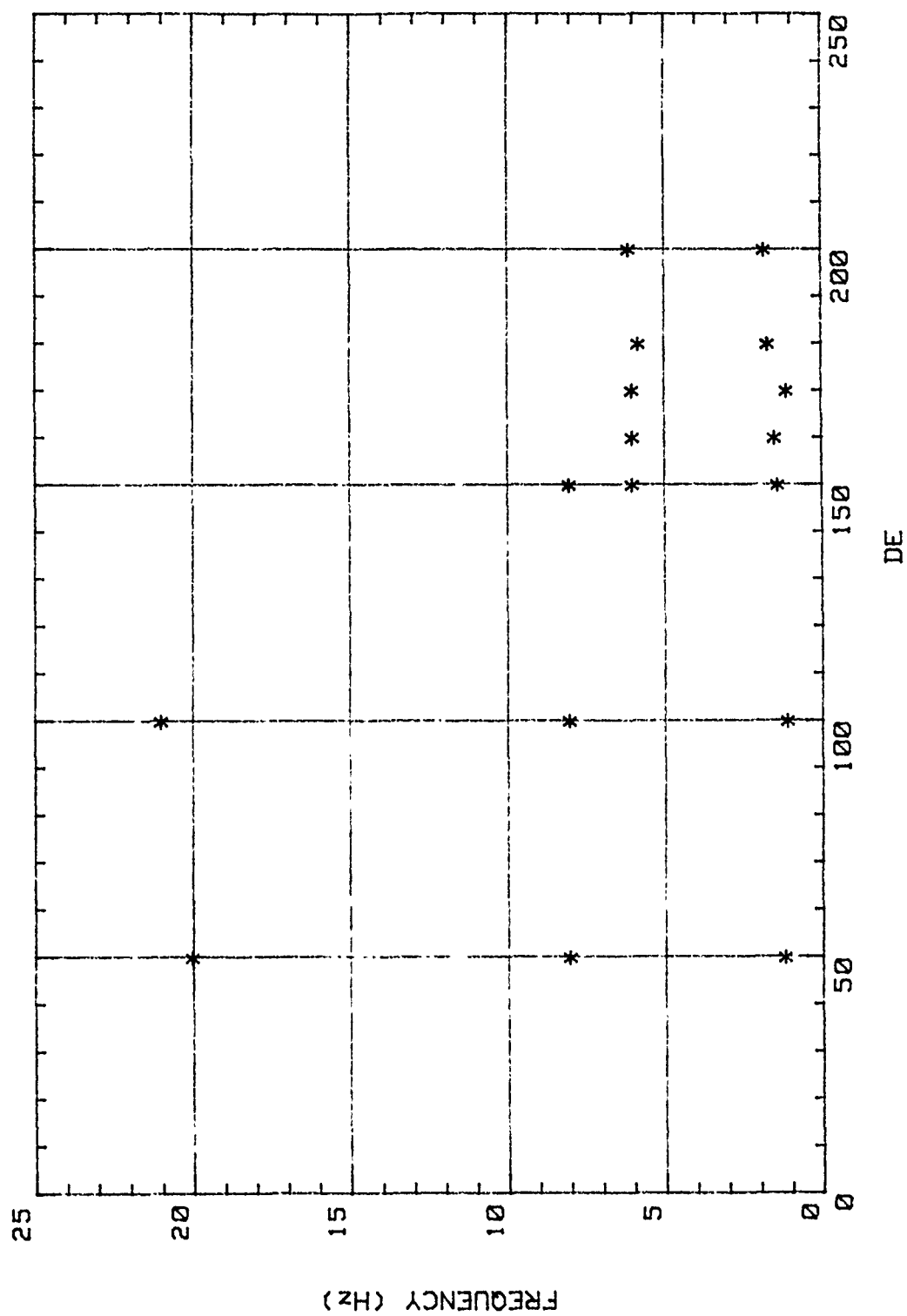


Figure 86. Peak Frequency vs. De, Position 2

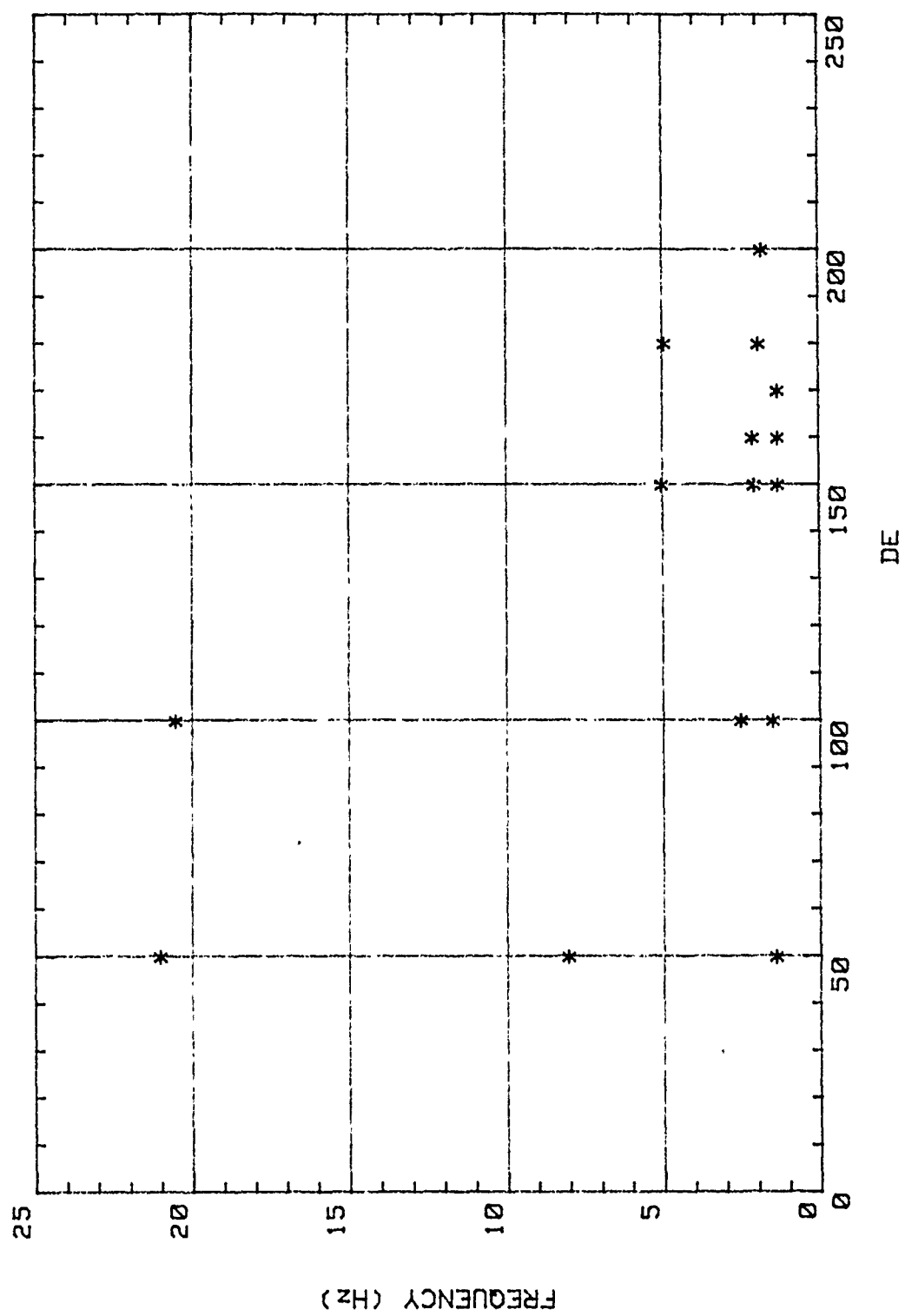


Figure 87. Peak Frequency vs. De, Position 3

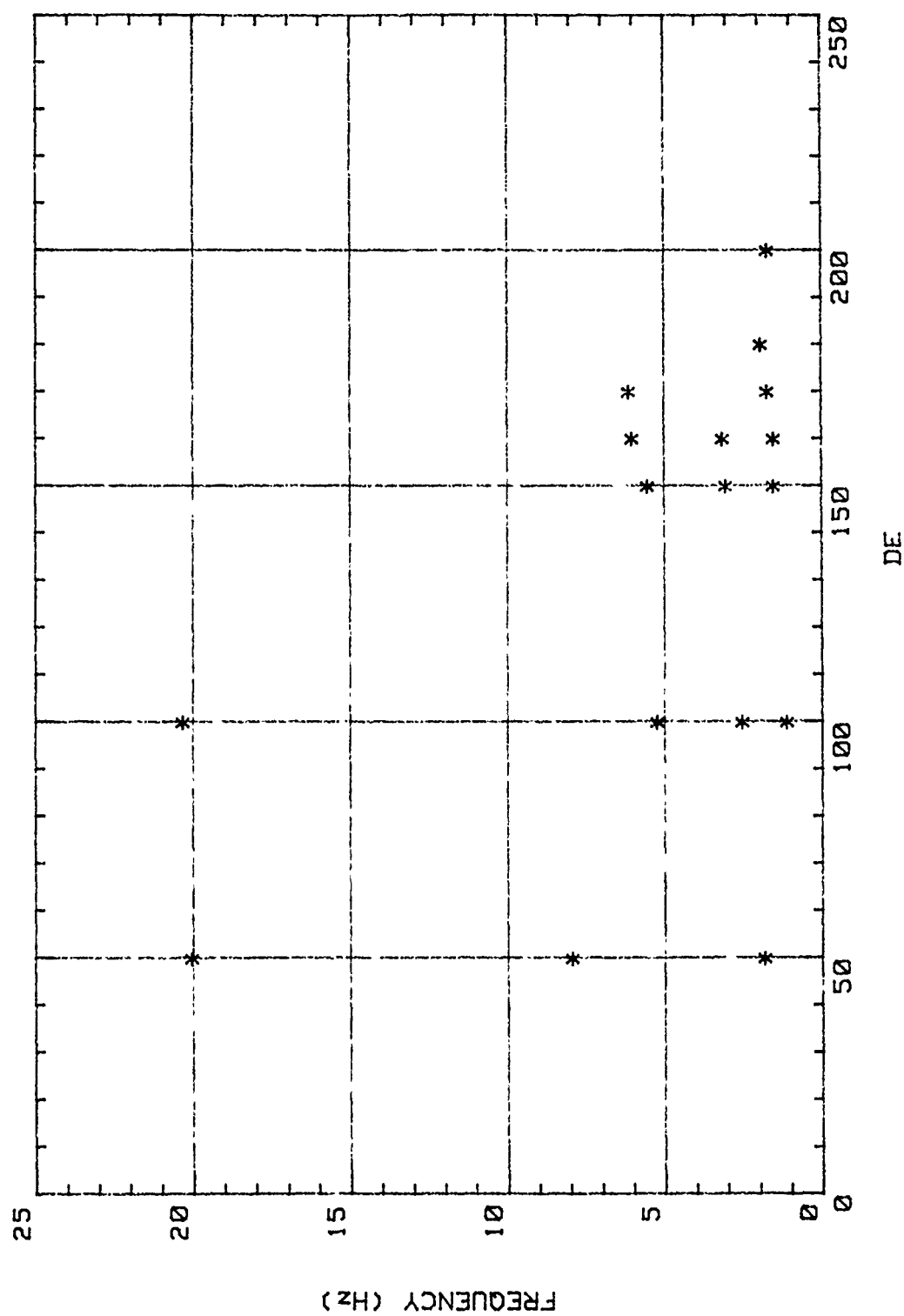


Figure 88. Peak Frequency vs. De, Position 4

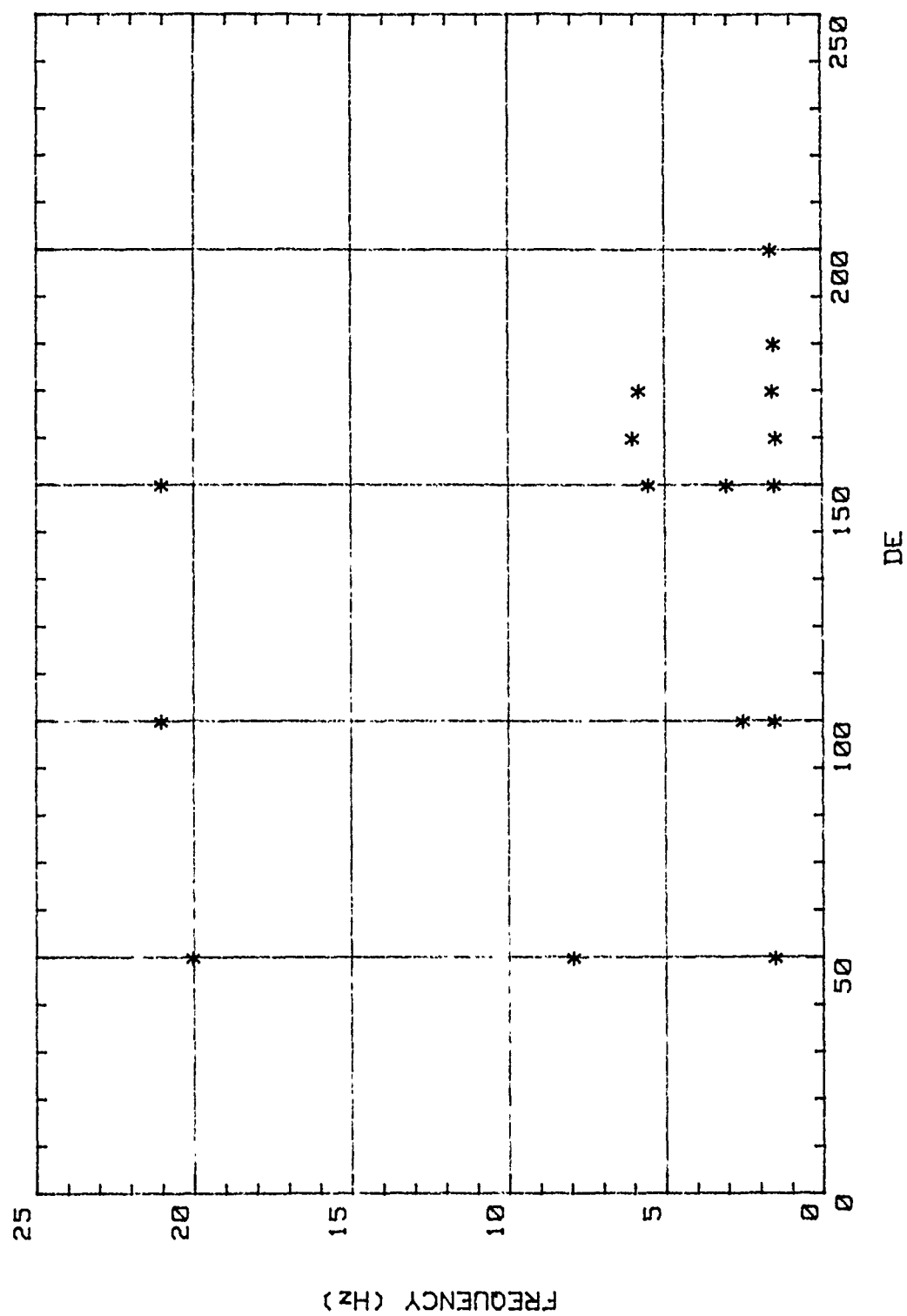


Figure 89. Peak Frequency vs. De, Position 5

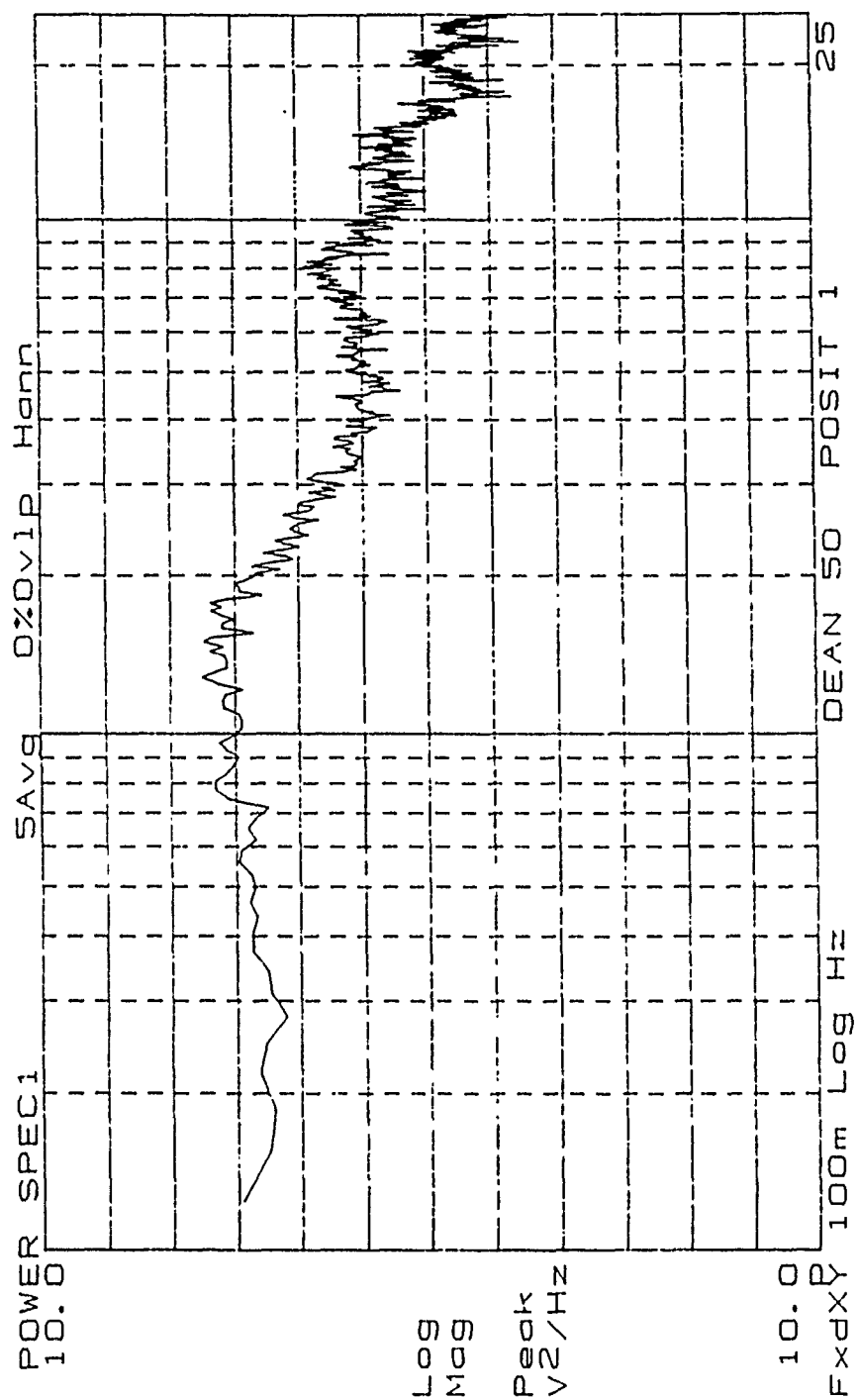


Figure 90. Low Frequency Power Spectrum, De=50, Position 1

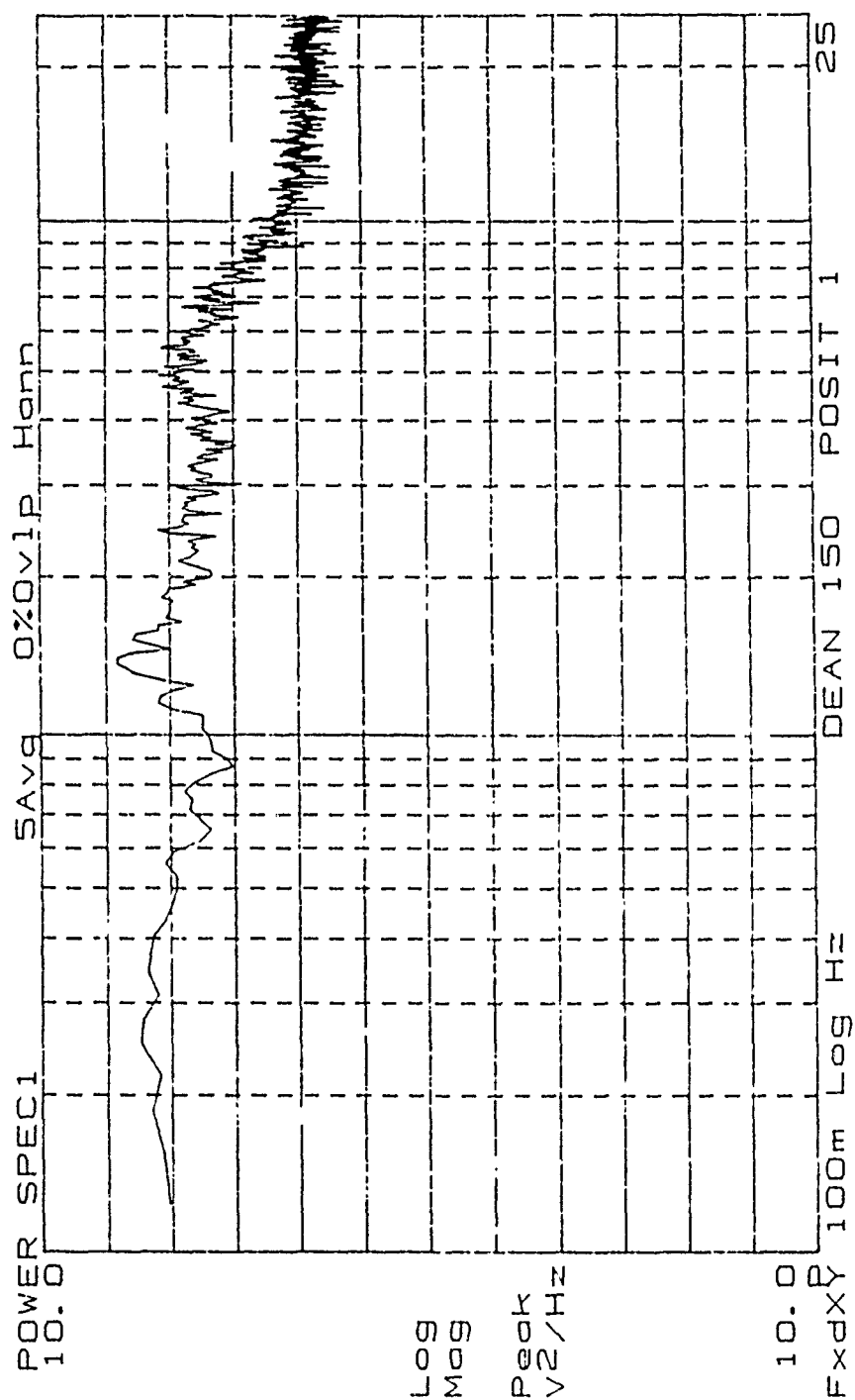


Figure 91. Low Frequency Power Spectrum, De=150, Position 1

Linear Resolution						
MEASURE:	CHAN 1 Power Spec	CHAN 2 Off				
WINDOW:	CHAN 1 Hanning	CHAN 2 Hanning				
AVERAGE:	TYPE Stable	# AVG 10	OVERLAP 0%	TIME Off	AVG Off	
FREQ:	CENTER 5 kHz		SPAN 10.0kHz	BW 18.7 Hz		
	REC LGTH 80.0ms	Δt 78.1 μ s				
TRIGGER:	TYPE FreeRun	LEVEL 0.0 Vpk	SLOPE Pos	PREVIEW Off		
INPUT:	RANGE	ENG UNITS	COUPLING	DELAY		
CH 1	AutoRng \uparrow	1.0 V/EU	DC (Flt)	0.0 S		
CH 2	AutoRng \uparrow	1.0 V/EU	DC (Flt)	0.0 S		
SOURCE:	TYPE Off	LEVEL 0.0 Vpk	OFFSET 0.0 Vpk			

Figure 152. Hot-wire Probe High Frequency Power Spectra Settings

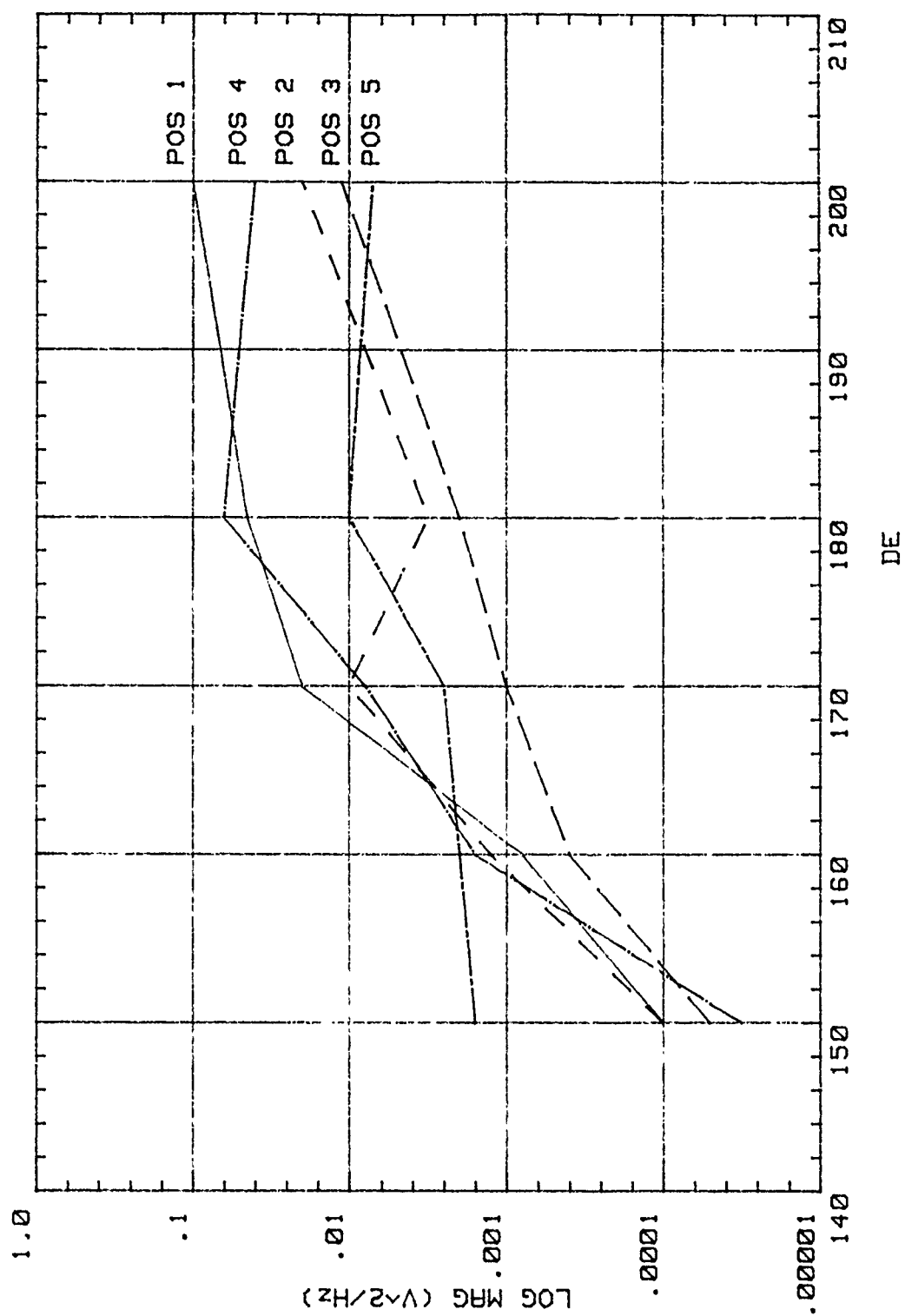


Figure 153. Peak Magnitude vs. De, Positions 1,2,3,4,5

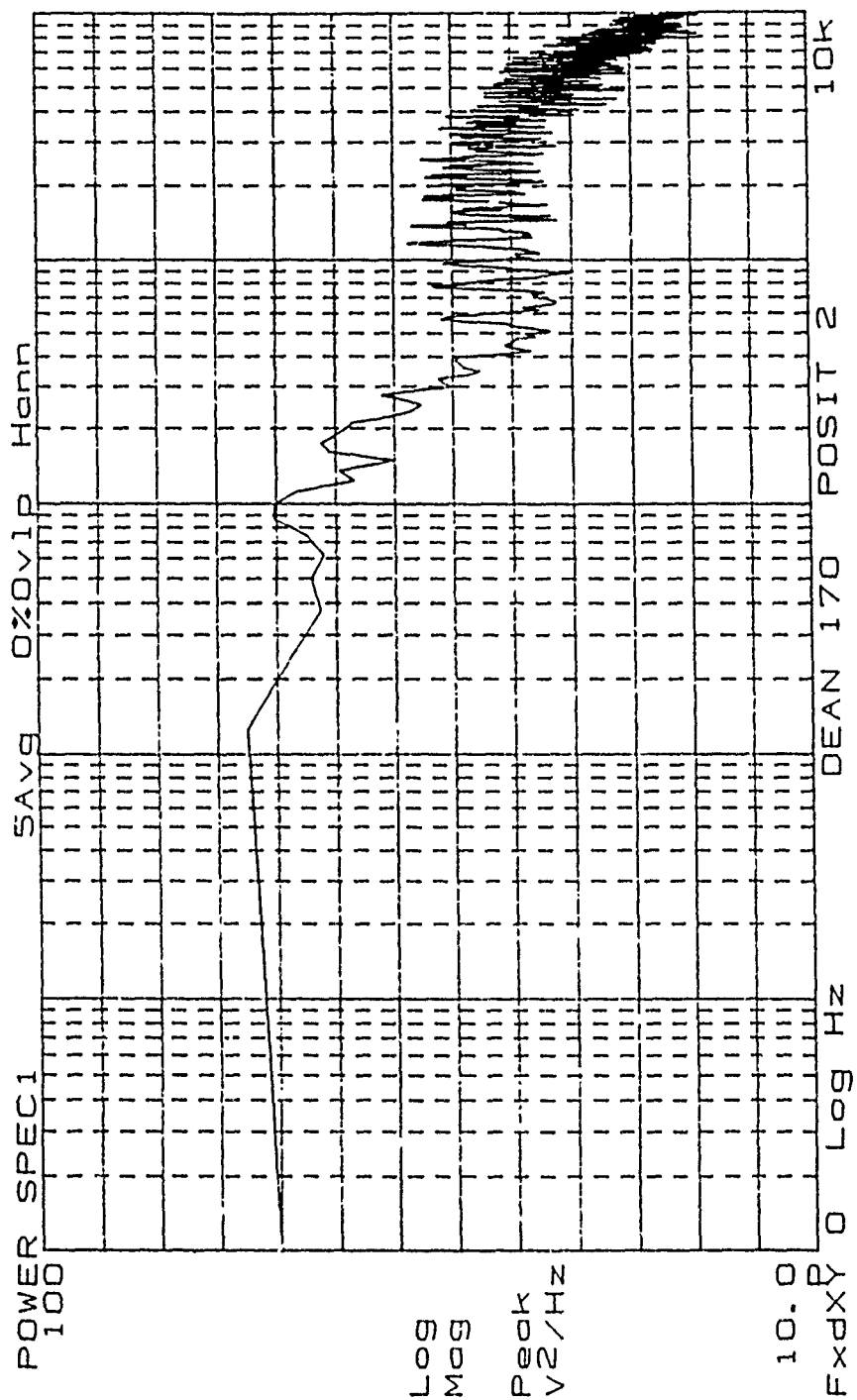


Figure 154. High Frequency Power Spectrum, De=170, Position 2

Frame 1

2

3

4

5

6

7

8

9

10

11

12

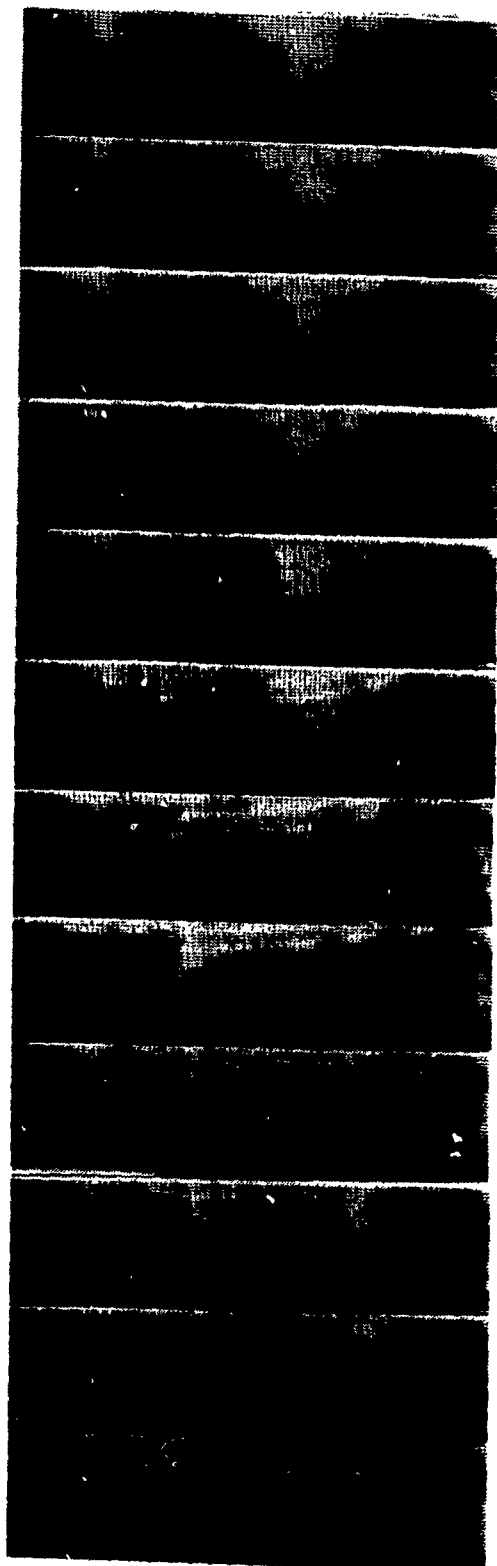


Figure 215. Vortex Pair Split Visualization, $De=100$, $\theta=115^\circ$
Interval $1/30$ s

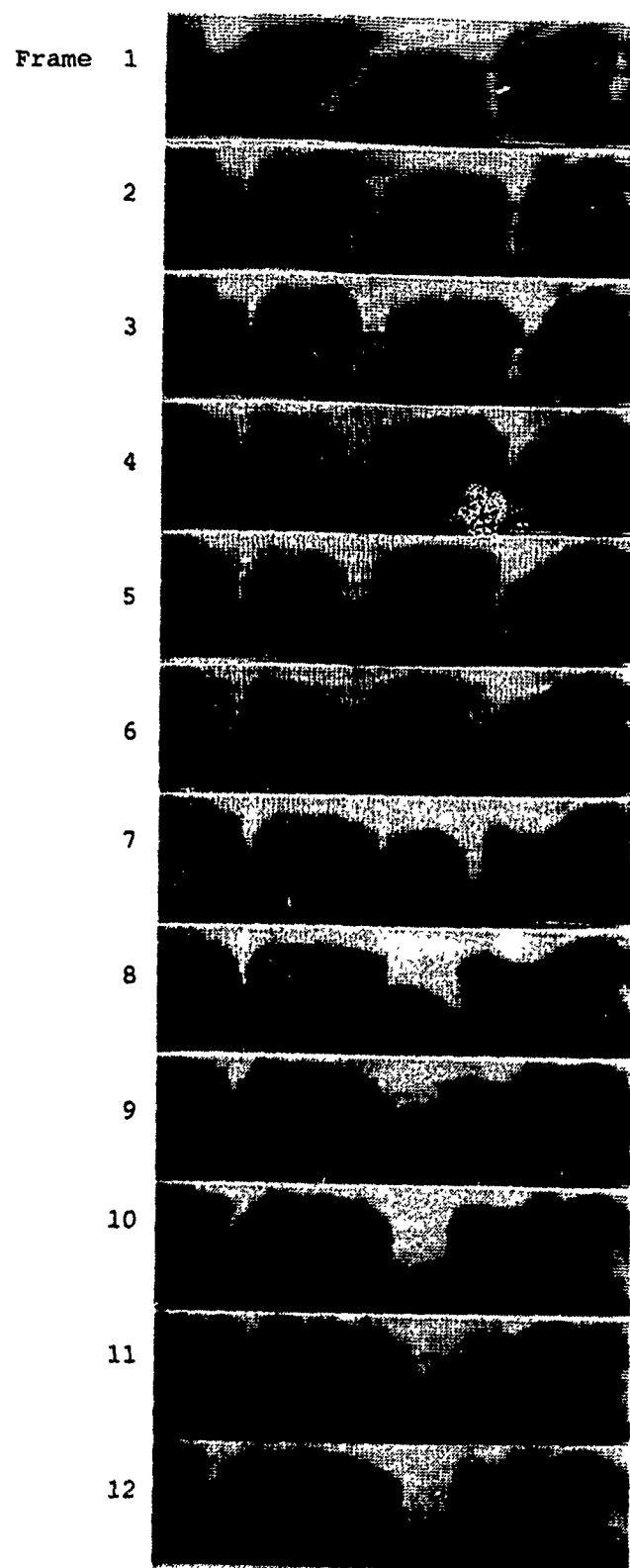


Figure 216. Vortex Pair Collapse Visualization, $De=100$, $\theta=115^\circ$
Interval $1/30$ s

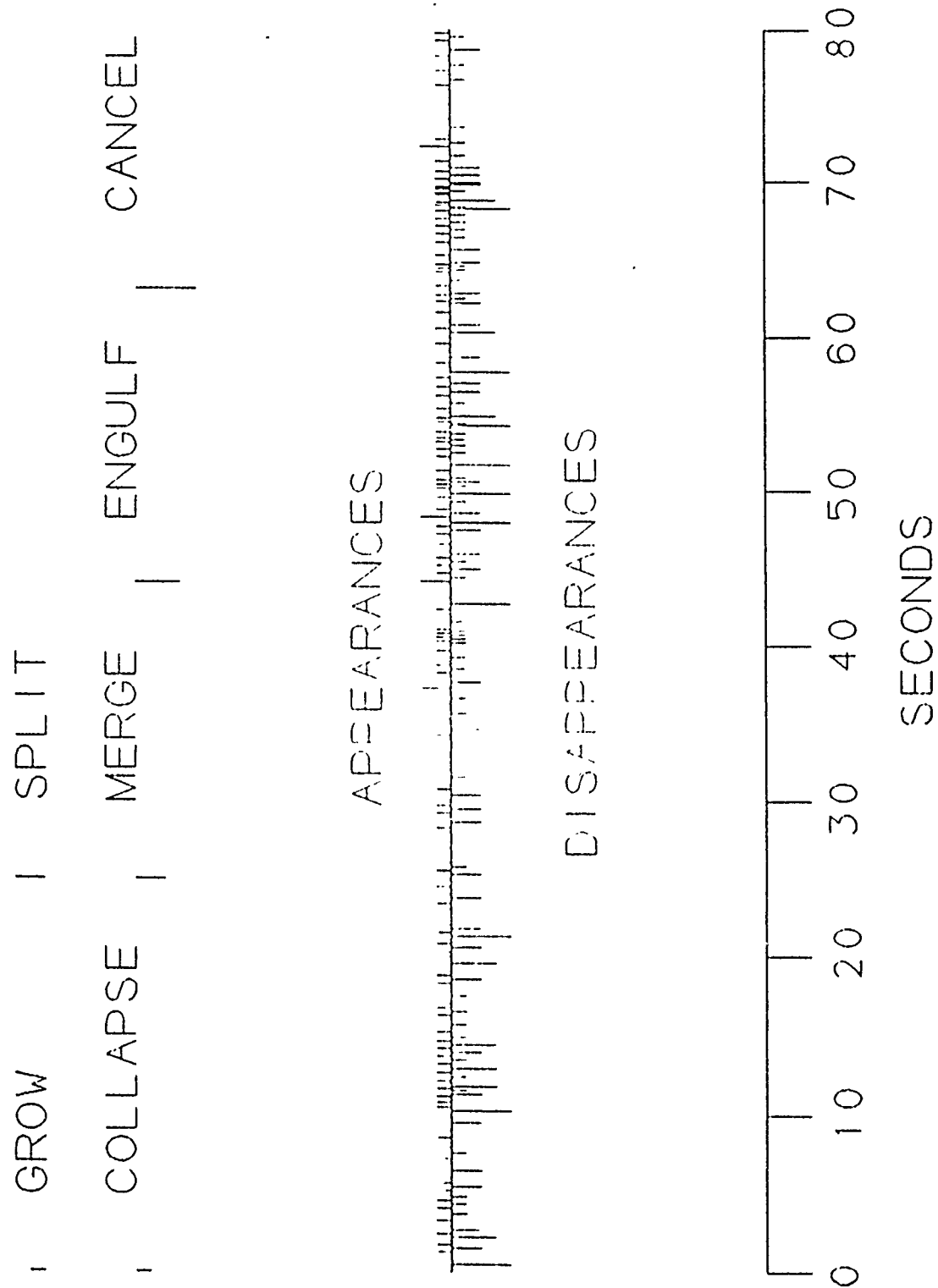


Figure 217. Vortex Pair Appearances and Disappearances Macroscopic Time
Line, $De=100$, $\theta=115^\circ$

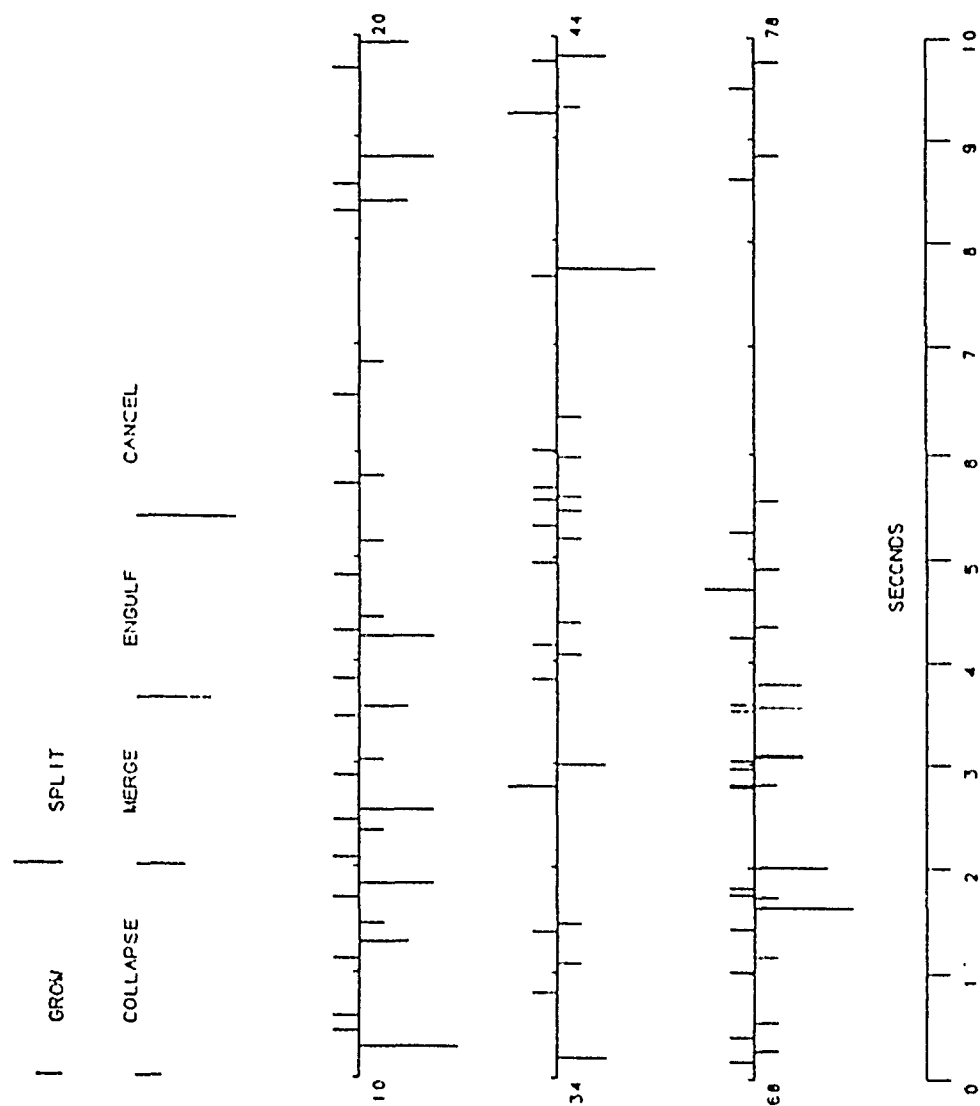


Figure 218. Vortex Pair Appearances and Disappearances Microscopic Time Lines, $De=100$, $\theta=115^\circ$

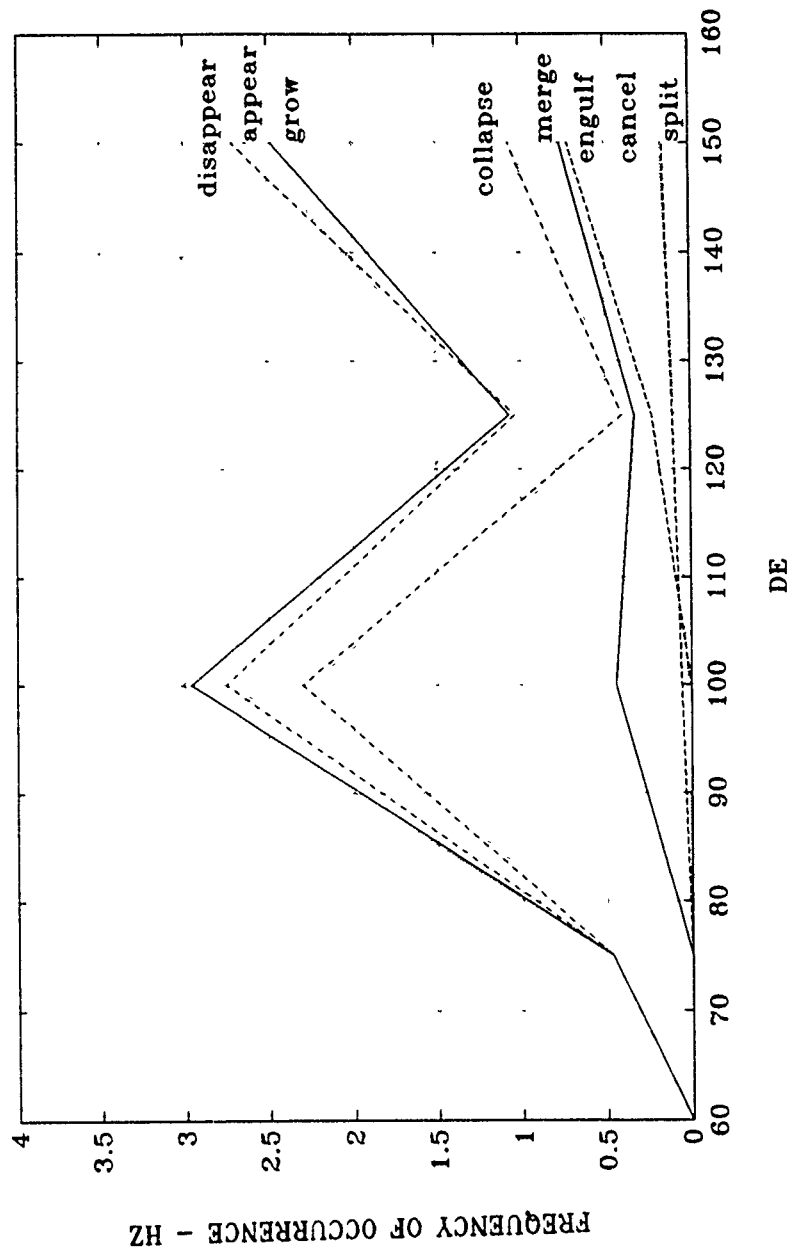


Figure 219. Vortex Pair Appearance and Disappearance Frequencies vs. De , $\theta=85^\circ$

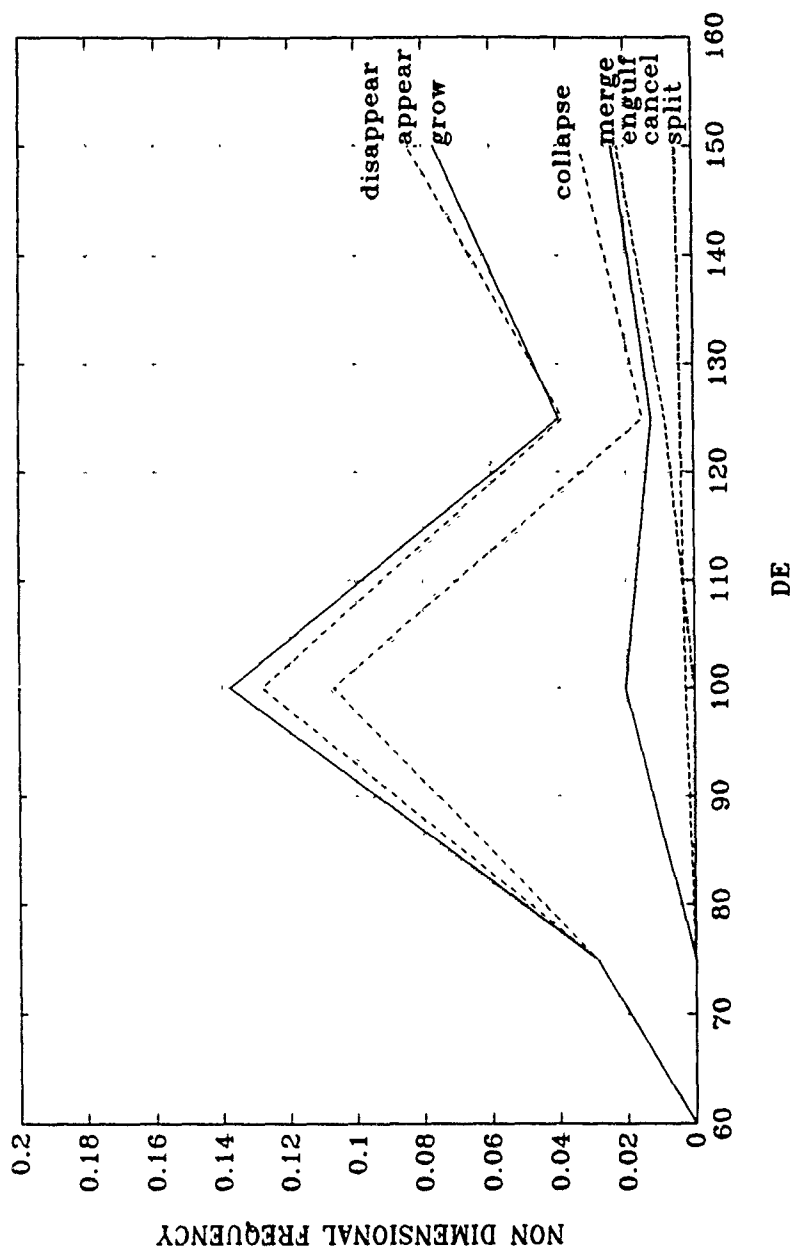


Figure 220. Vortex Pair Appearance and Disappearance Non-dimensional Frequencies ($\pi fd/\bar{U}$) vs. De , $\theta=85^\circ$

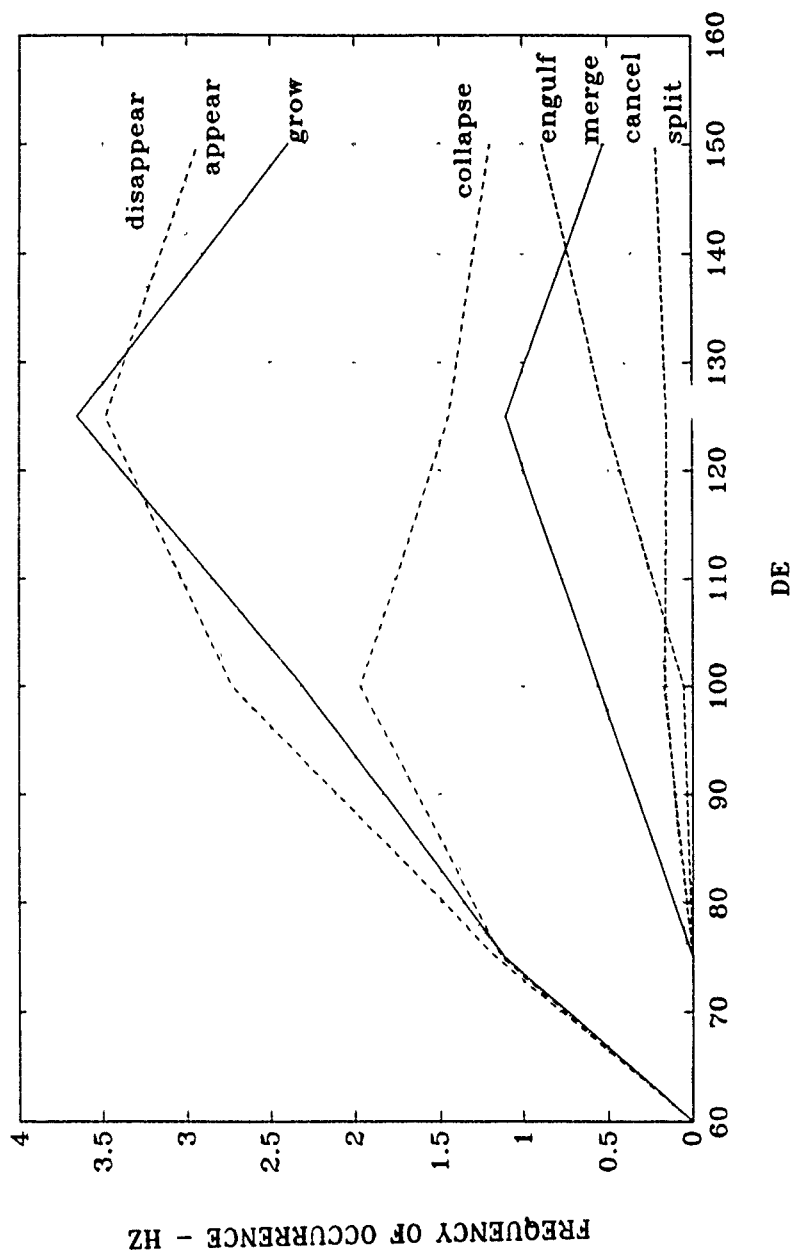


Figure 221. Vortex Pair Appearance and Disappearance Frequencies vs. De , $\theta=95^\circ$

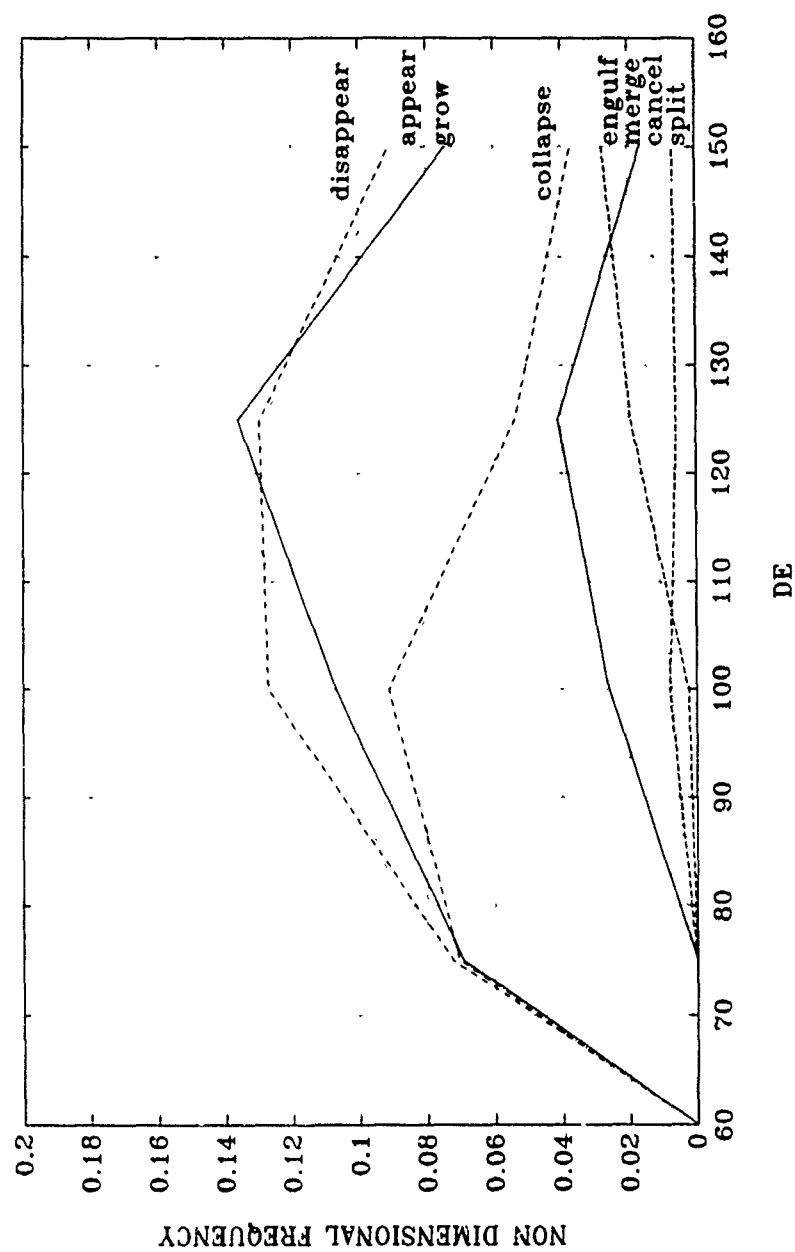


Figure 222. Vortex Pair Appearance and Disappearance Non-dimensional Frequencies ($\pi fd/\bar{U}$) vs. De , $\theta=95^\circ$

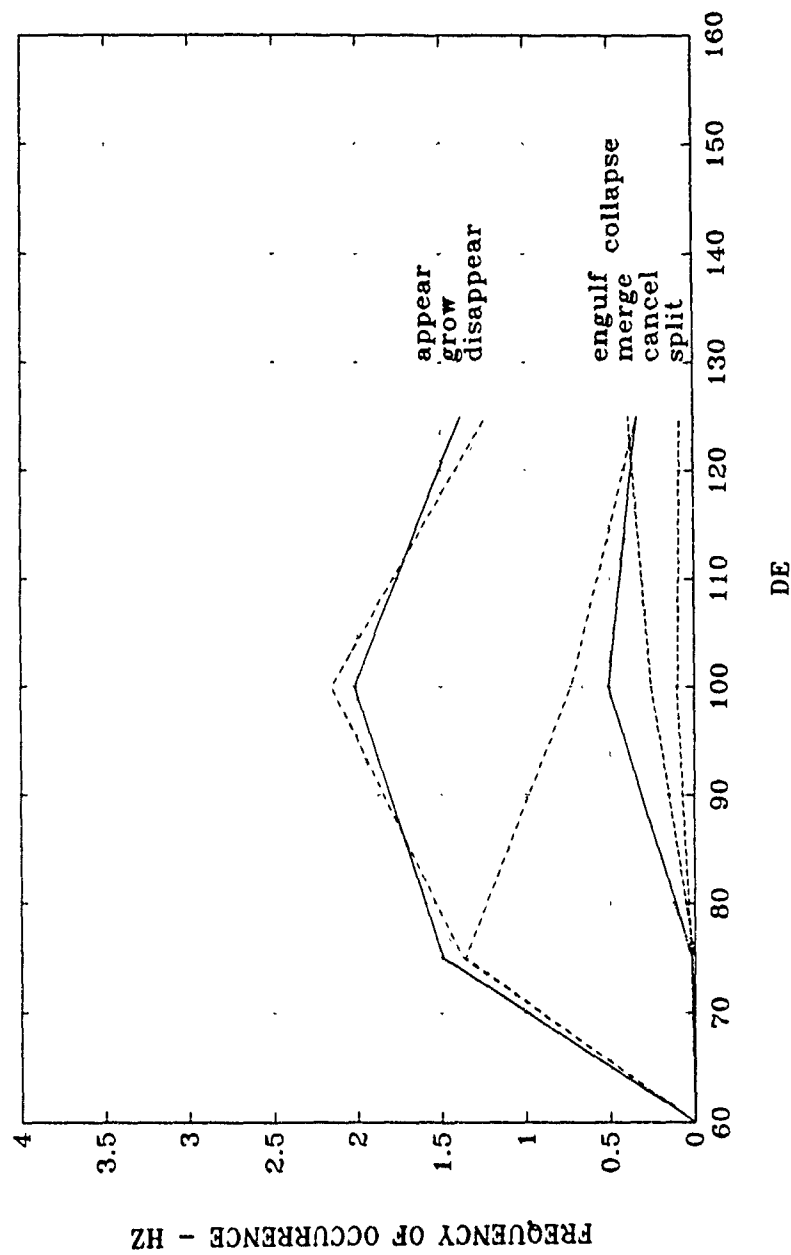


Figure 223. Vortex Pair Appearance and Disappearance Frequencies vs. De , $\theta=105^\circ$

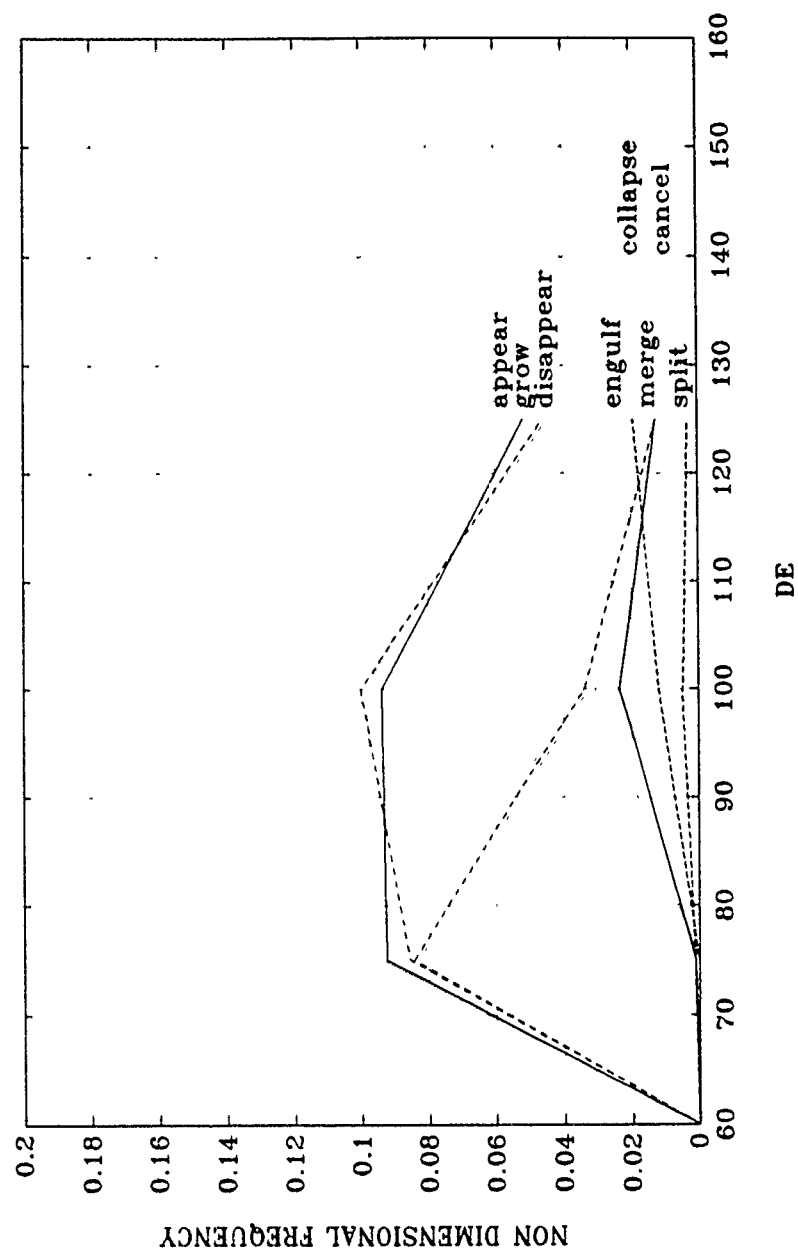


Figure 224. Vortex Pair Appearance and Disappearance Non-dimensional Frequencies ($\pi fd/\bar{U}$) vs. De , $\theta=105^\circ$

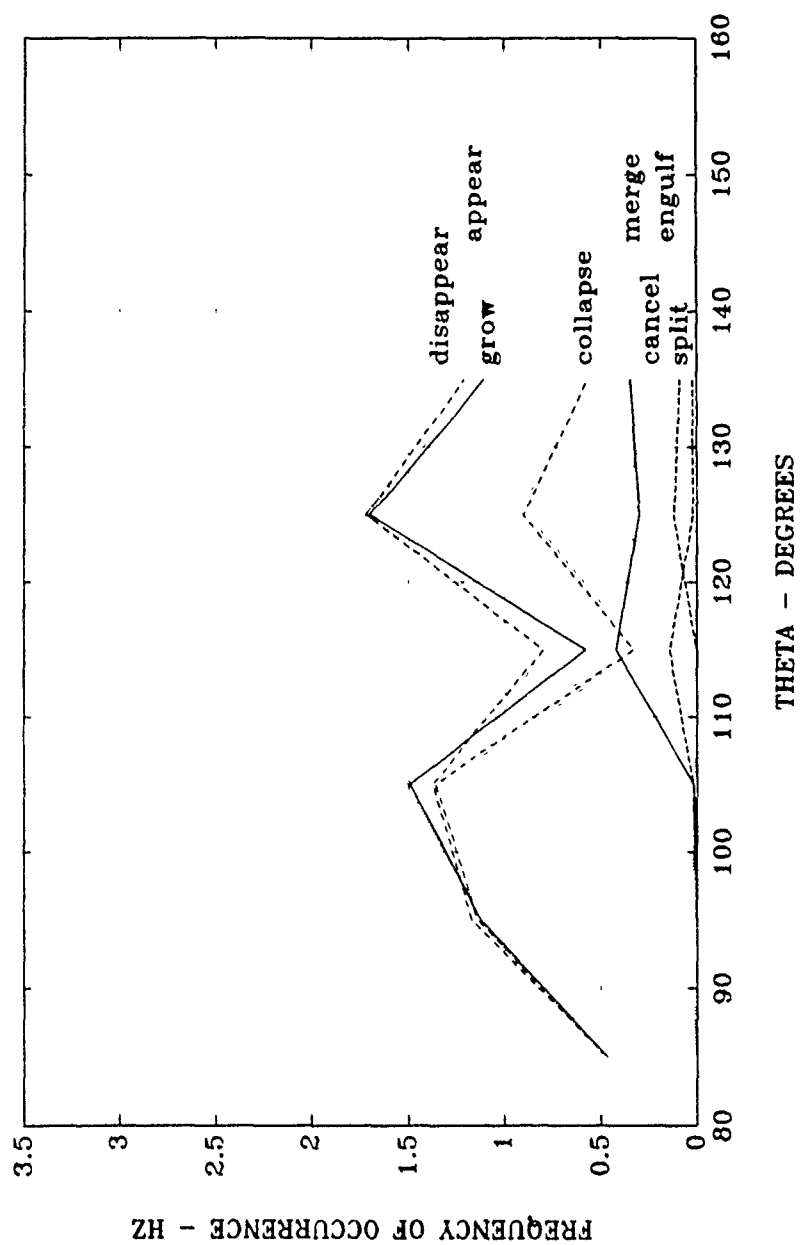


Figure 225. Vortex Pair Appearance and Disappearance Frequencies vs. θ , $De=75$

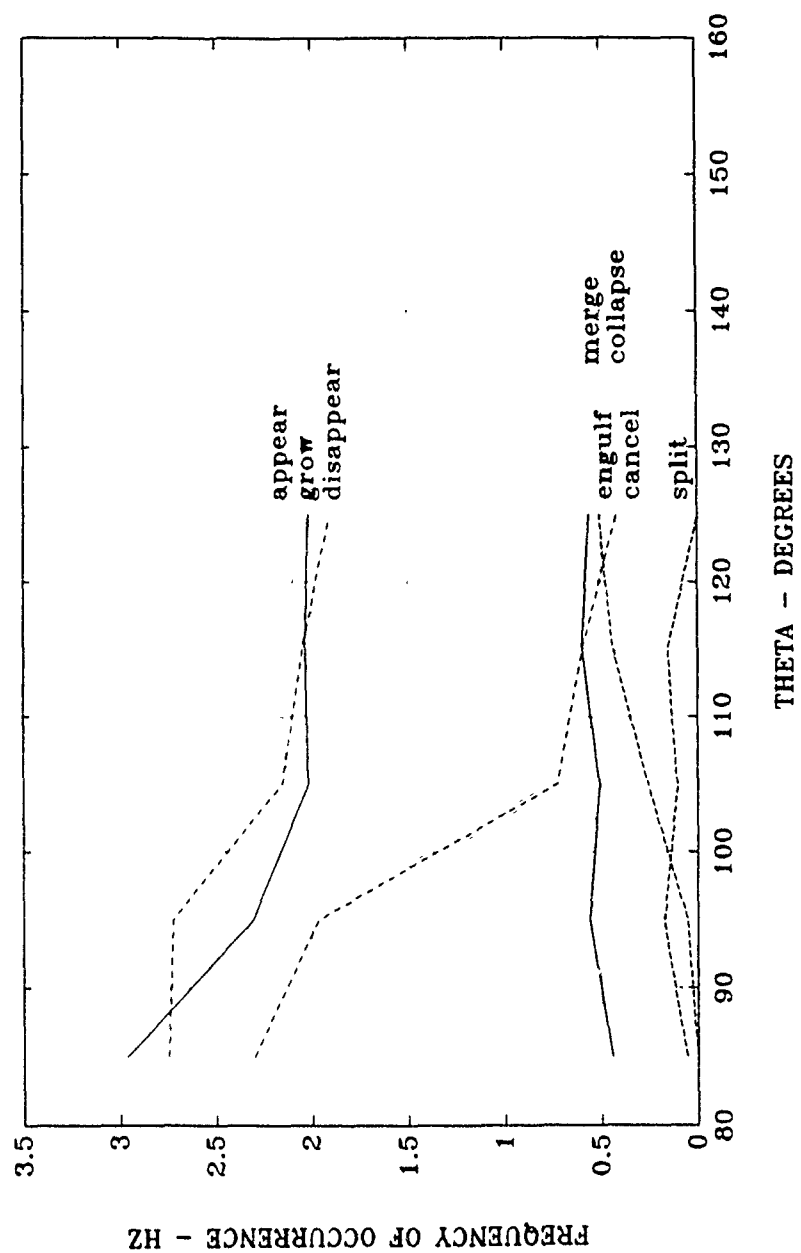


Figure 226. Vortex Pair Appearance and Disappearance Frequencies vs. θ ,
 $De=100$

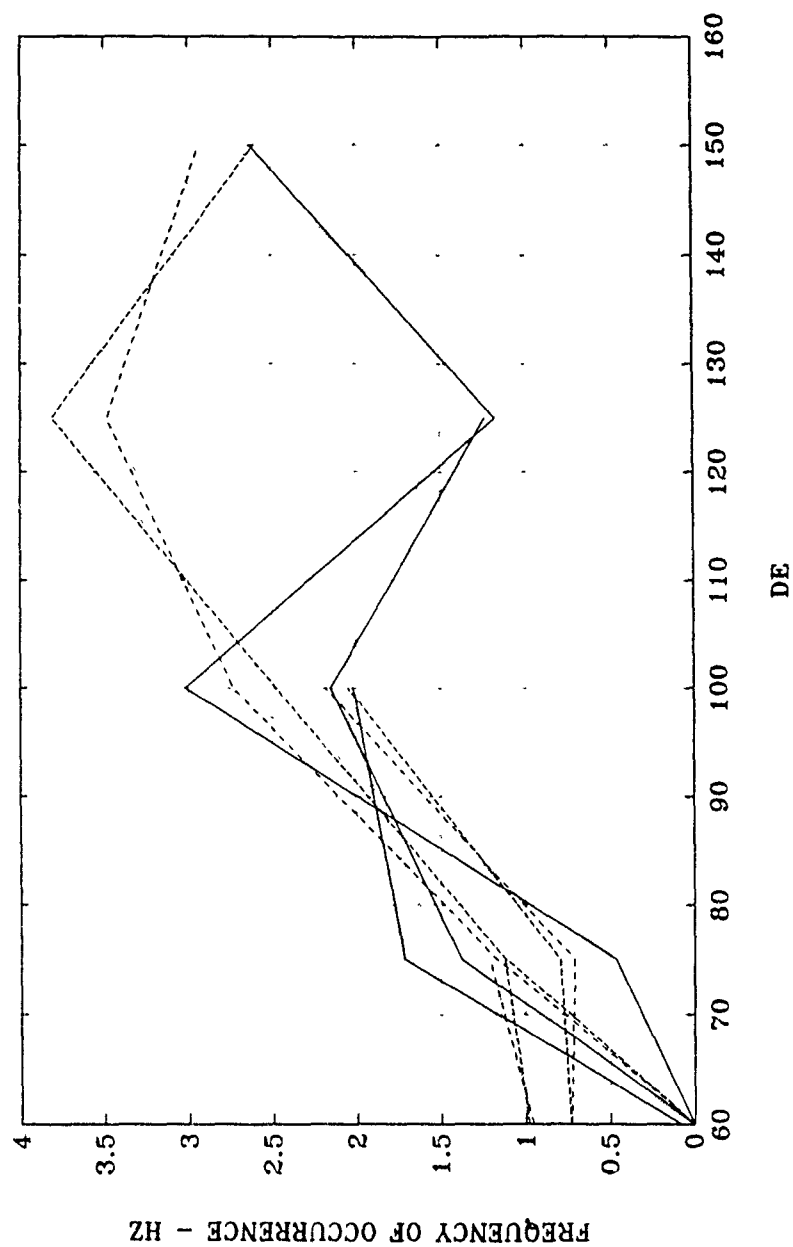


Figure 227. Vortex Pair Appearance and Disappearance Frequencies vs. De , $\theta = 85^\circ$ to 135° Composite w/o Curve Identification

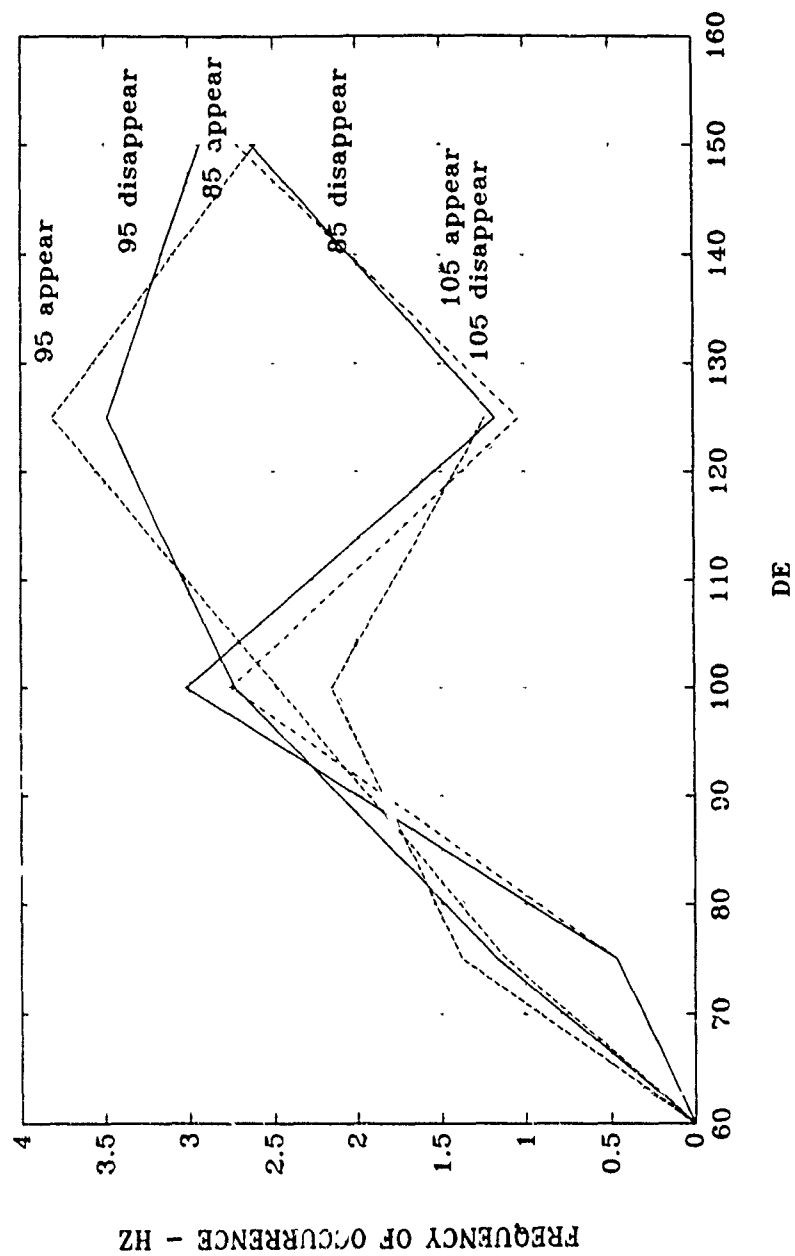


Figure 228. Vortex Pair Appearance and Disappearance Frequencies vs. De , $\theta = 85^\circ$ to 105°

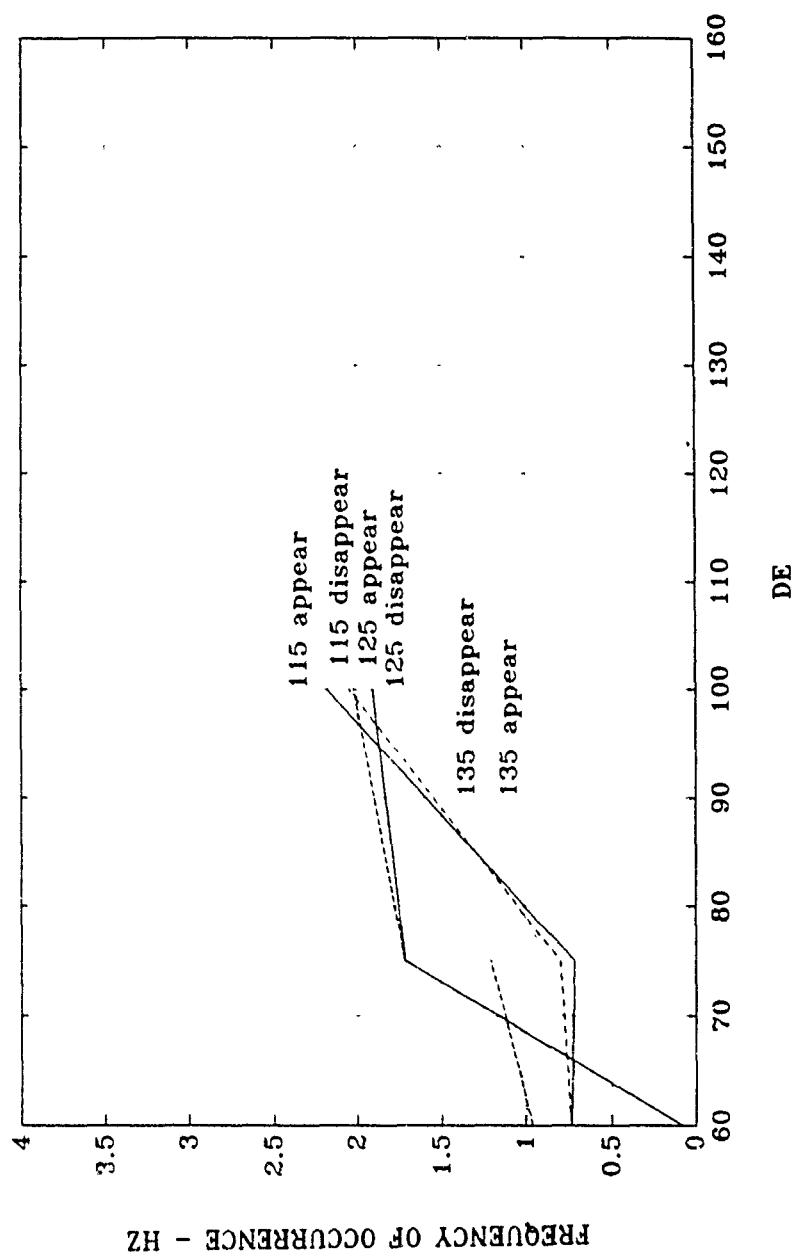


Figure 229. Vortex Pair Appearance and Disappearance Frequencies vs. De , $\theta = 115^\circ$ to 135°

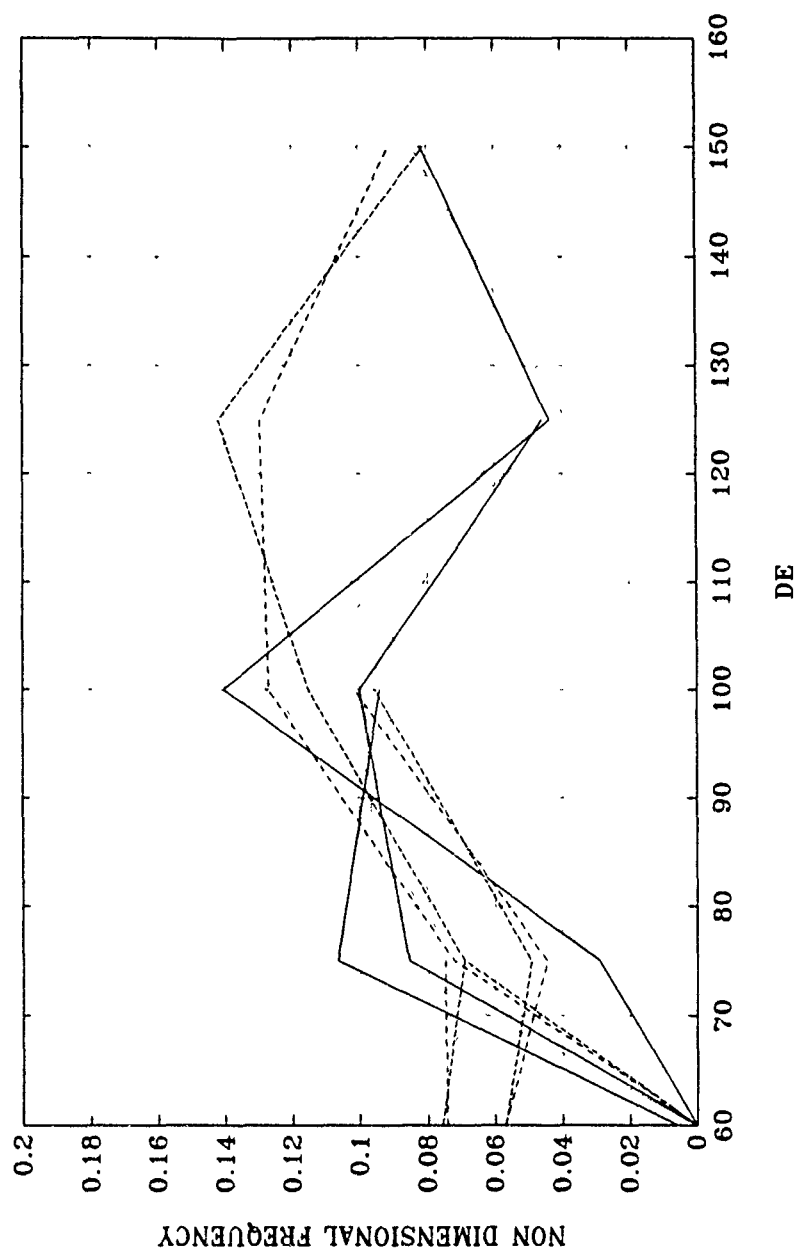


Figure 230. Vortex Pair Appearance and Disappearance Non-dimensional Frequencies ($\pi fd/\bar{U}$) vs. De , $\theta=85^\circ$ to 135° Composite w/o Curve Identification

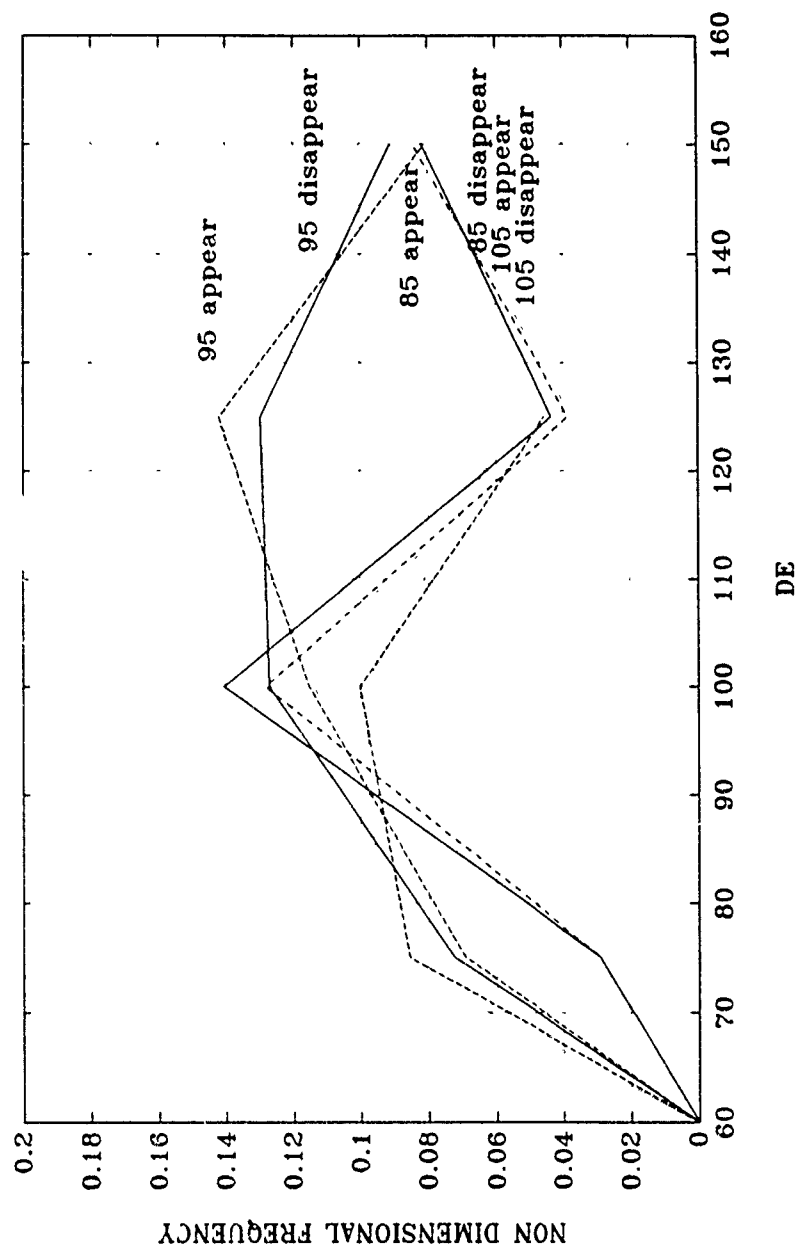


Figure 231. Vortex Pair Appearance and Disappearance Non-dimensional Frequencies ($\pi fd/\bar{U}$) vs. De , $\theta=85^\circ$ to 105°

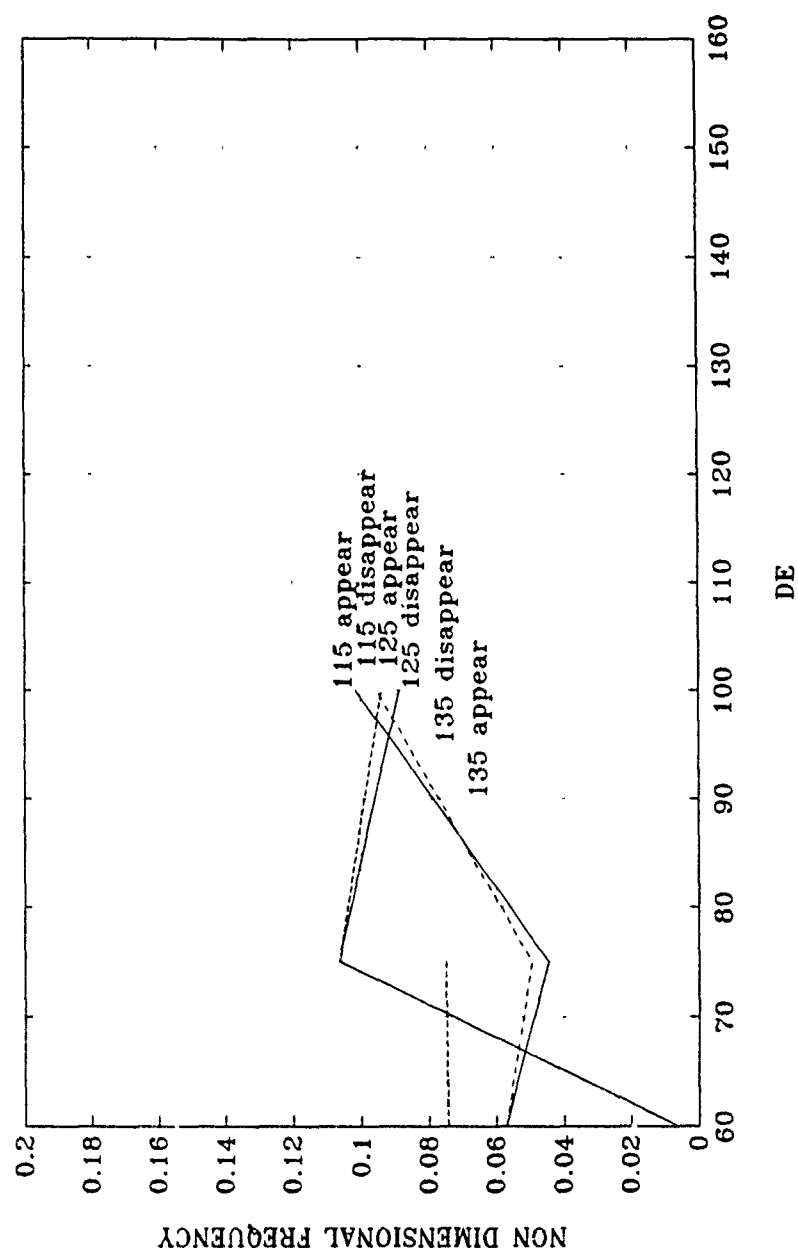


Figure 232. Vortex Pair Appearance and Disappearance Non-dimensional Frequencies ($\pi fd/\bar{U}$) vs. De , $\theta=115^\circ$ to 135°

APPENDIX F - INDIVIDUAL SPECTRA

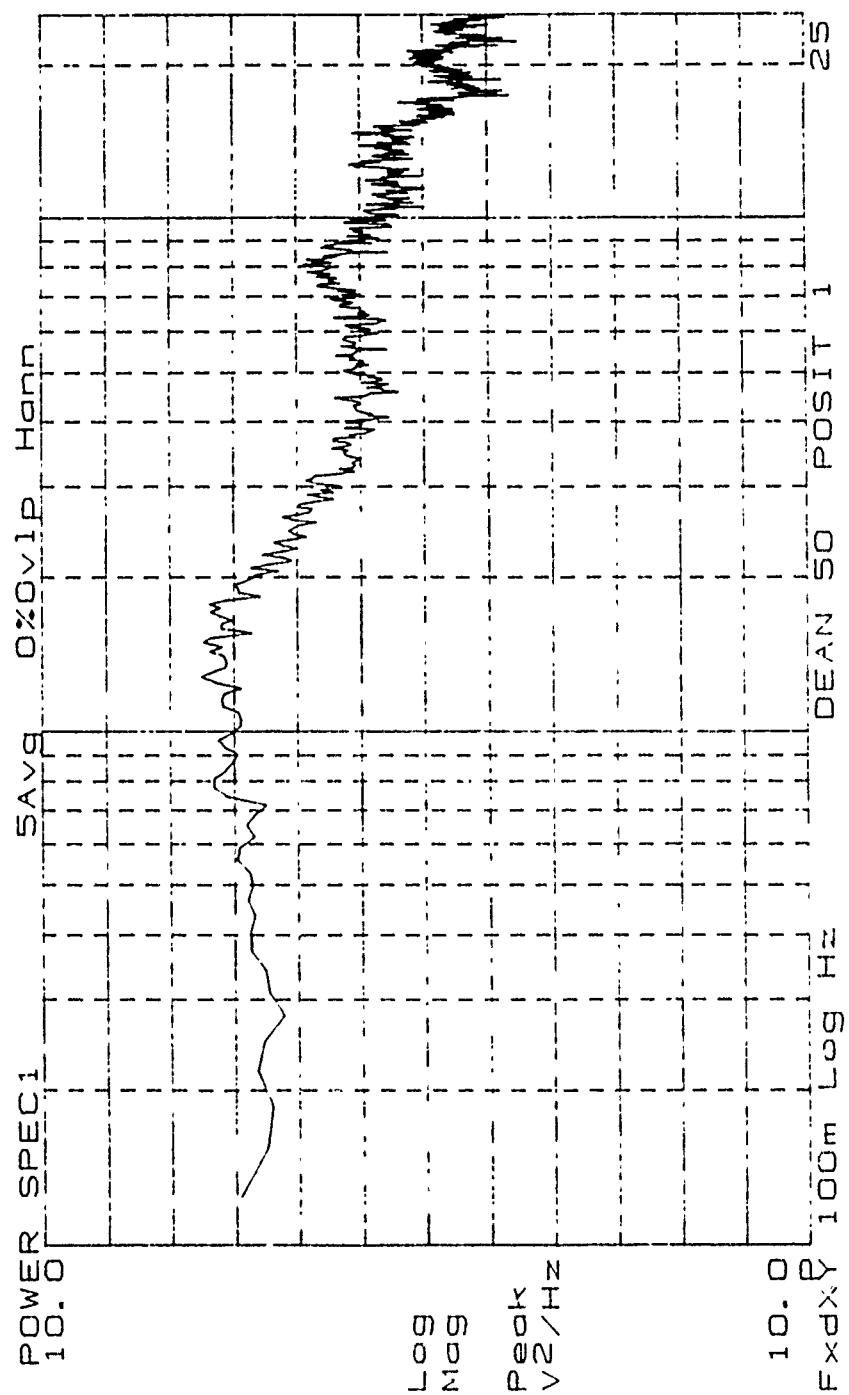


Figure 92. Low Frequency Power Spectrum, De=50, Position 1

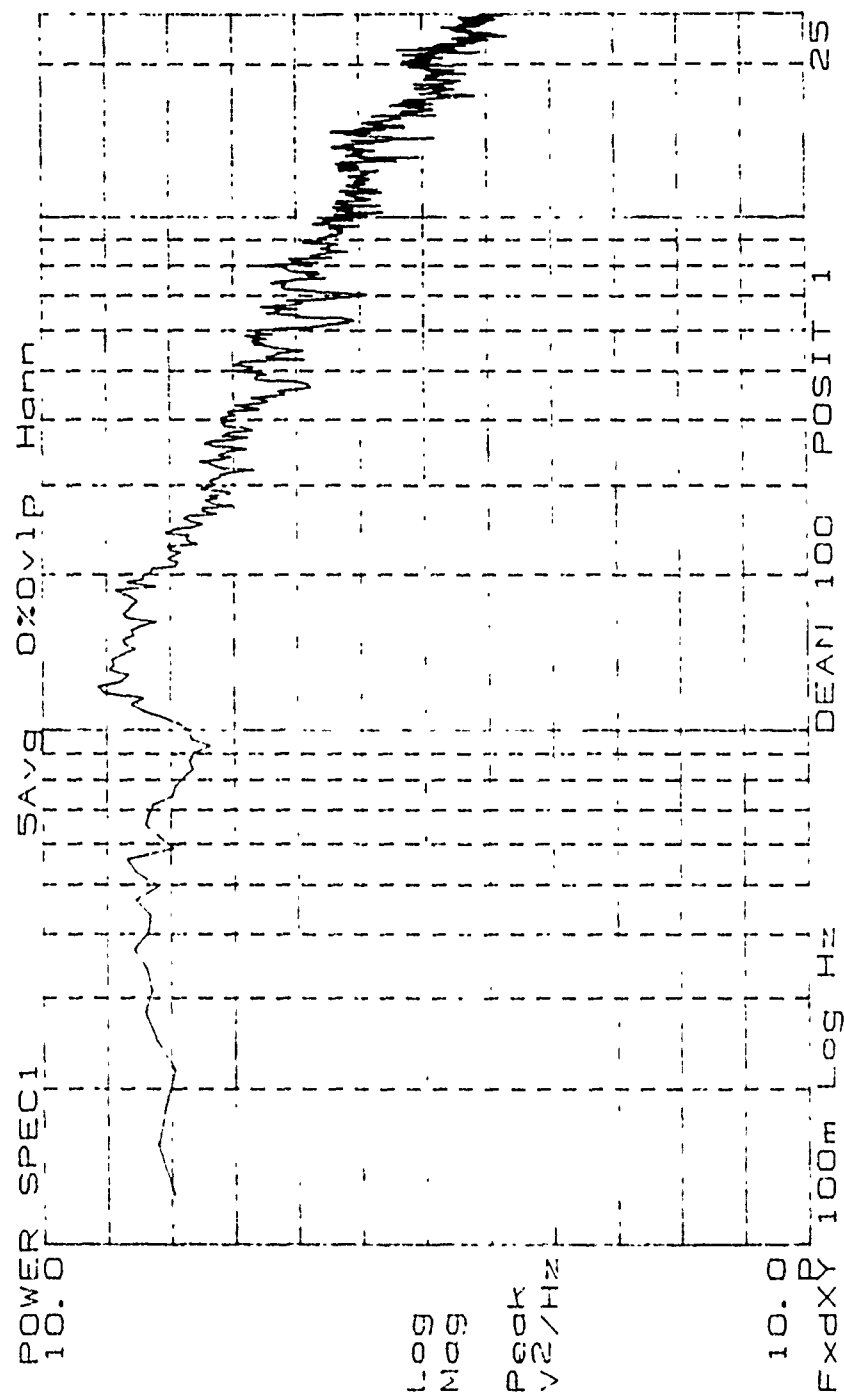


Figure 93. Low Frequency Power Spectrum, De=100, Position 1

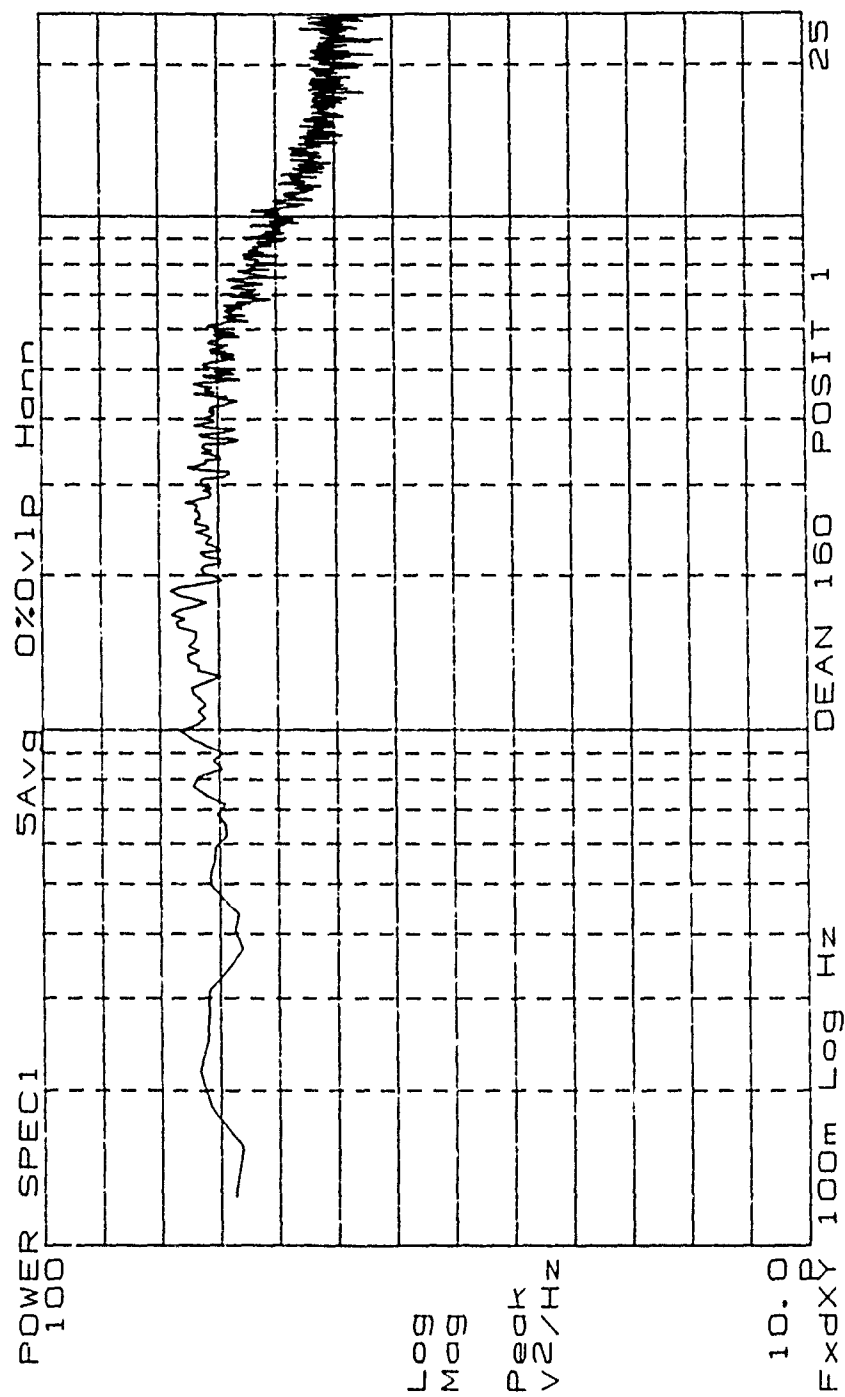


Figure 95. Low Frequency Power Spectrum, De=160, Position 1

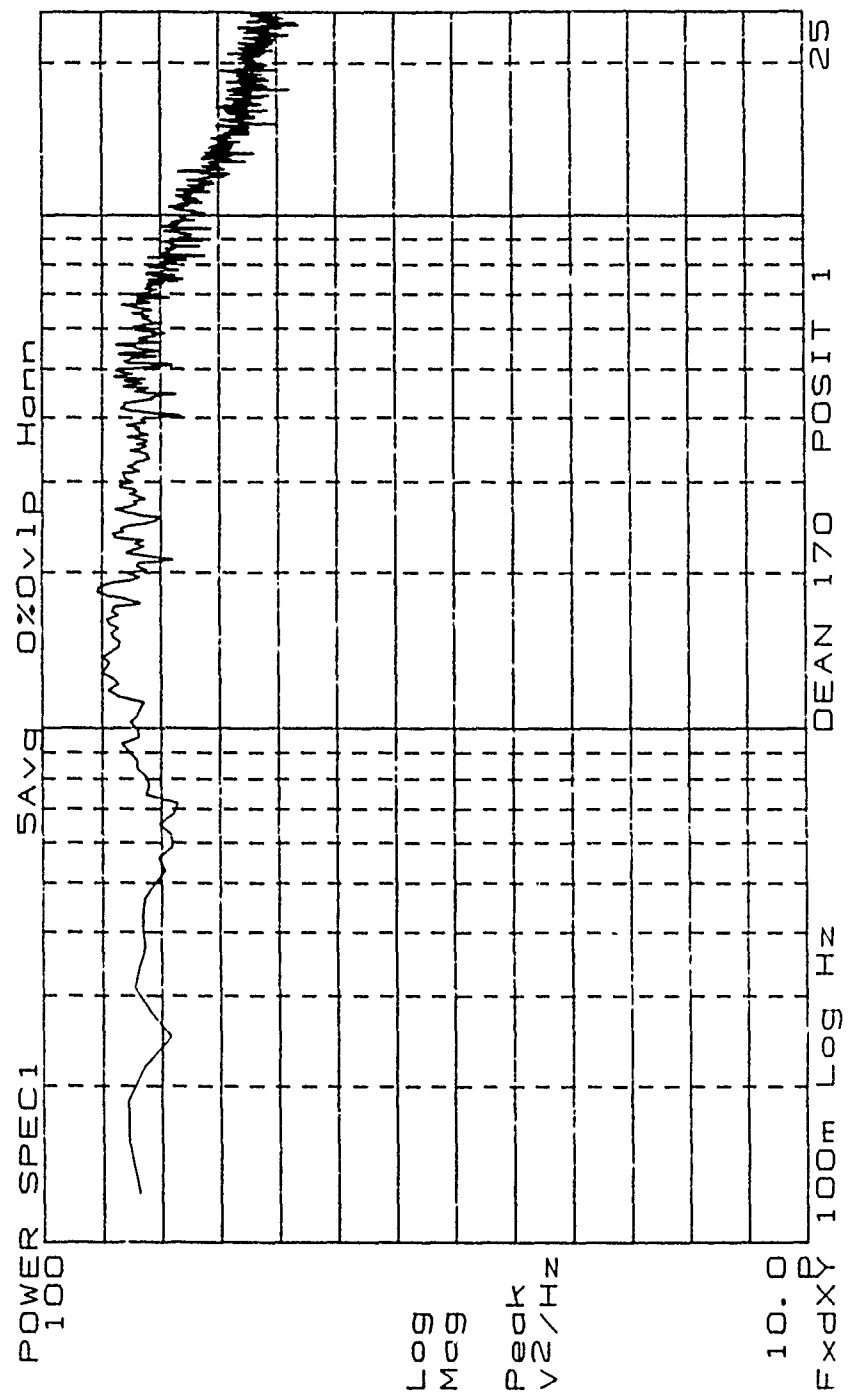


Figure 96. Low Frequency Power Spectrum, De=170, Position 1

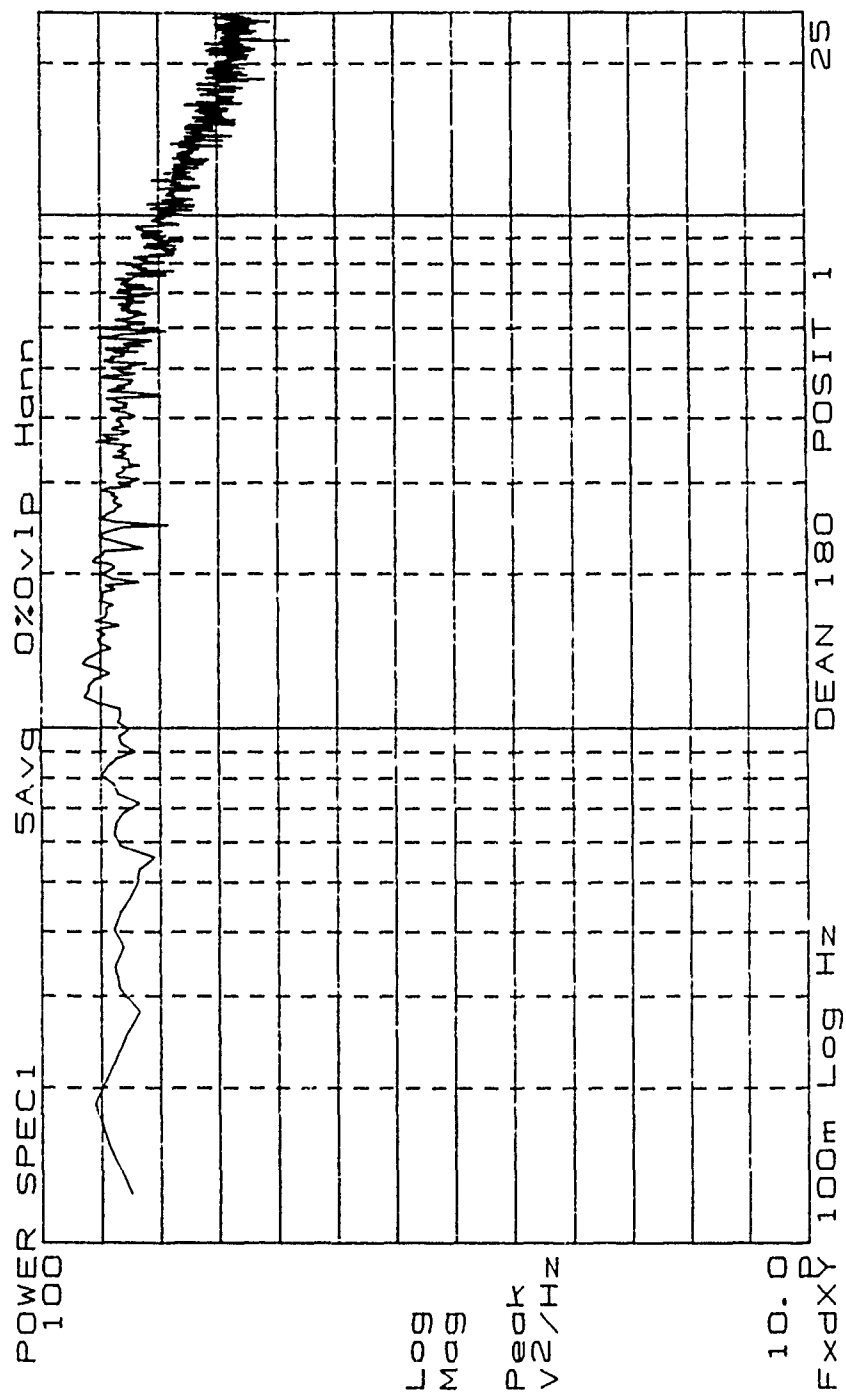


Figure 97. Low Frequency Power Spectrum, De=180, Position 1

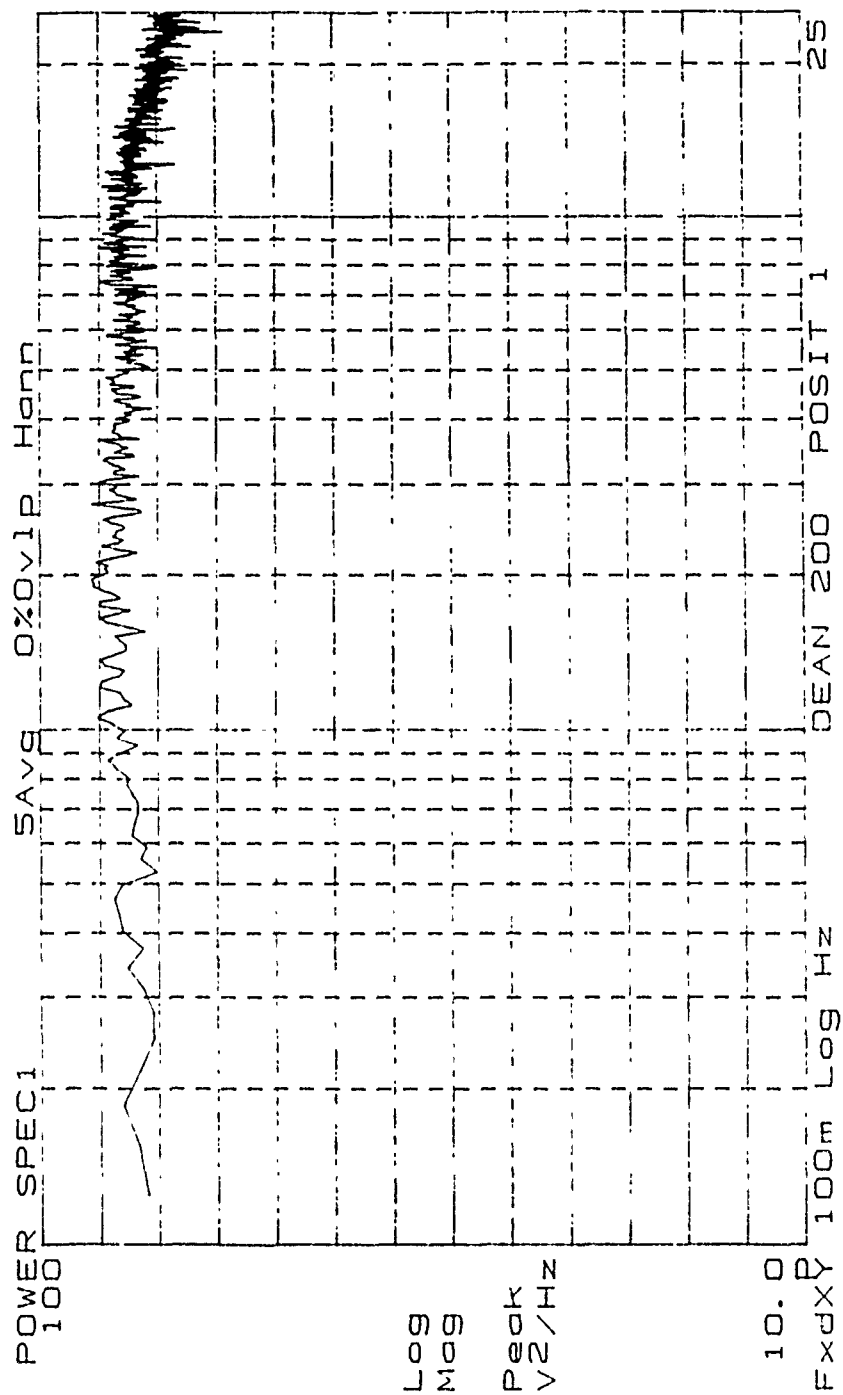


Figure 98. Low Frequency Power Spectrum, De=200, Position 1

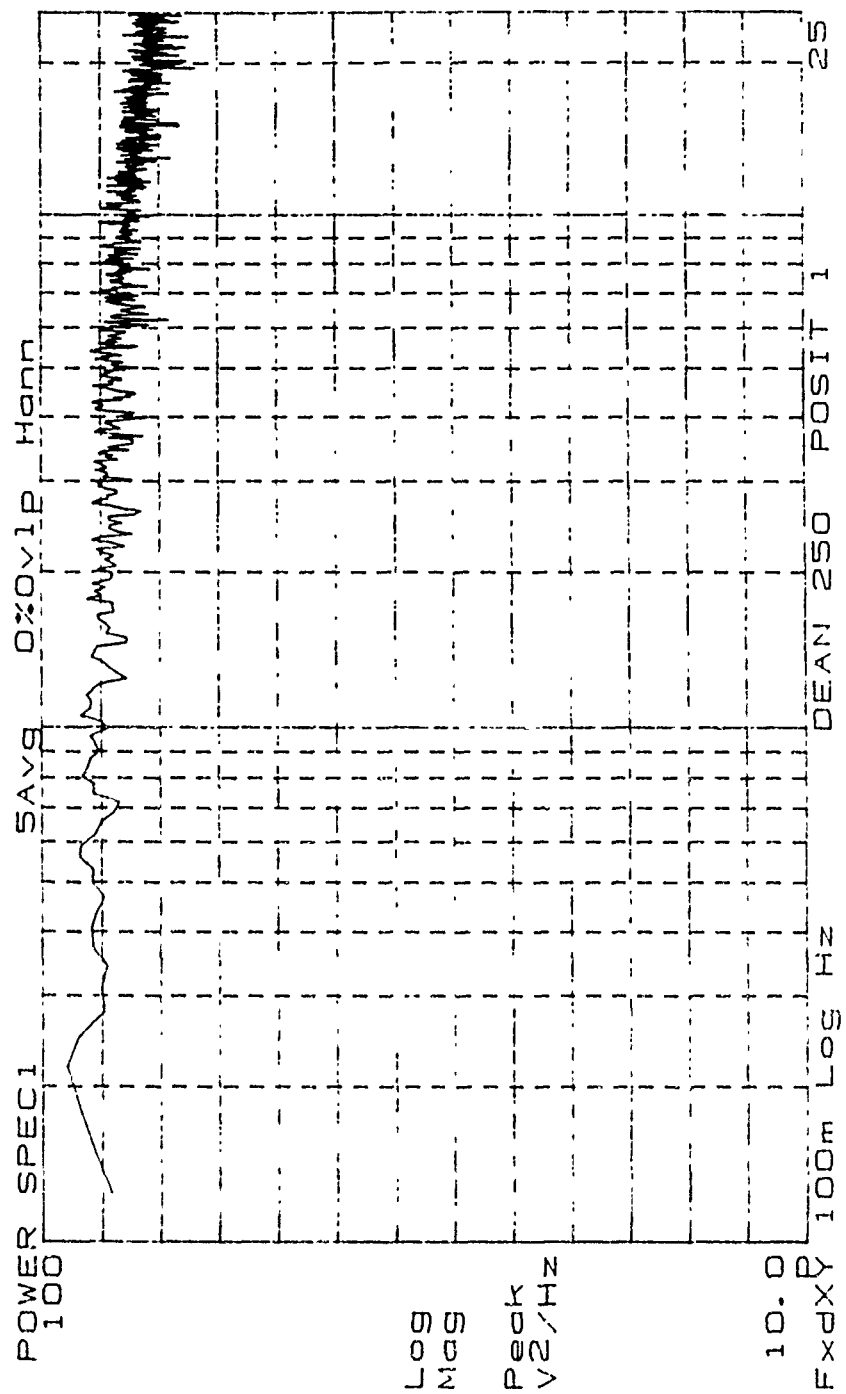


Figure 99. Low Frequency Power Spectrum, De=250, Position 1

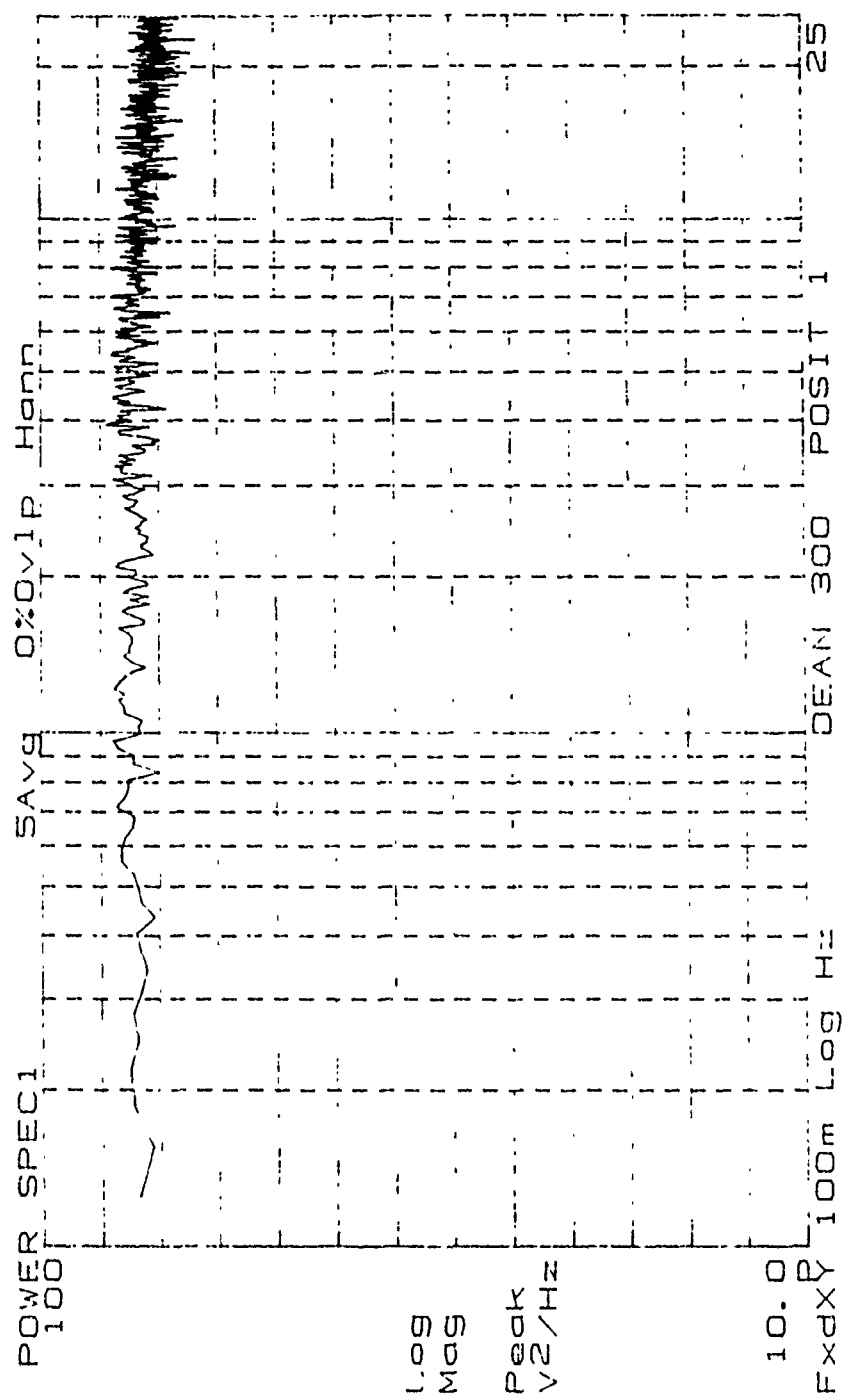


Figure 100. Low Frequency Power Spectrum, De=300, Position 1

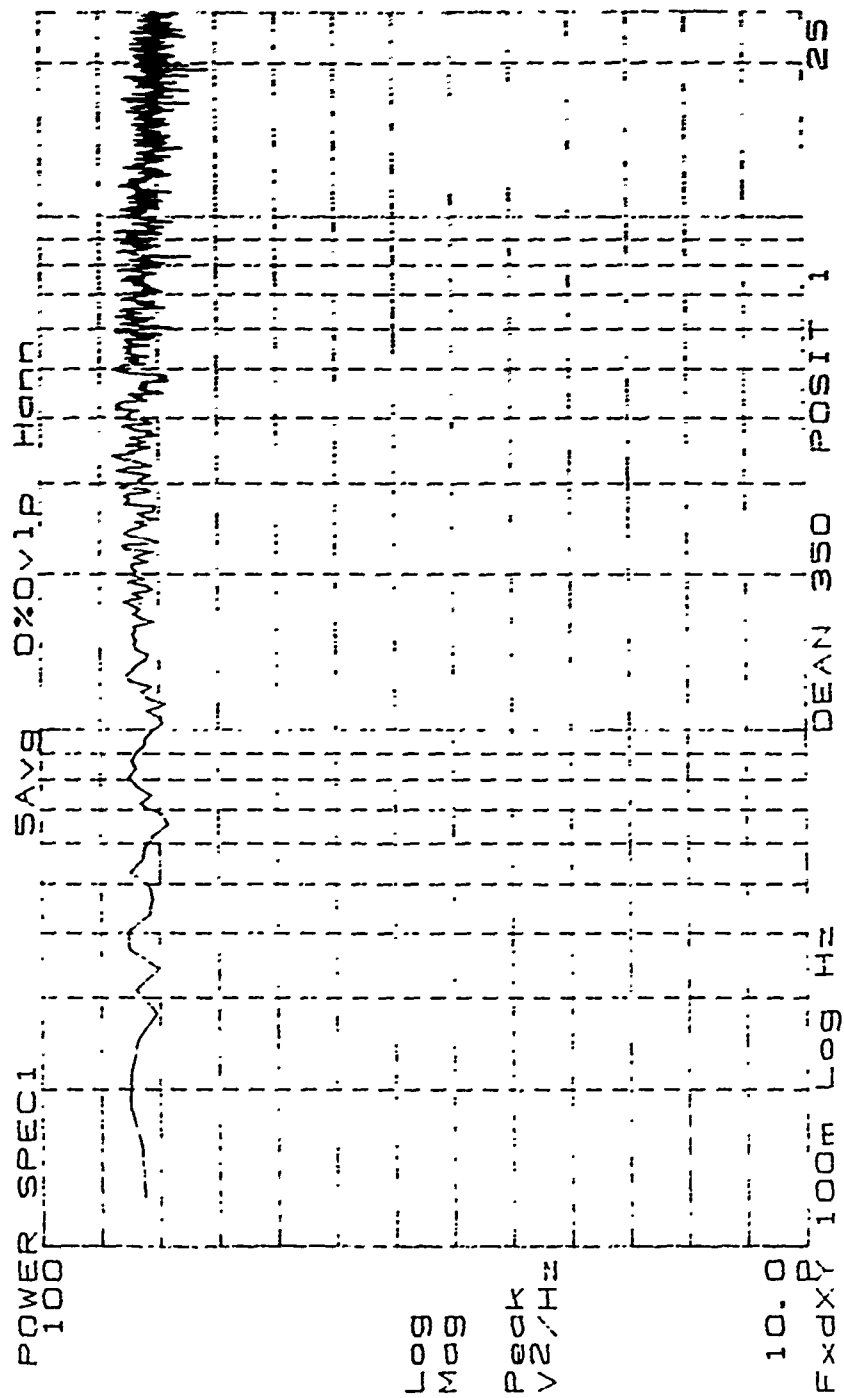


Figure 101. Low Frequency Power Spectrum, De=350, Position 1

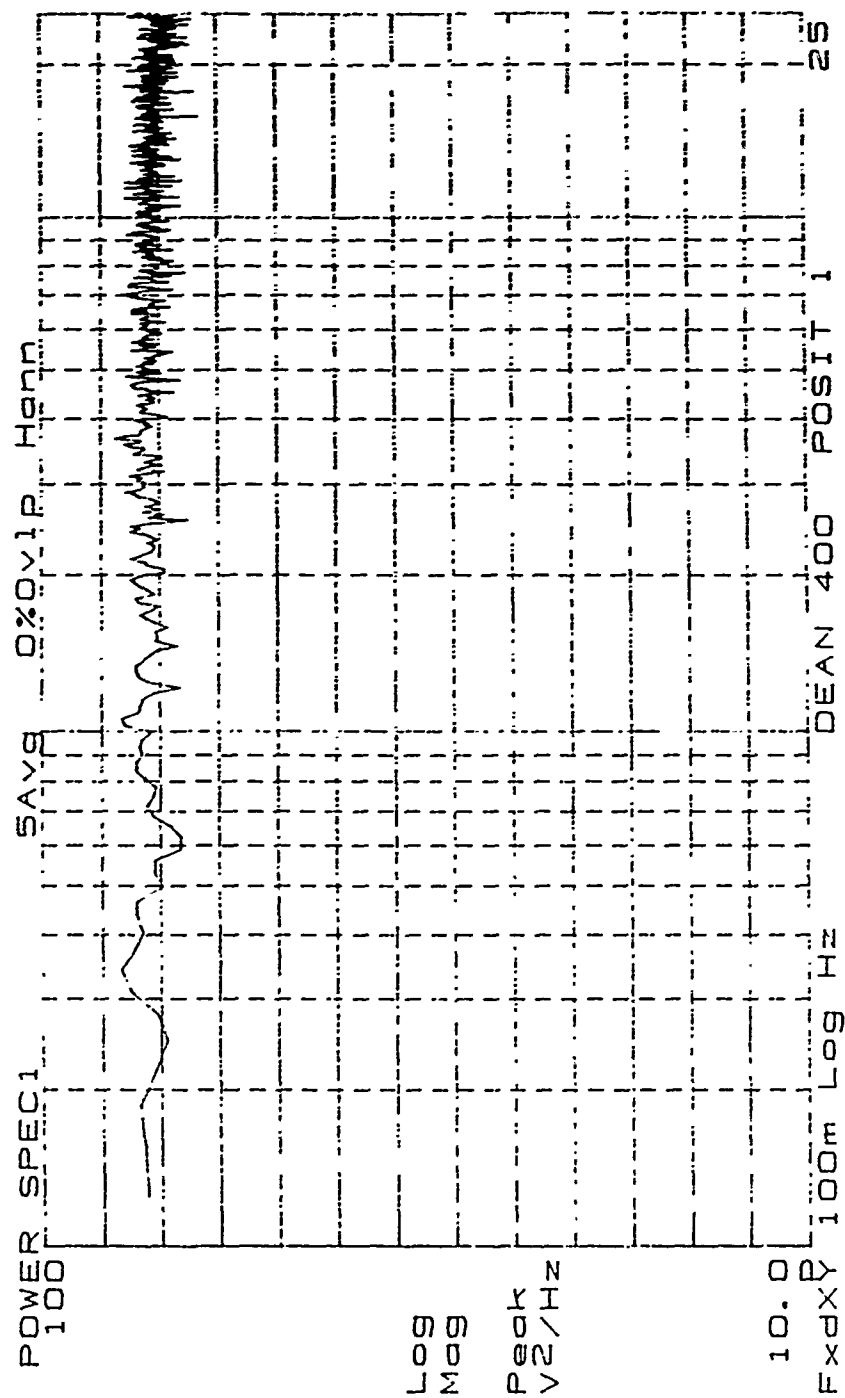


Figure 102. Low Frequency Power Spectrum, De=400, Position 1

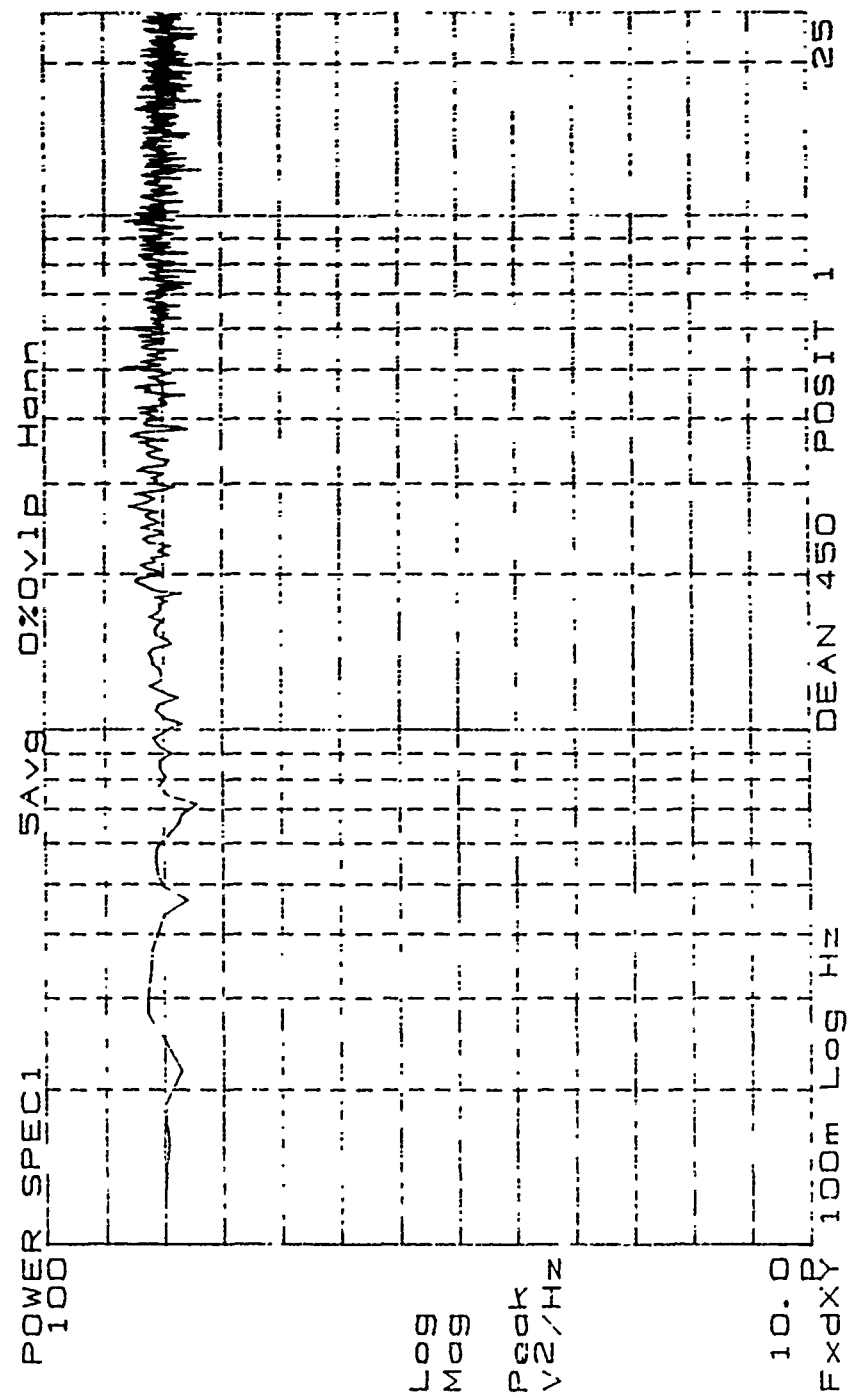


Figure 103. Low Frequency Power Spectrum, De=450, Position 1

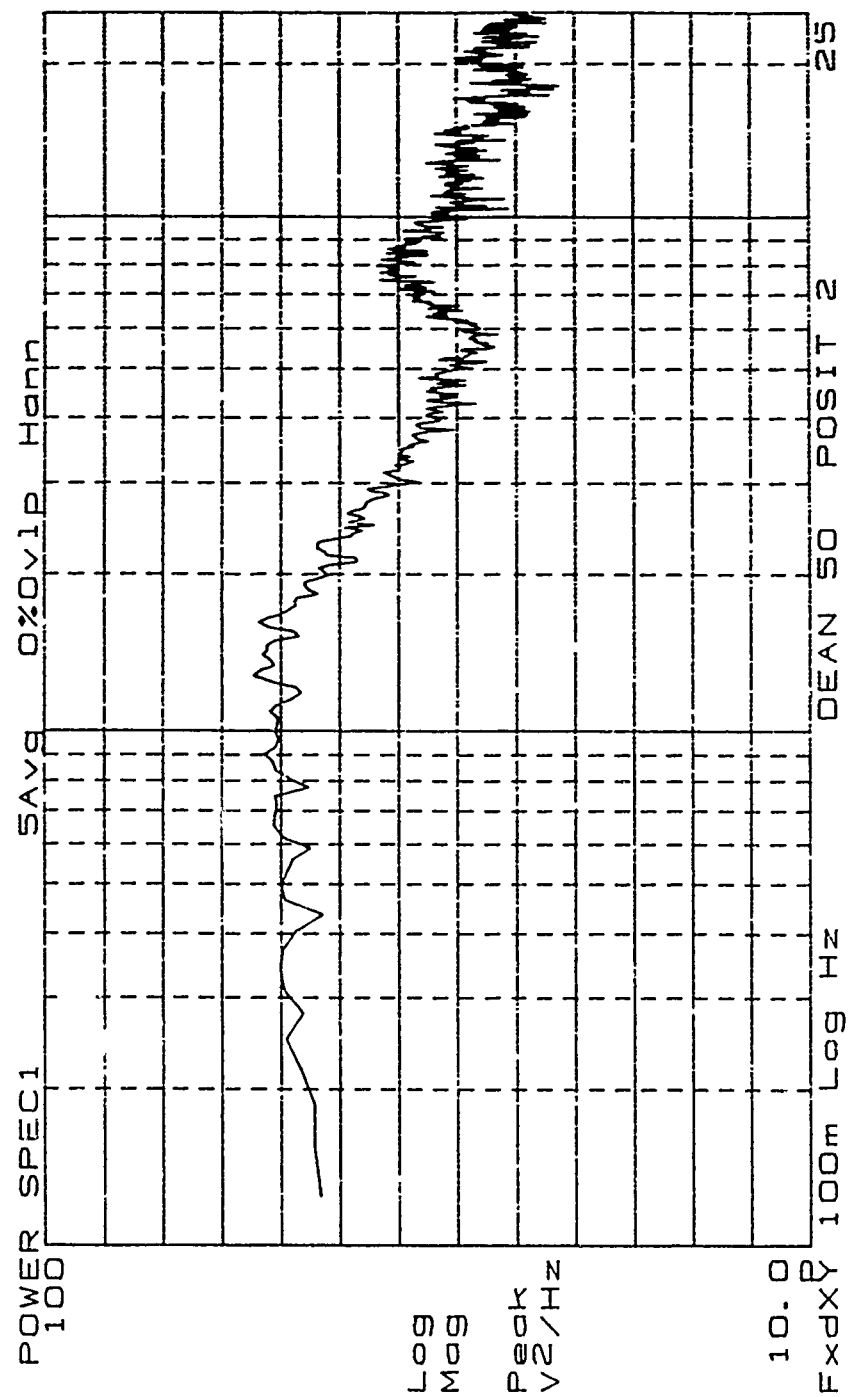


Figure 104. Low Frequency Power Spectrum, De=50, Position 2

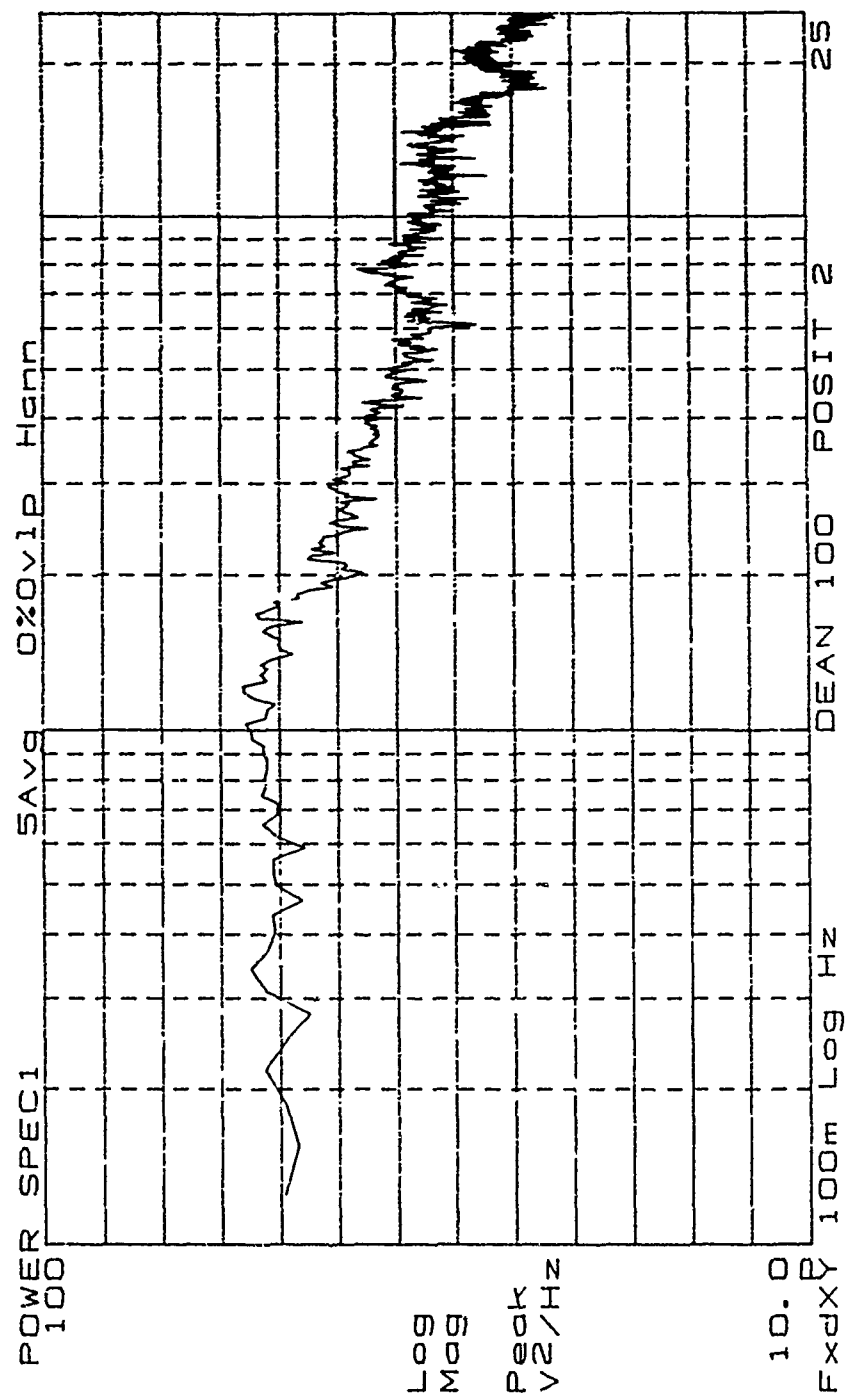


Figure 105. Low Frequency Power Spectrum, De=100, Position 2

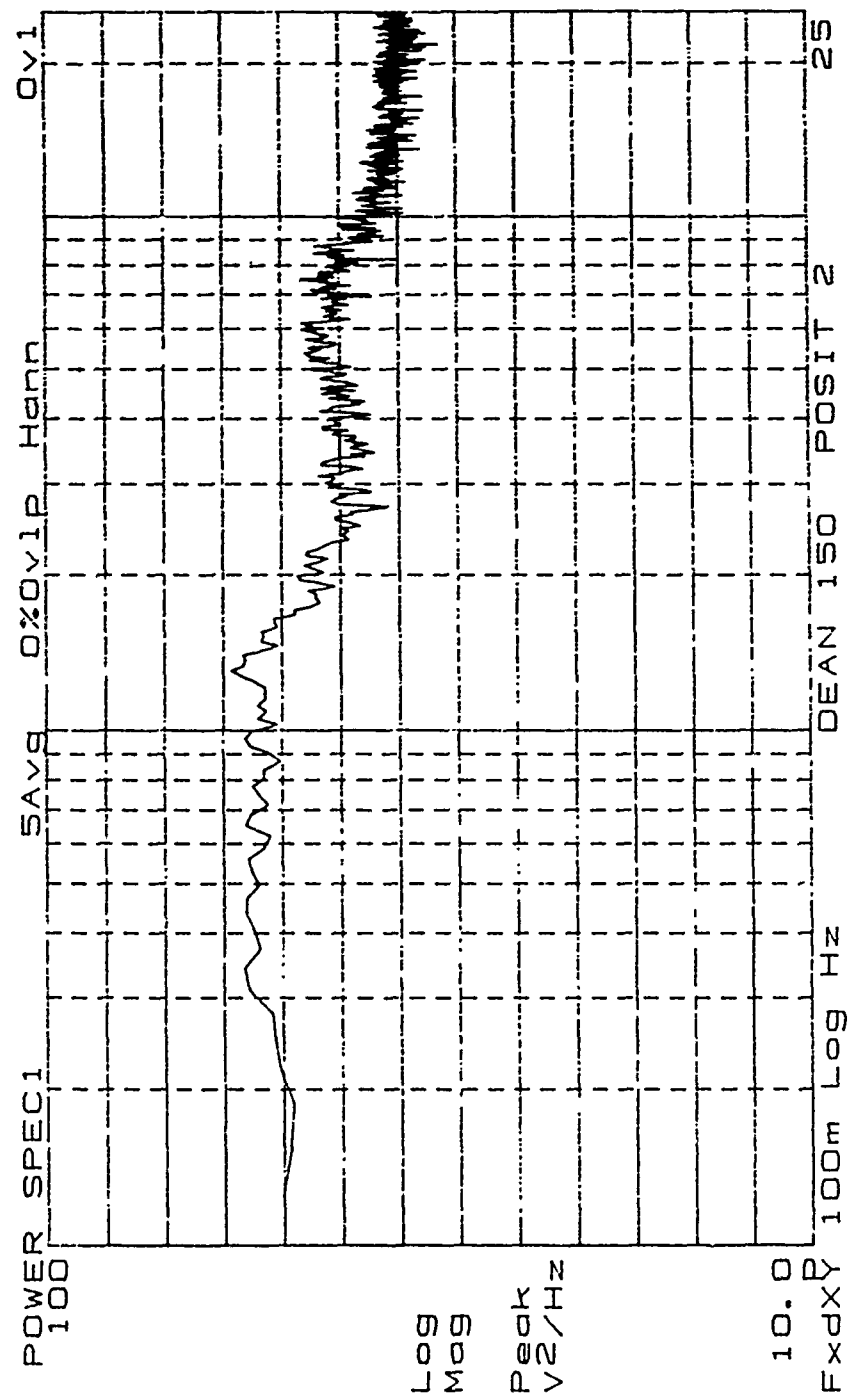


Figure 106. Low Frequency Power Spectrum, De=150, Position 2

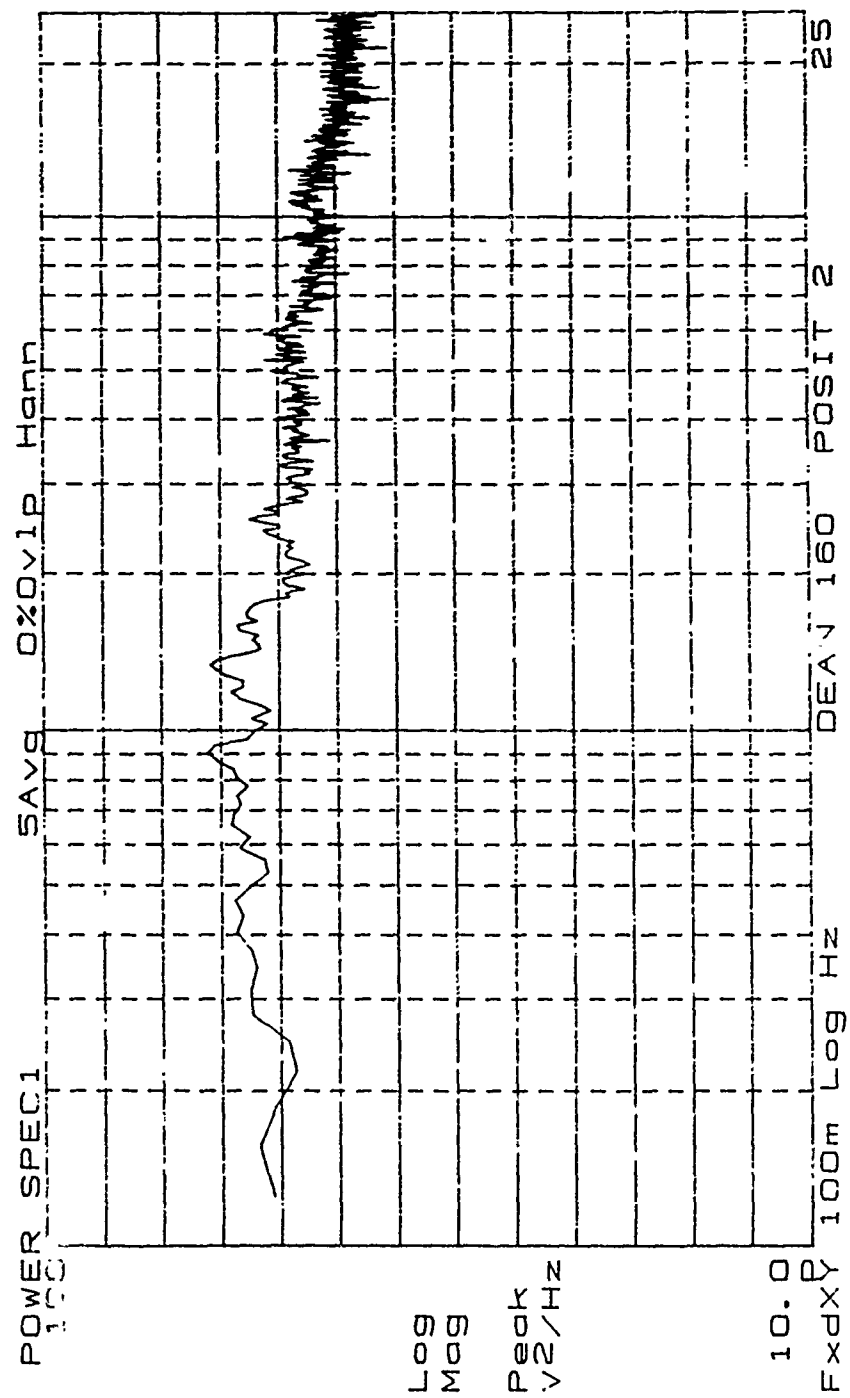


Figure 107. Low Frequency Power Spectrum, De=160, Position 2

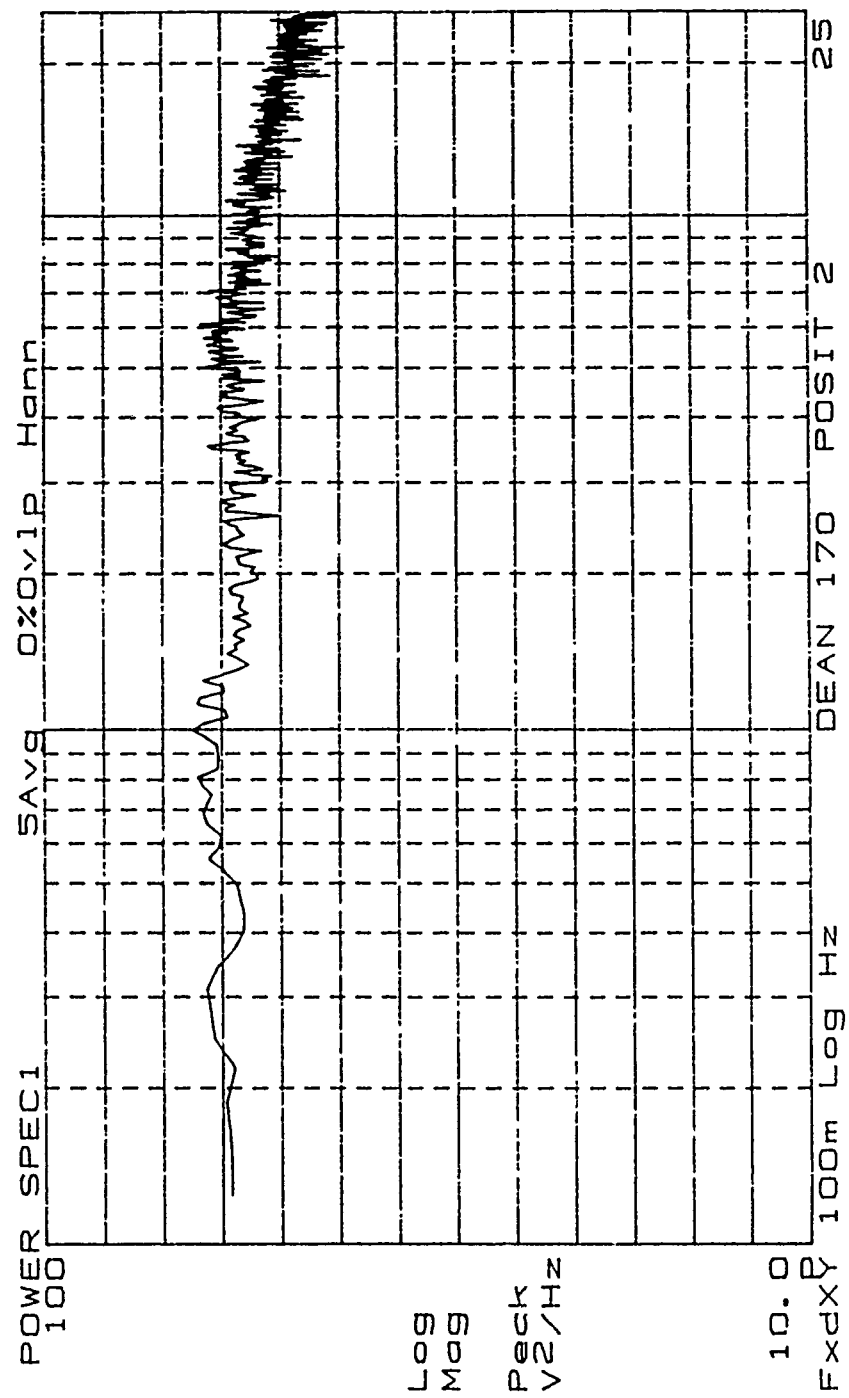


Figure 108. Low Frequency Power Spectrum, De=170, Position 2

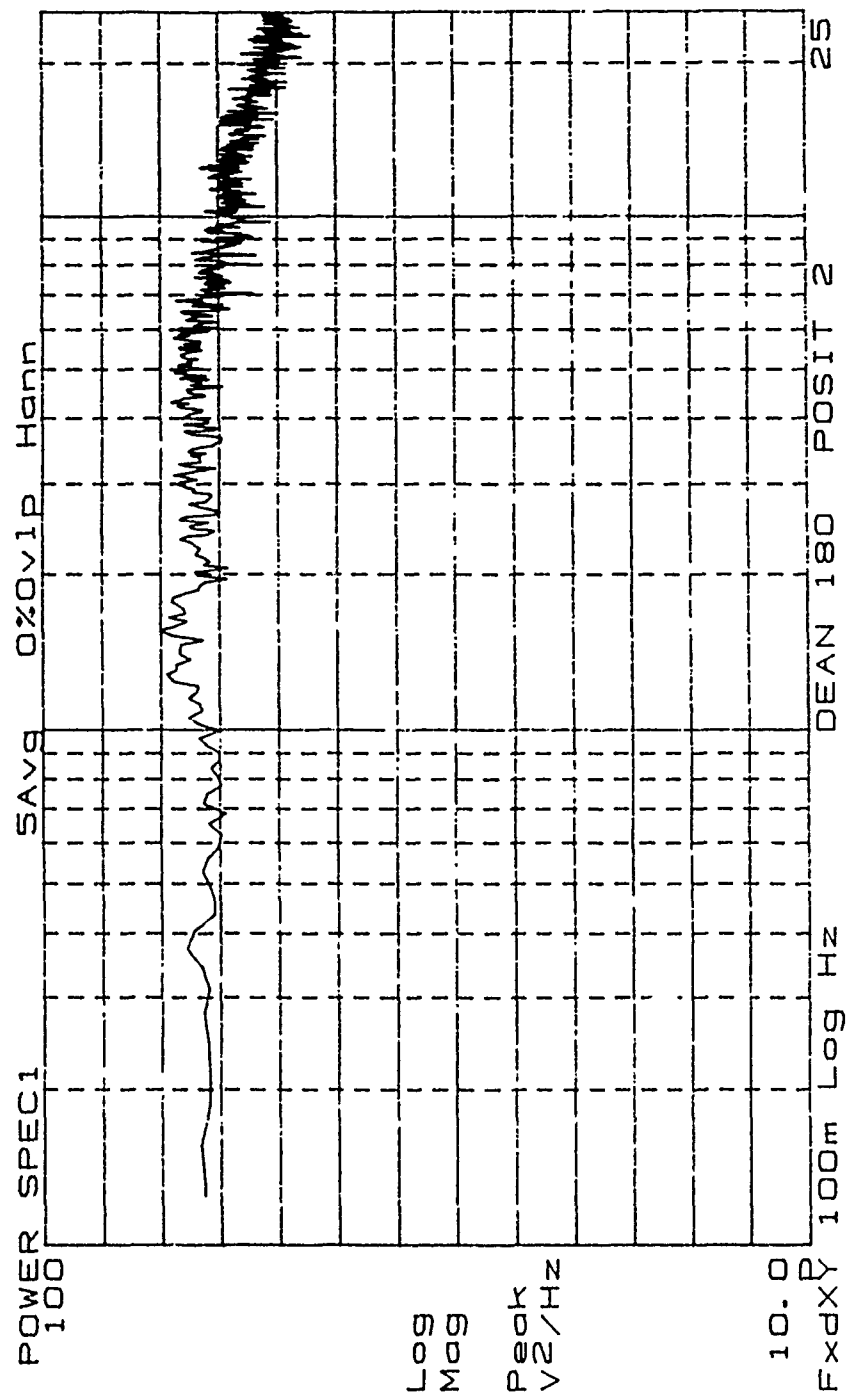


Figure 109. Low Frequency Power Spectrum, De=180, Position 2

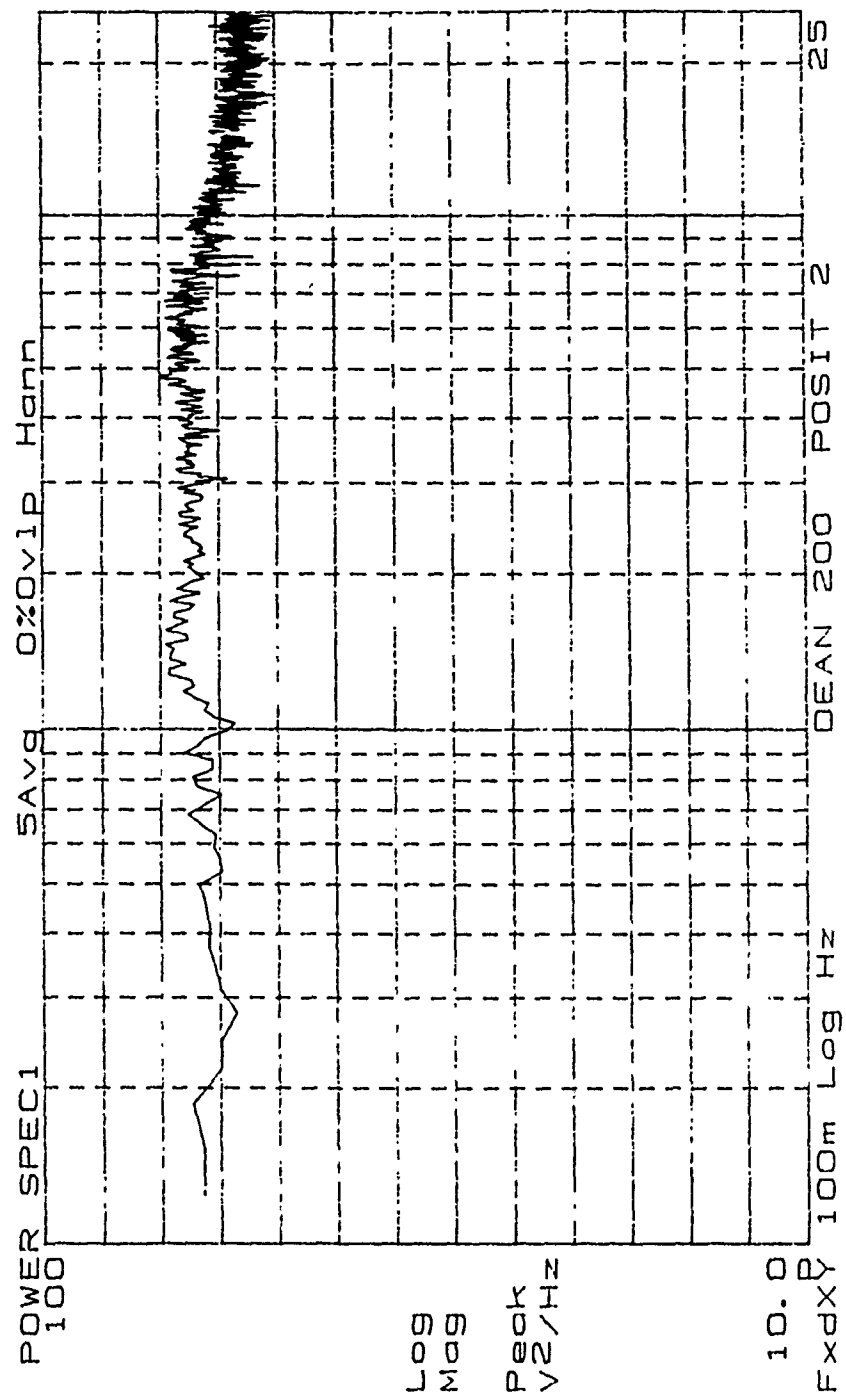


Figure 110. Low Frequency Power Spectrum, De=200, Position 2

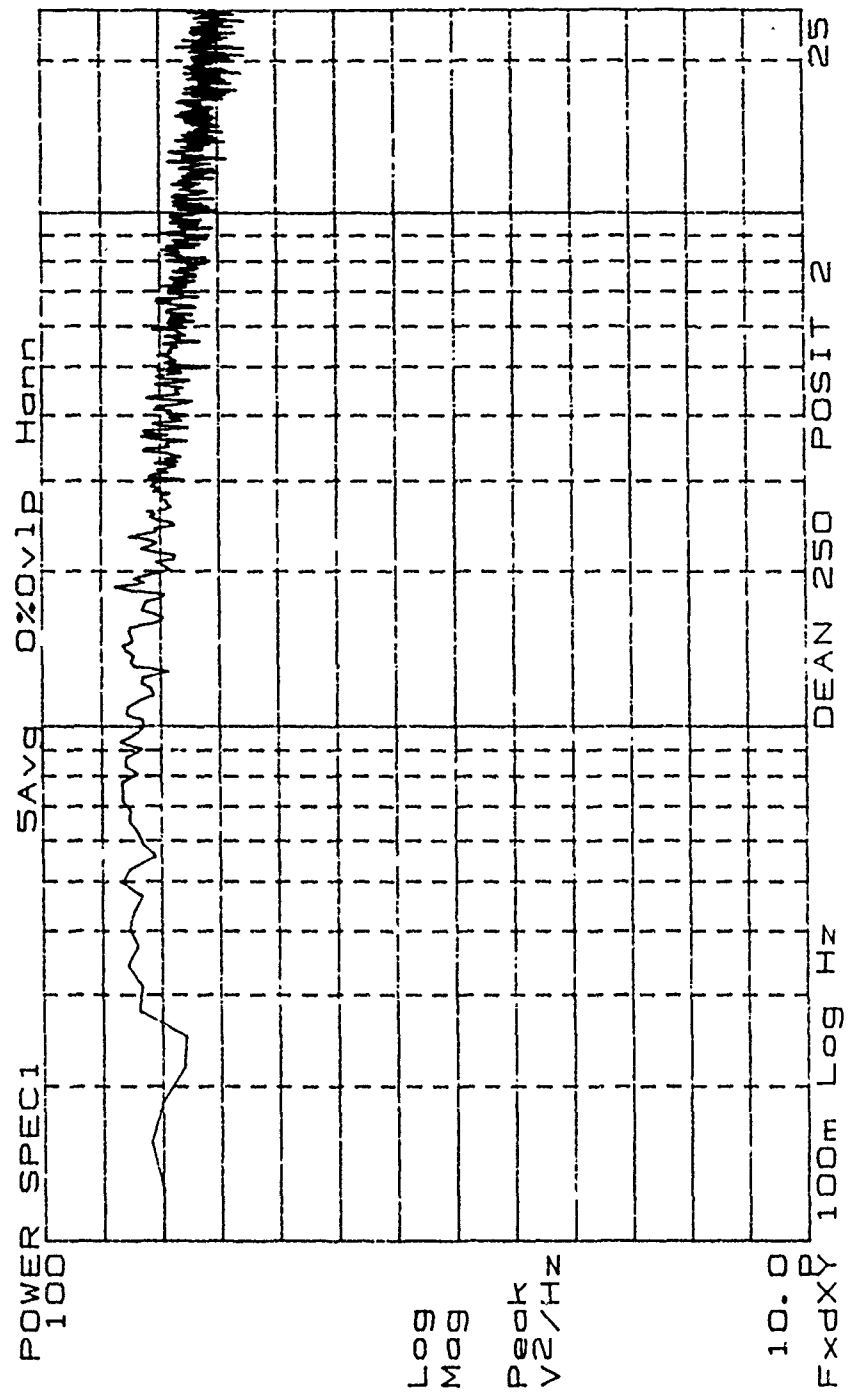


Figure 111. Low Frequency Power Spectrum, De=250, Position 2

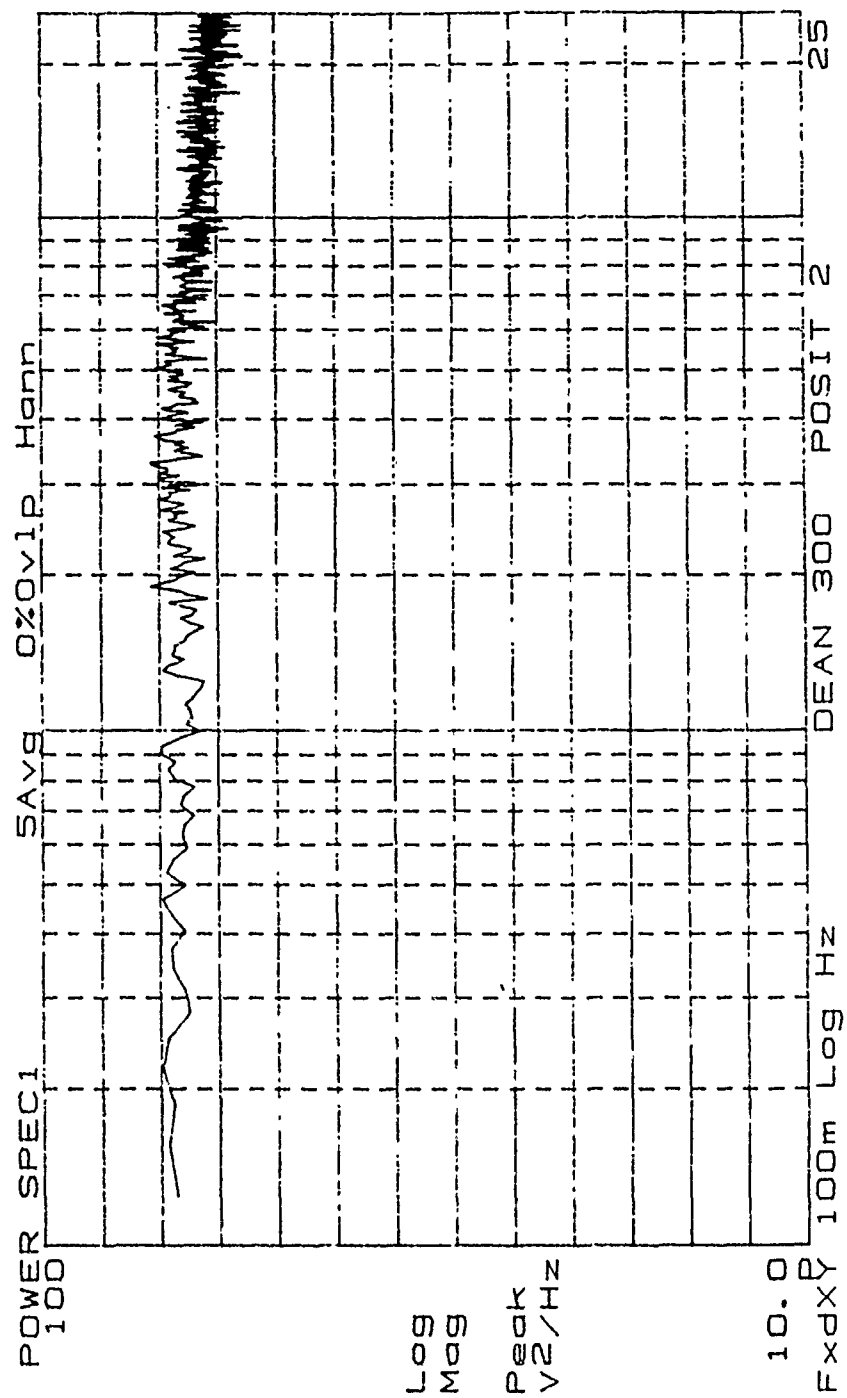


Figure 112. Low Frequency Power Spectrum, De=300, Position 2

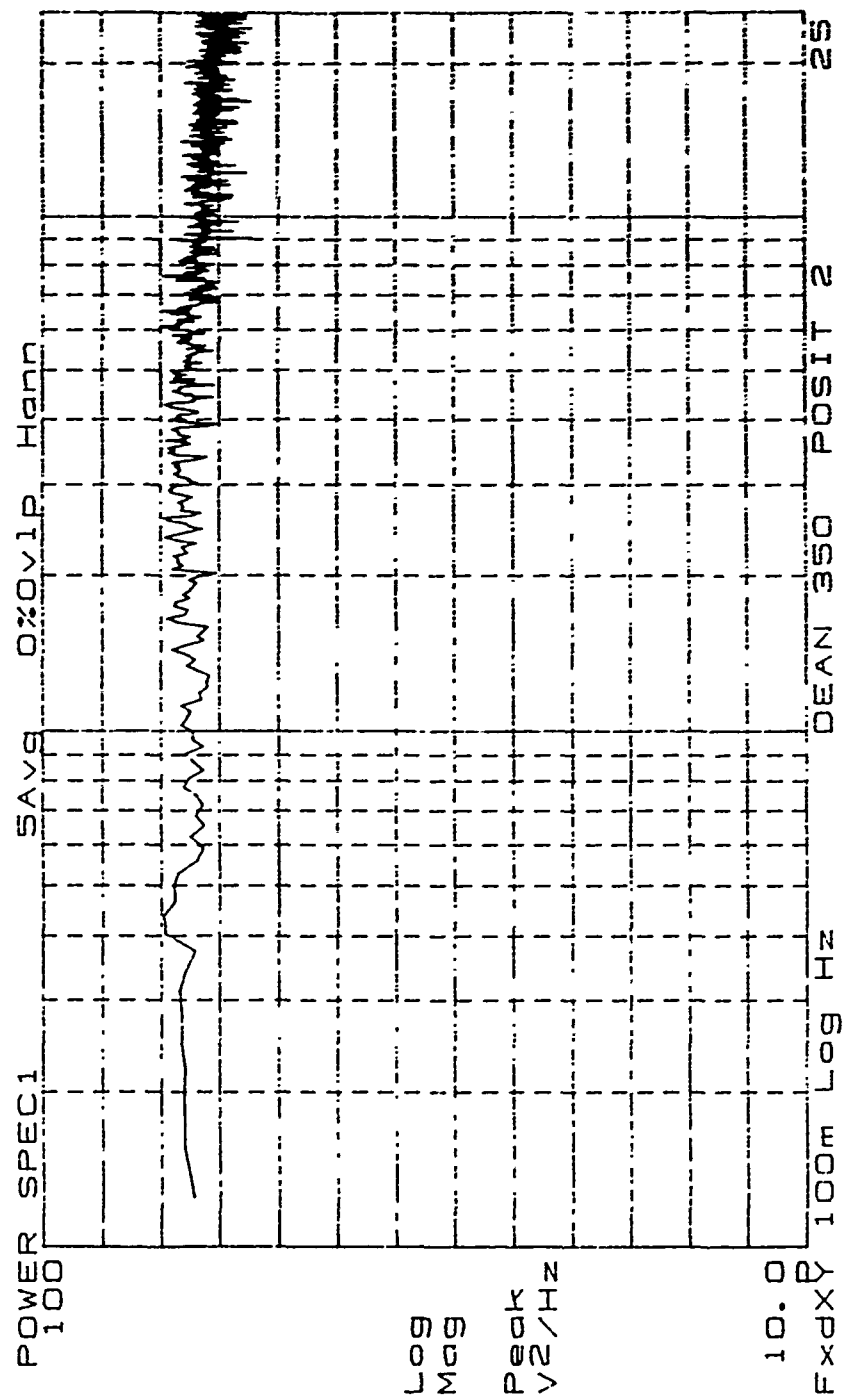


Figure 113. Low Frequency Power Spectrum, De=350, Position 2

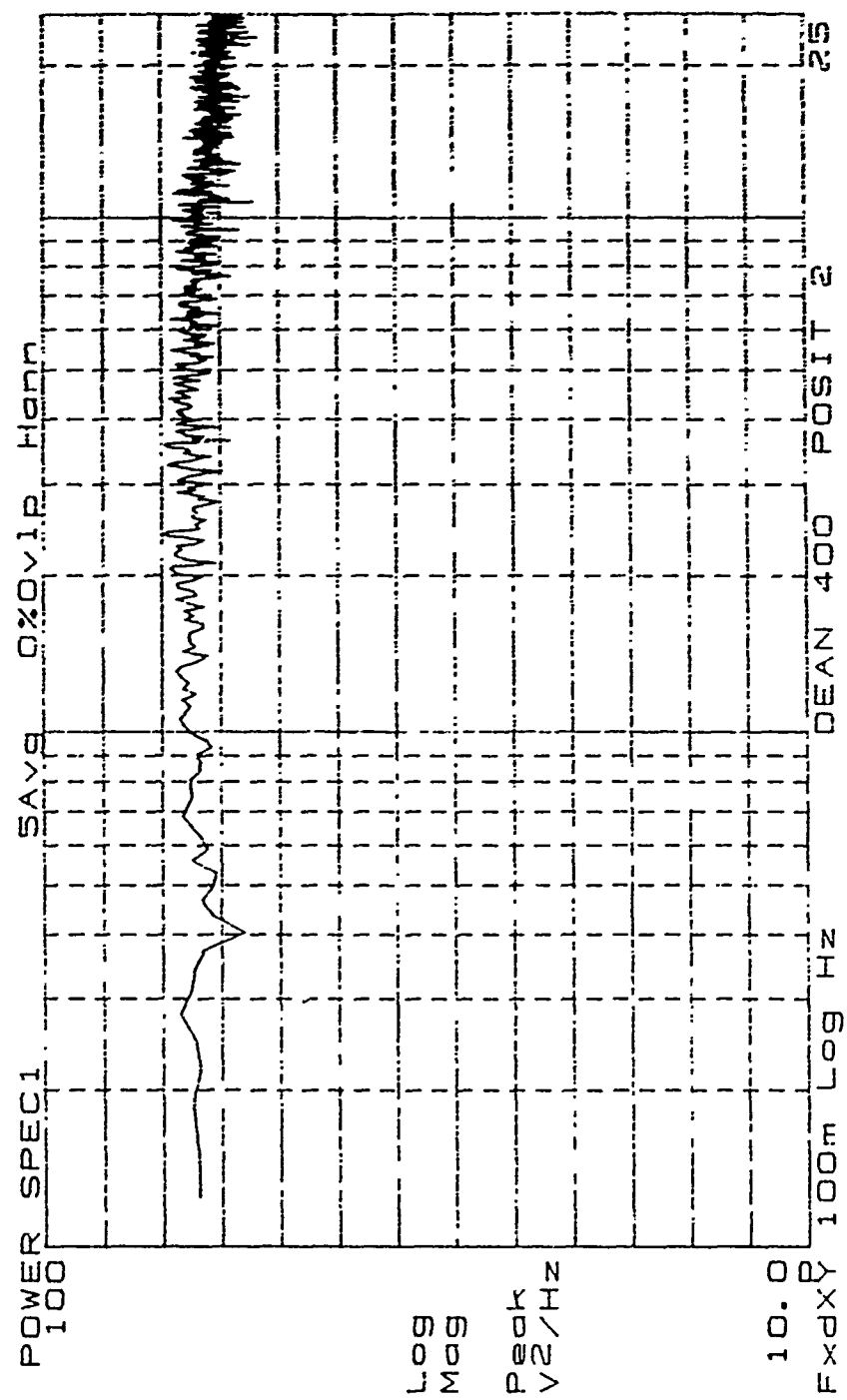


Figure 114. Low Frequency Power Spectrum, De=400, Position 2

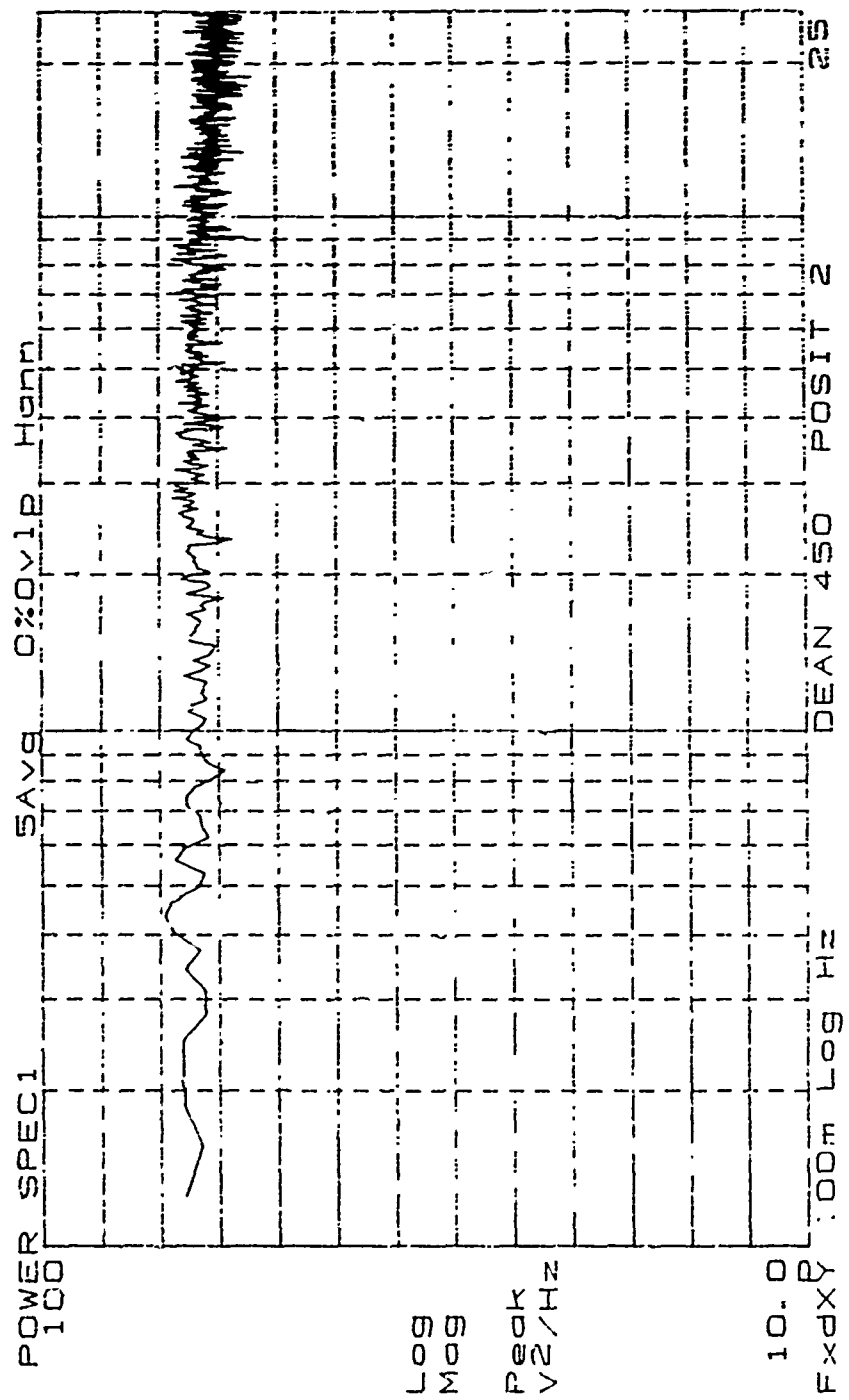


Figure 115. Low Frequency Power Spectrum, De=450, Position 2

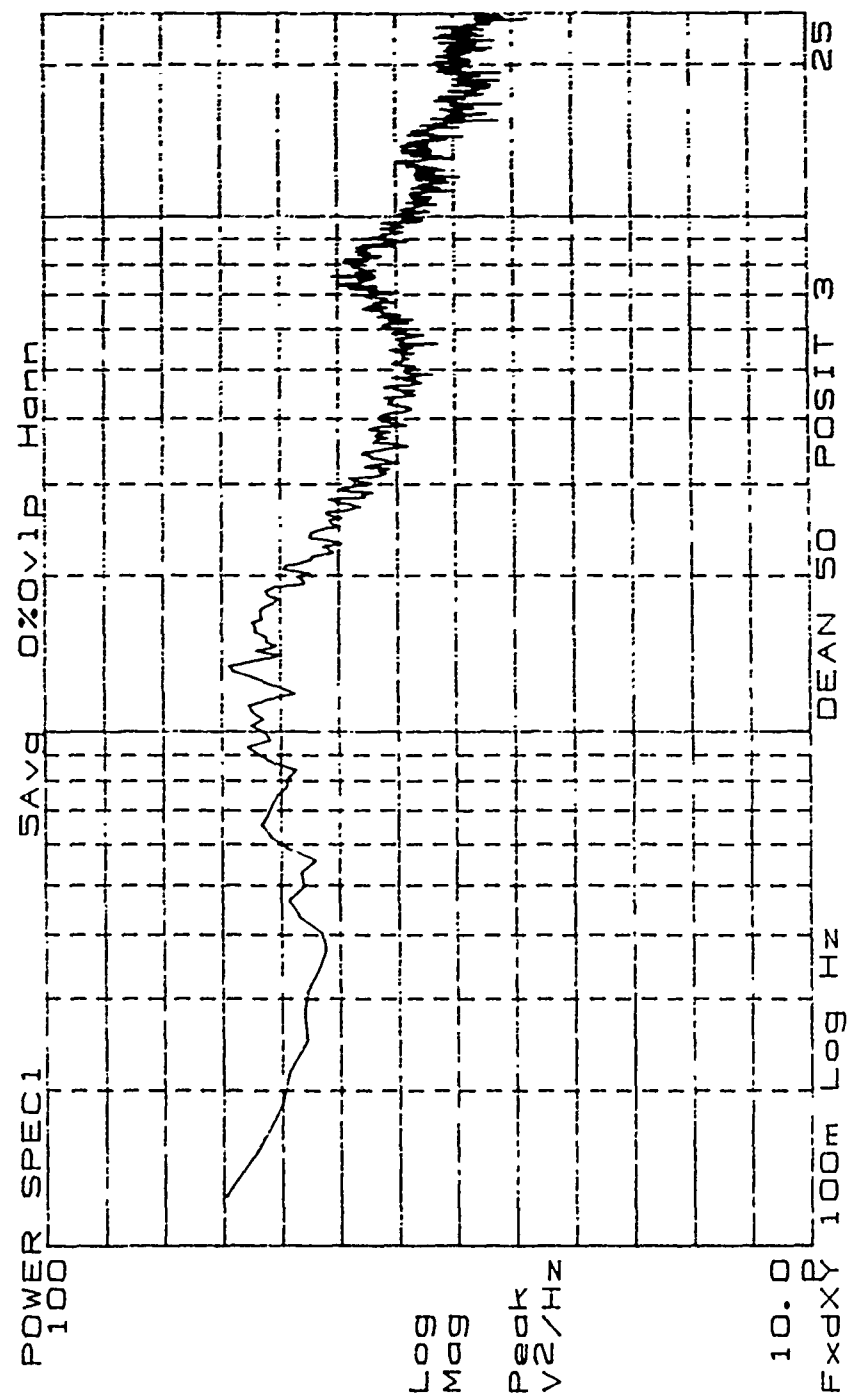


Figure 116. Low Frequency Power Spectrum, De=50, Position 3

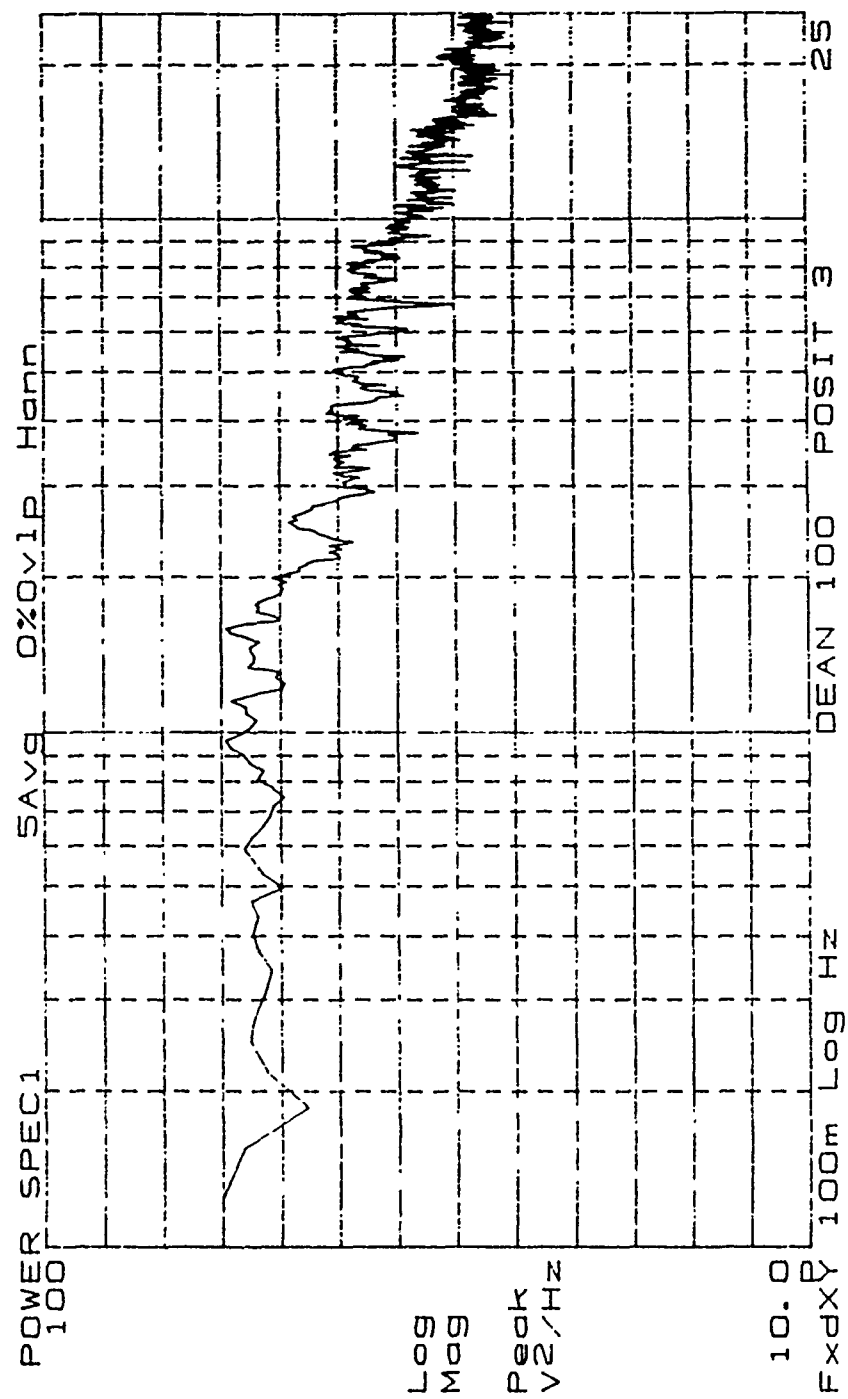


Figure 117. Low Frequency Power Spectrum, De=100, Position 3

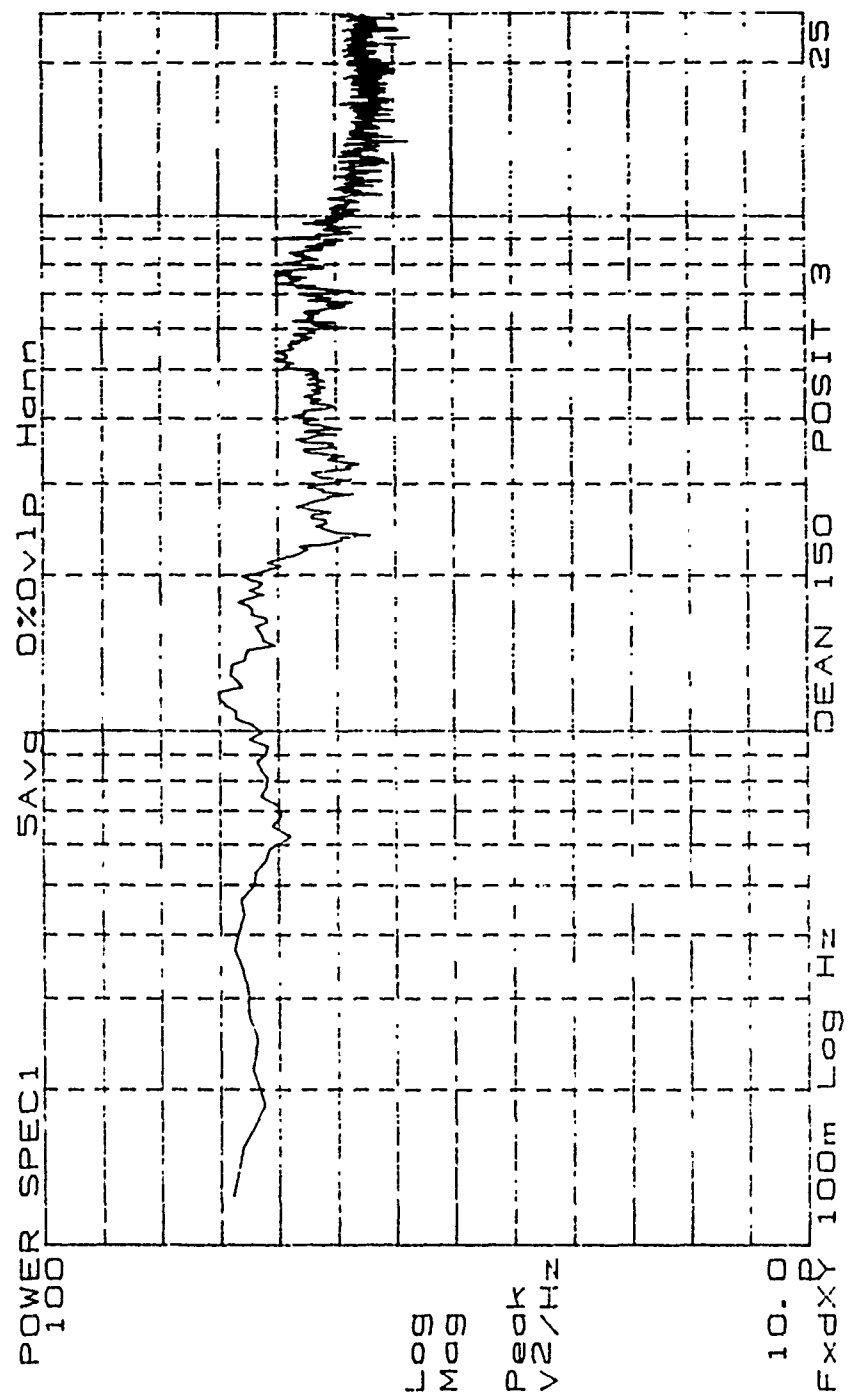


Figure 118. Low Frequency Power Spectrum, De=150, Position 3

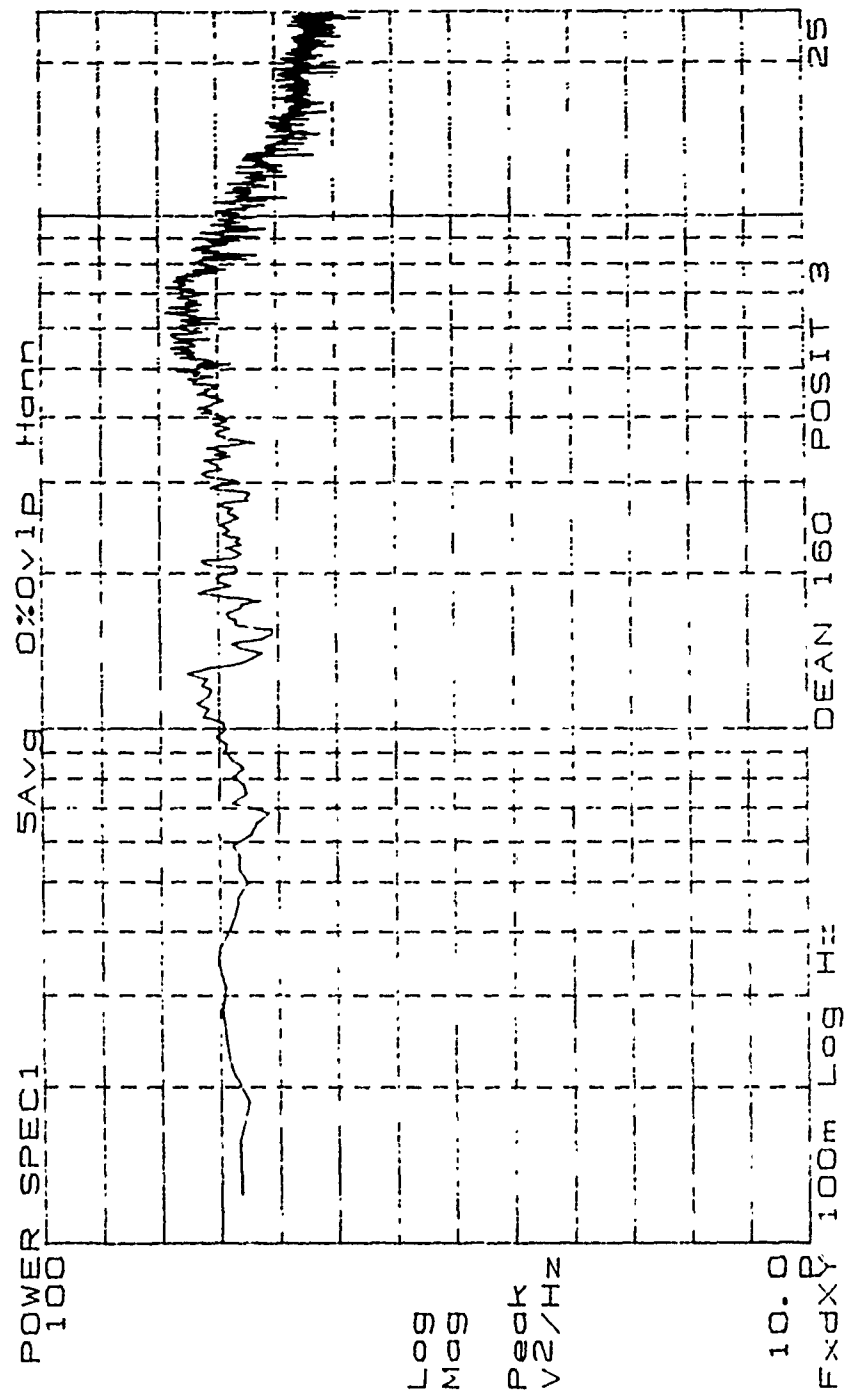


Figure 119. Low Frequency Power Spectrum, De=160, Position 3

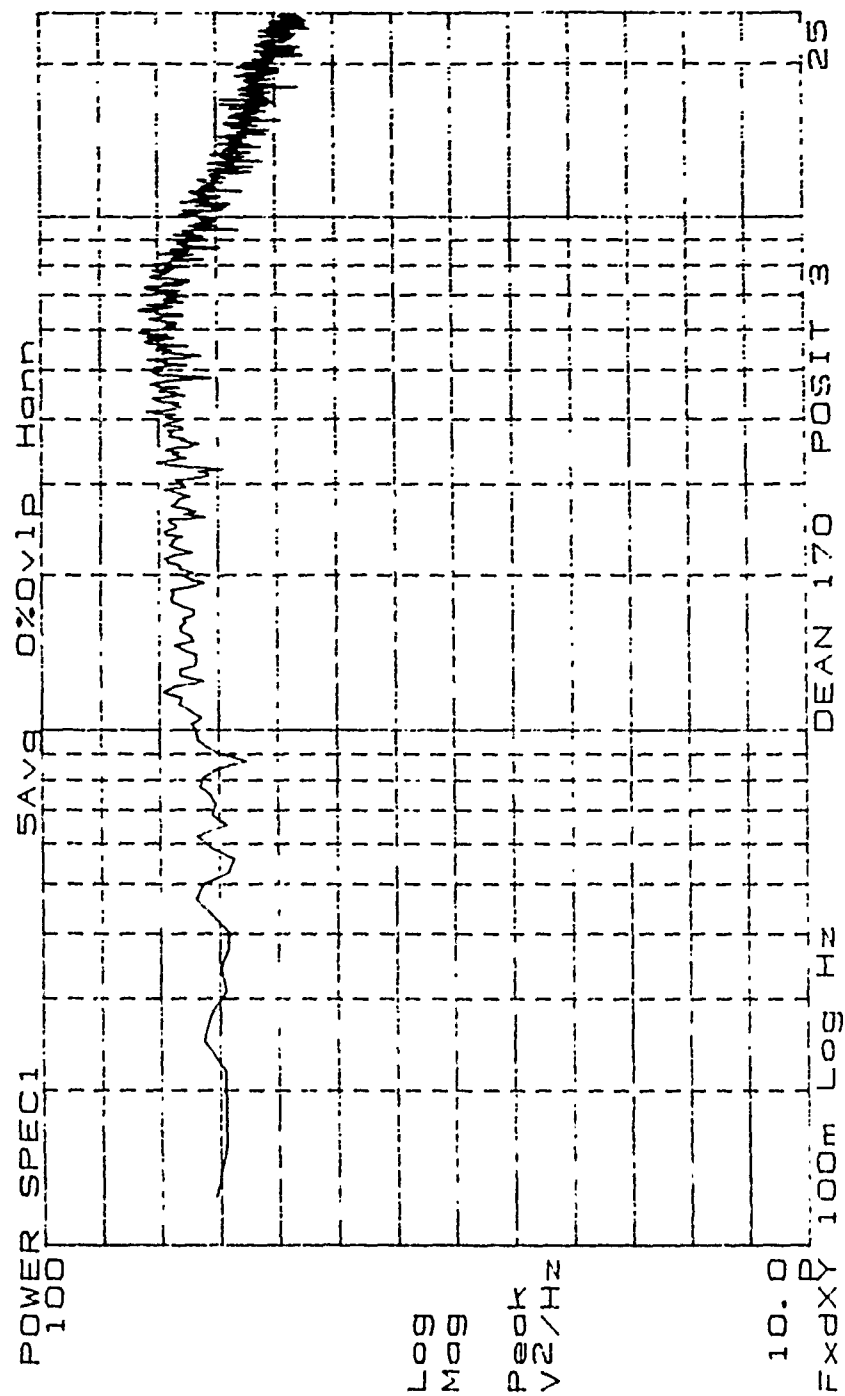


Figure 120. Low Frequency Power Spectrum, De=170, Position 3

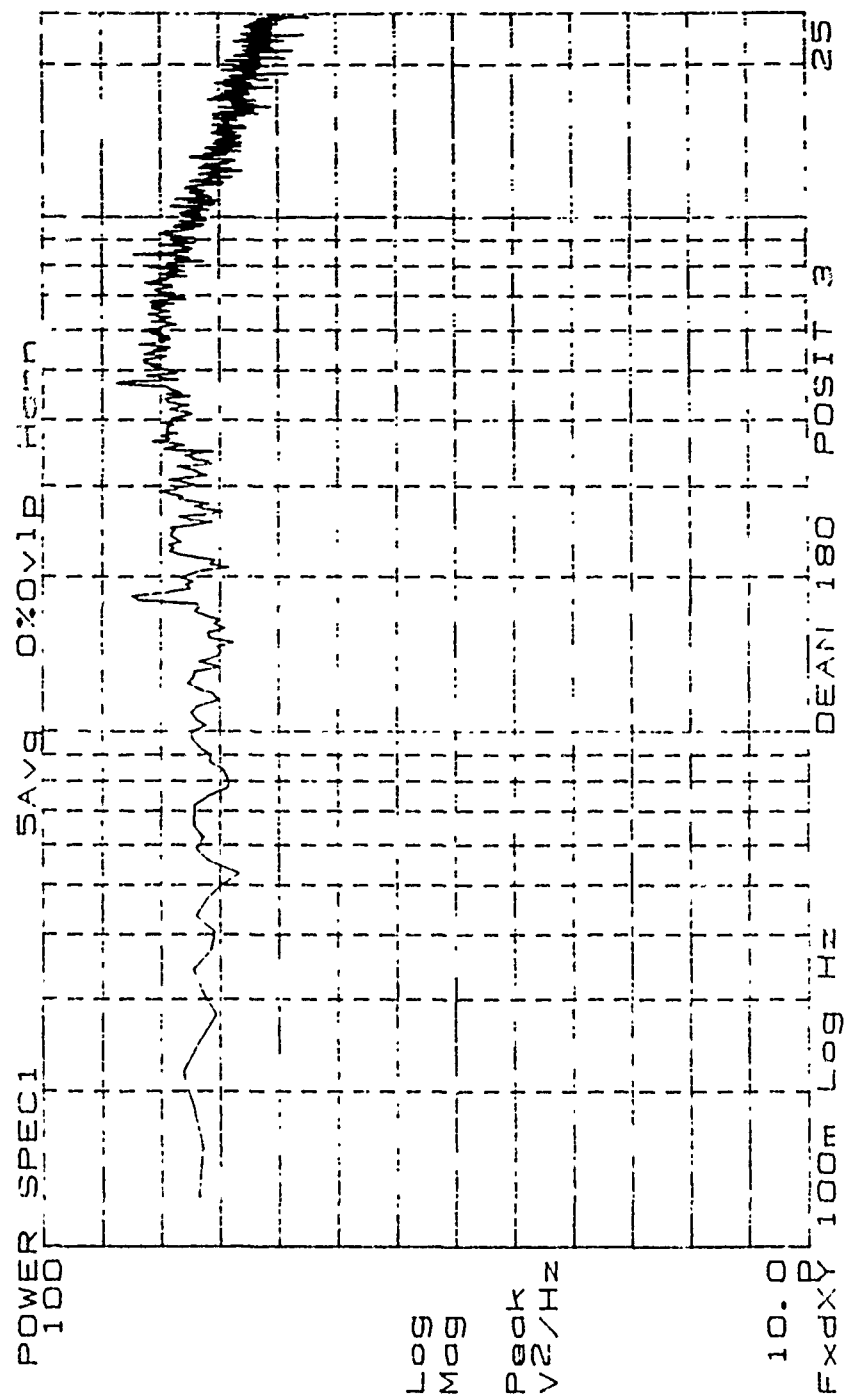


Figure 121. Low Frequency Power Spectrum, De=180, Position 3

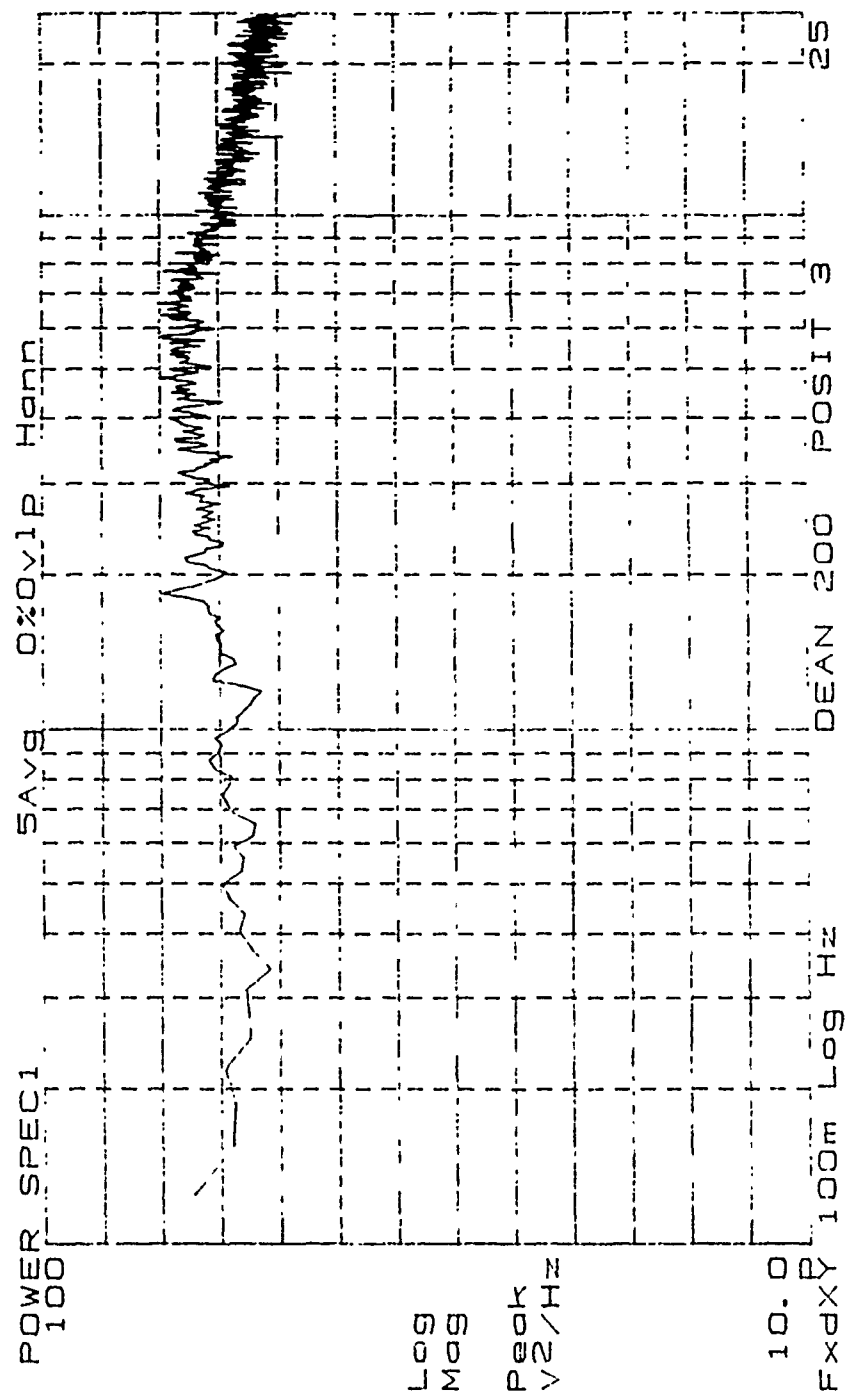


Figure 122. Low Frequency Power Spectrum, De=200, Position 3

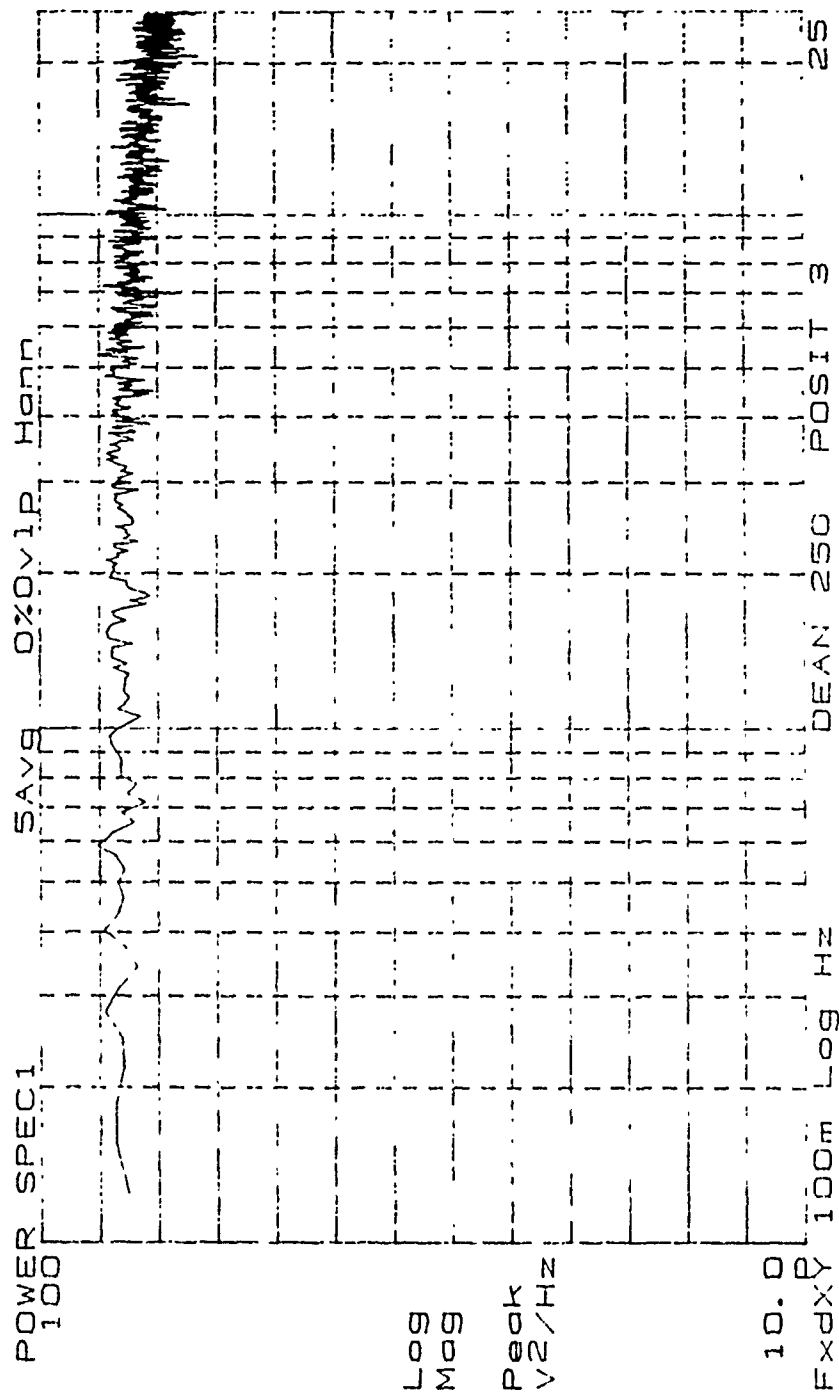


Figure 123. Low Frequency Power Spectrum, De=250, Position 3

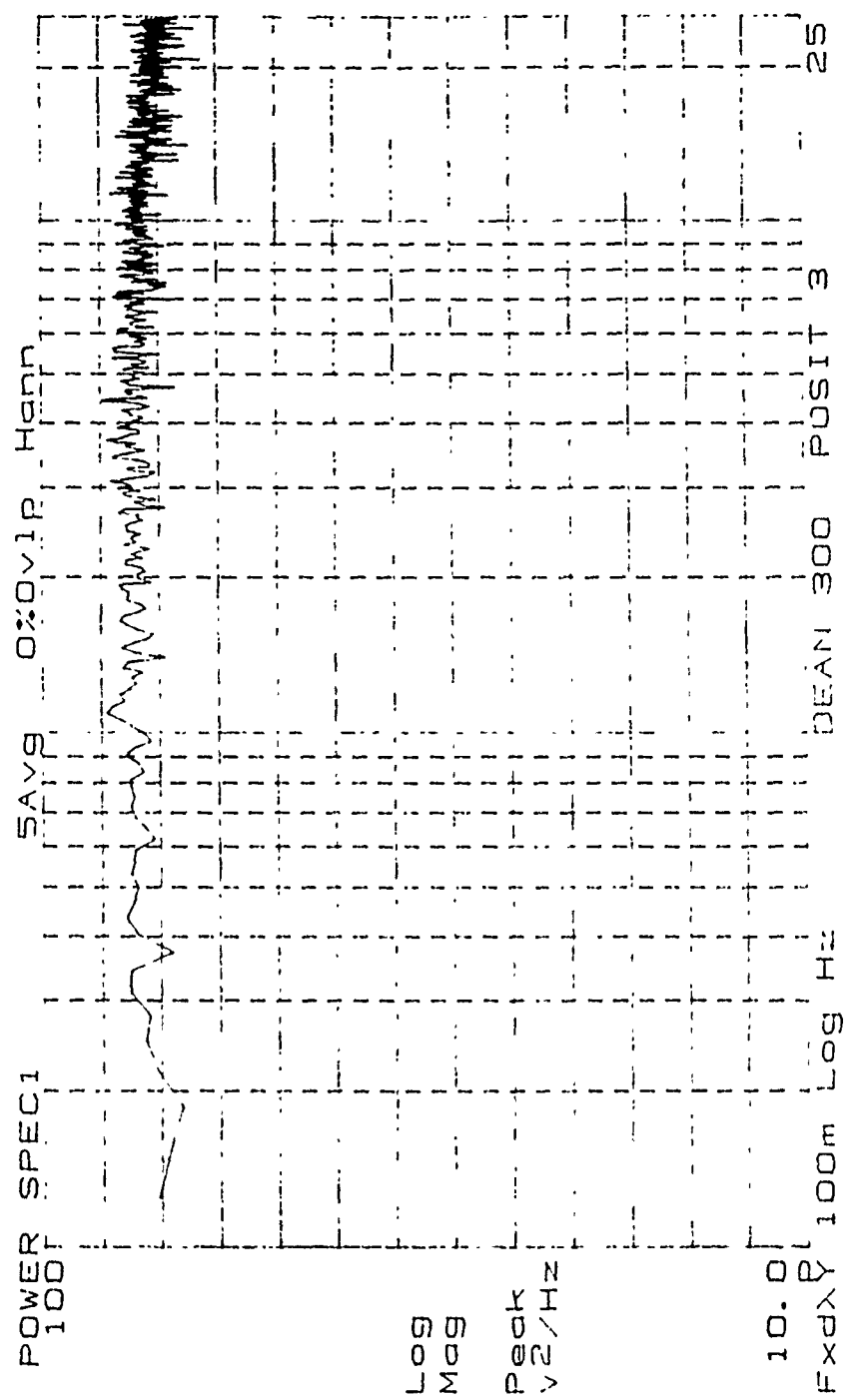


Figure 124. Low Frequency Power Spectrum, De=300, Position 3



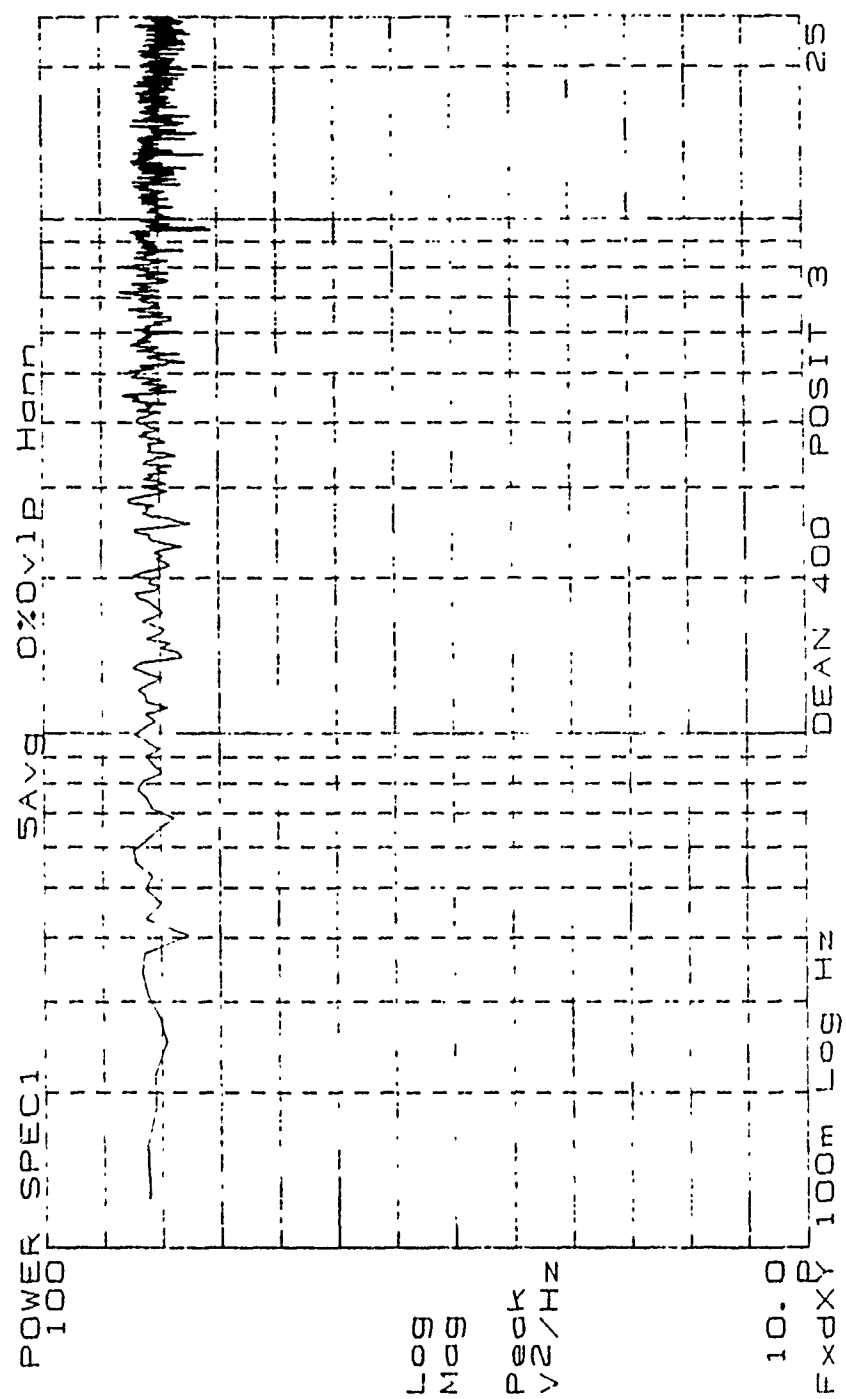


Figure 126. Low Frequency Power Spectrum, De=400, Position 3

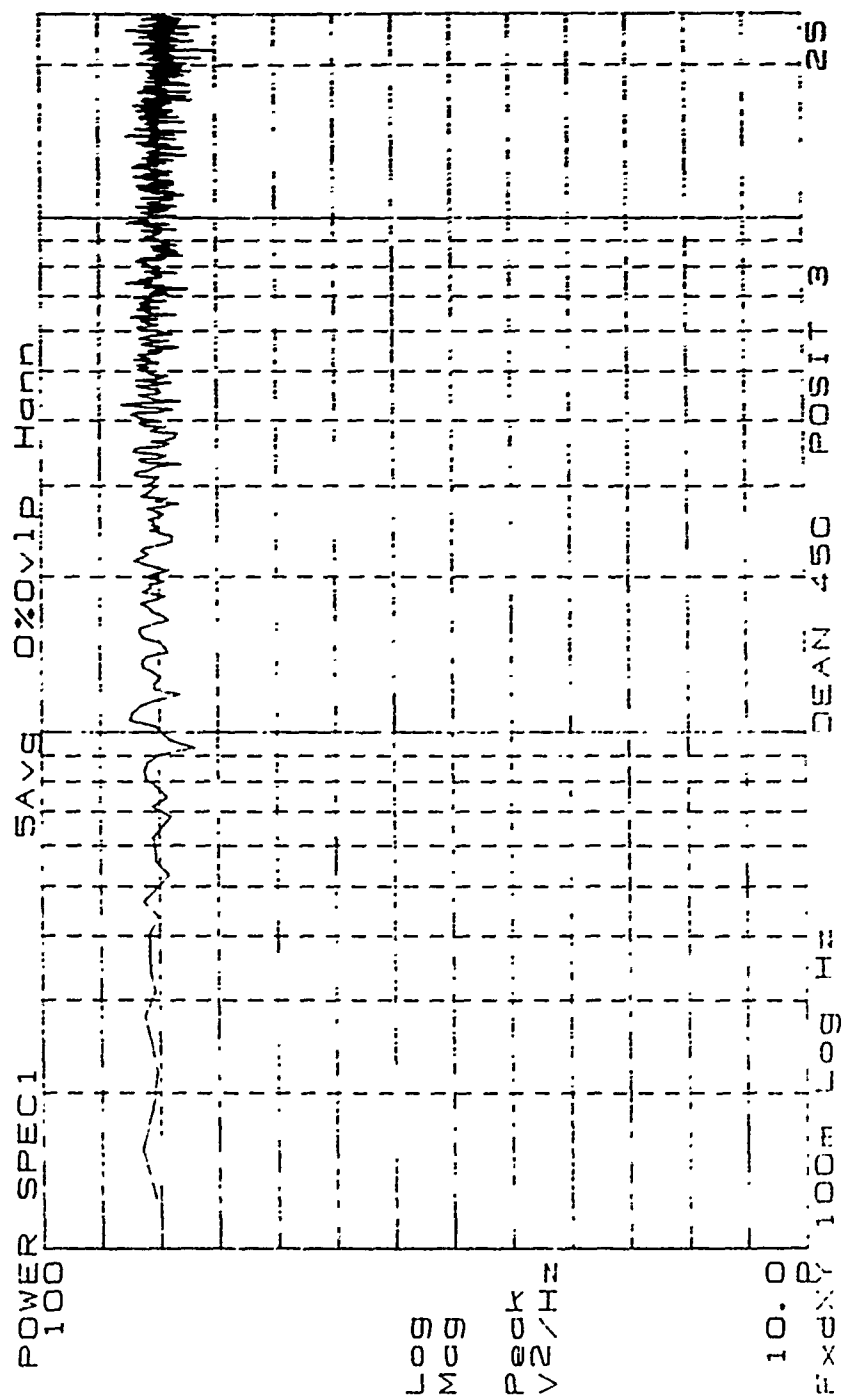


Figure 127. Low Frequency Power Spectrum, De=450, Position 3

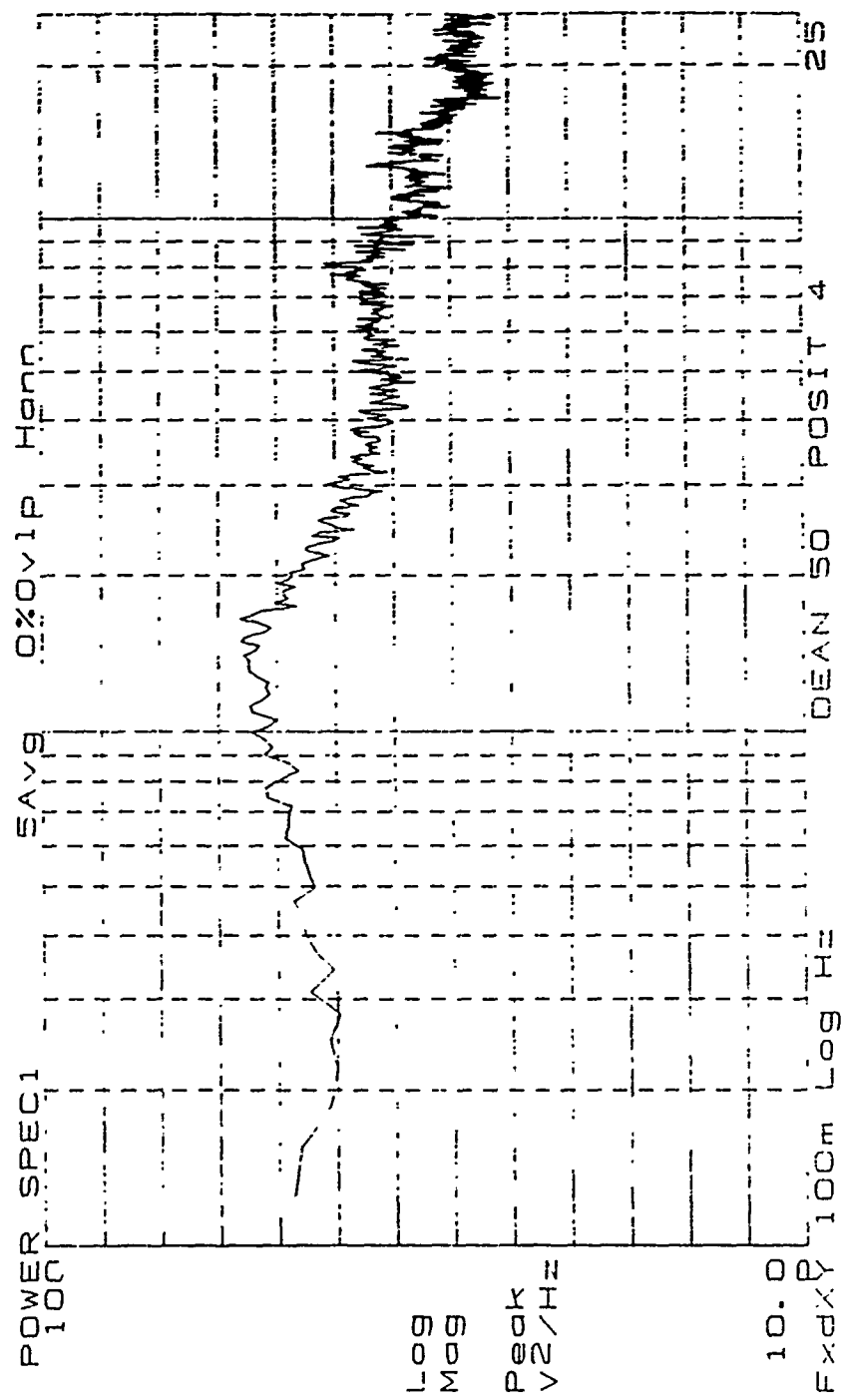


Figure 128. Low Frequency Power Spectrum, De=50, Position 4

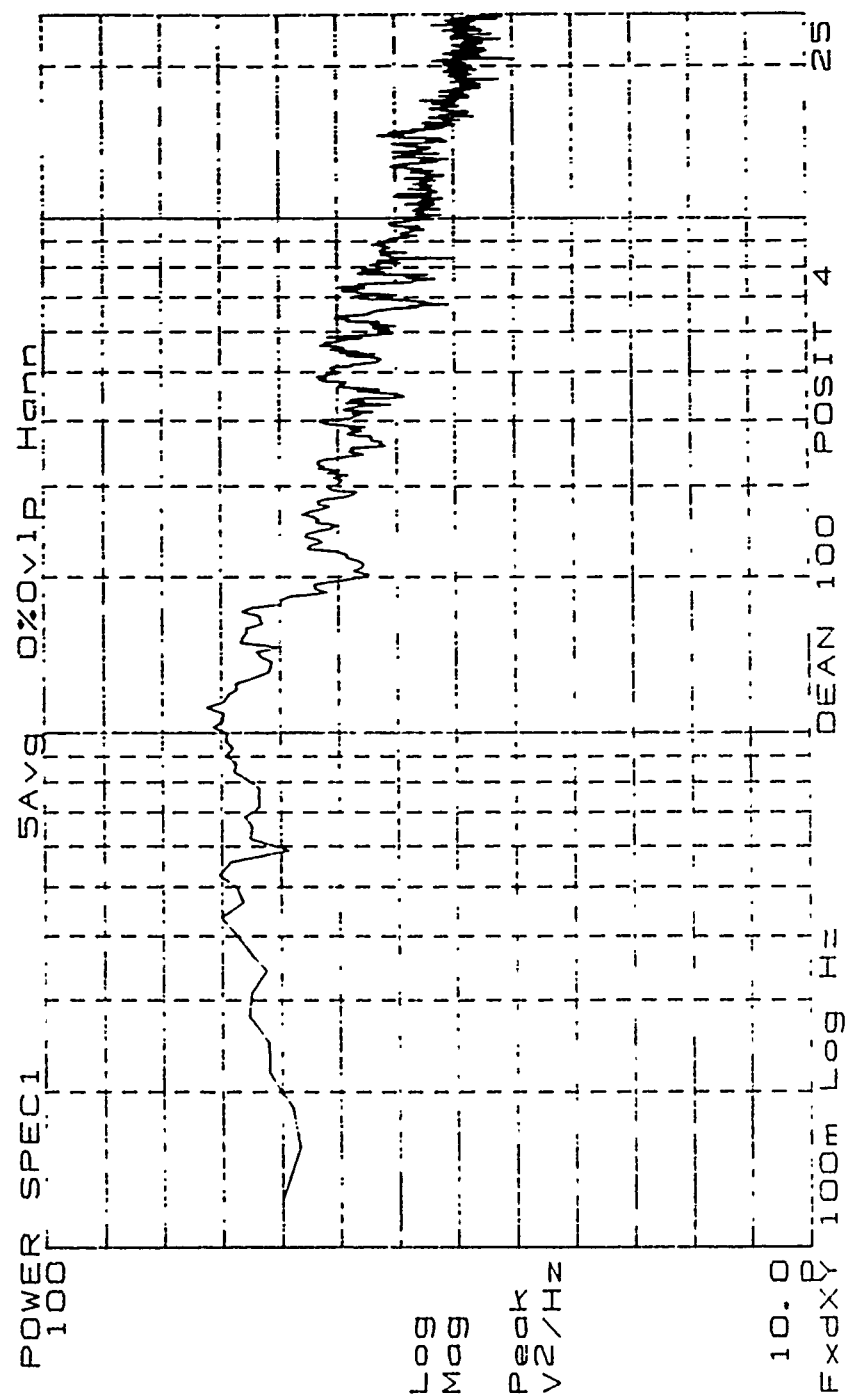


Figure 129. Low Frequency Power Spectrum, De=100, Position 4

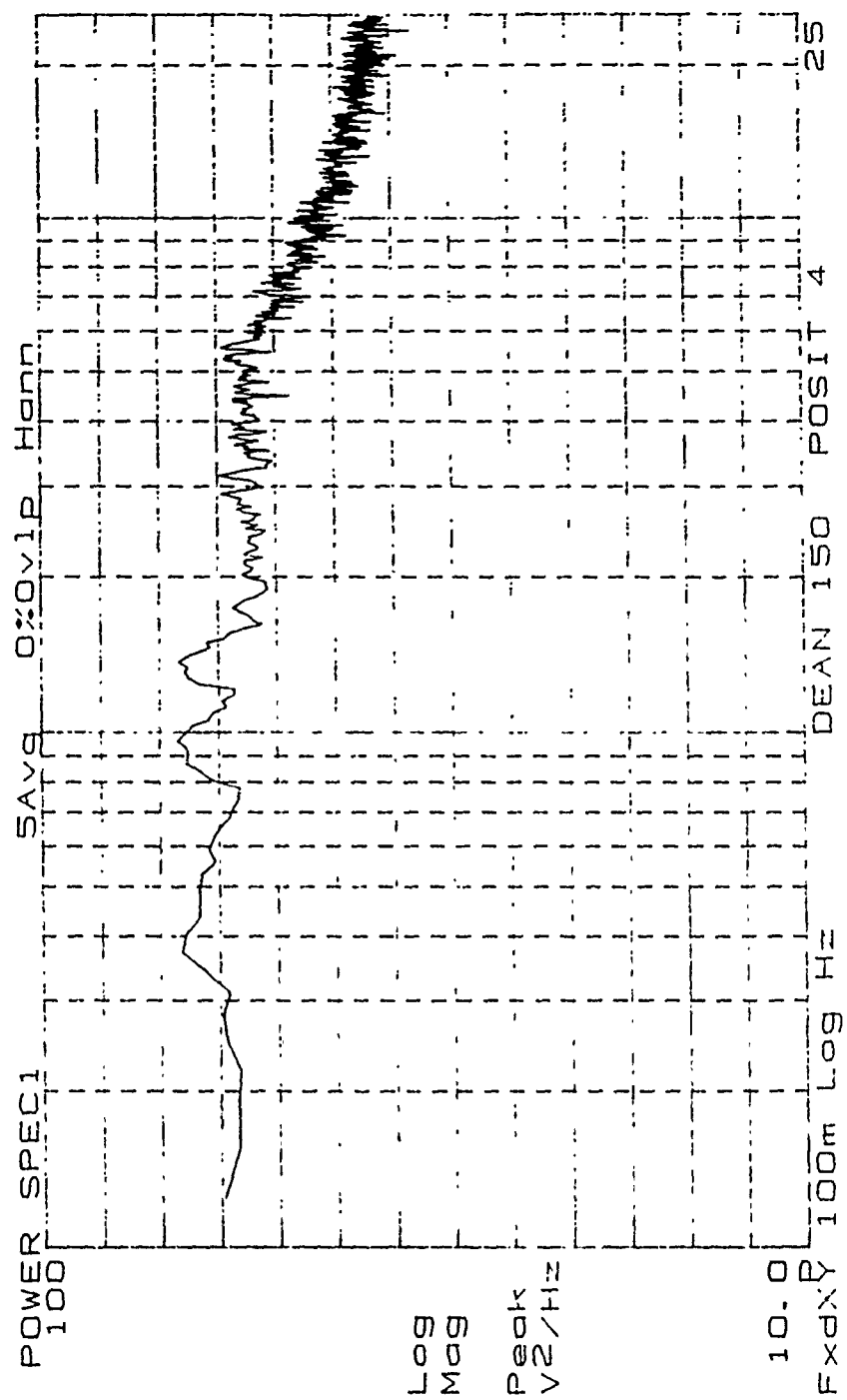


Figure 130. Low Frequency Power Spectrum, De=150, Position 4

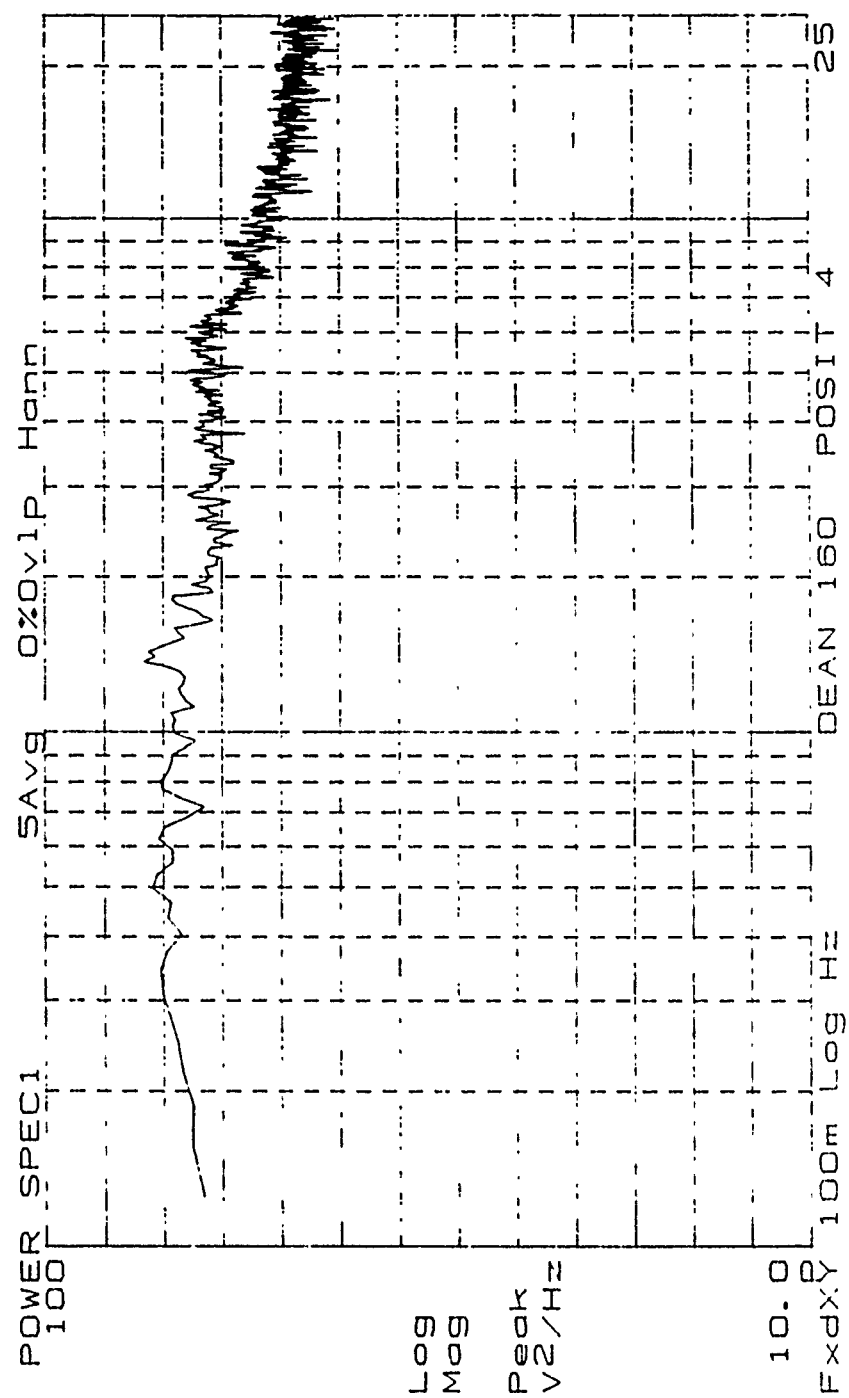


Figure 131. Low Frequency Power Spectrum, De=160, Position 4

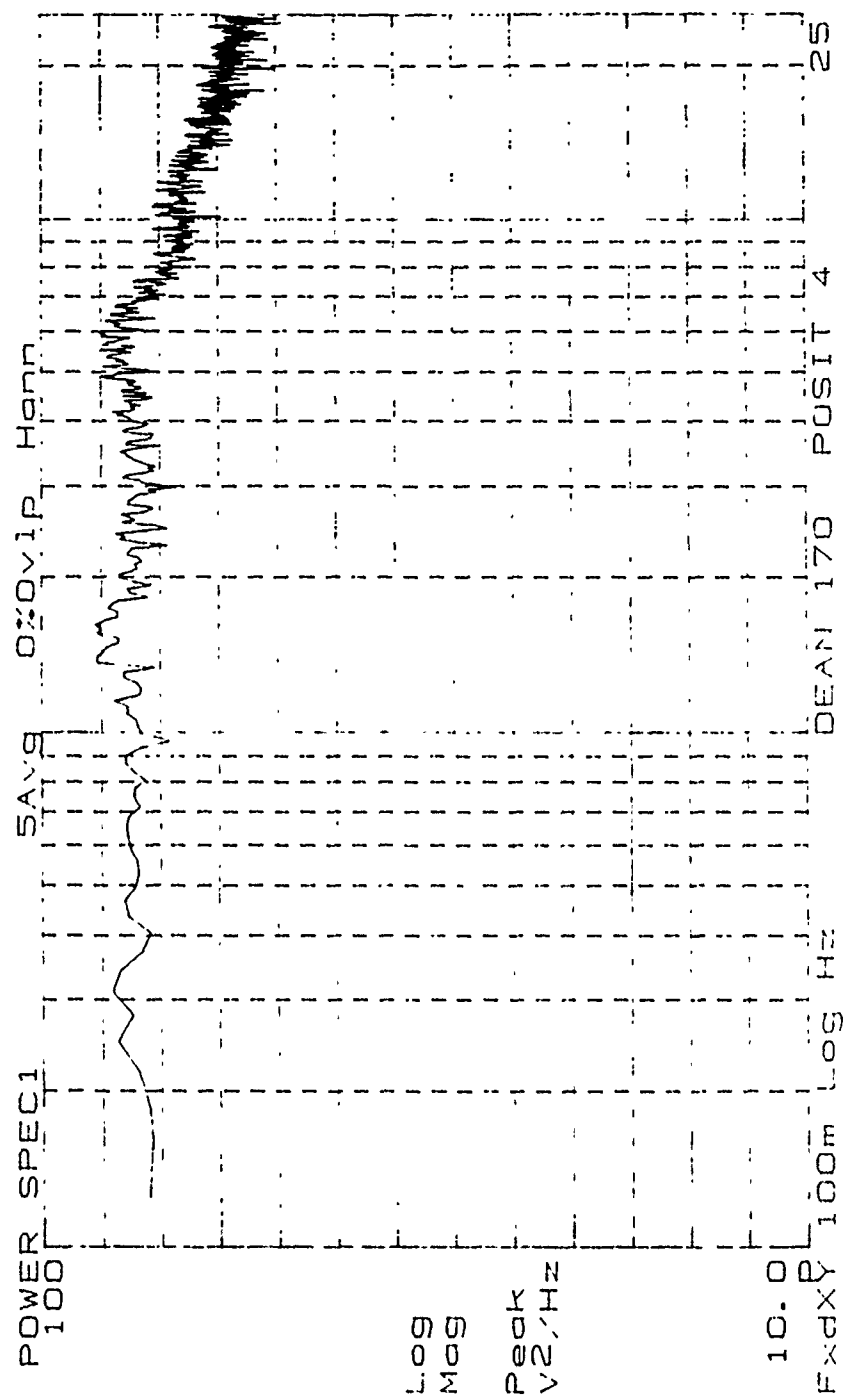


Figure 132. Low Frequency Power Spectrum, De=170, Position 4

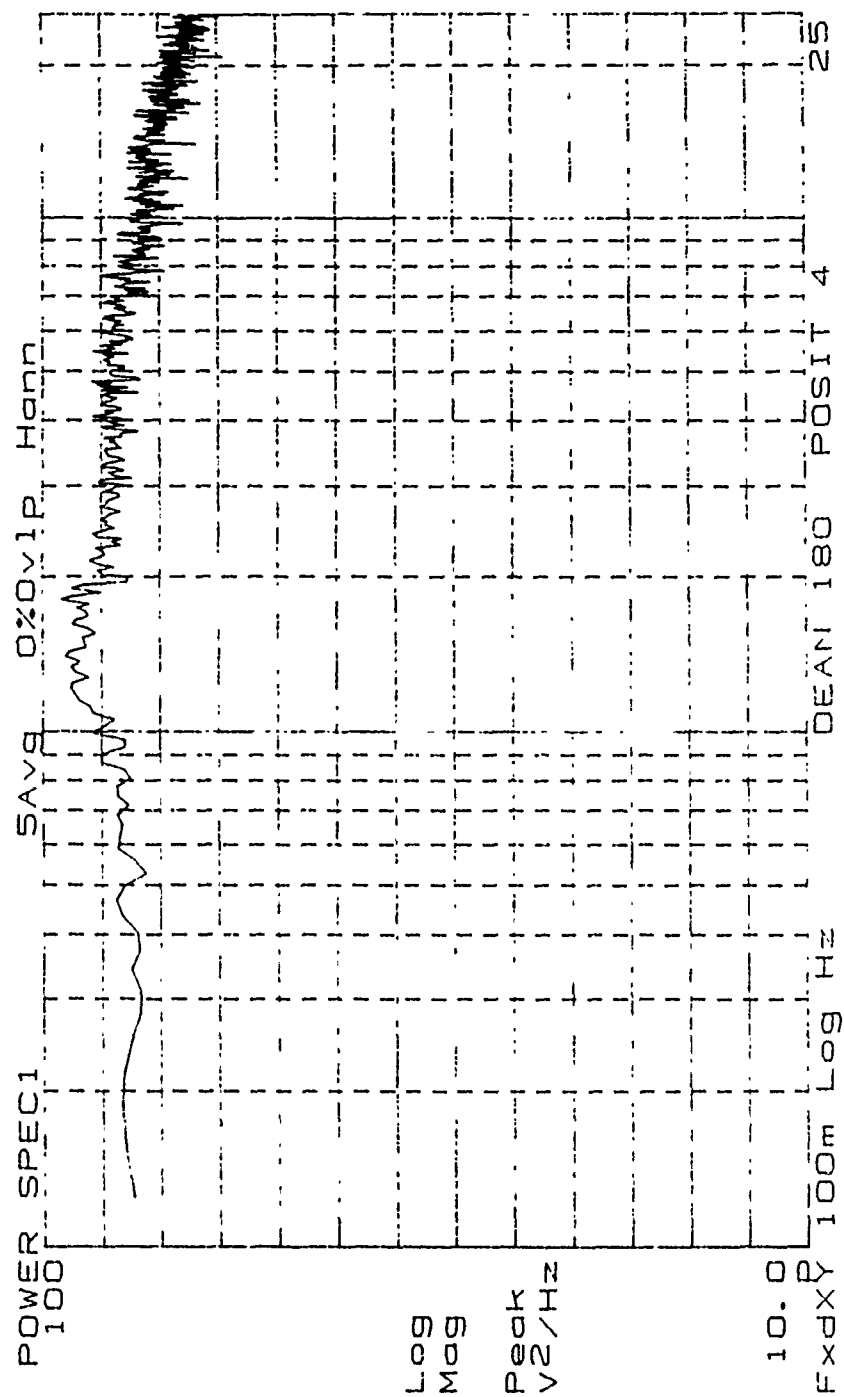


Figure 133. Low Frequency Power Spectrum, De=180, Position 4

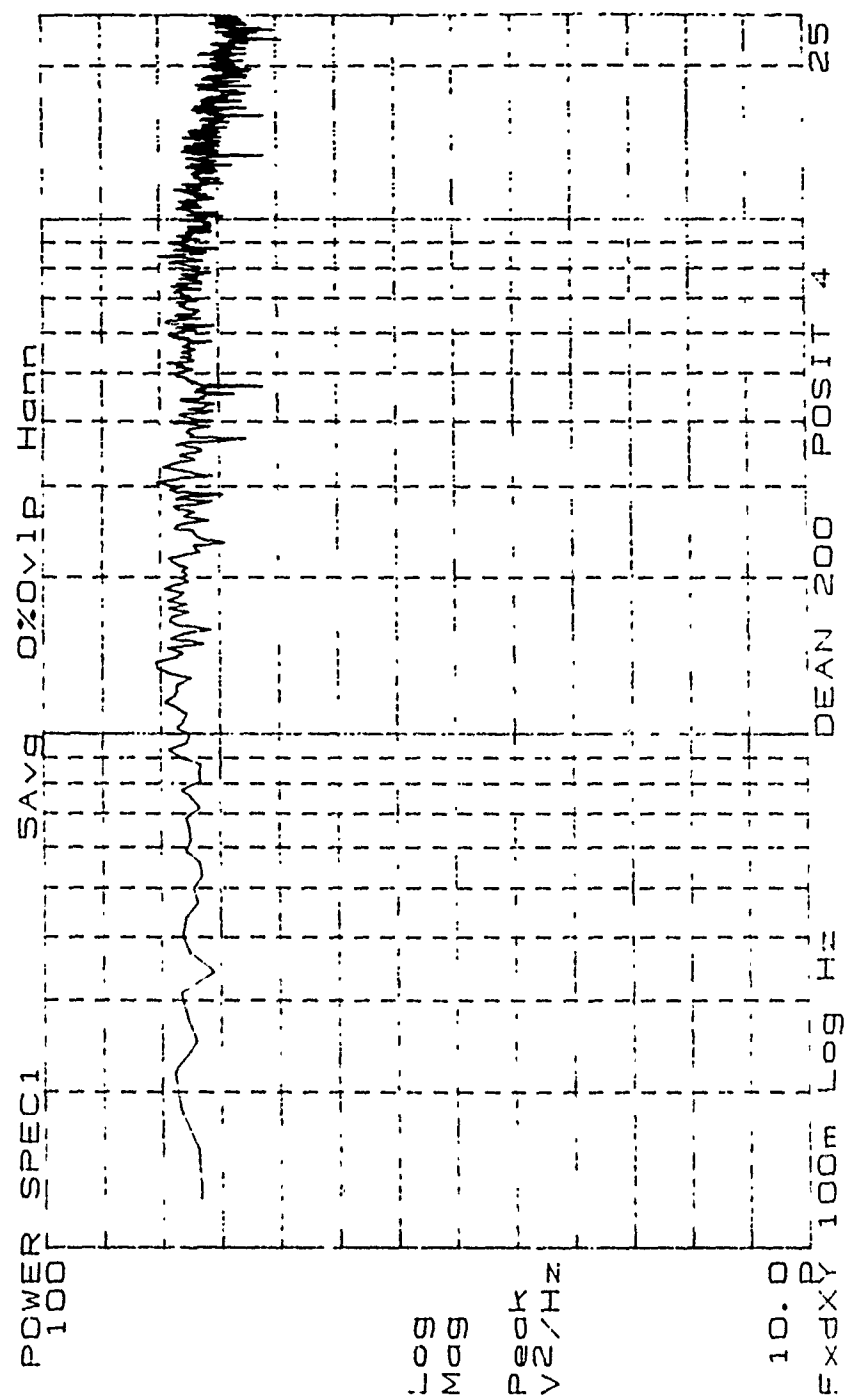


Figure 134. Low Frequency Power Spectrum, De=200, Position 4

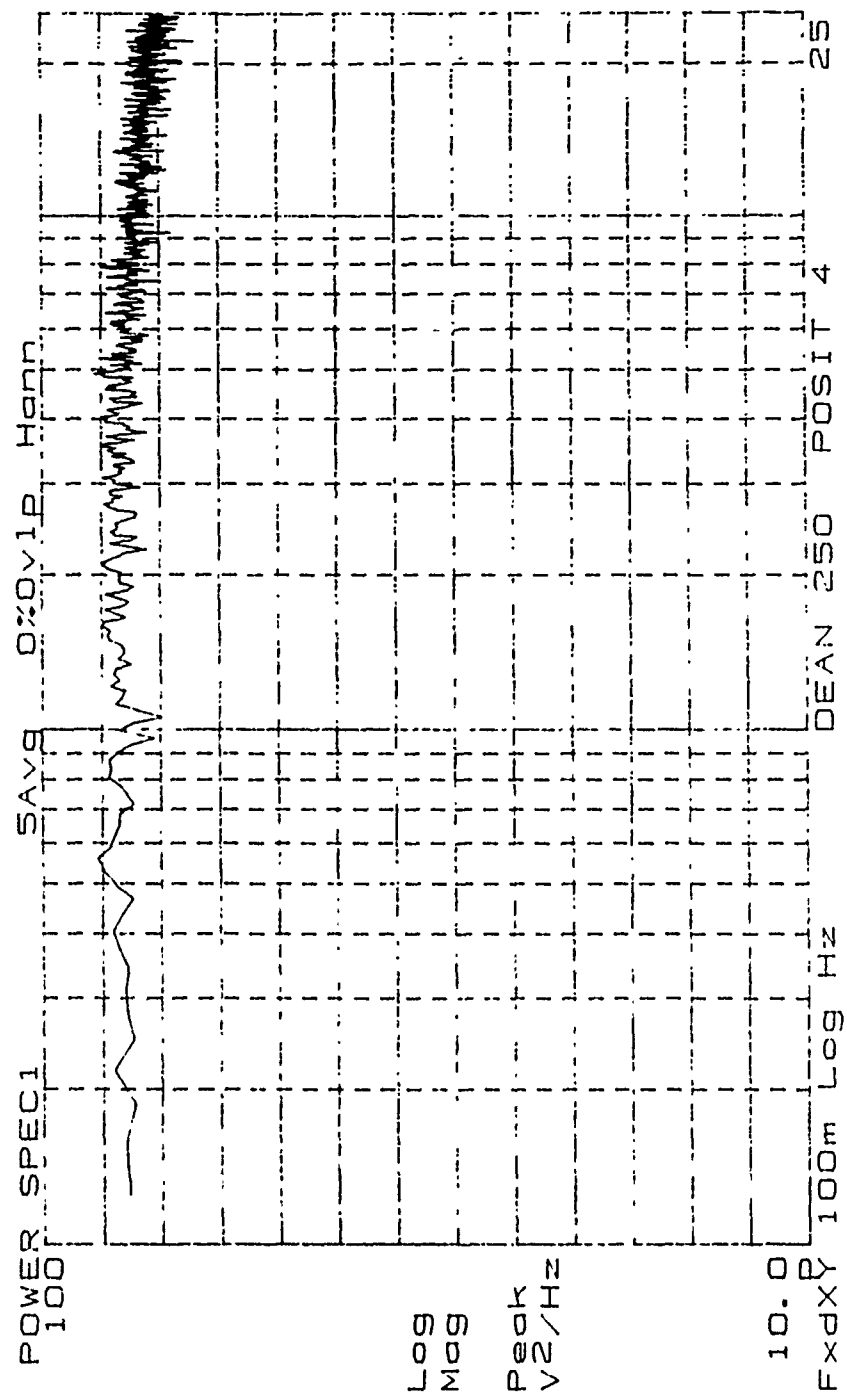


Figure 135. Low Frequency Power Spectrum, De=250, Position 4

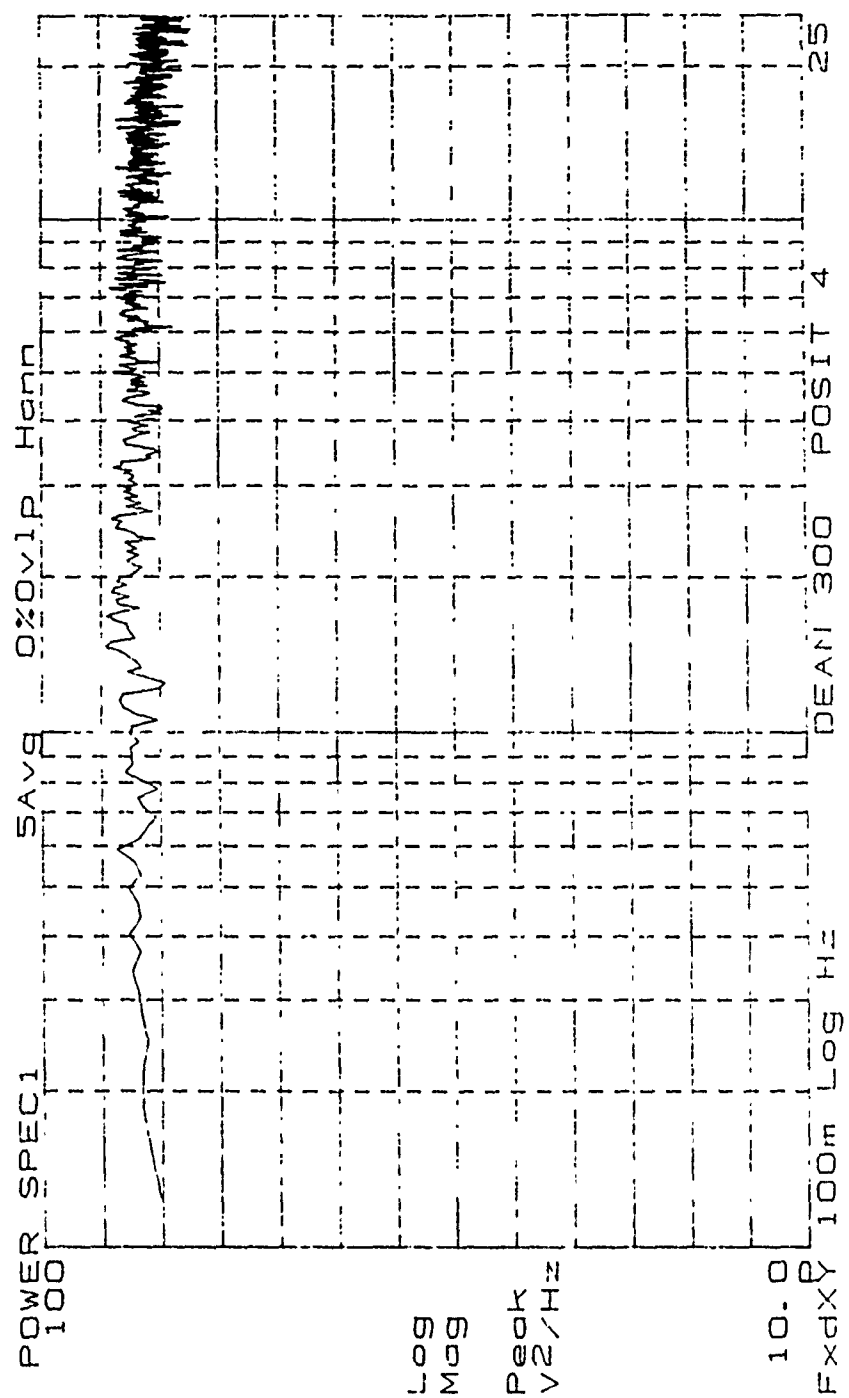


Figure 136. Low Frequency Power Spectrum, De=300, Position 4

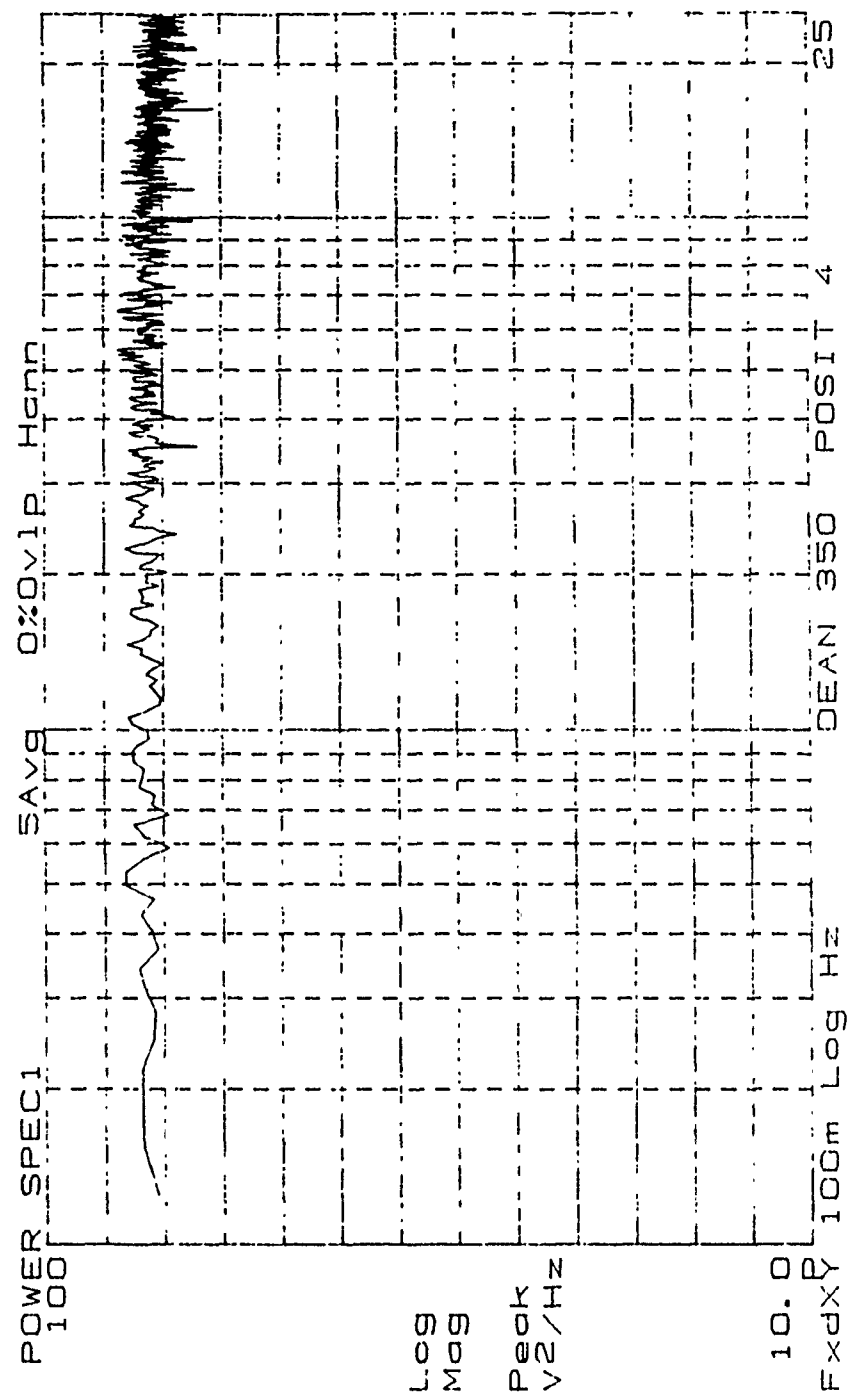


Figure 137. Low Frequency Power Spectrum, De=350, Position 4

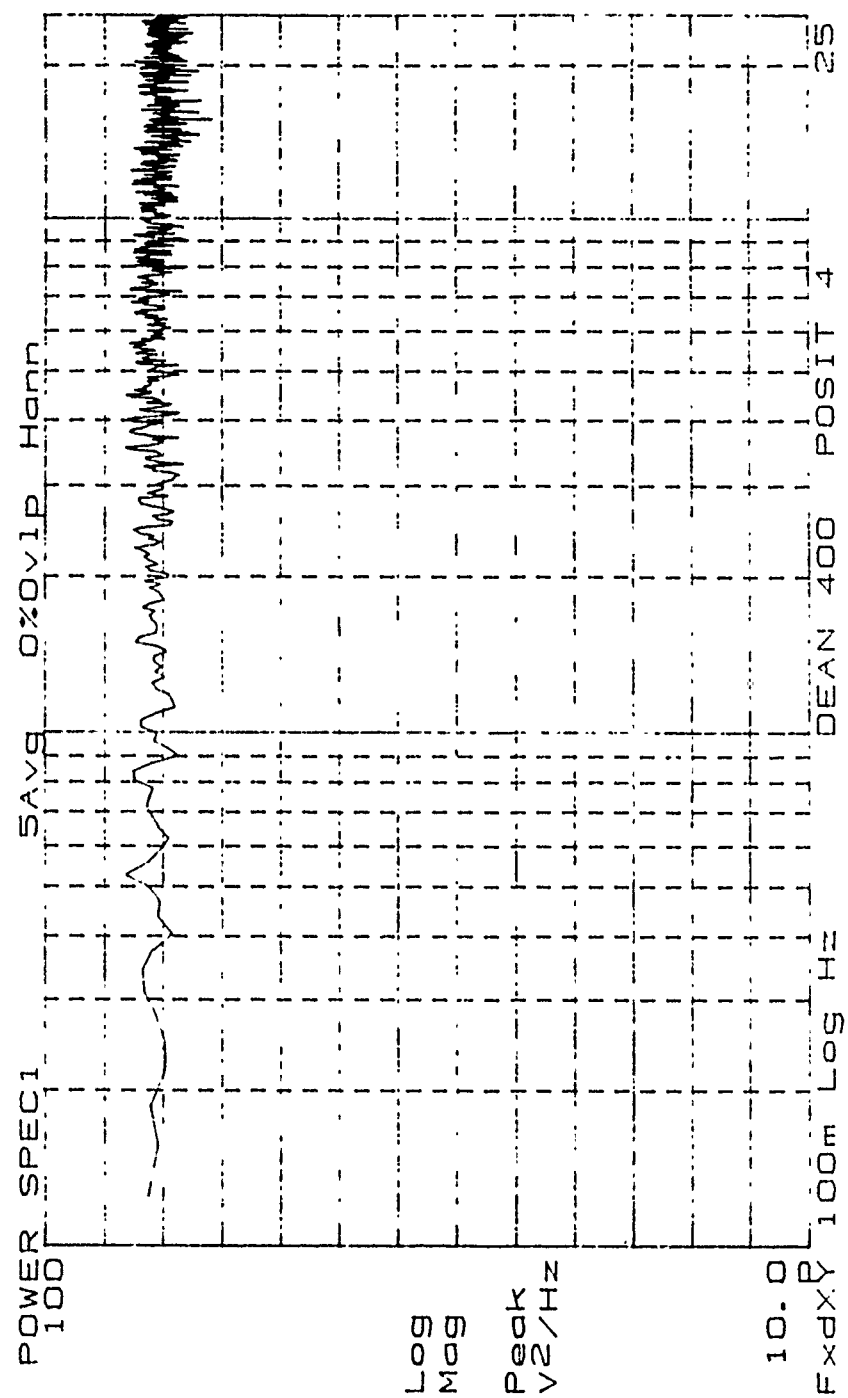


Figure 138. Low Frequency Power Spectrum, De=400, Position 4

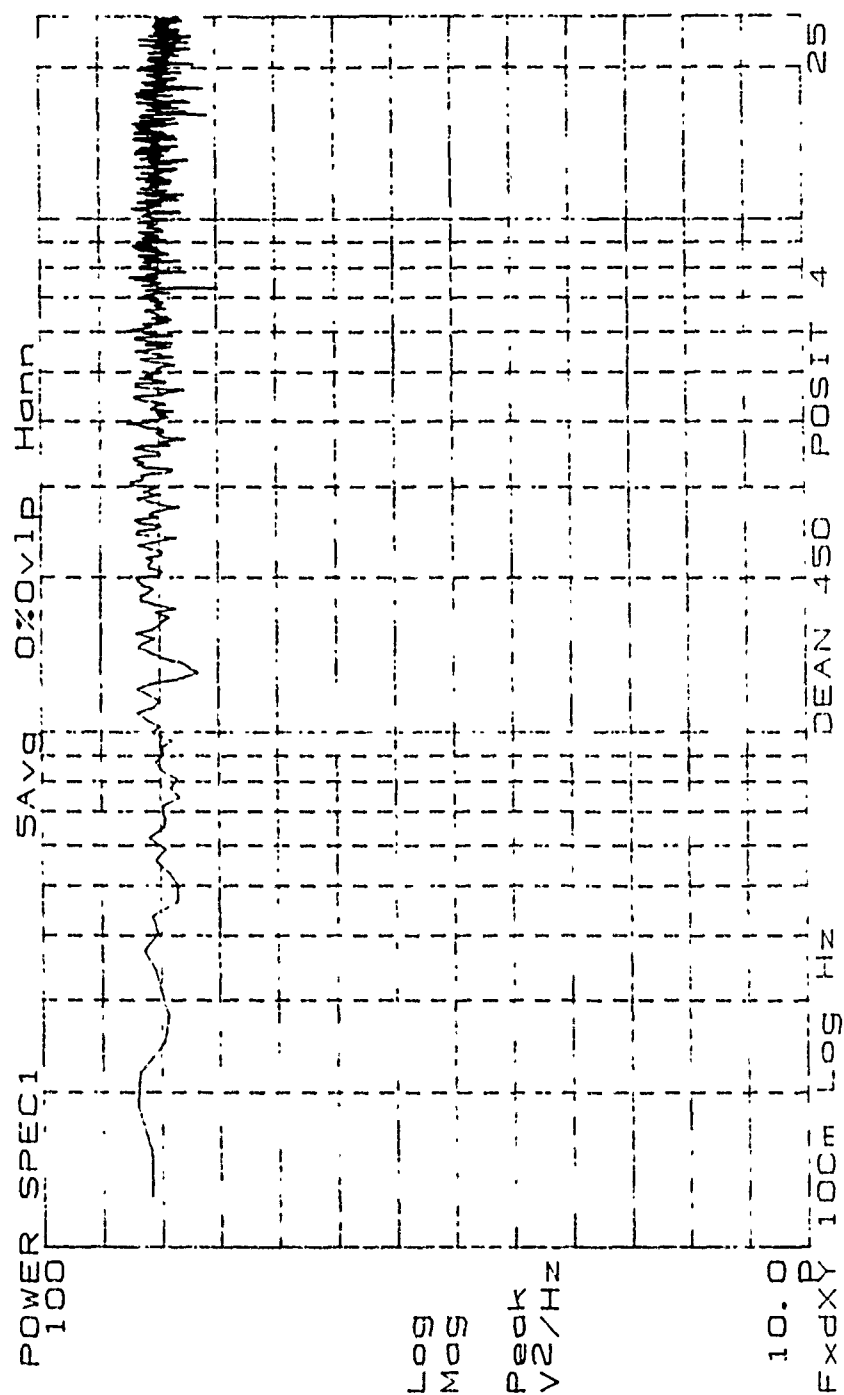


Figure 139. Low Frequency Power Spectrum, De=450, Position 4

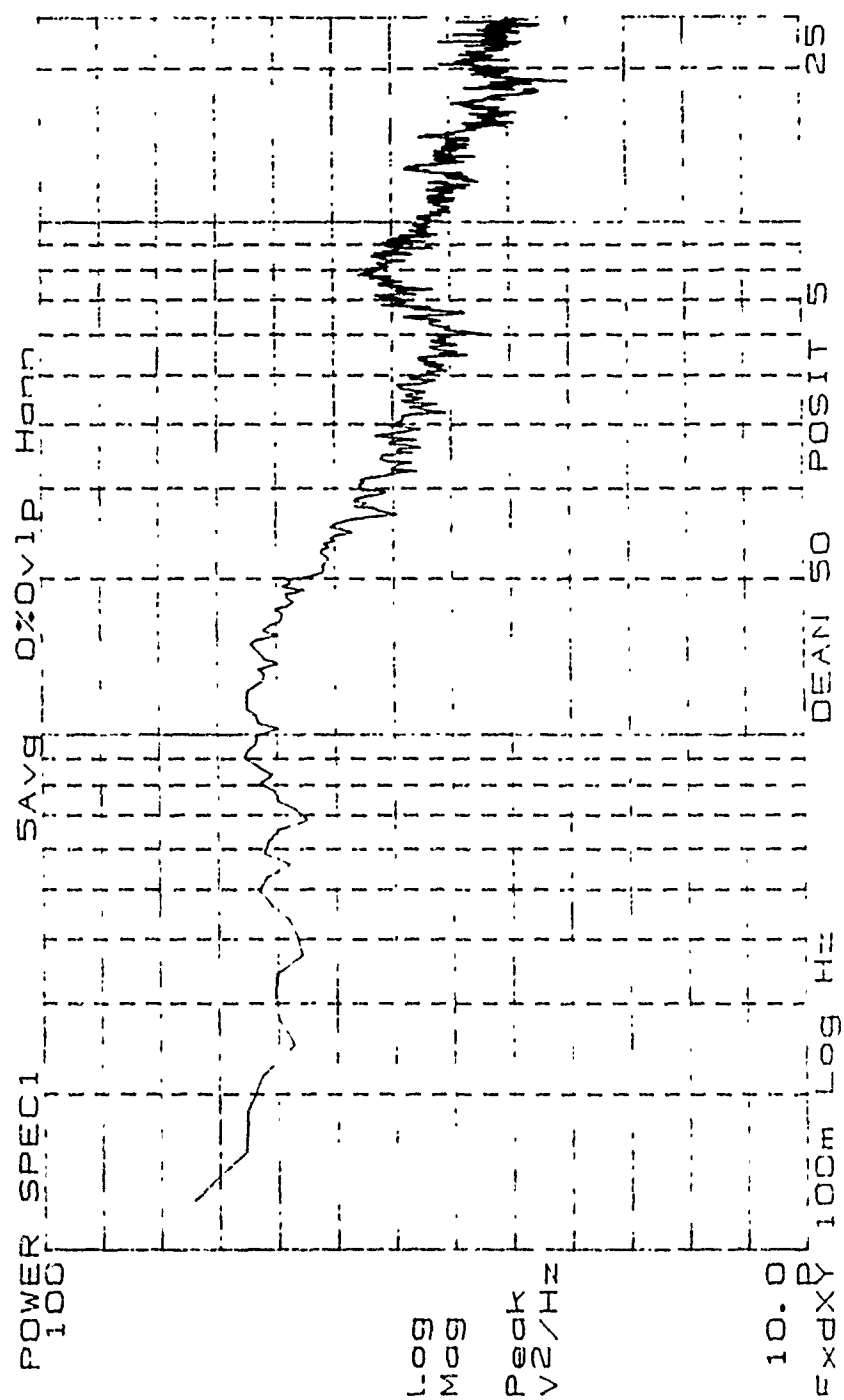


Figure 140. Low Frequency Power Spectrum, De=50, Position 5

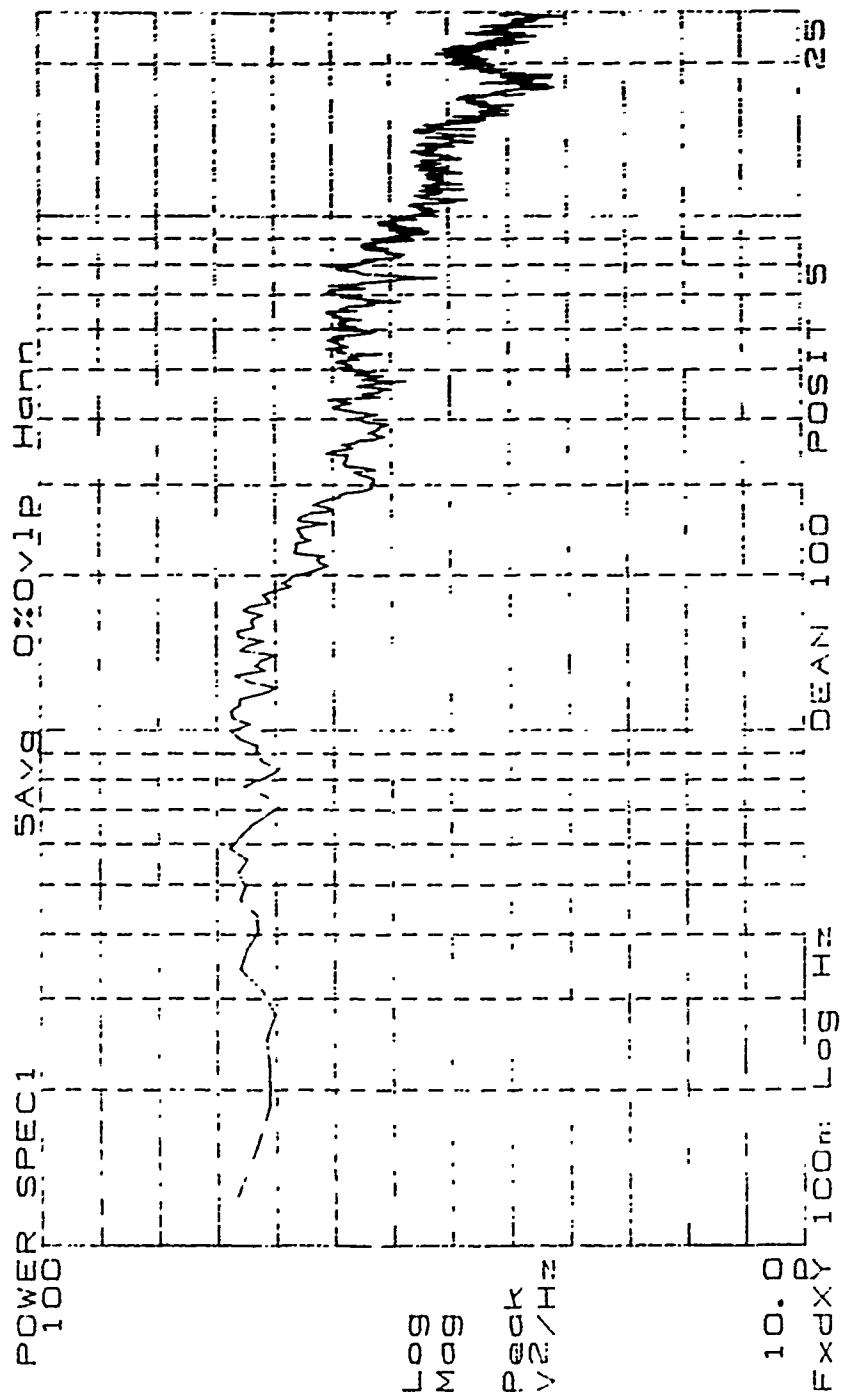


Figure 141. Low Frequency Power Spectrum, De=100, Position 5

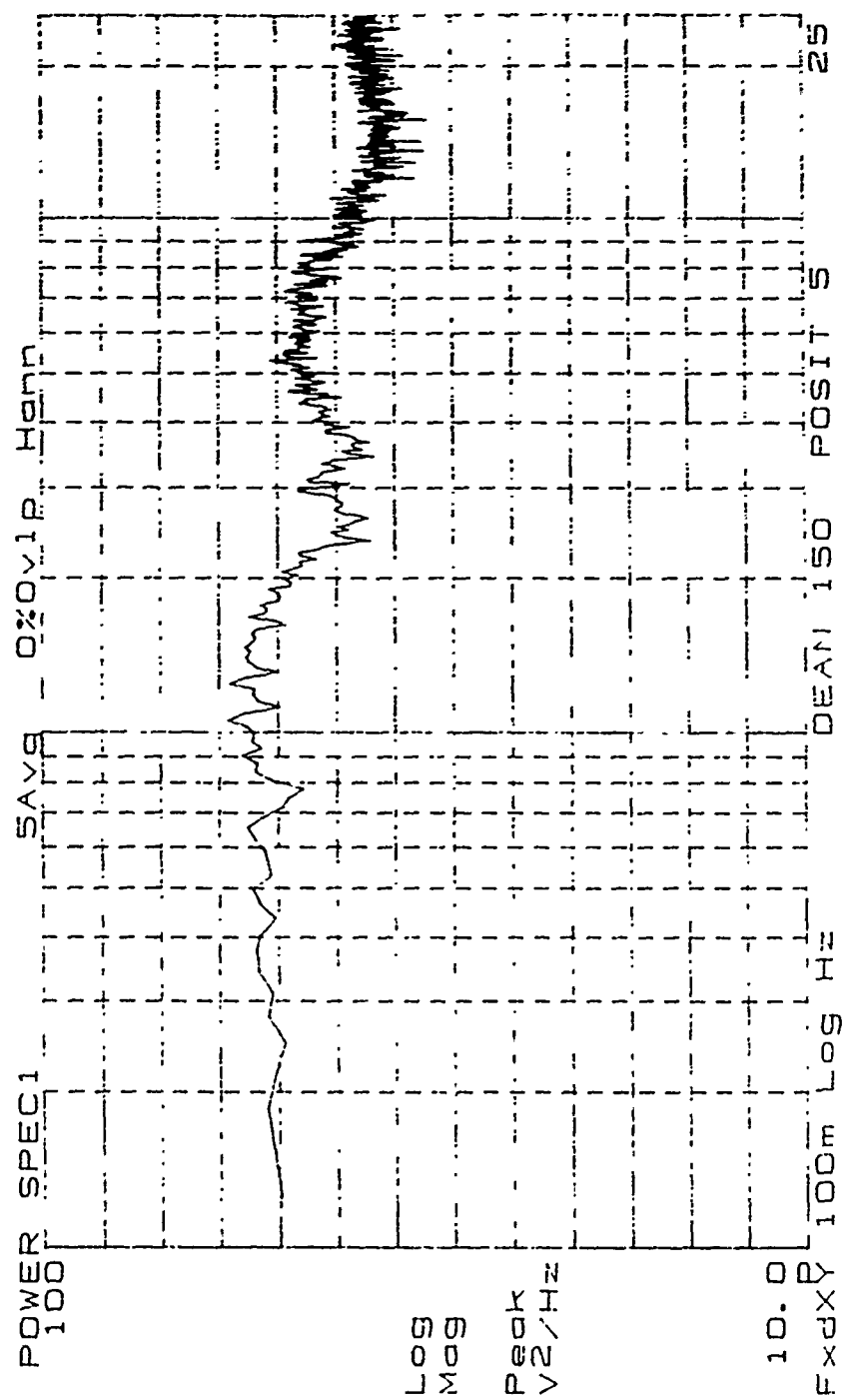


Figure 142. Low Frequency Power Spectrum, De=150, Position 5

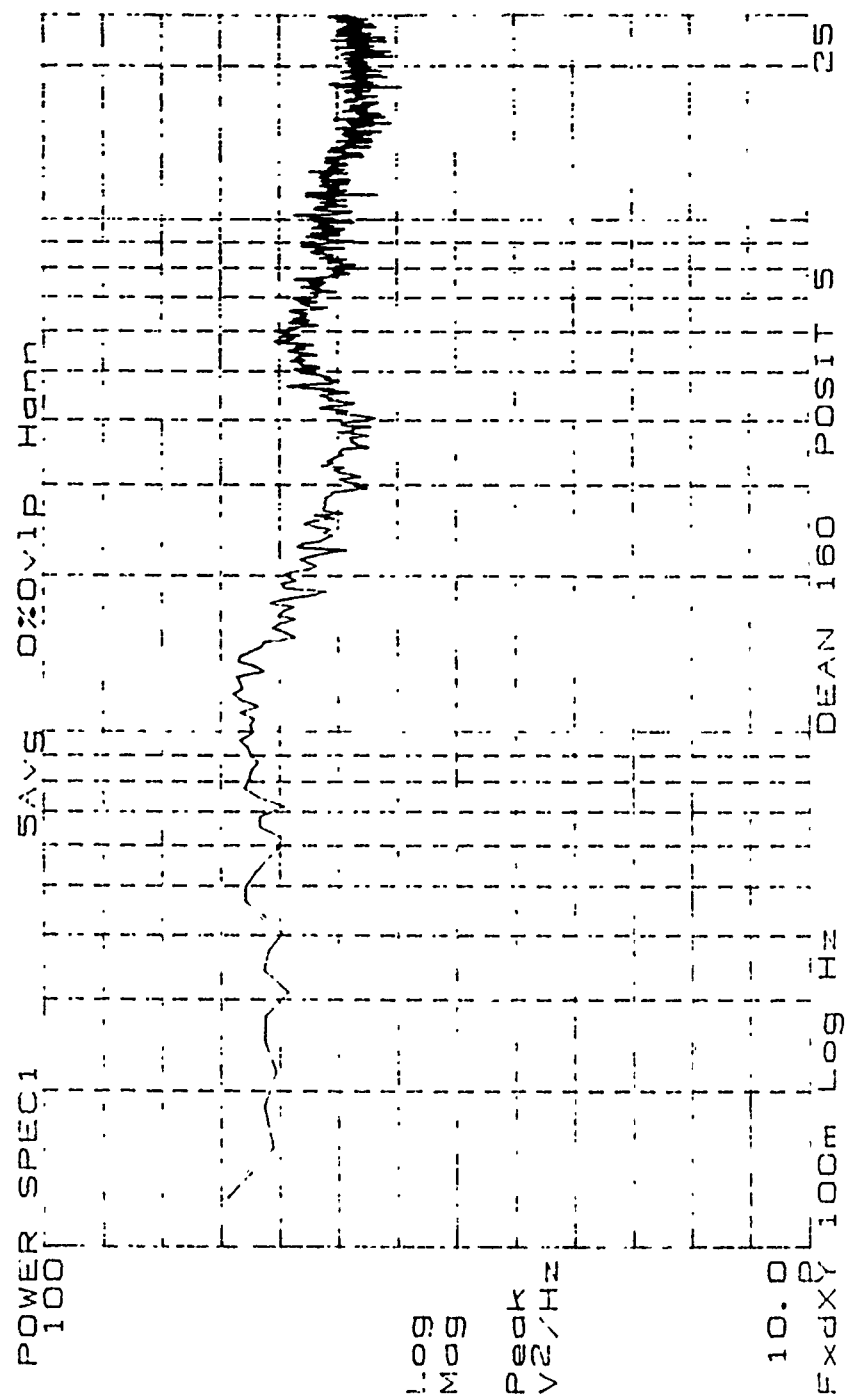


Figure 143. Low Frequency Power Spectrum, De=160, Position 5

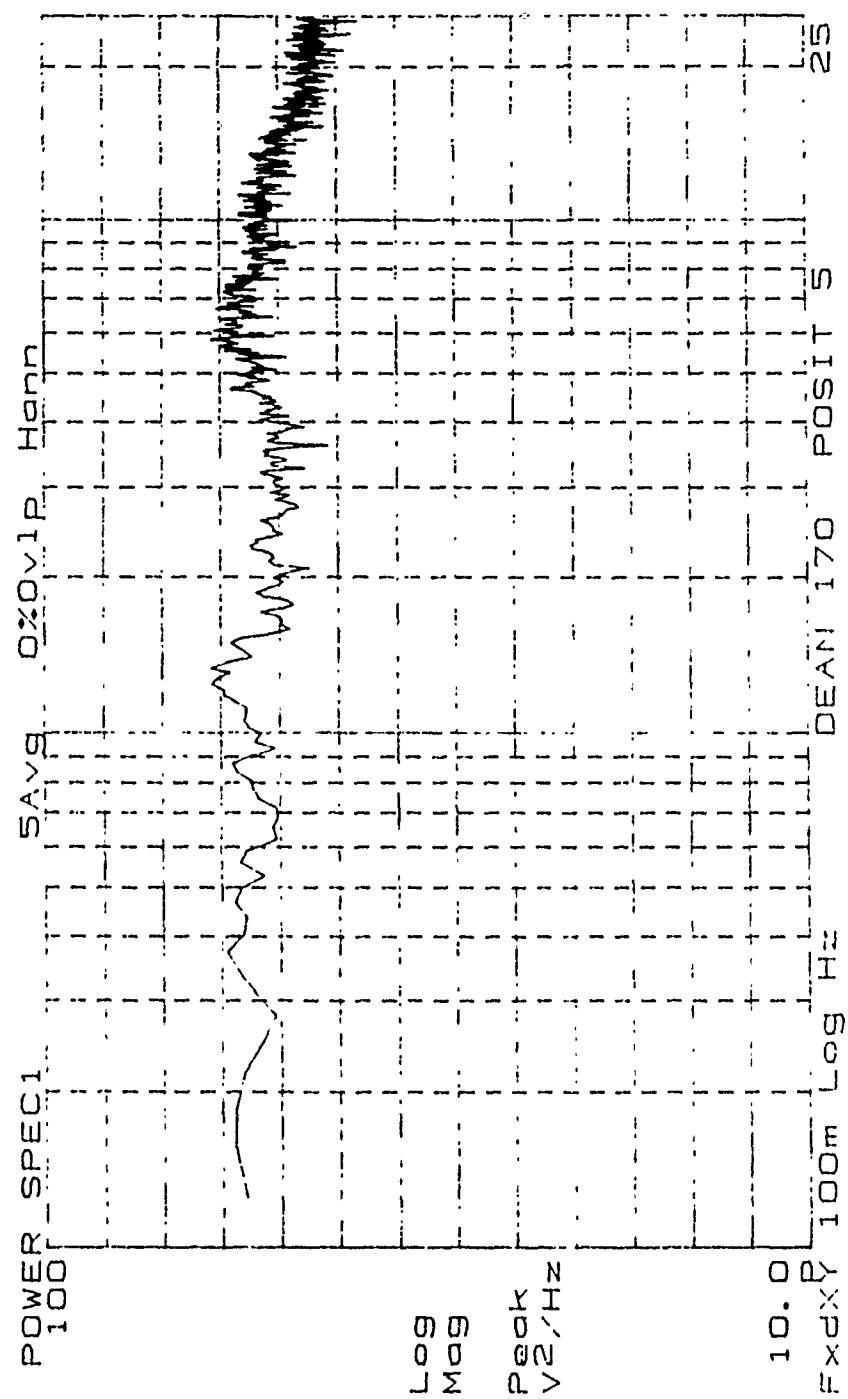


Figure 144. Low Frequency Power Spectrum, De=170, Position 5

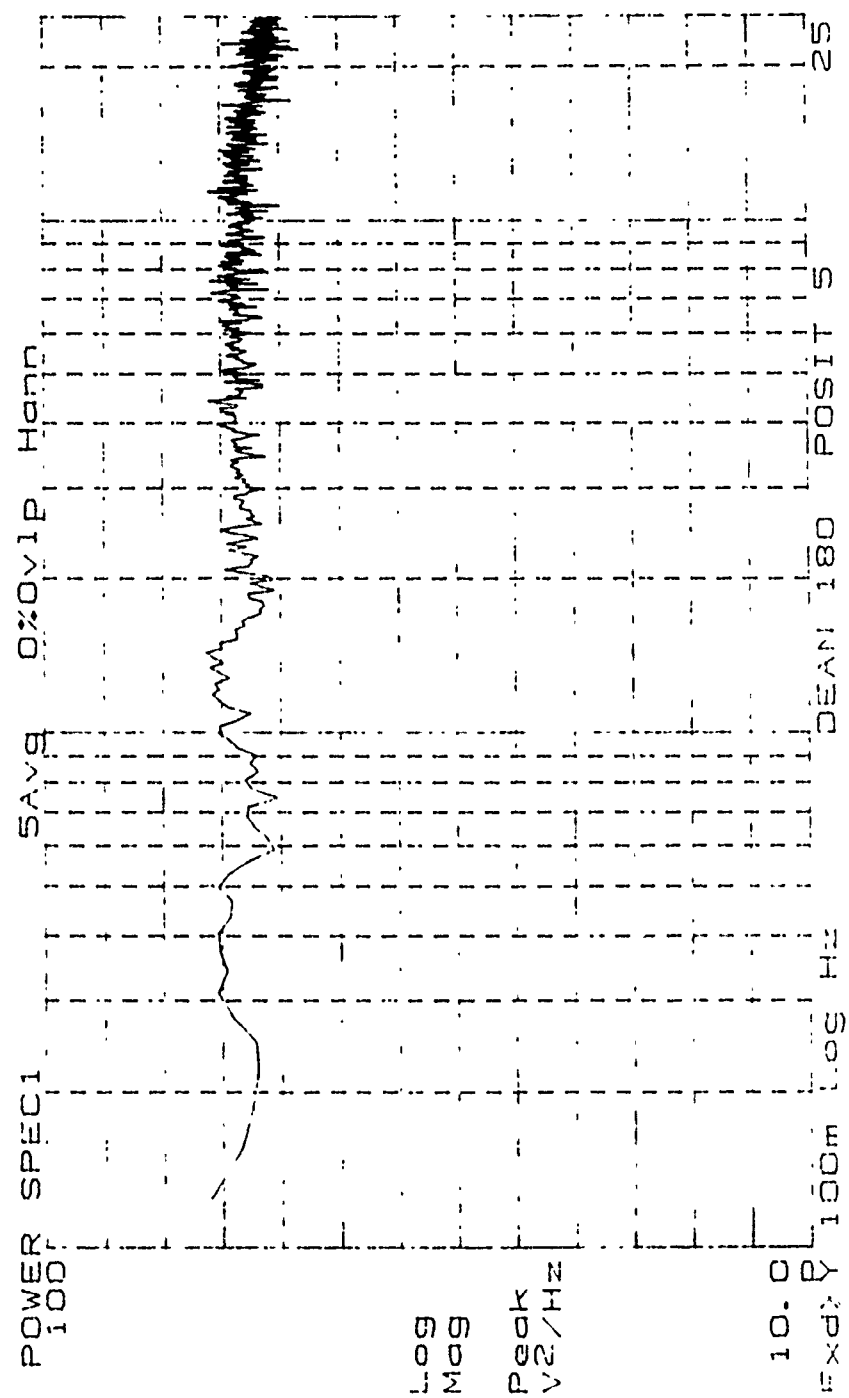


Figure 145. Low Frequency Power Spectrum, De=180, Position 5

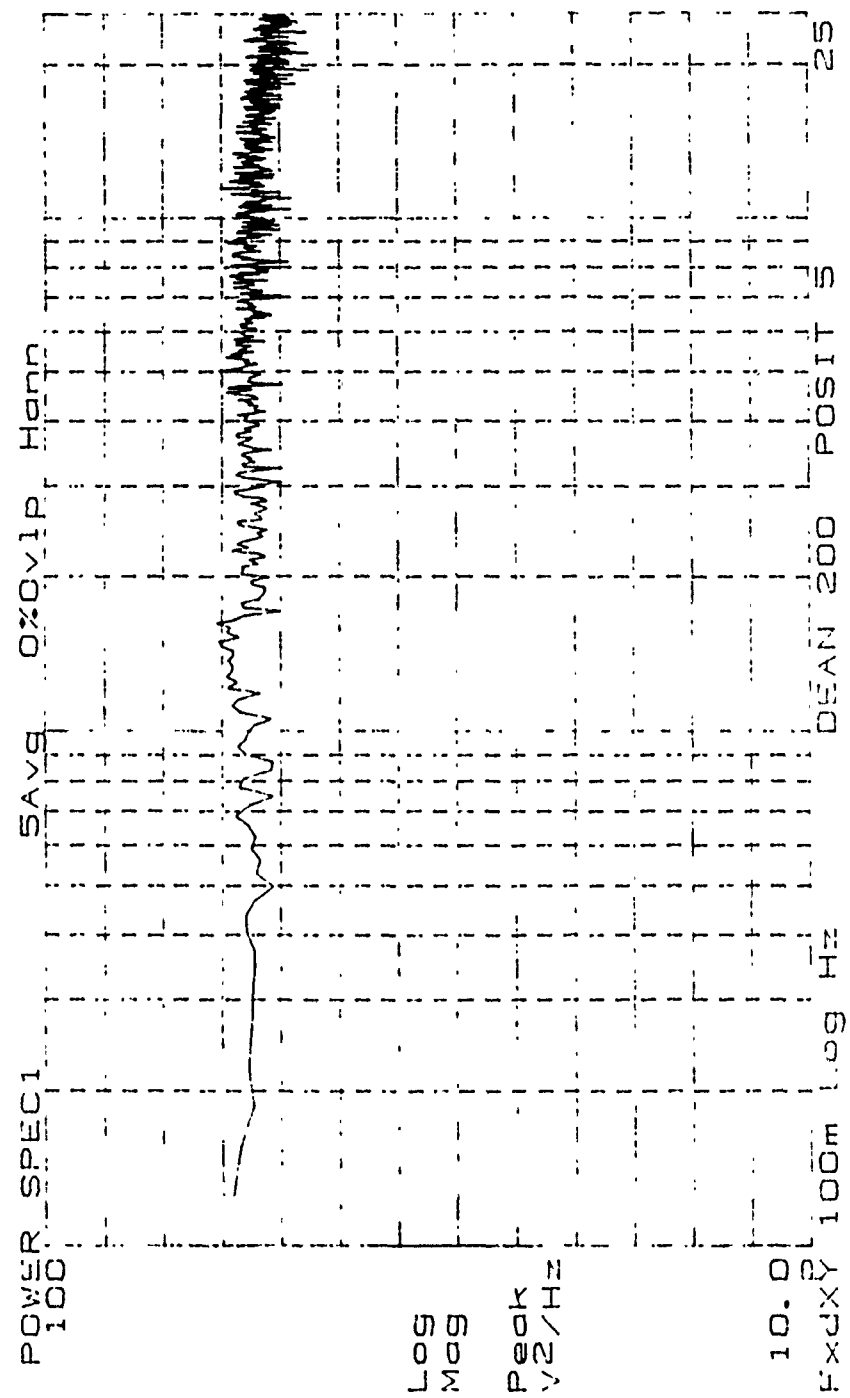


Figure 146. Low Frequency Power Spectrum, De=200, Position 5

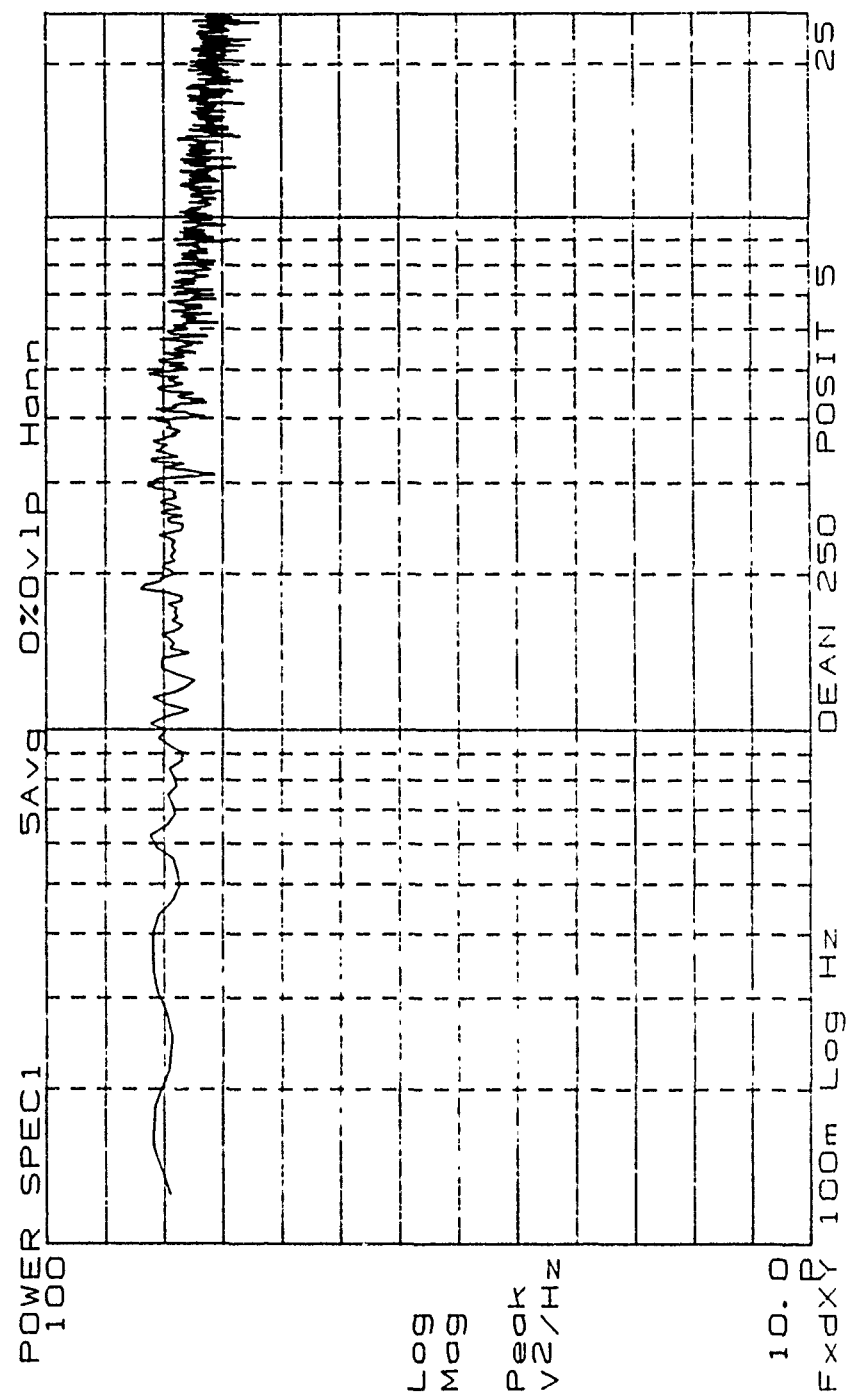


Figure 147. Low Frequency Power Spectrum, De=250, Position 5

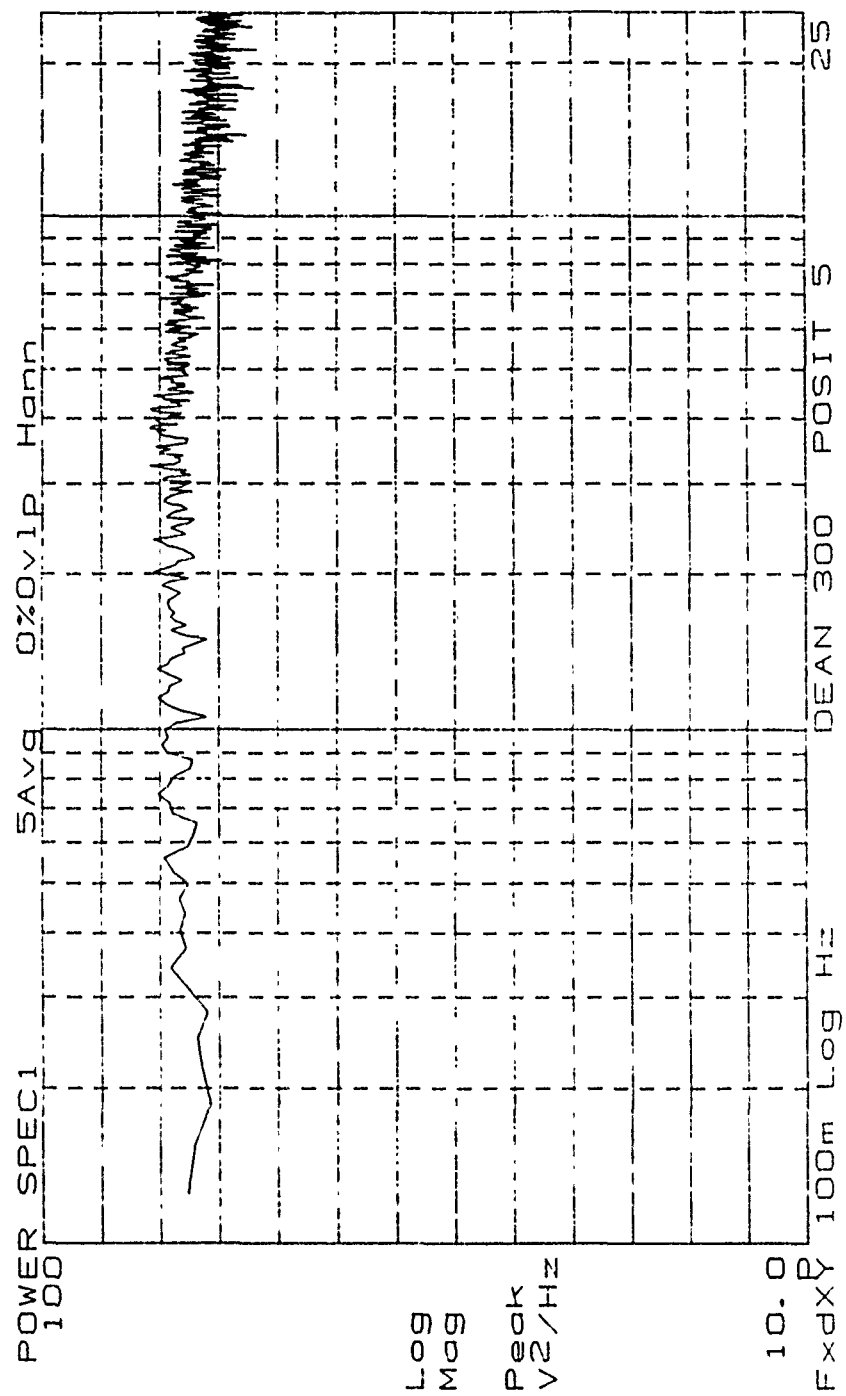


Figure 148. Low Frequency Power Spectrum, De=300, Position 5

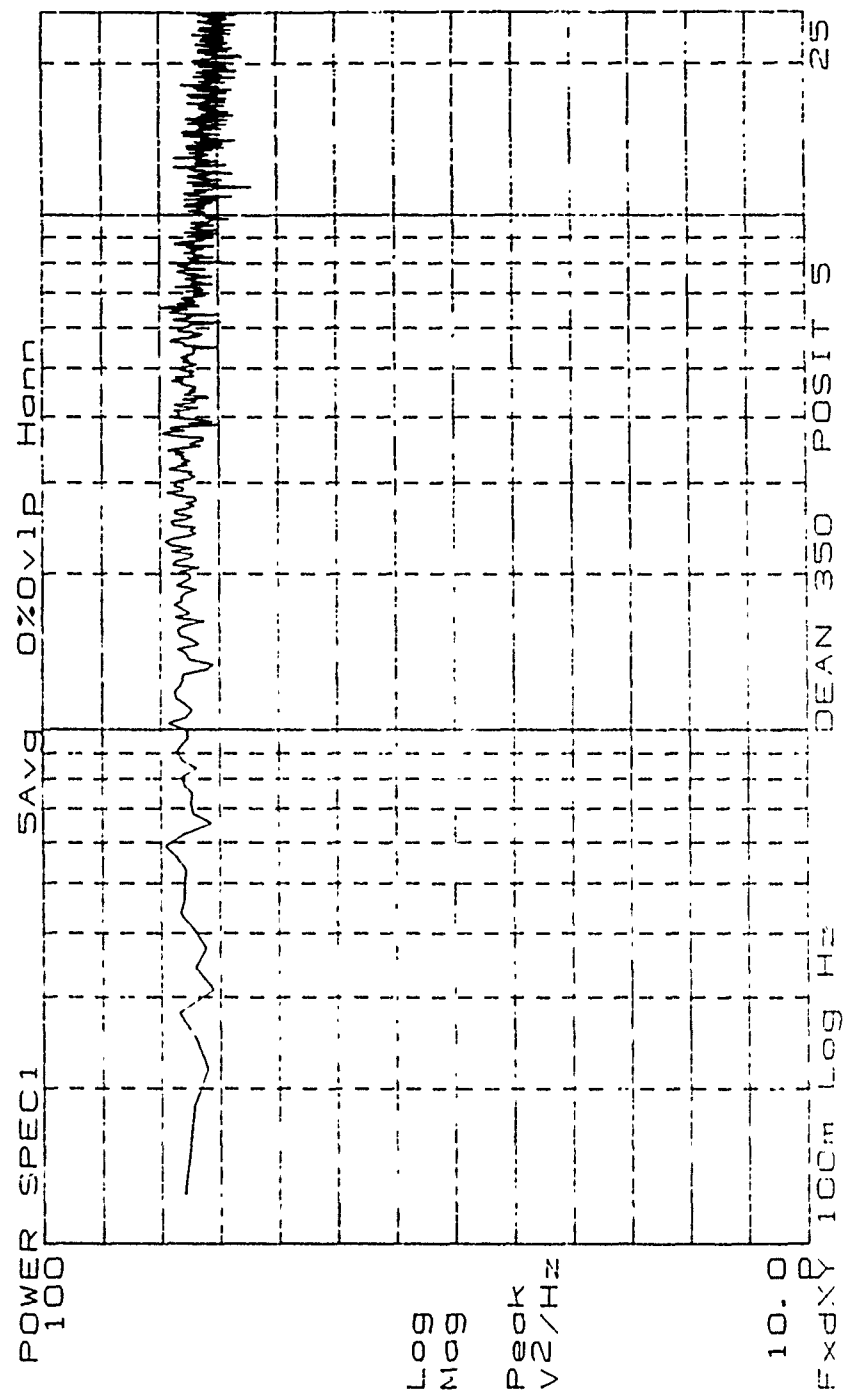


Figure 149. Low Frequency Power Spectrum, De=350, Position 5

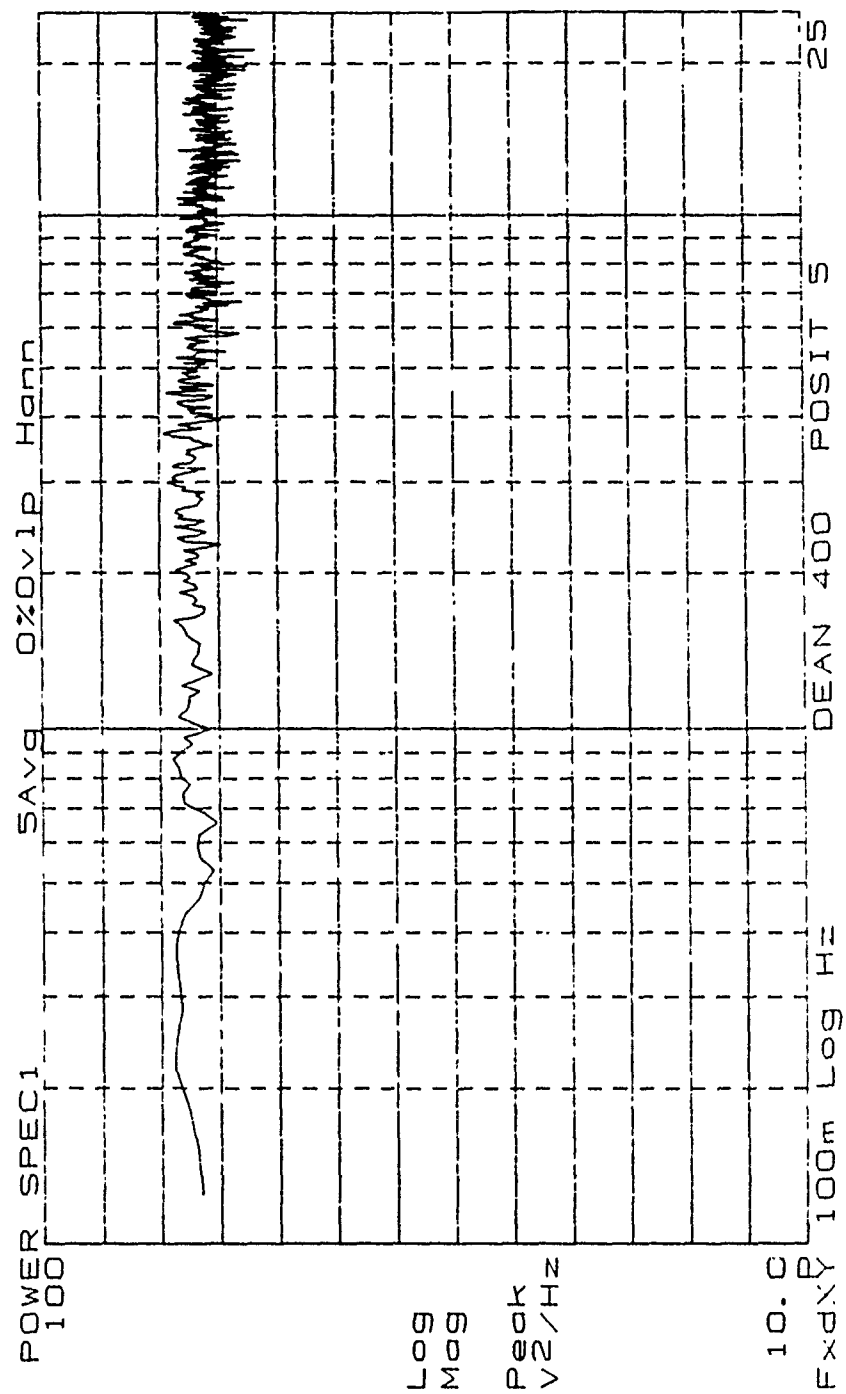


Figure 150. Low Frequency Power Spectrum, De=400, Position 5

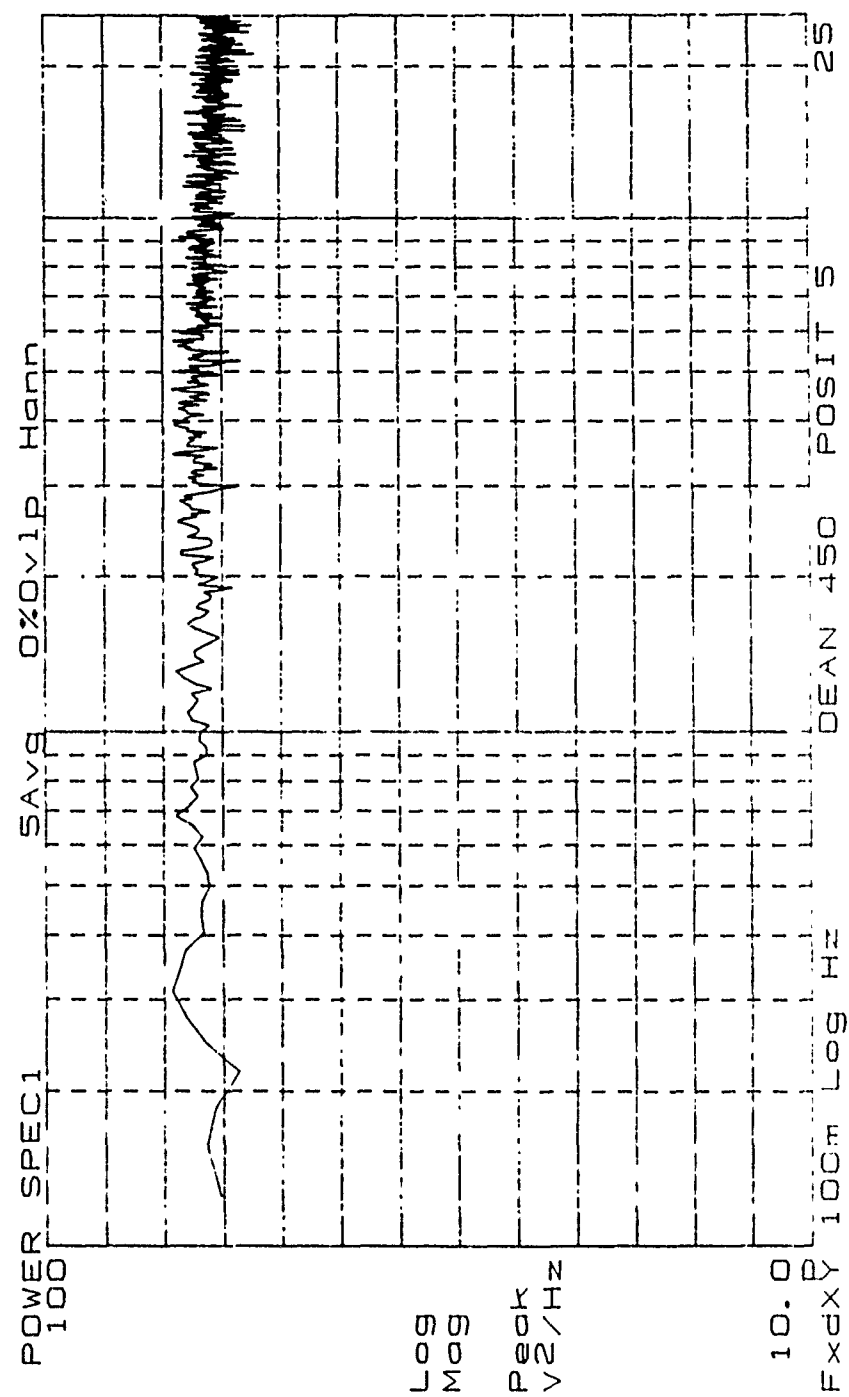


Figure 151. Low Frequency Power Spectrum, De=450, Position 5

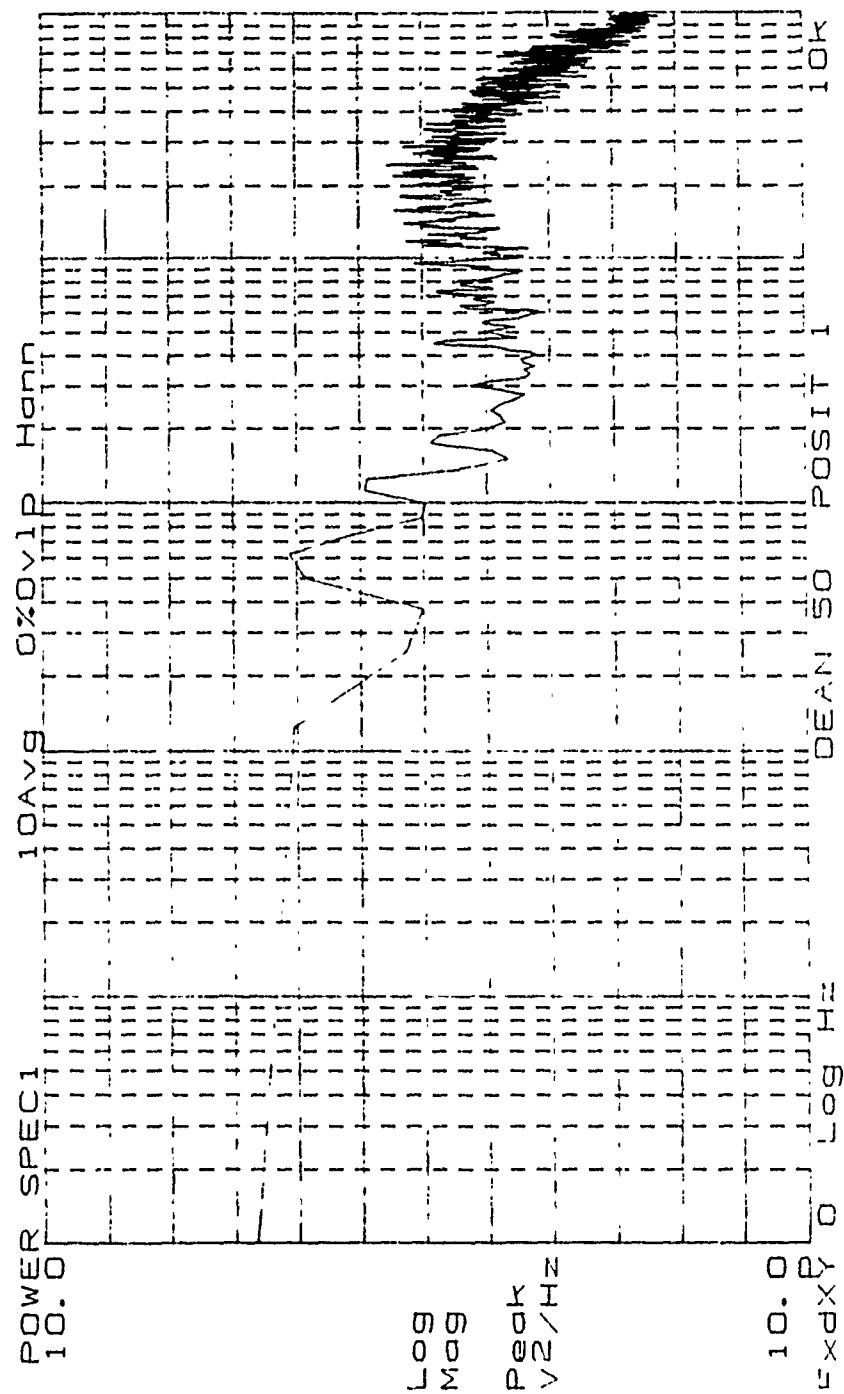


Figure 155. High Frequency Power Spectrum, De=50, Position 1

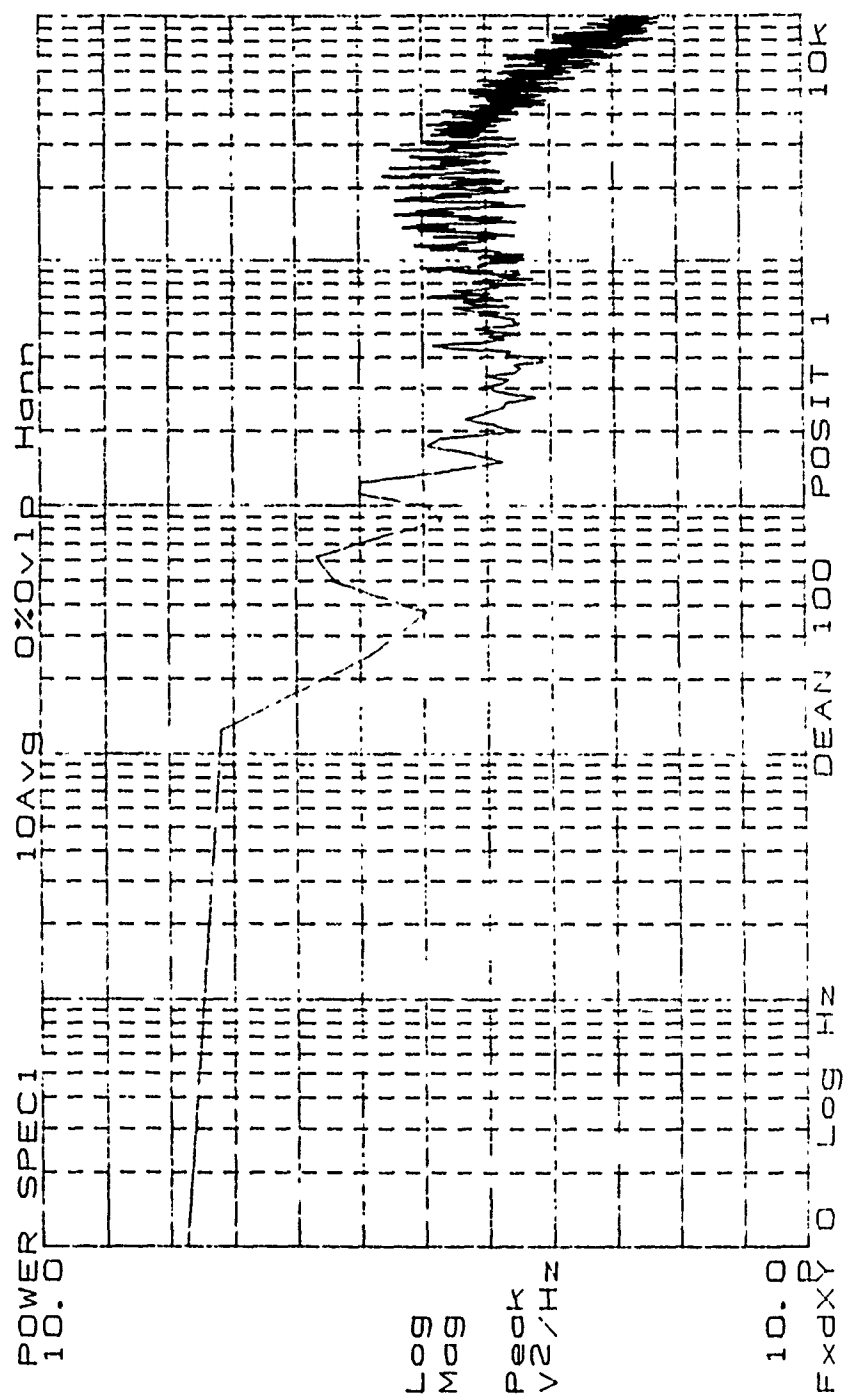


Figure 156. High Frequency Power Spectrum, De=100, Position 1

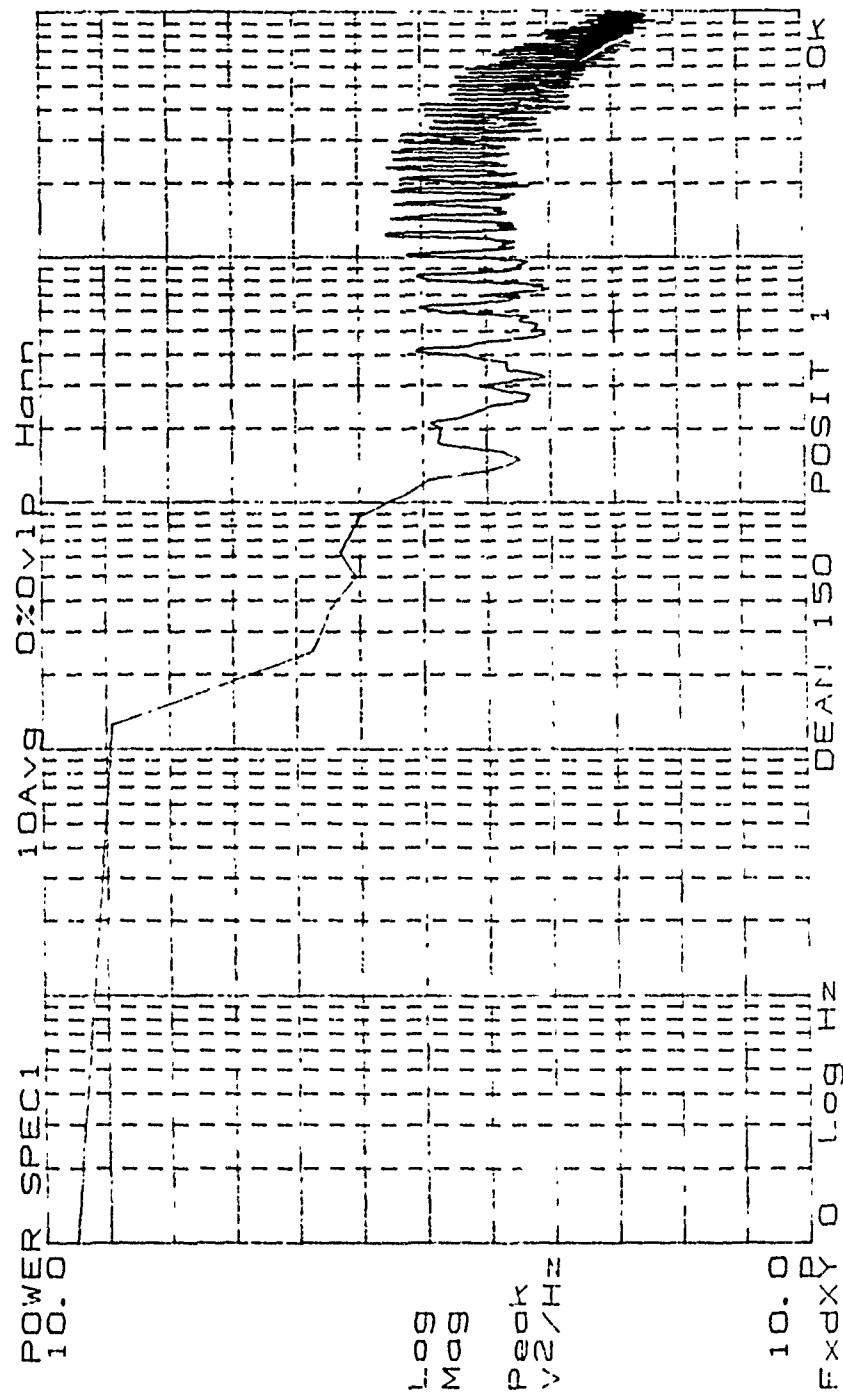


Figure 157. High Frequency Power Spectrum, De=150, Position 1

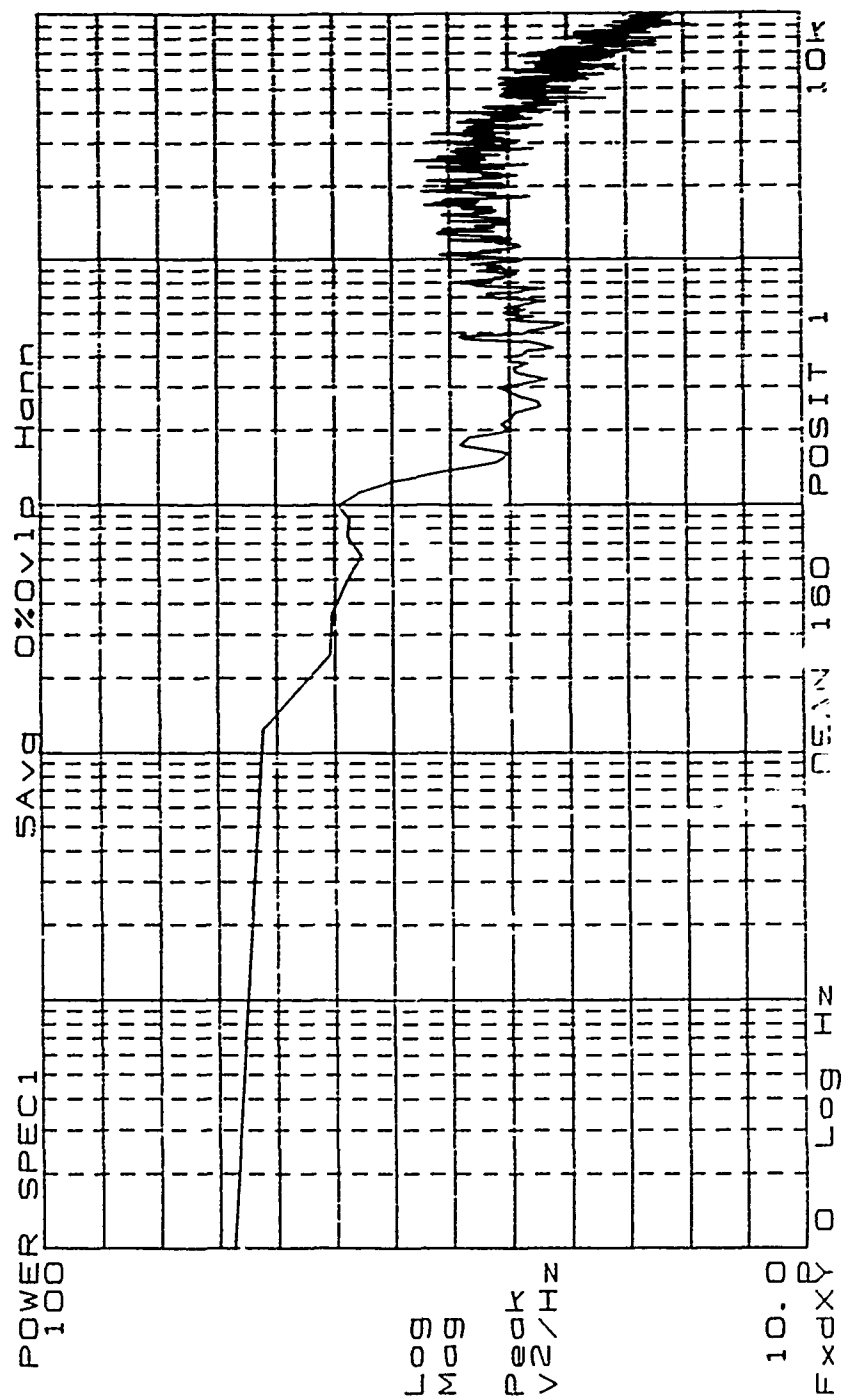


Figure 158. High Frequency Power Spectrum, De=160, Position 1

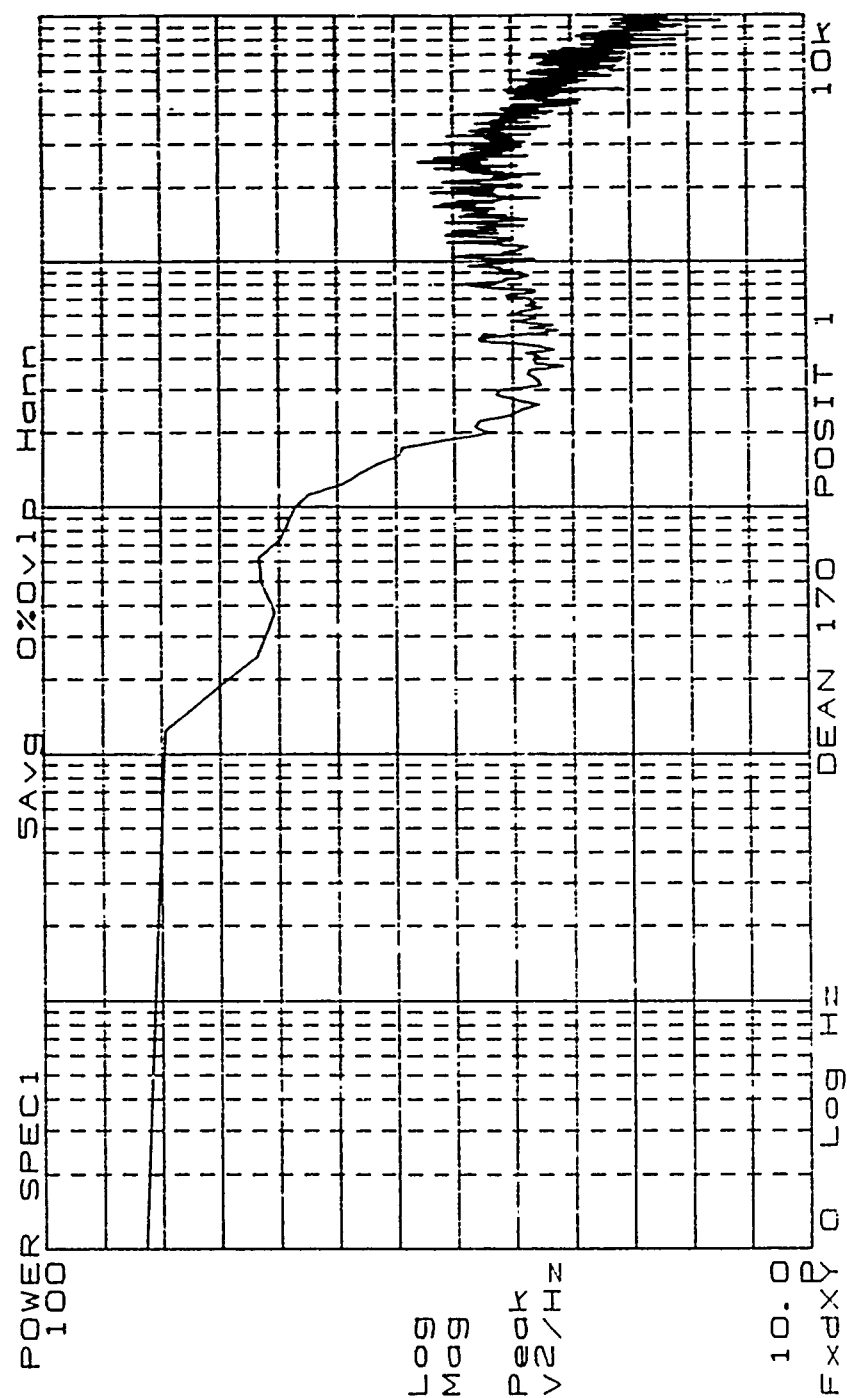


Figure 159. High Frequency Power Spectrum, De=170, Position 1

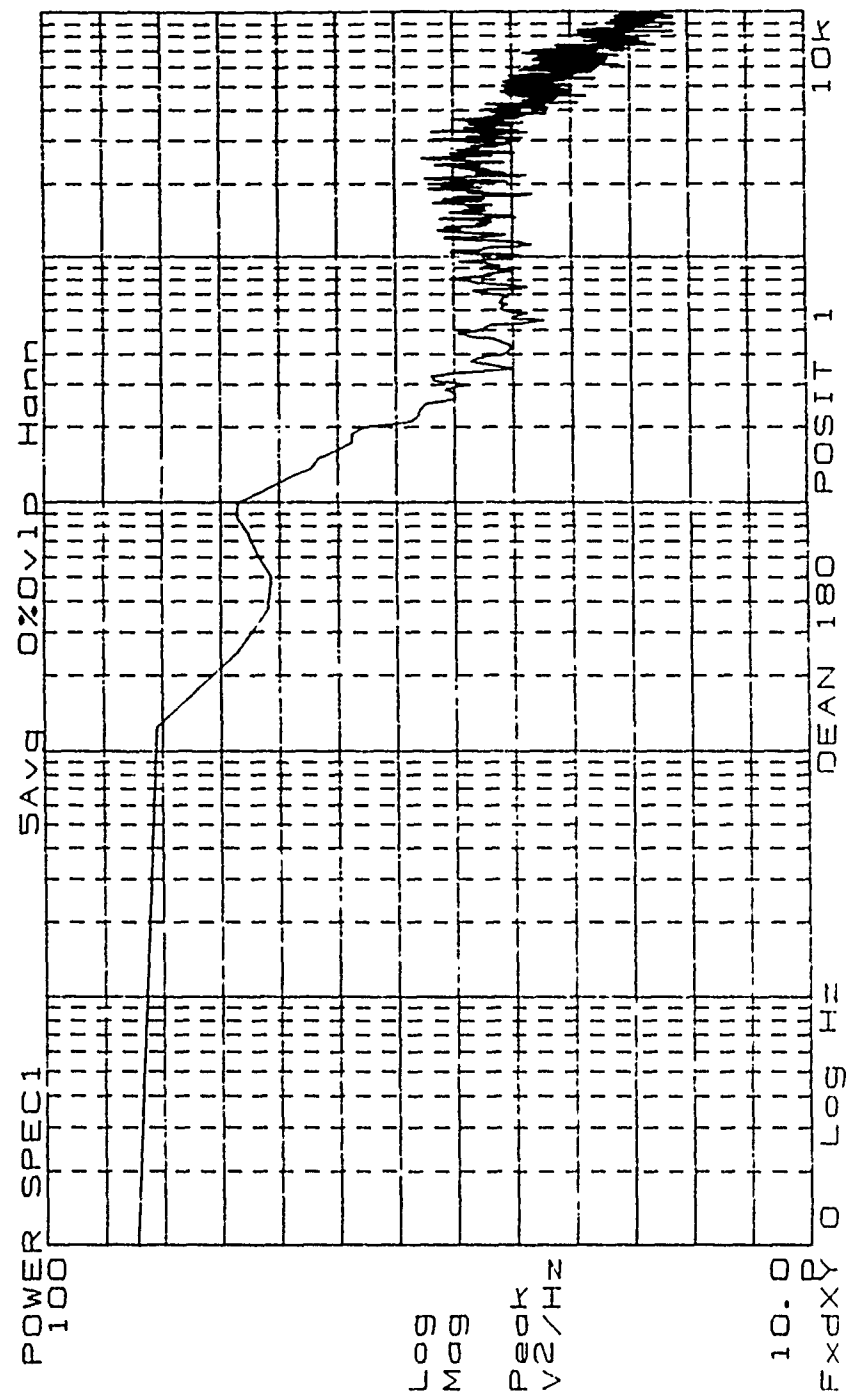


Figure 160. High Frequency Power Spectrum, De=180, Position 1



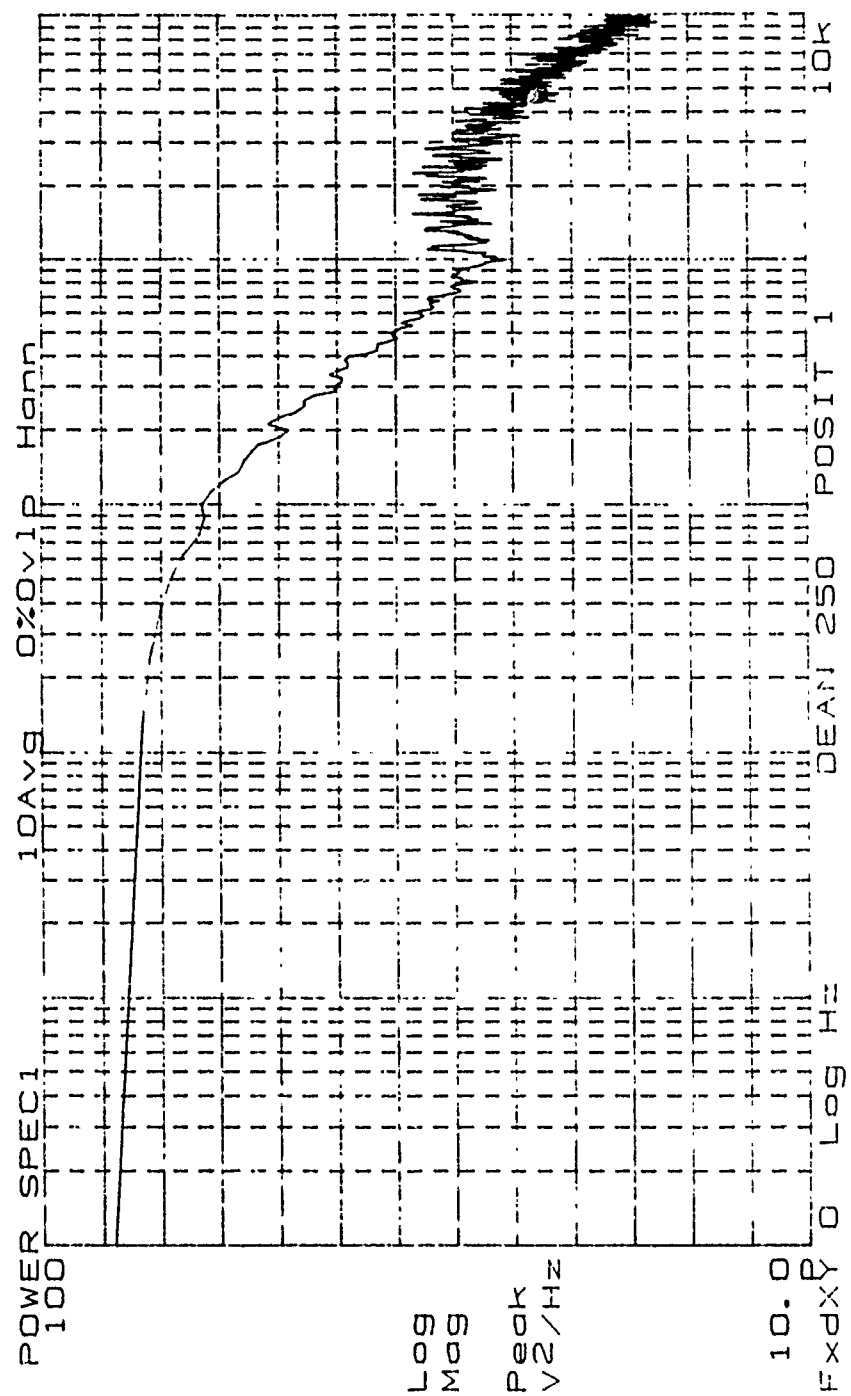


Figure 162. High Frequency Power Spectrum, De=250, Position 1

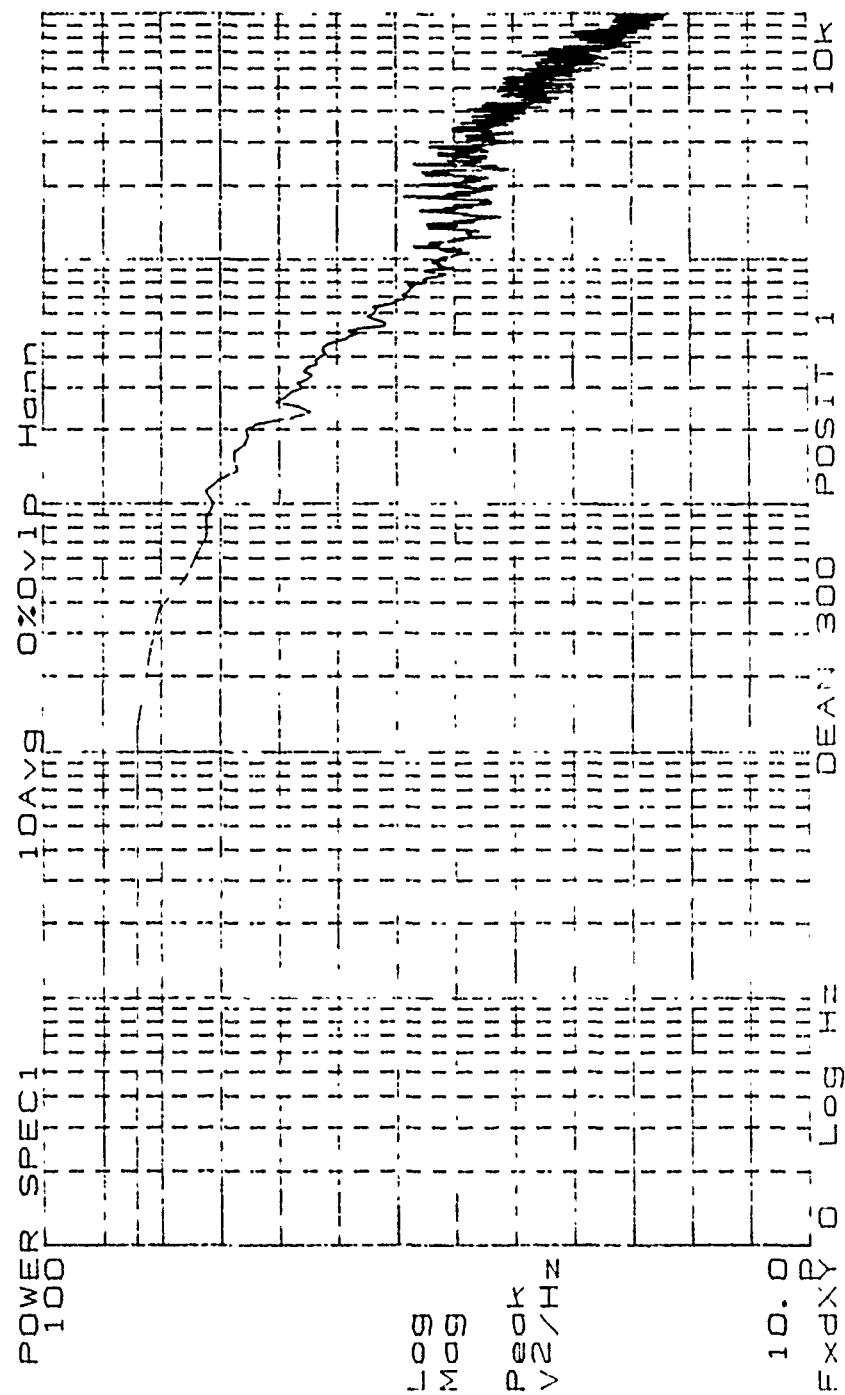


Figure 163. High Frequency Power Spectrum, De=300, Position 1

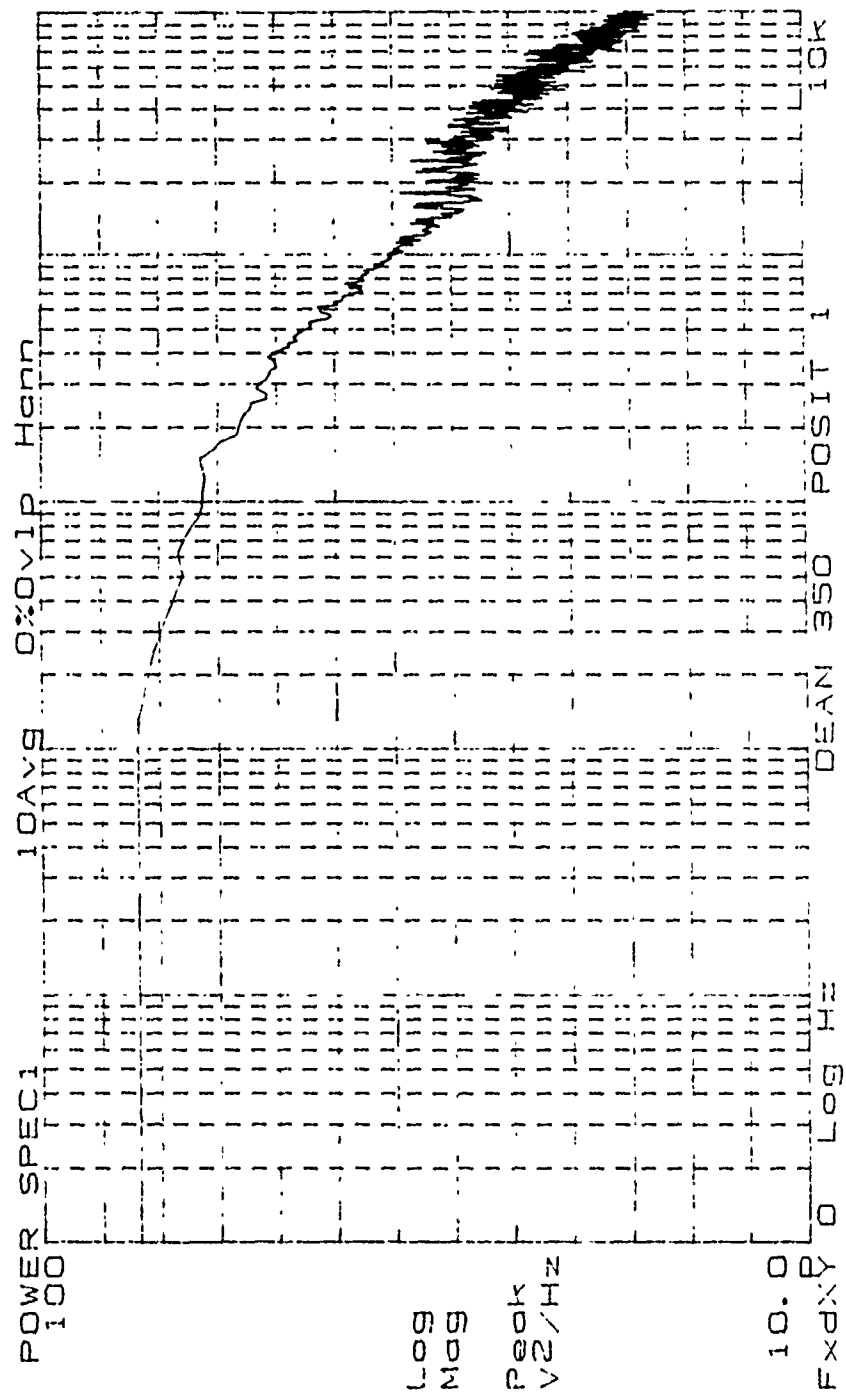


Figure 164. High Frequency Power Spectrum, De=350, Position 1

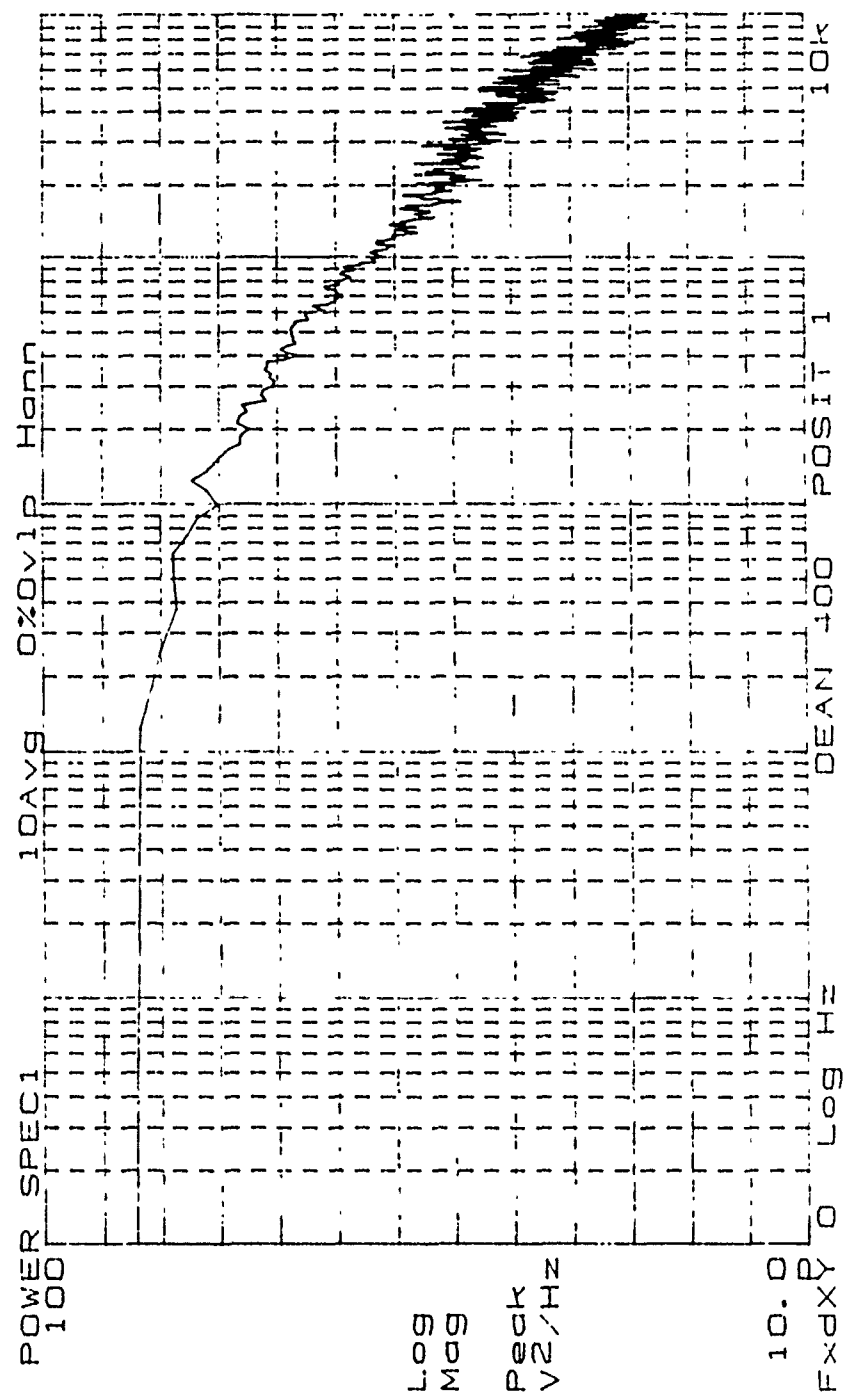


Figure 165. High Frequency Power Spectrum, De=400, Position 1

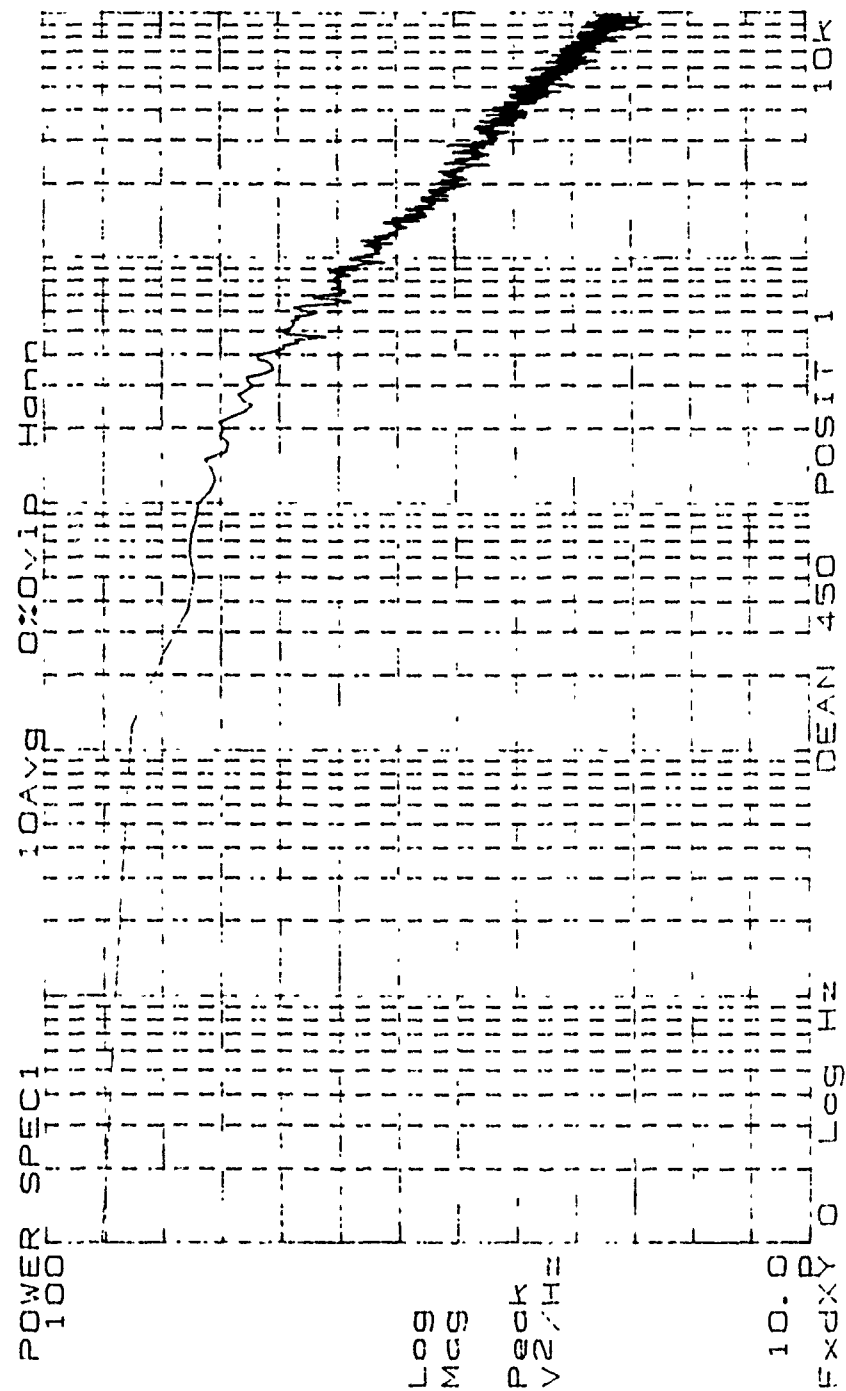


Figure 166. High Frequency Power Spectrum, De=450, Position 1

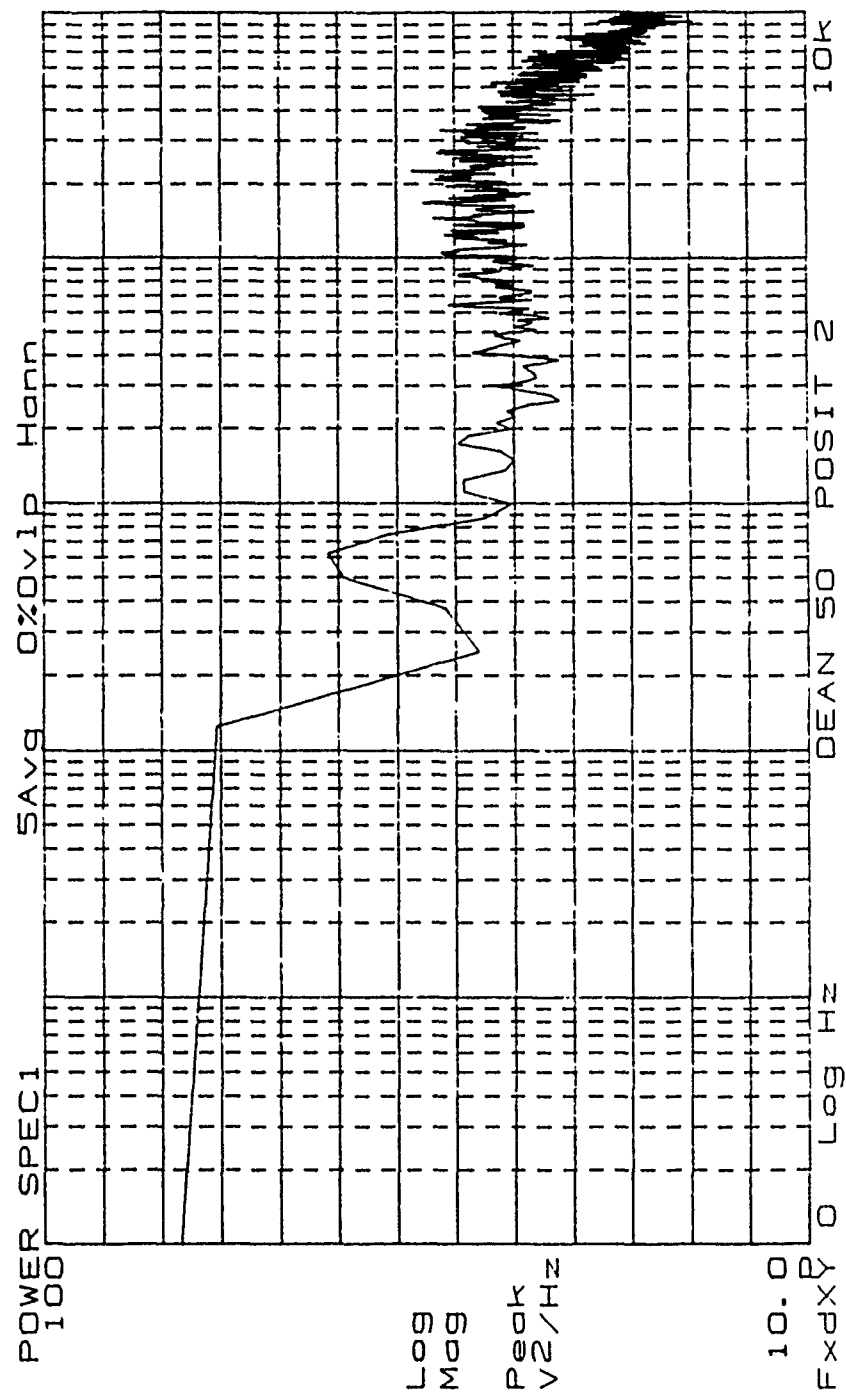


Figure 167. High Frequency Power Spectrum, De=50, Position 2

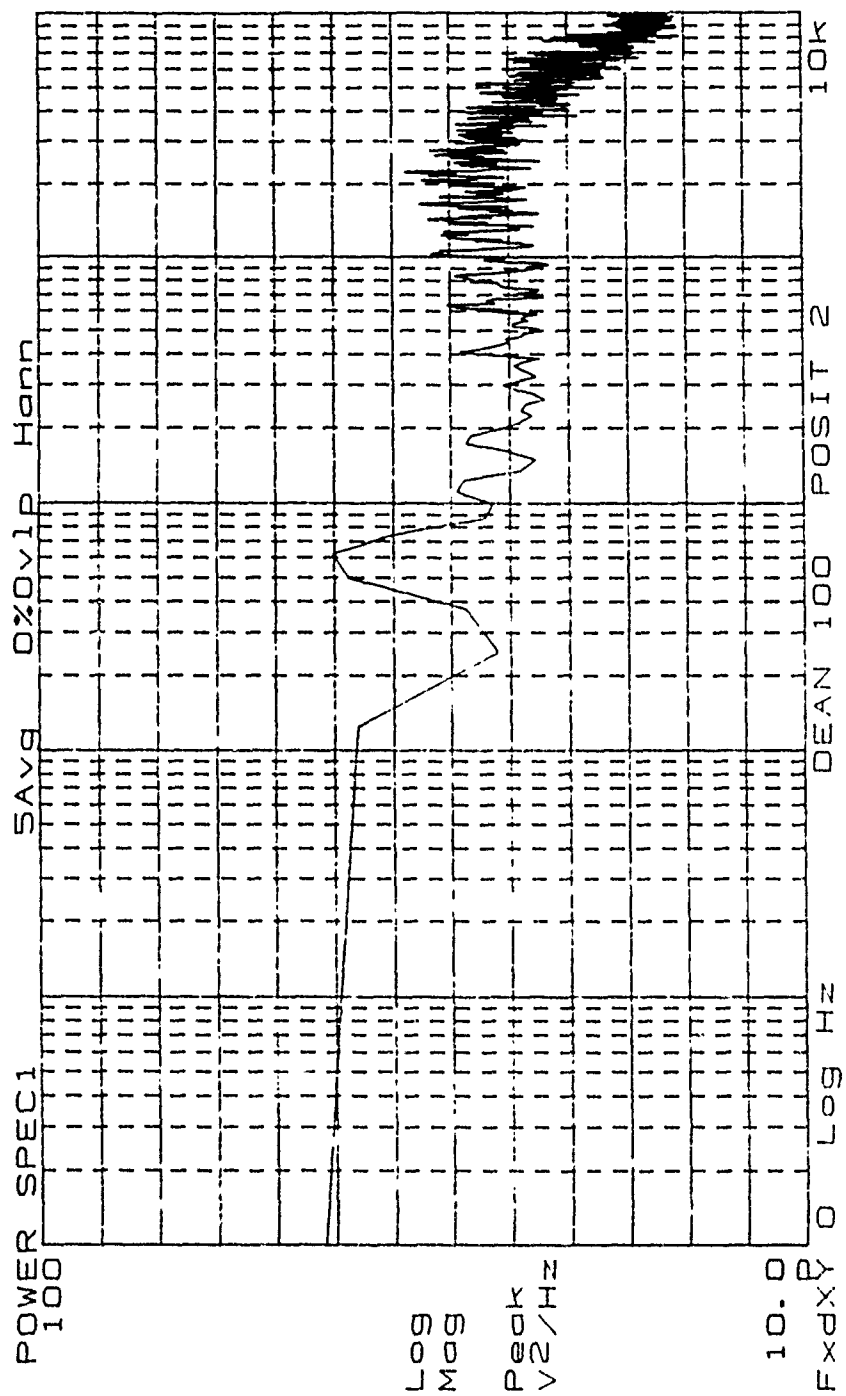


Figure 168. High Frequency Power Spectrum, De=100, Position 2

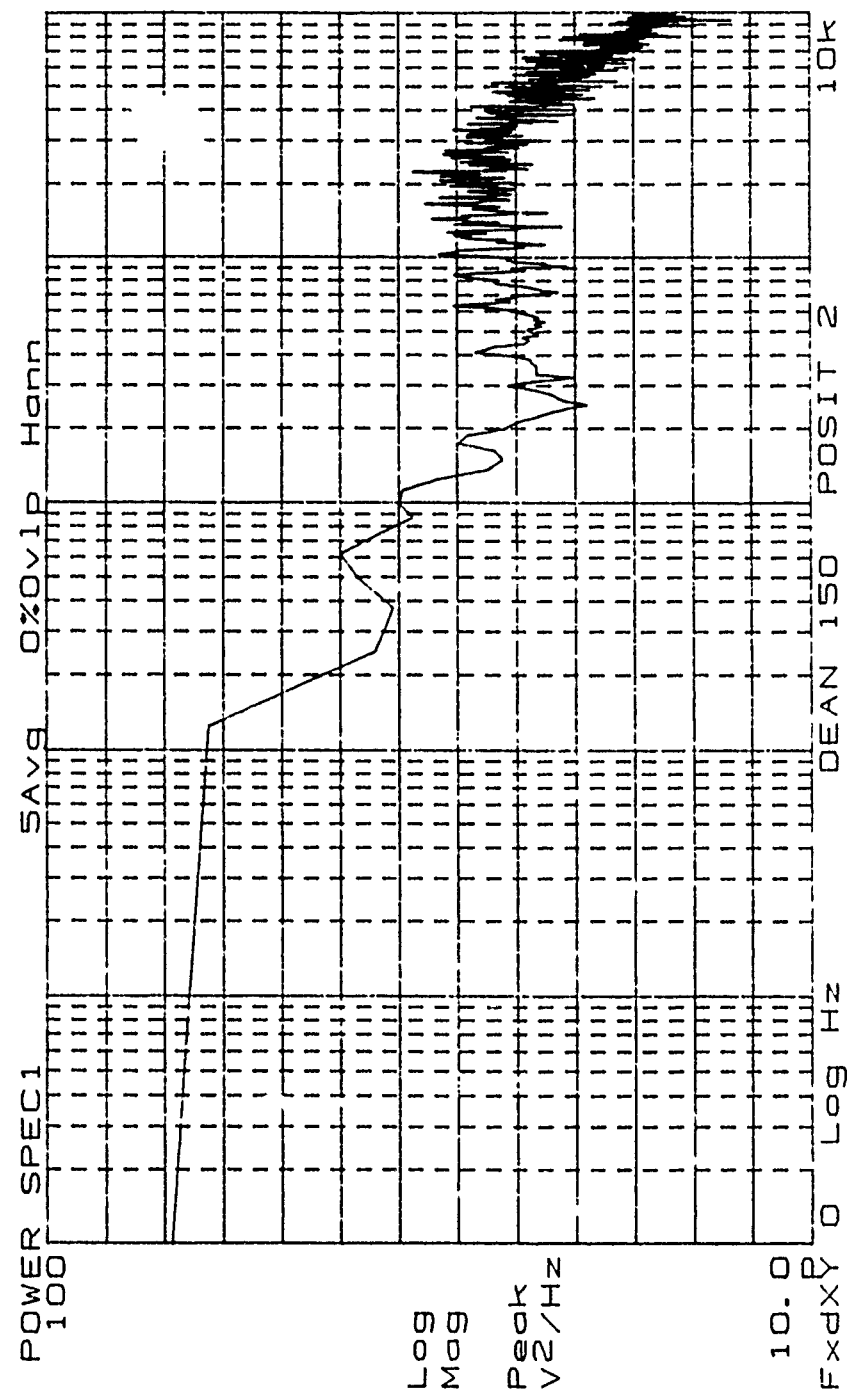


Figure 169. High Frequency Power Spectrum, De=150, Position 2

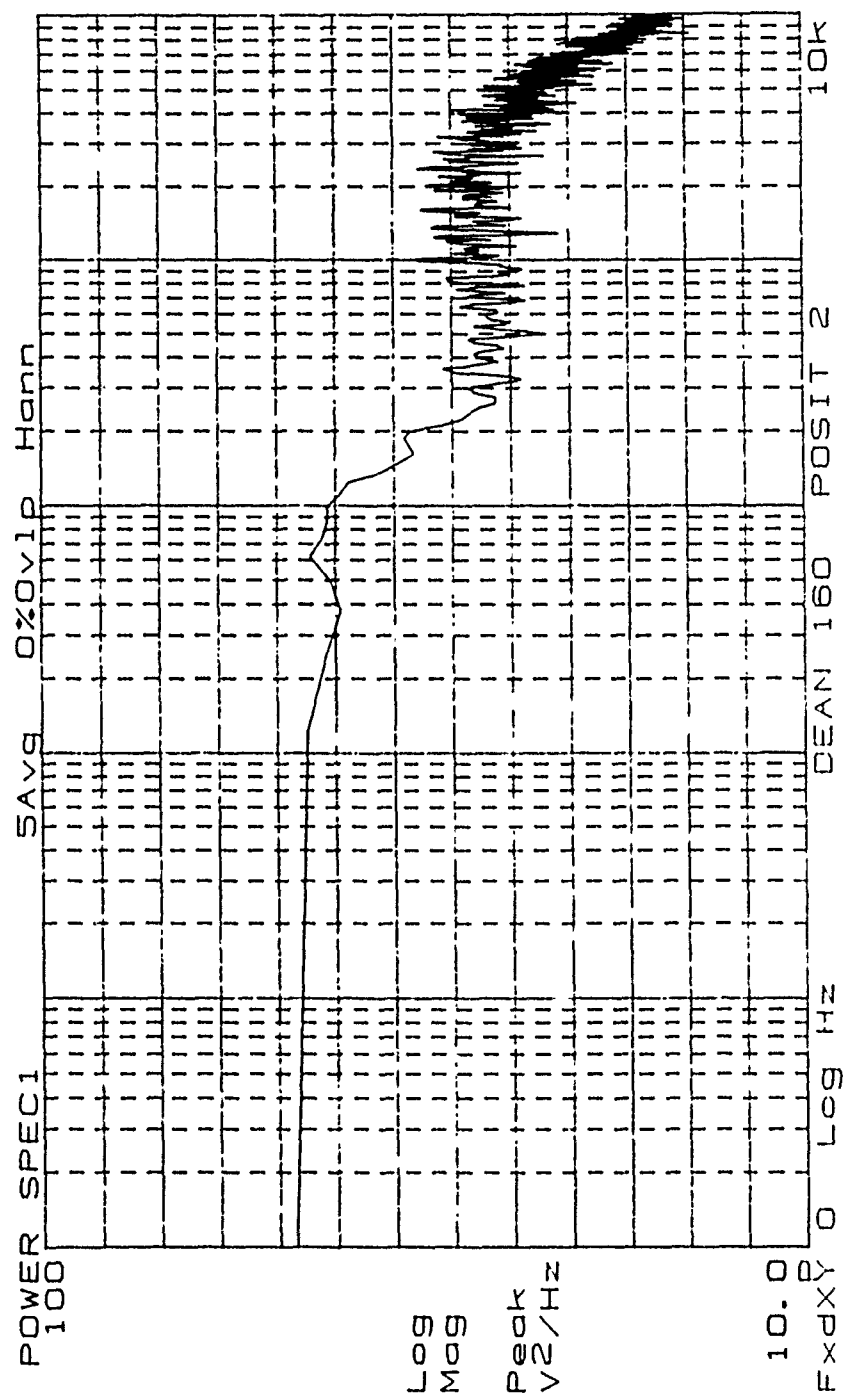


Figure 170. High Frequency Power Spectrum, De=160, Position 2

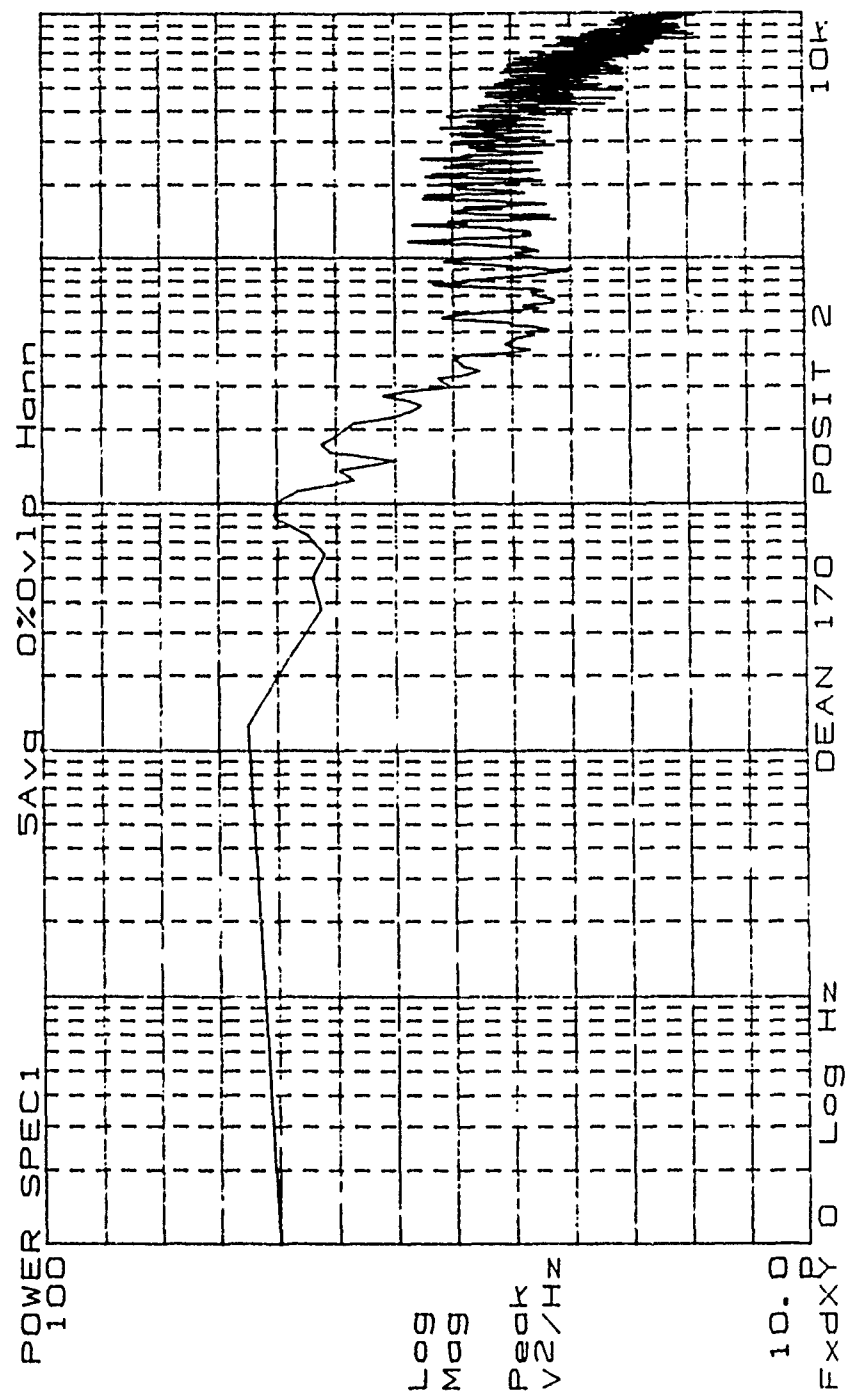


Figure 171. High Frequency Power Spectrum, De=170, Position 2

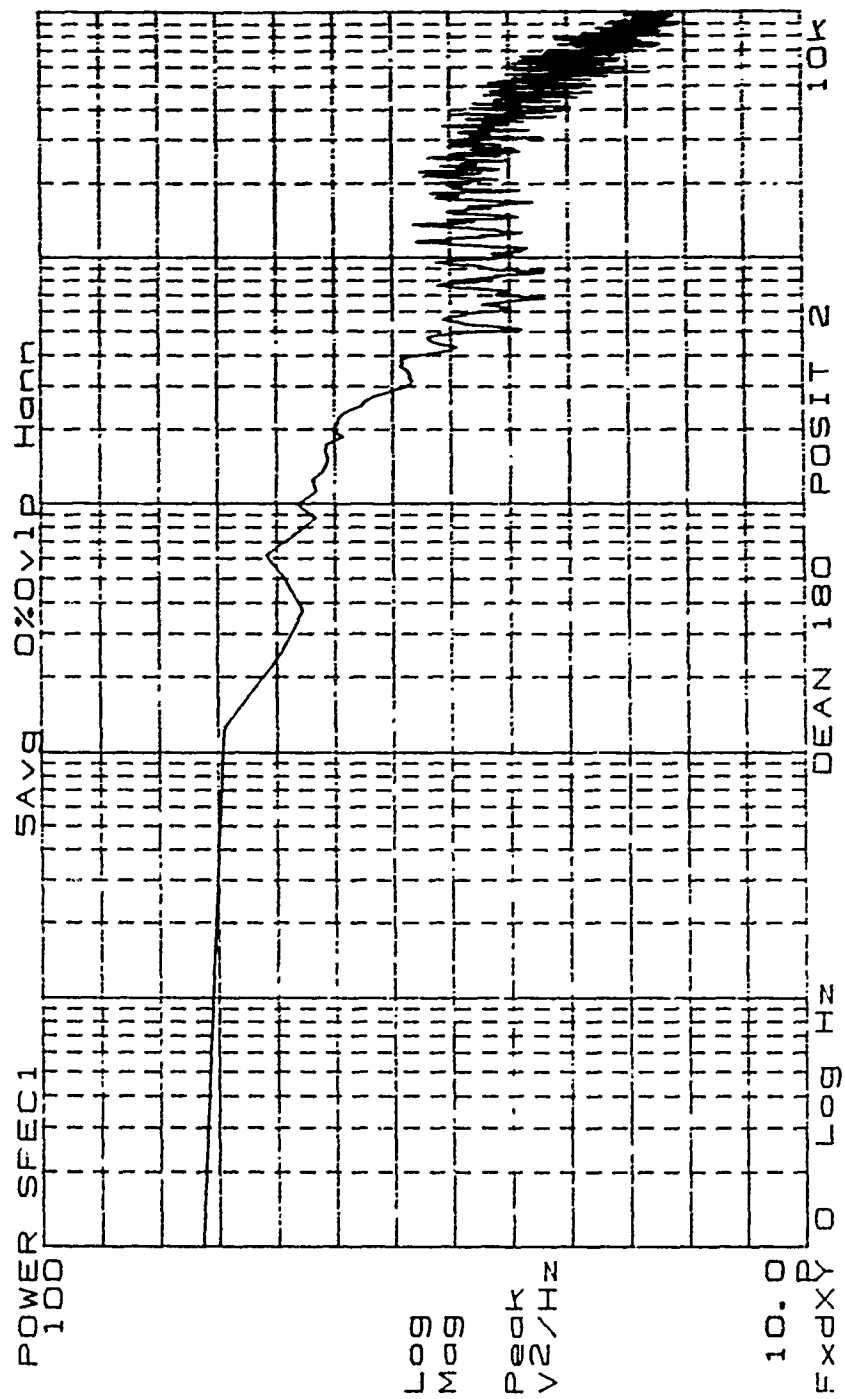


Figure 172. High Frequency Power Spectrum, De=180, Position 2

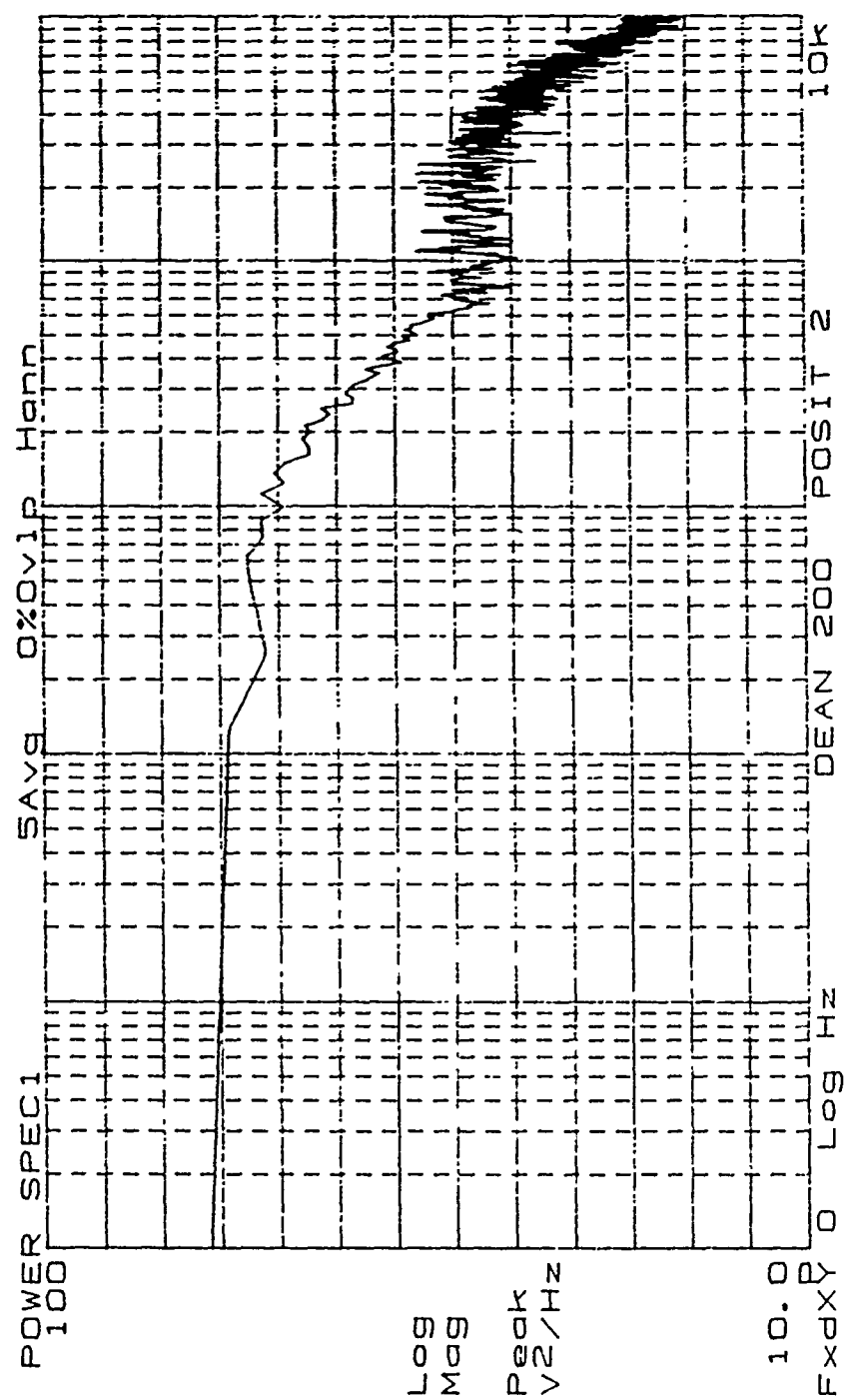


Figure 173. High Frequency Power Spectrum, De=200, Position 2

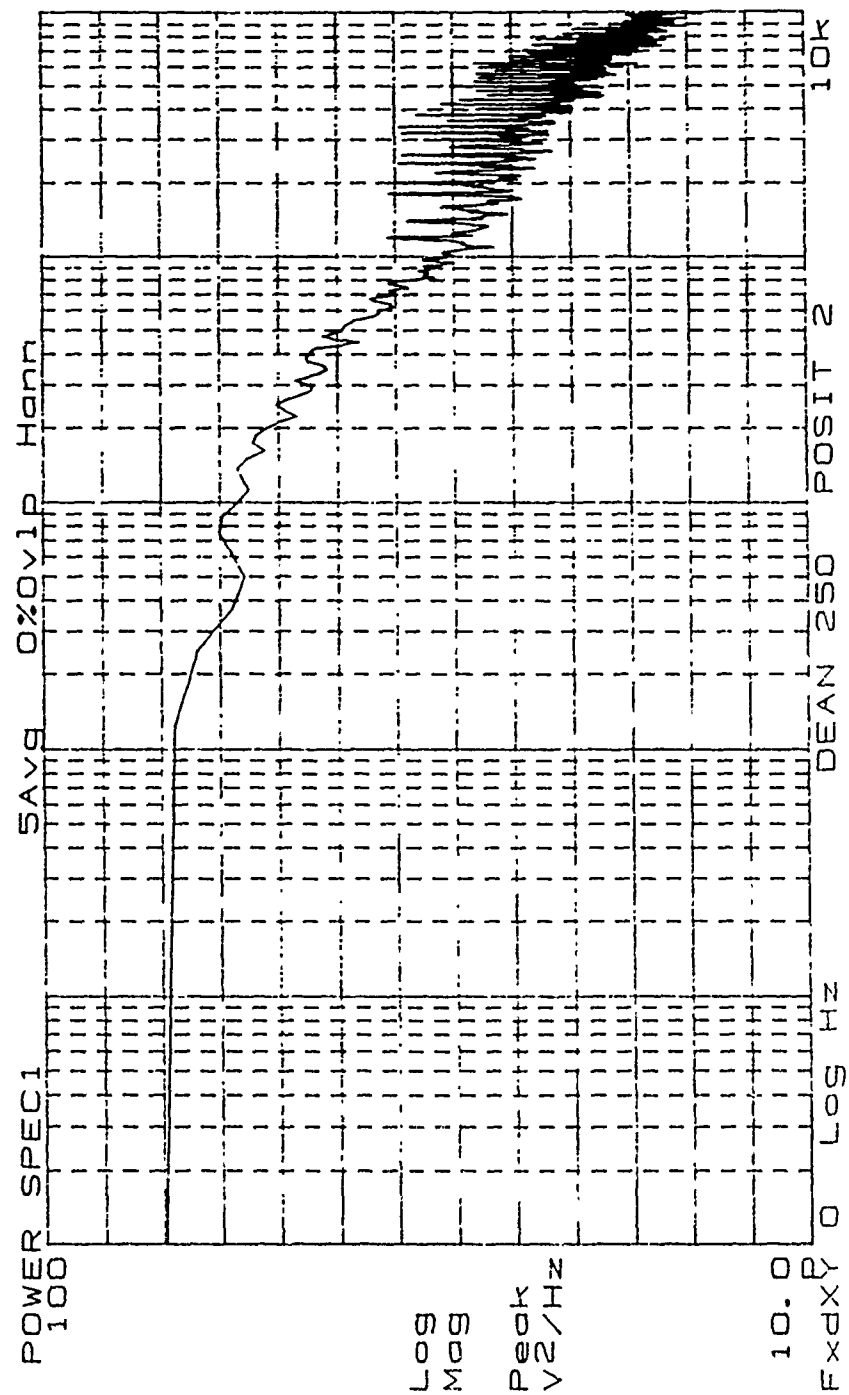


Figure 174. High Frequency Power Spectrum, De=250, Position 2

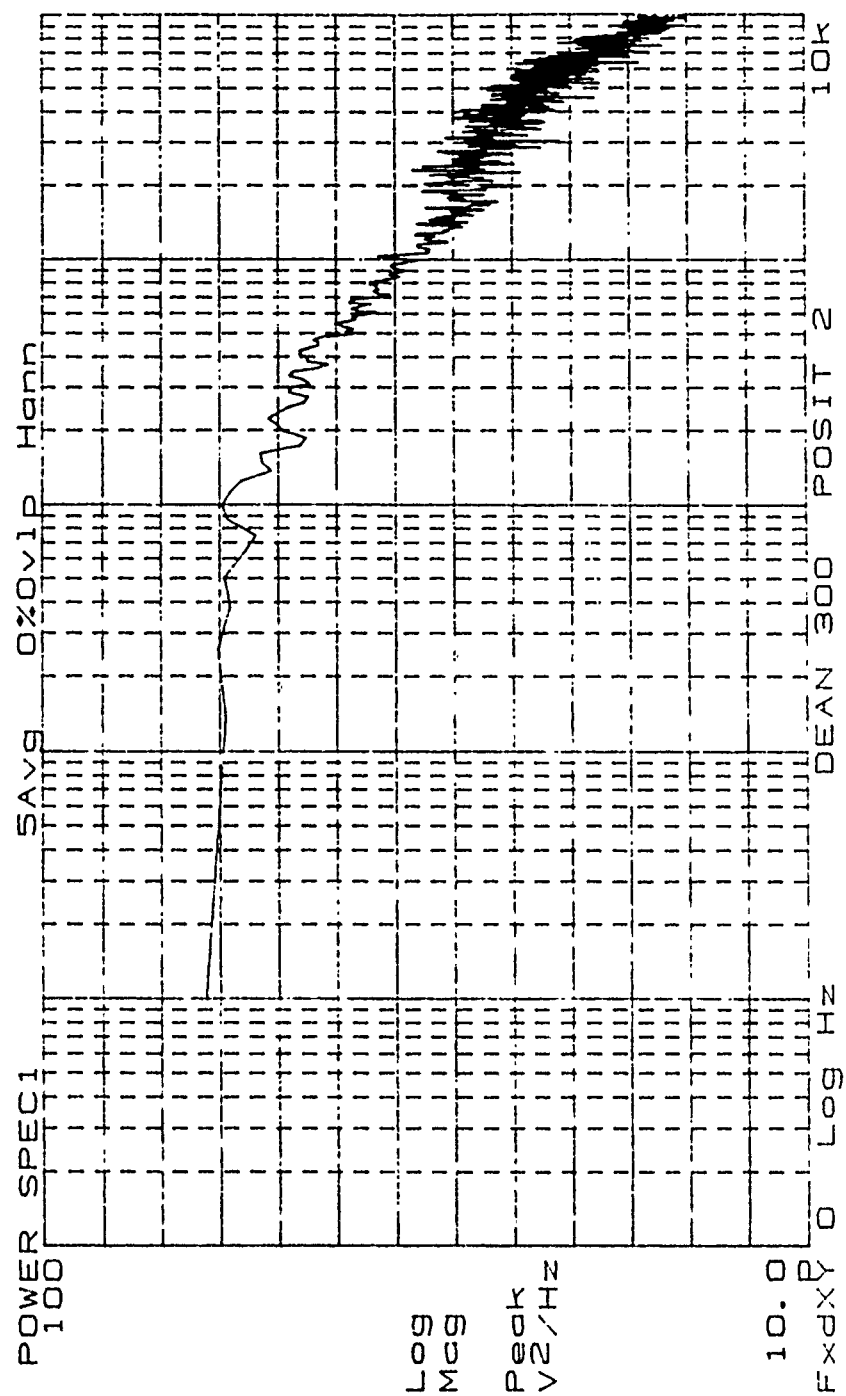


Figure 175. High Frequency Power Spectrum, De=300, Position 2

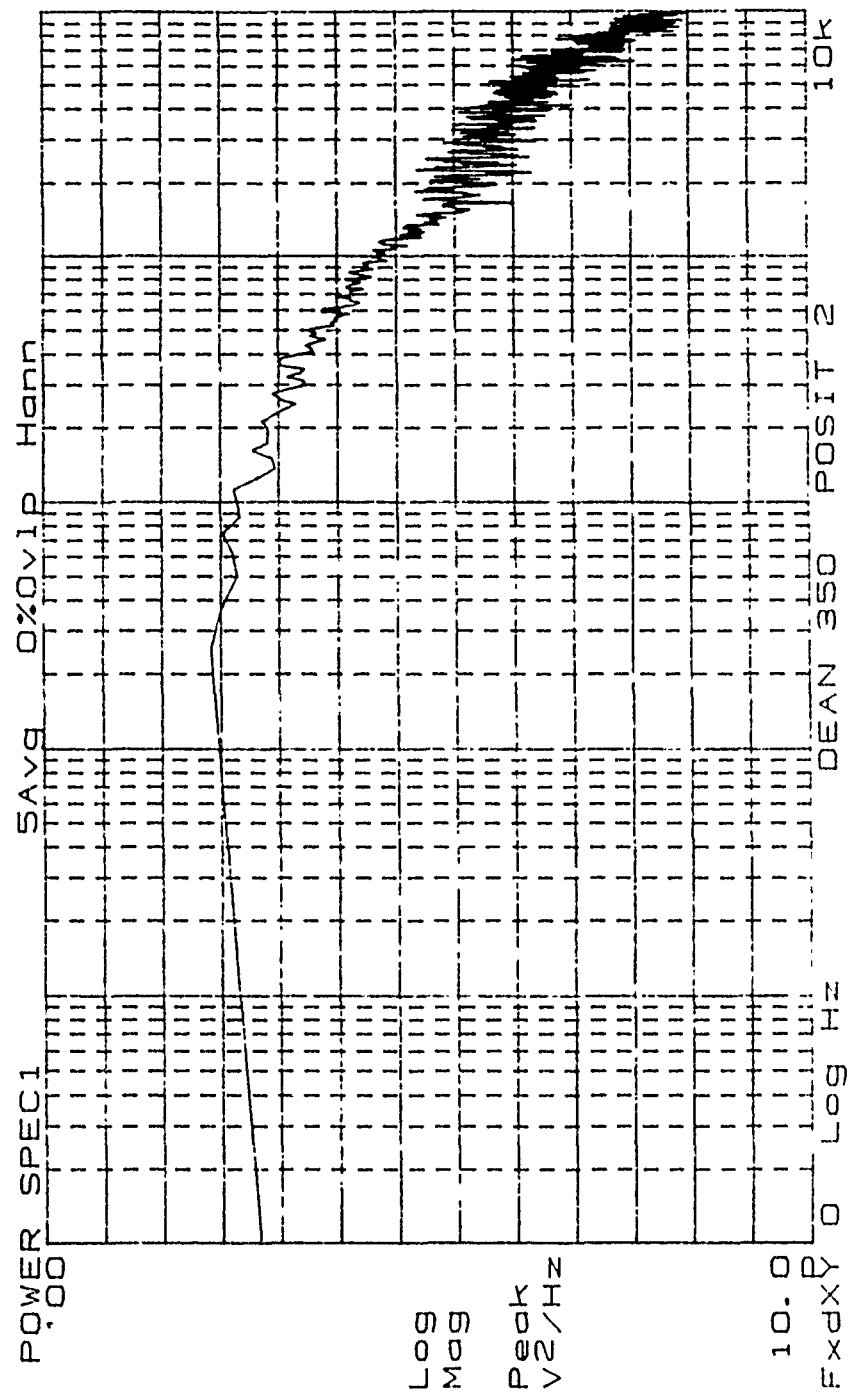


Figure 176. High Frequency Power Spectrum, De=350, Position 2

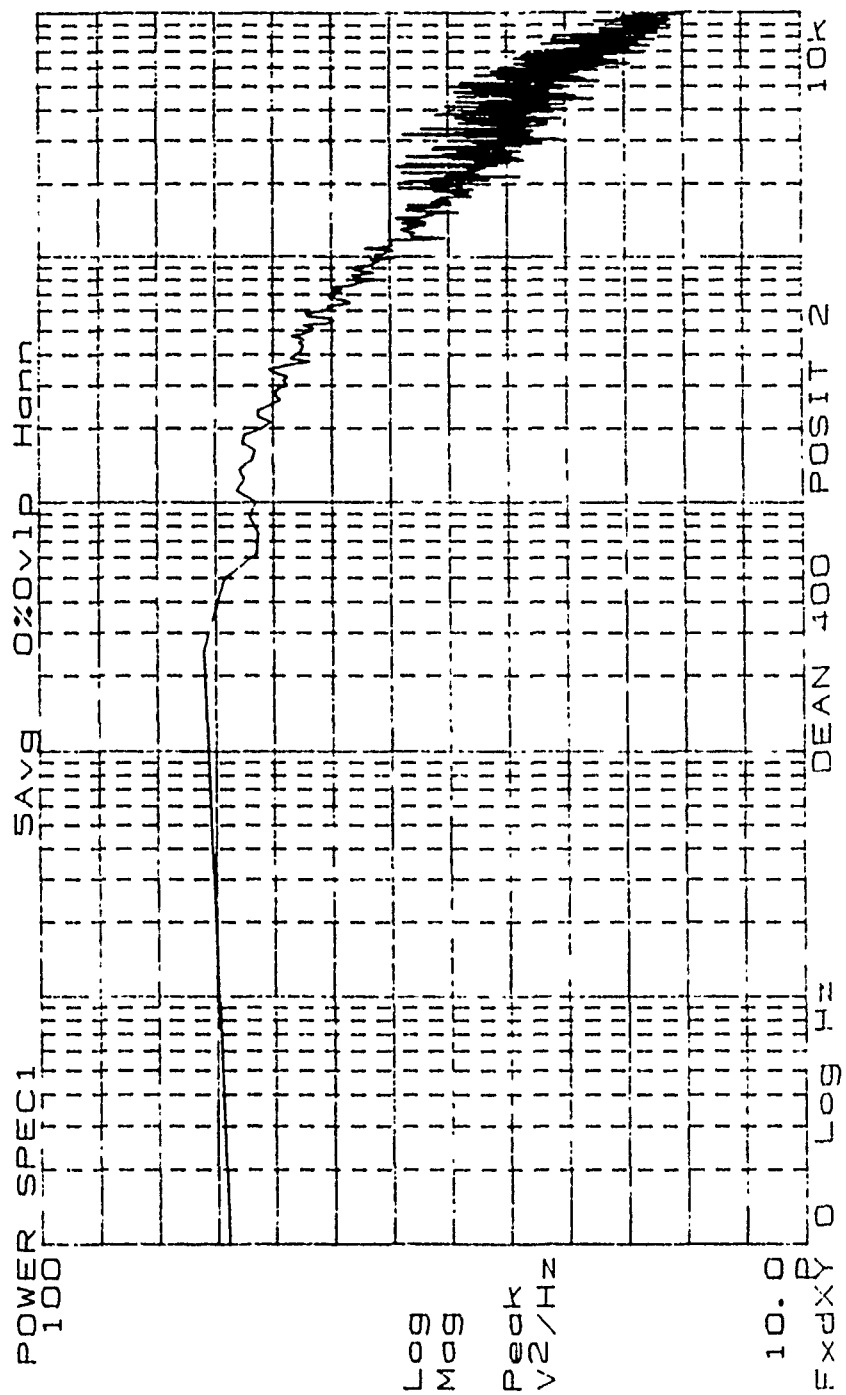


Figure 177. High Frequency Power Spectrum, De=400, Position 2

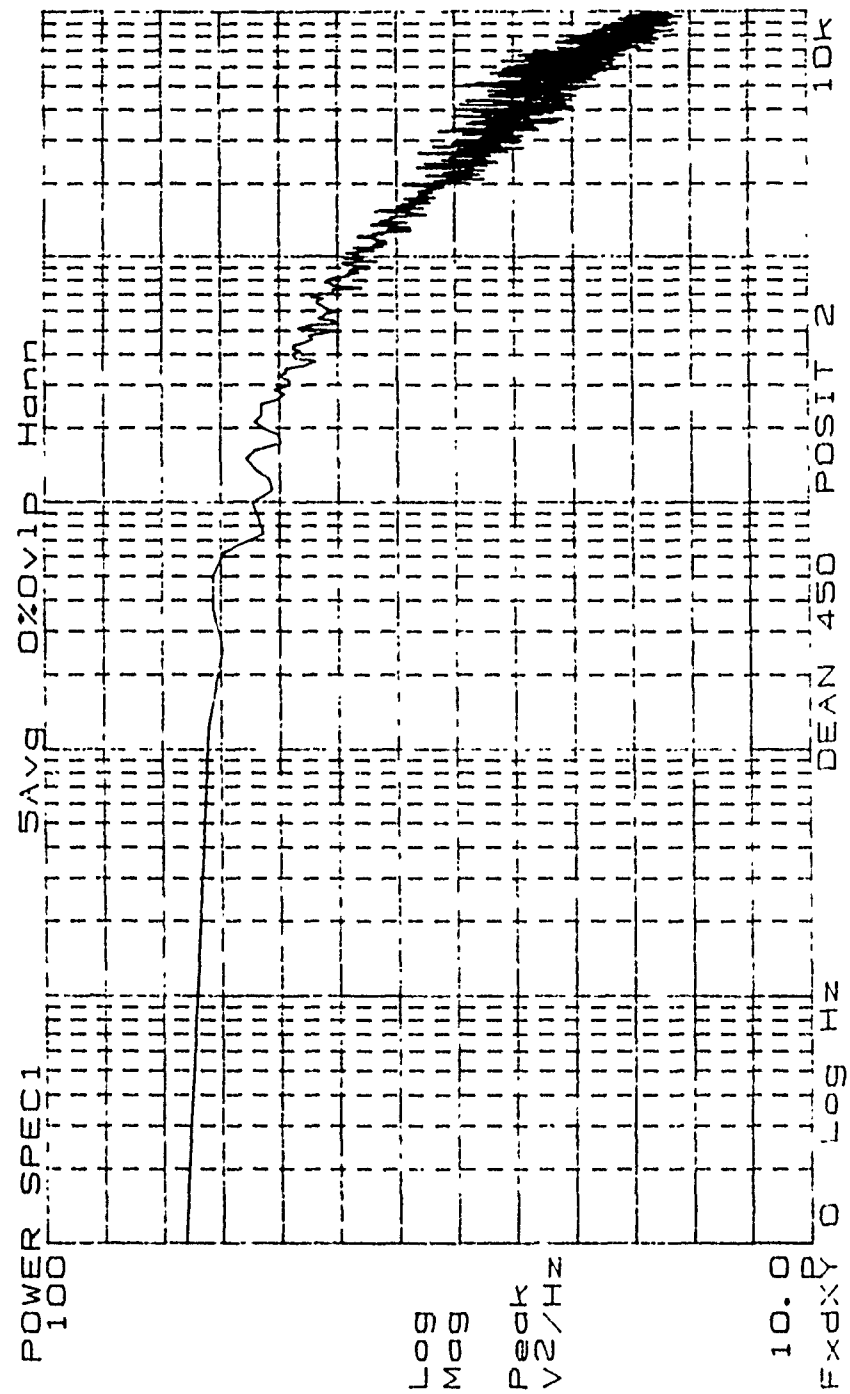


Figure 178. High Frequency Power Spectrum, De=450, Position 2

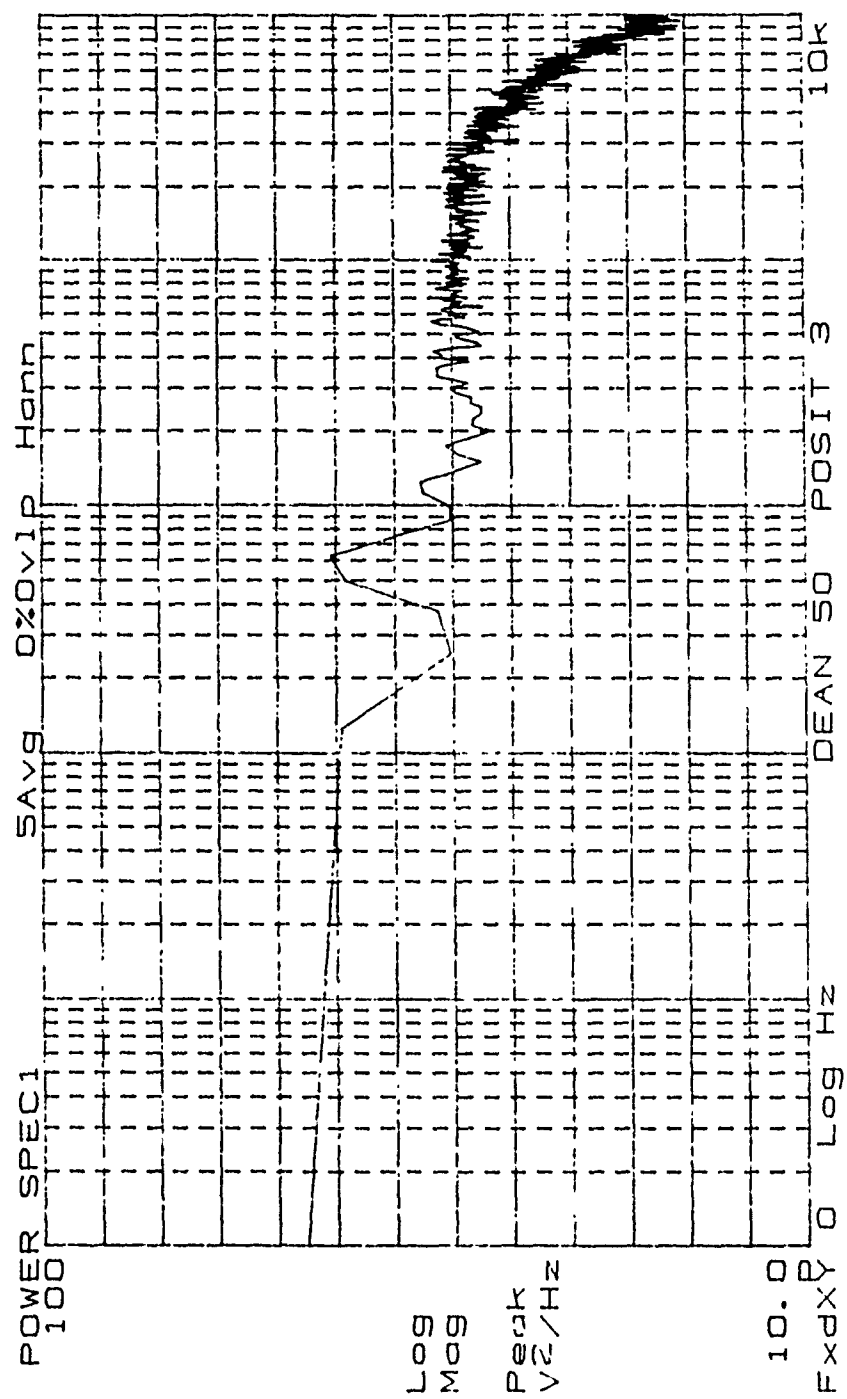


Figure 179. High Frequency Power Spectrum, De=50, Position 3

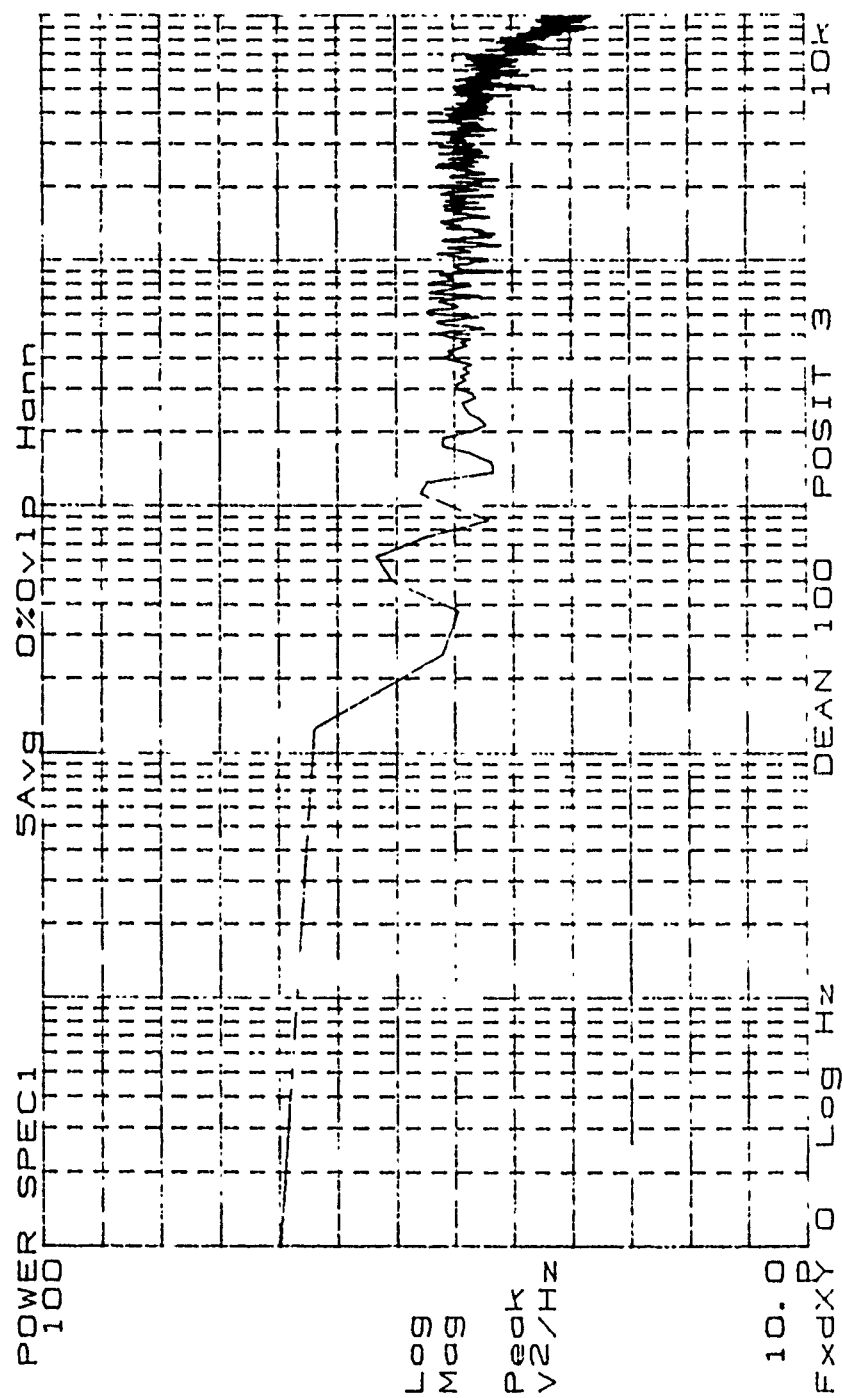


Figure 180. High Frequency Power Spectrum, De=100, Position 3

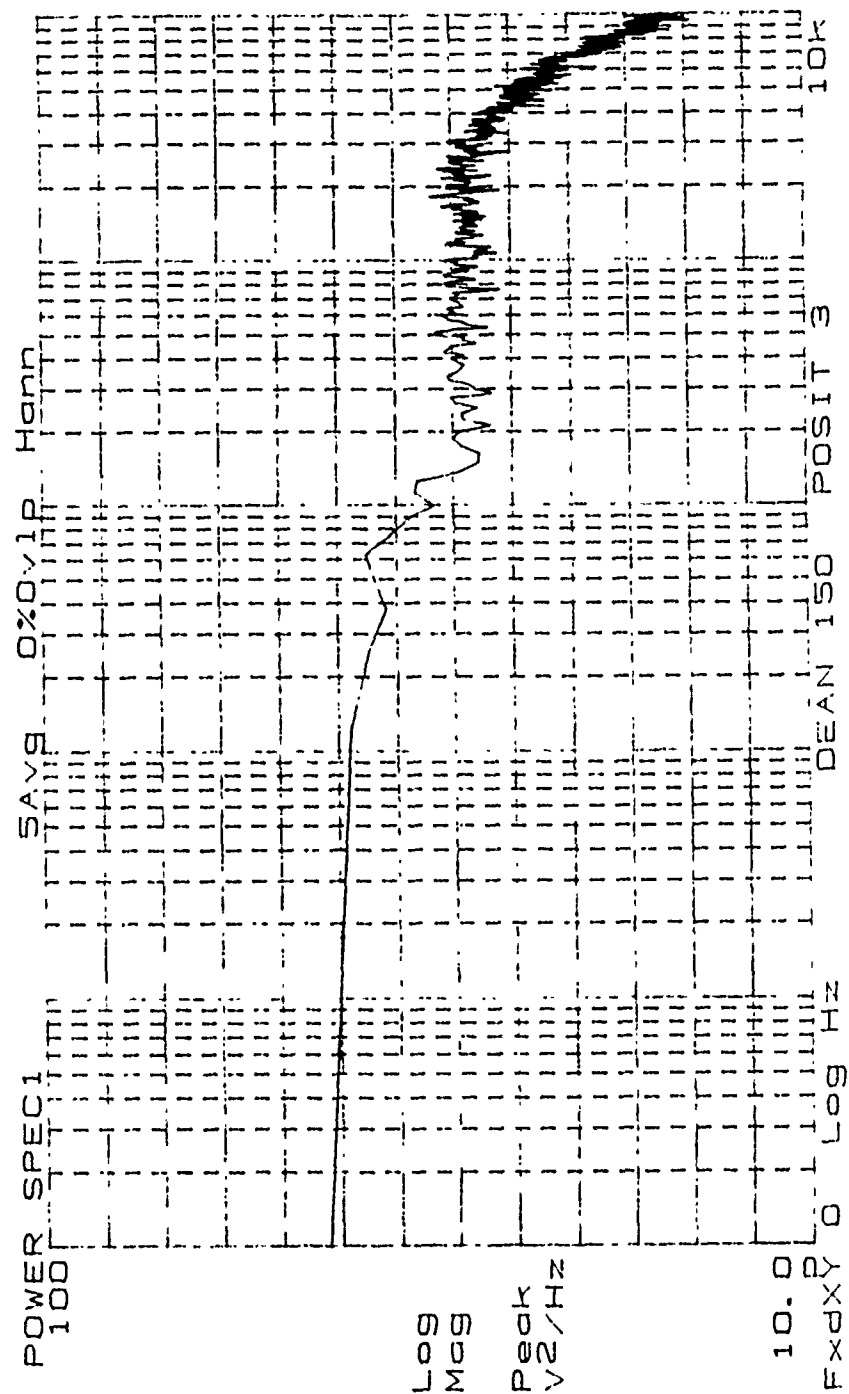


Figure 181. High Frequency Power Spectrum, De=150, Position 3

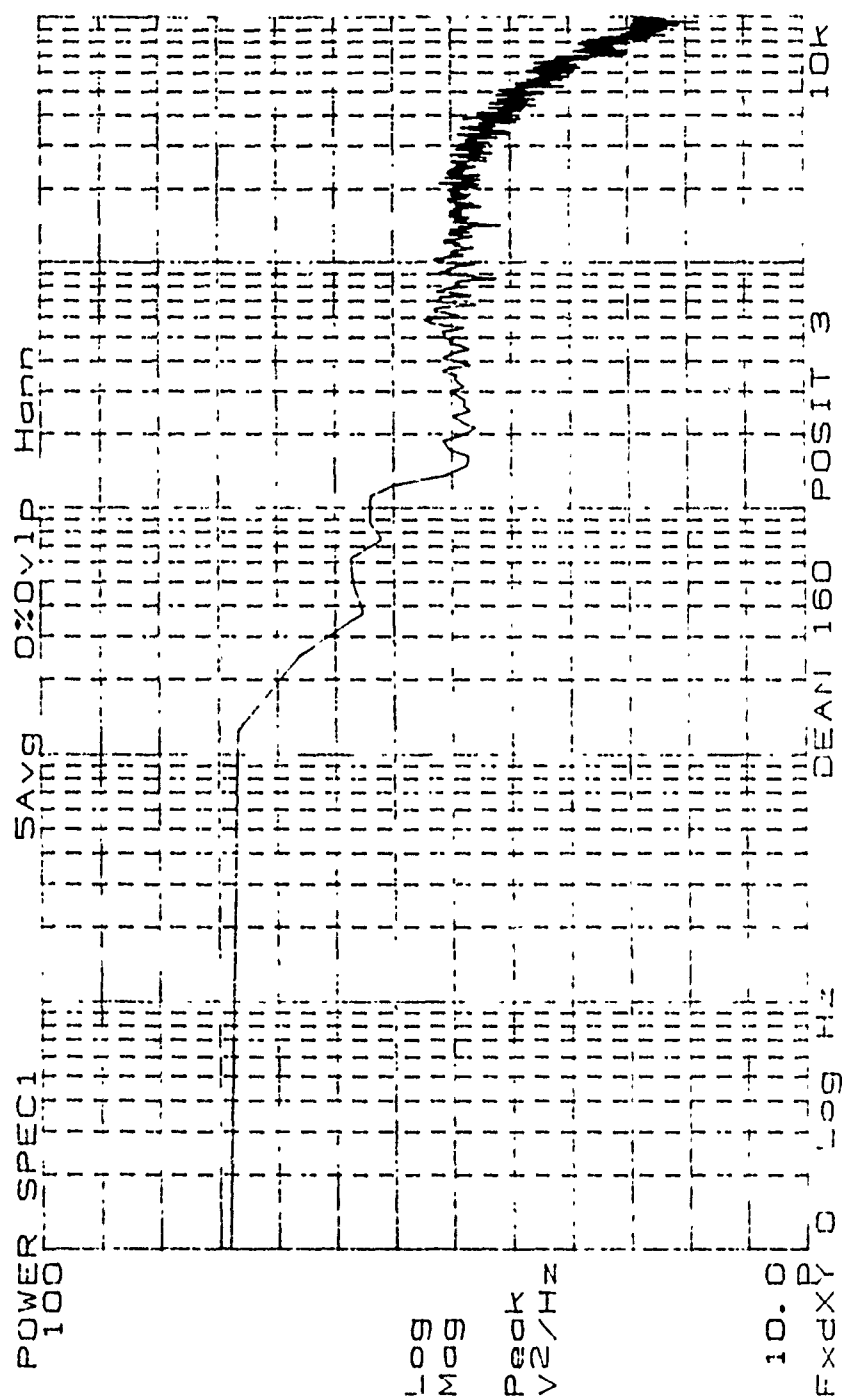


Figure 182. High Frequency Power Spectrum, De=160, Position 3

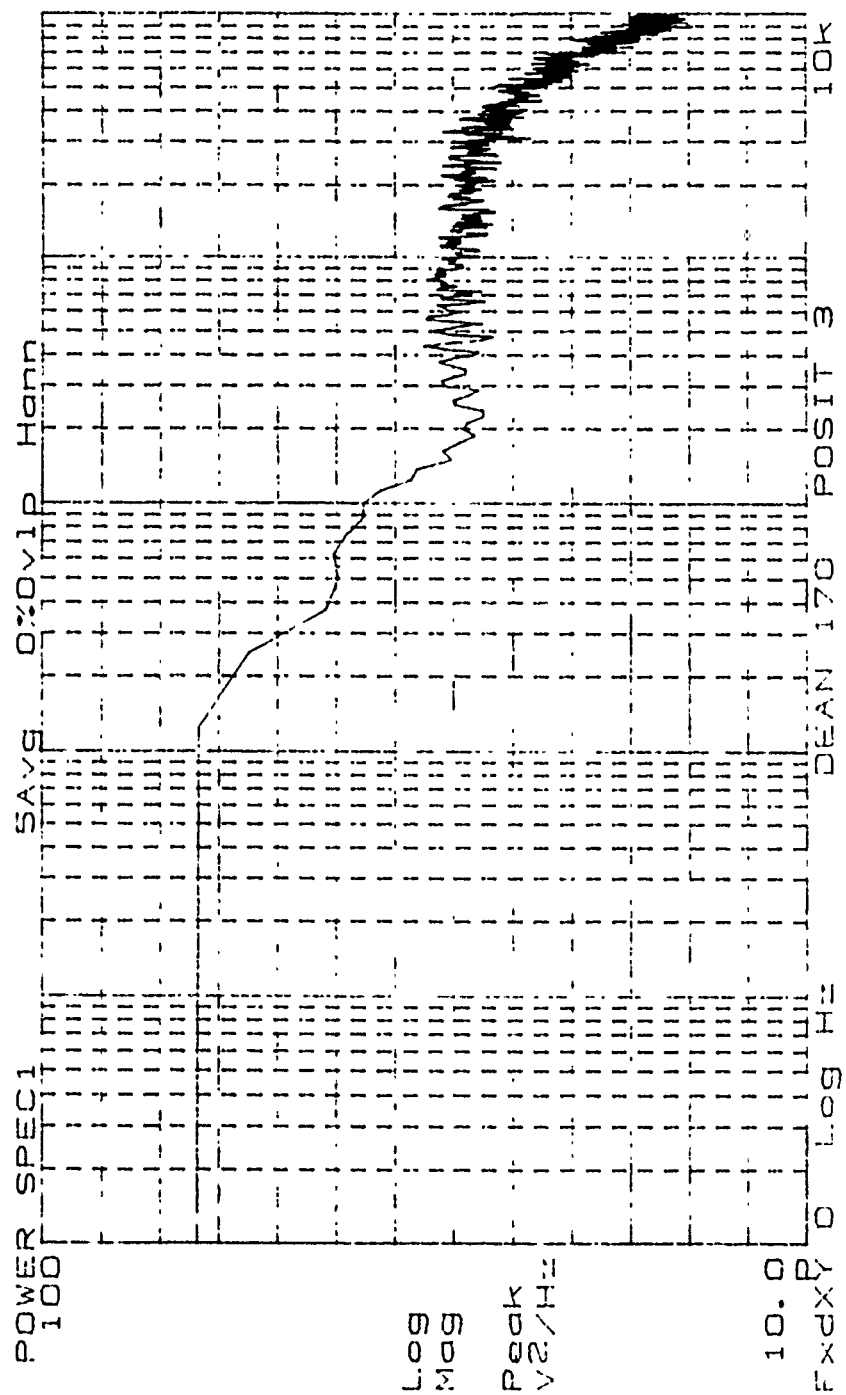


Figure 183. High Frequency Power Spectrum, De=170, Position 3

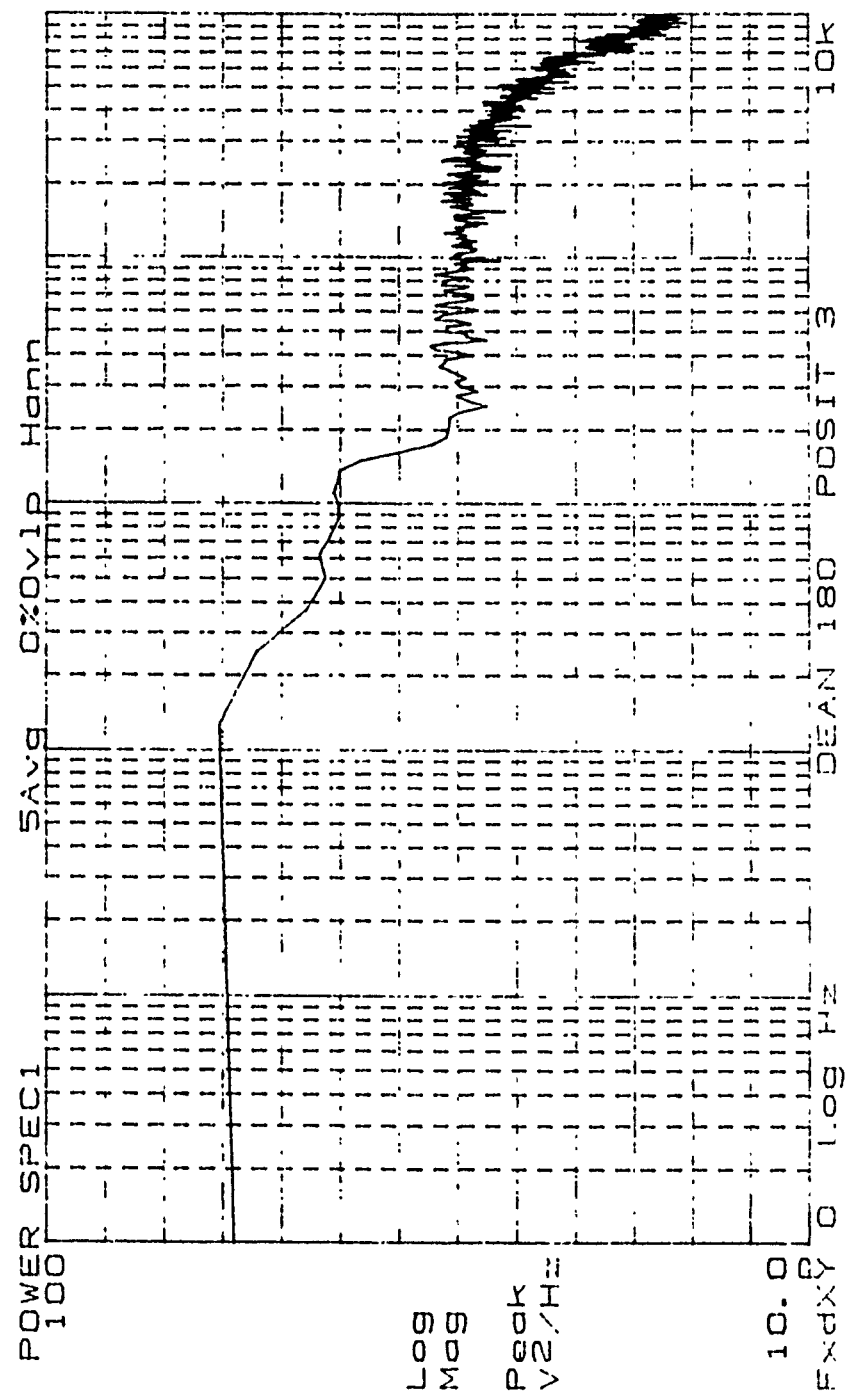


Figure 184. High Frequency Power Spectrum, De=180, Position 3

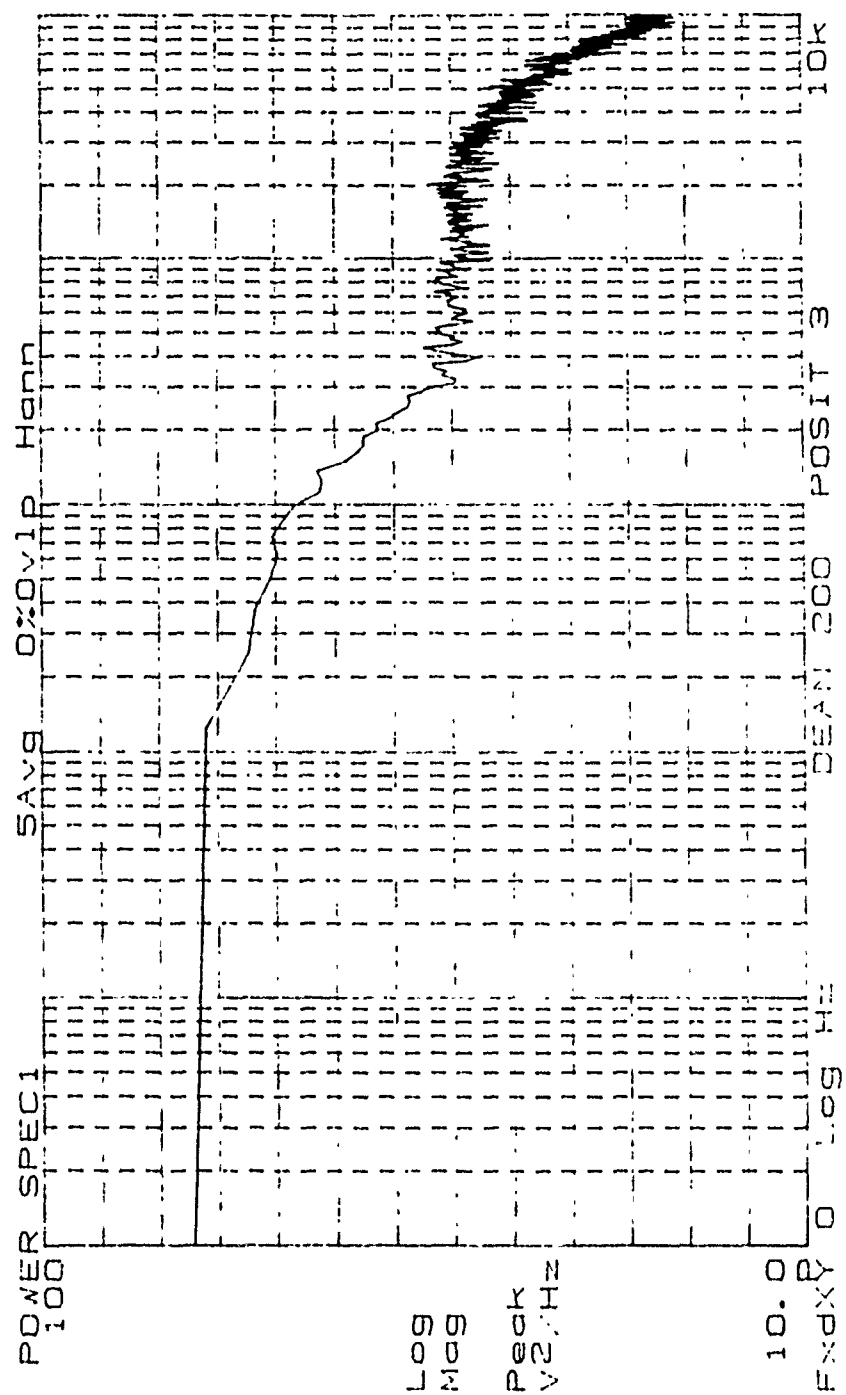


Figure 185. High Frequency Power Spectrum, De=200, Position 3

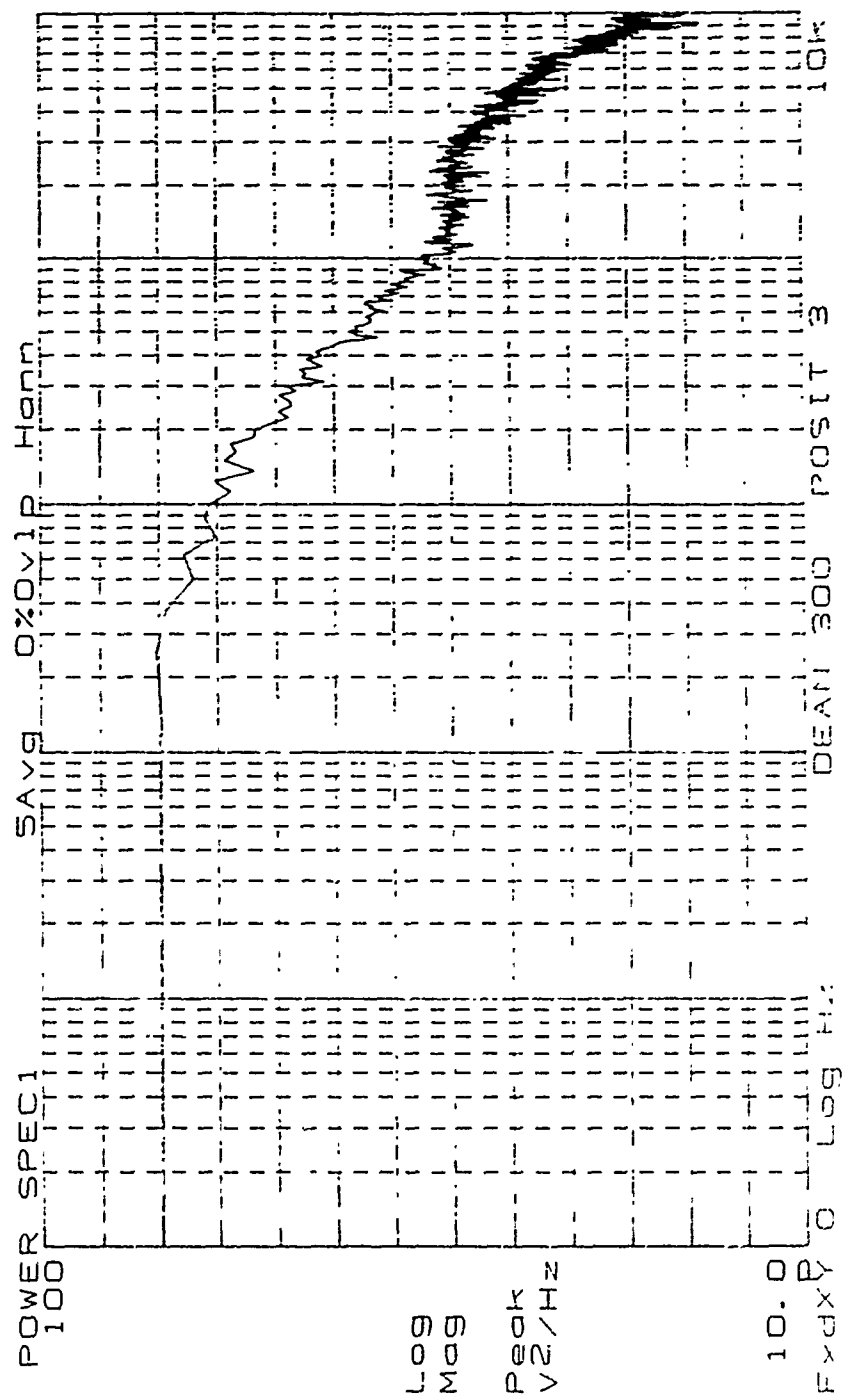


Figure 187. High Frequency Power Spectrum, De=300, Position 3

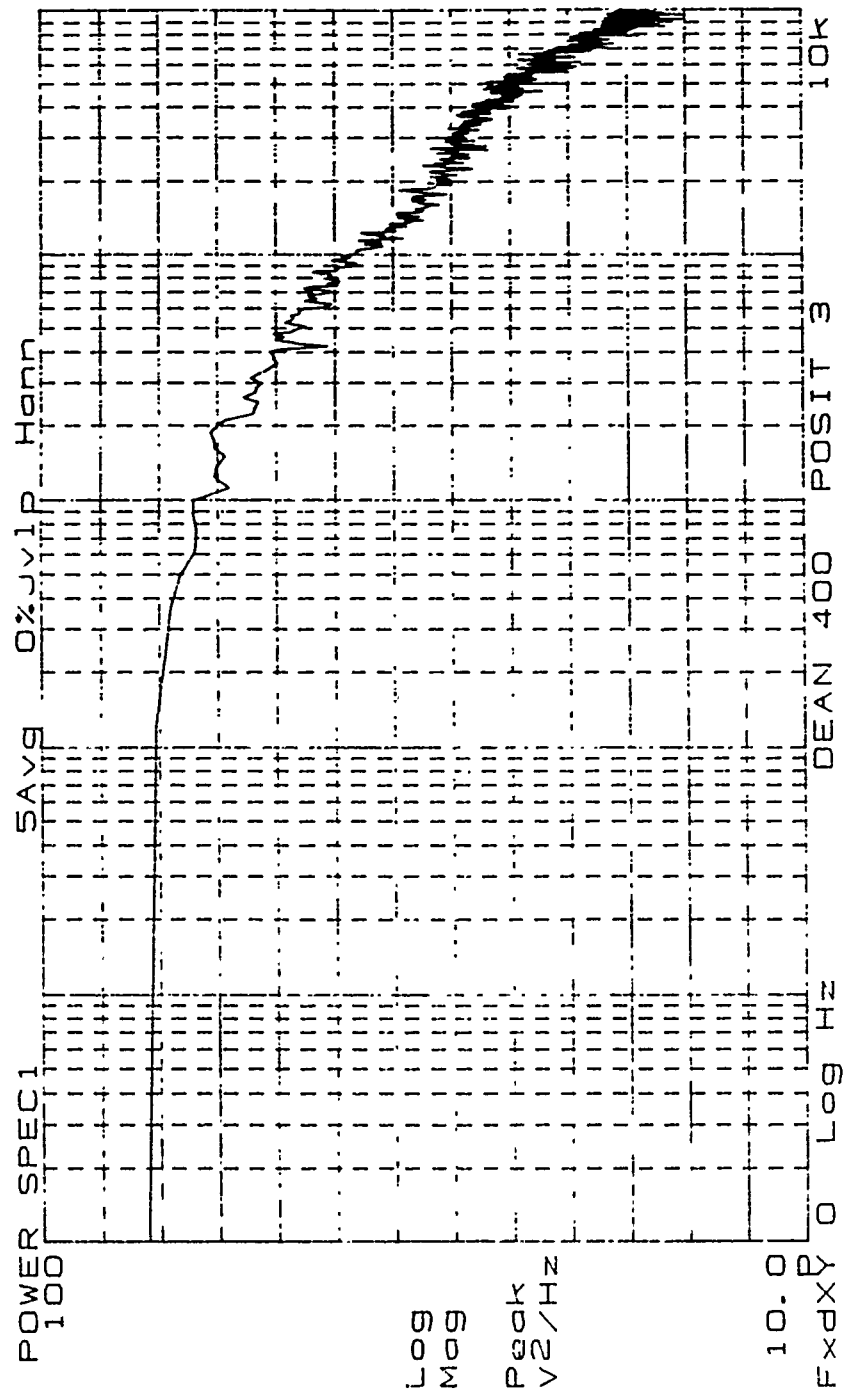


Figure 189. High Frequency Power Spectrum, De=400, Position 3

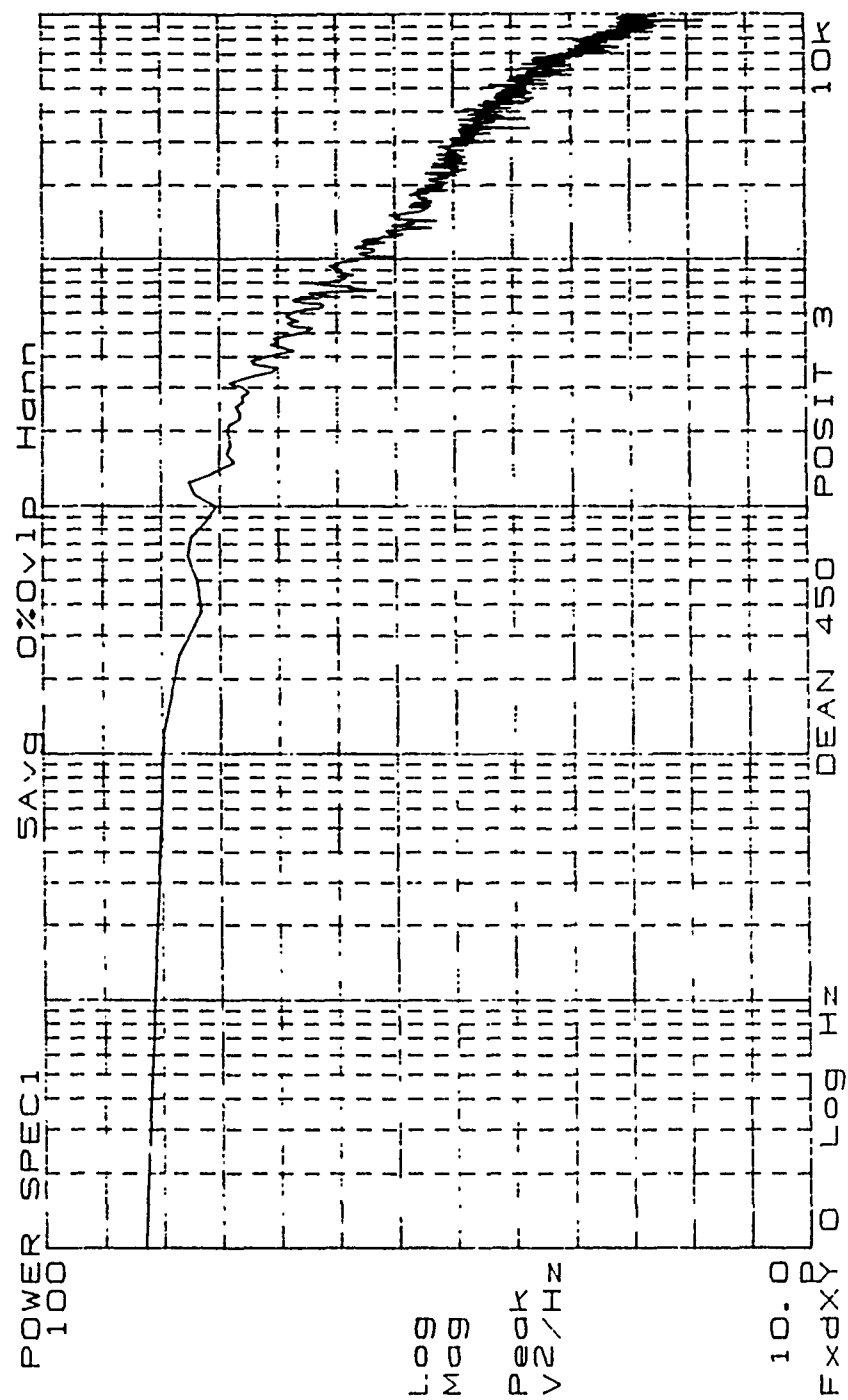


Figure 190. High Frequency Power Spectrum, De=450, Position 3

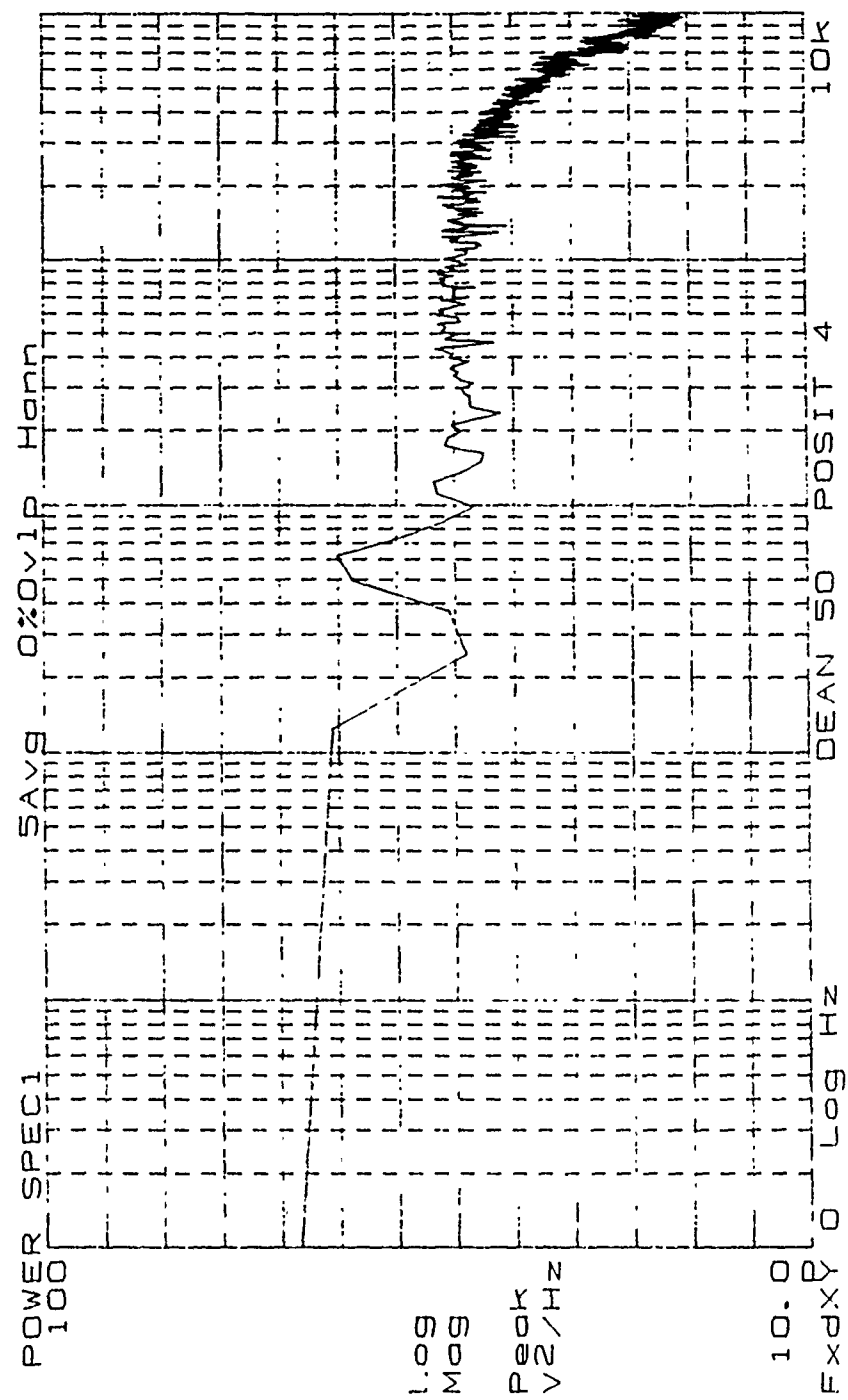


Figure 191. High Frequency Power Spectrum, De=50, Position 4

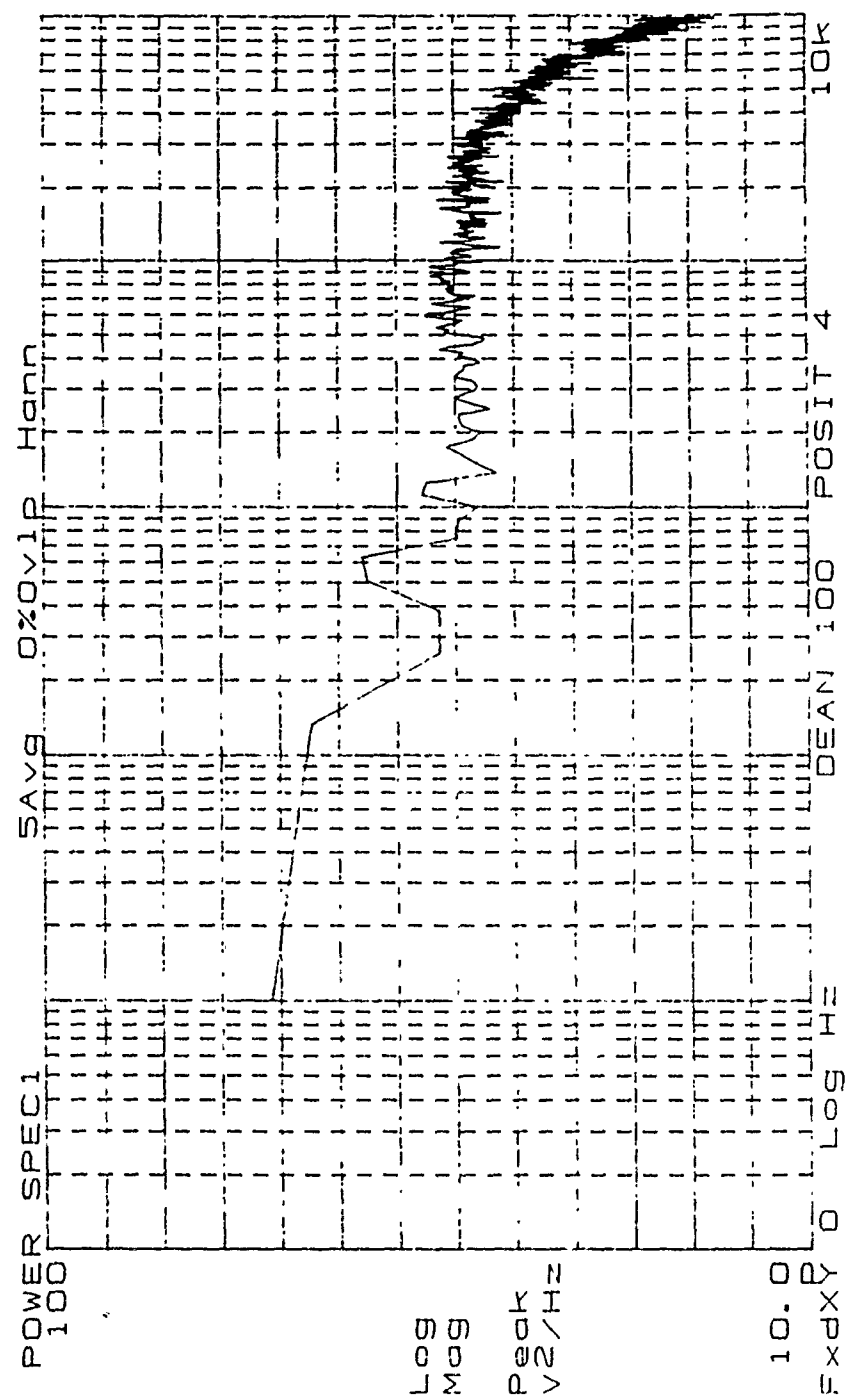


Figure 192. High Frequency Power Spectrum, De=100, Position 4

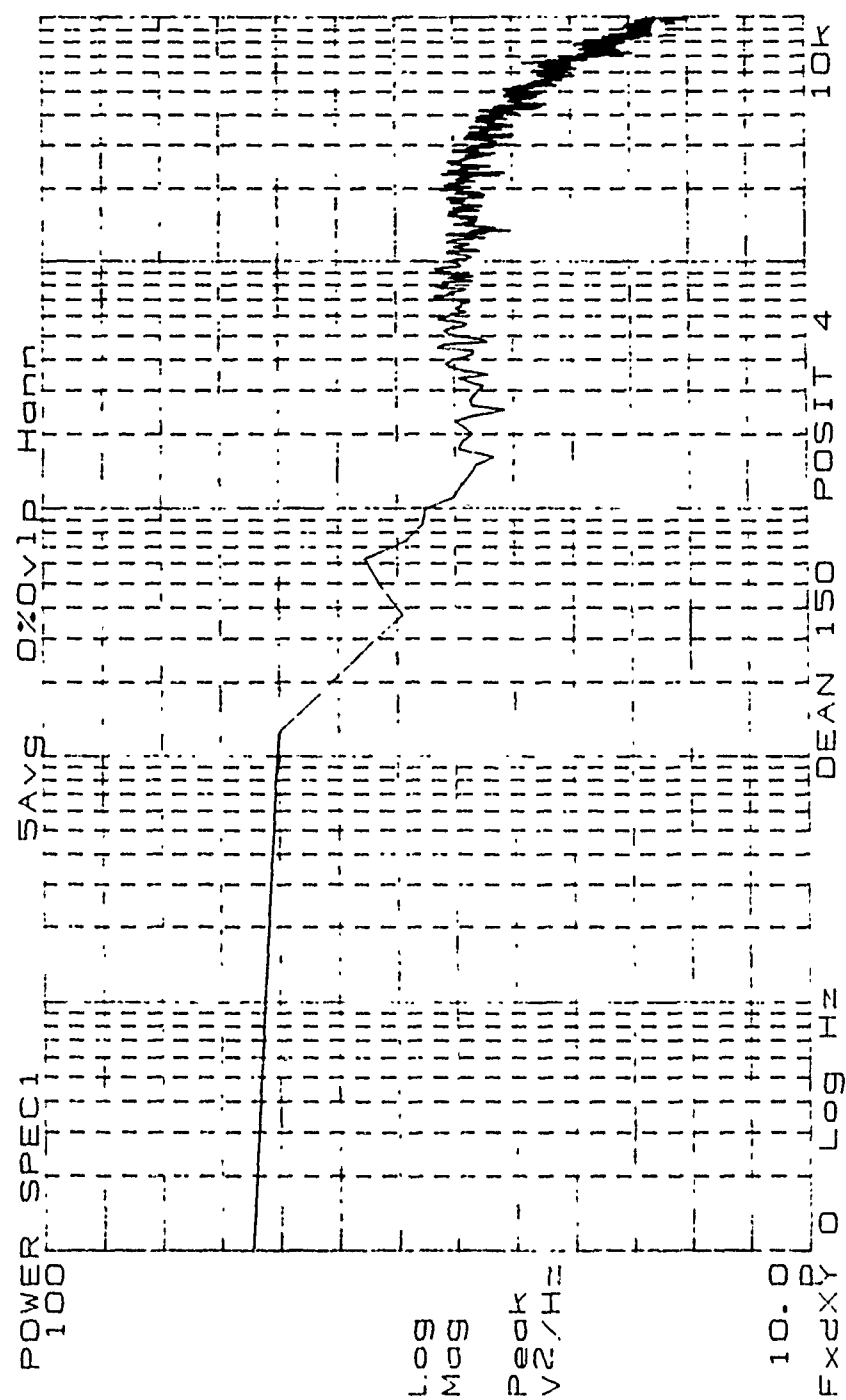


Figure 193. High Frequency Power Spectrum, De=150, Position 4

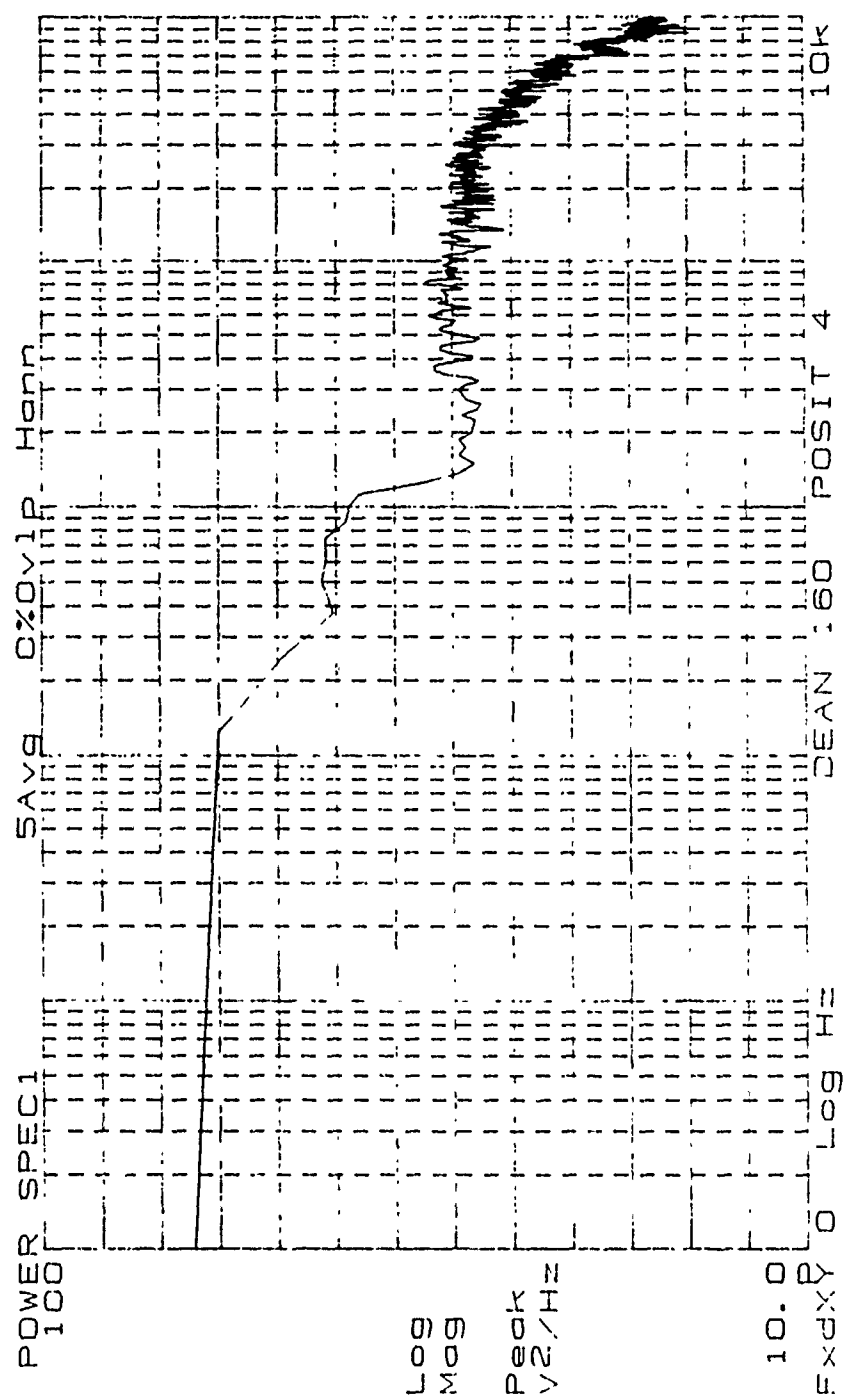


Figure 194. High Frequency Power Spectrum, De=160, Position 4

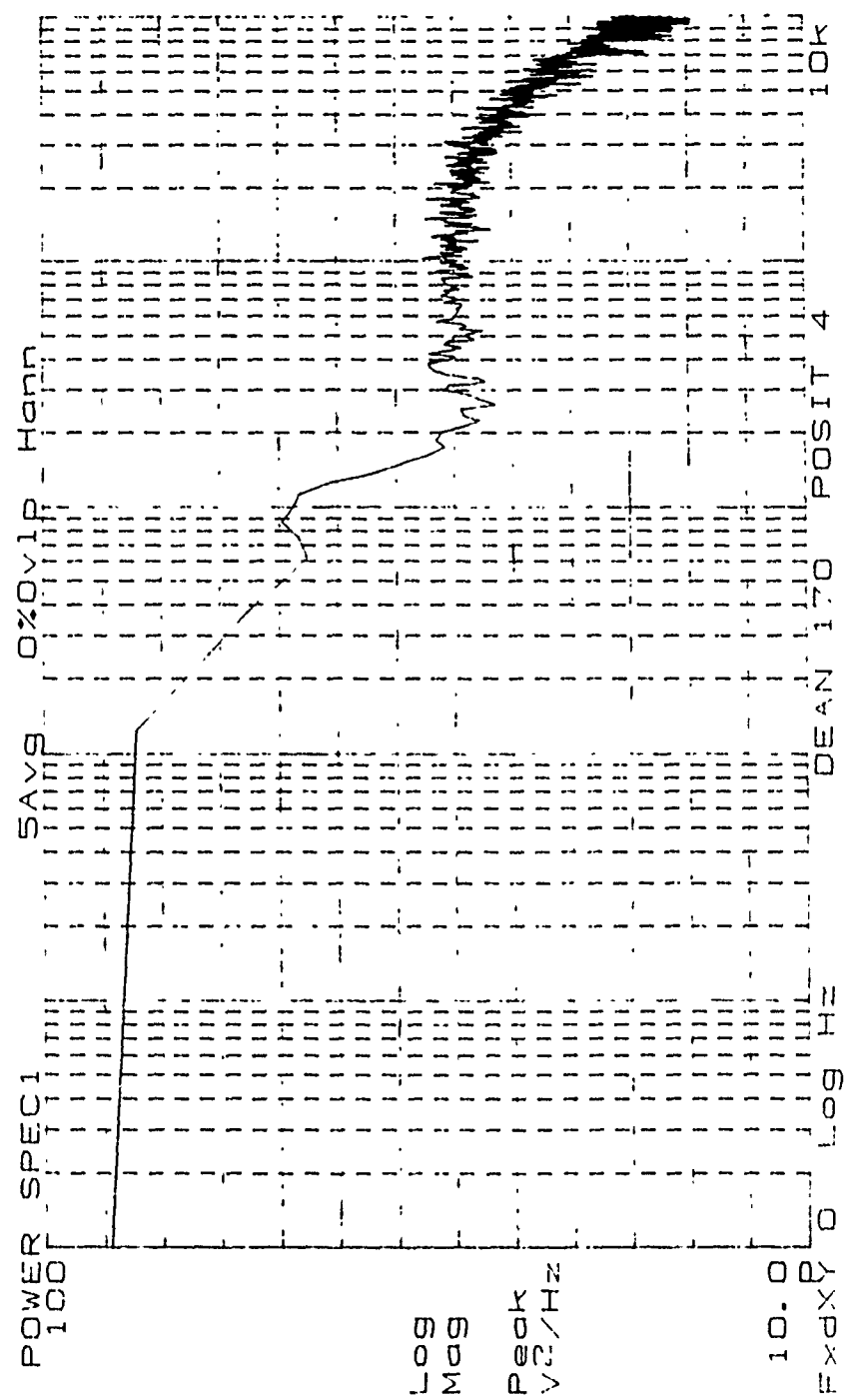


Figure 195. High Frequency Power Spectrum, De=170, Position 4

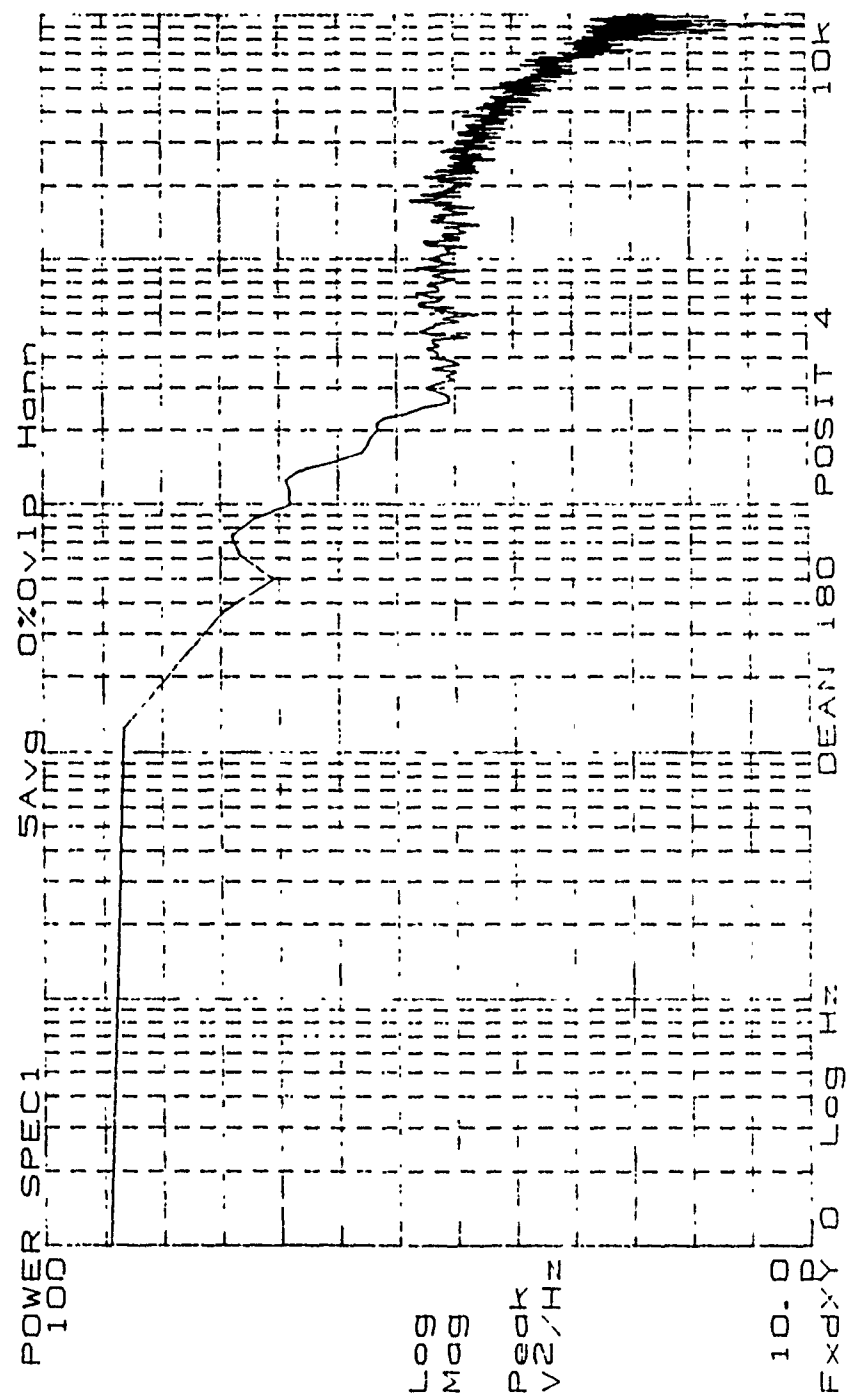


Figure 196. High Frequency Power Spectrum, De=180, Position 4

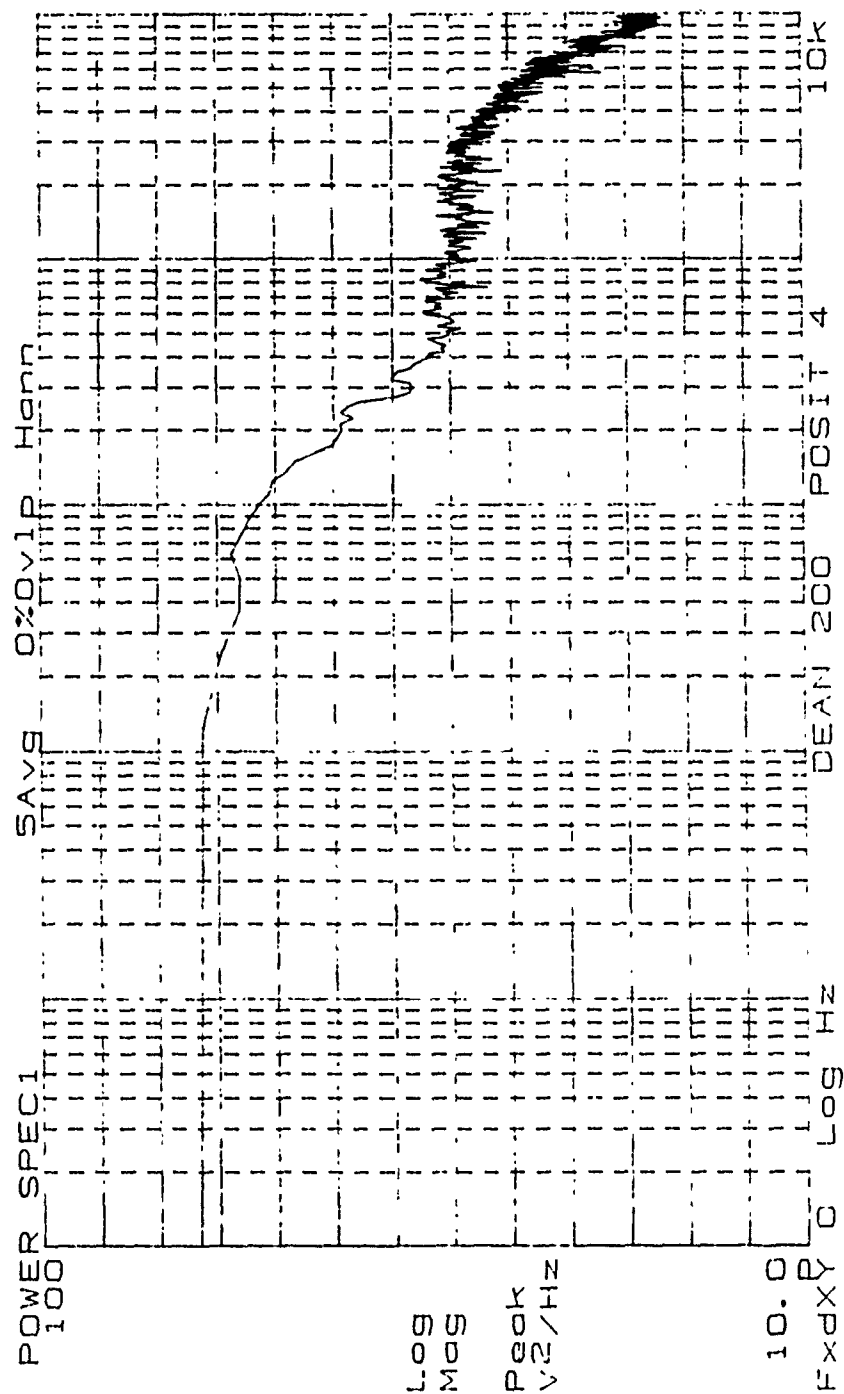


Figure 197. High Frequency Power Spectrum, De=200, Position 4



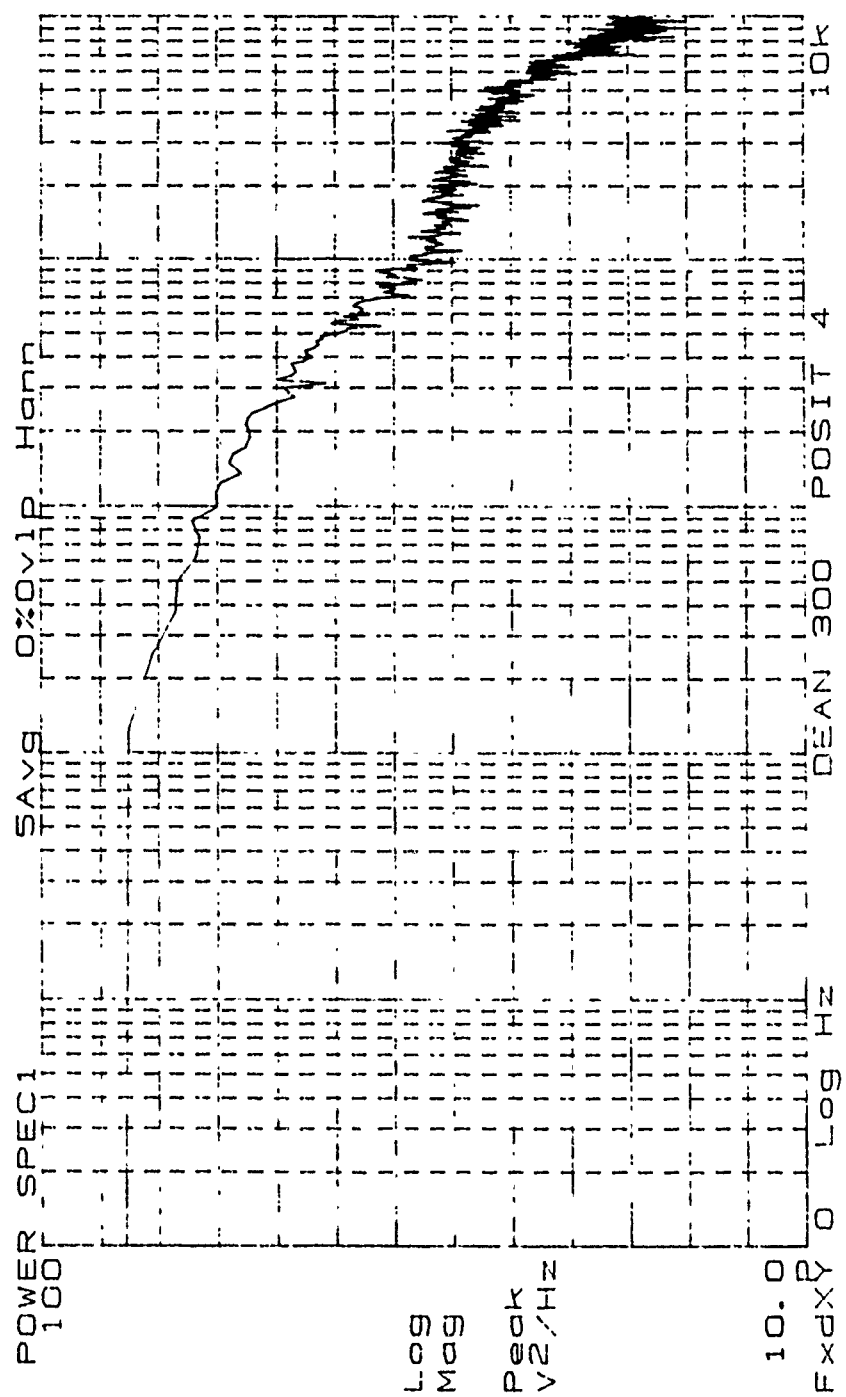


Figure 199. High Frequency Power Spectrum, De=300, Position 4

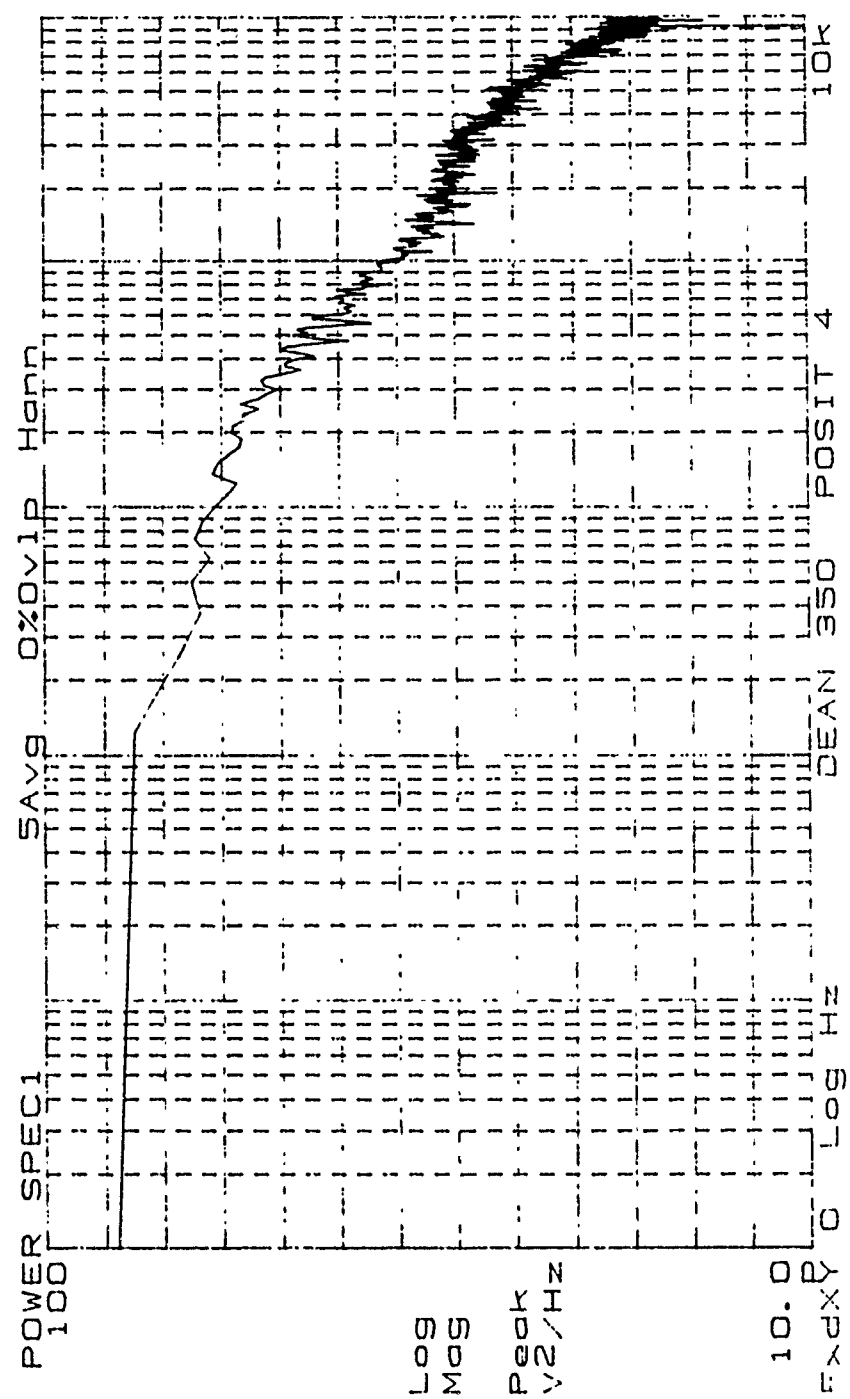


Figure 200. High Frequency Power Spectrum, De=350, Position 4

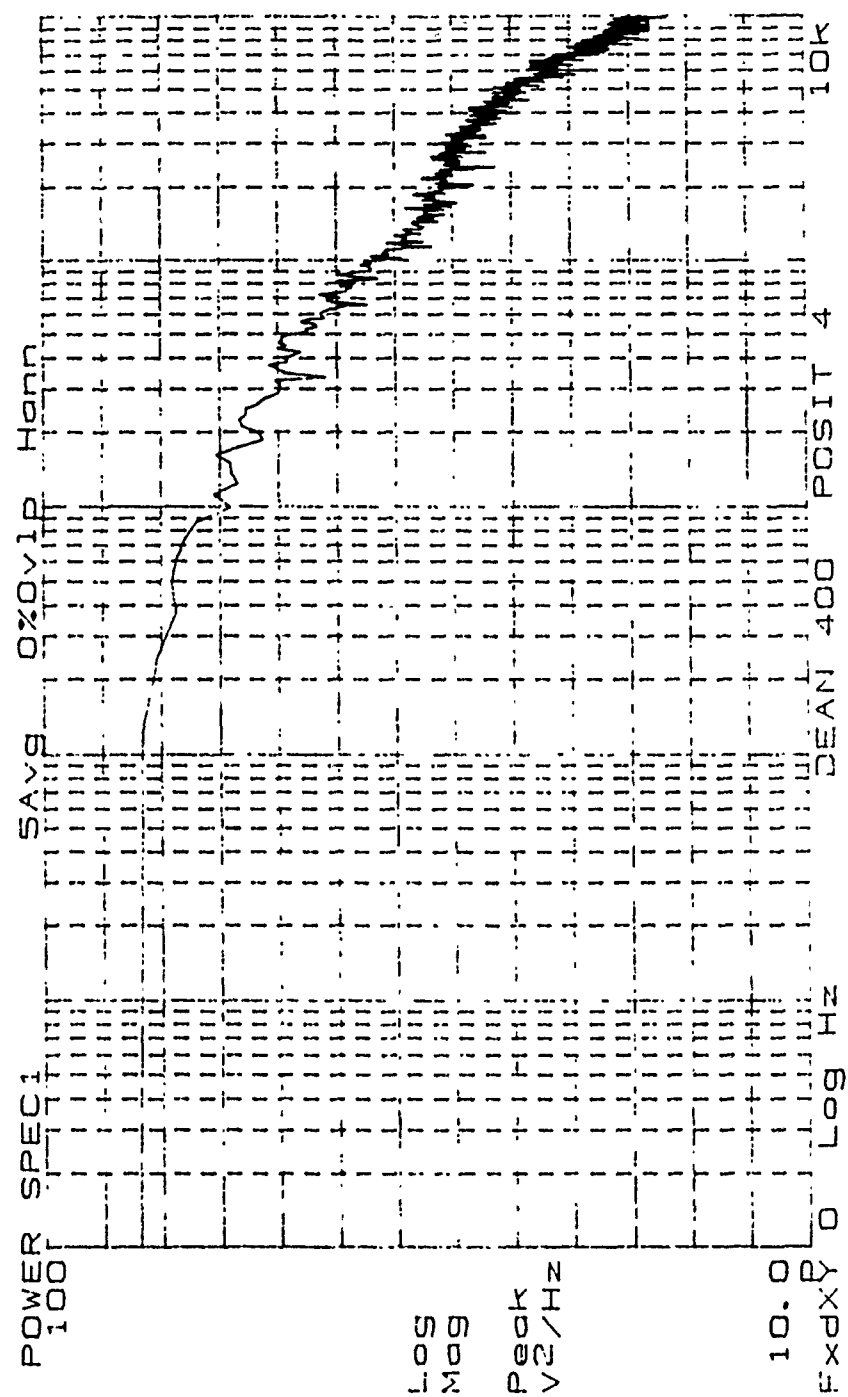


Figure 201. High Frequency Power Spectrum, De=400, Position 4

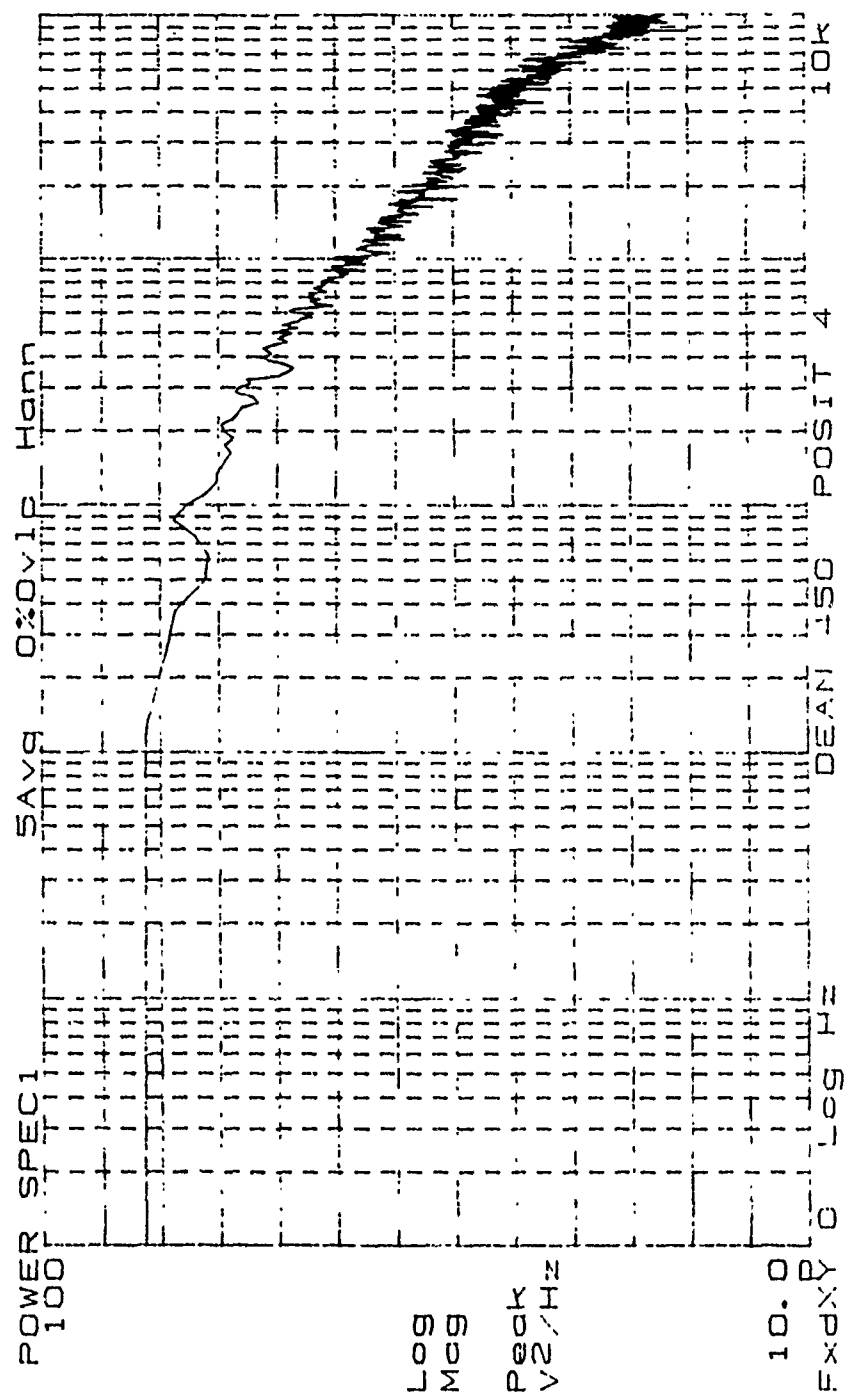


Figure 202. High Frequency Power Spectrum, De=450, Position 4

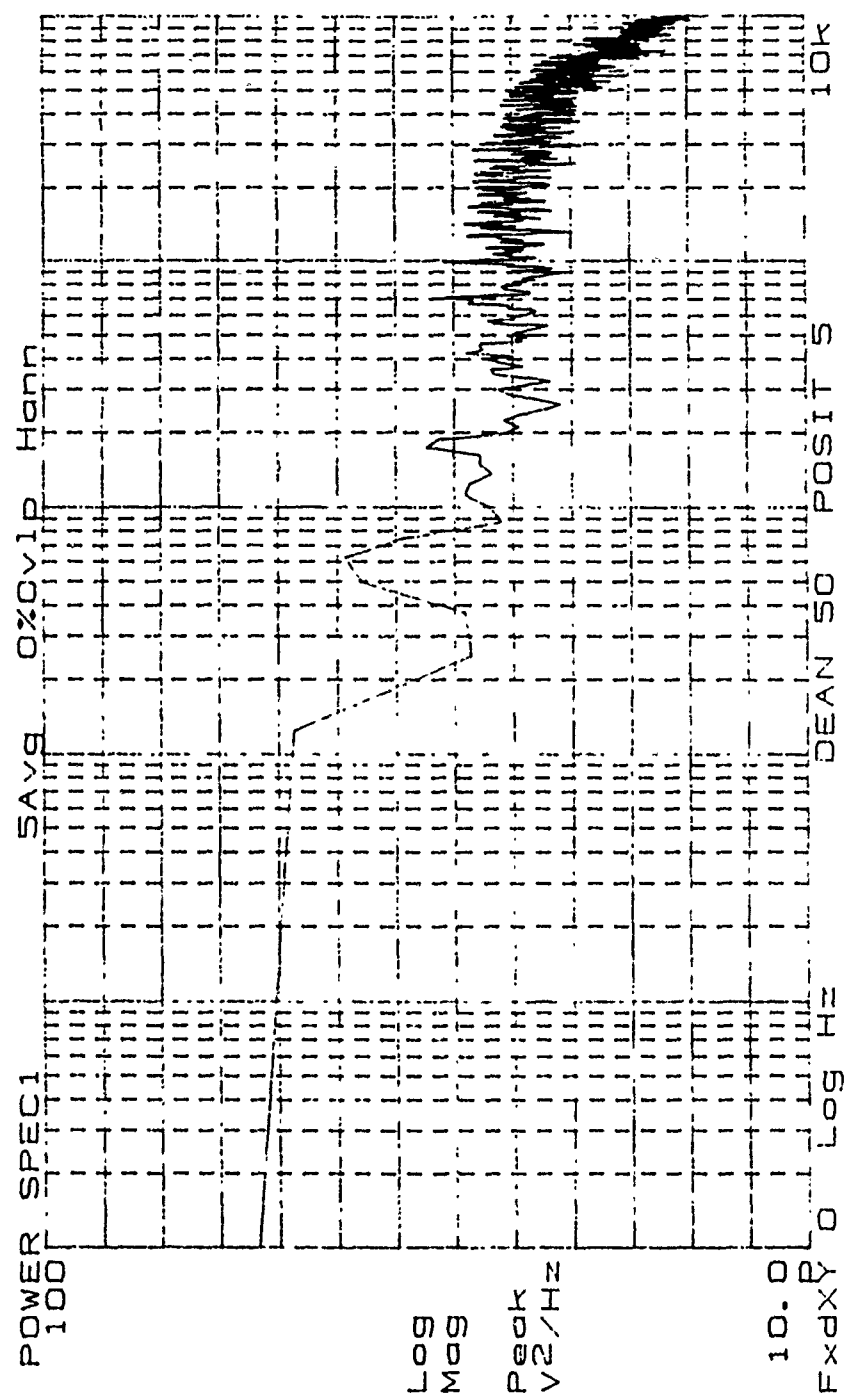


Figure 203. High Frequency Power Spectrum, De=50, Position 5

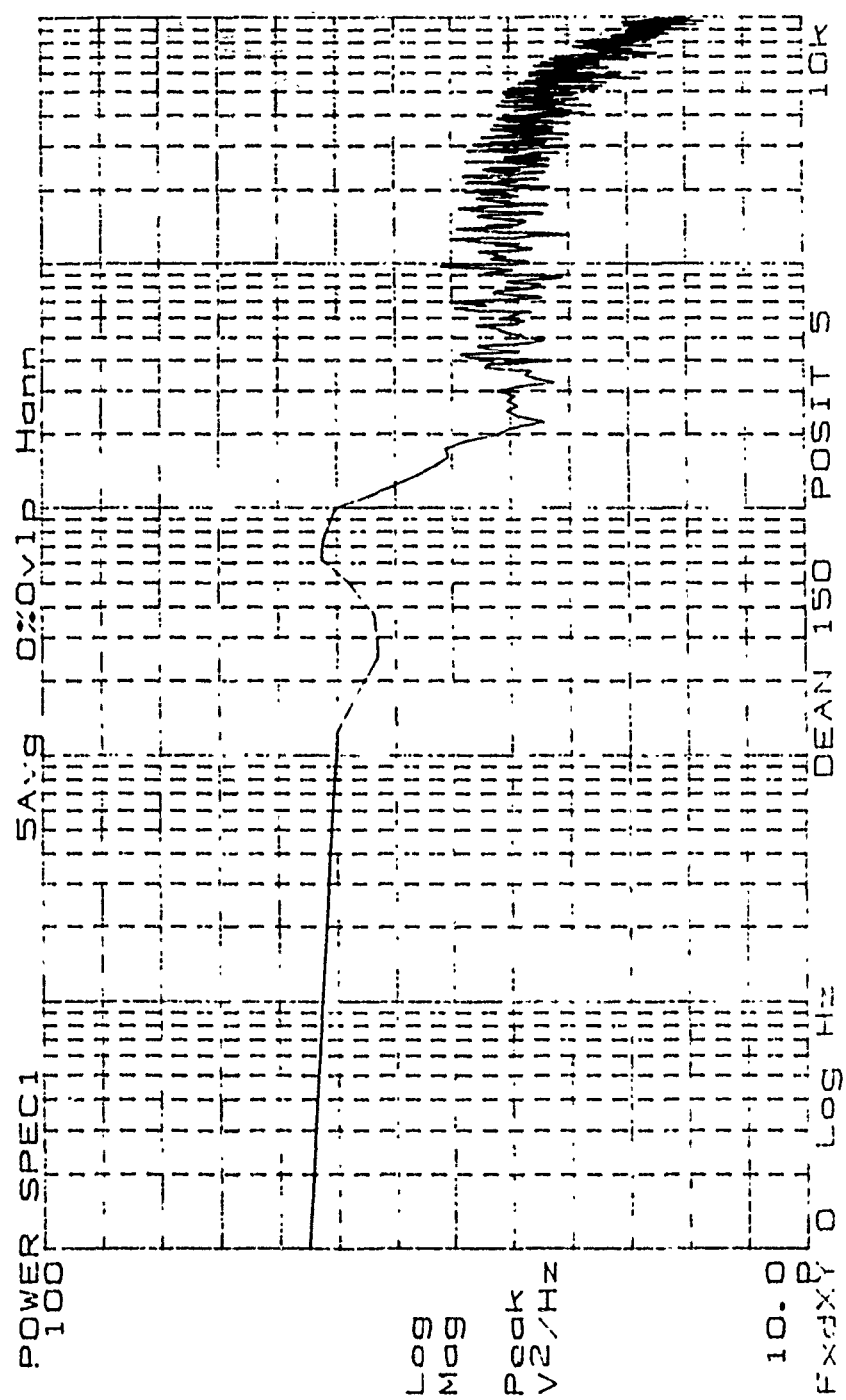


Figure 205. High Frequency Power Spectrum, De=150, Position 5

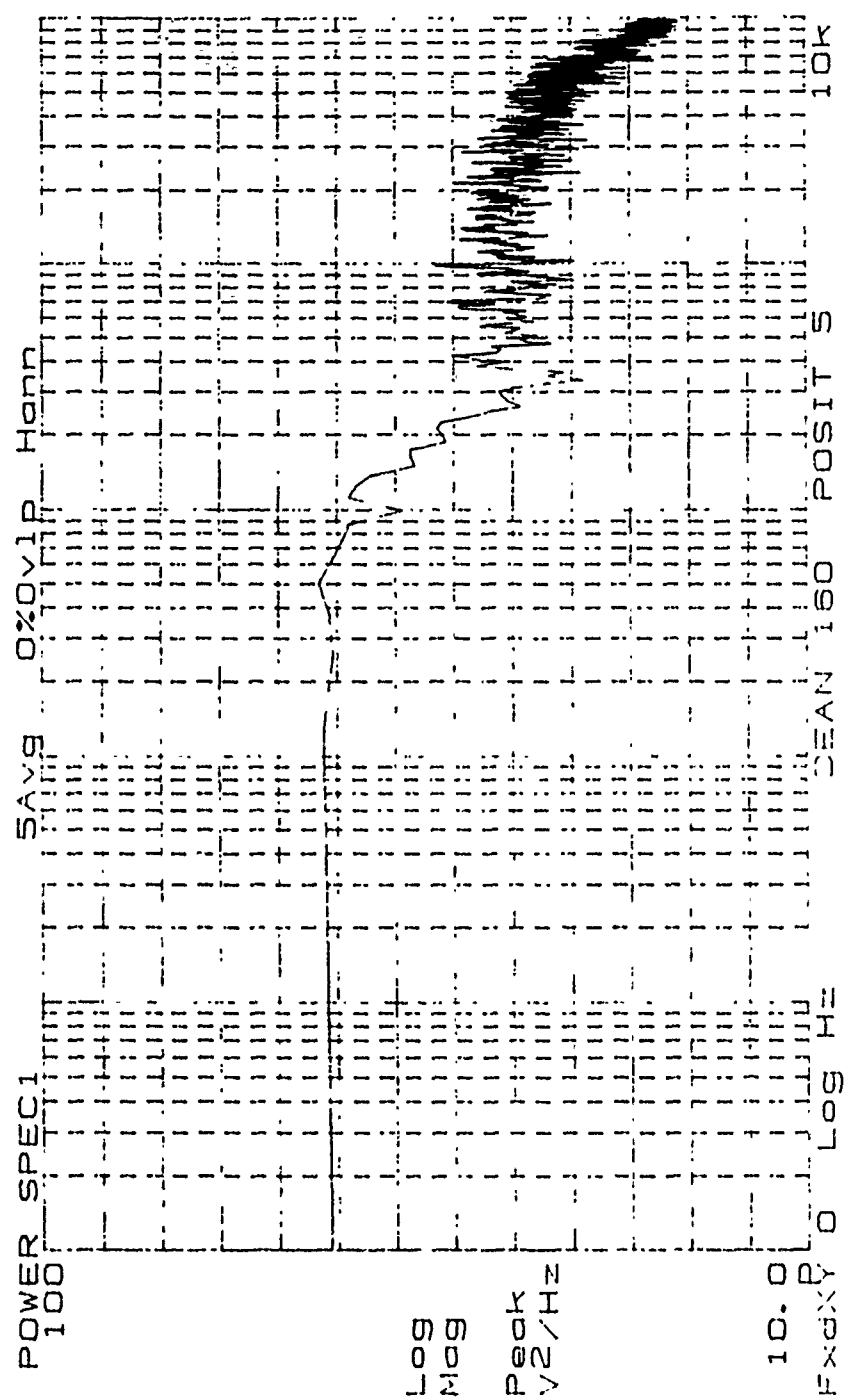


Figure 206. High Frequency Power Spectrum, $D_e=160$, Position 5



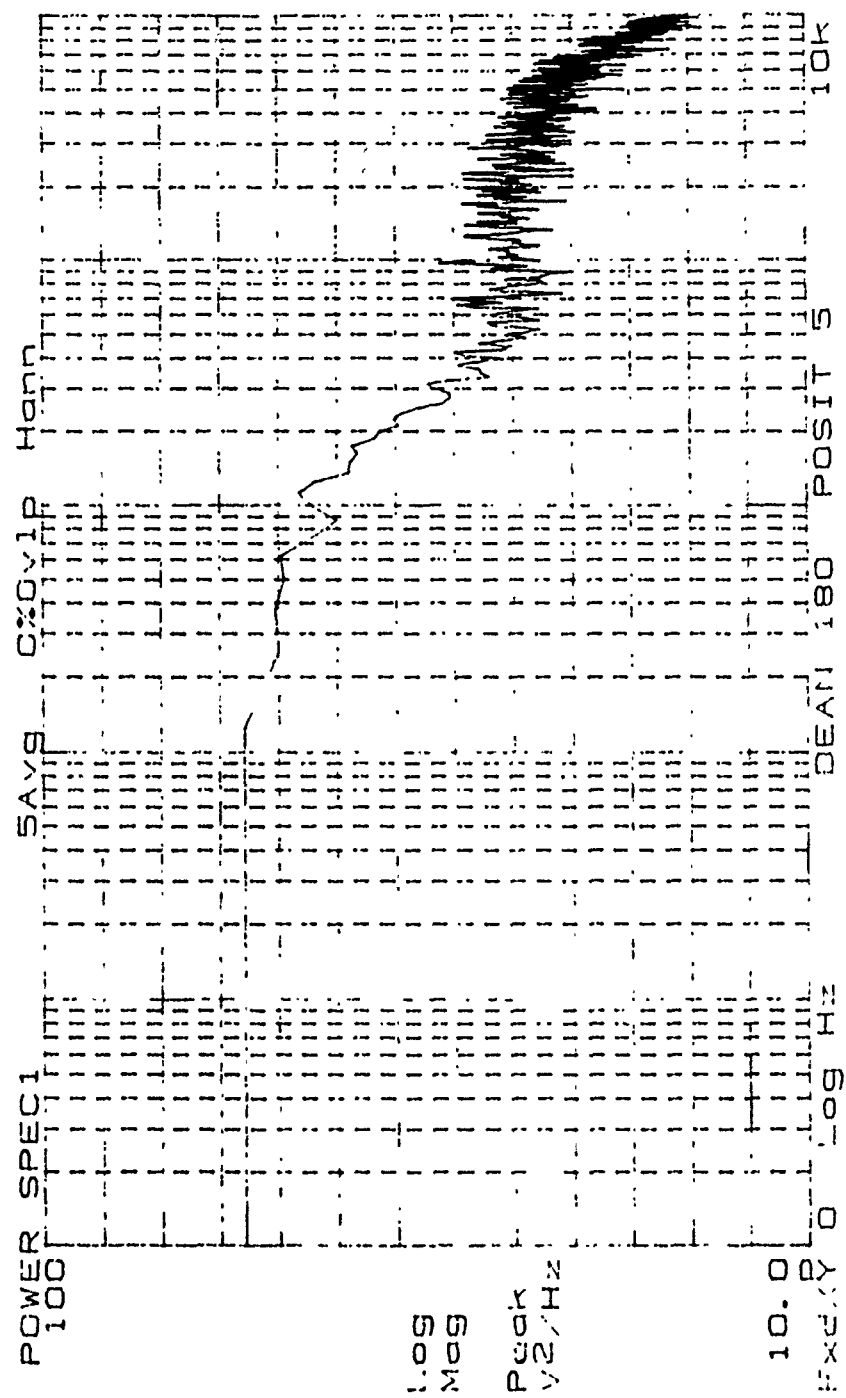


Figure 208. High Frequency Power Spectrum, De=180, Position 5

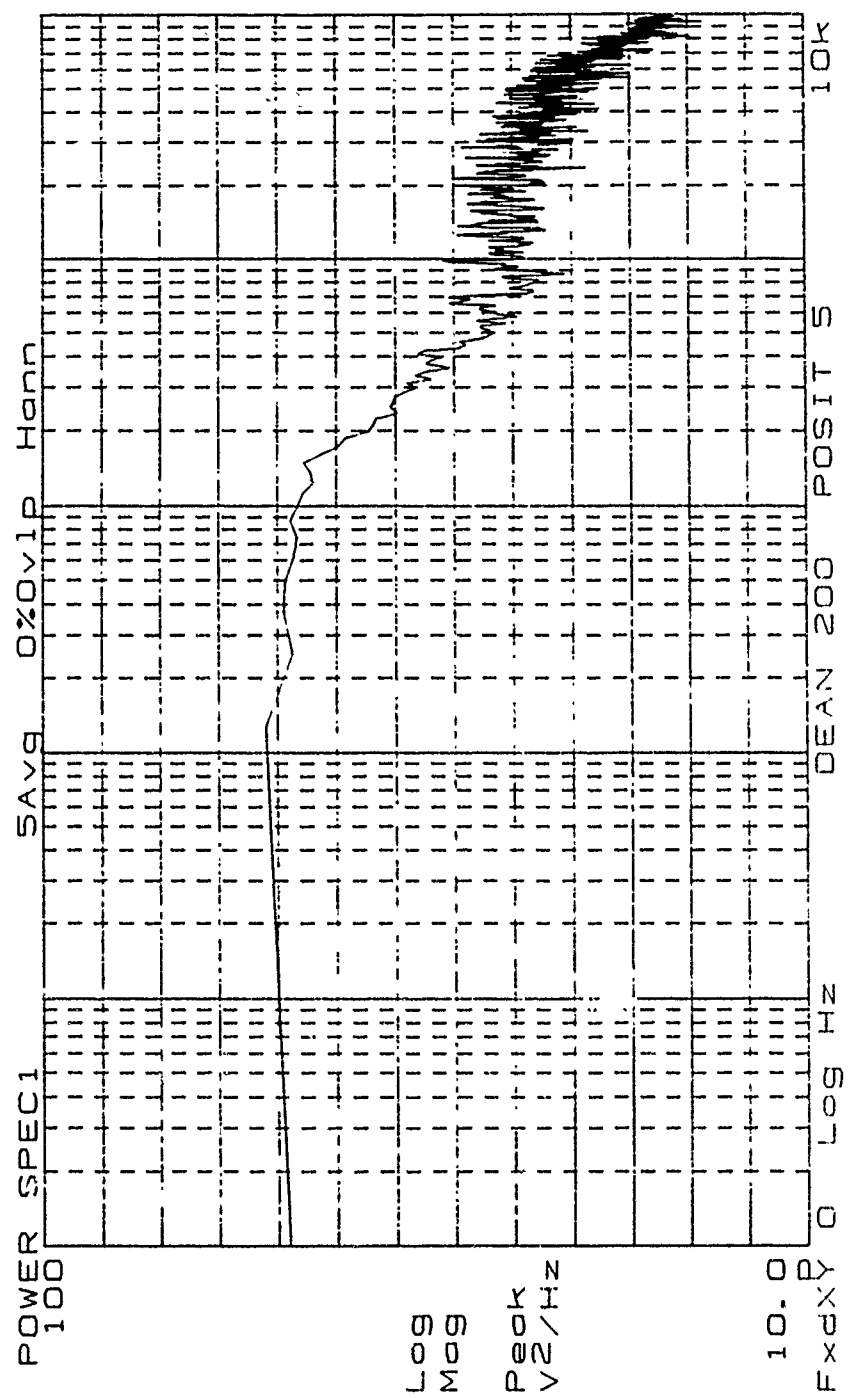


Figure 209. High Frequency Power Spectrum, De=200, Position 5

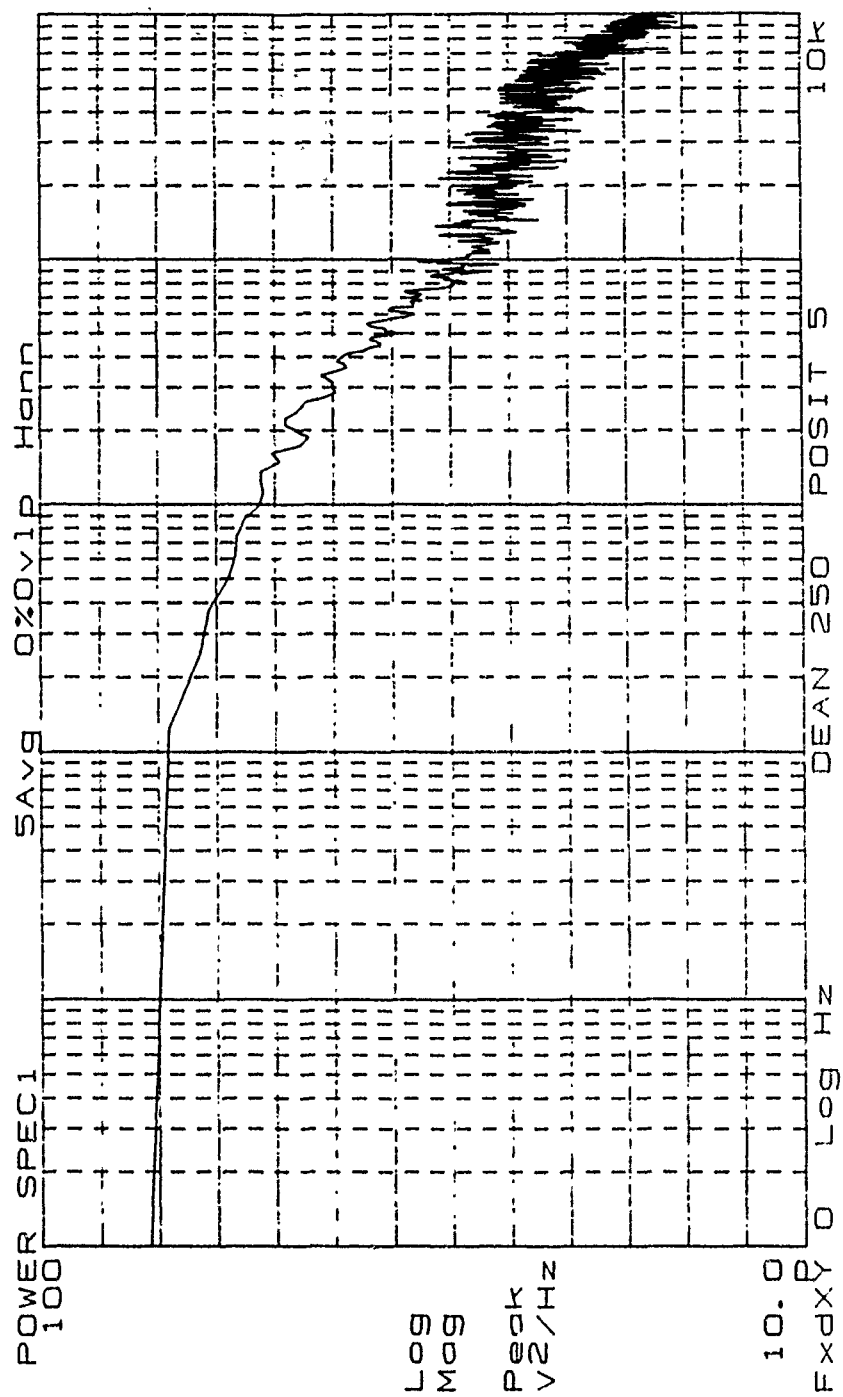


Figure 210. High Frequency Power Spectrum, De=250, Position 5

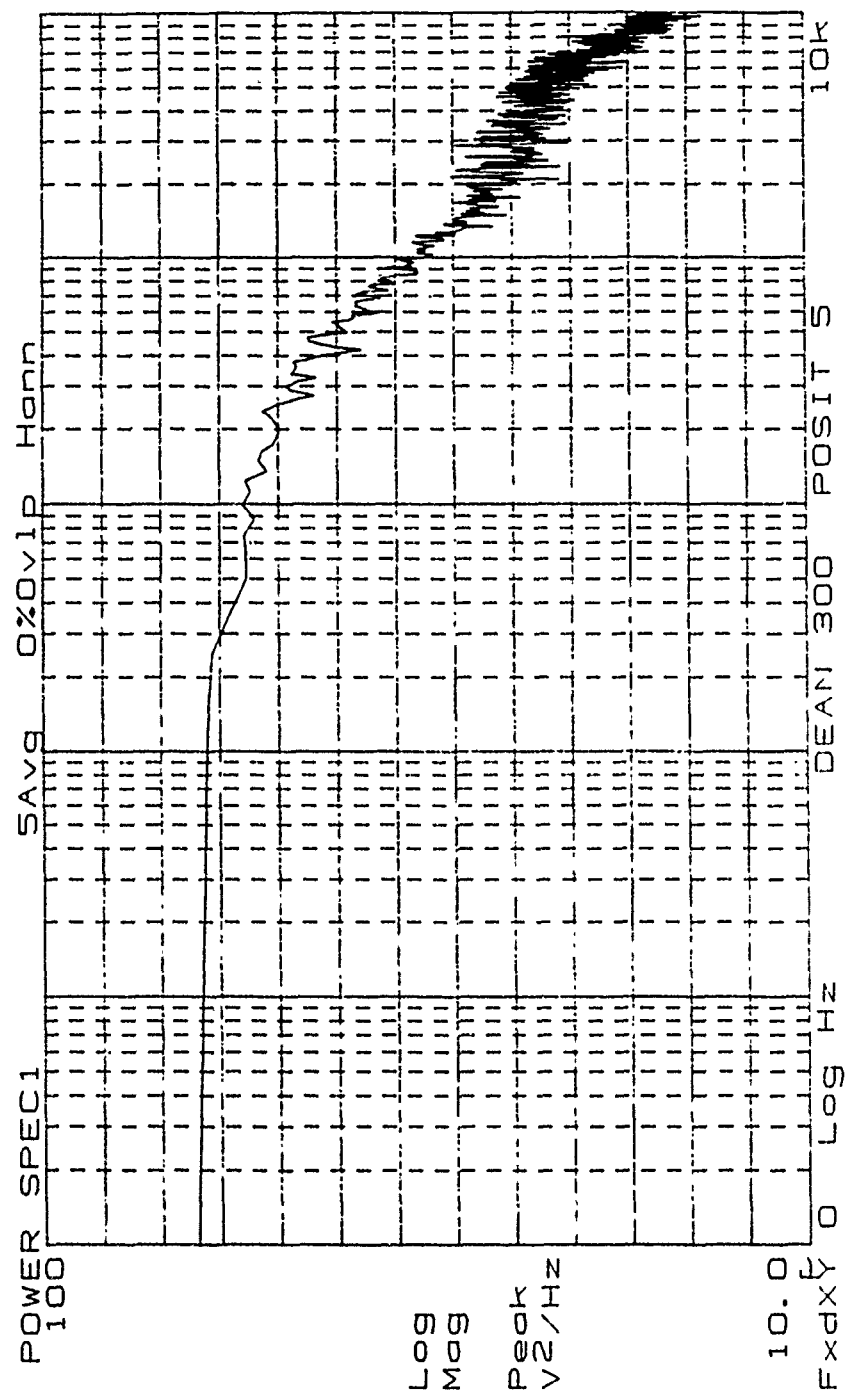


Figure 211. High Frequency Power Spectrum, De=300, Position 5

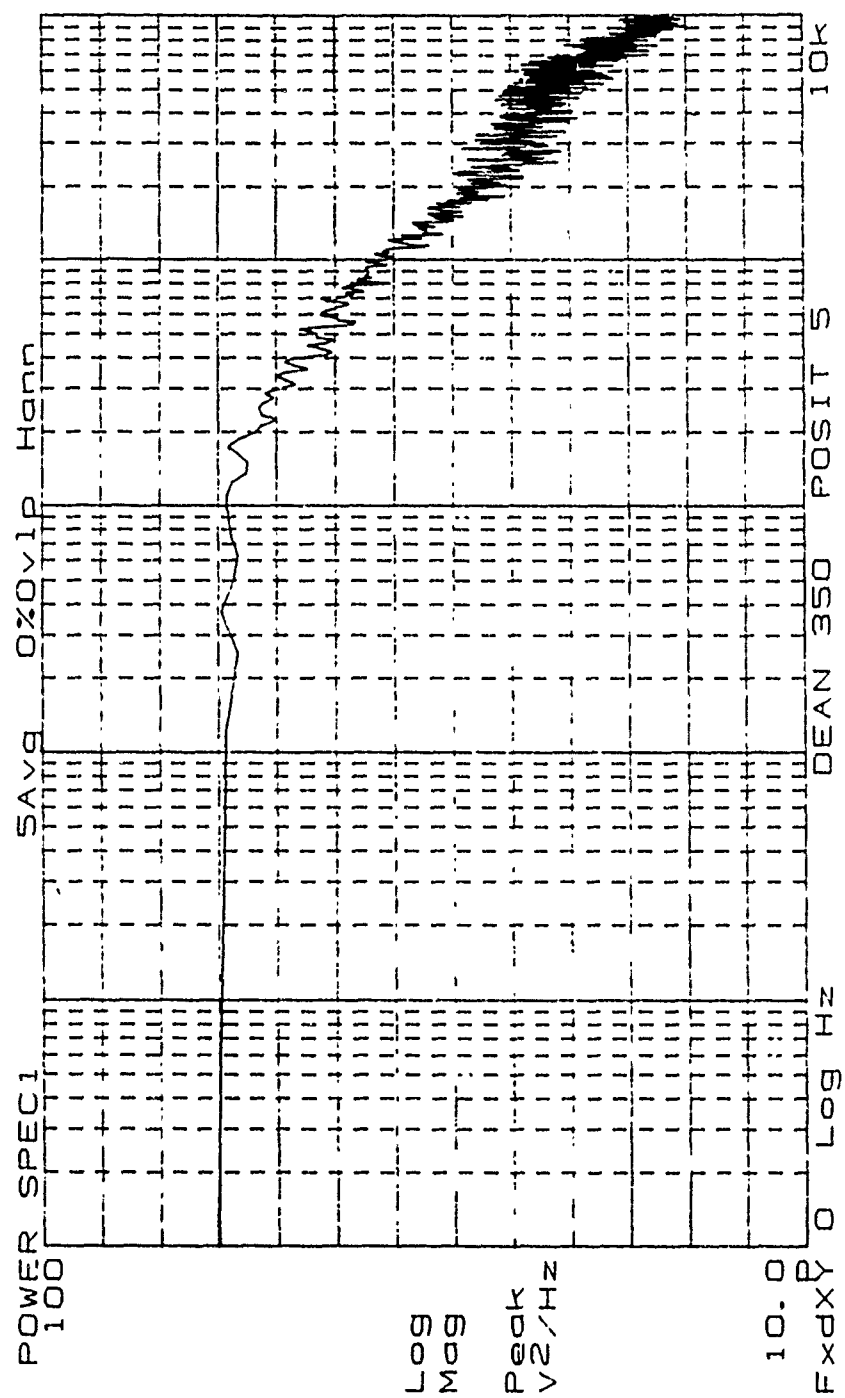


Figure 212. High Frequency Power Spectrum, De=350, Position 5

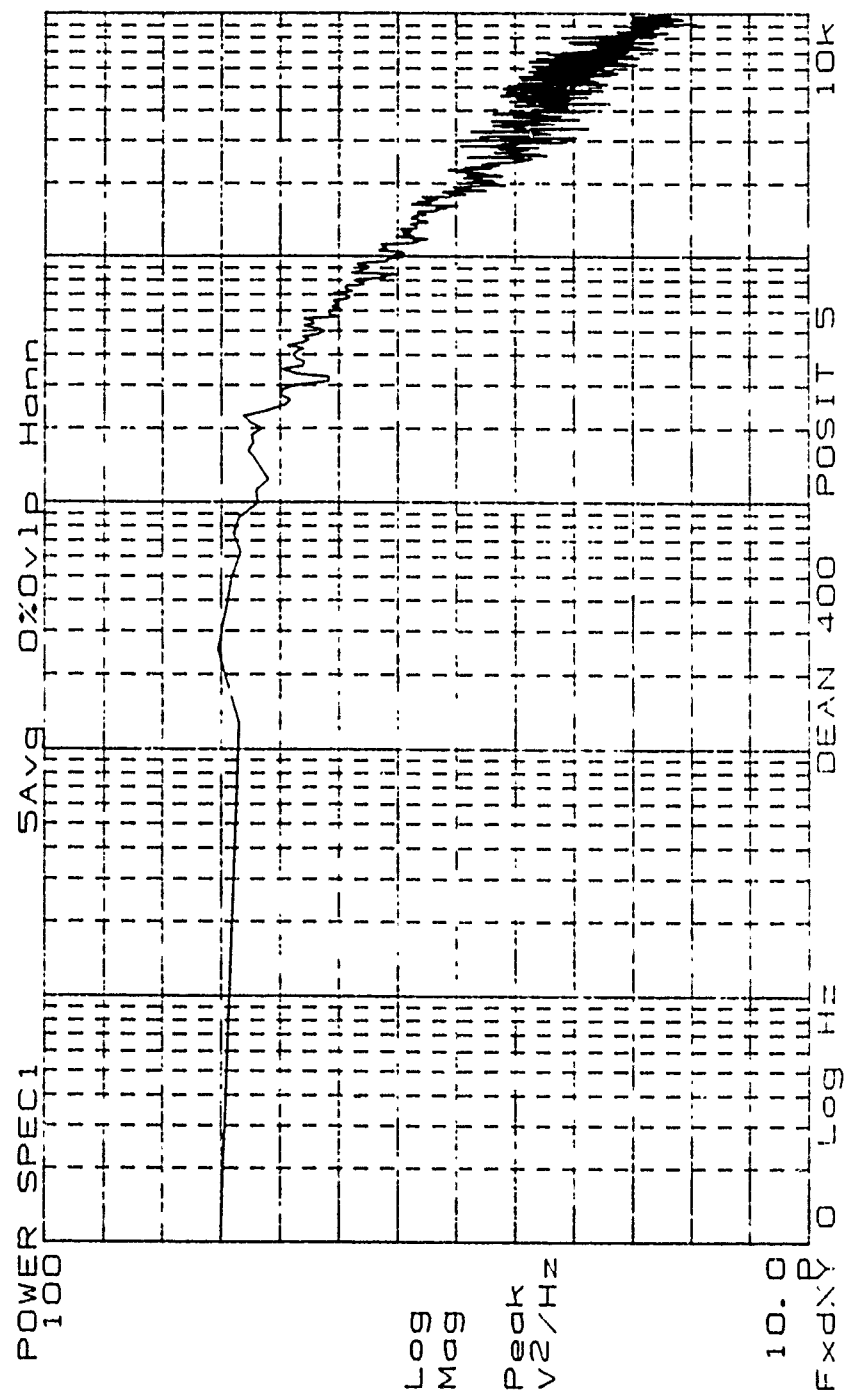


Figure 213. High Frequency Power Spectrum, De=400, Position 5

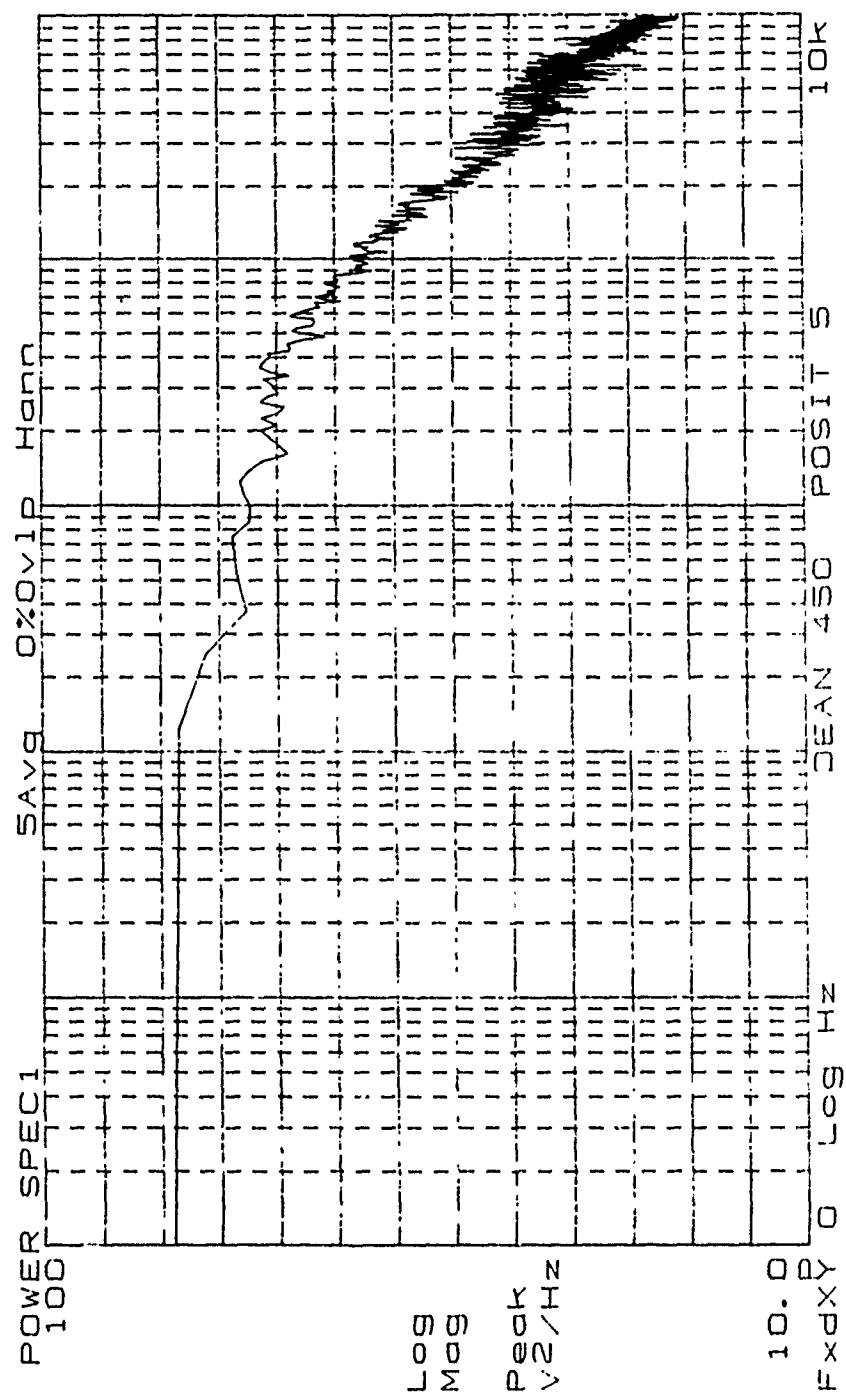


Figure 214. High Frequency Power Spectrum, De=450, Position 5

LIST OF REFERENCES

1. Finlay, W.H., Keller, J.B., and Ferziger, J.H., "Finite Amplitude Vortices in Curved Channel Flow," *Journal of Fluid Mechanics*, v. 194, pp. 417-456, September 1988.
2. Kelleher, M.D., Flentie, D.L., and McKee, R.J., "An Experimental Study of the Secondary Flow in a Curved Rectangular Channel," *ASME Journal of Fluids Engineering*, v. 102, pp. 92-96, 1980.
3. Ligrani, P.M., and Niver, R.D., "Flow Visualization of Dean Vortices in a Curved Channel with 40 to 1 Aspect Ratio," *Physics of Fluids A - Fluid Dynamics*, v. 31, pp. 3605-3617, December 1988.
4. Matsson, O.J.E., and Alfredsson, P.H., "Curvature- and Rotation-Induced Instabilities in Channel Flow," *Journal of Fluid Mechanics*, v. 210, pp. 537-563, 1990.
5. Finlay, W.H., and Nandakumar, K., "Onset of Two-Dimensional Cellular Flow in Finite Curved Channels of Large Aspect Ratio," *Physics of Fluids A - Fluid Dynamics*, v. 2, pp. 1163-1174, July 1990.
6. Ligrani, P.M., Longest, J.E., and Kendall, M.R., "Appearance, Disappearance and Spanwise Wavenumber Selection of Dean Vortex Pairs in a Curved Rectangular Channel," in preparation, 1991.
7. Ligrani, P.M., Singer, B.A., and Baun, L.R., "Miniature Five Hole Pressure Probe for Measurement of Three Mean Velocity Components in Low Speed Flows," *Journal of Physics E - Scientific Instruments*, v. 22, pp. 868-876, October 1989.
8. Hughes, R.E., *Development, Qualification and Measurements in Two Curved Channels with 40 to 1 Aspect Ratio*, Master's Thesis, Naval Postgraduate School, Monterey, California, September 1989.
9. Baun, L.R., *The Development and Structural Characteristics of Dean Vortices in a Curved Rectangular Channel*, Engineer's Thesis, Naval Postgraduate School, Monterey, California, September 1988.
10. Holman, J.P., and Gajda, W.J., Jr., *Experimental Methods for Engineers*, 4th ed., pp.238-247, McGraw-Hill, 1984.
11. Niver, R.D., *Structural Characteristics of Dean Vortices in a Curved Channel*, Master's Thesis, Naval Postgraduate School, Monterey, California, June 1987.
12. ASME Power Test Committee, *ASME Power Test Codes, (Supplement on Instruments and Apparatus)*, part 5, chapter 4, p. 25, American Society of Engineers, 1959.
13. Treaster, A.L., and Houtz, H.E., "Fabricating and Calibrating Five-hole probes," *Proceedings of the Fluid Measurements and Instrumentation Forum*, v. 34, ed. Bajura, R.A., and Billet, M.L., (ASME-Fluids Engineering Division, AIAA/ASME 4th Fluid Mechanics, Plasma Dynamics and Lasers Conference, Atlanta Georgia)

14. Ligrani, P.M., Singer, B.A., and Baun, L.R., "Spatial Resolution and Downwash Velocity Corrections for Multiple-Hole Pressure Probes in Complex Flows," *Experiments in Fluids*, v. 7, pp. 424-426, June 1989.
15. Fields, W.A., *Study of the Effects of Centrifugal Instabilities on Flow in a 40 to 1 Aspect Ratio Rectangular Curved Channel, for Dean Numbers from 35 to Fully Turbulent Conditions*, Engineer's Thesis, Naval Postgraduate School, Monterey, California, December 1990.
16. Longest, J.E., *Flow Visualization Studies in (1) A Curved Rectangular Channel with 40 to 1 Aspect Ratio and (2) A Straight Channel with Bulk Flow Unsteadiness*, Master's Thesis, Naval Postgraduate School, Monterey, California, June 1989.
17. Perry, A.E., *Hot-wire Anemometry*, Oxford University Press, 1982.
18. Finlay, W.H., Ligrani, P.M., and Bland, S.B., "Features of Wavy Vortices in a Curved Channel from Experimental and Numerical Studies," *Physics of Fluids A - Fluid Dynamics*, 1991.

INITIAL DISTRIBUTION LIST

1. Defense Technical Information Center 2
Cameron Station
Alexandria, Virginia 22304-6145
2. Library, Code 52 2
Naval Postgraduate School
Monterey, California 93943-5002
3. Dean of Science and Engineering, Code 06 1
Naval Postgraduate School
Monterey, California 93943-5000
4. Research and Administration Office, Code 012 1
Naval Postgraduate School
Monterey, California 93943-5000
5. Department Chairman, Code 69 1
Department of Mechanical Engineering
Naval Postgraduate School
Monterey, California 93943-5000
6. Naval Engineering Curricular Office, Code 34 1
Department of Mechanical Engineering
Naval Postgraduate School
Monterey, California 93943-5000
7. Professor P.M. Ligrani, Code 69Li 3
Department of Mechanical Engineering
Naval Postgraduate School
Monterey, California 93943-5000
8. Professor C.S. Subramanian, Code 69Su 1
Department of Mechanical Engineering
Naval Postgraduate School
Monterey, California 93943-5000
9. Dr. K.C. Civinskas 2
Propulsion Directorate
U.S. Army Aviation Research and Technology Activity
AVSCOM
NASA-Lewis Research Center
Cleveland, Ohio 45433
10. LT M.R. Kendall 1
1253 Leahy Road
Monterey, California 93940